Differential cross section and polarization extractions for $\gamma p \rightarrow K^+\Sigma^0$ and $\gamma p \rightarrow \phi p$ using CLAS at Jefferson Lab, and a partial wave analysis in search of missing baryon resonances

by

Biplab Dey

A dissertation submitted in partial fulfillment of the requirements
for the degree of

Doctor of Philosophy

in the Department of Physics

Carnegie Mellon University

June 28, 2011

Abstract

In the first part of this work, we present differential cross-section and polarization measurements for the reactions $\gamma p \to K^+\Sigma^0$ and $\gamma p \to \phi p$. The data were collected using the almost-hermetic CLAS detector stationed in Hall B at Jefferson Lab. An unpolarized energy tagged photon beam produced via bremsstrahlung and a liquid hydroden target was used for this, during the so-called $g11a$ experimental run-period. The kinematic coverage of our results is from near production threshold to $\sqrt{s} = 2.84$ GeV in energy and $-0.95 \leq \cos\theta_{\rm c.m.} \leq +0.95$ in the meson production angle $\theta_{\rm c.m.}$. For the most part our results are finely binned in 10-MeV-wide $\sqrt{s}$ bins. For the ϕp channel, we analyze both the charged ($\phi \to K^+K^-$) and the neutral ($\phi \to K^0_S K^0_L$) decay modes. For $K^+\Sigma^0$, our work corresponds to a 300 MeV increase in energy coverage for the differential cross-sections and forms the first extensive recoil polarization world dataset. For ϕp, where previous world data is either non-existent or exist with wide energy bins and very limited statistics, our results will be the first extensive world dataset for both the cross-sections and the spin density matrix elements $\rho^0_{MM'}$. Our $K^+\Sigma^0$ results are now published as PRC 82, 025202 (2010) and the ϕp results are also nearing completion of internal Collaboration analysis review. In addition, we have also been able to extend upon a previous $K^+\Lambda$ analysis in the backward angles and near threshold kinematic regimes, using a higher statistics dataset.

The second segment consists of setting up a general framework for performing a coupled-channel partial wave analysis (PWA) on these extracted data results. Our goal is to search for the so-called "missing" baryon resonances, that is, states predicted by quark models, but absent in conventional πN analyses. We construct the amplitudes and polarization observables required for this PWA. For polarizations in the pseudoscalar sector, sign discrepancies due to different conventions adopted by different authors in the field are treated in a systematic manner and this study has been published as PRC 83, 055208 (2011). During our preliminary PWA, we found that certain normalization discrepancies exist between CLAS and older higher energy data from SLAC/DESY/CEA. A systematic global study of these normalization issues and their effect on the coupling constants in hadrodynamic model is presented. Our PWA remains incomplete, but the rich set of data results and analysis tools obtained here will provide impetus for future work.

Contents

Chapter 1

Introduction

The goal of this work is to understand the nature of the strong interaction, the fundamental force holding together sub-nuclear objects like the proton. This chapter gives an introduction to the problem and an overview of our approach towards investigating it using Hadron Spectroscopy experiments and Partial Wave Analysis theoretical tools.

1.1 The strong force or QCD

We tried to put a little color into QED and we got into a considerable mess.
- Predrag Cvitanović, Field Theory

Fig. 1.1 shows the Standard Model of particle physics with all the known fundamental matter particles and interaction forces. Quantum Chromodynamics (QCD) is part of this Standard Model and is the theory of the strong interaction. As the word "strong" suggests, it is like the big brother of Quantum Electrodynamics, or QED, the quantum field theory of the electromagnetic (EM) force. QCD is responsible for gluing together point-like objects called quarks to form composite nuclear particles such as the proton and the neutron. However, unlike the ordinary EM interaction which has a single type of charge (the ordinary electric charge), QCD has three types of charges, fancifully termed as "color". The color charges are called red (r), blue (b) and green (g), and all physical particles occurring in nature must be color singlets, i.e., one can only have color neutral combinations like $\mathrm{r\bar{r}}$ or rbg existing in nature. Since quarks carry one unit of color charge, this implies that a single quark can never be isolated, but must always be confined inside a multi-quark system. This so-called "confinement" is just one of the many mysterious properties of QCD.

Strongly interacting particles are called hadrons. "Normal" hadrons are made up of quarks and are of two types, $|q_{\mathrm{c}}\bar{q}_{\bar{\mathrm{c}}}\rangle$ pairs called mesons (the pi-meson or pion) or color singlet $|q_{\mathrm{r}}q_{\mathrm{g}}q_{\mathrm{b}}\rangle$ objects called baryons (like the proton). Here, q_{c} is a quark of color charge "c" and $\bar{q}$ is an anti-quark with anti-color charge "$\bar{\mathrm{c}}$". In addition to quarks, the theory also includes "force carriers" that transmit the interaction force. Just like the photon is the carrier of the EM force, the force-carrying "glue" particles in QCD are called gluons and there are eight of them. Another important property of QCD is that unlike the photon which is charge-neutral, the QCD gluons carry color charges themselves. Therefore, one can have "exotic" hadrons made up of pure glue called glueballs, or even quark-glue hybrid states. In principle, tetraquark and pentaquark states are also not ruled out, as long as they are color singlets. The fact that nature has chosen these exotic particles to be elusive is yet another puzzle. In this work, we will be concerned with the usual ground state mesons and baryons.

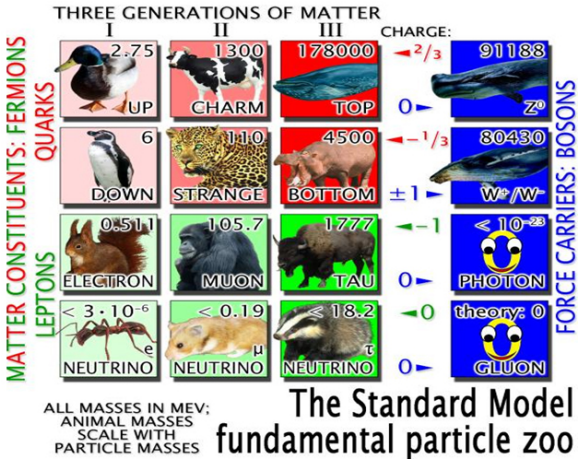

Figure 1.1: The Standard Model particle "zoo" with all the known fundamental point-like matter particles and interaction forces.

Having described the bare essentials of QCD, we now turn to why Dr. Cvitanović finds the transition from QED to QCD so messy. The general structure of any quantum field theory derive from internal gauge symmetries [1]. A *representation* of such a gauge symmetry is a set of objects (quarks carrying color charge, for example) that transform among themselves according to the symmetry transformation laws, akin to a rotation in real space. Furthermore, to make these gauge transformations local (i.e., the transformations are functions of space-time as well) one needs an additional set of fields called gauge fields (the gluons). The most general gauge invariant Lagrangian density that one can write down is

$$\mathcal{L} = -\bar{\psi}(\gamma^\mu \mathcal{D}_\mu + m)\psi - \frac{1}{4} F^\alpha_{\mu\nu} F^{\mu\nu}_\alpha, \tag{1.1}$$

where γ^μ are the Dirac matrices, ψ are the matter fields with mass m and $\mathcal{D}$ is the gauge-covariant derivative

$$\mathcal{D}_\mu \psi = (\partial_\mu - igA^\alpha_\mu t_\alpha)\psi. \tag{1.2}$$

The gauge fields A^α_μ are massless spin-1 particles carrying the gauge charge indexed by α. They transform in the so-called adjoint representation of the symmetry group. For the gauge group SU(N), $\alpha = \{1, \ldots, (\mathrm{N}^2 - 1)\}$; for QCD, $\mathrm{N} = 3$ and there are 8 gauge fields. The t_α's are generators of the gauge transformation for a given representation of the matter fields, and g is a generalized charge representing the strength of the interaction. Overall, the gauge fields are constructed in such a fashion that the derivative $\mathcal{D}_\mu \psi$ remains locally gauge invariant. The last term in Eq. 1.1 involves the covariant field tensor defined as the commutator of the covaraint derivative

$$F^\alpha_{\mu\nu} = [D_\mu, D_\nu]^\alpha = \partial_\mu A^\alpha_\nu - \partial_\nu A^\alpha_\mu - g f^{\alpha\beta\gamma} A^\beta_\mu A^\gamma_\nu, \tag{1.3}$$

where $f^{\alpha\beta\gamma}$ are the structure constants of the Lie algebra in the commutators $[t^\beta, t^\gamma] = i f^{\alpha\beta\gamma} t^\alpha$. For QED, the symmetry group is U(1), which is a local phase transformation, and the $f^{\alpha\beta\gamma}$'s are all zero. For QCD, the fact that SU(3) is a non-Abelian group means that the structure constants are non-zero and it is this little difference that results in drastically different properties of QCD vis-à-vis QED.

The first new property of QCD is the presence of pure gauge field interaction vertices due to the last term in Eq. 1.3. Both 3- and 4-gluon vertices are possible now, which would be absent if the f's

were zero. Another important property is asympotic freedom, discovered simultaneously in 1973 by Gross, Wilczek and Politzer [2, 3] for which they received a Nobel prize. The strong coupling constant $\alpha_s \approx g^2$ is dependent on the energy scale. Asptotic freedom means that high enough energies (small distances), α_s approaches zero asymptotically and perturbative calculations are possible. At lower energies (larger distances), $\alpha_s \sim \mathcal{O}(1)$ and calculations become non-perturbative. This non-perturbative nature of low-energy QCD coupled with interacting gluons and eight different color charges results in a highly complex and non-linear interacting theory. As of this writing, no analytical solution exists for QCD and the theory remains essentially untested at low energies. Given that QCD is an essential part of the Standard Model of particle physics and is well tested in the high energy regime at particle colliders like LHC, Fermilab, SLAC, DESY, *et al.*, this is a highly undesirable situation. Inkeeping with this goal, Jefferson Lab was built to specifically study medium- and low-energy QCD.

1.2 QCD and Baryon Spectroscopy

In ordinary optics, one of the ways to understand the properties of a system is to photo-excite it and observe the emitted spectrum. For example, one can identify different chemical elements from their the emission spectrum and this process is called spectroscopy. Similarly, a strongly interacting hadronic system can be photo-excited and as these excited states (called "resonances") decay back to the ground states, they follow many different paths (or "channels"), emitting a wide variety of particles. By measuring the angular distributions of the emitted particles it is possible to decipher the properties of these excited states. Given that an exact solution of QCD is not available, we can construct QCD-"inspired" effective theory models and cross-check the predictions from these models with experiment. Of course hadrons include mesons, glueballs, hybrids, *et al.*, in addition to baryons. To be more specific, in this work we will be chiefly concerned with the excited baryon spectrum. Furthermore, the excited baryons we are interested in will be made up of only the light quarks (u and d) that make constitute the proton (uud) and the nucleon (udd). That is, we are looking at excited N^* and Δ^* resonances.

1.2.1 Pre-QCD strong interaction models

Even before the realization of QCD as the fundamental theory of strong interactions, the hadronic spectrum was a rich playground for strong physics. In the 1960's, as multitudes of strongly interacting particles were being discovered in particle accelerators, it was slowly realized that several patterns were emerging in the spectrum. The strong interaction seemed to preserve various "quantum numbers" and one could predict selection rules for the allowed decays, in complete analogy with atomic spectroscopy, again. It was ultimately realized that all hadrons were composite particles made up of quarks (Feynman called them partons). For our purposes, quarks come in three "flavors": up (u), down (d) and strange (s) that form a representation of flavor SU(3). In addition, each quark also has an $S = \pm\frac{1}{2}$ spin quantum number, giving rise to the an approximate SU(6) spin-flavor symmetry for the strong interaction. Of course, with the advent of QCD, it was realized that each quark carries a color SU(3) charge as well. Furthermore, within the flavor SU(3) group, the u and d quarks form a smaller isospin SU(2) subgroup. Isospin symmetry connects the proton and the neutron.

Around the same time as the evolution of the quark model, it was noticed that the spin (J) and mass (M) of hadrons seemed to follow a simple linear relationship

$$J \approx J_0 + \alpha' M^2, \tag{1.4}$$

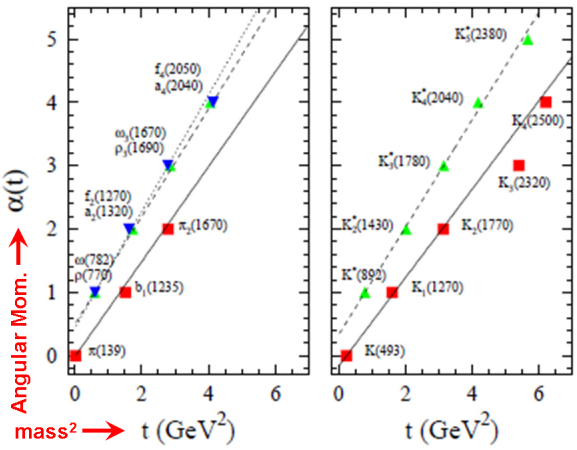

Figure 1.2: The spins of several mesons when plotted against their mass^2 approximately lie on linear trajectories called Regge trajectories

called a Regge trajectory [5]. Fig. 1.2 shows some of these plots (called Chew-Frautschi plots). Such an approximate linear relationship between the angular momentum and M^2 is known to arise in String Theory with $1/2\pi\alpha'$ as the string tension. The early Regge work strove to understand strong interactions from the analyticity of the scattering matrix (or S-matrix) and crossing properties between the variables s, t and u (see Ref. [4] for example). The situation is shown in Fig. 1.3 for a simple $2 \to 2$ scattering with equal masses for all particles. The Mandelstam variables are defined as

$$s = (p_A + p_B)^2 \tag{1.5a}$$
$$t = (p_A - p_C)^2 \tag{1.5b}$$
$$u = (p_A - p_D)^2. \tag{1.5c}$$

Since $s + t + u = m_A^2 + m_B^2 + m_C^2 + m_D^2$, the most general amplitude would be of the form $\mathcal{A}(s,t)$ with s, t and u treated on an equal footing (crossing-symmetry) and poles (singularities) at the physical masses of the exchanged particles. The exchange of an s-channel resonance is equivalent to the exchange of several particles in the t-channel and the Regge trajectory effectively sums up the combined exchange of all particles lying on a given trajectory. At low energies close to threshold, however, a few s-channel resonances should dominate, but at higher energies the non-resonant t- and u-channel processes should take over. Furthermore, the principle of duality, proposed by Bloom and Gilman [6], links the resonant and the non-resonant contributions as

$$\sum s\text{-channel} = \sum t\text{-channel}, \tag{1.6}$$

that is, the average of *all* the s-channel contributions should equal the average of *all* the t-channel processes. The Bloom-Gilman conjecture leads to the problem of double-counting; that is, one has to be careful while including *both* s- and t-channels in the production amplitude.

Although QCD has certainly taken over S-matrix theory and Regge theory as the fundamental theory of strong interactions, a full explanation of why nature exhibits Regge trajectories still eludes us. A specifically important case is the so-called Pomeron ($I\!P$) trajectory. The Pomeron is a universal object appearing in all high-energy processes, especially in the diffractive regime $t \to 0$ (very forward angle scattering). This universality of the Pomeron indicates that it has the quantum numbers of the vacuum. Another property is $\alpha_{I\!P}(t = 0) \approx 1$, which saturates the so called Froissart

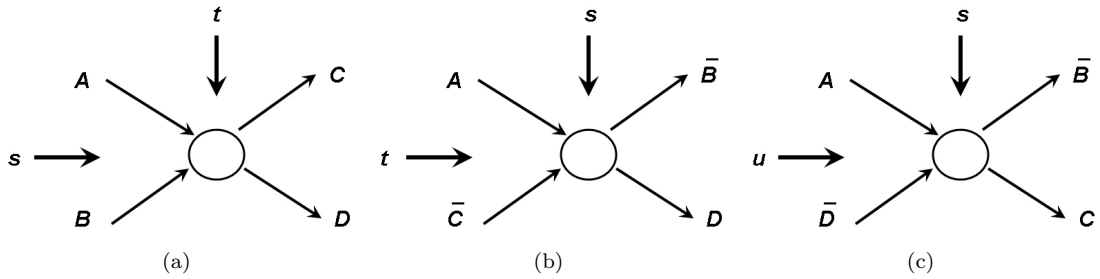

Figure 1.3: Crossing relations for an $AB \to CD$ scattering process: (a) s-channel, (b) t-channel and (c) u-channel.

bound $\alpha(t = 0) \leq 0$ that comes from very general unitarity principles (see Refs. [7, 8]). Aside from these features, there are very little is known about its fundamental properties, and a first-principle QCD derivation is yet to come. For example, we do not know exactly how the Pomeron couples to hadrons. Since the Pomeron is supposed to be a glue-rich non-perterbative object and is known to dominate the ϕ photoproduction process, studying the Pomeron is one of the chief motivations of the present ϕ analysis.

1.2.2 CQM, the Missing Baryon Resonance Problem and efforts at CMU

Given that an analytic solution of low-energy QCD is too hard, it is prudent to start by simplifying the problem down to its bare essentials. One idea propounded by Dalitz [9] was to consider baryons as excitations of a basic three-quark system. Only the valence quarks are included here and this is called the Constituent Quark Model (CQM). With just the u, d and s quarks, this gives a basic SU(6) spin-flavor symmetry group to work with. In the harmonic potential model [10], the quarks interact via a radial harmonic oscillator potential force (O(3) rotational symmetry), and the baryon spectrum emerges as the supermultiplets of the full SU(6)×O(3) symmetry group. A glaring problem arising from this model is that the number of states predicated is much higher than the number of excited states observed in πN phase-shift analyses. This over-abundance of predicted states is called *missing baryon resonance problem*.

Extensive work by Isgur (1980) and co-workers [11] later added aspects of QCD to the basic CQM model and calculated the excited baryon spectrum as well as their decay couplings into various channels. Capstick (1992) and co-workers [12, 13] further extended the Isgur calculations by adding relativistic corrections. A prominent feature of these extracted couplings was that the experimentally known states had strong couplings to the πN channels, which is where the bulk of the data lie. This leads to the question: have we not seen the "missing" states because they couple to the non-πN sector, where there is very little data? Two papers by Captick and Roberts, on the non-strange [14] and the strange [15] indeed showed that some of the previously unseen resonances had strong couplings to non-πN sector. These Capstick-Roberts predictions have instigated an extensive worldwide program at several experimental nuclear facilities to hunt for the missing states. Using data from the CLAS detector at Jefferson Lab, the Carnegie Mellon PWA group has already published high-statistics results for the ωp [16, 17], $\eta p/\eta' p$ [18] and $K^+\Lambda$ [19] channels. The latest results for the $K^+\Sigma^0$ channel, which will be presented in this work are also published now [20] and the ϕp results are currently undergoing internal Collaboration review. The final goal is to perform a full coupled-channel PWA on these and other available world data.

Figure 1.4: In the diquark model of Lichtenberg *et al.* [21], two out of the three quarks in a baryon are tightly bound together. The reduced degrees of freedom leads to fewer number of predicted resonance states.

1.2.3 Diquark Model and Lattice QCD predictions

The diquark model, first proposed by Lichtenberg *et al.* [21], tries to solve the missing baryon problem by clustering together two of the quarks inside a baryon as shown in Fig. 1.4. This reduces the number of degrees of freedom, and thereby, the number of predicted resonance states. The diquark model mass spectrum has been claimed to be in better agreement with the observed mass spectrum [22]; however there is little direct experimental evidence of the clustering process itself.

In the Lattice QCD (LQCD) framework, one tries to solve the full non-perturbative QCD numerically on a discretized space-time "lattice". The usual Minkowskian metric is converted to a 4-dimensional Euclidian metric by a technique known an Wick rotation that allows the analytic continuation of the time variable t to imaginary it. Quarks sit on the lattice sites and local gauge symmetry is maintained by assigning a transformation (the gluons) at each lattice site that is an element of SU(3). Finally, the lattice spacing provides a natural regularization scale and the proof that QCD can be properly renormalized in this fashion was shown by Kenneth Wilson (this work led to a Nobel Prize). Although these numerical calculations are very computationally expensive, with novel algorithms and computing technology, LQCD has seen tremendous progress in recent years. In Ref. [23], the full baryon spectrum upto $J^P = \frac{7}{2}^{\pm}$ has been calculated on the lattice, for the first time. Interestingly, these latest lattice results lend support to the CQM models, over diquark and other models. This will provide a further impetus to search for the missing states.

1.3 Introduction to the $K^+\Sigma^0$ and ϕp channels

Table 1.1 lists some basic properties of the particles of interest in this work. The kaons, the ϕ and the two hyperons ($Y = \{\Lambda, \Sigma^0\}$) are all hadrons with strangeness content, due to the presence of the strange quark. Therefore, in a sense, this thesis really is about ground-state strangeness physics. In the hyperon sector, Λ is an iso-singlet ($I = 0$), while Σ^0 is part of an iso-triplet ($I = 1$). Therefore, the $K^+\Lambda$ channel acts as an isospin filter (only $I = \frac{1}{2}$ N^* resonances are accessible), while both N^* and Δ^* ($I = \frac{3}{2}$) can couple to the $K^+\Sigma^0$ channel. The ϕ is intereresting because it is a vector meson and in the quark model, it is an almost pure $s\bar{s}$ state. Assuming the nucleons to be made up of mostly the light quark sector, OZI rule (see Ref. [24], for example) suppresses quark (meson) exchanges and the ϕp is expected to be a "clean" channel for the production of glue-rich objects [25].

1.3.1 Previous $K^+\Sigma^0$ measurements

In previous hyperon photoproduction measurements, it was more or less customary to treat both $K^+\Lambda$ and $K^+\Sigma^0$ channels together. One usually detected a K^+ (the kaon identification part) and the missing mass spectrum off the kaon showed two clear peaks at 1.115 and 1.192 GeV, which was the Λ and the Σ^0, respectively. Furthermore, the K^+Y channels were usually treated as a by-product, so to say, of πN analyses that had much larger statistics. In some sense, the present $g11a$ analyses

Hadron	$I(J^P)$	Mass	Charge	Valence quarks	Decays (b.f.)
$\pi^{\pm}$	$1(0^-)$	139.57	±1	ud, $d\bar{u}$	
$K^{\pm}$	$\frac{1}{2}(0^-)$	493.67	±1	$u\bar{s}$, $\bar{u}s$	
K^0	$\frac{1}{2}(0^-)$	497.64	0	$d\bar{s}$	
ϕ	$0(1^-)$	1019.46	0	$s\bar{s}$	K^+K^- (49.2%), $K^0_SK^0_L$ (34%)
p	$\frac{1}{2}(\frac{1}{2}^+)$	938.27	+1	uud	
Λ	$0(\frac{1}{2}^+)$	1115.68	0	uds	$p\pi^-$ (63.9%)
Σ^0	$1(\frac{1}{2}^+)$	1192.64	0	uds	$\gamma\Lambda$ (100%)

Table 1.1: Characteristics listed in the PDG [53], of particles we will commonly encounter in this thesis. Here, I, J, and P denote isospin, spin, and parity quantum numbers; the mass unit is MeV and the charge is in units of the electron charge. The last column gives the decay-mode(s) and branching fraction (b.f.) relevant to this work.

are an exception in these aspects. The unique event trigger for this experiment (see Sec. 2.5) does not allow for πN analyses. Also, the high statistical precision and control over systematics in $g11a$ made it worthwhile to treat the two hyperon analyses independently. As a result, the $K^+\Lambda$ channel has been investigated separately in the thesis work of Mike McCracken [26]. Here we concentrate on the $K^+\Sigma^0$ channel.

1.3.1.1 Pre-CLAS/SAPHIR era

In the 1960's, several groups at SLAC [200, 203], Cambridge [201, 202] and elsewhere used low-intensity untagged photon beams and limited-acceptance magnetic spectrometers to conduct photoproduction experiments. "Untagged" signifies that the energy of the photon (usually produced from an electron beam) was not known event-by-event. The energy binning of these early measurments were coarse and only a handful of data points were produced. Aside some normalization issues, discussed in Ch. 11, these results will not be discussed further in this work.

1.3.1.2 Modern Large-Acceptance Experiments: CLAS and SAPHIR

The earlier SLAC/Cambridge measurements had very small angular coverage (mostly in the forward angles), while, uncovering reaction dynamics requires measurements over a large part of the scattering angle. The wide-angle measurenets were possible only after the emergence of large-acceptance spectrometers like SAPHIR at the University of Bonn, Germany, and CLAS at Jefferson Lab. Although there were some previous work, we focus on the most recent SAPHIR-2004-Glander results [88]. About 54388 $K^+\Sigma^0$ events were reconstructed here with an energy-tagged photon beam, and incident photon energy E_γ from 0.85 to 2.65 GeV. The data were binned in 50-MeV-wide E_γ bins and 0.1-unit-wide $\cos\theta^{K^+}_{\rm c.m.}$ bins. Due to the nature of the $\Lambda \to p\pi^-$ weak-decay process, where the Λ is produced via $\Sigma^0 \to \Lambda\gamma$, the Σ^0 polarization normal to the production place can be measured even with an unpolarized beam. This is called the recoil polarization (see Sec. 8.3 for more details). The SAPHIR-Glander results included both cross-section and recoil polarization results.

Previous CLAS results consist of CLAS-McNabb-2004 [107] and CLAS-Bradford-2006 [87], based on the unpolarized $g1$ and circularly-polarized-beam $g1c$ datasets, respectively. Since $g1c$ had a polarized beam, Bradford *et al.* also published a subsequent dataset [87] containing the double polarization variables C_x and C_z. The current experiment does not have a polarized beam, so we will not be discussing the C_x and C_z variables further. The coverage of these previous CLAS results were from near threshold till $\sqrt{s} \sim 2.53$ GeV. Around 440,000 $K^+\Sigma^0$ events were reconstructed for the

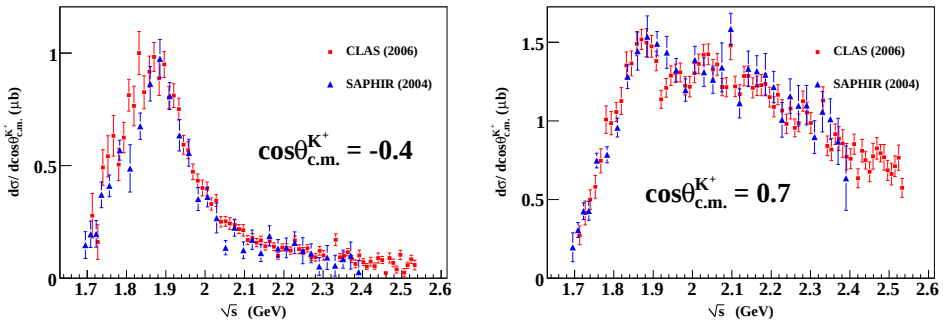

(a) (b)

Figure 1.5: Comparison of differential cross-sections between the SAPHIR-2004-Glander [88] and CLAS-2006-Bradford [87]: (a) backward- and (b) forward angles. Agreement is generally fair to good.

$g1c$ experiment, and the increased statistics allowed for a finer 25-MeV E_γ binning, compared to the SAPHIR results. Fig. 1.5 shows comparisons between the Glander and Bradford results. Agreement is generally fair to good.

While the cross-section results were of reasonable statistical precision, the recoil polarization from both the SAPHIR [88] and CLAS [107] datasets had very poor resolution. Part of the problem arises because the Σ^0 polarizations in these measurements were "twice diluted" (see Sec. 8.3 for details). Our current set of results will far supercede these previous polarization measurements.

1.3.1.3 Modern Limited-Acceptance Experiments: LEPS

The LEPS Collaboration (Sumihama-2006 [90]) at the Spring-8 facility has also published high-statistics differential cross-section results recently. Unlike SAPHIR and CLAS, the LEPS detector can only detect very forward-going particles. In addition their photon beam energy range is limited to $E_\gamma = 2.4$ GeV. However, within these limited kinematic coverage, their statistical precision is quite good, and as wel shall show later, our present CLAS results are in excellent agreement with the LEPS-2006-Sumihama data.

1.3.2 Previous ϕp measurements

Experimentally, most of the world data exist in the high energy diffractive region. This includes results from DESY (Erbe 1968 [121]; Alvensleben 1972 [122]; Behrend 1978 [115]), Cornell (McClellan 1971 [123]; Berger 1972 [124]), SLAC (Anderson 1970 [126]; Anderson 1973 [125]; Ballam 1973 [114]), Fermilab (Egloff 1979 [113]; Busenitz 1989 [127]), Daresbury (Barber 1978 [117]; Barber 1982 [118]) and HERA (Derrick 1996 [119]; Breitweg 2000 [128]). Due to the inherently small ϕ cross sections, these data are generally sparse with wide energy bin-widths and limited statistical precision.

The earliest low energy near-threshold measurement (the ABBHHM results [121] had some low energy data as well) was at Bonn (Besch 1978 [120]), with more recent results coming from SAPHIR (Barth 2003 [65]) and LEPS (Mibe 2005 [66]). Although both the Bonn and SAPHIR results covered the $E_\gamma = 2.0$ GeV energy region, it was the LEPS 2005 paper that first took note of a localized "bump" around $E_\gamma = 2.0$ GeV, when a simple Pomeron exchange model predicts a smooth rise from threshold, as shown in Fig. 1.6. The first CLAS measurement at $E_\gamma = 3.6$ GeV (Anciant

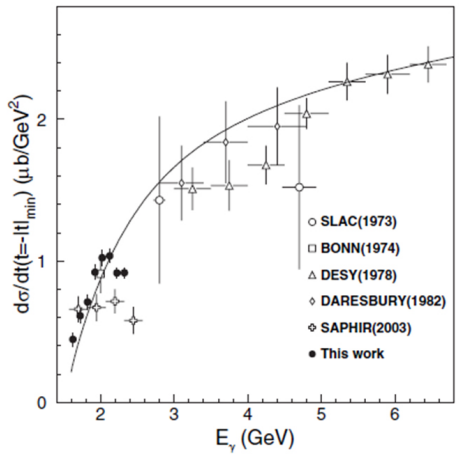

Figure 1.6: The forward-angle "bump" seen in the LEPS-2005-Mibe ϕp data. Image source: Ref. [66]

2000 [60]) also noted an interesting feature, a slight rise in the cross section at the backward-angles from nucleon exchanges via the u-channel. As mentioned earlier, the strangeness content of ordinary nucleons is usually assumed to be very small. However, u-channel nucleon exchanges points directly towards an appreciable strangeness content (possibly sea quarks) of the nucleon, or a violation of the OZI rule. As we show later, our current results confirm this backward-angle rise as well.

1.4 Summary and Structure of this Thesis

In this introductory chapter, we presented an overview of Hadron Spectroscopy studies in general and two specific photoproduction channels, $K^+\Sigma^0$ and ϕp, that are the primary goals for this work. The rest of this thesis is structured as follows. Ch. 2 gives an overview of our experiment at Jefferson Lab, and the almost-hermetic CLAS detector system where all our data were taken. Ch. 3 details with our data analysis procedure starting from the raw data as measured by CLAS, to clean samples of $K^+\Sigma^0$ and ϕp events, ready for further physics analysis. A complex detector system like CLAS has inefficiences that must be accounted for, prior to a PWA on the data. This step is called acceptance correction. Ch. 4 explains how we deal with this important step using monte carlo data and GEANT, a generic detctor simulation software package. An important part of this thesis involves PWA and extractions of baryon resonances. Ch. 5 explains our PWA formalism and construction of the amplitudes that will be needed for theoretical investigations. Chs. 6 and 9 pertain to the extraction of differential cross-sections for the $K^+\Sigma^0$ and ϕp channels, respectively. The Λ hyperon travels a finite distance before decaying to a proton and a π^-. This causes a subtle difference in the event triggering system for our experiment for the $K^+\Sigma^0$ channel. Ch. 7 explains all the systematic studies that went into understanding and correcting for this feature. Chs. 8 and 10 deal with extraction of polarization information for the pseudoscalar- ($K^+\Sigma^0$) and vector-meson (ϕp) sectors respectively. Ch. 11 is a preface to future PWA fits and conducts a global survey of certain normalization discrepancies that currently exists between different world datasets. Ch. 12 summaries the main achievements of this work and lays out our future analysis plans. Lastly, as a side project, we were also able to extend upon an earlier set of results for the $K^+\Lambda$ channel with increased statistics and kinematic coverage. These new data are presented in App. A.

Chapter 2

Jefferson Lab, CEBAF and the CLAS Detector

The data used in this analysis were taken during the so-called "$g11a$" run-period in the summer of 2004 at the Thomas Jefferson National Accelerator Facility (TJNAF), also referred to as Jefferson Laboratory or JLab, in Newport News, Virginia. $g11a$ ran as part of experiment E-04-021 [27], *Spectroscopy of Excited Baryons with CLAS: Search for Ground and First Excited States*. The main goal of this experiment was to carry out a high-statistics search for the exotic Θ^+ pentaquark state [28]. At that time, the pentaquark had attracted a huge amount of attention within the field of nuclear and particle physics and pentaquark-search had become one of the top priorities at several experimental nuclear facilities across the globe. As of this writing, the Θ^+ has never been conclusively shown to exist, neither by $g11a$, nor by any other experiment anywhere in the world. However, being a high-statistics precision experiment, designed to detect an exotic particle, the $g11a$ dataset received very careful attention during its calibration and has since become a rich source of data for the analysis of a number of other final states, including $K^+\Sigma^0$ and ϕp.

At JLab, there are three experimental halls, denoted as A, B and C, with an upcoming Hall D under construction which will be dedicated to the GlueX project [29], along with the main CEBAF electron accelerator and a number of other research and manufacturing facilities. An aerial view of the lab is shown in Fig. 2.1. The detector used in this analysis was the CEBAF Large Acceptance Spectrometer (CLAS) housed in Hall B. CLAS is optimized for the detection of multi-particle final states. The large acceptance of the CLAS detector, along with the continuous nature of the CEBAF electron beam and the fast data acquisition system of Hall B led to production of the world's largest $K^+\Sigma^0$ and ϕp photoproduction dataset. In this chapter, we provide details of the CEBAF accelerator, the CLAS detector and several other hardware devices that played key roles during the $g11a$ experiment.

2.1 CEBAF

The Continuous Electron Beam Accelerator Facility (CEBAF) at JLab delivers electron beams to the three experimental halls. At present, the end-point electron energy of the accelerator is 6 GeV (scheduled to be upgraded to 12 GeV in the near-future [32]). In general, particles beams used in high energy physics come in three different types, strong, electromagnetic, and weak, according to the interaction category of the beam particles. The interaction used at JLab is the electromagnetic intection, that is, a real (photoproduction) or virtual (electroproduction) photon is used as the probe. Early electromagnatic probes in the 1960's existed at SLAC, Cornell, Cambridge and DESY.

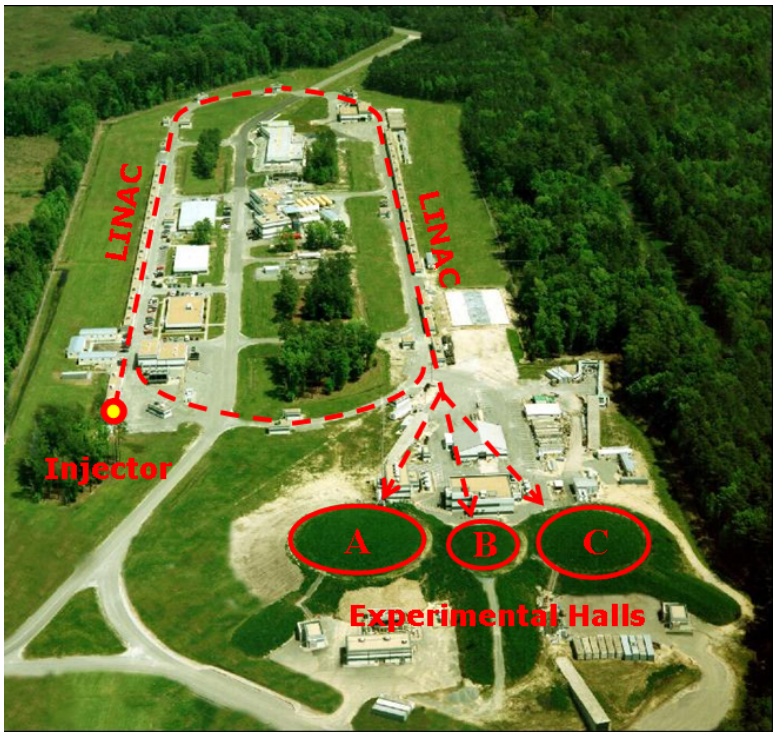

Figure 2.1: An aerial view of the Thomas Jefferson National Accelerator Facility (TJNAF), also referred to as JLab. Shown are the mile long race-course track linear accelerator (LINAC) and the three experimental halls, A, B and C. The CLAS detector is housed inside Hall B. Image source: Ref. [30].

However, since the electromagnetic interaction is inherently weak, these were low-duty machines that were decommissioned and replaced with hadronic machines. The salient feature of electromagnetic probes, however, is that they are also relatively *clean*, the photon or the electron being a point particle. In comparison, a pion or a proton probe is a messy bag of strongly interacting quarks and gluons. It was not until the 1980's that interest in photon-hadron interactions re-emerged with newer technologies for producing the desired reactions at high enough rates. The major advancement employed at CEBAF was the creation of an acceleration gradient using superconducting radio frequency (RF) cavities. Prior to CEBAF, copper RF cavities had been used. The resistivity of the copper caused the cavities to heat up during use which, in turn, required significant cooling time between beam spills. Superconducting cavities are non-resistive, allowing CEBAF to obtain a 100% duty factor and the continuous delivery of electrons permits quick acquisition of high-statistics datasets.

A schematic diagram displaying the major components of CEBAF is shown in Fig. 2.2. Production of the CEBAF electron beam begins at the injector, consisting of a photoemission electron gun, an RF accelerating cavity, and a chopper. The electrons are obtained by illuminating a GaAs photocathode with electron gun that consists of three diode lasers. pulsed individually and at 120° out of phase with each other. The use of three separate lasers allows for independent tuning of the beam characterestics (current, polarization) for each hall. The laser pulses are driven at 499 MHz, so that each experimental hall receives electron bunches every 2 ns. After extraction from the photocathode, 2 1/4 superconducting RF cavities are used to accelerate the electrons to 45 MeV [33]. The

injector system then employs an optical chopper to cleanly separate the bunches prior to sending them to CEBAF's recirculating linear accelerators (LINACs).

Each recirculating LINAC contains 168 superconducting RF niobium cavities; Fig. 2.3 shows a picture of a RF cavity assembly. Each cavity is cooled to -271°C by immersing in liquid helium, when it becomes superconducting. The acceleration gradient for the electron beam is provided by setting up radio frequency standing waves in the cavities, using klystrons. The standing waves are kept in phase with the electron bunches resulting in a continuous positive electric force on each bunch as it passesu through a cavity (see Fig. 2.4). CEBAF has two such LINACs located along the "straightaways" of the 7/8 mile "race-track" course. Each LINAC is capable of providing 600 MeV of acceleration, which will get doubled with the 12 GeV upgrade. The LINACs are connected by nine recirculating arcs, allowing the beam to make up to five passes through each LINAC, obtaining a maximum energy of $\sim$ 6 GeV prior to extraction by the experimental halls. The recirculation is achieved by bending magnets in the arcs (see Fig. 2.2). Extraction of the beam by the halls is performed using RF separator cavities. Each hall can choose to extract the beam after any number of passes (not exceeding the maximum number of five), giving them flexibility to run at different beam energies and currents, simultaneously. It is to be noted however, that, while any number of halls at JLab can run at the maximum energy, no two halls can run with a single lower energy [33].

After extraction, each beam pulse was then directed towards either Hall A, B or C. CEBAF is able to supply each hall with up to on the order of 100μA of electron current, although for Hall B the beam delivered is typically measured of the order of a few tens of nA. For $g11a$, the current was about 60 to 65 nA [34]. Although $g11a$ was an unpolarized photoproduction run, CEBAF is also capable of delivering polarized electron beams which can then be transferred to the radiated photon in different ways, and several experiments before and after $g11a$ have use this feature.

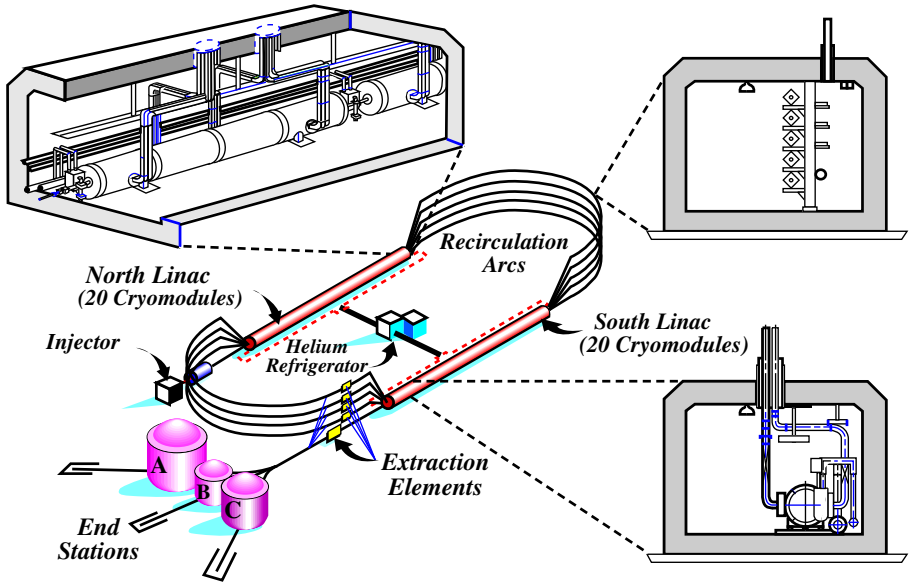

Figure 2.2: A schematic diagram of the "race-track"-shaped Continuous Electron Beam Accelerator Facility (CEBAF). The electron beam, which begins its first orbit at the injector, is accelerated by the two LINACs (shown in red) up to a maximum energy of 6 GeV at the time of $g11a$, prior to being directed towards one of the experimental halls (A, B or C). At top-right is a magnified view of the five separate bending magnet assemblies for up to five beam passes. Image source: Ref. [31].

Figure 2.3: A pair of CEBAF's superconducting RF cavities, shown here with support hardware and beam pipe. Image source: Ref. [30].

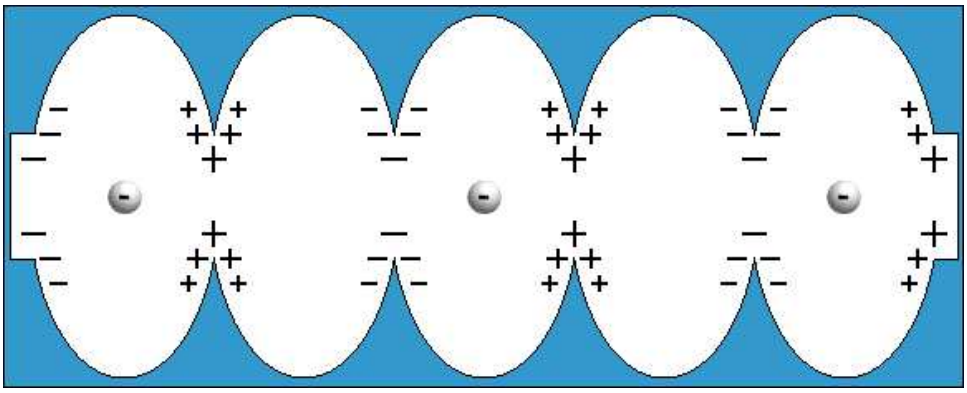

Figure 2.4: The acceleration gradient in the CEBAF LINACSs are provided by establishing standing waves tuned such that an electron always experienced a positive electric force while propagating through the cavity [35].

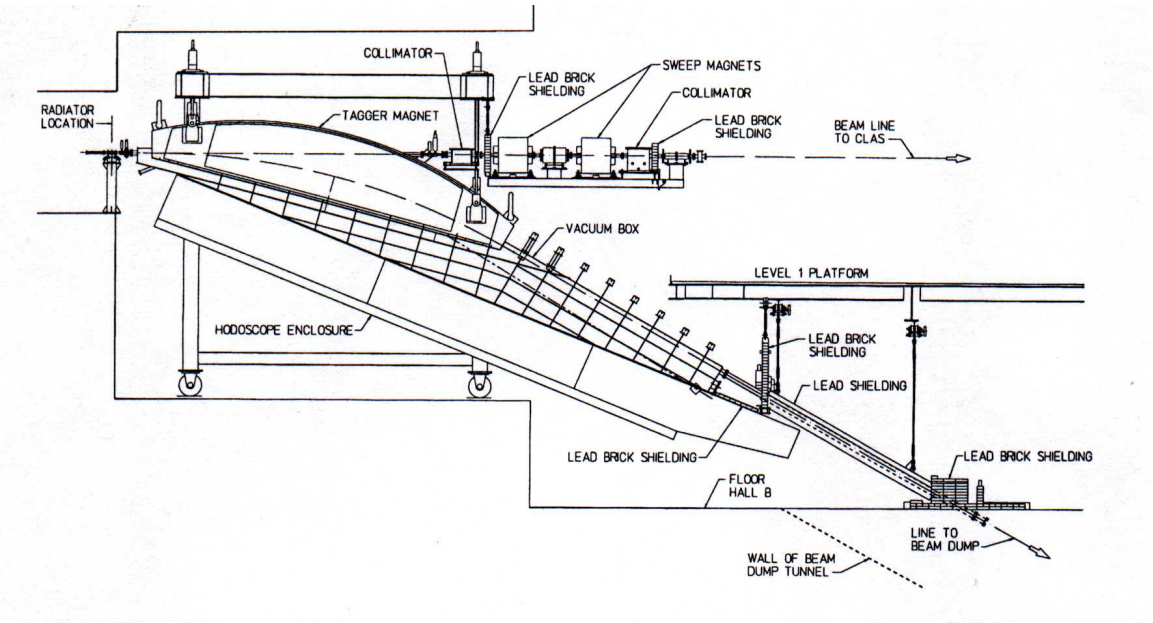

Figure 2.5: The Hall B photon tagging system. The main components include the radiator, magnetic spectrometer and collimators. Image source: Ref. [36].

2.2 The Photon Tagger

For a photoproduction experiment like $g11a$, the electron beam provided by the accelerator has to be converted into a photon beam. Production and energy determination of the photon beam is the job of the Hall B tagging system [36]. This comprises of a radiator that first converts the electron beam into a photon beam using bremsstrahlung, a magnetic spectrometer that sweeps the recoil electrons away from the path of the photon beam (and also makes energy and timing measurements), and finally, a series of collimators. A schematic diagram of the Hall B tagging system is shown in Fig. 2.5.

2.2.1 Radiator

When the electron beam interacts with a gold foil radiator, photons are produced via bremsstrahlung radiation. The nuclear electric field of the radiator decelerates the electron, and the energy change change appears in the form of a photon. Hence the name bremsstrahlung ("braking radiation"). The high atomic number of gold helps reduce contamination of photons produced by electron-electron scattering. A radiator of thickness 10^{-4} radiation lengths was used during $g11a$ production runs, while a much thinner radiator was used during *normalization* runs.

2.2.2 Magnetic Spectrometer

After passing through the radiator, the beam is a mixture of non-interacting electrons, recoil electrons and photons. A dipole magnetic field then sweeps the electrons out of the beam, allowing the photons to proceed towards the CLAS target. Since the bremsstrahlung spectrum is not monochromatic, the energies of the individual photons in the beam need to be measured as well. Assuming the energy transferred to the heavy nucleus (during bremsstrahlung) is small, the photon beam energy is given by $E_\gamma = E_0 - E_e$, where E_0 is accelerator energy and E_e is the energy of the recoiling

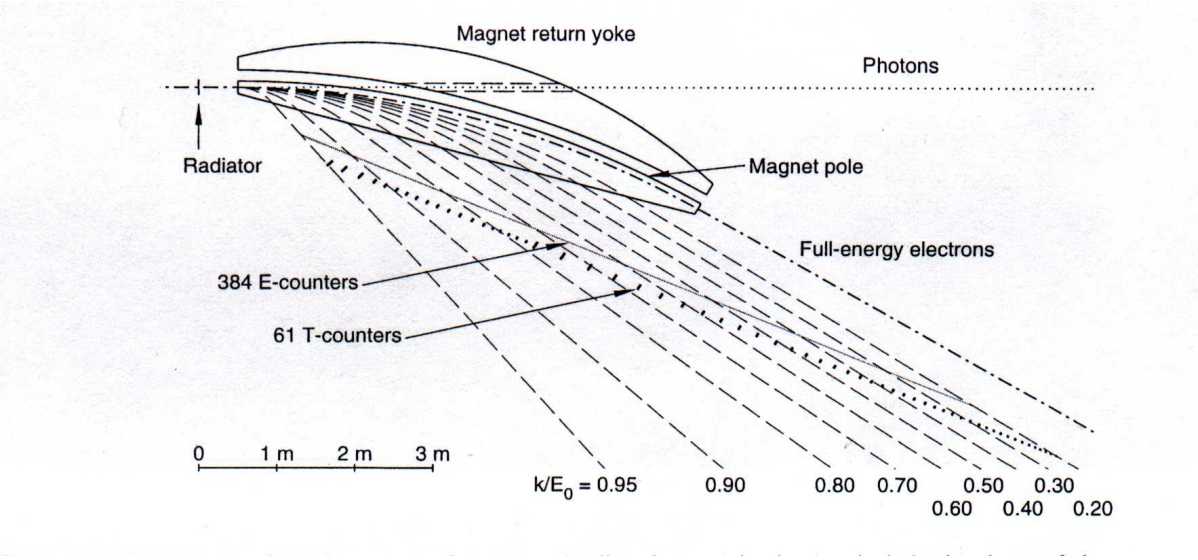

Figure 2.6: Schematic diagram of the tagger spectrometer. The dashed lines show the trajectories followed by recoil electrons of various fractional energies transferred to the outgoing photon. Both hodoscope scintillator planes, the E- and T-planes, are accurately depicted geometrically and with the correct segmentation. Image source: Ref. [36].

electron. Therefore, E_γ for the individual photons can be measured by measuring E_e of the corresponding recoil electron. This is the job of the magnetic spectrometer of the Hall B tagging system.

The tagger magnetic field directs the recoil electrons towards two hodoscope planes, each made of overlapping arrays of scintillators. The field is also tuned to match the accelerator energy E_0, so that the non-interacting electrons can be directed into a shielded beam-dump. The first scintillator plane, referred to as the E-plane, is used to determine the momentum (and thereby, the energy) of the recoiling electrons. It consists of 384 scintillator paddles ("E-counters") that are 20 cm long, 4 mm thick and from 6 to 18 mm in width, arranged in an overlapping fashion to give an increased number of 767 logical paddles. The momentum resolution achieved due to this highly segmented design is about 1×10^{-3}, while the intrinsic resolution of the tagger magnet is $\sim 2\times10^{-4}$. The second scintillator plane, referred to as the T-plane, is used to make accurate timing measurements of the recoiling electrons. To correctly associate a tagged electron with the corresponding 2 ns beam-bunch provided by the accelerator, and thereby, the physics event to be induced by the tagged photon, a timing resolution of at least $\sigma = 300$ ps is required. To achieve this, the T-plane is made up of 61 scintillator paddles ("T-counters"), each 2 cm thick, the added thickness allowing for sufficient light to accurately determine the pulse-shapes. The widths of the paddles varies from 9 to 20 cm, so that each paddle has a uniform counting-rate, despite the $1/E_\gamma$ dependence of the bremsstrahlung cross-section. The final timing resolution was 110 ps and the spectrometer was able to tag photons ranging from 20–95% of the incident electron beam energy. Fig. 2.6 shows a schematic diagram of the tagger spectrometer, with some typical trajectories for the recoiling electrons corresponding to various fractional energies transferred to the outgoing photon.

The signals produced by the scintillator paddles are read out using photomultiplier tubes (PMTs). The T-counter PMT signals were passed through a fast (200 MHz, Philips 715) discriminator before being fed to the "Master OR" (MOR) and an array of FASTBUS TDCs. The MOR is an

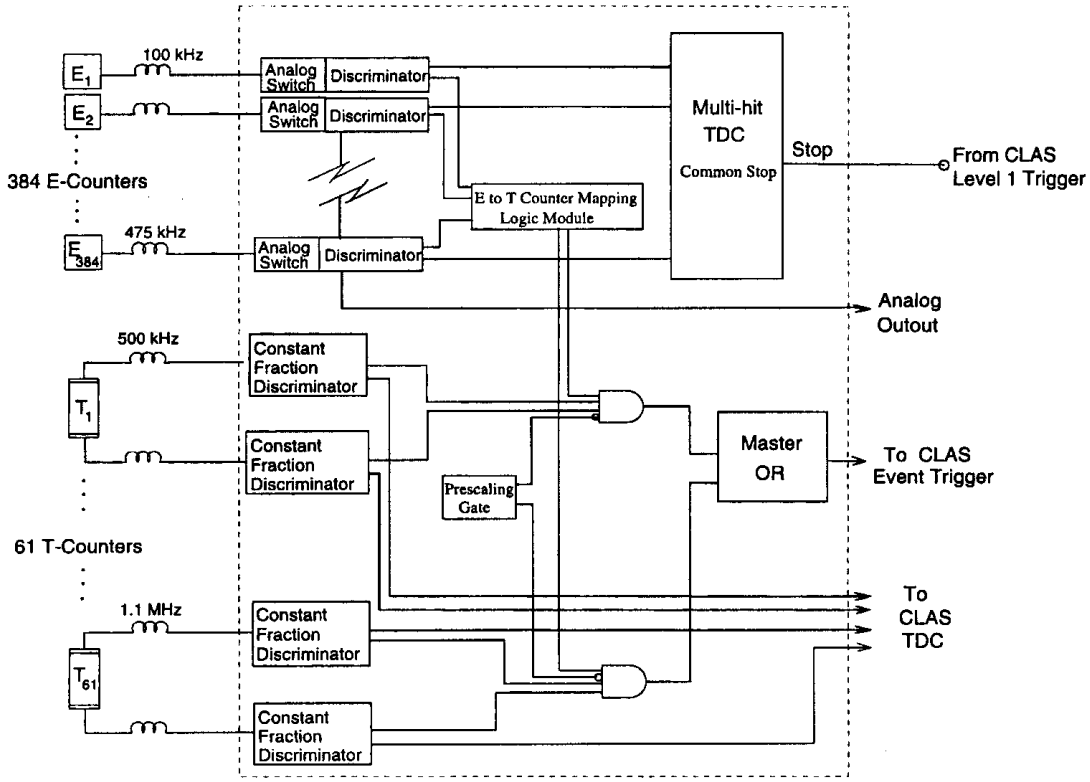

Figure 2.7: Schematic diagram of the readout electronics of the Hall B photon tagging system. Image source: Ref. [36].

important part of the $g11a$ trigger, discussed in Sec. 2.5. The TDC array was used to extract the timing information from all 61 T-counters and also to count the total number of hits registered in the tagger for use during normalization calculations. This timing information was used to correctly associate photons with events in the CLAS detector as multiple photons per event were typically written to tape during readout (see Sec. 3.5 for details). The E-counter PMT signals were also sent through a discriminator and then forwarded to a multi-hit TDC. The timing signals from both the E- and T-counters were written into the data stream and used during offline analysis to establish coincidence between paddles, *ie* used to determine which sets of signals corresponded to an electron passing through the two planes of the tagger spectrometer. Fig. 2.7 shows a schematic diagram of the front-end electronics of the Hall B tagging system. As mentioned earlier, the timing resolution of the tagger precise enough to correctly identify which RF beam bucket each photon is associated with. The RF signal obtained from the accelerator is the most accurate timing information available in the entire experiment. The *event vertex time*, or the time at which all the final state particles produced in the interaction were at the same point in space, is calculated by propagating (temporally) the RF time from the radiator to the event interaction vertex.

To trim the beam halo, before reaching the CLAS detector, the photon beam also passes through a pair of collimators. Sweeping magnets were placed between the two collimators to remove any charged particles created by interactions of photons with the first collimator. More detailed information on the Hall B tagging system can be found in Ref. [36].

Figure 2.8: Photograph of the CLAS detector taken during a maintenance period for which the time-of-flight scintillator walls, forward region Cerenkov counters and electromagnetic calorimeters were pulled away from the interior detector elements. Image source: Ref. [30].

2.3 The CLAS Detector

The CEBAF Large Acceptance Spectrometer (CLAS) is the main physics detector in Hall B. CLAS comprises of several subsystems like the start counter, drift chambers, time-of-flight scintillators, along with Cerenkov counters and electromagnetic calorimeters in the forward region. The latter two forward region detector elements are for electroproduction experiments and will not be discussed here. Our analysis also did not incorporate any timing information from the start counter. However, the start counter plays an important role in the $g11a$ event trigger. The drift chambers are used to track charged particles, which are bent by a superconducting toroidal magnetic, as they travel through the detector. By reconstructing a particle's flight path, one is able to determine its momentum. The time-of-flight scintillator walls are used for particle identification purposes. In this section, we will discuss the detector subsystems which played important roles in our analysis. A photograph and schematic drawing of CLAS is shown in Figs. 2.8 and 2.9, respectively, and a general description of CLAS can be found in Ref. [38].

2.3.1 The $g11a$ Cryotarget

Over the years, target cells with a variety of shapes, sizes and material types (both solid and liquid) have been employed by experiments using CLAS. The $g11a$ target cell, which was cylindrical in shape, was constructed out of kapton by CLAS technician Steve Christo. The cell was 40 cm long with a radius of 2 cm, and a schematic diagram is shown in Fig. 2.10. The target material for $g11a$ was liquid hydrogen and the temperature and pressure was monitored approximately once per hour. Calculations of the target density (an important quantity for making cross-section measurements) have been made by Mike Williams. The average value over the $g11a$ run-period is 0.07177 g/cm^3. with a relative run-by-run fluctuation of about 1.4% [51].

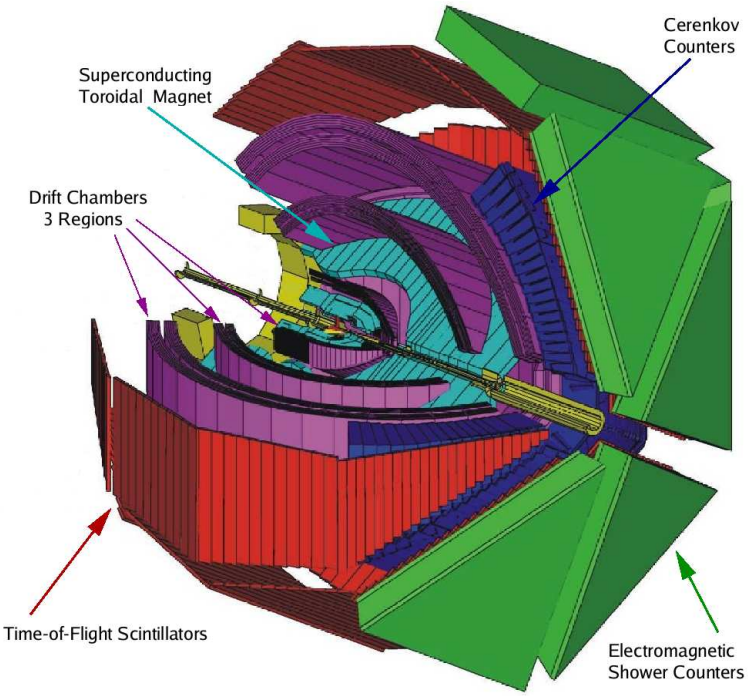

Figure 2.9: Schematic of the CLAS detector showing all of the major subsystems. The detector, which is approximately 8 m in diameter, is housed in experimental Hall B at Jefferson Lab. Image source: Ref. [37].

Figure 2.10: Target cell used during the $g11a$ run period. Image source: Ref. [39].

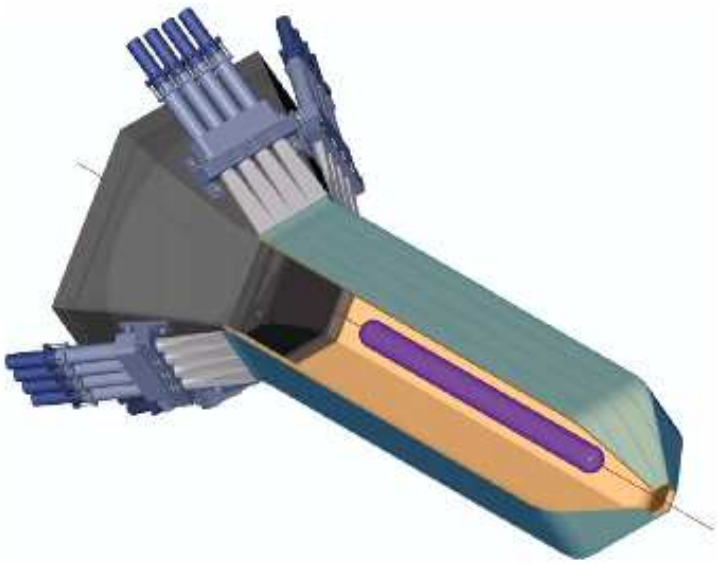

Figure 2.11: Schematic diagram of the new CLAS start counter installed just prior to running $g11a$. Image source: Ref. [40].

2.3.2 Start Counter

Although the most precise timing information was provided by the RF signals from the accelerator, this happened during offline analysis. During actual data collection, it was important to be able to promptly correlate (in real-time), a sub-nanosecond co-incidence between the tagging spectrometer (T-counters) and time of a hadronic interaction within the target cell. This is achived by placing a start counter surrounding the target region. For a 99% confidence level determination of the correct RF beam bucket, the requisite resolution of the counter has to be $\sim$ 388 ps. Earlier versions of the CLAS start counter proved to be inadequate for high-intensity runs like $g11a$. Therefore, a completely new start counter was installed for the $g11a$ run period. Like the CLAS detector itself, the start counter is divide into six sectors each with four scintillator paddles (see Fig. 2.11). The main improvements in the new start counter design were a higher degree of segmentation (needed for better timing resolution), greater hermiticity and increased length (to match that of the $g11a$ target cell). Though we did not incorporate the timing information obtained from the start counter in our analysis, it was included in the Level 1 trigger during $g11a$. As described later in Sec. 7.1. the start counter played a critical role for the $K^+\Sigma^0$ analysis. More information on this detector element, including details on its construction, can be found in Ref. [40].

2.3.3 Superconducting Toroidal Magnet

The functionality of CLAS as a *magnetic spectrometer* derives from the magnetic field due to its superconducting toroidal magnetic system. The magnetic field bends the trajectories of charged particles traversing CLAS, and together with the a tracking system, enables accurate determination of the particle momenta. Fig. 2.12 shows a picture of the bare torus coils during construction of the CLAS detector.

The magnet comprises of six kidney-shaped superconducting coils, designed and tested by Oxford Instruments Ltd. in Witney, UK. The coils are separated by 60^0 in the azimuthal direction

Figure 2.12: The coils of the CLAS toroidal magnet prior to installation of the rest of the detector subsystems. Image source: Ref. [30].

about the beam-line. For the *normal field* configuration, used during $g11a$, negatively charged particles are bent in towards the beam-line and positively charged particles away from the beam-line. CLAS has a "hole" (zero-acceptance) in the forward-direction to accomodate for the beam-dump. As a consequence of the particular magnetic field setting for $g11a$, the acceptance for forward-going negative-tracks (bent into the beam-dump) is lower than that of the forward-going positive-tracks (bent into the fiducial region of the detector). The peak current the magnet can support is 3861 A, resulting in a maximum field strength of 3.5 T, although the current for $g11a$ was limited to about half the 1920 A. Running at higher currents provides better momentum resolution but further decreases the acceptance for negative particles, due to the forward hole. Since the physics goals of $g11a$ demanded a high overall forward-angle acceptance, running at a lower current was found to be the optimal choice. During operation, the magnet was cooled down to 4.4 K using liquid helium obtained from the central CEBAF refrigerator [41].

2.3.4 Drift Chambers

As mentioned above, the momenta of charged particles are measured by tracking the particles as they travel through the field generated by the toroidal magnet. The charged particles are tracked using three separate "regions" of drift chambers. Region 1, the inner-most chamber, is positioned radially below the torus cryostats where the magnetic field is weak. Region 2 is mounted directly to the magnet's cryostats and occupies the space where the magnetic field is the strongest. Region 3 is positioned outside of the torus coils, and further away from the target, again in a region of weak magnetic field. Fig. 2.14 shows a cut-away diagram of the CLAS detector, depicting the geometrical positions of the three drift chamber regions relative to the torus coils.

For track-reconstruction purposes, each of the three drift chamber regions is further divided into two *superlayers*, one with axially oriented wires (relative to the magnetic field direction) and one with wires oriented at a 6° stereo angle (for azimuthal information). Each superlayer consists of six wire layers of hexagonal drift cells arranged such that neighboring layers are offset by half a cell width. Each cell has a 20 μm gold-plated tungsten sense wire (positive potential) located at its

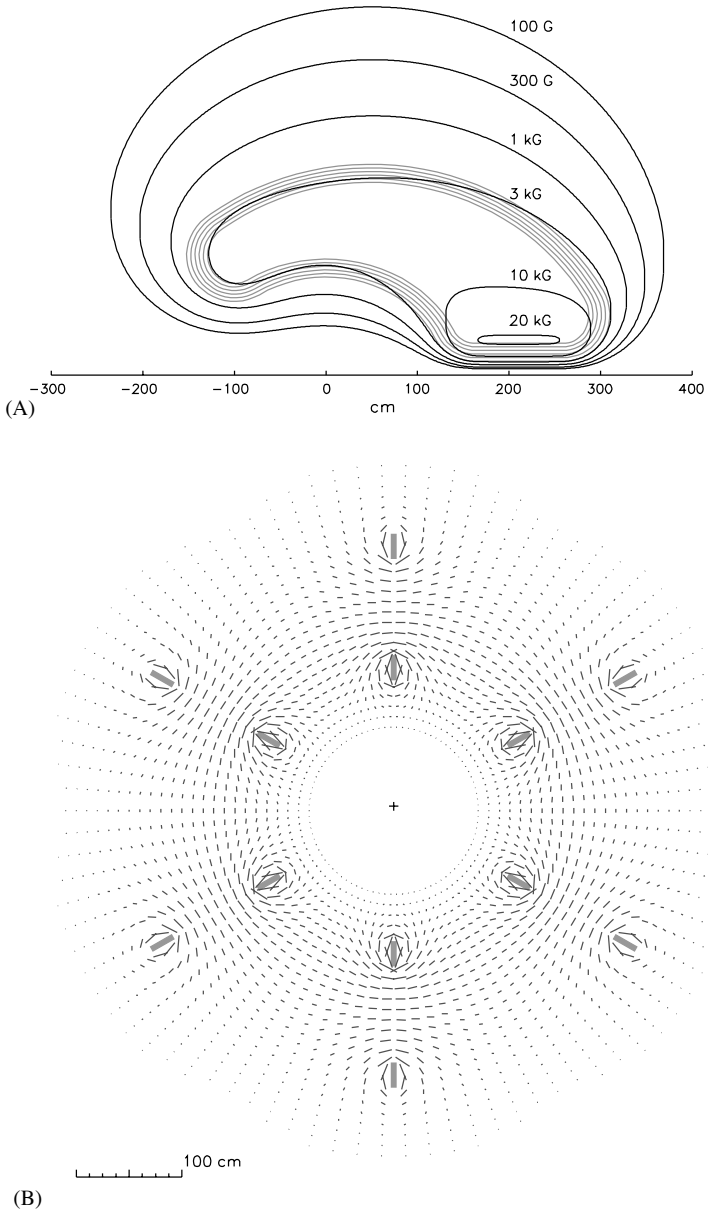

Figure 2.13: The magnetic field strength and direction of the CLAS toroidal magnet: (A) shows the contours of constant magnetic field strength. The magnetic field is strongest in the forward region; (B) shows the magnetic field vectors in a plane transverse to the beam direction, centered at the target. The length of each line segment is proportional to the field strength at that point. Image source: Ref. [38].

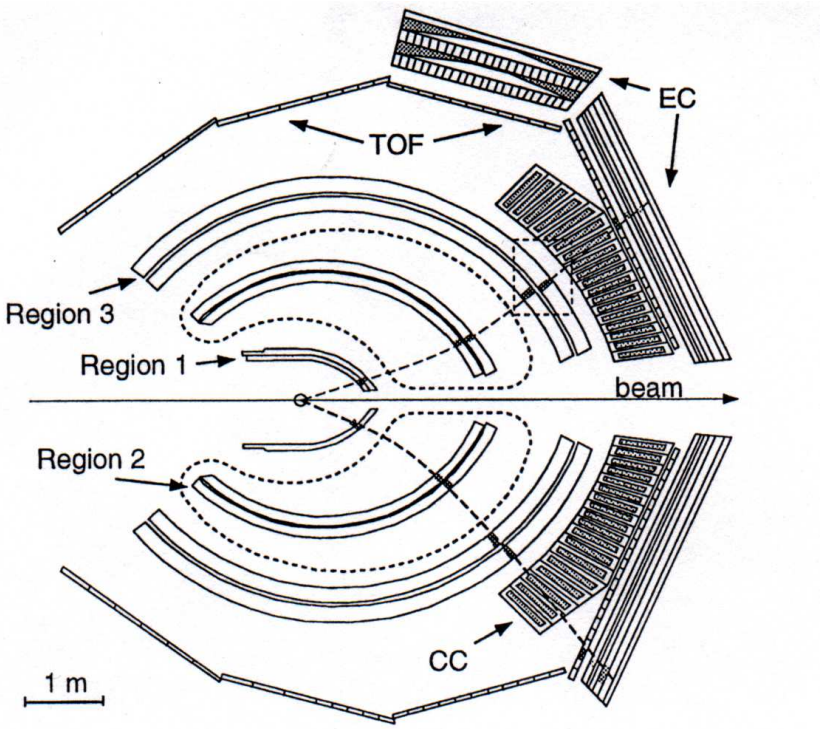

Figure 2.14: Cut away diagram of CLAS showing the relative positions of the detector subsystems. The kidney shaped dashed lines outline the location of the toroidal magnet coils. Image source: Ref. [42].

center surrounded by six 140 μm gold-plated aluminum alloy field wires (negative potential). The drift gas mixture was chosen to be 90% Argon and 10% CO_2, due to its ionization properties and because it is non-flammable. More information pertaining to the CLAS drift chambers can be found in Refs. [42, 43, 44, 45].

2.3.5 Time-of-Flight Scintillators

The outer shell of the CLAS "onion" is made up of six segmented time-of-flight (TOF) scintillator walls, one for each sector, located approximately four meters from the cryotarget. The scintillator wall in each sector has four panels and a total of 57 bars (TOF-counters) of varying lengths and widths, mounted in a fashion such that their lengths project perpendicularly onto the beam-line (see Fig. 2.15). The counters in the forward-region (scattering-angle less than 45°) are 15 cm wide with lengths of 32-276 cm, while the large-angle counters are 22 cm in width and 271-445 cm in length. The signals from the scintillators were collected via photo-multiplier tubes (PMTs) mounted at each end of the bars. The timing resolution was 80–160 ps, depending on the length of the bar (longer bars had worse resolution). The TOF-system plays a central role in this analysis, being a part of the Level 1 $g11a$ trigger (Sec. 2.5) and also for performing particle identification (Sec. 3.6.3). A more detailed description of the TOF system, construction and performance, is given in Ref. [46].

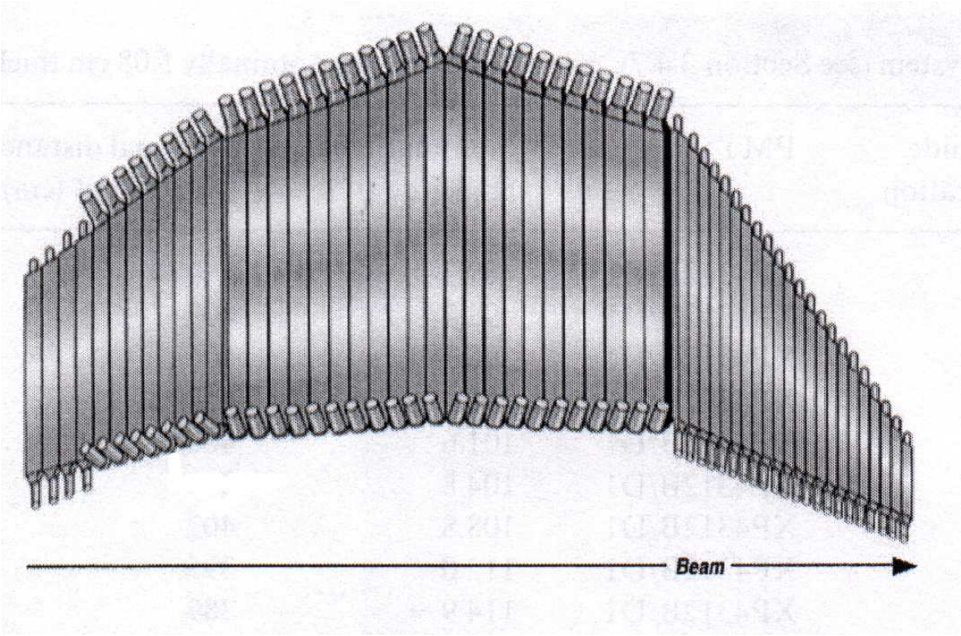

Figure 2.15: Diagram of the time-of-flight (TOF) scintillator shell from one CLAS sector. Image source: Ref. [46].

2.4 Beamline Devices

A number of beamline devices were used in Hall B during $g11a$. Devices placed upstream from the CLAS detector were used to monitor the quality of the beam. These included beam position monitors (BPMs), harps and devices which measured the current of the beam. Downstream devices, such as the total absorption shower counter (TASC), pair spectrometer (PS) and pair counter (PC), were used to measure the photon flux. The TASC was used by *gflux* [47], the standard CLAS photon flux calculation method, to obtain the *tagging ratio* of the T-counters. It consisted of four lead glass blocks, with 100% photon detection efficiency, each instrumented with a phototube. The TASC could provide an absolute measurement of the photon flux, but only if the beam current was less than 100 pA [36]. Thus, low current *normalization runs* were taken periodically so that the flux calculated by the tagger could be calibrated against the TASC.

2.5 Triggering and Data Acquisition

Since the goal of $g11a$ was specifically to search for the pentaquark, predicted to decay via channels with multiple charged final states, $g11a$ used a more restrictive event trigger than previous CLAS runs. This helped reduce the number of unwanted background events that were not relevent to the physics goal. A number of extraneous sources could also produce signals, such as cosmic radiation passing through a detector element, electronic noise, etc. It was the job of the *trigger system* to determine which sets of signals constituted a physics event. Once this decision had been made, the data acquisition system (DAQ) collected the signals and wrote them to magnetic tape for future *offline* analysis. At the time $g11a$ was run, the DAQ was capable of running at $\sim$ 5 kHz. The $g11a$ trigger required coincidence between the tagger Master OR (MOR) and the CLAS Level 1 trigger. Although the entire tagger focal plane was kept on and recorded data, only the first 40

(highest energy) tagger T-counters were enabled in the trigger (see also Sec. 4.10.3). Effectively, this truncation ensured that most of the triggered events lay above $E\gamma \approx 1.5$ GeV, where most of the interesting physics was supposed to lie. For an individual CLAS sector to satisfy the Level 1 trigger, a signal was required from any of the 4 start counter paddles and any of the 48 TOF paddles (in that same sector) within a coincidence window of 150 ns. The Level 1 trigger, as a whole, was only passed if at least two sector-based triggers were registered. The final requirement for the $g11a$ trigger was a coincidence between the tagger MOR and the start counter OR within a timing window of 15 ns [48]. This was done to reduce the coincidence window between the Hall B tagging system and the CLAS detector.

2.6 Summary

Prior to performing our analysis, we required an experimental setup which could produce, observe and record $K^+\Sigma^0$ and ϕp photoproduction events. Production of the desired events employed the tagged photon facility at JLab comprising of the CEBAF accelerator and the Hall B tagging system, and the CLAS cryogenic liquid hydrogen target. The events were observed by the various components of the CLAS detector and recorded by the data acquisition system. At this stage of the $g11a$ experiment, we had $\sim$21 TB of electronic signals stored on magnetic tape. In the following chapters, we will detail the process of converting this *raw* information into meaningful physics observables.

Chapter 3

Event Selection

The $g11a$ dataset consists of about 20 billion event triggers and around 21 TB of data collected by the CLAS collaboration at Jefferson Lab between May 17th and July 29th, 2004. Next, the data underwent a step known as *cooking*, where raw signals recorded by the various detector subsystems were repackaged into a form suitable for physics analysis. This included recording of tracking information and assignment of particle kinematics for every event. Each detector component was also calibrated and checked for functionality at this point. The chef for $g11a$ cooking was Maurizio Ungaro at INFN [49]. After cooking, the actual physics analysis began.

At the time of this writing, $g11a$ is by far the largest strangeness photoproduction dataset in the world to have been fully analyzed. However, cross sections for strangeness photoproduction generally being much smaller compared to the non-strange sector, most of the data consisted of $N\pi$, $N\pi\pi$, $p\omega$, $p\rho$, ... production, which were "background" events for the $K^+\Sigma^0$ and ϕp channels. In this chapter, we describe all the steps involved in the extraction of good $K^+\Sigma^0$ and ϕp events from this very large dataset.

3.1 Reaction Topologies

3.1.1 $K^+\Sigma^0$: "Three-track" and "Two-track" Topologies

The Σ^0 is a neutral particle. Upon production, it decays ~100% of the time via $\Sigma^0 \to \Lambda\gamma_f$. This is an electromagnetic $M1$ transition and occurs almost intantaneously. The Λ subsequently undergoes a weak decay via both charged ($p\pi^-$, 63.9%) and neutral ($n\pi^0$, 35.8%) decay modes. Since CLAS is optimized for detecting charged tracks, we will be concerned with the Λ charged decay mode only. The $g11a$ Level 1 trigger was a sector-wise two-prong trigger. Therefore, for a major portion of the $K^+\Sigma^0$ analysis, our selected events have tracks detected for all the three final-state charged particles concerned: K^+, p and π^-. The undetected outgoing photon, γ_f, is reconstructed as the total missing 4-momentum. Henceforth, we will refer to $\gamma p \to K^+ p\,\pi^-(\gamma_f)$ as the "three-track" topology for the $K^+\Sigma^0$ channel.

We also examine the full two-track dataset by detecting only the K^+ and the proton, and we will refer to $\gamma p \to K^+ p(\pi^-\gamma_f)$ as the "two-track" topology for $K^+\Sigma^0$. Since the π^- tracks are negatively charged, they are bent *inwards* toward the beamline by the torus magnets and have a greater chance of escaping undetected through the beam-dump hole in the downstream region of the detector. Therefore, by not requiring the π^- to be detected, the two-track topology has a higher overall acceptance. However, to make Σ^0 polarization measurements with the Λ-Σ^0 polarization transfer preserved, and our event-based partial wave analysis setup as well, requires knowledge of all

Channel	Topology	Reaction-chain	Features
$K^+\Sigma^0$	Three-track	$\gamma p \to K^+\Sigma^0 \to$ $K^+\Lambda(\gamma_f) \to K^+p\pi^-(\gamma_f)$	PWA-based acceptance calculation. Less "diluted" polarization measurements.
$K^+\Sigma^0$	Two-track	$\gamma p \to K^+\Sigma^0 \to K^+p(\pi^-\gamma_f)$	Higher statistics. Greater kinematic coverage.
ϕp	Charged-mode	$\gamma p \to \phi p \to K^+(K^-)p$	Effect of ϕ-$\Lambda(1520)$ overlap. Higher statistics.
ϕp	Neutral-mode	$\gamma p \to \phi p \to K^0_S(K^0_L)p \to$ $\pi^+\pi^-(K^0_L)p$	No ϕ-$\Lambda(1520)$ overlap.

Table 3.1: Summary of the reaction topologies for the $K^+\Sigma^0$ and ϕp channels used in this analysis. The undetected final-state particles are shown within parentheses.

four final-state particle momenta. Since the missing momentum for the two-track topology is the sum of the π^- and γ_f momenta, the individual momenta of these tracks could be reconstructed. Hence, our two-track topology analysis is mostly limited to differential cross-section measurements only. As shown in Sec. 6.7, in regions where the kinematics overlap and statistics are high enough, the two- and three-track $K^+\Sigma^0$ results are found to be in good agreement with each other, even though the two analyses are independent of each other with quite different event selection and analysis schemes. This in turn serves as an internal check for our understanding of the $g11a$ dataset and the detector acceptance.

3.1.2 ϕp : "Charged-mode" and "Neutral-mode" Topologies

The ϕ primarily decays into two kaons via charged- ($\phi \to K^+K^-$, 49%) and neutral-mode ($\phi \to K^0_SK^0_L$, 34%) decays. For the charged-mode, both two-track $\gamma p \to \phi p \to K^+(K^-)p$ and three-track $\gamma p \to \phi p \to K^+K^-p$ topologies are possible. Since the ϕ cross-section is inherently small, the three-track topology has quite limited statistics. Therefore, we only use the two-track dataset for the "charged-mode" topology in the analysis. This has the highest statistics and forms the primary source of results for this channel.

Along with the charged mode, we also analyze the neutral-mode decay of the ϕ. Below $\sqrt{s} \sim$ 2.2 GeV, the charged-mode topology overlaps in phase-space with the reaction $\gamma p \to K^+\Lambda(1520) \to K^+K^-p$, while the neutral-mode kinematics is impervious to the $\Lambda(1520)$. It is therefore crucial to compare results between the charged and the neutral modes to understand any effect the $\Lambda(1520)$ might have on ϕ photoproduction below 2.2 GeV. It is to be noted that all previous world data utilized only the charged decay mode by detecting the K^+. The present results represent the first analysis of the neutral decay mode of the ϕ. Hemceforth, we define the "neutral-mode" topology as $\gamma p \to \phi p \to K^0_S(K^0_L)p \to \pi^+\pi^-(K^0_L)p$ with the undetected K^0_L being reconstructed as the missing 4-momentum. Being a three-track topology, statistics is again rather limited here. To bolster statistics, our energy bins are wider and our angular coverage is limited to the forward- and some of the mid-angles regions only.

Excluded runs	Description
43490-43525	Commissioning runs.
44108-44133	5.021 GeV beam-energy.
43675-43676, 43777-43778, 44013	Alternate trigger configurations.
43989, 43990-43991, 44000-44002, 44007-44008, 44010-44012	TOF problem in sector 2.
43586-43589, 43590-43596	TOF problem in sector 3.
43588, 43585, 43657, 44036, 44101	Abnormal data yields.
43526, 43527, 43532, 43533, 43540, 43541, 43547-43553, 43561	Damaged magnetic tape during full two-track data transfer (for two-track topologies only).

Table 3.2: Table of $g11a$ runs excluded from this analysis

3.2 Excluded Runs

Data acquisition (DAQ) in CLAS proceeds on a run-by-run basis, each "run" consisting of about 10 million events. This subdivision helps in diagnosing detector and DAQ problems that might creep in over time. The $g11a$ run period includes CLAS runs 43490 to 44133. Runs 43490 to 44107 were taken with an electron beam-energy of 4.019 GeV, while for runs 44108 to 44133, the beam-energy was 5.021 GeV. Since the latter set of runs forms only a small fraction of the entire dataset and will not reduce our statistical uncertainties by any considerable amount if removed, but can lead to possible differences in systematics, we use only the 4.019 GeV beam-energy runs in this analysis. We also exclude the very first few runs from 43490 to 43525; these were *commissioning* runs taken for diagnostic reasons and were not meant to be used for any actual physics analysis.

There were several other runs which were later found to be unreliable and are excluded from this analysis. While $g11a$ was being recorded, a logbook was kept of all shift workers' observations. The CLAS $g11a$ logbook entries for runs 43981-43982 show that there were problems with the drift chambers during these runs. Similarly, logbook entries for runs 43989-43991 show problems with the DAQ system. In order to study the $g11a$ trigger, runs 43675-6, 43777-8, 44013 were taken with different triggering configurations than the standard production trigger. Several runs showed systematic problems with the DC power supply to the TOF counters in sector 2 (runs 43989, 43990-1, 44000-2, 44007-8, 44010-2) and sector 3 (runs 43586-9, 43590-6). Lastly, run 43588 was found to have abnormalities in previous $g11a$ analyses and runs 43585, 43657, 44036 and 44101 exhibited abnormal flux-normalized $K^+\Sigma^0$ yields (see Sec. 4.10). All of the runs listed above are excluded from our analysis.

For three-track analyses in both channels, all $g11a$ runs between 43525-44107 not mentioned as "excluded" in Table 3.2 are included. During the full two-track data transfer (this was done separately, at a later stage in the analysis), one particular magnetic tape containing about a hundred files was found to be physically damaged at the Jefferson Lab end. These hundred odd files spill on to 15 runs (see Table 3.2) and are further excluded from the two-track analyses for both channels (two-track mode for $K^+\Sigma^0$ and charged-mode for ϕp).

3.3 Kinematic Fitting

3.3.1 Introduction

Our particle identification methods (except for the $K^+\Sigma^0$ two-track dataset), as well as our tagger and momentum corrections make heavy use of a method known as *kinematic fitting*. For the $g11a$ datset, this powerful tool was developed by Mike Williams, a former CMU graduate student [50, 51]. In this section we sketch out very briefly how this method works.

To start with, we consider a set of n measured quantities, denoted by the n-vector $\vec{\eta}$. For example, these can be the momenta of different tracks measured by CLAS. Each measurement has an associated error, given similarly by the n-vector $\vec{\epsilon}$. The *actual* values of the observables being measured are $\vec{y}$, with the relation

$$\vec{\eta} = \vec{y} + \vec{\epsilon}. \tag{3.1}$$

The idea is to estimate $\vec{y}$ from $\vec{\eta}$ using a set of *kinematic* constraints, in our case, the conservation of energy and momentum. For example, in the $K^+\Sigma^0$ channel, we have an outgoing photon which we do not detect. The constraint equation is therefore the requirement of a zero total missing mass, and the fit is a one constraint (1-C) fit. If we had detected *all* the final particles we would have required every component of the total missing 4-momenta to be zero and the fit would have been a 4-C fit. Note here that the fit parameters all go inside the constraint equations. Then, consider the following n-vector, $\vec{\delta}$, given by

$$\vec{\delta}_i = \vec{y}_f - \vec{y}_i \tag{3.2}$$

where $\vec{y}_f$ are the final required fit results, $\vec{y}_i$ is the improved measurement at the i^{th} iteration step and the starting $\vec{y}_0$ taken as the *measured* $\vec{\eta}$. If the covariance matrix for the measured quantities is C_η, then the quantity we want to minimize is $\vec{\delta}^T C_\eta^{-1} \vec{\delta}$. However, this minimization has to be done in tandem with the aforementioned constraint equations. This is done by employing the standard procedure of Lagrange multipliers. Lastly, the actual fits are run by utilizing the method of least squares.

3.3.2 Event Selection Scheme using Kinematic Fitting

The way we use the above procedure to select good events is as follows. First, we require every event to be of the form "$+:+$", where at least two positively charged tracks have to be detected and ascribed to the particular event in question. For all three-track analyses, we also require an additional negatively charged track and the event topologies take the form "$+:+:-$". An important point to note here is that the CLAS event reconstruction software typically assigns several charged tracks to the same event and incorrect particle track assignments can thereby be associated an event at this stage. However, as we will show later, these incorrect assignments will not escape our cuts. In the next step, we make a *physics hypothesis* of which particles these tracks refer to. For example, for the $K^+\Sigma^0$ three-track analysis, the physics hypothesis can be either "$K^+ : p : \pi^-$" or "$p : K^+ : \pi^-$". That is, the negatively charged track is assumed to be a π^- and the positively charged tracks have to be either a proton and a K^+, or vice versa. Similarly, for the ϕp charged-mode topology, our event hypotheses are of the forms "$p : K^+$" or "$K^+ : p$", with a missing K^+. We reiterate upon the fact here that throughout this analysis, *all* possible particle hypothesis combinations are looped over and each hypothesis is treated as an *independent event hypothesis*. This serves to minimize any initial bias in our particle identification procedure.

3.3.3 Confidence Levels

The "goodness of fit" from our kinematic fitting is given by the *confidence level* for a given *physics hypothesis*. The fit errors are contained in $\vec{\epsilon}$ vector; if all measurements were independent of each

other so that the covariance matrix C_η was diagonal, the minimization quantity would have taken the familiar χ^2 form $\sum_{j=1}^{n} \epsilon_j^2/\sigma_j^2$. However, for the general case, the covariance matrix will *not* be diagonal and the minimization quantity follows a χ^2 distribution with $d = k - m$ degrees of freedom, where m is the number of fit parameters and k is the number of constraint equations. A measure of the "goodness of fit" for the least squares method is then given by the *confidence level*:

$$CL = \int_{\chi^2}^{\infty} f(z;d)dz, \tag{3.3}$$

where $f(z;d)$ is the χ^2 probability density function with d degrees of freedom. The confidence level indicates how real and repeatable and not just random, a certain fit result is. It is the probability that another random event from the same distribution would have given a χ^2 from the fit which was at least as large as the event in question. If the errors are normally distributed, the confidence levels from "good" events will populate the range $(0, 1]$ evenly and "background" events which fail the hypotheses will have very small confidence levels.

The quality of error estimation from the above procedure are given by the *pull* distributions for each measured quantity. These are defined as $z_i = \epsilon_i/\sigma(\epsilon_i)$ with $\epsilon_i = \eta_i - y_i$ and standard deviation $\sigma(\epsilon_i)$. Recasting this as

$$z_i = \frac{\eta_i - y_i}{\sqrt{\sigma^2(\eta_i) - \sigma^2(y_i)}}, \tag{3.4}$$

puts them in a calculable form (the covariance matrix C_y for calculating $\sigma(y_i)$ is obtained here by standard error propagation techniques from C_η). If all the errors are accounted for properly, the pull distributions are normal distributions, centered around zero with $\sigma = 1$.

The kinematic fitter for $g11a$ has undergone extensive testing and has been applied to several other channels with outstanding results [16, 18, 26]. The confidence level from kinematic fits are therefore one of the main handles for event selection and background reduction for this analysis. Since the confidence levels for good events is given by a flat distribution, by demanding that we accept events only with confidence level greater than a certain percentage, we are throwing away a *known* and *well understood* fraction of actual good events, but as we show later, this effectively trims out most of the background.

3.4 Energy, Momentum and Tagger Corrections

3.4.1 Energy Loss Corrections

Energy loss by particles as they pass through various materials in the CLAS detector happens ubiquitously. Even before a particle hits any component of the tracking system, energy losses occur in the target material (liquid Hydrogen) and walls, the beam pipe, the start counter, the air gap between the start counter and the inner regions of the drift chamber, and so on. The PDG [53] lists a comprehensive list of all such energy losses during the passage of high energy particles through matter. Thus these losses had to be properly corrected for. For CLAS, these corrections were handled by the `eloss` package written by Eugene Pasyuk, then at ASU (currently at JLab) [54].

3.4.2 Vertex Reconstruction Corrections

For the $K^+\Sigma^0$ three-track topology (as opposed to the two-track analysis), the Λ decay vertex is reconstructable using tracking information. For the three-track case, since we detect the π^- along

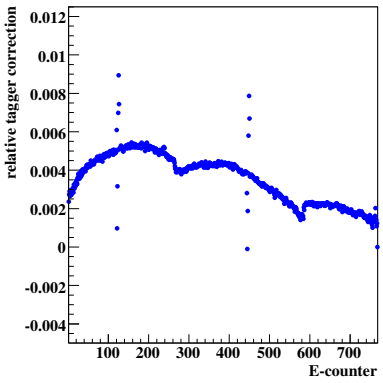

Figure 3.1: Shown above are the *relative* tagger corrections for each tagger E-counter for the $g11a$ dataset as calculated in [51]. The four dips correspond to the sagging of the E-counter focal plane between its four support yokes. There are a few points off the general trend. These are due to wrong cable connections for the counters during data recording. Image source [51].

with the proton, we can use tracking information to find the point of closest approach between the π^- and the proton tracks and assign to this as the Λ decay vertex position. We then set the π^- and proton vertices as the Λ decay vertex position. Similarly, for both the two-track and the three-track $K^+\Sigma^0$ analyses, the *event* vertex position is set as the point of closest approach between the K^+ track and an idealized beam along the z-axis. All vertex calculations were performed using *MVRT*, a vertexing package written by J. McNabb [55]. In earlier CLAS analyses and the early stages of the present analysis, the event vertex was being calculated by projecting back all the detected tracks to one single point and the energy loss for any particle was being calculated assuming it emanate from this point. Due to the multiple decays in the $K^+\Sigma^0$ channel and the fact that the Λ has a macroscopic pathlength of several centimeters, the proton and the π^- tracks inevitably get "kinks" in the direction at each decay vertex. It is thus inappropriate to project all the tracks to a single point. Once we have reconstructed the more accurate event and Λ decay (for the three-track case) vertices, we are also able to calculate the improved energy loss corrections accordingly.

For the ϕp charged-mode, all the final-state particles emanates from a single event vertex. For the neutral-mode, the K^0_S has a finite path-length of $c\tau \sim 2.68$ cm. The K^0_S vertex is therefore different from the event vertex. The K^0_S vertex is reconstructed as the point of closest approach between the π^+ and the π^- tracks. Energy loss corrections are also employed accordingly after the the improved vertex reconstructions.

3.4.3 Tagger Corrections

The photon energy (E_γ) for an event ccomes from the E-counters of the photon tagger in CLAS. However, physical distortions of the tagger's focal plane gave rise to inaccuracies in this measurement. This effect was examined earlier by studying the inclusive $(\gamma)p \rightarrow p\pi^+\pi^-$ reaction via a kinematic fit. This was an inclusive reaction in the sense that the measurements for the incoming photon were ignorned and a 1-C kinematic fit was made to zero total missing mass corresponding to a missing photon. Only events with a high enough confidence level were selected in this study (here one is concerned not about throwing away good events, but that the events selected *really* be good events). This was done for both the CLAS $g11a$ [51] and $g1c$ [56] datasets. Tagger corrections

were then ascribed as the difference between the *measured* photon energy and the energy from the fit result. By taking the Gaussian mean over the entire $\sqrt{s}$ range, a systematic correction was found for each tagger E-counter (see Fig. 3.1). These results have been interpreted as due to sagging of the focal plane between its four support yokes [57]. This sag displaced the narrow E-counters from their ideal locations, causing them to detect electrons with slightly different energies. In this analysis, we have applied the derived $g11a$ tagger corrections to each event according to its associated tagger E-counter.

3.4.4 Momentum Corrections

Momenta for the various particles are measured in CLAS from tracking information as the particles bend during their flight though the toroidal magnetic field. Therefore, any discrepancy between the "ideal" field map from survey information and the "actual" field during the experiment gives rise to incorrectly reconstructed momenta. Similarly for misalignments and sagging in various parts of the drift chamber.

Momentum corrections for the $g11a$ run period have been derived using the $\gamma p \to p\pi^+\pi^-$ channel [58]. Tagger and energy-loss corrections were applied to each $p\pi^+\pi^-$ event in which all final-state tracks were reconstructed by CLAS. Three separate kinematic fits were then performed, each treating one of the detected final-state particles as "missing": $\gamma p \to p\pi^+(\pi^-)$, $\gamma p \to p(\pi^+)\pi^-$, and $\gamma p \to (p)\pi^+\pi^-$ hypotheses. The measured momenta for the "missing" particles were then compared to the missing momenta from the kinematic fits. Corrections were calculated for each CLAS sector and particle charge. Each sector was divided into twelve 5° bins in the azimuthal angle ϕ. Each ϕ bin was then divided into fifteen polar angle (θ) bins: nine 5° bins in the range $5° \leq \theta < 50°$, four 10° bins in $50° \leq \theta < 90°$, and two 25° bins in $90° \leq \theta < 140°$. Corrections to the magnitude of momentum for each track charge were calculated in each of the angular bins, and were typically found to be less than 10 MeV.

3.4.5 Effectiveness of the Corrections

To check the effectiveness of these corrections, we employ the $K^+\Sigma^0$ channel and look at the missing mass off K^+ and the invariant $(p\,\pi^-)$ mass distributions in the three-track dataset. The former corresponds to the Σ^0 mass (∼1.1926 GeV) and the latter to the Λ mass (∼1.1156 GeV). We choose events by kinematically fitting to $\gamma p \to K^+ p\,\pi^-(\gamma_f)$ and applying a 1% confidence level cut (the validity of this cut is described in detail in Sec. 3.6.1) keeping only events with missing mass off K^+ between 1.14 GeV and 1.24 GeV. Fig. 3.2 shows the two distributions as they looked before and after the corrections were made (but before kinematic fitting). All events are taken from runs 43810-43819. There is a distinct shift in the peaks between the pre and post-correction distributions. The corrections pulled the mass peaks closer to their PDG values, demonstrating the effectiveness of our corrections.

3.5 Photon Selection

For photoproduction experiments in CLAS, the interaction time for an event can be measured in two different ways. Each event has a number of tagged photons. As mentioned in Sec. 2.2, the timing resolution of the tagging spectrometer in CLAS is 110 ps and this is good enough to identify the RF beam bucket the tagged photon is associated with. The next step is to temporally propagate the photon time from the radiator to the interaction vertex. This *tagger vertex time*, derived from

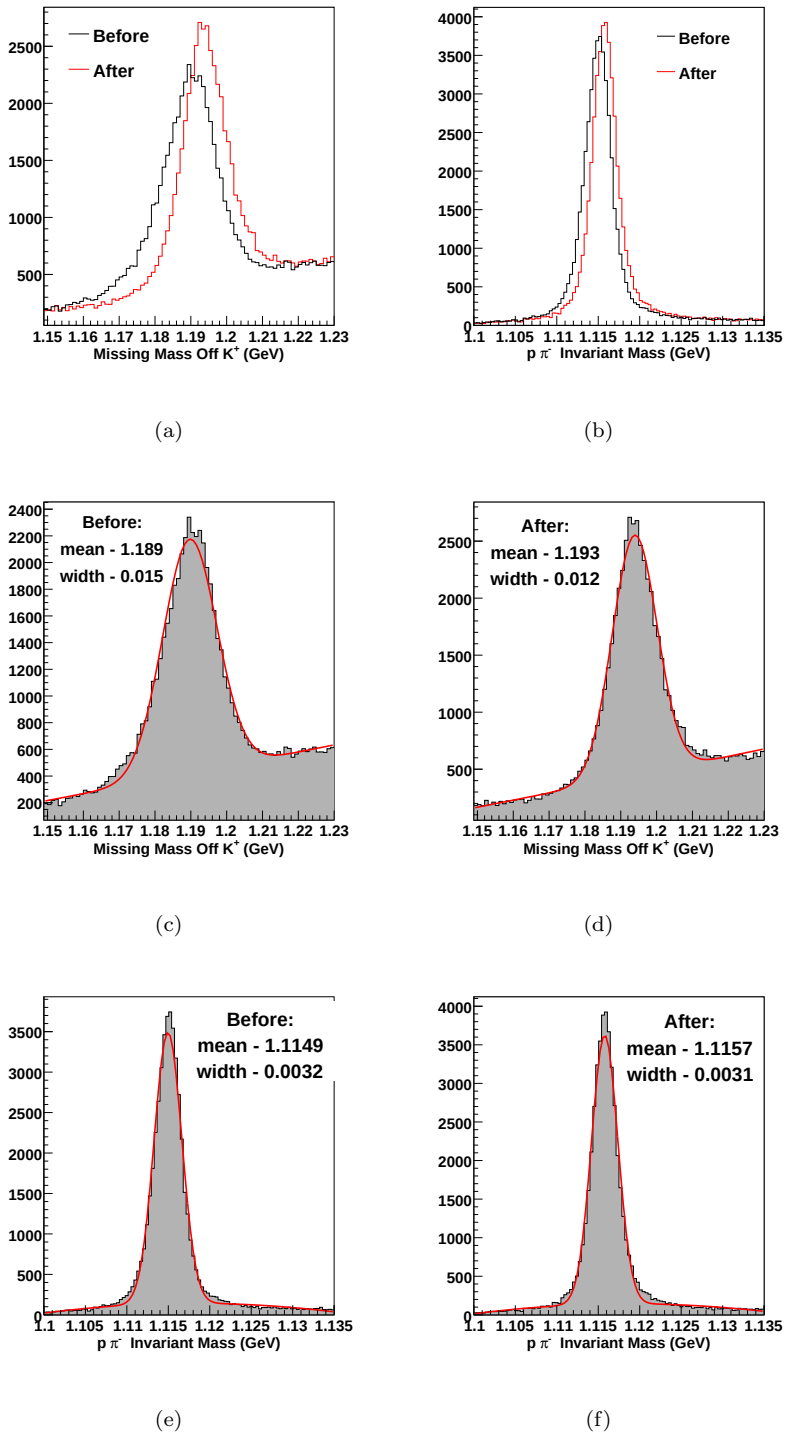

Figure 3.2: Effectiveness of energy, momentum and tagger corrections using the $K^+\Sigma^0$ channel: shifts in the (a) Σ^0 and (b) Λ mass peaks respectively, before and after the corrections. Fits to the distributions in (c) and (d) for Σ^0, (e) and (f) for Λ show that the peaks are pulled closer to the masses listed in PDG after the corrections. Note that the events are *selected* using a kinematic fit cut, but the momenta used to compute the above variables use the corresponding pre-kinematic fit values.

the RF signal time is the most accurate timing information available in the entire experiment and *this is the event vertex time that we use in this analysis.* For a given event, every tagged photon [1] is looped over independently, as "the" photon. Photons associated with the wrong RF bucket are removed by cuts later on. An alternative way of determining the event vertex time is to use timing information from the start counter. The start conter is the first detector system that a charged track trigger after it leaves the target. Timing information from the start counter is propagated backward temporally to the event vertex by using the track's momentum and tracking information and a *start counter vertex time* is obtained from here. In some CLAS analyses (see Bob Bradford's CLAS $g1c$ analysis [52] for example), an initial ± 1 ns photon selection cut was placed between the tagger and start counter vertex times for every detected track. We examined the effect of this cut in the very initial stages of our analysis, and though we found it to be a loose enough cut, we *do not employ this cut in this analysis.*

3.6 Event Selection – $K^+\Sigma^0$ Three-track Topology

3.6.1 Kinematic Fitting of $\gamma p \to K^+ p\pi^-(\gamma)$

As noted earlier, the $g11a$ dataset is swamped by events from the non-strange physics sector. For the $K^+\Sigma^0$ three-track topology, the first step towards cleaning up the data is to perform a very loose *skim* using the kinematic fitter, aimed at trimming out this large and all pervasive background.

As described in Sec. 3.3.2, we begin by selecting "$+:+:-$" events and making a physics hypothesis, where the tracks are assigned as "$K^+ : p : \pi^-$" or "$p : K^+ : \pi^-$". To save computation time, we reject events we can realistically assume to be background by placing the following two *extremely* loose cuts:

1. require total missing mass to be less than 400 MeV, and,
2. require missing mass off K^+ to be less than 1.45 GeV.

These cuts greatly reduce the number of ineligible background events that we kinematically fit. We then employ a 1-C kinematic fit to $\gamma p \to K^+ p\,\pi^-\,(\gamma)$ and place a 1% confidence level cut.

Before proceeding to describe the results of this skim, we note that for any of the two combinatorial physics hypotheses we make, prior to applying kinematic fitting, we applied all the appropriate energy, momentum and tagger corrections. Also, post-skim, only events with missing mass off K^+ between 1.14 GeV and 1.3 GeV are retained. Clearly, the Σ^0, for which the PDG [53] lists as mass of $\sim$1.192 GeV, lies well within this range. The upper limit is intentionally kept higher to facilitate our background subtraction method.

The results of the fit are shown in Fig. 3.3. The confidence level distribution for all events is shown in Fig. 3.3a. The distribution is almost flat above 0.4. Note that effectively (aside from the two *very* loose cuts mentioned above) we have not applied any cut at all and the $K^+\Sigma^0$ channel is completely swamped by background at this stage (Fig. 3.3b). Upon further requiring the total missing mass to be within ± 60 MeV, the Σ^0 peak finally shows up (this last cut is just for visualization purposes here and was not included in the actual skimming). There is still a large amount of background, most of which is removed by the 1% confidence level cut (shown in blue in Fig. 3.3c). Since we have not made any particle identification cuts at this stage and even our confidence level cut is pretty loose, expectedly, some amount of background leaks in, but the post-confidence-level dataset is reasonably clean (shown in red in Fig. 3.3c). The crucial point is that events rejected by

[1] For this analysis, this means having a status word 7 or 15 in the TAGR bank.

the 1% confidence level cut (blue, Fig. 3.3c) hardly shows sign of any peak and we can fairly claim that we are throwing away very few "good" events.

3.6.2 Effectiveness of the Confidence Level cut

If the kinematic fitter is working perfectly and errors are all Gaussian, we expect to lose ∼1% signal with a 1% confidence level cut. We check this by comparing the estimated total signal from a Gaussian (signal) plus quartic (background) fit to the event distributions prior to and after making the confidence level cut. This is shown in Fig. 3.4. The cut hardly changes the signal Gaussian characterestics, the mean (∼1.193 GeV) and the width (∼0.011 GeV) of the signal Gaussians are almost equal in going from Fig. 3.4a to Fig. 3.4b. The signal yield is then estimated by integrating the fit Gaussian function over $\mu \pm 2.5\sigma$. The estimated signal is found to be 34672 and 34335 before and after the cut, in excellent correspondence with a ∼1% signal loss.

3.6.3 Particle Identification − Timing Cuts

The main motivation behind the *skim* was to reduce the $g11a$ dataset to a manageable size while losing as few good events as possible. We have seen that we were able to achieve this very efficiently using the kinematic fitter. To further our event selection process we have to decide upon, and fine tune the next level of cuts. Recall that the kinematic fitter used only kinematic information about the particle trajectories, the various momenta. A second source of information for particle identification (PID) are *timing* information recorded by CLAS for the tracks. We will assume here that the negatively charged track is a π^- (positive and negative tracks bend differently in the magnetic field inside the detector and are distinguished quite easily). Then the main job of the PID is to identify the positively charged tracks as either a proton or a K^+ and trim out the π^+'s leaking in. By judiciously selecting timing based cuts, we are able to arrive upon a very clean dataset with minimal loss of good events.

Timing information for any particle is chiefly encoded in its *time-of-flight* (tof). This is the time difference between the event vertex time and time at which the particle hit the time-of-flight scintillator walls on the outer shell of the detector. Consider the quantity:

$$\Delta\, tof = tof_{meas} - tof_{calc}, \tag{3.5}$$

where tof_{meas} is the *measured* time-of-flight and tof_{calc} is the time-of-flight *calculated* for the mass hypothesis for the particle in question. The latter is given by

$$tof_{calc} = \frac{L}{c}\sqrt{1 + \left(\frac{m}{p}\right)^2}, \tag{3.6}$$

where L is the path length from the target to the scintillator, c is the speed of light, m is the hypothesized mass and p is the magnitude of the 3-momentum. Obviously, the closer to zero $\Delta\, tof$ is, the more confidence we have in our hypothesis. An equivalent way of looking at this is to look at the *calculated* mass (m_{calc}) for a particular track, given by

$$m_{calc} = \frac{p}{\gamma\beta\, c} = \sqrt{\frac{p^2(1-\beta^2)}{\beta^2 c^2}}, \tag{3.7}$$

where

$$\beta = \frac{1}{c} \times \frac{L}{tof_{meas}}. \tag{3.8}$$

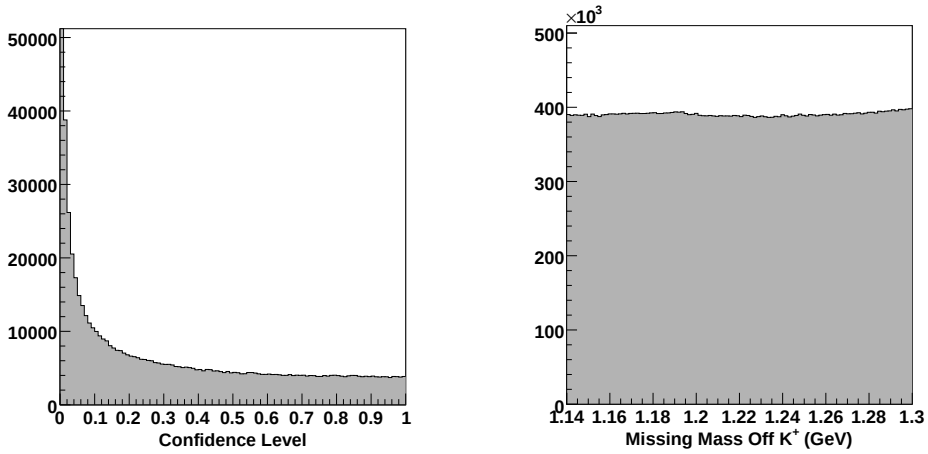

(a) (b)

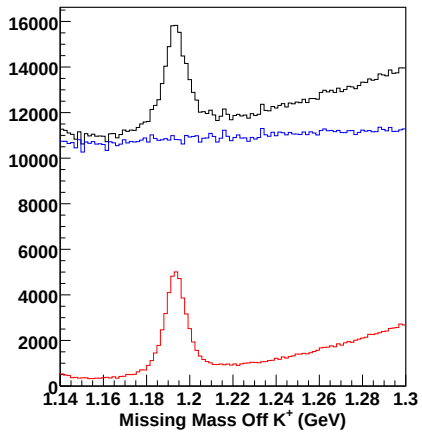

(c)

Figure 3.3: Kinematic fit to $\gamma p \to K^+ p\,\pi^-$ (γ) for the $K^+\Sigma^0$ three-track topology analysis. Events are from runs 43810-43819: (a) confidence level from all the events – the distribution is fairly flat above 0.4. (b) Missing mass off K^+ distributions for all events (with the two loose skim cuts described in the text). (c) Includes a total missing mass requirement between ±60 MeV (see text). There is still a large amount of background, but the Σ^0 peak is visible. Shown are all the events (black), events rejected by a 1% confidence level cut (blue) and events passing the 1% confidence level cut (red).

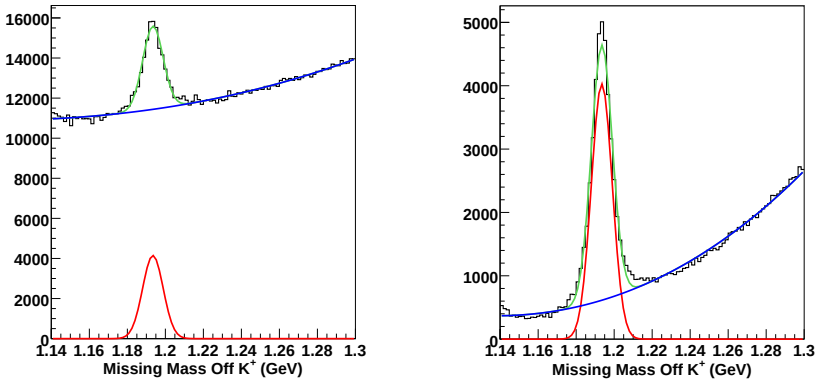

(a) (b)

Figure 3.4: Effectiveness of the confidence level cut for the $K^+\Sigma^0$ three-track dataset. Events are from runs 43810-43819 and include a $|MM| \leq 60$ MeV cut. The total fit function (in green) consists of a Gaussian signal (in red) plus a quartic background (in blue). Fits are to the following event distributions: (a) all events, prior to confidence level cut. Estimated signal − 34672 events. (b) events surviving a 1% confidence level cut. Estimated signal − 34335 events.

For our analysis purposes, we will go back and forth between these two pictures to show the legitimacy and effectiveness of our cuts.

Note that the momenta used in Eqs. 3.5 to 3.8 are the track momenta as CLAS measured it, prior to our corrections and kinematic fitting. The other caveat to note is that the Δtof and the *calculated* mass plots that are to follow (which we based our cut selections on) includes only events with missing mass off K^+ between 1.14 GeV and 1.24 GeV. That is, events with missing mass off K^+ between 1.24 GeV and 1.3 GeV, although included in the *skim*, were excluded for our PID studies. This was to ensure that events which we *apriori* knew to be background did not influence the selection of our cuts.

Fig. 3.5a and 3.5b show Δtof and m_{calc} respectively for the particle passing the kinematic fit under the K^+ hypothesis plotted against that for the particle passing under a proton hypothesis. There are a couple of things that are easy to see from the very outset:

1. in Fig. 3.5a, the clusters of events around $(\pm 2, \pm 2)$, $(\pm 4, \pm 4)$,..., are due to photons associated with the wrong RF bucket (recall from Chapter 2 that the accelerator delivered bunches of elections to Hall B every 2 ns).

2. the band of events inside the boxed region "II" in Fig. 3.5b corresponds to events where our particle hypothesis call a particle a proton when it was actually a kaon, and vice versa. Likewise, in the same region one can also see $p\,\pi^+$ combinations which passed the kinematic cut under a K^+p hypothesis. Such incorrectly assigned events could pass the 1% confidence level cut if the tracks had a high enough momentum relative to the particle masses so that the kinematic fitter could not reliably distinguish between the two. This band actually continues vertically upwards till and beyond where the calculated mass distributions for the two combinations meet − which means also that we could not *reliably* separate signal from background in this region using timing information. To further clean the data we utilize our powerful

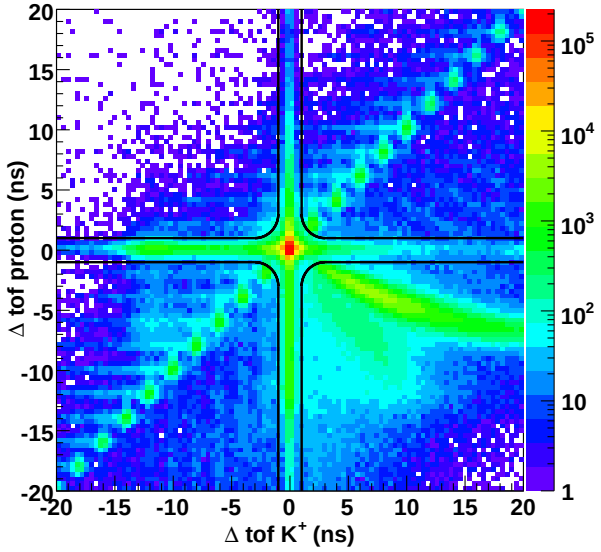

(a)

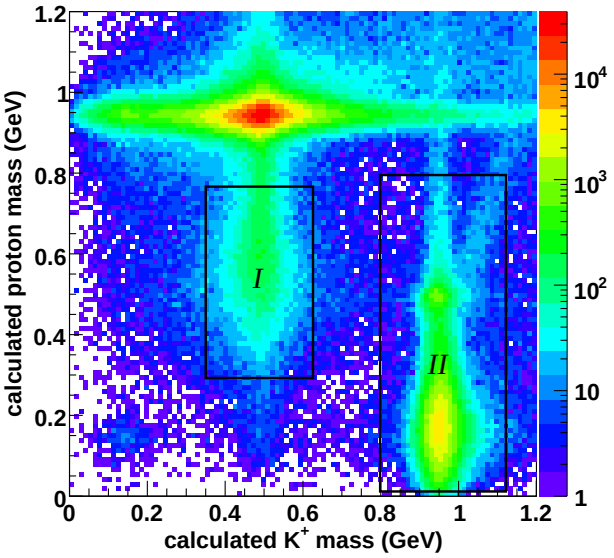

(b)

Figure 3.5: Cumulative skimmed $K^+\Sigma^0$ three-track dataset: (a) $\Delta\, tof$ and (b) calculated masses for p and K^+ (see text for regions marked "I" and "II"). The "iron cross" in (a) shows our PID timing cut. Only events with missing mass off K^+ between 1.14 GeV and 1.24 GeV are included in these plots.

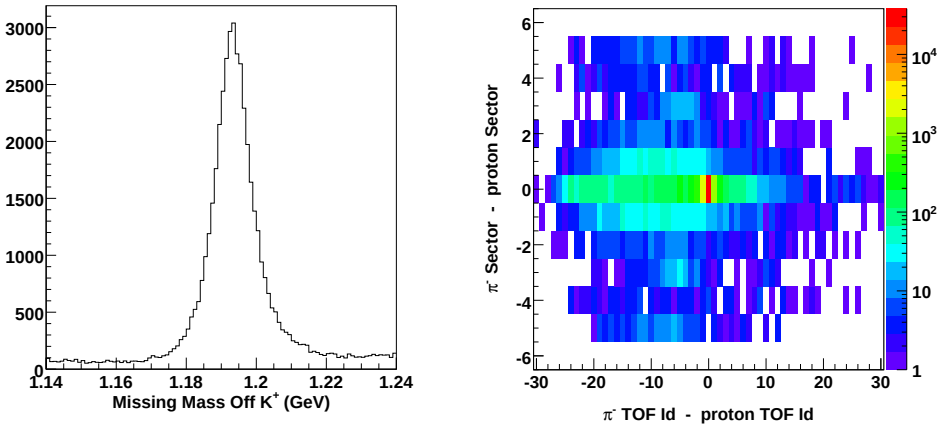

(a) (b)

Figure 3.6: Incorrect Proton timing for region "I" of Fig. 3.5b: (a) Missing Mass off K^+ for these events (b) sector Id difference vs TOF Paddle Id difference between π^- and proton − the blob at the center corresponds to both the tracks hitting the same physical TOF counter.

signal-background separation method to be described in the next section.

3.6.4 A subtlety

Region "I" in Fig. 3.5b deserves special attention. The K^+'s seem to have been correctly identified here but the protons look more like K^+'s. One is first led to suspect that these events somehow resulted from the production of double strangeness cascade events. However, firstly, it is hard to imagine that such events would pass even a loose 1% confidence level cut from a kinematic fit to zero missing mass. Secondly, we have constrained the missing mass off K^+ to be less than 1.24 GeV and any double strangeness exotic particle itself would have a much higher mass. Thirdly, and most importantly, the missing mass off K^+ for these events contain a very clean peak around the Σ^0 mass (Fig. 3.6a).

Upon further investigation it is found that these events *are* good $K^+\Sigma^0$ events after all, save that CLAS recorded the proton timing information incorrectly. Recall that the breakup momentum of the Λ particle is relatively small. This means that the breakup angle in the laboratory frame is also small. The proton and the π^- coming from the Λ decay are then almost collinear, as seen in the laboratory/CLAS frame and can hit the same TOF scintillator paddle. This is indeed what happened for these particular events, as shown in Fig. 3.6b. The big blob at $(0, 0)$ is where CLAS recorded the same TOF paddle Id and the same sector Id, and thus the same physical TOF paddle, for the proton and the π^- tracks. TOF scintillators in CLAS are single-hit counters. CLAS therefores assign the *same* one time-of-flight to both the proton and the π^-. The π^- being lighter, typically arrives first and are assigned the correct time-of-flight. The proton which follows are then assigned a shorter time-of-flight which reduces its calculated mass, bringing it closer to the kaon mass region. However, as long as we were careful not to use the proton timing information anywhere else in our analysis, we can still include these events. Also, note that the K^+ goes completely unaffected by this.

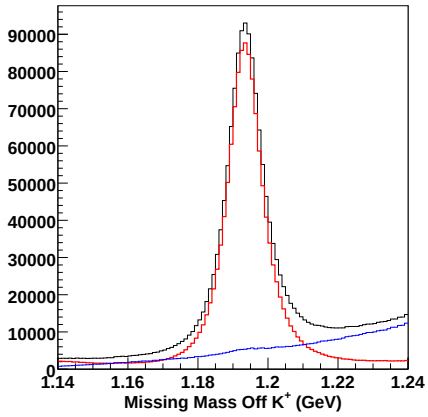

Figure 3.7: PID cut on the cumulative $K^+\Sigma^0$ three-track skimmed dataset. In red are events that passed the cut and in blue are the events rejected by the cut.

3.6.5 The "Iron-cross" Cut

The PID cut chosen for the $K^+\Sigma^0$ three-track analysis is shown by the quadruplet of black lines in Fig. 3.5a taking the shape of an "iron-cross". That is, we reject events lying outside the cross. The cut is essentially based on the idea of accepting tracks with $\Delta tof \leq 2$ns, executed in a 2-dimensional fashion. It is meant to be both loose enough to minimize signal loss but stringent enough to reduce the background substantially. The result of the cut is shown in Fig. 3.7. Fig. 3.8a shows the calculated mass distribution for events rejected by our cut while Fig. 3.8b shows that for events passing the cut. One can ask here whether our cut is too loose and we should also trim out region "I" (containing $\pi^+ p$ background) and region "II" (containing pp background) in Fig. 3.8a. However plotting the missing mass off K^+ for these regions (Fig. 3.9), we find that there is sufficient amount of signal in these regions to retain them. Furthermore we show in Sec. 4.4 that for the Accepted Monte Carlo, which we know to have almost negligible $\pi^+ p$ and pp background, also have events populating these regions. The few events remaining in region "III" (Fig. 3.8a), though can reliably be claimed to have a wrong PID assignment, will be retained at this stage to give enough leverage to our background fitter for pulling out the background underneath region "II".

This completes all our PID cuts for the three-track dataset. All remnant background will be removed by our signal-background separation method (Sec. 3.11).

3.6.6 PID uncertainty

As evident from Fig. 3.7, our PID cuts throw away very few good events. We can make an estimate of how much signal we are throwing away by fitting the missing mass off K^+ distribution before the cut and that for events rejected by the cut with a Gaussian plus a quartic. This is shown in Fig. 3.10. Fig. 3.10a shows the fit to the entire skimmed dataset. The total fit function seems to slightly fall short of the total histogram peak though the background function describes the background pretty well. We thus chose to estimate the total signal by subtracting the background integral from the

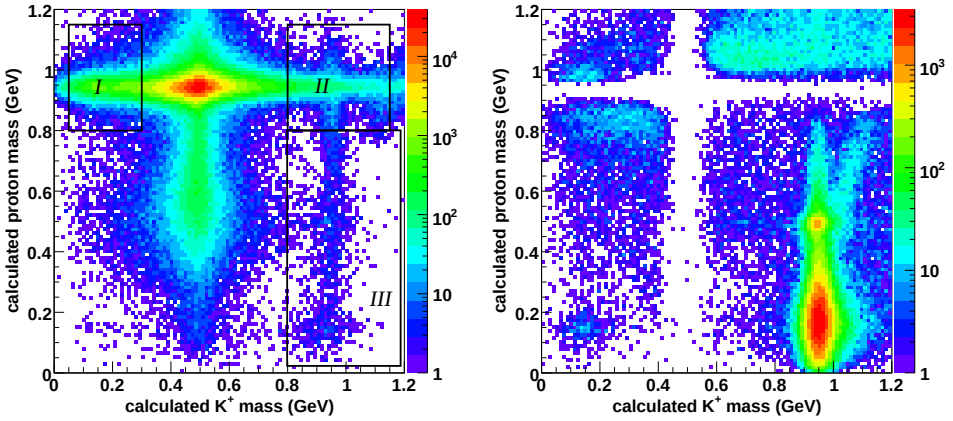

(a) (b)

Figure 3.8: Calculated masses after the PID cut for the cumulative skimmed $K^+\Sigma^0$ three-track dataset: (a) events passing the cut. Regions marked as "I" and "II" here contain possible $\pi^+ p$ and $p\,p$ background respectively which survive the cut (see Fig. 3.9). Region "III" is also retained at this point (see text). (b) events rejected by the cut.

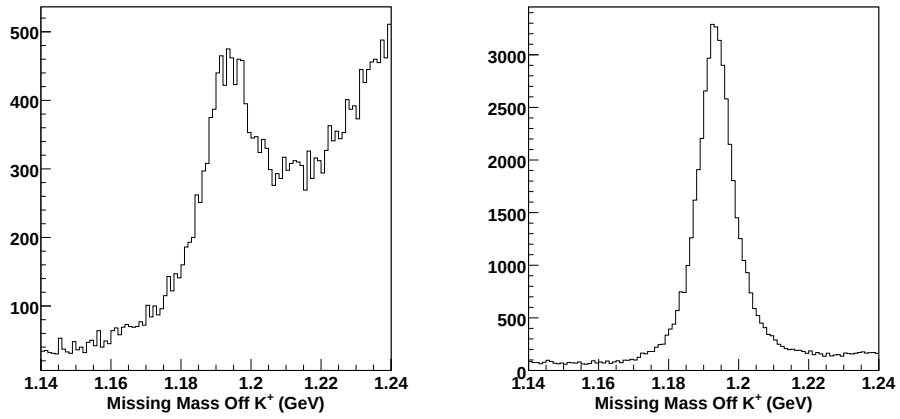

(a) (b)

Figure 3.9: Missing Mass off K^+ for events in regions "I" and "II" from Fig. 3.8a: (a) Region "I" $-$ π^+p background mostly (b) Region "II" $-$ possible pp background. There is sufficient signal in both regions to not throw them away completely. The remaining background will be removed by our signal-background separation method.

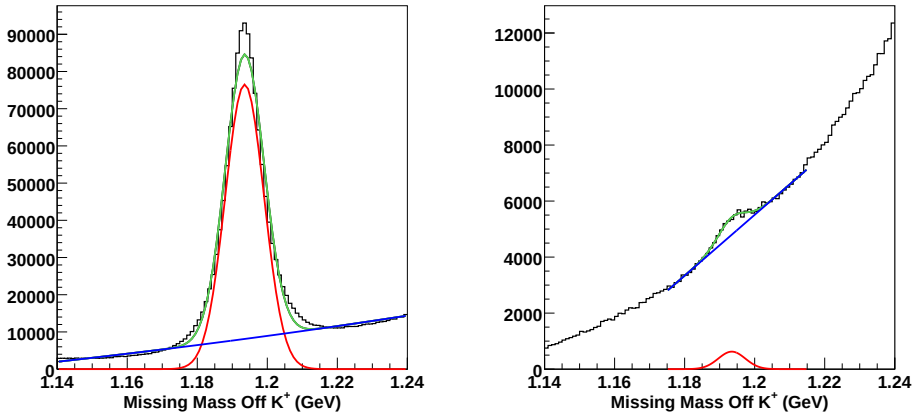

(a) (b)

Figure 3.10: PID uncertainty for the $K^+\Sigma^0$ three-track topology. Fits were to a Gaussian signal (red) plus quartic polynomial (blue). In green is the total fit function. (a) Cumulative skimmed dataset before PID cuts. Estimated signal ∼1.068 million (b) Events rejected by PID cuts. Estimated "signal" being lost due to PID cut ∼6610. The ratio ∼0.62% is the estimated uncertainty in our PID scheme.

total histogram in the range $[\mu - 2.5\sigma, \mu + 2.5\sigma]$, where μ (= 1.1935 GeV) and σ (= 0.005 GeV) are from the signal Gaussian fit. Our signal estimate is thereby found to be ∼1.068 million events.

Next, we fit the distribution of events rejected by the cut. The small signal we are trying to pull out here made the fits sensitive to the starting values of the fit parameters as well as range that the fit was being run over. A good fit was found on running it between 1.175 GeV and 1.215 GeV and is shown in Fig. 3.10b. For this range, the total fit function seems to match the event distribution very well in this case. The estimated signal content is thus found by a 2.5σ integral of the signal Gaussian (μ = 1.1934 GeV, σ = 0.004 GeV) about the mean and amounts to ∼6610 events. The percentage of signal lost by the PID cuts is therefore ∼0.62%. We will quote this as the uncertainty in our PID scheme for the $K^+\Sigma^0$ three-track analysis.

3.6.7 $K^+\Lambda$ Background Removal

Recall from Sec. 3.6.1 that during kinematic fitting, we fit each event to a $K^+p\pi^-$ hypothesis with zero total missing mass. While this is appropriate for $K^+p\pi^-$ events with a missing outgoing photon, events with the same toplogy but with *no* missing particle would also pass the kinematic fit cuts. In the present context, the latter set of events originates from a long $K^+\Lambda$ "tail". There are two kinematic regimes where this occurs more predominantly.

First, note that the higher one goes in $\sqrt{s}$, the higher the momenta of the various decay particles generally get. Momentum resolution in CLAS worsens with increasing particle momenta. Thus, the $K^+\Lambda$ signal peak (at ∼1.115 GeV) widens as we go higher in $\sqrt{s}$ and the $K^+\Lambda$ tail will encroach more and more under the $K^+\Sigma^0$ peak. This effect is clearly visible in going from Fig. 3.11a to 3.11b. Second, the breakup energy (and correspondingly, the breakup angle) of Σ^0 is small (∼77 MeV). This means most of the time the Λ will continue to move in the same direction as the Σ^0 it originates

from. When this opening angle is small enough, the kinematic fitter *can* end up wiggling the various momenta to make a Λ look like a Σ^0. Fig. 3.11c demonstrates this effect. Note that given the information which is supplied to the fitter, this is not a pathology at all but a peculiarity of the kinematics.

Given the above considerations, we expect to see the Λ tail in higher $\sqrt{s}$ and smaller Σ^0 breakup angle regions. Note that for the plots in Fig. 3.11, we have already applied our 1% confidence level (from a kinematic fit to $\gamma p \to K^+ p\pi^-$, zero total missing mass) and PID cuts, which means that neither of these cuts remove the $K^+\Lambda$ background. This was actually a good sign, because the way we tuned these cuts, neither of them were *supposed* to remove $K^+\Lambda$ events in the first place.

The solution to the problem at hand employs the kinematic fitter again. To efficiently skim out the $K^+\Lambda$ events, we can fit every event which we included in our skim to $\gamma p \to K^+ p\pi^-$ with *nothing missing* − that is, we fit to every component of the missing 4-momenta being zero. This is a much tighter 4-C fit than fitting to a zero total missing mass (a 1-C fit). Real $K^+\Sigma^0$ events have near-zero confidence level to this fit while $K^+\Lambda$ events would have evenly distributed confidence levels over the range $(0, 1]$. Fig. 3.11d demonstrates this, where we have plotted the confidence level from $\gamma p \to K^+ p\pi^-$ (nothing missing) fit against missing mass off K^+. The higher confidence level region corresponds to the $K^+\Lambda$ tail. We can thus effectively remove the $K^+\Lambda$ background by rejecting events with confidence level (from a kinematic fit to $\gamma p \to K^+ p\pi^-$, nothing missing) greater than 0.1% (Fig. 3.11(e)). The effect of the cut is shown in Fig. 3.11(f) − our cut is remarkably efficient in skimming out the $K^+\Lambda$ background with minimal signal loss (the blue histogram in 3.11f for events rejected by the cut, representing a long $K^+\Lambda$ tail, shows no sign of a Σ^0 peak).

Note that to accentuate the effect of the $K^+\Lambda$ background we have used events only with higher $\sqrt{s}$ (between 2.7 and 2.84 GeV) for the plots shown in Fig. 3.11b through 3.11f.

3.7 Event Selection − $K^+\Sigma^0$ two-track topology

3.7.1 "Dalitz" Cut

Consider the decay chain $\Sigma^0 \to \Lambda\gamma \to p\pi^-\gamma$, treating it as an overall three-body decay. In the standard "Dalitz" analysis of a three-body decay $M \to m_1 m_2 m_3$, for a given value of the invariant mass m_{12}, m_{23} is bound between

$$\left(m_{23}^2\right)_{max} = \left(E_2^* + E_3^*\right)^2 - \left(\sqrt{E_2^{*2} - m_2^2} - \sqrt{E_3^{*2} - m_3^2}\right)^2 \quad \text{and} \tag{3.9a}$$

$$\left(m_{23}^2\right)_{min} = \left(E_2^* + E_3^*\right)^2 - \left(\sqrt{E_2^{*2} - m_2^2} + \sqrt{E_3^{*2} - m_3^2}\right)^2, \tag{3.9b}$$

where

$$E_2^* = \left(m_{12}^2 - m_1^2 + m_2^2\right)/2m_{12} \quad \text{and} \tag{3.10a}$$

$$E_3^* = \left(M^2 - m_{12}^2 - m_3^2\right)/2m_{12}. \tag{3.10b}$$

In our case, if we assign M as Σ^0, m_1 as p, m_2 as π^-, m_3 and γ, m_{12} is the $(p\pi^-)$ mass corresponding to the Λ mass. Then m_{23} is the invariant $(\pi^-\gamma)$ mass, which is also the total missing mass $MM\,(pK^+)$ for the two-track topology. Substituting the physical values of the masses, we find the condition:

$$0.176 \text{ GeV} \leq m_{23} \leq 0.251 \text{ GeV}. \tag{3.11}$$

We call a cut based on this requirement, a "Dalitz" cut.

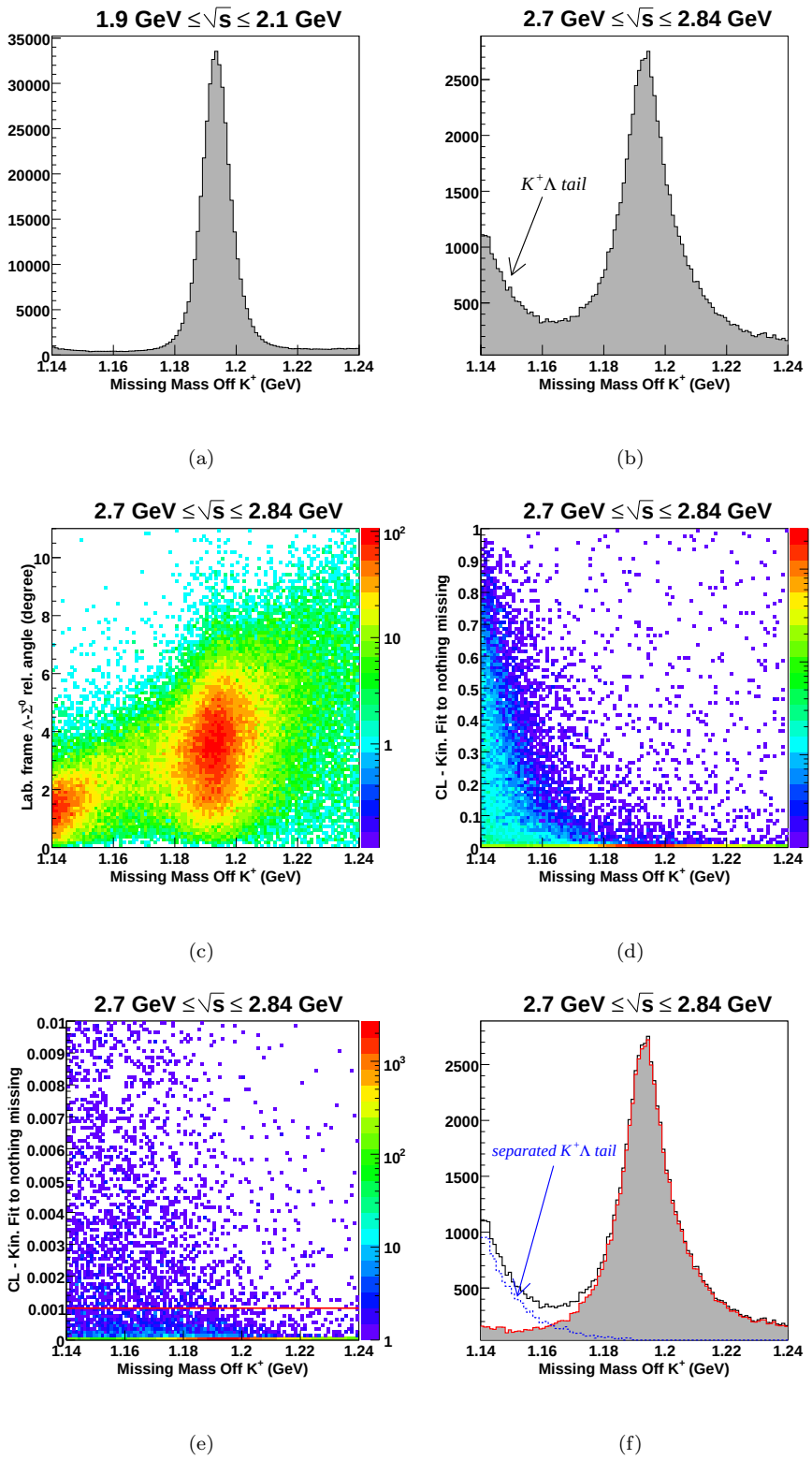

Figure 3.11: $K^+\Lambda$ background removal ($K^+\Sigma^0$ three-track topology): the $K^+\Lambda$ tail is more prominent at higher $\sqrt{s}$ (compare (a) and (b)) and smaller relative angle between Σ^0 and Λ (from (c)). (d) and (e) show the 0.1% CL cut we make (red horizontal line in (e)) and (f) shows the efficiency of the cut. See text for details.

3.7.2 Initial Skim

Our event selection for the two-track topology follow the general itinerary set up earlier for the three-track case. We choose events of the type "$+:+$" having at least two positively charged tracks. We then make the *physics hypotheses* "$p:K^+$" and "$K^+:p$" for these two tracks, looping over all possible combinations. The event and the K^+ vertices are set as for the three-track case, but since information on the π^- track is unavailable, we are not able to locate the Λ decay vertex any longer. As our next best approximation, we set the p vertex as the event vertex. Energy, momentum and tagger corrections are then applied corresponding to each hypothesis.

Since both the outgoing photon and the π^- momenta remain unknown, we can not avail of the kinematic fitter. For our initial *skim*, we place the following four cuts:

1. missing mass off K^+ between 1.14 GeV and 1.3 GeV,
2. calculated mass of p between 0.3 GeV and 1.2 GeV,
3. calculated mass of K^+ between 0.2 GeV and 0.85 GeV and
4. total missing mass between 0.15 GeV and 0.28 GeV.

These cuts are intentionally kept loose at this stage to keep the loss of good events at a minimum. Cut (4) corresponds to the "Dalitz" cut after allowance for energy-momentum resolution. Fig. 3.13 shows the signal shape, calculated masses and total missing mass in the cumulative skimmed dataset. The total number of events which pass the skim is ~ 6.4 million.

3.7.3 Particle Identification − 2-D Calculated Mass and "Dalitz" Cut

Our first PID cut consists of a 2-D cut on the calculated masses of the hypothesized K^+ and p tracks. The cut is shown in Fig. 3.12a − events lying outside the quadruplet of black lines are removed. The second cut we employ is a "Dalitz" cut, accepting events only that satisfy the criterion:

$$0.16 \text{ GeV} \leq MM\left(pK^+\right) \leq 0.265 \text{ GeV}. \tag{3.12}$$

The two limits are marked by the two horizontal lines in Fig. 3.12c. The cut limits are kept looser than given in Eq. 3.11 to account for momentum resolutions. Fig. 3.12b and 3.12d show the effect of the calculated mass and Dalitz cuts individually.

Fig. 3.13 shows the combined effect of both cuts (the histograms include around a third of the full 2-track dataset). The black histogram is the skimmed dataset. In green are events that pass the calculated mass cut. Events retained after a subsequent application of the Dalitz cut appears in red. The blue histogram shows the events that fail either cut. The estimated "signal" for the skimmed dataset and for events failing the PID cuts are ~ 2.28 million and $\sim 41,738$ respectively. Thus the upper limit on the signal loss due to the PID cuts is $\sim 1.8\%$. We quote this as our PID error for the two-track topology.

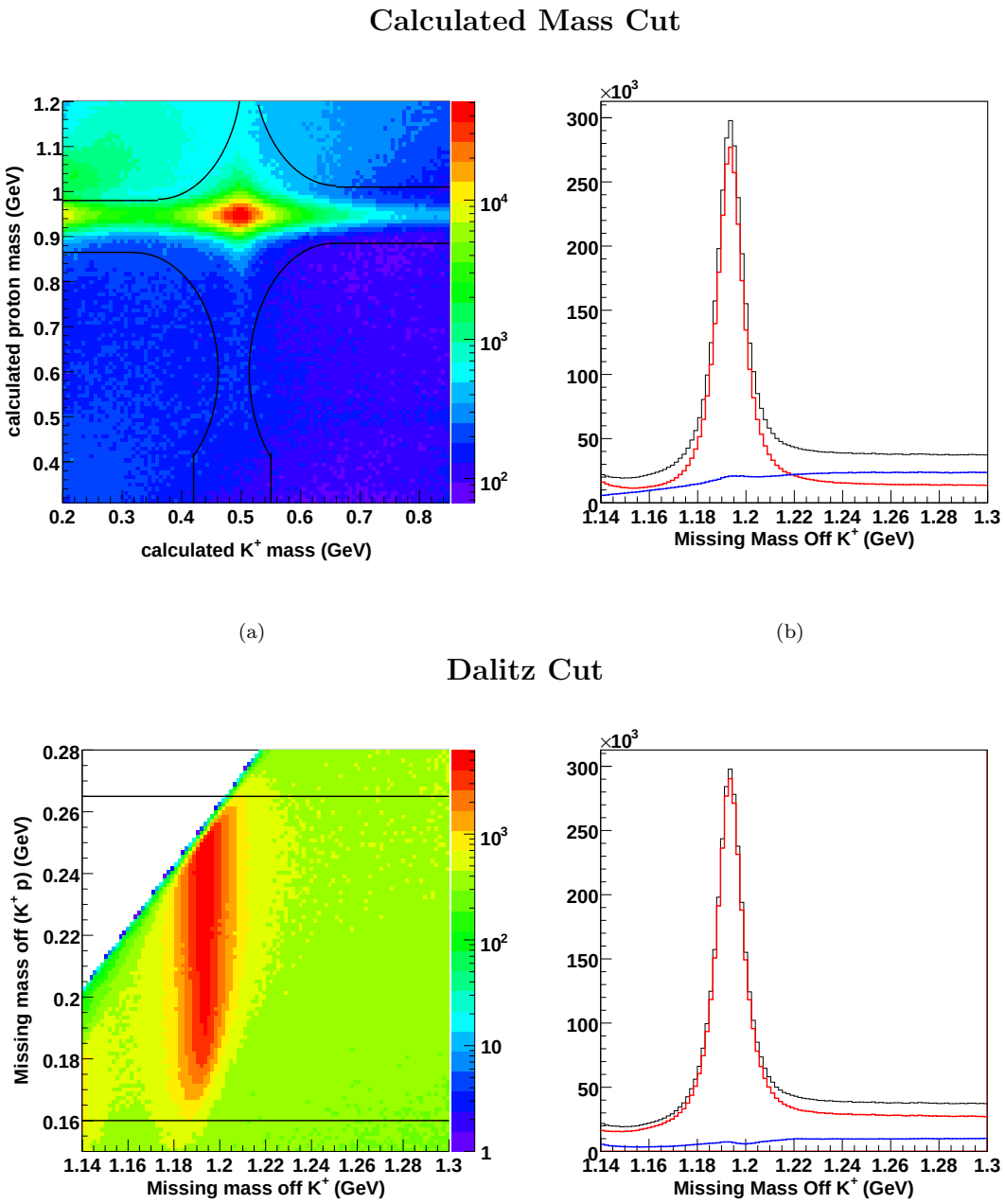

Figure 3.12: PID cuts on the skimmed $K^+\Sigma^0$ two-track dataset: (a) Calculated masses for proton and the kaon. Events lying outside the quadruplet of black lines are rejected. (b) Effect of the calculated mass cut – the black histogram is the original skimmed dataset, in red are the accepted events and in blue are the rejected events. (c) Total missing mass (which, for real $K^+\Sigma^0$ events, should correspond to the invariant $(\pi^-\gamma)$ mass) plotted versus missing mass off K^+. The two horizontal lines show the "Dalitz" cut – only events lying in between the two lines are kept. (d) Effect of the Dalitz cut – black histogram is the original skimmed dataset, in red are the accepted events and in blue are the rejected events.

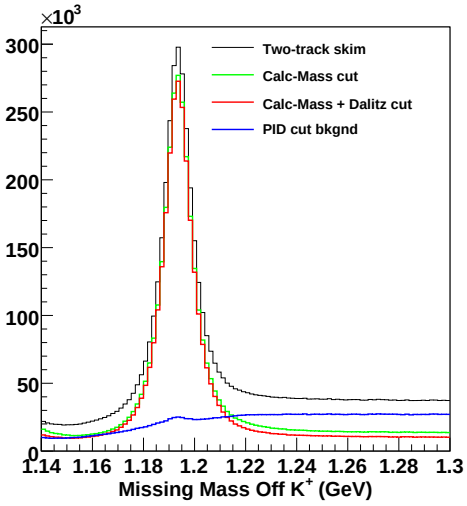

Figure 3.13: $K^+\Sigma^0$ two-track topology, PID cuts: green histogram shows just the calculated mass cut. Red histogram shows the effect of subsequently applying the Dalitz cut. The blue histogram is the background removed after both cuts are applied. Total signal loss is $\sim 1.8\%$.

3.8 Event Selection – ϕp Charged-mode Topology

3.8.1 Kinematic Fitting of $\gamma p \to K^+(K^-)p$

For the charged-mode, the first step in the event selection process is a kinematic fit to $\gamma p \to K^+(K^-)p$. This is a 1-C fit to total missing mass $m_{K^-} = 0.493$ GeV with the K^- 4-momentum reconstructed as the total missing momentum. As always, both combination of proton and K^+ assignments to the two positively charged tracks were looped over. To save computation time, we placed an initial *extremely* loose constraint of $|MM(p) - 1.019| \leq 0.5$ GeV to select out possible ϕ events. Fig. 3.14a shows the confidence level distribution. To avoid an overwhelming amount of background, we have placed an additional $|MM - 0.493 \text{ GeV}| \leq 100$ MeV cut here (this is only for illustrative purposes and was not used during the actual kinematic fitting). Fig. 3.14b shows the effect of placing a 10% confidence level cut. The red histogram shows the $MM(p)$ distribution after the cut and the blue histogram shows the events rejected by the cut.

To facilitate further analysis, a "skimmed" ϕ dataset was formed by applying the 10% confidence level cut and two additional calculated mass cuts of 0.4 GeV $\leq m_{calc,p} \leq$ 1.2 GeV and 0.2 GeV $\leq m_{calc,K^+} \leq$ 0.8 GeV. The dataset was binned in $\sqrt{s} = 10$ MeV-wide energy bins after this.

3.8.2 Particle Identification – Timing Cuts

Fig. 3.15a shows the Δtof distribution for the two positively tracks hypothesized as proton and K^+, for the entire skimmed dataset. The preliminary timing cut we apply is the "iron-cross" cut, shown by the quadruplet of black curves. This cut was described earlier in Sec. 3.6.5 and is an *extremely* loose cut. Fig. 3.15b shows the effect of applying the iron-cross cut. The blue histogram represents the events removed by the cut and the red histogram are events passing the cut; there is hardly any signal loss at this point. However, there is still a preponderance of pion background, as shown

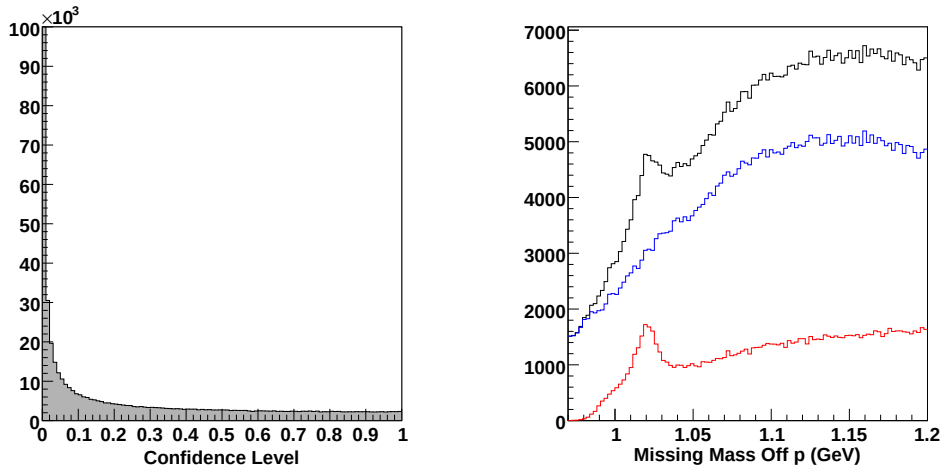

(a) (b)

Figure 3.14: Kinematic fit to $\gamma p \rightarrow K^+(K^-)p$ for the ϕp charged-mode topology: (a) shows the confidence level distribution and (b) shows the effect of placing a 10% confidence level cut. In blue are the events rejected and in red are the events accepted by the cut. All events belong to the runs 43800-43839.

by plotting the calculated masses of the proton and K^+ tracks (*after* application of the iron-cross cut) in Fig. 3.15c. To further reduce this significant pion background, we have chosen to place an additional two-dimensional cut on the calculated masses. This is shown by the two black curves in Fig. 3.15c where events on the left side of the "pinch" are removed. The "pinch" shape has been tuned to remove as much of the pion background as possible, while keeping signal loss at a minimum. Finally, we also place a hard cut on the calculated masses of the proton as:

$$0.8 \text{ GeV} \leq m_{calc,p} \leq 1.1 \text{ GeV} \tag{3.13}$$

The progressive effect of the two timing cuts are shown in Fig. 3.15d. The black histogram is the full skimmed dataset. The green histogram represents the events surviving the iron-cross Δtof cut and the red histogram, those after both the iron-cross and the two-dimensional calculated mass cuts have been applied. The blue histogram represents the cumulative events rejected by our timing cuts (Δtof and calculated mass cuts applied in succession). Figs. 3.16a and 3.16b show fits to the cumulative yield prior to the timing cuts and set of events rejected by the cuts. The signal function used in the fit is a Voigtian with a mass-dependent Breit-Wigner width and the background function has been taken to be of the ansatz (a suitable polynomial function would also work):

$$f(x) = a\sqrt{x^2 - 4m_K^2} + b(x^2 - 4m_K^2), \tag{3.14}$$

since $MM(p) = 2m_K$ is the threshold for the $\phi \rightarrow KK$ decay (see also Ref. [59]). The estimated signal loss due to the timing cuts is $\sim 4.2\%$. We will quote this as the upper limit of the systematic uncertainty due to the timing cuts for the the ϕp charged-mode topology.

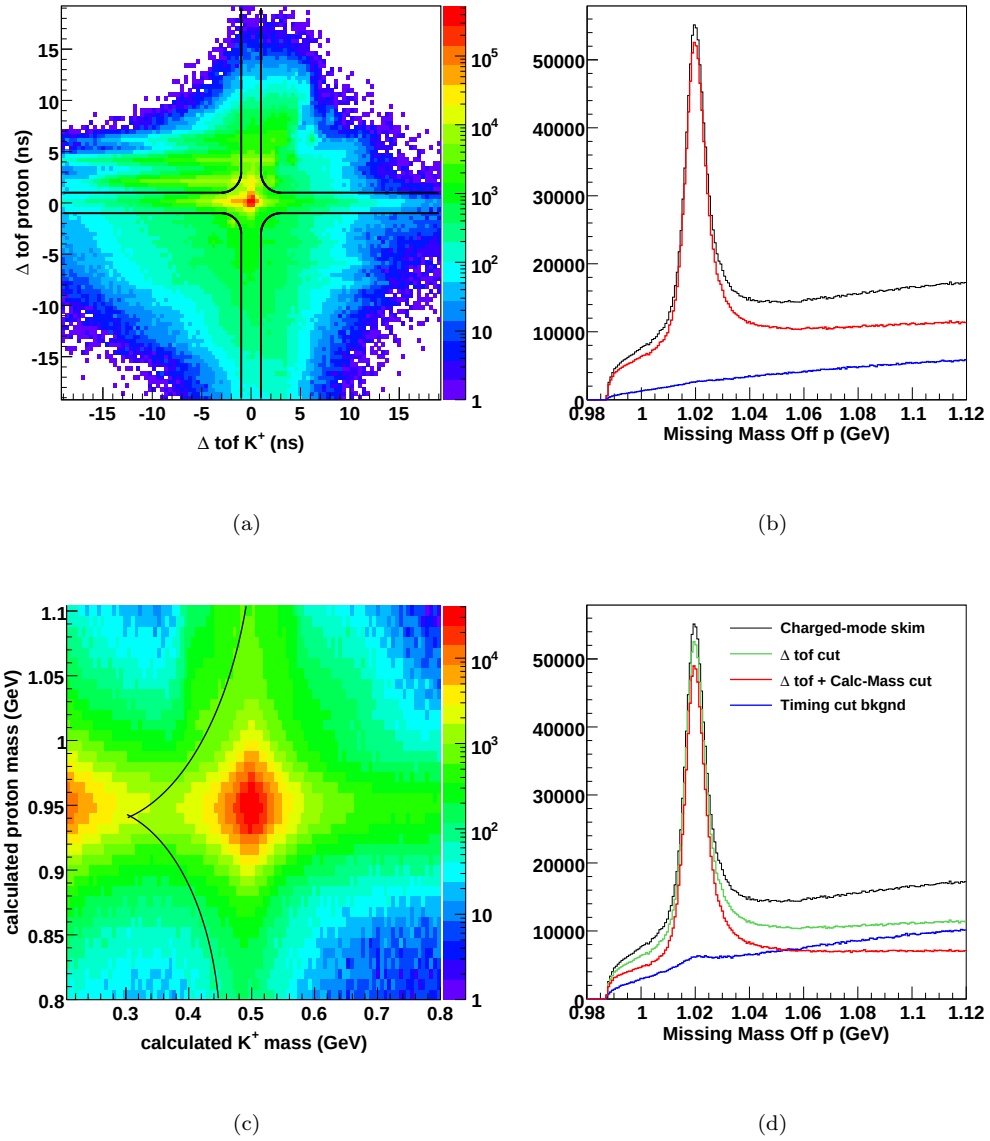

Figure 3.15: Timing cuts for the ϕ charged-mode topology: (a) shows the Δtof distribution for proton and K^+ for the entire skimmed dataset. The "iron-cross" cut is shown by the quadruplet of black lines; events outside the iron-cross are removed. The effect of this cut is shown in (b) where the red and blue histograms are the events accepted and rejected by the cut, respectively. (c) shows the calculated mass distribution *after* the iron-cross cut has been placed; there is a significant amount of remnant pion background which is removed by rejecting events on the left side of the "pinch-shaped" doublet of black curves. Events with the proton calculated mass higher than 1.1 GeV or lower than 0.8 GeV are also removed. (d) shows the progressive effect of applying the two-step timing (Δtof and calculated mass) cuts. The blue histogram represents events rejected by this two-step timing cut.

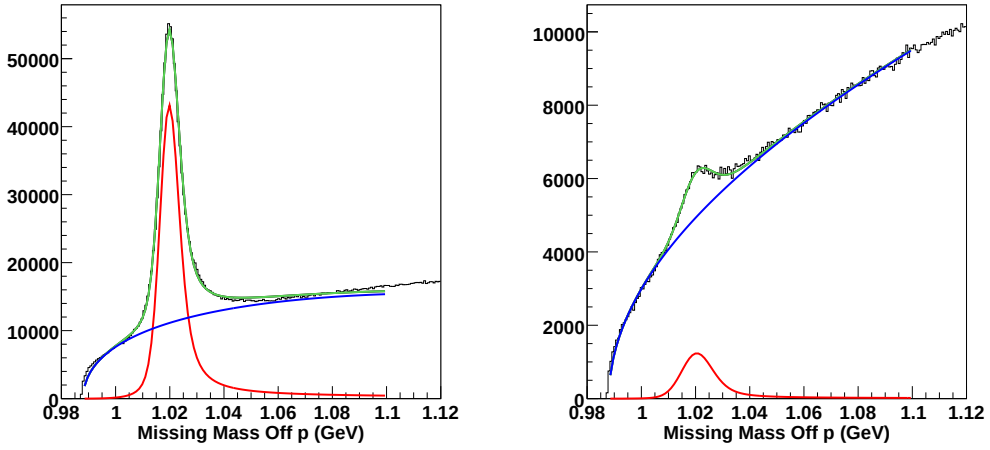

(a) (b)

Figure 3.16: The estimated signal in the $MM(p)$ distribution prior to the timing cuts is ~ 713380 events and in that rejected by the timing cuts is ~ 29965. The percentage signal loss is ~ 4.2.

3.8.3 $\Lambda(1520)$ Cut

Consider the reaction chain $\gamma p \to K^+\Lambda(1520) \to K^+K^-p$. Since the final-state particles in this reaction are the same as in the ϕp charged-mode topology, the two reactions can overlap in certain regions of phase space. For further insight, we look back at our $K^+\Sigma^0$ "Dalitz" cut discussion in Sec. 3.7.1. In Eq. 3.10b, if we put $M = \sqrt{s}$, $m_1 = m_{K^+}$, $m_2 = m_{K^-}$, $m_{12} = M(K^+, K^-) = m_\phi$ and $m_3 = m_p$, we obtain a $\sqrt{s}$ dependent constraint on the minimum and maximum values of $m_{23} = M(K^-, p)$. Fig. 3.17a shows the variation of the $m_{23}(\sqrt{s})$ limits with $\sqrt{s}$, where $M(K^-p) = 1.52$ GeV is shown by a horizontal dashed line in red. Therefore, in the region roughly corresponding to 2.0 GeV $\leq \sqrt{s} \leq$ 2.2 GeV, the $K^+\Lambda(1520)$ and ϕp channels can kinemtically overlap in phase space.

In the region of overlap, if the $K^+\Lambda(1520)$ background does not interfere with ϕp production process, our background subtraction procedure (Sec. 3.12) should be able to remove the $K^+\Lambda(1520)$ events under the ϕ mass peak. If, however the $K^+\Lambda(1520)$ and the ϕp channels do interfere, then the situation becomes more complicated. To study this effect, we can apply a hard cut around the $\Lambda(1520)$ mass as $|M(K^-, p) - 1.52 \text{ GeV}| \leq \delta$ and the width δ can be varied as 10, 15, or even 20 MeV.

3.9 Event Selection – ϕp Neutral-mode Topology

3.9.1 Kinematic Fitting of $\gamma p \to p\pi^+\pi^-(K^0_L)$

For the neutral-mode topology, a kinematic fit to $\gamma p \to p\pi^+\pi^-(K^0_L)$ was first performed. This was a 1-C fit to total missing mass $m_{K^0} = 0.497$ GeV with the K^0_L 4-momentum reconstructed as the total missing momentum. The K^0_S was reconstructed as the sum of the π^+ and π^- 4-momenta and both combination of proton and π^+ assignments to the two positively charged tracks were looped

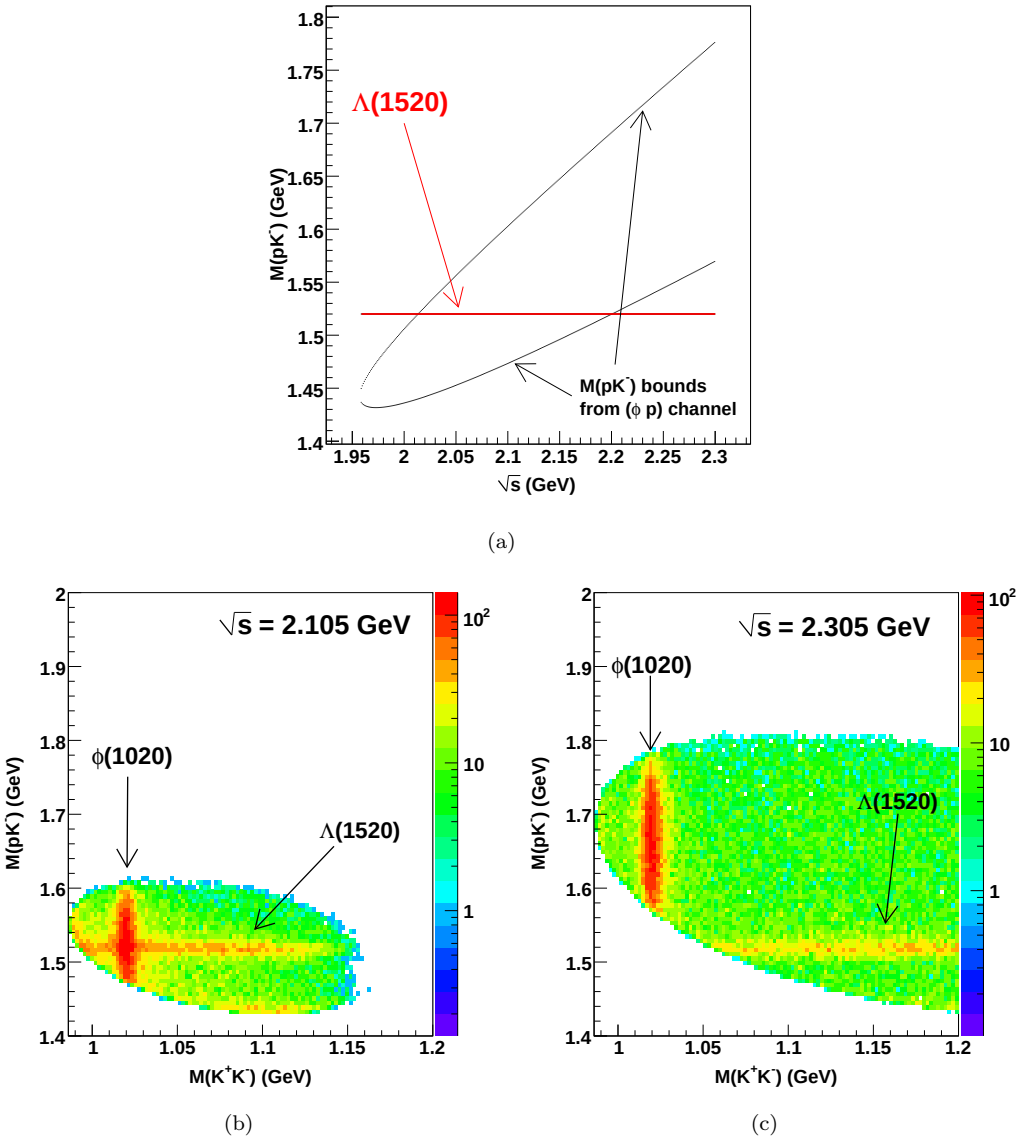

Figure 3.17: In the process $\gamma p \to \phi p \to K^+K^-p$, the invariant mass $M(K^-p)$ is constrained to lie between the two black curves as shown in (a), depending on $\sqrt{s}$. Between 2.0 GeV $\leq \sqrt{s} \leq$ 2.2 GeV, $M(K^-p) = 1.52$ GeV falls within these limits and the ϕp and $K^+\Lambda(1520)$ channels are kinematically allowed to overlap in phase space. (b) shows $M(K^-p)$ *vs.* $MM(p)$ in the overlap region, while (c) shows the same in a region where the $\Lambda(1520)$ and ϕ are separated.

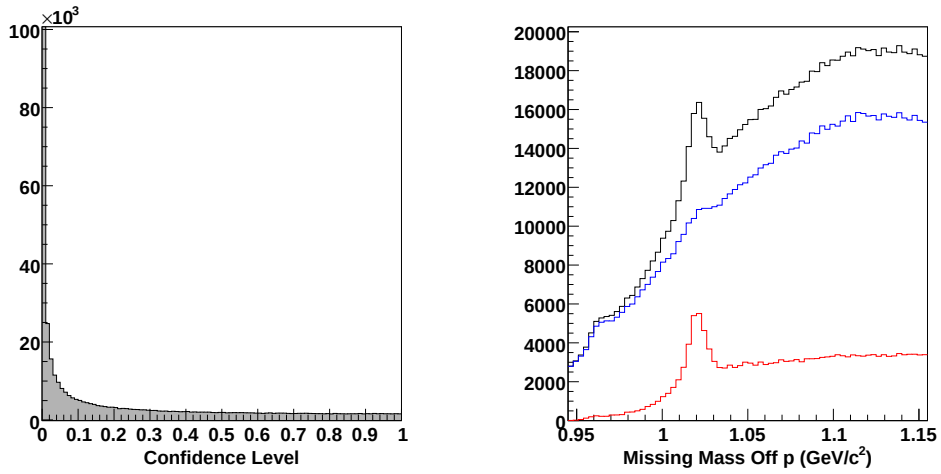

(a) (b)

Figure 3.18: Kinematic fit to $\gamma p \to p\pi^+\pi^-(K_L^0)$ for the ϕ neutral-mode topology: (a) shows the confidence level distribution and (b) shows the effect of placing a 10% confidence level cut. In blue are the events rejected and in red are the events accepted by the cut.

over. The confidence level distribution is shown in Fig. 3.18a. Fig. 3.18b shows the effect of a 10% confidence level cut. The blue histogram are the events rejected and in red are the events that passed the cut.

3.9.2 Timing Cuts

Given that the neutral-mode was a three-track topology, in conjunction with the inherently low statistics for the ϕp channel, we employed PID cuts that were as loose as possible. Fig. 3.19a shows the Δtof_{proton} plotted against Δtof_{π^+} for the entire skimmed neutral-mode dataset along with the "iron-cross" cut described earlier in Sec. 3.6.5. The effect of applying this cut is shown in Fig. 3.19b. Events that passed the cut are in red, while those rejected are in blue. The latter shows no sign of a peak around $MM(p) = 1.019$ GeV, depicting the fact that the cut was extremely loose.

3.9.3 K_S^0 Selection Cut

Fig. 3.20a shows the invariant $M(\pi^+\pi^-)$ mass spectrum of the skimmed ϕp neutral-mode dataset, after the application of the timing cuts. The peak around 0.5 GeV represents the K_S^0 mass. Fig. 3.20b shows the distribution of $M(\pi^+\pi^-)$ with $MM(p)$. The dot-dashed lines in Figs. 3.20a and 3.20b show the boundaries of a 0.488 GeV $\leq M(\pi^+\pi^-) \leq$ 0.508 GeV K_S^0 selection cut. Fig. 3.20c shows the effect of this cut – the red histogram represents events that pass the cut, while the blue histogram are events that fail the cut.

To estimate the amount of signal lost due to this cut, we fit the original $MM(p)$ distribution prior to applying the cut and that of the events removed by the cut, to a mass-dependent Voigtian plus a general quartic background. These are shown in Figs. 3.21a and 3.21, respectively. To accentuate the effect of the final cut-limits, we have also applied a loose 0.47 GeV $\leq M(\pi^+\pi^-) \leq$ 0.53 GeV

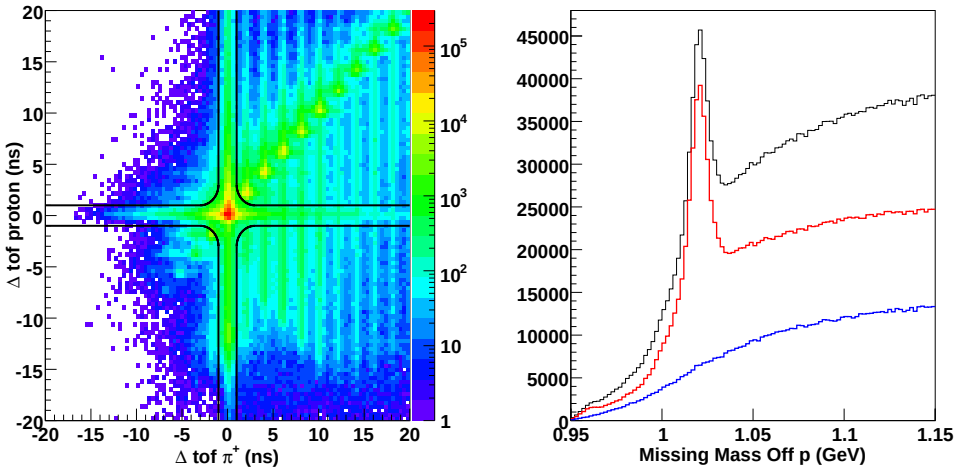

(a) (b)

Figure 3.19: Timing cuts for the ϕp neutral-mode topology: (a) shows the "iron-cross" cut on proton-π^+ Δtof distribution. The effect of the cut is shown in (b). The rejected events in blue hardly show any sign of a peak at $MM(p) = 1.019$ GeV, since the cut was very loose. The set of events that passed the cut is shown in red.

cut for these plots. The estimated signal (by integrating the signal Voigtian function) before the cut is $\sim 190,000$ and that removed by the cut is $12,500$, a roughly 6.5% estimated loss in signal. However, we note that the same cut is also applied to the Monte Carlo, with a comparable signal loss (see Sec. 4.7). Therefore, as a reasonable *upper-bound* on the systematic uncertainty due this cut, we quote 5% as the systematic uncertainty in our K^0_S selection cut.

3.10 Detector Performance Cuts

A crucial part of our analysis depended on how well we understand the acceptance of the CLAS detector. Our acceptance calculations employed Monte Carlo $K^+\Sigma^0/\phi p$ events and GSIM, a GEANT based simulation of the CLAS detector, as described in the next chapter. At this point, we simply note that if there are regions, or particular elements, of the detector which were not well understood, to allow a reliable acceptance calculation, they had be removed from our analysis. This section deals with these types of cuts that went into our analysis.

3.10.1 Minimum Proton Momentum Cut

Slow moving protons, because of greater susceptability to interactions with the detector material, were difficult to model accurately. Studies by Matt Bellis, a then post-doctoral researcher at CMU compared the acceptance of the data and Monte Carlo, both of which were calculated empirically using the $\gamma p \to p\pi^+\pi^-$ channel.

For example, one could require only a π^+ and a π^- to be detected and kinematically fit to a missing proton. For events passing this fit with a high enough confidence level, one could then cross check whether a proton was *actually* detected in the correct sector in CLAS or not. Using a large

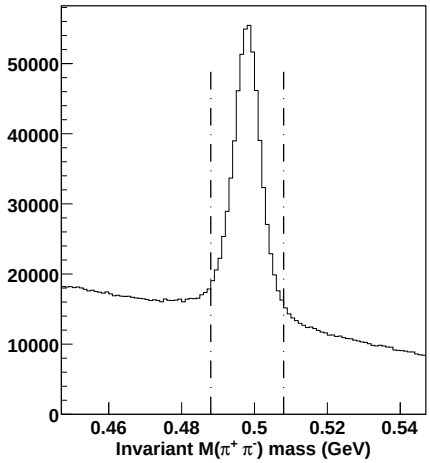

(a)

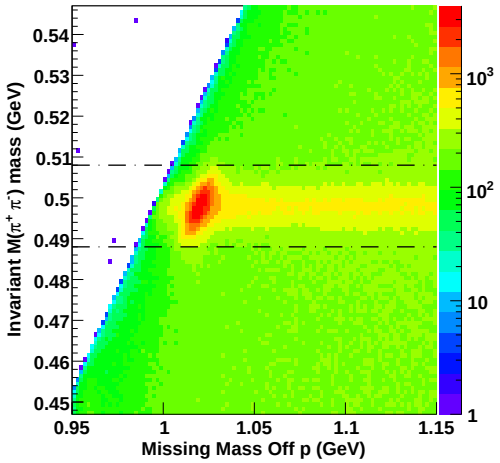

(b)

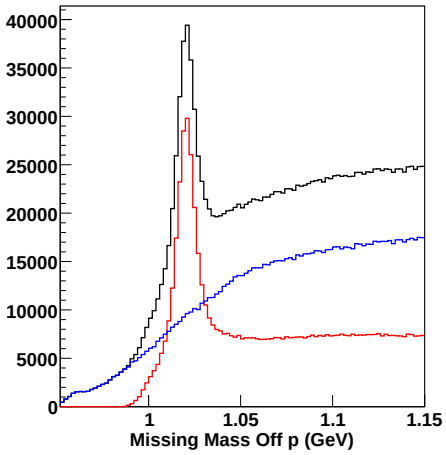

(c)

Figure 3.20: K^0_S selection cut for the ϕp neutral-mode after application of timing cuts: (a) shows the K^0_S peak and (b) shows the $m_{K^0_S}$-m_ϕ distribution. (c) shows the effect of a 0.488 GeV $\leq m_{K^0_S} \leq$ 0.508 GeV K^0_S cut, where the red histogram shows the events passing the cut and the blue histogram shows those that failed the cut. The cut boundaries are shown by the dot-dashed lines in (a) and (b).

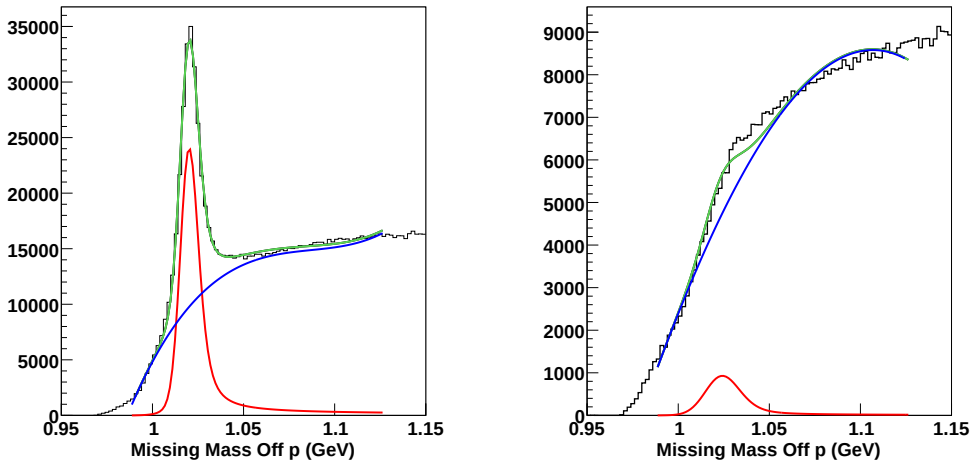

(a) (b)

Figure 3.21: Signal loss due to K^0_S selection cut in the ϕp neutral-mode topology: (a) and (b) show fits to the $MM(p)$ distrubutions prior to applying the cut and the events rejected by the cut, respectively, in Fig. 3.20c. The signal, background and total fit functions are in red, blue and green, respectively. The signal loss is estimated to be $\sim 6.5\%$.

enough sample of events, the acceptance of each particle type could be calculated in each kinematic region of the detector in this way. This was carried out both for the Data and the Monte Carlo, upon which we defined the *acceptance assymmetry* in the following manner

$$A = \frac{|\mathcal{A}_{data} - \mathcal{A}_{mc}|}{\mathcal{A}_{data} + \mathcal{A}_{mc}}, \tag{3.15}$$

where $\mathcal{A}_{data}, \mathcal{A}_{mc}$ were the acceptances of the data and Monte Carlo respectively. In regions where this was near zero, we could claim to have been reliably modeled the acceptance.

Fig. 3.22 shows A for protons, plotted as a function of the magnitude and direction of the track momentum. In most areas, A was found to be close to zero, signifying good agreement betwen the real data and the Monte Carlo. Two regions where problems are evident, are forward-angle track and low momentum track regions. The former region were to be removed by our fiducial cuts as discussed below while the latter, we cut out by placing a minimum proton momentum cut at 375 MeV.

3.10.2 Fiducial Cuts

The acceptance study from the previous section also led to the need for removing events with tracks going into certain regions of the detector. For example, near the superconducting torus coils, the magnetic field varies too rapidly to be properly modeled by GSIM. Events with any track going into these regions will thus be removed from this analysis. This effect is most prominent in the forward direction where the coils occupy a greater amount of space. Similarly, CLAS has a hole in the very forward direction (the beam dump). We thus place a hard cut in the forward direction for tracks with $\cos\theta_{lab} \geq 0.985$. CLAS is also limited in detecting very backward angle tracks to accomodate

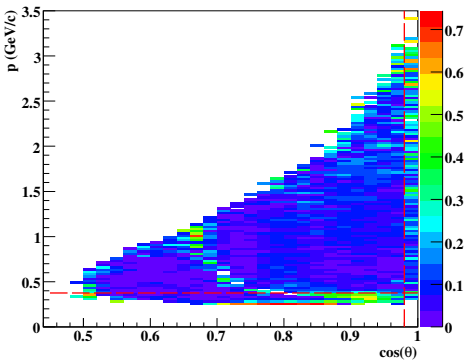

Figure 3.22: Acceptance asymmetry defined in Eq. 3.15 plotted as a function of 3-momentum magnitude p and $\cos\theta$ for protons in Matt Bellis' acceptance study. The curved band of large asymmetries was due a problematic 11^{th} TOF counter in sector 3 which was removed from this analysis. The vertical dashed line at $\cos\theta = 0.985$ shows a hard fiducial cut placed on foward going tracks. The horizontal dashed line at $p = 375$ MeV indicates the minimum proton momentum cut that we employed.

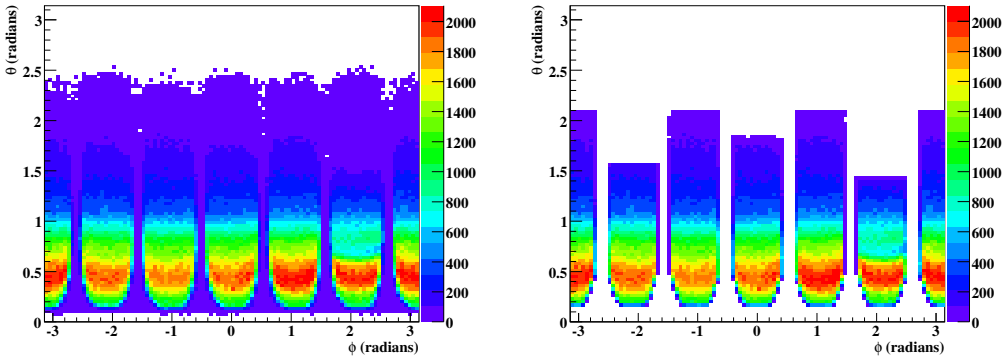

(a) (b)

Figure 3.23: Fiducial cuts: (a) All tracks in run 43582 (three-track dataset). (b) Tracks which pass our fiducial cuts for the same run. Note that the effect of the cuts is most dramatic at the sector boundaries and the forward-angle regions where the torus coils occupy a large fraction of the available space.

Sector	Removed Paddles	
	configuration I	configuration II
1	18, 26, 27, 33	18,23,26,27,33
2	none	23
3	11, 24, 25	11,23
4	26	23,26
5	20, 23	20,23
6	25, 30, 34	23,25,30,34

Table 3.3: The two configurations of removed problematic TOF paddles studied during this analysis. Configuartion II has the 23rd paddle removed in all the sectors and was used for the $K^+\Sigma^0$ results, while the ϕp results use configuration I. See text for more details.

space for the incoming beam. There is a sector-dependent backward angle cut to account for this. Finally, fiducial cuts remove events with any track having an unphysical sector or TOF paddle index assigned to it due to some glitch at the time of recording. The results of the fiducial cuts are shown in Fig. 3.23.

3.10.3 Problematic TOF Paddle Removal

There are also certain *specific* TOF paddles which we remove from our analysis. These problematic paddles are known to cause discrepancies in the occupany distribution between the Data and the Monte Carlo. Note that this is independent of the kind of particle track. For TOF paddles known to have problems, this would show up for protons, pions, kaons, *et al.* A sector-wise list of these TOF paddles is given in Table 3.3. Two different configurations of the set of removed paddles were tried out for this analysis, denoted as configurations I and II in Table 3.3. Configuration I is more or less the "basic" configuration of knocked-out paddles used in previous CLAS analyses [51, 16, 18]. In configuration II, paddle 23 is removed in all six sectors. The 23^{rd} paddle is located at the boundary between the first and second sections of the TOF wall which gives rise to an overlap in the logical output between paddle 23 and 24. For tracks that hit both paddles 23 and 24, tracking is sometimes inconsistent (assigned a default zero value). The effect of the 23^{rd} paddle was studied in detail during systematic checks on $g11a$ (see Ref. [26] and also Sec. 7.4) for the $K^+\Sigma^0$ and $K^+\Lambda$ channels [26]. The overall difference in results from two configurations was found to negligible, although the final results for both the $K^+\Sigma^0$ and $K^+\Lambda$ channels still had the 23^{rd} paddle removed (configuration II). For the ϕp analysis, which was done at a later stage, we reverted back to the more "standard"

Description	$K^+\Sigma^0$ Topology	
	Three-track	Two-track
Confidence level cut	Sec. 3.6.1	–
$K^+\Lambda$ removal cut	Sec. 3.6.7	–
Timing cuts	Sec. 3.6.5	Sec. 3.7.2
Total MM cut	–	Sec. 3.7.3
Fiducial cuts	Sec. 3.10.2	Sec. 3.10.2
TOF paddle knockout	Sec. 3.10.3	Sec. 3.10.3
Final $MM(K^+)$ cut	Sec. 7.5.3	Sec. 7.5.4

Table 3.4: Table of cuts applied to the two topologies for the $K^+\Sigma^0$ channel.

Description	ϕp Topology	
	Charged-mode	Neutral-mode
Confidence level cut	Sec. 3.8.1	Sec. 3.9.1
Timing cuts	Sec. 3.8.2	Sec. 3.9.2
$\Lambda(1520)$ removal cut	Sec. 3.8.3	–
K^0_S selection cut	–	Sec. 3.9.3
Fiducial cuts	Sec. 3.10.2	Sec. 3.10.2
TOF paddle knockout	Sec. 3.10.3	Sec. 3.10.3
Final $MM(p)$ cut	Sec. 3.12.4	Sec. 3.12.4

Table 3.5: Table of cuts applied to the two topologies for the ϕp channel.

configuration I.

3.11 Signal Background Separation

After the application of all our cuts (Tables 3.4 and 3.5), some amount of background still remains. A great deal of effort in the CMU PWA group had gone into devising a signal-background separation technique which suits our needs − both analytically/computationally and physics-wise. Traditionally, background separation has been performed using the side-band subtraction method. That is, one tries to estimate the background under the signal by looking at the side-band regions where there is presumably no signal and only background. The problem with using such a method in our case is two-fold. First, for a reaction like $\gamma p \to K^+\Sigma^0 \to K^+\Lambda\gamma \to K^+p\pi^-\gamma$ with multiple decays and thus multiple independent decay angles, the background will generally depend on the region of phase space one is looking at, because the physics is different in each localized region of phase space. One could bin in, say, $\cos\theta^{K^+}_{c.m.}$ and *then* apply the side-band technique individually for every bin. But again, given that there are multiple independent decay angles, such a process will not suffice. What one needs instead is a technique that simultaneously incorporates *all* the relevent independent decay angles.

Secondly, our partial wave fits are event-based fits using unbinned likelihood fits. Normally for extracting yields for cross sections or assymetries for polarization one employs a binned method where the collective background in a particular bin is what matters, as opposed to an event by event evaluation. Therefore, in our case it is required to have a signal-background separation method at individual event level for the kind of fits we wanted to run.

Inkeeping with the above two considerations, one would ideally want a binary 1 or 0 for every event to be a signal or a background. While this is not possible, we can however assign a *signal probability* to every event by fitting a select group of events lying in the vicinity of the event in question in phase space to a signal plus a background fit function. By making this particluar choice of events close lying together in phase space we are ensuring that that background shape remains roughly similar between all of them. To make the definition of "closeness in phase space" more specific we define the following metric between the i^{th} and j^{th} events

$$g^2_{ij} = \sum_{k=1}^{d} \left[\frac{\xi^i_k - \xi^j_k}{r_k} \right]^2 , \tag{3.16}$$

where $\vec{\xi}$ represents the d independent kinematic angles in phase space and $\vec{r}$ are the corresponding ranges.

For the $K^+\Sigma^0$ three-track case, the angular variables were $\cos\theta^{K^+}_{c.m.}$, $\cos\theta^{\Lambda}_{\Sigma HF}$, $\phi^{\Lambda}_{\Sigma HF}$, $\cos\theta^{p}_{\Lambda HF}$ and $\phi^{p}_{\Lambda HF}$ (the superscript denotes the particular track in question and the subscript denotes the particular frame the angle is being measured in; HF refers to the Helicity Frame, which is loosely the same as the Rest Frame, but defined in Sec. 8.3). Thus, $d = 5$ and $\vec{r} = \{2, 2, 2\pi, 2, 2\pi\}$. For the two-track case, the variables were $\cos\theta^{K^+}_{c.m.}$ and $\cos\theta^{p}_{\Sigma HF}$. Then, $d = 2$ and $\vec{r} = \{2, 2\}$. Once we had defined a metric, we chose N_c events closest to the particular event in question and fit the missing mass off K^+ (denoted simply by m, from now on) distribution for these N_c+1 events to a gaussian signal $\mathcal{S}(m)$ and a suitably chosen background function $\mathcal{B}(m)$. The fits were unbinned likelihood fits ran using different choices of N_c (50, 100, 200) and the background function $\mathcal{B}(m)$. The latter consisted of two parts − a Gaussian centered at the Λ mass (the tail of the Gaussian encroaching into the Σ^0 mass region only matters) and another function which was test run as a linear, a quadratic, a quartic and finally as another Gaussian tail coming from above the Σ^0 mass peak from general pion background.

3.11.1 Q-values and Error Estimation

Once the fit functions $\mathcal{S}_i(m)$ and $\mathcal{B}_i(m)$ for the i^{th} event have been extracted, the event is assigned the following *quality factor* or Q-value as its signal probability

$$Q_i = \frac{\mathcal{S}_i(m_i)}{\mathcal{S}_i(m_i) + \mathcal{B}_i(m_i)}. \tag{3.17}$$

Furthermore, if the N_f fit parameters are denoted by the vector $\vec{\eta}$ and the Covariance matrix from the fit as C_η, we can extract the errors in the Q values as the following

$$\sigma^2_Q = \sum_n^{N_f}\sum_m^{N_f} \frac{\partial Q}{\partial \eta_m}(C^{-1}_\eta)_{mn}\frac{\partial Q}{\partial \eta_n}. \tag{3.18}$$

The use of these errors in yields calculation for differential cross section measurements is described in Sec. 6.6.2.

3.11.2 Application of the Procedure for $K^+\Sigma^0$

Fig. 3.24 shows the signal-background separation as a function of the missing mass off K^+ in three different $\sqrt{s}$ regions for the two topologies. The shaded histograms have each event weighted by its Q-value and represent the extracted signal. The blue histograms use $(1 - Q)$ as the weight, representing the background. The fits were run with $N_c = 200$ and the background as a sum of two Gaussian tails − one $K^+\Lambda$ and the other from a general π^+ background coming from above the Σ^0 mass peak as mentioned earlier. The background estimation seems quite reasonable.

If we weigh each event by its Q-value, the cumulative yield after all our cuts and background separation is $\sim 655,500$ for the three-track topology and 4.64×10^6 for the two-track topology. We will quote these as the number of "good" events for this analysis. The Q-value weighted $\sqrt{s}$ distributions is shown in Fig. 3.25. To check for systematic effects, fits with different N_c's and different background fit functions were run simultaneously. No significant shift in the fit results were observed. For example, with $N_c = 200$ and $\mathcal{B}(m)$ as a sum of a Gaussian (for the $K^+\Lambda$ background tail) and a quartic, the Q-value weighted cumulative yield for the three-track topology was found to be $\sim 653,200$, a less than 1% deviation from the earlier quoted value. A global fit to the same dataset with a Gaussian signal and quartic background also gave a very similar signal yield.

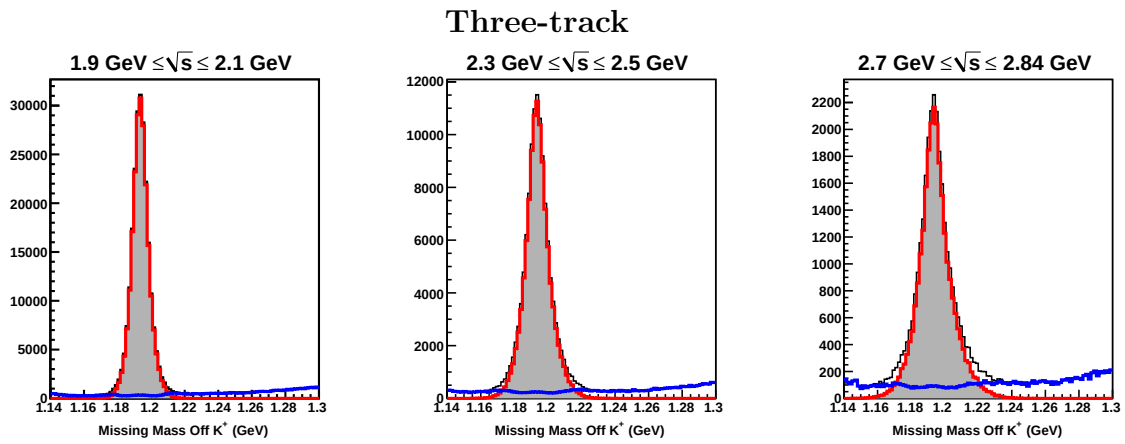

(a)

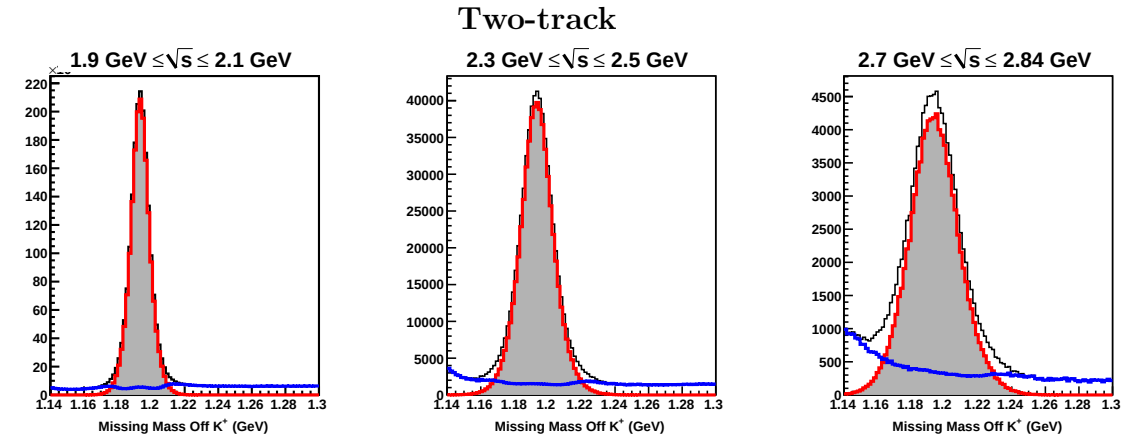

(b)

Figure 3.24: Signal Background Separation in three different $\sqrt{s}$ ranges for the $K^+\Sigma^0$ (a) three-track and (b) two-track topologies. The black histograms are the unweighted distributions. The shaded histograms (bordered in red) are the Q-value weighted distributions representing the signal. The blue histograms are the same distributions but weighted by (1-Q), representing the background.

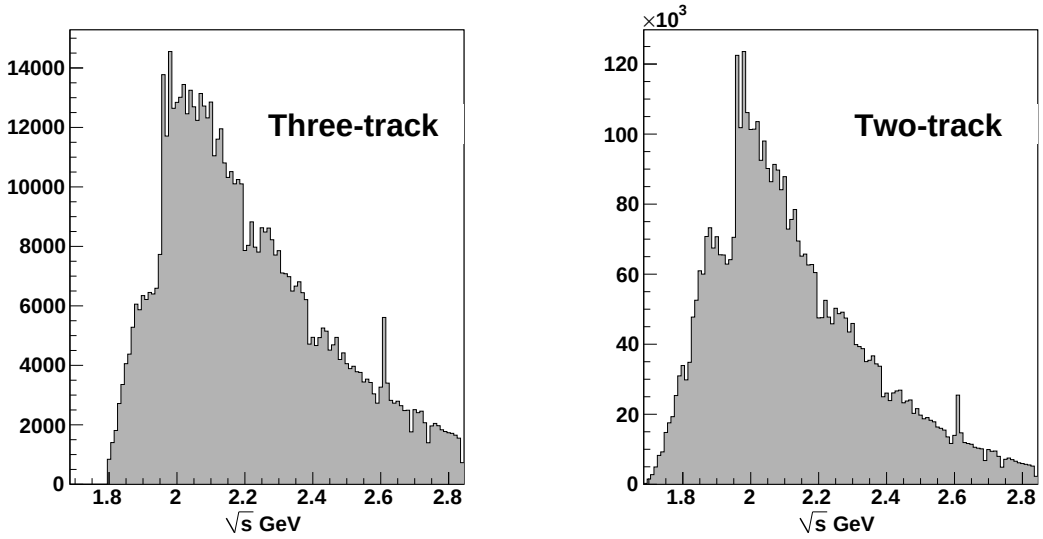

(a) (b)

Figure 3.25: Q-value weighted occupancy as a function of $\sqrt{s}$ for the two topologies. Each $\sqrt{s}$ bin in the x-axes is 10 MeV wide so that the occupancies reflect the signal content in each $\sqrt{s}$ bin where we will extract differential cross sections. The discontinuity near $\sqrt{s} \sim 1.95$ GeV is an artifact of the $g11a$ trigger (see Sec. 4.10.3) while the "hot" region at $\sqrt{s} \sim 2.61$ GeV is due to a discontinuity in the length of the T-counter scintillators. The total number of "good" events after all our cuts and background separation is ~ 0.655 million for the three-track and ~ 4.64 million for the two-track dataset.

3.12 Systematic Study of the Background for ϕp

Since the ϕ lies very close to the edge of the KK production threshold, the background subtraction procedure for the ϕp channel had some unique issues not present in the $K^+\Sigma^0$ analysis. The main problem is that side-band subtraction is not always possible because the $MM(p)$ distribution on the lower side of the ϕ mass peak has very low occupancy. Additionally, the ϕ has a finite signal-width of ~ 4 MeV and strictly speaking, the ϕ line-shape is also not known exactly. Previous ϕ analyses have often employed a Gaussian signal line-shape, which is, at best, an approximation. Here, we try to employ a better approximation by taking the signal function as

$$S(m,\vec{\xi}) = F_s(\vec{\xi})V(m,\mu,\sigma,\Gamma(m)), \tag{3.19}$$

where

$$V(m,\mu,\sigma,\Gamma(m)) = \frac{1}{\sqrt{2\pi}\sigma} Real\left[w\left(\frac{1}{2\sqrt{\sigma}}(m-\mu) + i\frac{\Gamma(m)}{2\sqrt{2}\sigma}\right)\right], \tag{3.20}$$

is the convolution of a Gaussian of width σ and a non-relativistic Breit-Wigner of width $\Gamma(m)$ with mean μ, known as a Voigtian ($w(z)$ is the complex error function) and $F_s(\xi)$ is the unknown kinematic dependence of the signal distribution. The set of angular variables were chosen as $\vec{\xi} = \{\cos\theta^{\phi}_{c.m.}, \cos\theta^{K}_{Hel}, \phi^{K}_{Hel}\}$ where θ^{K}_{Hel} and ϕ^{K}_{Hel} describe the $\phi \to KK$ decay in the helicity frame, and m is the ϕ mass variable, $MM(p)$.

Note that the Breit-Wigner width $\Gamma(m)$ is mass dependent. The $\phi \to KK$ decay is an $L = 1$ P-wave decay. In the ϕ rest frame, the maximum orbital angular momentum L of the KK system is limited by the break-up momentum $q(m) = \sqrt{m^2 - m_K^2}/2$ for a ϕ mass m. The daughter K particles moving slowly with an impact parameter (meson radius) d of the order of 1 fm ($d = 0.1973$ GeV) have difficulty in generating sufficient L to conserve the overall angular momentum. Each angular momentum amplitude therefore has to be weighted by the barrier factor given by the Blatt-Weisskopf function B_L [53]. For $L = 1$, $B_L = \sqrt{2z/(1+z)}$, where $z = q/d$. The mass dependent Breit-Wigner width is then given by

$$\Gamma(m) = \Gamma_0 \left(\frac{q}{q_0}\right)^{2L+1} \left(\frac{m_0}{m}\right) \left(\frac{B_0}{B}\right), \tag{3.21}$$

where the subscript 0 denotes evaluation at the ϕ mean mass $m_0 = 1.01946$ GeV, and $\Gamma_0 = 4$ MeV.

Three types of background functions were studied. The first one was a general quartic, the second was a general quadratic and the third was of the form $f(x)$, as given by Eq. 3.14. The set of angular variables were $\cos\theta^{\phi}_{c.m.}$, $\cos\theta^{K}_{Hel}$ and ϕ^{K}_{Hel} (the particular choice of reference frame for the $\phi \to KK$ decay did not matter here).

3.12.1 Review of Yield Extraction Methods Used in Previous Analyses

As mentioned above, the yield extraction for the ϕ is complicated by several factors. The ϕ mean mass is very close to the KK threshold, it has a significant decay-width (the Σ^0 and Λ widths are negligible, by comparison), the ϕ lineshape is not known precisely, there is a small S-wave (a_0/f_0) underneath the P-wave (ϕ), and for the charged-mode, there is the additional complication (in certain kinematic regime) due to the $K^+\Lambda(1520)$ channel. We will present detailed comparisons of our final results with previous world data in Sec. 9.5, but in this section, we briefly go over some of the techniques used in these older analyses. It is also worth noting that all previous analyses had limited control over the systematics due to wide energy bins and low statistics. The impetus in many of these older results had been towards the overall shape and gross features, instead of more minute details.

We first look at the Anciant [60] results. This was a CLAS analysis on the $g6a$ dataset published in 2000. From the available analysis note [61] and Eric Anciant's thesis [62], it appears that two types of background subtraction were tried out: a "flat" background (Fig. 14 in Ref. [61]) and a simulated a_0/f_0 plus KK phase space background (Fig. 15 in Ref. [61]). The yield extraction fits were performed till the ϕ mass of 1.2 GeV, with a rather coarse binning in the ϕ mass variable. Fig. 15 in Ref. [61] is questionable from a different aspect: the a_0/f_0 contribution is shown to be comparable to the ϕ. While there is certainly an S-wave underneath the ϕ, the extent of the S-wave contribution shown here is suspicious, the presently accepted estimated being at the percent level [63, 64]. By assigning the total $MM(p)$ yield as a sum of the P-wave plus S-wave plus KK phase space, Ref. [61] also implies that their particle identification is perfect. That is, each event under the $MM(p)$ peak (Fig. 15 in Ref. [61]) is presumed to be a pKK event. This is certainly questionable, because a large portion of the background underneath the ϕ is undoubtedly populated by non-strange (non-pKK) events, generic pion production, possibly.

For the SAPHIR [65] and LEPS [66] results, similar "templates" were used to model the $\Lambda(1520)$ and KK phase-space backgrounds. Given the coarse binning and wide ranges for the $MM(p)$ (ϕ mass) distributions shown in the papers [65, 66], is difficult to ascertain the what the systematic uncertainties were in these yield extractions. For example, one might question whether the $\Lambda(1520)$ contribution underneath the ϕ could have been "over-subtracted", since no information about is given what the ϕ lineshape looked after the background had been subtracted out.

In this work, we avoid the use of such "templates" to model the background. Instead, we adopt the mass-dependent ϕ lineshape as described earlier and enforce this lineshape in our fits, while allowing for generic background shapes. Therefore, there is some difference in philosophy between our approach and that in some of the previous ϕ analyses – instead of "subtracting out the background", we are "pulling out the signal". Furthermore, by performing independent fits in very small regions of phase-space for each event (where the background shape is assumed to be roughly constant), we are not making any a priori guesses about the global features of the background. Even if there is an f_0/a_0 or $\Lambda(1520)$ background, unless this background interferes strongly with the ϕ, our method should work properly and provide a much better handle on the systematics of the signal-background separation process than in the older methods.

3.12.2 Charged-Mode Topology

Being a two-track topology, the charged-mode has higher statistics than the neutral-mode. Therefore a 10-MeV $\sqrt{s}$ binning was preserved here. For each of the background function forms, the quality of signal extraction was studied with the number of closest points N_c as 100 and 200. The results we present here were with $N_c = 200$ and a quartic background. Initially, no hard cut was placed around the $\Lambda(1520)$ mass ($\delta = 0$ from Sec. 3.8.3). However the Q-values seemed to be unable to cleanly remove the $\Lambda(1520)$ background. This was true for all values of N_c and all types of background functions that were tried out. Fig. 3.26 shows $M(pK^-)$ plotted againt $MM(p)$ in three angular regions for the bin $\sqrt{s} = 2.085$ GeV. The $\Lambda(1520)$ background ($M(pK^-) \approx 1.52$ GeV) is still faintly visible, especially in the mid-angles. As mentioned earlier, our signal-background separation method assumes that the background does not interfere with the signal. It is possible however, that there is some interference between the charged-mode ϕp and $K^+\Lambda(1520)$ channels (due to the same final-states), in which case our method would fail. In this case, the separation has to be done at the amplitude level in a coupled-channel partial wave analysis.

Inkeeping with the above discussion, we placed an additional cut of $|M(pK^-) - 1.52| > 15$ MeV. The quality checks for the energy regime $\sqrt{s}$ between 2.12 and 2.15 GeV are shown in Figs. 3.27- 3.29 where the Q-value weighted ϕ signal-distributions are in red and the $(1 - Q)$ weighted background

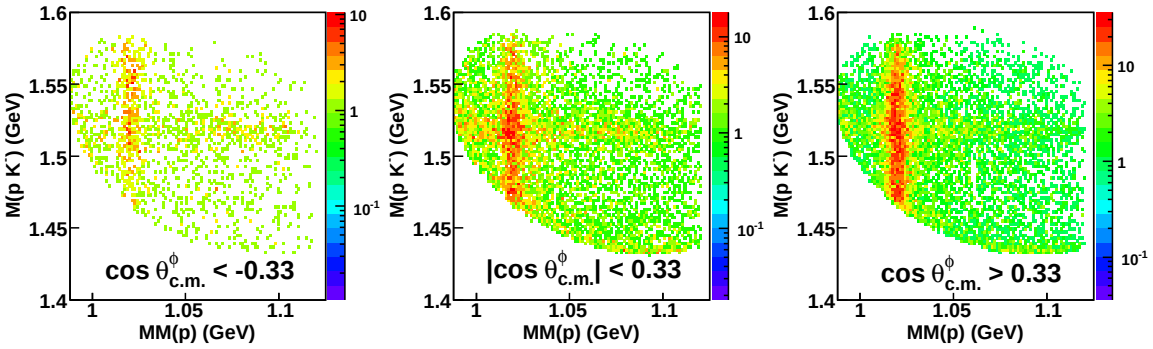

Figure 3.26: ϕ-$\Lambda(1520)$ overlap for the charged-mode topology for the bin $\sqrt{s} = 2.085$ GeV. Q-value weighted $M(pK^-)$ *vs.* $MM(p)$ distribution after cuts and background removal. The $\Lambda(1520)$ "band" is still visible, with the most relative prominence in the mid-angles.

distributions are in blue. The three plots cover the backward-, mid- and forward-angle regions, individually. Further, in each plot, we have broken the $\phi \to KK$ decay phase-space into 3×3 segments and show the quality checks in each region of phase space. It is clear that the background level (both shape and scale) depends on the phase-space region one is in. Roughly speaking, there is an f_0/a_0 peak below the ϕ mass, and a general background above the ϕ peak. Similar checks were also done in the other energy regimes. Fig. 3.33a shows the weighted $\sqrt{s}$ occupancies for the charged-mode, the dashed histogram corresponding to no hard cut around the $\Lambda(1520)$ mass, while the shaded histogram corresponds to a 15 MeV hard cut around the $\Lambda(1520)$. Our estimated signal yields are around 0.456 and 0.423 million events for the two cases, respectively. To compare the systematics due to using different values of N_c and different background functions (while preserving the $\Lambda(1520)$ cut), the overall yield using $N_c = 200$ and a quadratic background was ~ 0.4255 million, clearly, a deviation at the sub-percentage level.

3.12.3 Neutral-Mode Topology

Being a three-track case, the neutral-mode has a reduced detector acceptance. Additionally, the ϕ cross sections are inherently small. Therefore, this topology had an overall limited statistics. To bolster statistics, a wider energy binning was chosen (at least 30-MeV wide $\sqrt{s}$ bins), though statistics was still quite limited in the backward-angles. We also note here that unlike the charged-mode, the "detected" kaon (K^0_S) for the neutral-mode is not detected directly, but reconstructed via the detection of two other tracks. Therefore the resolutions for the neutral-mode are inherently worse than that of the charged-mode. All three background-functional forms mentioned earlier in this section were tried out and were found to give similar results. Our signal-background separation quality checks for the neutral-mode using a general quartic background and $N_c = 200$, $\sqrt{s}$ between 2.12 and 2.15 GeV are shown in Figs. 3.30-3.32. As for the charged-mode, we make these checks in localized regions of phase-space. The estimated neutral-mode signal yield is around 0.097 million events, roughly a fifth that of the two-track charged-mode dataset. With the background function form given by Eq. 3.14 and $N_c = 200$, the cumulative yield was ~ 0.095 million, again pointing to the fact that as long as the background functional form is generic enough, the signal-extraction process gives similar results. We reiterate that the main problem with the background subtraction here is that the ϕ mass lies so close to the KK threshold. This is especially prominent in the forwrad-angle plots (Fig. 3.32), since there are so few events below the ϕ mass, there is no easy way to model the background. This is why we have chosen to model the signal-function instead and the fuction function is flexible enough to represent the remnant background in each localized phase-space region.

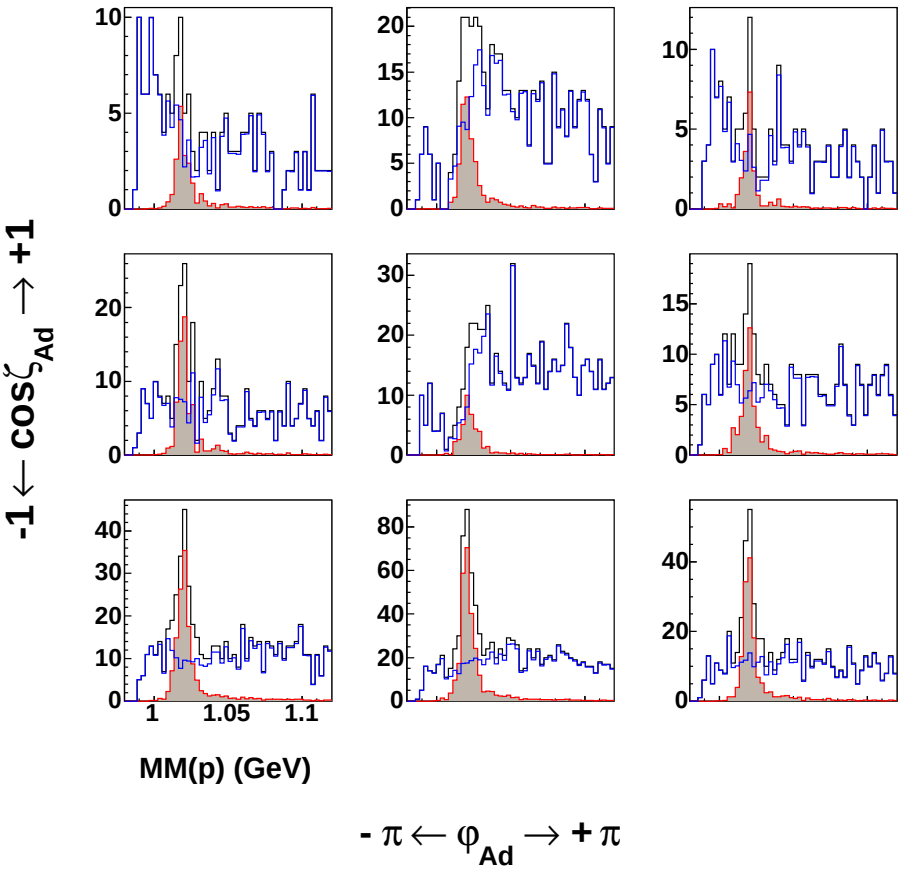

Figure 3.27: Charged-mode signal-background separation quality checks for $\sqrt{s}$ between 2.12 and 2.15 GeV and $\cos\theta^{\phi}_{\rm c.m.} < -0.33$, in different phase-space regions of the $\phi \to KK$ decay angles. The red histograms correspond to the signal (each event being weighted by Q), while the blue histograms are the backgrounds (each event being weighted by $(1-Q)$). See text for details.

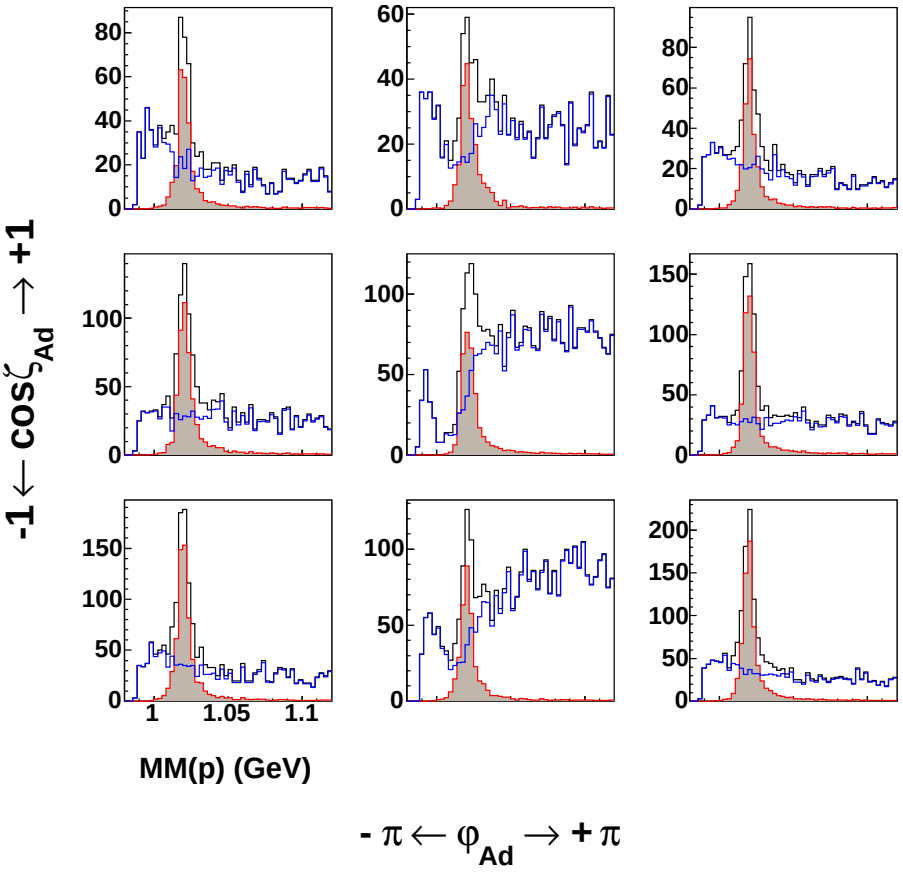

Figure 3.28: Charged-mode signal-background separation quality checks for $\sqrt{s}$ between 2.12 and 2.15 GeV and $|\cos\theta^{\phi}_{\rm c.m.}| < 0.33$, in different phase-space regions of the $\phi \to KK$ decay angles. The red histograms correspond to the signal (each event being weighted by Q), while the blue histograms are the backgrounds (each event being weighted by $(1-Q)$). See text for details.

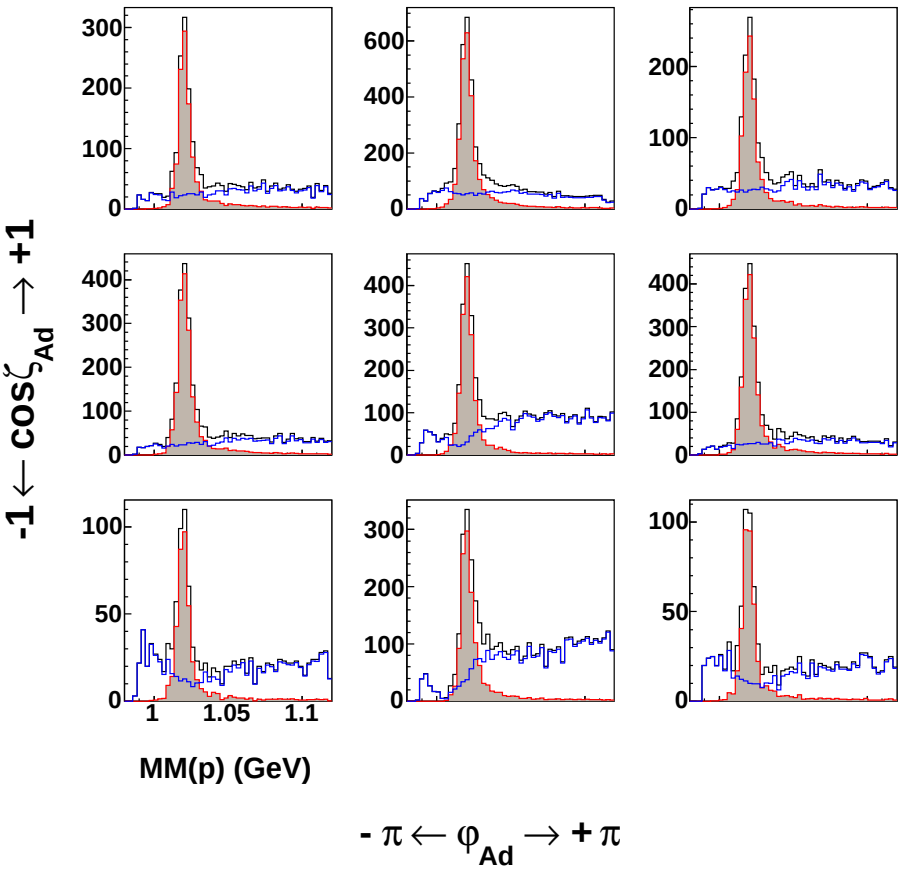

Figure 3.29: Charged-mode signal-background separation quality checks for $\sqrt{s}$ between 2.12 and 2.15 GeV and $\cos\theta^{\phi}_{\rm c.m.} > 0.33$, in different phase-space regions of the $\phi \to KK$ decay angles. The red histograms correspond to the signal (each event being weighted by Q), while the blue histograms are the backgrounds (each event being weighted by $(1-Q)$). See text for details.

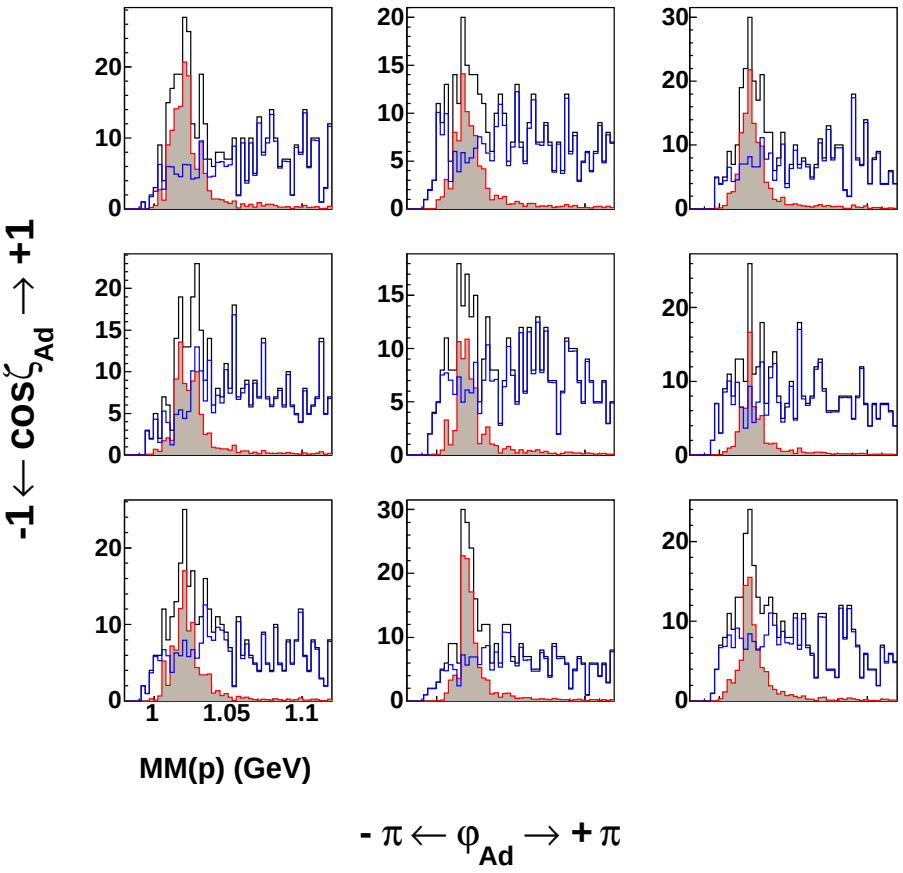

Figure 3.30: Neutral-mode signal-background separation quality checks for $\sqrt{s}$ between 2.12 and 2.15 GeV and $\cos\theta^{\phi}_{\rm c.m.} < -0.33$, in different phase-space regions of the $\phi \to KK$ decay angles. The red histograms correspond to the signal (each event being weighted by Q), while the blue histograms are the backgrounds (each event being weighted by $(1-Q)$). See text for details.

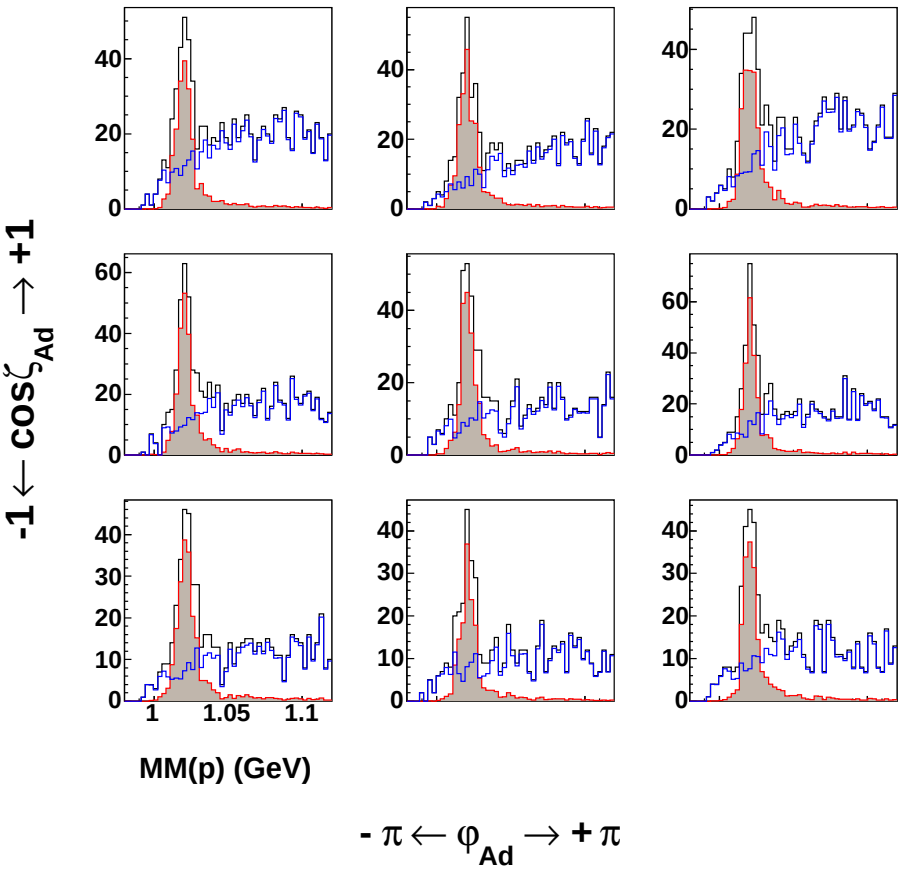

Figure 3.31: Neutral-mode signal-background separation quality checks for $\sqrt{s}$ between 2.12 and 2.15 GeV and $|\cos\theta^{\phi}_{\rm c.m.}| < 0.33$, in different phase-space regions of the $\phi \to KK$ decay angles. The red histograms correspond to the signal (each event being weighted by Q), while the blue histograms are the backgrounds (each event being weighted by $(1-Q)$). See text for details.

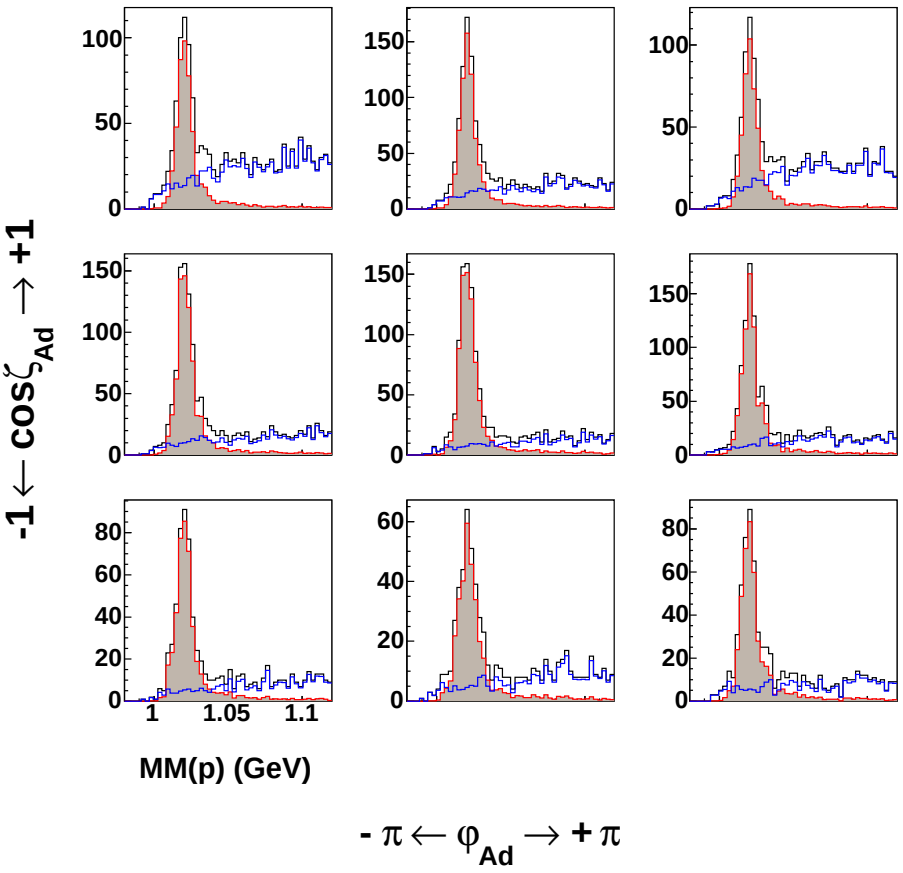

Figure 3.32: Neutral-mode signal-background separation quality checks for $\sqrt{s}$ between 2.12 and 2.15 GeV and $\cos\theta^{\phi}_{\rm c.m.} > 0.33$, in different phase-space regions of the $\phi \to KK$ decay angles. The red histograms correspond to the signal (each event being weighted by Q), while the blue histograms are the backgrounds (each event being weighted by $(1-Q)$). See text for details.

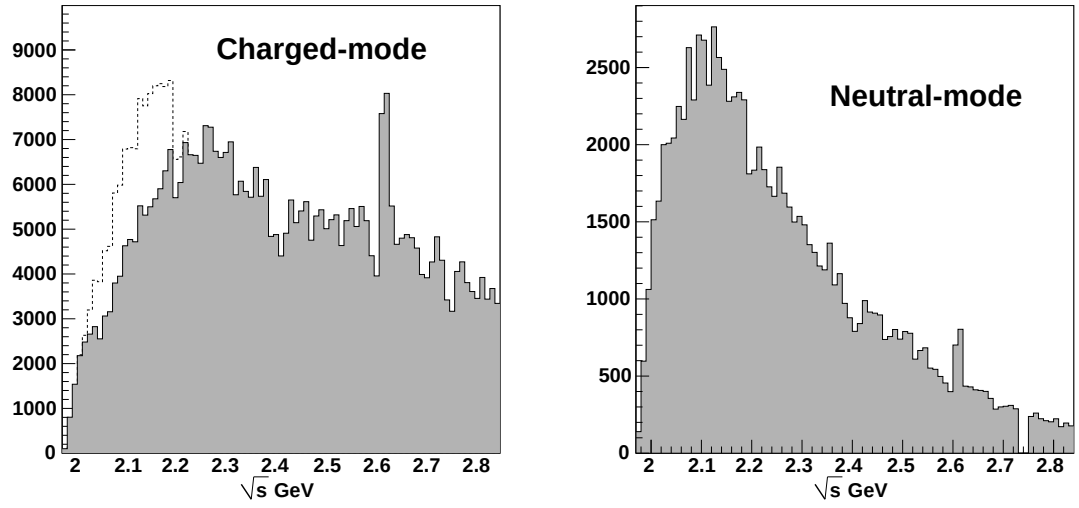

(a) (b)

Figure 3.33: Q-value weighted occupancy for the ϕ channel as a function of $\sqrt{s}$ for (a) charged- and (b) neutral-mode topologies. Each $\sqrt{s}$ bin in the x-axes is 10 MeV wide. The dashed histogram in (a) represents the occupancies *without* the 15-MeV-wide cut around the $\Lambda(1520)$ mass for the charged-mode (≈ 0.456 million signal events) while the shaded histogram is *with* the $\Lambda(1520)$ hard cut (≈ 0.423 million signal events). Above $\sqrt{s} \approx 2.2$ GeV, this cut makes no difference any more. For the three-track neutral-mode dataset, the total estimated signal yield was ≈ 0.097 million, that is, around a fifth that of the two-track charged-mode dataset.

3.12.4 Additional $MM(p)$ cut after signal-background separation

To effectively perform the signal-background separation process, till now, we have intentionally kept a wide range for the ϕ mass. After the completion of the signal-extraction (Q-values) process, we placed an additional 1.00 GeV $\leq MM(p) \leq$ 1.08 cut for both the charged- and neutral mode ϕp topologies. As for all PID/event-selection cuts, the cut was applied on both the Data and the Monte Carlo. The main purpose of the cut was to remove any extraneous events below the ϕ mass and in the long "tail", that might have slipped through the background-removal process.

3.13 Summary

To extract a clean sample of $\gamma p \rightarrow K^+\Sigma^0$ events from the $g11a$ dataset, we have selected events using two different final-state topologies, a series of cuts and employment of a signal-background separation procedure. Similarly, for the $\gamma p \rightarrow \phi p$ channel, we have selected events corresponding to two different decay modes of the ϕ. Some of the cuts employed pre-existing detector performance studies whilst others were specific to these channels. At every step we have detailed both the validity and utility of the cut we make. The results are a set of highly clean yields of $K^+\Sigma^0$ and ϕp events, ready for further physics analyses.

Chapter 4

Detector Acceptance and Normalization

Extraction of signal yields, which was covered in detail in the last chapter, was just one of the steps towards the measurement of differential cross sections, the other two being *detector acceptance* and *flux normalization*. The CLAS detector is a complex device. The mere production of an event with a particular kinematics does not mean that the event will actually be successfully detected and recorded by CLAS. The yields from the previous chapter will therefore have to be properly corrected for the *acceptance* of the detector. *Normalization* refers to the number of photons impinging on the target. If the photon flux is high, this will ratchet up the signal yields. The differential cross sections thus have to be normalized by the inverse of the flux factor. Additionally, the electronics of the detector have a finite dead time when it is not ready to record events because it is writing out previously recorded data, or for some other reasons. This fractional live time needs to be accounted for too in the normalization. All these calculations and corrections, we cover in the this chapter.

4.1 Detector Simulation

4.1.1 "Raw" Monte Carlo

To simulate detector acceptance, we first generated "raw" Monte Carlo events according to phase-space distributions. For the $K^+\Sigma^0$ channel, 300 million events were generated for the three-track and around 337 million for the two-track topology. For ϕp, around 100 million events were generated for both the charged- and neutral-mode topologies (the event-generator used the same ϕ lineshape as described in Sec. 3.12). The events were thrown such that after all cuts and background separation, the E_γ occupancy for the Monte Carlo was roughly three times that of the data. Ideally, one needs to throw Monte Carlo events based on some physics model. Except for the $K^+\Sigma^0$ two-track analysis, our acceptance calculation was obtained by weighing the Monte Carlo by a PWA fit to the actual data distribution, so that no *a priori* physics generator was needed.

For the $K^+\Sigma^0$ two-track case, this remained a concern, since a fit to the data could no longer be effected (our PWA setup required knowledge of all the final state particles). We were thus forced to use the unweighted Monte Carlo for this case. Fortuitously, due to the break-up momenta being small in both Σ^0 and Λ decays, the difference between the weighted and unweighted acceptance calculations was found to be minimal (see Sec. 7.3). Were this not the case, it would have been considerably more difficult to use the two-track dataset for making measurements.

Parameter	Setting
AUTO	1
KINE	1
MAGTYPE	2
MAGSCALE	0.4974 0.0
FIELD	2
GEOM	ALL
NOSEC	OTHE
TARGET	g11a
TGPOS	0.0 0.0 0.0
STZOFF	-10.00
STTYPE	1
SAVE	'LEVL' 1 'HADR' 0.93
RUNG	43852 1
BEAM	4.023

Table 4.1: Some of the values used for input to the GSIM `ffread` card for this analysis. The items marked in blue were only used for the two-track topology.

4.1.2 GSIM

The "raw" events were next passed through GSIM, a GEANT based simulation software for the CLAS detector, and the collaboration's standard simulation package [67]. GSIM's main task was to simulate detector signals for each subsystem of CLAS based on the kinematics for each particle. To do so, GSIM took as input, the initial particle types, momenta, and positions for each raw MC (Monte Carlo) event and used spatial information regarding the CLAS detector materials and toroidal magnetic fields to "swim" particles through the detector. GSIM also knew how to decay the various unstable particles (K^0, K^+, Σ^0, Λ, π^-, ...) so that we did not need to put in any branching fractions while calculating the cross-sections − these are already included in the acceptance. The only exception was the $\phi \to KK$ decay. This decay was effected by hand. That is, our thrown events already had the ϕ decayed either into K^+K^- or $K^0_S K^0_L$ according to the corresponding branching fractions. Therefore the ϕ differential cross sections needed to be scaled up by the corresponding branching fractions.

GSIM accepts parameters in the form of an `ffread` "card". Table 4.1 shows some of the typical values used for this analysis. One element that needs additional mention here is the set of parameters marked in blue. It is the peculiarity of the $K^+\Sigma^0$ and $K^+\Lambda$ channels in the $g11a$ dataset (see Sec. 7.1 for explanations) that knowledge of the secondary vertex for the Λ decay was essential. At the time of this writing, no previous CLAS analysis at CMU required knowledge of secondary decay vertices. For the three-track topology, the vertex could be *re-constructed* from tracking information and the Λ momentum. Since the Λ momentum was unknown in the two-track case, even this approach failed. Since it was not required, the earlier existing local versions of GSIM at CMU was not set up to retrieve secondary decay vertex information directly from GEANT though the BOS banks which stored this information, namely, MCVX and MCTK, were already built in and compiled. One simply needed to instruct GSIM to correctly write out the information into these banks using the `SAVE` command in the `ffread` card. For our purposes, it sufficed to save the first decay vertex (`'LEVL' 1`) where the decay products include a "`'HADR' 0.93`", that is, a hadron with mass greater than 0.93 GeV (a proton, in our case) − this addition is shown in blue font in Table 4.1. We subsequently double checked our code using a small three-track topology test-run by fitting t_{rf},

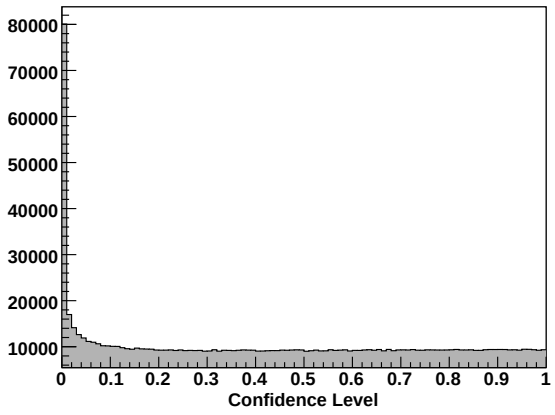

Figure 4.1: Confidence levels from kinematic fitting to $\gamma p \to K^+ p\pi^-(\gamma)$ after GPP and momentum smearing. The confidence level distribution is flat beyond 0.2 which suggests that the resolution of the accepted Monte Carlo is of the same order as the data.

the flight time of the Λ in its rest frame (this calculation requires knowledge of the Λ momentum and thus the necessity of the three-track topology) to an exponential and retrieved the value of $c\tau = 7.89$ cm, as quoted in PDG, to a fairly high precision.

4.1.3 GPP

The output from GSIM was next processed by GPP, a CLAS software package which smeared the detector signals to match the actual detector resolutions more accurately. Signals from the TOF scintillator paddles were smeared according to their lengths, a longer scintillator requiring a more diffused smearing function. Timing signals from the drift chambers were similarly diffused according to the distance of closest approach (DOCA) to set the momentum resolution in the Monte Carlo. After applying all these smearings, however, it was found that the Monte Carlo still had higher a resolution than the data [51]. Since GPP also allowed for user specified "degree of smearing", a minimal smearing of 1.0 was applied to the drift chamber, and instead, an emperical smearing algorithm tuned to produce a more accurate resolution over all regions of the detector was applied.

The empirical algorithm took the reported values of the tracking angles as the mean and $1.85\sigma_{track}$ as the width of a Gaussian function and randomly sampled from this Gaussian distribution (σ_{track} was the resolution obtained from the tracking code). The momentum magnitudes were also smeared by ~ 2 MeV on the average. Fig. 4.1 shows the confidence level distribution from a subsequent $\gamma p \to K^+ p\pi^-(\gamma)$ kinematic fit for the accepted Monte Carlo. Since the covariance matrix of the kinematic fitter was tuned to give a globally flat confidence level for the $g11a$ data, the flatness for the accepted Monte Carlo distribution suggests a good resolution match between the two.

4.2 Trigger Simulation

The role of GSIM was to account for inefficiences in the various detector components once a set of tracks triggers an "event" (see for the details on the $g11a$ triggering criteria). However the trigger-

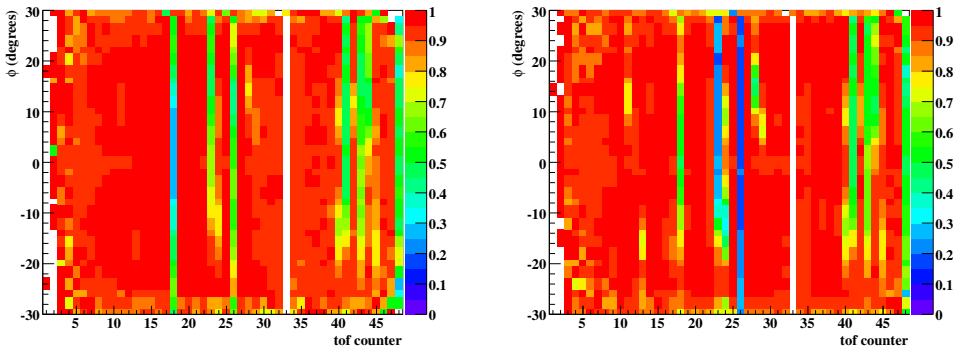

(a) (b)

Figure 4.2: Trigger efficiency map as a function of ϕ(degrees) and TOF-counter for Sector 1: (a) proton (b) π^- (Source: [51]).

ing itself was not without inefficiencies, so the next step was to account for these in the Monte Carlo.

Trigger inefficiencies in $g11a$ were first noticed by the Genova group [48] through discrepancies in the $\gamma p \to p\omega$ differential cross-sections between the two topologies $\gamma p \to p\pi^+(\pi^-\pi^0)$ and $\gamma p \to p\pi^+\pi^-(\pi^0)$. This was investigated further in great detail by Krahn *et al* [58] by utilizing the *trigger word* written into the data stream when events were being recorded. The CLAS Level 1 trigger requires a coincidence between the start counter time and the TOF scintillator time within a time window for two charged tracks in two different sectors. The *trigger word* contains information on which sectors met this trigger condition. By using the kinematic fitter and a high enough confidence level cut to select good $\gamma p \to p\pi^+\pi^-$ events, one can look at the trigger word and see how many times one of the three final state particles did not meet the trigger condition (at least two of the tracks must have triggered for the event to have been recorded). In this manner Krahn *et al* built up a "trigger map" for each particle type (proton, π^+ and π^-) as a function of sector, TOF paddle and azimuthal angle ϕ. Fig. 4.2 shows this for the proton and π^-.

One can immediately make out the problematic TOF paddles from Fig. 4.2. For example paddle 33 in Sector 1 is non-functioning for both the proton and the π^-. Paddles 12 and 13 have localized regions of lower efficiencies, either due to defective scintillator materials in these regions or due to high threshold settings of the TDC's in the PMT's located at the ends of each paddle. Note that many of the problematic paddles are already excluded altogether, as mentioned in Sec. 3.10.3. To correct for the localized inefficiencies for the remaining paddles, we use the trigger map as follows. For every track, we generate a random number between 0 and 1. If this is lesser than the efficiency read out from the map, we set the trigger word as positive for that particular track. The event as a whole is accepted if two or more tracks are "triggered" in this way. For the K^+, we utilized the π^+ trigger map (see also Sec. 7.5.2).

4.3 Start Counter Correction

Due to the peculier simultaneity of certain nuances lying in the $g11a$ start counter, the $g11a$ trigger, and the kinematics involving the decay of a Λ, an additional trigger correction is required for the accepted Monte Carlo in this analysis. Events for which the Λ decays outside the geometrical boundary of the start counter fail to trigger in the data, but might be included in the Monte Carlo.

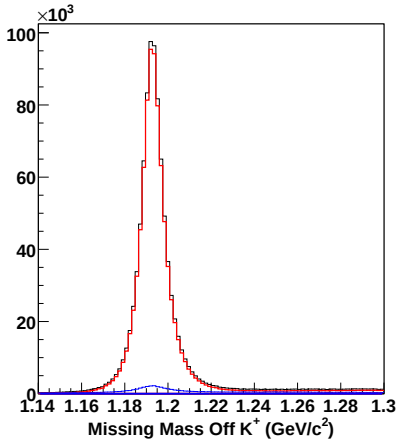

Figure 4.3: Accepted Monte Carlo from kinematic fit to $\gamma p \to K^+ p\pi^-(\gamma)$: in red are events after a 1% confidence level cut and in blue are events rejected by the cut. All histograms produced after a $|MM| < 60$ MeV cut to compare with data (Fig. 3.3c).

Thus, these events must be separately removed in the Monte Carlo by a cut. Both the effect and the cut are detailed in Sec. 7.1 and we direct the reader there to avoid repetition.

4.4 Event Selection – $K^+\Sigma^0$ Three-track topology

After passage through GSIM and GPP, the Monte Carlo is the form of raw events as was obtained from the detector. Here on, it undergoes cooking and skimming using the same versions of the software that the data was processed with. This ensures any systematic inefficiencies to be reflected in the same way in the Monte Carlo as in the data.

Event selection follows suit along the same philosophy – kinematic fitting, particle identification and event selection are replicated on the Monte Carlo as was applied on the data. Fig. 4.3 shows the effect of a 1% confidence level cut after a kinematic fit to $\gamma p \to K^+ p\pi^-(\gamma)$. In red are events surviving the cut and in blue are events rejected by the cut. As for the data, we have applied a total missing mass between ±60 MeV cut prior to making this plot. There is no "background" per se for the Monte Carlo, except for a proton-K^+ swap misidentification, which the latter cut removes. We have added this cut here for comparision with the corresponding plot for data – while skimming the Monte Carlo, as in the case of data, no such cut was applied. Fits to the black and red histograms (*i.e.*, before and after the cut) yeild a signal loss of about 1.5%, in tune with what we had found for the data.

Fig. 4.4a shows the Δtof plot for the proton hypothesis vs. the K^+ hypothesis, inlayed with the "iron-cross". As for the data, events outsode the "cross" are rejected. Fig. 4.4b shows the calculated masses of the proton and the K^+, while Fig. 4.4c (Fig. 4.4d) show the calculated mass distributions for events accepted(rejected) by the iron cross cut. It is to be noted that the feature in Region "I" of Fig. 3.5(b) due to incorrect timing information of the proton occurs for the Monte Carlo as well.

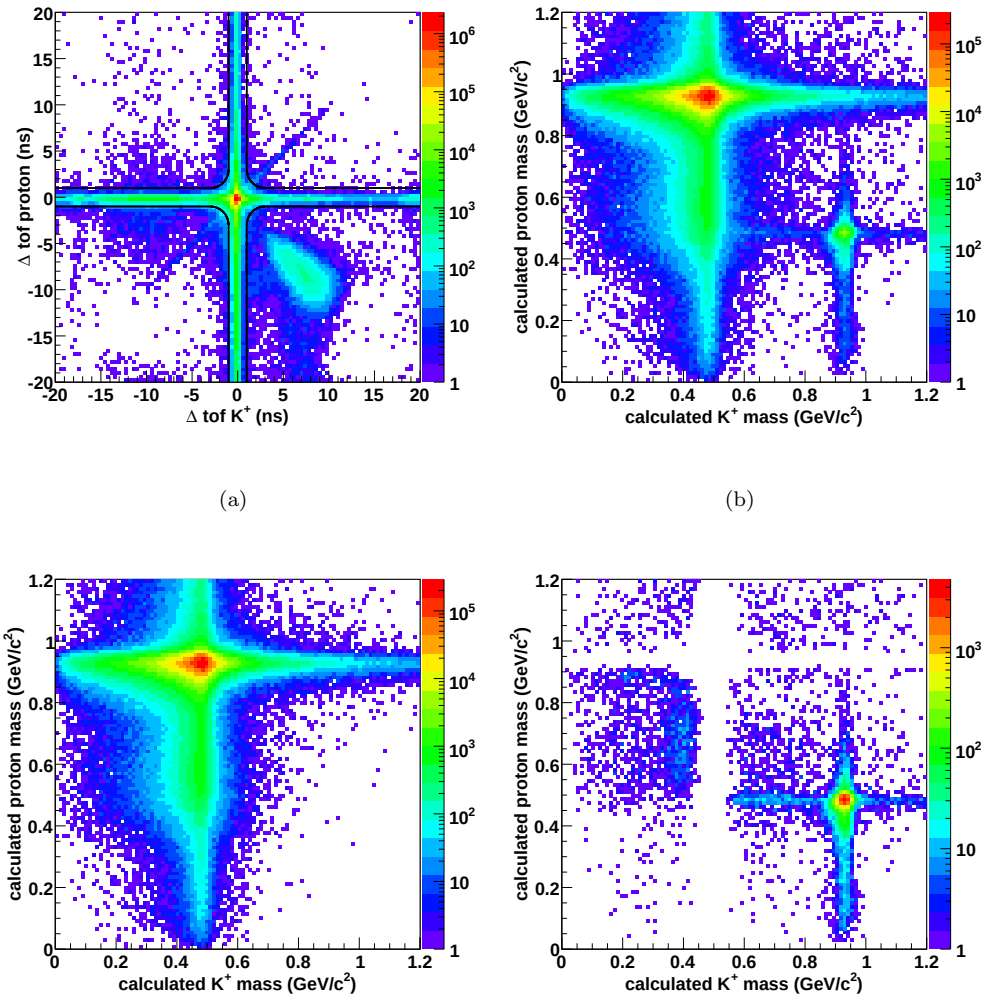

Figure 4.4: Accepted Monte Carlo PID for the $K^+\Sigma^0$ three-track topology: (a) Δtof – events outside the "iron-cross" are rejected. Calculated masses – (b) before cut, (c) events accepted by cut, and (d) rejected by cut. See text for details.

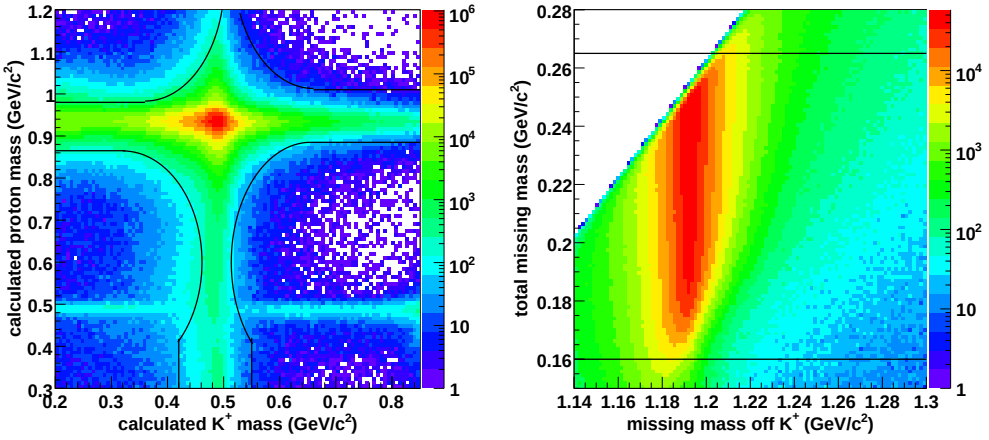

(a) (b)

Figure 4.5: Accepted Monte Carlo PID for the $K^+\Sigma^0$ two-track topology: (a) calculated masses for the entire skimmed dataset. The black lines denote our cut – events outside the "iron-cross" region are rejected. (b) Total missing mass, corresponding to the invariant $(\pi^-\gamma)$ mass, plotted against missing mass off K^+ – only events lying between the two horizontal lines were accepted.

4.5 Event Selection – $K^+\Sigma^0$ Two-track topology

For the $K^+\Sigma^0$ two-track case, the only "background" is an identification-swap between the proton and K^+, which is mostly removed during the initial skimming process (using the same calculated mass and Dalitz cuts as in the two-track data skim) itself. Thus the skimmed dataset is very clean already. Fig. 4.5 shows the calculated masses and the total missing mass distributions for this. However, to avoid any systamtic "bias" between data and Monte Carlo, the same PID cuts as applied on the data were applied on the Monte Carlo as well. The number of events rejected by these cuts were found to be nearly negligible. Energy, momentum and tagger corrections were also applied as was for the two-track data.

4.6 Event Selection – ϕp Charged-mode topology

Following the general norm for this analysis, as noted earlier, the accepted Monte Carlo for the ϕp channel was processed in exactly the same fashion as the real data. Fig. 4.6a shows a plot of the the proton and K^+ Δtof for the accepted Monte Carlo ϕp charged-mode topology skimmed dataset (after a 10% confidence level cut from kinematic fitting to $\gamma p \rightarrow K^+ p(K^-)$). The quadruplet of black curves shows the "iron-cross" cut limits. Fig. 4.6b shows the calculated masses after the "iron-cross" Δtof cut has been applied. Events on the left of the "pinch" shaped doublet of black curves were also rejected, as in the Data. Fig. 4.6c shows the cumulative effect of the timing cuts. The blue histogram represents the signal loss due to the cuts. A simple event count (without fits) gave a signal loss of $\sim 4\%$, in very good agreement with the 4.2% loss for the Data in Sec. 3.8.2.

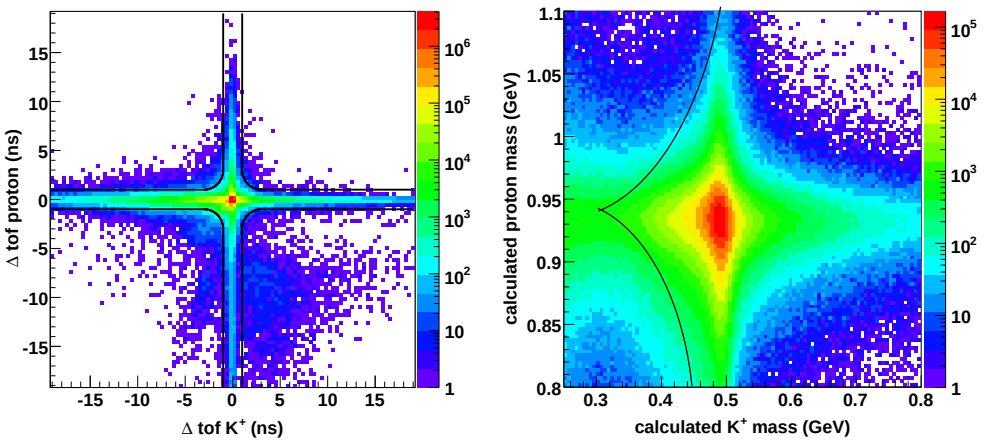

(a) (b)

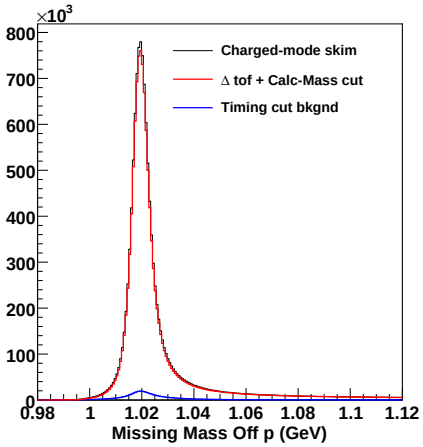

(c)

Figure 4.6: Accepted Monte Carlo timing cuts for the ϕp charged-mode topology: (a) Δtof plots for the entire skimmed dataset. The quadruplet of black lines denote our cut; (b) shows calculated masses of the proton and K^+ after the "iron-cross" Δtof cut has been applied. The events on the left of the black curves were also rejected, as in the Data. The effect of the timing cuts is shown in (c).

4.7 Event Selection – ϕp Neutral-mode topology

Figs. 4.7a and 4.7b show the "iron-cross" timing cut and the K^0_S selection cut, respectively, for the ϕp neutral-mode topology on the accepted Monte Carlo skimmed dataset (after a 10% confidence level cut from kinematic fitting to $\gamma p \to \pi^+\pi^-(K^0_L)p$). The cut boundaries are shown by the black curves (Fig. 4.7a) and horizontal lines (Fig. 4.7b). As in the case of the Data, the iron-cross cut results in very little signal loss. Fig. 4.7c shows the effect of the K^0_S selection cut – the red histogram represents events that pass the cut, while the blue histogram are events that fail the cut. A simple counting of events under the histograms in Fig. 4.7c gives a $\sim 6.6\%$ loss of events due to our K^0_S selection cut. This is comparable to the $\sim 6.5\%$ estimated signal loss for the Data that was given in Sec. 3.9.3.

4.8 Systematic Uncertainties

Since both the beam and target were unpolarized for $g11a$, the $K^+\Sigma^0$ photoproduction yields must be isotropic in the azimuthal production angle. To estimate systematic uncertainties in our acceptance calculation, we compare the acceptance normalized yields for each of the six (azimuthally symmetric) sectors the K^+ goes into. Tagging the sectors by the K^+ helps in mapping over the acceptance to useful quantities like $\cos\theta^{K^+}_{c.m.}$ and t. Since each sector has its own set of acceptance inefficiencies, if we have properly accounted for them in our acceptance calculation, we should get the same acceptance corrected yield for each sector. Fig. 4.8a and 4.8b show the yields before and after acceptance correction for $\sqrt{s} = 2.05$ GeV. The localized depletions in $\cos\theta^{K^+}_{c.m.}$ in Fig. 4.8a correspond to knocked out TOF paddles (for a given $\sqrt{s}$, each $\cos\theta^{K^+}_{c.m.}$ and $\phi^{K^+}_{c.m.}$ corresponds to a particular sector based TOF paddle). Since the same cuts that were applied on the data goes into the acceptance calculation, the acceptance correction removes these depletions and brings all the individual sector-wise yields into alignment, as evident from Fig. 4.8b.

Some discrepancies still exist between the sector-wise yields and the mean. Following [51], we next investigate whether these discrepancies can be accounted for by the statistical errors or whether one needs to assign supplementary uncertainties. If the errors were only statistical, then assuming a normal distribution, we expect that 68% of the time the deviation from the mean should be within 1σ, or,

$$\sum_{c,s} \Theta(\sigma^2_{c,s} - (y_{c,s} - \mu_c)^2) \approx 0.68N, \tag{4.1}$$

where s denotes the sector, c is the $\cos\theta^{K^+}_{c.m.}$ bin, $\sigma_{c,s}$ is the statistical error for each point and Θ is the Heaviside step function. Before proceeding further, we pause to note that one of the differences between the $K^+\Sigma^0$ channel and the $p\omega$ channel analysis of [51] is that we have much lower statistics due to the inherent low cross-sections of strangeness production compared to non-strange channels. Thus, upon initial survey, it was found that the fraction within 1σ from Eq. 4.1 was more than 68%, indicating that $\sigma_{statistical}$ was being over-estimated. A check on the occupancies per sector based $\cos\theta^{K^+}_{c.m.}$ bin (see Fig. 8.4) revealed that due to TOF paddle knockouts, localized occupancy distribution could be as low as a single event per bin, which kicks up $\sigma_{statistical}$. However, the acceptance corrected yields are much closer to the mean ($|y_{c,s} - \mu_c| \sim 0$), since our acceptance was devised to correct for these deficiencies in the first place). So if acceptance correction is being handled properly, these bins on the average, will have $\sigma^2_{c,s} > (y_{c,s} - \mu_c)^2$ more than 68% of the time, which is what we see. In other words, in a way, this confirms our faith in the acceptance calculation.

Similar issues with low statistics were encountered in the CLAS $g11a$ $K^+\Lambda$ channel analysis [26]. Taking a cue from there, we first bolster our statistics by simply merging bins. For instance, bins were merged from $\sqrt{s} = 2.0$ GeV to 2.04 GeV. Now, since Eq. 4.1 is valid only in a statistical sense

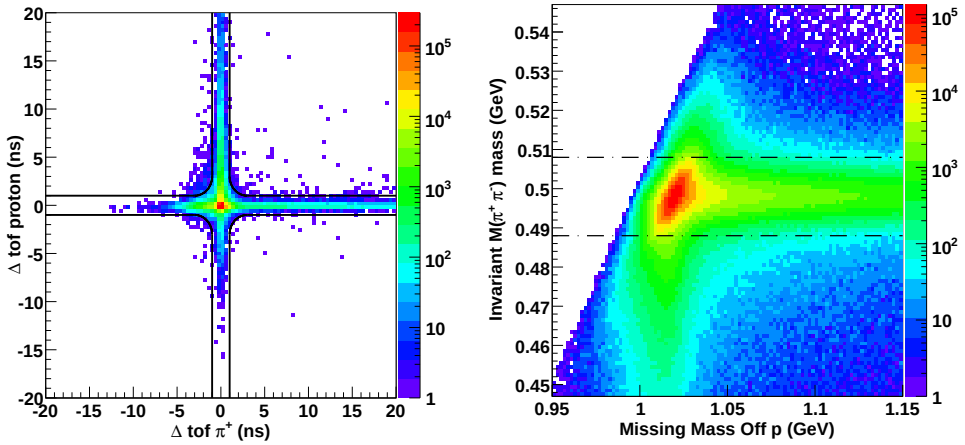

(a) (b)

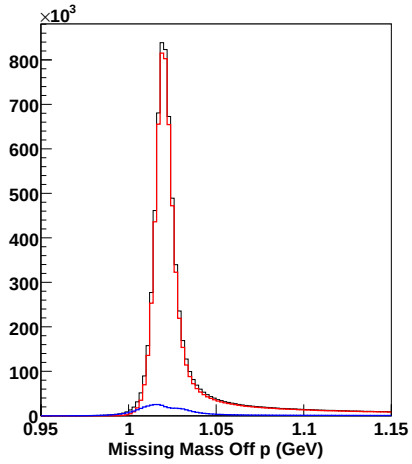

(c)

Figure 4.7: Accepted Monte Carlo PID and event selection cuts for the ϕp neutral-mode topology: (a) Δtof for the entire skimmed dataset. The quadruplet of black lines denote our "iron-cross" timing cut. (b) Shows the cut on the reconstructed K^0_S mass as $M(\pi^+\pi^-)$. The cut limits are shown by the two horizontal lines. (c) shows the effect of the K^0_S selection cut, where the red histogram shows the events passing the cut and the blue histogram shows those that failed the cut. Note that the histograms in (b) and (c) were produced after the application of the Δtof cut.

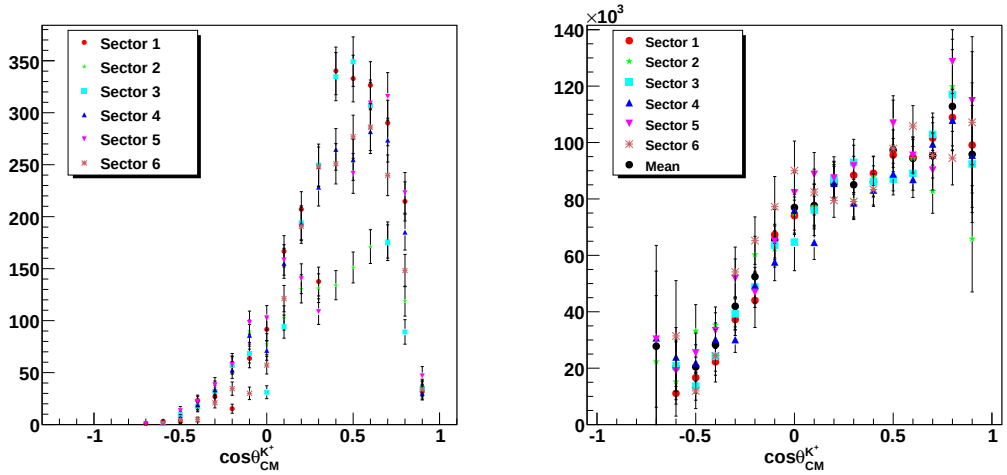

(a) (b)

Figure 4.8: Acceptance normalization for $\sqrt{s} = 2.005$ GeV for the $K^+\Sigma^0$ channel: (a) sector-wise data yields before acceptance correction, and (b) normalized yields after acceptance correction. Post-correction, the occupancies are much more similar between the different sectors.

and we seem to be statistics limited here, we next arrive upon the following compromise – demand that the minimum occupancy (pre acceptance corrected yield) in every sector-wise $\cos\theta^{K^+}_{c.m.}$ bin is greater than 40 and that there are at least 40 such bins. Having enforced a higher statistics, we go back and check on Eq. 4.1 again. The percentage of points within 1σ is now reduced to $\sim 62\%$ which means that there Eq. 4.1 must be modified to

$$\sum_{c,s} \Theta(\sigma^2_{c,s} + (\sigma_{acc} y_{c,s})^2 - (y_{c,s} - \mu_c)^2) \approx 0.68N \tag{4.2}$$

where σ_{acc} is the (relative) systematic error from our acceptance calculation. Note that since no particular dependence on $\cos\theta^{K^+}_{c.m.}$ can be noticed in the errors from Fig. 4.8, we will assume that σ_{acc} does not depend on this variable.

The discrete nature of Eq. 4.2 means that it cannot be solved analytically. In order to determine σ_{acc} we plot the percentage of points satisfying Eq. 4.2 versus incremental σ_{acc} as shown in Fig. 4.9. We see that 68% is hit at around $\sigma_{acc} = 0.04$ which is then our estimate for the systematic error in acceptance for a mean $\sqrt{s}$ of 2.2 GeV.

Similar studies were undertaken for higher energies with wider bin summations. However, the higher in $\sqrt{s}$ one goes the more forward peaked the yields become so that summing over $\sqrt{s}$ bins often do not help too much. Since the study in [51] involved a much higher statistics channel but was on the same dataset (CLAS $g11a$) and the errors that are of concern here depend "mostly" on hardware/recording/cooking malfunctions independent of the particular reaction under analysis, we will use the σ_{acc} values for higher $\sqrt{s}$ as quoted there. Namely,

$$\sigma_{acc}(\sqrt{s}) = 0.0217\sqrt{s} + 0.002791. \tag{4.3}$$

Fig. 4.10 shows the comparison between studies on the $p\omega$ and $K^+\Lambda$ channel. The errors are mostly within half a percent of each other for two completely different channels, easily within the

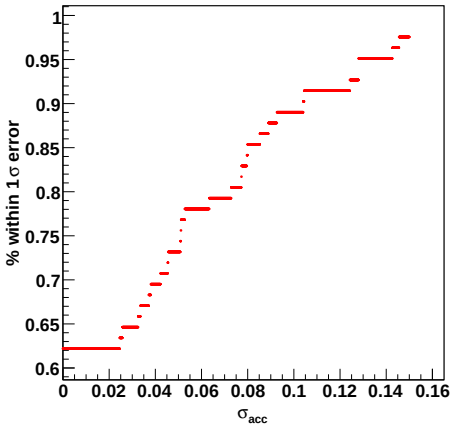

Figure 4.9: Percentage of points satisfying Eq. 4.2 plotted *vs.* incremental σ_{acc}. 68% is hit at around $\sigma_{acc} = 0.04$

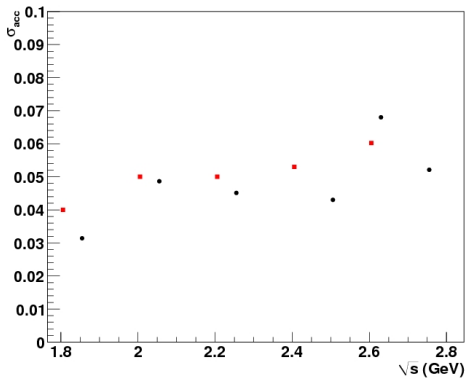

Figure 4.10: Variation of the acceptance uncertainty with center-of-mass energy ($\sqrt{s}$) for two different reactions, $p\omega$ (in red) [51] and $K^+\Lambda$ (in black) [26]. The agreement is mostly within sub-percent. Further, σ_{acc} goes from $\sim$ 4% to $\sim$ 6% over a $\sqrt{s}$ range of $\sim$ 1000 MeV so that *within* a $\sqrt{s}$ bin (10 MeV wide) the variation in σ_{acc} due to $\cos\theta^{K^+}_{c.m.}$ dependence is concievably quite small.

limits of statistical fluctuations. Furthermore, in the region where there is enough statistics (the $\sqrt{s} \approx 2.2$ GeV region that we analysed above), our σ_{acc} estimate of 4% agrees well with [51]. This further bolsters our confidence in using Eq. 4.3.

Since the ϕ (both charged- and neutral-mode topologies) has even lower statistics, it becomes even more difficult to conduct a similar sector-based study. Production-amplitude-wise, the ϕ channel is more akin to the ω. Particle-identification-wise, the difference between a kaon and a pion detection should not have too much of an effect on the acceptance uncertainty, as shown by the comparison between the ωp and $K^+\Lambda$ channels in Fig. 4.10. We therefore adopt Eq. 4.3 for the ϕp channel as well.

4.9 Target Density

One of the factors going into the cross-section calculation is the density of the liquid hydrogen target. Like the rest of the assembly in CLAS, the density characterstics of the target changes with time and can be emperically written as a function of the pressure P, and temperature T of the target. CLAS records the latter quantities run by run and thus the density can be calculated on a run by run basis too. It was found in [51] that during the $g11a$ run period, the average target density was

$$\bar{\rho} = 0.07177 \frac{g}{cm^3}, \tag{4.4}$$

with a variance of

$$\sigma^2 = 6.776 \times 10^{-9} \frac{g^2}{cm^6}. \tag{4.5}$$

That is, the relative fluctuations are of the order of 0.11%.

4.10 Photon Flux Normalization

The final piece of information we require to calculate a physical cross-section from the quantum mechanical amplitudes is the total number of photons incident on the target. This quantity is called the *photon flux* and goes into the cross-section calculation as a factor in the denominator to give the *flux normalized* yields. The standard CLAS normalization utilizes the *gflux* package developed by Pasyuk *et al* [54]. We will give a brief description of the *gflux* next.

4.10.1 gflux

The basic idea is the following. Recall from that the Hall B tagging system converts a fraction of the electron beam provided by the CEBAF accelerator into a photon beam using bremsstrahlung. The remnent electron beam is thereafter bent by magnetic fields into the tagging system. However, only a fraction of these electrons are actually be associated with any physical bremsstrahlung re-scattering, the rest of the electrons being the so called "out of time" electrons. Assuming Poissonian statistics for the "out of time" electron hits, one can estimate the total number of "good" (reliably detected) electrons entering the tagging system within a certain time window. One the defines the *tagging efficiency* as the number of "good" electrons relative to the number of photons impinging on the target. To calibrate the tagging efficiency, special *normalization* runs with lower beam intensity and and thinner bremsstrahlung radiators were taken, the resultant lower photon flux being directly measured by a total absorption counter (TAC) placed directly in the photon beam. The efficiency was found to be around 85% and was generally dependent on the photon energy but independent of the flux. *gflux* also corrects for the detector *live time*, the fraction of the run time when the

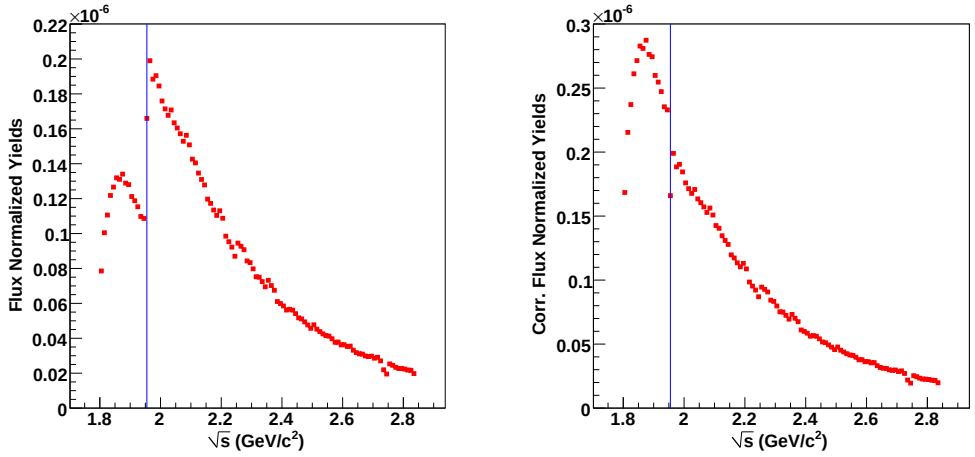

(a) (b)

Figure 4.11: Flux normalized yields for the three-track topology: (a) Before and (b) After the correction for the $g11a$ trigger. The correction makes the yields look continuous across the cutoff bin $\sqrt{s} = 1.955$ GeV marked by the blue vertical line.

detector was "ready" to record data (CLAS experiences *dead time* when its data acquisition system is busy writing recorded information to the output stream). Finally, since the TAC was located some distance downstream from the target there were some additional corrections for the photon attenuation between the target location and the TAC [68].

4.10.2 Current-dependent Normalization Correction

During preliminary analysis, inconsistencies in current dependence of flux-normalizations were found for the $g11a$ dataset, which was traced back to the live-time correction going into the *gflux* calculation [51]. Generally, live time in CLAS is calculated by the scaler clocks in the DAQ system, but can also be measured by an additional component called the Faraday cup, a downstream device normally used for measuring the electron beam current, but which essentially measures electronic noise for a photon beam. Though the Faraday cup measurements are less precise for photons, no systematic discrepancies are expected with the clock measuements. However what was seen in practice was that the ratio LT_{FCUP}/LT_{CLOCK} showed a monotonic deviation from unity with an increasing beam current. Furthermore, the deviation went away with another factor of LT_{CLOCK} in the denominator, that is, LT_{FCUP}/LT^2_{CLOCK} seemed to hold at a constant unity over a range of beam currents. Thus replacing LT_{CLOCK} by LT^2_{CLOCK} in *gflux* correspondingly removed the current dependence of the flux and here onwards LT^2_{CLOCK} will be taken as the *corrected* time. For a more detailed account of this effect, see [51].

4.10.3 Trigger Correction for Flux

Recall from Sec. that the $g11a$ trigger required a signal from the first 40 T-counters in the Master OR (MOR). These T-counters correspond to the higher end of the photon energy spectrum. An event with a lower E_γ would have been recorded only if it fell within the time window of a separate electron hit on any of the first 40 T-counters. The exact cutoff E_γ whereon only the first 40 T-counters are hit varies from run to run, but the average is $E_\gamma \sim 1.57$ GeV or $\sqrt{s} \sim 1.956$ GeV as

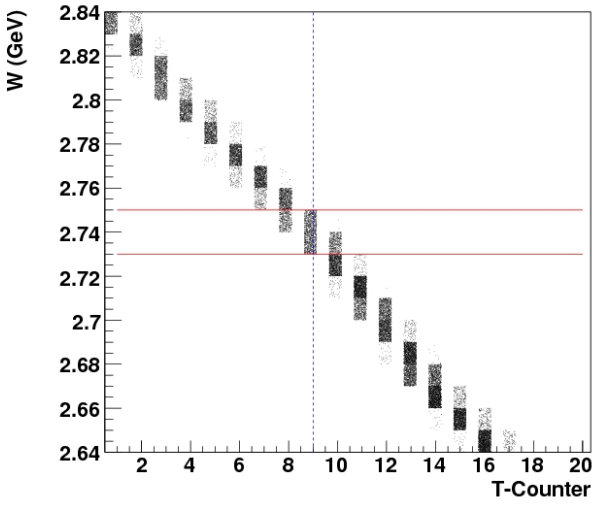

Figure 4.12: Photons corresponding to T-counter 9 spill on to the two W-bins (bin-centers 2.74 GeV and 2.75 GeV) where we see an abnormal photon flux.

found in [51]. However, *gflux* was programmed to accumulate photon flux over all the T-counters for any particular run. Thus for $\sqrt{s} \leq 1.956$ GeV, the photon flux (for events that were triggered) is over-estimated by *gflux*. It was shown in [51] that the average probability over all runs that at least one photon hit any of the first 40 T-counters is ~ 0.47. Thus if *gflux* recorded N photons in all, only $\sim 0.47N$ would correspond to the first 40 T-counters. Correspondingly, below $\sqrt{s} \leq 1.956$ GeV, the photon flux has to be scaled down by a 0.47 multiplicative factor.

Fig. 4.11 shows the flux normalized yield before and after the correction. Note that the correction brings continuity in the normalized yields across the cut-off energy 1.956 GeV though at the crossover bin itself, the yield seems abnormal. We shall henceforth exclude the $\sqrt{s} = 1.955$ GeV bin from this analysis. Also the two bins $\sqrt{s} = 2.735$ GeV and $\sqrt{s} = 2.745$ GeV show higher fluxes recorded than their surrounding bins. Fig. 4.12 shows a plot of W ($= \sqrt{s}$) vs. T-counter. Clearly photons from T-counter 9 are common to these two bins (and do not spill on to any other W-bin as well), so this effect is most probably due to a malfunction in T-9. Both these bins will thus also be excluded hereon.

4.10.4 Systematic Error

Fig. 4.13 shows the flux-normalized yields for the $K^+\Sigma^0$ three-track topology, as a function of the run number. The photon flux was recorded as a function of the photon beam energy E_γ, or equivalently, the center of mass energy $\sqrt{s}$. The flux normalized yield for a particular run was then obtained by

$$\mathcal{N}_r = \sum_s \frac{Y_s}{\mathcal{F}_s}, \tag{4.6}$$

where Y_s and $\mathcal{F}_s$ are the $K^+\Sigma^0$ yield and corrected photon flux for each $\sqrt{s}$ bin in the run r. A fit to the distribution gave a mean $\mu = 1.38192 \times 10^{-6}$ and standard deviation $\sigma = 4.44843 \times 10^{-8}$.

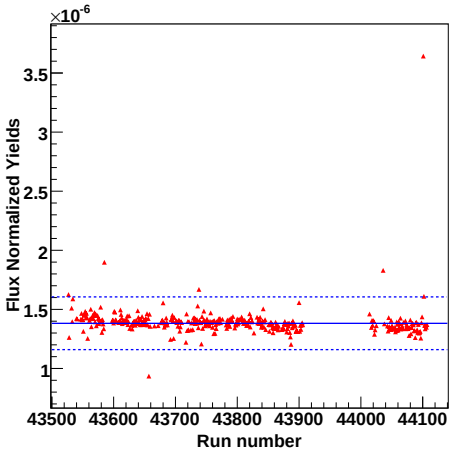

Figure 4.13: Flux normalized yields run by run for the $K^+\Sigma^0$ three-track topology. The mean $\mu = 1.38192 \times 10^{-6}$ and standard deviation $\sigma = 4.44843 \times 10^{-8}$ was found by fitting the distribution to a Gaussian. The continuous blue line shows the position of the mean and the dashed blue lines represent $\mu \pm 5\sigma$ limits.

Thus, $\sigma/\mu \sim 3.2\%$ which represents an *adhoc* estimate of the systematic error for the flux normalization. Generally flux normalization systematics are studied by comparing cross-sections for different reactions between different experiments/datasets. A wider study encompassing the $p\omega$, $K^+\Lambda$ and $p\eta$ photo-production channels [16] gives a 7% systematic error for the flux. Combined in quadrature with the 3.2% run-by-run error (this number is 1.8 for the $p\omega$ case [16]) gives a 7.7% error for the flux.

Lastly, note that runs 43585, 43657, 44036 and 44101 seem to have abnormal flux-normalized yields. They were also found to have low statistics and will be removed from our analysis hereon.

4.11 Summary

To calculate the acceptance of the CLAS detector, we generated 300(200) million $\gamma p \to K^+\Sigma^0$ events for the three(two)-track topology, which were subseqently passed through GSIM, a GEANT based detector simulator. For the ϕp channel, similarly, 100 million $\gamma p \to \phi p$ events were generated for the charged- and neutral-mode topologies and processed by GSIM. Every particle identification and event selection cut that was applied on the data was repeated on the Monte Carlo using the same set of softwares. In addition the Monte Carlo required other corrections from triggering and resolution issues. The overall effort resulted in the Monte Carlo resembling the actual data as near as possible apart from the fact that the Monte Carlo contained no physics, being generated flat in phase space. We also calculated the photon flux and flux normalized yields for each run, with corrections for a live time detector error and an error arising from the $g11a$ trigger. Our estimated systematic errors for each relevant factor were also calculated in this chapter.

Chapter 5

PWA Theoretical Formalism

In this chapter we discuss the construction of the amplitudes that we will be using in our partial wave analysis (PWA). Since our amplitudes will be written down in a manifestly covariant fashion, our language will be tensorial which is best equipped to deal with Lorentz covariance. We will first give a brief description of the representation theory of the Homogenous Lorentz Group (HLG). A particle of spin J and mass M is nothing but a member of a particular representation of the HLG. Furthermore, higher spin states are built up as tensor products of lower spin states, with supplementary conditions which are required to lower the number of independent components to that appropriate for a spin J state. The crucial point here is to do this while maintaining Lorentz covariance all the way. We describe this formalism, due to Rarita, Schwinger [69] and Zemach [70], in detail, following the setup of Refs. [51, 71]. Once we have constructed the spin states, we write out the amplitude for the entire decay chain. We also construct amplitudes for the non-resonant "background" processes and finally comment on how our formalism maintains the underlying gauge invariance of the theory.

5.1 Representation Theory of the Homogenous Lorentz Group

The group of continous space-time symmetries in special relativity consists of 4 space-time translations, 3 rotations and 3 boosts, a total of 10 generators. This group is called the Inhomogenous Lorentz Group or the Poincaré group [1, 72]. The group consisting of the 3 boosts and the 3 rotations, or 6 rotations in space-time, forms a sub-group called the Homogenous Lorentz Group or HLG. It is defined by the following group multiplication law

$$\Lambda^{\mu}_{\rho}\Lambda^{\rho}_{\nu} = g^{\mu}_{\nu} \tag{5.1}$$

where $g_{\mu\nu}$ is the metric tensor diag(1,-1,-1,-1). This is nothing but the unitarity condition $\Lambda\Lambda^{\dagger} = 1$ written out with the proper indices attached. An infinitesimal element of the HLG can then be written as

$$\Lambda^{\mu}_{\nu} \sim g^{\mu}_{\nu} + \omega^{\mu}_{\nu} \tag{5.2}$$

where we have assumed that every element is path connected to the unit element g^{μ}_{ν} so that the discrete translations − space reflections and time inversion, are not included. It is easy to see then that $\omega_{\mu\nu} = -\omega_{\nu\mu}$ so that the HLG is isomorphic to the group of 4×4 anti-symmetric matrices (which also has ${}^4C_2 = 6$ generators).

A *representation* of the HLG is then defined as a group of operators $D(\Lambda)$ acting on a "state" space, with the following group multiplication law

$$D(\Lambda_1)D(\Lambda_2) = D(\Lambda_1\Lambda_2), \tag{5.3}$$

with the generators $J^{\mu\nu}$ given by

$$D(\Lambda) = exp\,(\frac{i}{2}\omega_{\mu\nu}J^{\nu\mu}) = 1 + \frac{i}{2}\omega_{\mu\nu}J^{\nu\mu} + \cdots . \tag{5.4}$$

The "state" space will contain all our usual particles − scalars, vectors, *et al.* But to see the connection between spin and representations, we need to further work out the algebra for the generators of the representations.

5.1.1 The HLG algebra

The easist way to do is by invoking the the group multiplication law for the infinitesimal element $\bar{\Lambda} = 1 + \bar{\omega}$:

$$\begin{aligned} D(\Lambda)D(\bar{\Lambda})D(\Lambda^{-1}) &= D(\Lambda\bar{\Lambda}\Lambda^{-1}) && (5.5a)\\ &= D(1 + \Lambda\bar{\omega}\Lambda^{-1}) && (5.5b)\\ &= 1 + \frac{i}{2}(\Lambda\bar{\omega}\Lambda^{-1})_{\rho\sigma}J^{\rho\sigma} && (5.5c)\\ &= 1 + \frac{i}{2}\bar{\omega}_{\mu\nu}\Lambda^{\mu}_{\rho}\Lambda^{\nu}_{\sigma}J^{\rho\sigma}. && (5.5d) \end{aligned}$$

On the other hand,

$$D(\Lambda)D(\bar{\Lambda})D(\Lambda^{-1}) = 1 + D(\Lambda)\frac{i}{2}\bar{\omega}_{\mu\nu}J^{\mu\nu}D(\Lambda^{-1}). \tag{5.6}$$

Comparing Eqs. 5.5d and 5.6 we find that the generators $J^{\mu\nu}$ transform as second rank contravariant tensors:

$$D(\Lambda)J^{\mu\nu}D(\Lambda^{-1}) = \Lambda^{\mu}_{\rho}\Lambda^{\nu}_{\sigma}J^{\rho\sigma} \tag{5.7}$$

If we further take Λ be infinitesimal too, as $1 + \omega$, and keep all ω terms till the first order, Eq. 5.7 gives the following algebra:

$$[J^{\mu\nu}, J^{\rho\sigma}] = i(g^{\mu\sigma}J^{\rho\nu} + g^{\nu\sigma}J^{\mu\rho} - g^{\rho\mu}J^{\sigma\nu} - g^{\rho\nu}J^{\mu\sigma}). \tag{5.8}$$

Until now we have not made assumptions about the dimensionality of space-time − Eq. 5.8 will hold for $SO(1, d)$, the rotation group in $(d+1)$ space-time dimsensions. However $(n+1)$ space-time has the special property ${}^{n}C_2 = n$ for $n = 3$, so that we can write the following:

$$\begin{aligned} J_1 &\equiv J^{23} = J_{23} && (5.9a)\\ J_2 &\equiv J^{31} = J_{31} && (5.9b)\\ J_3 &\equiv J^{12} = J_{12} && (5.9c)\\ K_1 &\equiv J^{10} && (5.9d)\\ K_2 &\equiv J^{20} && (5.9e)\\ K_3 &\equiv J^{30}, && (5.9f) \end{aligned}$$

where the J_i's are the three rotation generators and the K_i's are the boosts. We can then recast Eq. 5.8 into the more physically transparent following three commutators [72]:

$$\begin{aligned} [J_i, J_j] &= i\epsilon_{ijk}J_k && (5.10a)\\ [J_i, K_j] &= i\epsilon_{ijk}K_k && (5.10b)\\ [K_i, K_j] &= -i\epsilon_{ijk}J_k && (5.10c) \end{aligned}$$

Note that the K_i's here are not Hermitian because the boost operator is not unitary (which is okay since the HLG is a non-compact group). Also, from Eqs. 5.10b and 5.10c, the rotations and boosts mix. This has consequences like the phenomenon of Thomas precession in relativity.

Next, consider the following linear combinations:

$$A_i \equiv \frac{1}{2}(J_i - iK_i) \tag{5.11a}$$

$$B_i \equiv \frac{1}{2}(J_i + iK_i), \tag{5.11b}$$

whereupon one finds,

$$[A_i, A_j] = i\epsilon_{ijk}A_k, \qquad [B_i, B_j] = i\epsilon_{ijk}B_k \tag{5.12}$$

together with the decoupling

$$[A_i, B_j] = 0. \tag{5.13}$$

The structure of the HLG unfolds now − it is simply a direct product of two rotation groups! General representations of the HLG are to be labelled as (A, B) where A and B are integers or half-intergers. Within a representation, a particular state is labelled as (a, b) where $a = -A, -A+1, ..., A$ and $b = -B, -B+1, ..., B$. Since the total angular momentum is $\vec{J} = \vec{A} + \vec{B}$, the "spin" j of any particle will come from Clebsch-Gordon decomposition of mixing two spins with j taking integral and half-integral values between $|A - B|$ and $|A + B|$.

5.2 Spin Half Representation

The simplest possible representations are fields transforming as $(0, \frac{1}{2})$ or $(\frac{1}{2}, 0)$. These 2-component spinors are called Weyl spinors. Now notice that the two discrete transformations − charge conjugation $\mathcal{C}$ and parity reversal $\mathcal{P}$ transforms (A, B) to (B, A). This is easy to see from Eq. 5.11 where A and B are evidently conjugate to each other. $\mathcal{C}$ interchanges A and B explicitly, while $\mathcal{P}$ reverses only $\vec{K}$ keeping $\vec{J}$ constant, whereby A and B are flipped again. Thus in theories like QED and QCD where both $\mathcal{C}$ and $\mathcal{P}$ are separately conserved, the fields must have both $(0, \frac{1}{2})$ and $(\frac{1}{2}, 0)$ components. These 4-component spinors transforming as $(\frac{1}{2}, 0) \oplus (0, \frac{1}{2})$ are called Dirac spinors. However, a spin half particle has only 2 independent components. To reduce the number of independent components from 4 to 2, we need a supplementary condition, which is nothing but the Dirac equation

$$(\gamma^\mu p_\mu - w)u(p, m) = 0, \tag{5.14}$$

where $u(p, m)$ is the Dirac spinor for a particle of mass w, 4-momentum p and spin projection $m(= \pm\frac{1}{2})$, while the 4 x 4 matrices γ^μ satisfy anti-commutation relations

$$\gamma^\mu\gamma^\nu + \gamma^\nu\gamma^\mu = 2g^{\mu\nu}. \tag{5.15}$$

In the *Dirac basis*, which we will use here, the γ matrices are defined as

$$\gamma^0 = \begin{pmatrix} 1 & 0 \\ 0 & -1 \end{pmatrix} \tag{5.16a}$$

$$\gamma^i = \begin{pmatrix} 0 & \sigma_i \\ -\sigma_i & 0 \end{pmatrix} \tag{5.16b}$$

where σ_i are the Pauli matrices. The "fifth" γ matrix, which anticommutes with all the other four is given by

$$\gamma^5 \equiv i\gamma^0\gamma^1\gamma^2\gamma^3 = \begin{pmatrix} 0 & 1 \\ 1 & 0 \end{pmatrix}. \tag{5.17}$$

The Dirac equation in the particle's rest frame then becomes

$$\begin{pmatrix} 0 & 0 \\ 0 & -2w \end{pmatrix} u(p_{rf}, m) = 0. \tag{5.18}$$

Therefore, the lower two components of $u(p_{rf}, m)$ are zero and the 4-component spinor takes the form

$$u(p_{rf}, m) = 2w \begin{pmatrix} \chi(m) \\ 0 \end{pmatrix}, \tag{5.19}$$

where

$$\chi(+\frac{1}{2}) = \begin{pmatrix} 1 \\ 0 \end{pmatrix}, \quad \chi(-\frac{1}{2}) = \begin{pmatrix} 0 \\ 1 \end{pmatrix}, \tag{5.20}$$

are the 2-component spinors. To get the 4-component spinor in any arbitrary frame, we simply boost it from the rest frame yielding [1]

$$u(p, m) = \Lambda_{\frac{1}{2}}(p)u(p_{rf}, m) = \sqrt{E+w} \begin{pmatrix} \chi(m) \\ \frac{\vec{\sigma}\cdot\vec{p}}{E+w}\chi(m) \end{pmatrix}, \tag{5.21}$$

where $\Lambda_{\frac{1}{2}}(p)$ is the spinor boost operator under which the γ's transform like a 4-vector:

$$D(\Lambda^{-1}_{\frac{1}{2}}(p))\gamma^\mu D(\Lambda_{\frac{1}{2}}(p)) = \Lambda^\mu{}_\nu(p)\gamma^\nu. \tag{5.22}$$

An important property of the gamma matrices is that $\left(\gamma^i\right)^\dagger = -\gamma^i$ for i from 1 to 3, whilst $\left(\gamma^0\right)^\dagger = \gamma^0$. This stems from the fact that the HLG is isomorphic to $SO(1,3)$ instead of $SO(4)$. Both these relations can be summed up as $(\gamma^\mu)^\dagger = \gamma^0\gamma^\mu\gamma^0$. An immediate consequence of this is that the adjoint of the Dirac spinor u is not $u^\dagger$ but $\bar{u} \equiv u^\dagger\gamma^0$, for only then does the hadronic current $u^\dagger\gamma^\mu u$ come out to be Hermitian. With u and $\bar{u}$, we can now build Lorentz scalars $\bar{u}u$, pseudo-scalars $\bar{u}\gamma^5 u$, vectors $\bar{u}\gamma^\mu u$, pseudo-vectors $\bar{u}\gamma^5\gamma^\mu u$ and tensors $\bar{u}\sigma^{\mu\nu}u$ ($\sigma^{\mu\nu} = \frac{i}{2}[\gamma_\mu, \gamma_\nu]$). We also define the spin $\frac{1}{2}$ projection operator

$$P^{(\frac{1}{2})}(p) = \frac{1}{2w}\sum_m u(p, m)\bar{u}(p, m) = \frac{1}{2w}(\gamma^\mu p_\mu + w), \tag{5.23}$$

which acting on an arbitrary spinor Π projects out the piece that is a solution to the Dirac equation

$$(\gamma^\mu p_\mu - w)P^{(\frac{1}{2})}(p)\Pi = \frac{1}{2w}(p^2 - w^2)\Pi = 0. \tag{5.24}$$

Note that this also sets the normlization of our Dirac spinors as $\bar{u}u = 2w$.

5.3 Integral Spin Formalism

Moving on to intergal spins now, the simplest case is for vectors − spin-1 massive particles (we will come back to the masless case in a bit). The transformation properties of these objects are

$$D(\Lambda_1^{-1})V^\mu D(\Lambda_1) = \Lambda^\mu{}_\nu V^\nu, \tag{5.25}$$

which leads to,

$$[J_i, V_j] = i\epsilon_{ijk}V_k, \qquad [K_i, V_j] = 0, \tag{5.26}$$

or, in terms of A and B,

$$[A_i, V_j] = \frac{i}{2}\epsilon_{ijk}V_k, \qquad [B_i, V_j] = \frac{i}{2}\epsilon_{ijk}V_k. \tag{5.27}$$

That is, these come from the $(\frac{1}{2}, \frac{1}{2})$ representation or the direct product $(\frac{1}{2}, 0) \otimes (0, \frac{1}{2})$ (note however that the vector representation is an irreducible representation). A 4-vector has four independent components, but we know that there are only three polarization states for a spin-1 particle. Thus we need a constraint equation, which comes in the form

$$p_\mu \epsilon^\mu(p, m) = 0 \tag{5.28}$$

for momentum p_μ, mass w and spin projection m. In the particle's rest frame this correctly implies that the time-component of ϵ^μ is 0. The spatial components are then chosen as

$$\vec{\epsilon}(\pm 1) = \mp\frac{1}{\sqrt{2}}(1, \pm i, 0), \qquad \vec{\epsilon}(0) = (0, 0, 1). \tag{5.29}$$

As earlier, the polarization vector in any general frame is gotten by making a boost on Eq. 5.29 from the rest frame. The spin-1 projection operator is then defined as

$$P^{(1)}_{\mu\nu}(p) = \sum_m \epsilon_\mu(p, m)\epsilon^*_\nu(p, m) = -g_{\mu\nu} + \frac{p_\mu p_\nu}{w^2} \equiv -g^\perp_{\mu\nu} \tag{5.30}$$

so that $y^\perp_\mu = P^{(1)}_{\mu\nu}(p)y^\nu$ is orthogonal to p for any y^ν. Note that in the center-of-mass (c.m.) frame, $g^\perp_{\mu\nu}$ takes the simple form

$$g^\perp_{\mu\nu,\text{c.m.}} = \begin{pmatrix} 0 & 0 & 0 & 0 \\ 0 & -1 & 0 & 0 \\ 0 & 0 & -1 & 0 \\ 0 & 0 & 0 & -1 \end{pmatrix}, \tag{5.31}$$

so that it projects out the spatial part of any 4-vector in which the angular momentum states "live".

5.3.1 Massless Case

For a massless particle like the photon, we cannot go to its rest frame. Eq. 5.28 now does not uniquely specify ϵ^μ, for if ϵ^μ is a solution, so is $\epsilon^\mu + \alpha p^\mu$ for any α. This is quite common in gauge theories where the extra gauge symmetry renders certain degrees of freedom unphysical (here, the longitudinal polarization component). One needs to place extra conditions called gauge conditions to fix the gauge completely and the theory/final result is completely blind as to what this condition may be. In QED, this is called the Gupta-Bleuler formalism [73] where the only allowed physical states are those with ϵ^0, or rather its expectation value, is equal to that of ϵ^3. Following this, in this work we will choose the two states as the left and right circular polarization states for the particle momentum in the $\hat{z}$ direction:

$$\epsilon^\mu(k\hat{z}, \pm 1) = \mp\frac{1}{\sqrt{2}}(0, 1, \pm i, 0). \tag{5.32}$$

Likewise, the massless spin projection operator cannot be written in the form of of Eq. 5.30 because the polarization now has only two independent components. Following [74], in photoproduction the photon projection operator is constructed for the $\gamma\, p$ system as a whole. Thus

$$g^{\perp\perp}_{\mu\nu} = \sum_{m_\gamma} \epsilon_\mu(m_\gamma)\epsilon^*_\nu(m_\gamma) = g_{\mu\nu} - \frac{P_\mu P_\nu}{P^2} - \frac{k^\perp_\mu k^\perp_\nu}{k^2_\perp}, \tag{5.33}$$

where P^μ is the total and k^μ is the relative momentum of the γp system and

$$k^\perp_\mu = k^\nu g^\perp_{\mu\nu} = k^\nu \left(g_{\mu\nu} - \frac{P_\mu P_\nu}{P^2} \right). \tag{5.34}$$

Then, in the c.m. frame, with the photon momentum parallel to the z-axis, $g^{\perp\perp}_{\mu\nu}$ takes the simple form

$$g^{\perp\perp}_{\mu\nu,\text{c.m.}} = \begin{pmatrix} 0 & 0 & 0 & 0 \\ 0 & -1 & 0 & 0 \\ 0 & 0 & -1 & 0 \\ 0 & 0 & 0 & 0 \end{pmatrix}. \tag{5.35}$$

5.3.2 Spin-2 (and higher) Tensors

Now that we have set up the formalism for spin-1 tensors, it is easy to couple them to form higher momentum tensors. A general spin-n tensor has n indices as $\epsilon_{\mu_1\mu_2\ldots\mu_n}$. For massive states these will be representations of $SO(d-1)$ for d space-time dimensions. The massless case, as for example the graviton $g_{\mu\nu}$ which transforms as a massless spin-2 particle, will be in a $SO(d-2)$ representation because there being no rest frame and one has to go to the helicity frame $p_{hel} = (E, 0, ..., E)$ to define the angular momentum states. Henceforth we will be concerned with massive higher spin states only.

The spin-2 polarization state is then formed as a direct product of two spin-1 states with the appropriate Clebsch-Gordon coefficients attached in the front:

$$\epsilon_{\mu\nu}(p,m) = \sum_{m_1,m_2} \langle 1 m_1 1 m_2 | 2 m \rangle \epsilon_\mu(p,m_1)\epsilon_\nu(p,m_2). \tag{5.36}$$

Since these are representations of $SO(3)$, they are also traceless and symmetric and must satisfy the appropriate generalization of Eq. 5.28. Or,

$$\begin{aligned} g^{\mu\nu}\epsilon_{\mu\nu}(p,m) &= 0 && \text{(5.37a)} \\ \epsilon_{\mu\nu}(p,m) &= \epsilon_{\nu\mu}(p,m) && \text{(5.37b)} \\ p^\mu \epsilon_{\mu\nu}(p,m) &= 0. && \text{(5.37c)} \end{aligned}$$

These supplementary conditions, known as Rarita-Schinger conditions correctly reduce the number of independent components from 16 (for a general rank-2 tensor) to 5 (for a spin-2 state). The generalization of Eq. 5.30 to spin-2 states is

$$\begin{aligned} P^{(2)}_{\mu_1\mu_2\nu_1\nu_2}(p) &= \sum_m \epsilon_{\mu_1\mu_2}(p,m)\epsilon^*_{\nu_1\nu_2}(p,m) && \text{(5.38a)} \\ &= \frac{1}{2}(g^\perp_{\mu_1\nu_1}g^\perp_{\mu_2\nu_2} + g^\perp_{\mu_1\nu_2}g^\perp_{\mu_2\nu_1}) - \frac{1}{3}g^\perp_{\mu_1\mu_2}g^\perp_{\nu_1\nu_2}, && \text{(5.38b)} \end{aligned}$$

which projects out that part of a general rank-2 tensor $T_{\mu\nu}$ which satisfies the Rarita-Schwinger conditions.

Further generalization to spin-J states is easy to see now. One builds up the spin-J states by coupling together spin-$(J-1)$ and spin-1 states as follows

$$\epsilon_{\mu_1\mu_2\ldots\mu_J}(p,m) = \sum_{m_{J-1},m_1} \langle (J-1) m_{J-1} 1 m_1 | J m \rangle \epsilon_{\mu_1\mu_2\ldots\mu_{J-1}}(p,m_{J-1})\epsilon_{\mu_J}(p,m_1). \tag{5.39}$$

The Rarita-Schwinger conditions remain the same except that every summation in Eq. 5.37 is done pairwise over all the indices now. And finally, the spin-J projection operator is defined as

$$P^{(J)}_{\mu_1\mu_2\ldots\mu_J\nu_1\nu_2\ldots\nu_J}(p) = \sum_m \epsilon_{\mu_1\mu_2\ldots\mu_J}(p,m)\epsilon^*_{\nu_1\nu_2\ldots\nu_J}(p,m). \tag{5.40}$$

The last object we need here is a projection operator for spin-J which is *not* of rank $2J$. In other words we want to project out the spin-J states of a rank r tensor when $J \neq r$ (we will need this during construction of amplitudes using the multipole basis). One of the ways in which this can be done is by coupling spin-$(r-1)$ and spin-1 states and using Clebsch-es to project out the spin-J part (note that J is constrained to be between $r-2$ and r now, which will suffice for our multipole construction as we will see). Thus,

$$\epsilon^J_{\mu_1\mu_2\ldots\mu_r}(p,m) = \sum_{m_{r-1},m_1} \langle (r-1)m_{r-1}1m_1|Jm\rangle \epsilon_{\mu_1\mu_2\ldots\mu_{r-1}}(p,m_{r-1})\epsilon_{\mu_r}(p,m_1), \tag{5.41}$$

and

$$P^{(J)}_{\mu_1\mu_2\ldots\mu_r\nu_1\nu_2\ldots\nu_r}(p) = \sum_m \epsilon^J_{\mu_1\mu_2\ldots\mu_r}(p,m)\epsilon^{J*}_{\nu_1\nu_2\ldots\nu_r}(p,m). \tag{5.42}$$

5.3.3 Orbital Angular Momentum

Consider a general decay reaction $a \to b+c$. We know that the combined state bc has orbital angular momentum $\vec{L}$ given by the spherical harmonics in the c.m. frame of the system. The trouble is that, with multiple decays, one cannot be in the c.m. frame for each individual decay all at the same time. Thus one needs to define orbital angular momentum in a covariant fashion, independent of any frame, but which boils down to the familiar spherical harmonics in the c.m. frame.

To proceed further, we first define $P = p_b + p_c$ and $p_{bc} = \frac{1}{2}(p_b - p_c)$ to be the total and relative momentum respectively. The angular momentum-ℓ state is formed by first building up a rank-ℓ tensor as the product of the relative momenta $p^{\nu_1}_{bc}p^{\nu_2}_{bc}\ldots p^{\nu_\ell}_{bc}$ and then projecting out the spin-ℓ part with $P^{(J)}_{\mu_1\mu_2\ldots\mu_J\nu_1\nu_2\ldots\nu_J}(P)$ (*cf.* Eq. 5.39). Thus,

$$L^{(\ell)}_{\mu_1\mu_2\ldots\mu_\ell}(p_{bc}) = P^{(\ell)}_{\mu_1\mu_2\ldots\mu_\ell\nu_1\nu_2\ldots\nu_\ell}(P)p^{\nu_1}_{bc}p^{\nu_2}_{cb}\ldots p^{\nu_\ell}_{bc}. \tag{5.43}$$

Note that the projection operator automatically enforces the Rarita-Schwinger conditions and ensures that there are $(2\ell+1)$ independent components only. For $\ell = 0, 1, 2$ and 3, these states are given as [74]

$$L^{(0)}(p_{bc}) = 1 \tag{5.44a}$$

$$L^{(1)}_\mu(p_{bc}) = p^{bc\perp}_\mu \tag{5.44b}$$

$$L^{(2)}_{\mu_1\mu_2}(p_{bc}) = \frac{3}{2}\left(p^{bc\perp}_{\mu_1}p^{bc\perp}_{\mu_2} - \frac{1}{3}p^2_{bc\perp}g^\perp_{\mu_1\mu_2}\right) \tag{5.44c}$$

$$L^{(3)}_{\mu_1\mu_2\mu_3}(p_{bc}) = \frac{5}{2}\left(p^{bc\perp}_{\mu_1}p^{bc\perp}_{\mu_2}p^{bc\perp}_{\mu_3} - \frac{1}{5}p^2_{bc\perp}(g^\perp_{\mu_1\mu_2}p^{bc\perp}_{\mu_3} + g^\perp_{\mu_1\mu_3}p^{bc\perp}_{\mu_2} + g^\perp_{\mu_2\mu_3}p^{bc\perp}_{\mu_1})\right) \tag{5.44d}$$

where $g^\perp_{\mu_1\mu_2} = g_{\mu_1\mu_2} - \frac{P_{\mu_1}P_{\mu_2}}{P^2}$ and $p^{bc\perp}_\mu = g^\perp_{\mu\nu}p^\nu_{bc}$.

5.4 Tensor-Spinor Combinations

Having covered Dirac spinors and tensors, we now want to combine them to form spin-J representations where $J = n + \frac{1}{2}$ for integral n. Consider for example the simplest case – spin-$\frac{3}{2}$. Note that a spin-$\frac{3}{2}$ particle can belong to any of the following representations $(\frac{3}{2}, 0)$, $(0, \frac{3}{2})$,

$(\frac{1}{2},1)$ or $(1,\frac{1}{2})$. This is a central feature of field theory − there is no unique correspondence between particles and fields. However, our aim here is to build up a spin-$\frac{3}{2}$ state out of a Dirac spinor and a vector, so we will look at the latter two, which are contained in the direct product $(\frac{1}{2},\frac{1}{2})\otimes\big((\frac{1}{2},0)\oplus(0,\frac{1}{2})\big) = (1,\frac{1}{2})\oplus(\frac{1}{2},1)\oplus(0,\frac{1}{2})\oplus(\frac{1}{2},0)$. As usual, on adding spin-1 and spin-$\frac{1}{2}$, we get spin-$\frac{3}{2}$ and another spin-$\frac{1}{2}$. One can also count the degrees of freedom here. A Dirac spinor has $2+2$ (spin-$\frac{1}{2}$ and its antiparticle) and a spin-1 vector, 3 independent components − the product, 12. In the product, these 12 components are divided into 8 components for a spin-$\frac{3}{2}$ and its antiparticle, along with $2+2$ components for another pair of conjugate spin-$\frac{1}{2}$'s (which must be set to zero to project out the spin-$\frac{3}{2}$ part). If $\psi^\mu(p) = \epsilon^\mu(p)u(p,m_{\frac{1}{2}})$ then the latter two spinors are formed by the two possible ways of contracting ψ^μ, viz. $\psi_1 = p_\mu\psi^\mu$ and $\psi_2 = \gamma_\mu\psi^\mu$. If ψ^μ satisfies the Dirac equation, it is easy to see that ψ_1 too must.

The case for ψ_2 is slightly trickier. In fact ψ_2 does *not* satisfy the Dirac equation − the sign of the mass comes out with a wrong sign, i.e., $(\gamma^\lambda p_\lambda + w)\psi_2 = 0$. One needs an extra γ^5 here. Thus, $\psi_2' = \gamma^5\gamma^\mu\psi_\mu$ is the other Dirac spinor. Alternatively, ψ_2 satisfies the Dirac equation for an antiparticle (which has the sign of p_μ reversed). Since γ^5 is block diagonal (or *equivalent* to a block diagonal form in some basis) setting either ψ_2 or ψ_2' to 0 will kill the extra 2 degrees of freedom floating around.

This formulation is easily generalizable to higher spins. The Rarita-Schwinger conditions for general spin-$(n+\frac{1}{2})$ tensor-spinor $\psi_{\mu_1\mu_2.....\mu_n}(p,m)$ takes the form [69]

$$\begin{aligned}
\psi_{\mu_1\mu_2\ldots\mu_i\ldots\mu_j\ldots\mu_n}(p,m) &= \psi_{\mu_1\mu_2\ldots\mu_j\ldots\mu_i\ldots\mu_n}(p,m) && (5.45a)\\
g^{\mu_i\mu_j}\psi_{\mu_1\mu_2\ldots\mu_i\ldots\mu_j\ldots\mu_n}(p,m) &= 0 && (5.45b)\\
(\gamma^\mu p_\mu - w)\psi_{\mu_1\mu_2.....\mu_n}(p,m) &= 0 && (5.45c)\\
p^{\mu_i}\psi_{\mu_1\mu_2\ldots\mu_i\ldots\mu_n}(p,m) &= 0 && (5.45d)\\
\gamma^{\mu_i}\psi_{\mu_1\mu_2\ldots\mu_i\ldots\mu_n}(p,m) &= 0. && (5.45e)
\end{aligned}$$

Eqs. 5.45d and 5.45e are the generalized versions of setting ψ_1 and ψ_2 to zero, as explained above.

5.4.1 Spin-Polarization Connection for Photon

Before ending this section we want to clarify the connection between the "spin" of the photon and its polarization given by ϵ^μ. The photon, even though a spin-1 particle, has only two polarization states. As we have mentioned before, this comes from the fact that it is massless − the longitudinal polarization is unphysical and can be gauged away. Thus the "spin" of the photon can only take values ±1 and there is no 0-spin state. Additionally, the "spin" quantization is along the longitidinal direction and these are called the helicity states, even though ϵ_z along the longitudinal direction is 0. This last part is slightly tricky to see, so we will demonstrate the connection here explicitly. Our proof follows Jackson [75] treating the problem semi-classically.

Classically, the angular momentum of the electromagnetic field is given by

$$\vec{J} = \int d^3x\, \vec{x}\times(\vec{E}\times\vec{B}) \tag{5.46}$$

where $\vec{E}$ is the electric field and $\vec{B}$ is the magnetic field given in terms of the vector potential $\vec{A}$ as $\vec{B} = \vec{\nabla}\times\vec{A}$. In field theory, A^μ is the photon field, proportional to ϵ^μ. Expanding $\vec{E}\times(\vec{\nabla}\times\vec{A})$ we get

$$\vec{J} = \int d^3x\, \vec{x} \times (E_\ell \vec{\nabla} A_\ell - E_\ell \partial_\ell \vec{A}) \tag{5.47a}$$

$$= \int d^3x\, (E_\ell (\vec{x} \times \vec{\nabla}) A_\ell - E_\ell x_i \partial_\ell A_j \epsilon^{ijk} \hat{k}) \tag{5.47b}$$

$$= \int d^3x\, (E_\ell (\vec{x} \times \vec{\nabla}) A_\ell + \vec{E} \times \vec{A}), \tag{5.47c}$$

where ϵ^{ijk} is the completely anti-symmetric tensor and the last step uses an integration by parts. If we identify the orbital angular momentum operator by $-i(\vec{x} \times \vec{\nabla})$ then the expression for the total angular momentum breaks down into an orbital part $\vec{L} = E_\ell (\vec{x} \times \vec{\nabla}) A_\ell$ and a "spin" part $\vec{S} = \vec{E} \times \vec{A}$.

Now in the radiation gauge, $\vec{A}$ is transverse to the propagation vector $\vec{k} = k\hat{z}$ with $\vec{E} = -\frac{\partial \vec{A}}{\partial t}$. This allows an expansion of $\vec{A}$ in the helicity basis $\vec{\epsilon}_\pm = (1/\sqrt{2})(\vec{\epsilon}_x \pm i\vec{\epsilon}_y)$ as

$$\vec{A} = a_+(k)\vec{\epsilon}_+ + a_-(k)\vec{\epsilon}_-, \tag{5.48}$$

and using the property $\vec{\epsilon_+} \times \vec{\epsilon_-} = -i\hat{z}$, one finds

$$\vec{S} \sim k(\,|a_+(k)|^2 - |a_-(k)|^2\,)\hat{z}. \tag{5.49}$$

Thus, semi-classically, the photon "spin" is always along $\hat{k}$ with the amplitudes for "up" or "down" given by $a_+(k)$ and $a_-(k)$ respectively.

5.5 $\Sigma^0 \to \gamma\Lambda \to \gamma p\pi^-$ and $\phi \to KK$ Decay Amplitudes

5.5.1 $\Sigma^0 \to \gamma\Lambda$

Since Σ^0 and Λ are both neutral, the $\Sigma^0 \to \gamma\Lambda$ transition can only be through a magnetic ($M1$) transition. The amplitude for this process is given by

$$\mathcal{A}_{\Sigma^0 \to \gamma\Lambda} = \epsilon^*_\mu\,(p_\gamma, m_\gamma)\,\langle \Lambda\,(p_\Lambda, m_\Lambda)\,|J^\mu|\,\Sigma^0\,(p_{\Sigma^0}, m_{\Sigma^0})\rangle, \tag{5.50}$$

where $\epsilon^*_\mu\,(p_\gamma, m_\gamma)$ is the polarization of the outgoing photon and J^μ is the electromagnetic hadronic current. Due to the $M1$ transition, the matrix element for the electromagnetic hadronic current can be written as

$$\langle \Lambda\,(p_\Lambda, m_\Lambda)\,|J^\mu|\,\Sigma^0\,(p_{\Sigma^0}, m_{\Sigma^0})\rangle = e g_{\Sigma^0\Lambda} \bar{u}_\Lambda\,(p_\Lambda, m_\Lambda)\,\sigma^{\mu\nu} p_\nu u_{\Sigma^0}\,(p_{\Sigma^0}, m_{\Sigma^0})\,, \tag{5.51}$$

where $p = p_\gamma = p_{\Sigma^0} - p_\Lambda$ and $g_{\Sigma^0\Lambda}$ is the effective coupling constant for the transition. In the Σ^0 rest frame, the amplitude expression then effectively boils down to

$$\mathcal{A}_{\Sigma^0 \to \gamma\Lambda} \sim \bar{u}_\Lambda\,(-p, m_\Lambda)\,\not{\epsilon}^*\,(p_\gamma, m_\gamma)\,\not{p} u_{\Sigma^0}\,(0, m_{\Sigma^0})\,, \tag{5.52}$$

where we have used the Feynman slash notation $\not{p} = p^\mu \gamma_\mu$.

To simplify this expression, from Eq. 5.21,

$$\bar{u}_\Lambda = u^\dagger \gamma^0 = \sqrt{E_\Lambda + w_\Lambda} \left(\chi^\dagger(m_\Lambda), -\chi^\dagger(m_\Lambda) \frac{\vec{\sigma} \cdot \vec{p}_\Lambda}{E_\Lambda + w_\Lambda} \right) \sim \left(\chi^\dagger(m_\Lambda), \chi^\dagger(m_\Lambda) \frac{\vec{\sigma} \cdot \vec{p}}{E_\Lambda + w_\Lambda} \right) \tag{5.53}$$

in the Σ^0 rest frame. Similarly,

$$u_{\Sigma^0} \sim \begin{pmatrix} \chi(m_{\Sigma^0}) \\ 0 \end{pmatrix}. \tag{5.54}$$

Now,

$$\not{p} = \begin{pmatrix} p & -\vec{\sigma}\cdot\vec{p} \\ \vec{\sigma}\cdot\vec{p} & -p \end{pmatrix} \tag{5.55}$$

(from here on, $p = |\vec{p}\,|$) so that

$$\not{p} u_{\Sigma^0} \sim \begin{pmatrix} p\,\chi(m_{\Sigma^0}) \\ \vec{\sigma}\cdot\vec{p}\chi(m_{\Sigma^0}) \end{pmatrix}. \tag{5.56}$$

We also know that the time component of ϵ^*_μ is 0, so that

$$\not{\epsilon}^* = \begin{pmatrix} 0 & -\vec{\sigma}\cdot\vec{\epsilon}^* \\ \vec{\sigma}\cdot\vec{\epsilon}^* & 0 \end{pmatrix} \tag{5.57}$$

and thus

$$\not{\epsilon}^*\not{p} u_{\Sigma^0} \sim \begin{pmatrix} -(\vec{\sigma}\cdot\vec{\epsilon}^*)(\vec{\sigma}\cdot\vec{p})\chi(m_{\Sigma^0}) \\ p(\vec{\sigma}\cdot\vec{\epsilon}^*)\chi(m_{\Sigma^0}) \end{pmatrix}. \tag{5.58}$$

Putting everything together, we arrive at the following expression for the decay amplitude, computed in the Σ^0 rest frame

$$\begin{aligned} \mathcal{A}_{\Sigma^0\to\gamma\Lambda} &\sim \left(\chi^\dagger(m_\Lambda), \chi^\dagger(m_\Lambda)\tfrac{\vec{\sigma}\cdot\vec{p}}{E_\Lambda + w_\Lambda}\right) \begin{pmatrix} -(\vec{\sigma}\cdot\vec{\epsilon}^*)(\vec{\sigma}\cdot\vec{p})\chi(m_{\Sigma^0}) \\ p(\vec{\sigma}\cdot\vec{\epsilon}^*)\chi(m_{\Sigma^0}) \end{pmatrix} \\ &= \left[-\chi^\dagger(m_\Lambda)(\vec{\sigma}\cdot\vec{\epsilon}^*)(\vec{\sigma}\cdot\vec{p})\chi(m_{\Sigma^0}) + \tfrac{p}{E_\Lambda + w_\Lambda}\chi^\dagger(m_\Lambda)(\vec{\sigma}\cdot\vec{p})(\vec{\sigma}\cdot\vec{\epsilon}^*)\chi(m_{\Sigma^0})\right] \end{aligned}. \tag{5.59}$$

The above expression can be further simplified as follows. First, note that since $p_\mu\epsilon^\mu = 0$ and we fixed the time component of ϵ^μ as 0 via our gauge choice, $\vec{p}\cdot\vec{\epsilon} = 0$, which means $\vec{p}\cdot\vec{\epsilon}^*$ is also 0. Thus $(\vec{\sigma}\cdot\vec{p})(\vec{\sigma}\cdot\vec{\epsilon}^*) = \vec{p}\cdot\vec{\epsilon}^* + (\vec{p}\times\vec{\epsilon}^*)\cdot\vec{\sigma} = (\vec{p}\times\vec{\epsilon}^*)\cdot\vec{\sigma} = -(\vec{\sigma}\cdot\vec{\epsilon}^*)(\vec{\sigma}\cdot\vec{p})$. Substituting this in the above expression, we get

$$\mathcal{A}_{\Sigma^0\to\gamma\Lambda} \sim -\left(\frac{p}{E_\Lambda + w_\Lambda} + 1\right)\left[\chi^\dagger(m_\Lambda)\left((\vec{p}\times\vec{\epsilon}^*)\cdot\vec{\sigma}\right)\chi(m_{\Sigma^0})\right]. \tag{5.60}$$

Let us now go to the helicity basis for the outgoing photon and expand $\vec{\epsilon}$ as $a_+\vec{\epsilon}_+ + a_-\vec{\epsilon}_-$. Then $\vec{\epsilon}^* = a_-\vec{\epsilon}_+ + a_+\vec{\epsilon}_-$ and $\vec{p}\times\vec{\epsilon}^* = -i(a_-\vec{\epsilon}_+ + a_+\vec{\epsilon}_+) = -i\vec{\epsilon}^*$, whence we can write finally write the amplitude expression stripped of all pre-factors as

$$\mathcal{A}_{\Sigma^0\to\gamma\Lambda} \sim \chi^\dagger(m_\Lambda)\left(\vec{\epsilon}^*\cdot\vec{\sigma}\right)\chi(m_{\Sigma^0}) \tag{5.61}$$

5.5.2 $\Lambda \to p\pi^-$

The $\Lambda \to p\pi^-$ decay is a weak decay. The most general form of the invariant amplitude for a spin-$\frac{1}{2}$ hyperon going into a spin-$\frac{1}{2}$ baryon and a spin-0 pseudo-scalar meson is given by [76]:

$$\mathcal{A}_{\Lambda\to p\pi^-} \sim \bar{u}_p(A - B\gamma^5)u_\Lambda. \tag{5.62}$$

To compute this in the Λ rest frame, from Eq. 5.21,

$$\bar{u}_p \sim \left(\chi^\dagger(m_p), \chi^\dagger(m_p)\frac{-\vec{\sigma}\cdot\vec{p}}{E_p + w_p}\right) \tag{5.63a}$$

$$u_\Lambda \sim \begin{pmatrix} \chi(m_\Lambda) \\ 0 \end{pmatrix}, \tag{5.63b}$$

where $\vec{p}$ is the proton momentum and E_p, the proton energy, in the Λ rest frame. Plugging these back, Eq. 5.62 becomes

$$\mathcal{A}_{\Lambda\to p\pi^-} \sim \left(\chi^\dagger(m_p), \chi^\dagger(m_p)\frac{-\vec{\sigma}\cdot\vec{p}}{E_p+w_p}\right)\begin{pmatrix} A & -B \\ -B & A\end{pmatrix}\begin{pmatrix}\chi(m_\Lambda)\\ 0\end{pmatrix} \tag{5.64a}$$

$$\sim \chi^\dagger(m_p)\,(s + p\,\vec{\sigma}\cdot\hat{n})\,\chi(m_\Lambda) \tag{5.64b}$$

$$\sim \chi^\dagger(m_p)\,(1 + x\,\vec{\sigma}\cdot\hat{n})\,\chi(m_\Lambda), \tag{5.64c}$$

where $s = A$, $p = |\vec{p}|B/(E_p + w_p)$, $x = p/s$, $\hat{n} = \vec{p}/|\vec{p}|$ and $\Delta = \delta_s - \delta_p$ is the phase between s and p (the s and p nomenclature here refers to the non-relativistic S and P wave decays respectively). To relate to experiments, we now define the following quantities

$$\alpha = 2Re(s^*p)/(|s|^2+|p|^2) = 2|x|\cos\Delta/(1+|x|^2) \tag{5.65a}$$

$$\beta = 2Im(s^*p)/(|s|^2+|p|^2) = -2|x|\sin\Delta/(1+|x|^2) \tag{5.65b}$$

$$\gamma = (|s|^2-|p|^2)/(|s|^2+|p|^2) = (1-|x|^2)/(1+|x|^2),\ \text{so that} \tag{5.65c}$$

$$\alpha^2+\beta^2+\gamma^2 = 1. \tag{5.65d}$$

$$\text{Also,}\quad \beta = (1-\alpha^2)^{1/2}\sin\phi \tag{5.65e}$$

$$\gamma = (1-\alpha^2)^{1/2}\cos\phi \tag{5.65f}$$

$$\tan\Delta = -\frac{1}{\alpha}(1-\alpha^2)^{1/2}\sin\phi. \tag{5.65g}$$

The PDG [53] lists $\alpha = 0.642\pm0.013$ and $\Delta = 7.7^\circ\pm4.0^\circ$, whence $x \simeq 2.71e^{-i\Delta}$ or $x \simeq 0.37e^{-i\Delta}$ from the quadratic equation 5.65a. The first value for x gives $\gamma = -0.76$ while the latter gives $\gamma = +0.76$. One can see the sign ambiguity arising from the square root in Eq. 5.65f. However, PDG lists γ as 0.76, so we will take $|x\,| = 0.37$. Finally, for the two body decay of $\Lambda \to p\pi^-$, $|\vec{p}| \simeq 0.1005$ GeV and $E_p \simeq 0.9436$ GeV so that $B/A \simeq 6.88e^{-i\Delta}$ and the final form of the amplitude is

$$\mathcal{A}_{\Lambda\to p\pi^-} \sim \bar{u}_p(1 - 6.88e^{-i\Delta}\gamma^5)u_\Lambda. \tag{5.66}$$

As a passing note, for $|x\,| = 2.71$, $B/A \simeq 50.83e^{-i\Delta}$.

5.5.3 $\phi \to KK$

The four kaons $K^\pm$, $K^0_{L,S}$ are all pseudo-scalars, while the ϕ is a vector, ϵ_ϕ. There is only one way to form a vector out of two pseudo-scalars, *viz.* $\partial_\mu K_1 - \partial_\mu K_2$, antisymmetric in the two kaons. Therefore, the general $\phi \to K_1K_2$ amplitude can be written as

$$\mathcal{A}_{\phi\to K_1K_2} \sim (\epsilon_\phi)^\mu (p_{K_1} - p_{K_2})_\mu. \tag{5.67}$$

In other words, this is a simple P-wave decay.

5.5.4 Normalization

The $\Sigma^0 \to \gamma\Lambda$ transition being an electromagnetic decay, occurs instantaneously before the Σ^0 can travel any significant macroscopic distance. The Λ pathlength is of the order ~ 10 cm, which means that the probability of its decaying outside the CLAS detector (roughly around 5 m, till the outer regions of the drift chambers) is around $1/\exp(50)$ which is negligible, that. Thus, aside acceptance issues, all the final states should be detected by CLAS. Quantum mechanically, this translates to:

$$\int |A_{\Sigma^0\to\gamma\Lambda\to\gamma p\pi^-}|^2 d\Phi_{\Sigma^0\to\gamma\Lambda\to\gamma p\pi^-} = 1, \tag{5.68}$$

where $\Phi_{\Sigma^0\to\gamma\Lambda\to\gamma p\pi^-}$ incorporates the phase space for the Σ^0 decay. This condition should thus be enforced by a normalization factor N. However, overall normalizations cancel out in our fitting procedure (see Sec. 6.1), so that N is not required to be included in our codes. Similarly, the ϕ decays strongly to KK almost instantaneously and CLAS is able to detect all the decay products.

5.6 The Non-resonant Amplitudes

5.6.1 Effective Lagrangians

We summarize below the requisite effective Lagrangians that we will need to build amplitudes for specific processes. To keep the form of these Lagrangians as general as possible, we will denote scalars ($J^P = 0^+$) as $S = \{\sigma(500), f_0(980), \ldots\}$, pseudo-scalars ($J^P = 0^-$) as $\varphi = \{\pi, \eta, \eta', K^+, \ldots\}$, vector mesons ($J^P = 1^-$) as $V = \{\rho, \omega, \phi, K^*(892), \ldots\}$, axial vectors ($J^P = 1^+$) as $V_a = \{K1(1270), \ldots\}$, tensor ($J^P = 2^+$) as $T = \{a2(1320), K2(1430)\ldots\}$ and $J^P = \frac{1}{2}^+$ baryons as $B = \{N, \Lambda, \Sigma^0, \ldots\}$. The photon field is denoted as A_μ and the vector meson and photon field tensors are $V_{\mu\nu} = \partial_\mu V_\mu - \partial_\nu V_\mu$ and $A_{\mu\nu} = \partial_\mu A_\mu - \partial_\nu A_\mu$, respectively.

$$\mathcal{L}_{SBB'} = g_{SBB'}\bar{u}_{B'}u_B S \tag{5.69a}$$

$$\mathcal{L}_{\gamma SV} = \frac{e g_{\gamma SV}}{2M_0} V^{\mu\nu} A_{\mu\nu} S \tag{5.69b}$$

$$\mathcal{L}_{\varphi BB'} = \left(-\zeta i g_{\varphi BB'}\varphi^\dagger \bar{u}_{B'}\gamma_5 u_B + (1-\zeta)\frac{f_{\varphi BB'}}{M_\varphi}\partial^\mu\varphi^\dagger\bar{u}_{B'}\gamma_\mu\gamma_5 u_B\right) \tag{5.69c}$$

$$\mathcal{L}_{\gamma\varphi\varphi} = -ie(\varphi^\dagger\partial_\mu\varphi - \varphi\partial_\mu\varphi^\dagger)A^\mu \tag{5.69d}$$

$$\mathcal{L}_{\gamma\varphi V} = \frac{e g_{\gamma\varphi V}}{4M_0}\epsilon^{\mu\nu\alpha\beta}V_{\mu\nu}A_{\alpha\beta}\,\varphi \tag{5.69e}$$

$$\mathcal{L}_{VBB'} = -g_{VBB'}\bar{u}_{B'}\left(\not{V} + \frac{\kappa_{VBB'}}{2(M_B+M_{B'})}\sigma_{\mu\nu}V^{\mu\nu}\right)u_B \tag{5.69f}$$

$$\mathcal{L}_{\gamma\varphi V_a} = \frac{e g_{\gamma\varphi V_a}}{2M_0}V_a^{\mu\nu}A_{\mu\nu}\,\varphi \tag{5.69g}$$

$$\mathcal{L}_{V_aBB'} = -\bar{u}_{B'}\left(g^E_{V_aBB'}\not{V}_a + \frac{g^M_{V_aBB'}}{2(M_B+M_{B'})}\sigma_{\mu\nu}V_a^{\mu\nu}\right)\gamma_5 u_B \tag{5.69h}$$

$$\mathcal{L}_{\gamma\varphi T} = -ie\frac{g_{\gamma\varphi T}}{M_0^2}\epsilon\alpha\beta\mu\nu A^{\mu\nu}(\partial^\alpha T^{\beta\rho} - \partial^\beta T^{\alpha\rho})\partial_\rho\varphi \tag{5.69i}$$

$$\mathcal{L}_{TBB'} = -2i\frac{g^{(1)}_{TBB'}}{M_B}\bar{B}'(\gamma_\lambda\partial_\sigma + \gamma_\sigma\partial_\lambda)BT^{\lambda\sigma} + 4\frac{g^{(2)}_{TBB'}}{M_B^2}\partial_\lambda\bar{B}'\partial_\sigma BT^{\lambda\sigma} \tag{5.69j}$$

The forms of these Lagragians represent the simplest possible way of constructing a scalar Lagrangian density function $\mathcal{L}$ out of the J^P properties of the particles at the interaction vertex. Gauge invariance is naturally incorporated by constructing the Lagrangians using the gauge invariant tensors $F_{\mu\nu}$ and $A_{\mu\nu}$. The variable ζ in Eq. 5.69c ranges between 1 and 0 and interpolates between a pseudo-scalar coupling $g_{\varphi BB'}$ and a pseudo-vector coupling $f_{\varphi BB'}$ that are related as

$$\frac{f_{\varphi BB'}}{M_\varphi} = \frac{g_{\varphi BB'}}{M_B + M_{B'}}. \tag{5.70}$$

The forms of the tensor couplings can be found in Ref. [190].

5.6.2 Feynman rules

In this section we summarize our Feynman rules to clarify the choices of the phases in our amplitudes. We start by writing the S-matrix element connecting the initial and final states as

$$S_{fi} = 1 - iT_{fi}, \tag{5.71}$$

where T_{fi} is the transition matrix element which is also identified with the Lorentz invariant amplitude $\mathcal{A}$. For the Feynman rules for obtaining S_{fi}, each vertex contributes a factor ig, where g is relevant coupling constant in the Lagrangian. The spinor propagator is $i(\not{p}+m)/(p^2-m^2+i\epsilon)$ and the spin-0 propagator is $i/(p^2-m^2+i\epsilon)$. The vector boson projection operator is $P_V^{\mu\nu} = \sum \varepsilon_V^{*\mu}\varepsilon_V^{\nu}$, where the sum is over the spin-projections. For the massless case (photon), this is given by $P_\gamma^{\mu\nu} = -g^{\mu\nu}$, while for the massive case, this is $P_V^{\mu\nu} = -g^{\mu\nu} + p^\mu p^\nu/p^2$. The corresponding (Feynman pole) propagators are $iP_V^{\mu\nu}/(p^2 - m^2 + i\epsilon)$. For any incoming (outgoing) paricle, the derivative operator ∂_μ brings down a factor of $-ip_\mu$ ($+ip_\mu$). Finally, we will add an overall factor of i to get $\mathcal{A}$ from S_{fi}. Unless otherwise mentioned, the 4-momenta for the incoming photon, outgoing meson, initial target proton and final outgoing baryon (a proton or a hyperon) as k, q, p and p', respectively.

5.6.3 $K^+\Lambda$ and $K^+\Sigma^0$ amplitudes

5.6.3.1 s- and t-channel Born terms

Denoting Y as a generic hyperon for both Λ and Σ^0, the s-channel proton and t-channel K^+ exchange amplitudes are:

$$\mathcal{A}_{KY}^{s-ch.\ \text{proton}} = ie\bar{u}_Y\left(\zeta g_{KYp}\gamma_5 + (1-\zeta)\frac{f_{KYp}}{M_K}\gamma_5\not{q}\right)\frac{\not{p}+\not{k}+M_p}{s-M_p^2}\left(\not{\varepsilon}_\gamma + \frac{\kappa_p}{2M_p}\not{k}\not{\varepsilon}_\gamma\right)u_i \tag{5.72a}$$

$$\mathcal{A}_{KY}^{t-ch.\ K^+} = \frac{2ieq\cdot\varepsilon_\gamma}{t-M_K^2}\bar{u}_Y\left(\zeta g_{KYp}\gamma_5 + (1-\zeta)\frac{f_{KYp}}{M_K}\gamma_5(\not{q}-\not{k})\right)u_i. \tag{5.72b}$$

For the t-channel Born term, it turns out that the pseudo-scalar ($\zeta = 1$) and pseudo-vector ($\zeta = 0$) forms are equivalent. This can be shown as follows:

$$\begin{aligned}
\mathcal{A}_{KY}^{K^+\,PV} &= \frac{2ieq\cdot\varepsilon_\gamma}{t-M_K^2}\left(\frac{f_{KYp}}{M_K}\right)\bar{u}_Y\gamma_5(\not{p}-\not{p}')u_i \\
&= i\frac{2ieq\cdot\varepsilon_\gamma}{t-M_K^2}\left(\frac{f_{KYp}}{M_K}\right)\bar{u}_Y(\not{p}'\gamma_5+\gamma_5\not{p})u_i \\
&= \frac{2ieq\cdot\varepsilon_\gamma}{t-M_K^2}\left(\frac{f_{KYp}}{M_K}\right)\bar{u}_Y(M_Y\gamma_5+\gamma_5 M_p)u_i \\
&= \frac{2ieq\cdot\varepsilon_\gamma}{t-M_K^2}g_{KYp}\bar{u}_Y\gamma_5 u_i = \mathcal{A}_{KY}^{K^+\,PS},
\end{aligned} \tag{5.73}$$

where we have invoked the Dirac equation ($\not{p}u_i = M_p u_i$ and $\bar{u}_Y\not{p}' = \bar{u}_Y M_Y$) and the connection between the pseudo-vector and pseudo-scalar couplings given by Eq. 5.70.

Eqs. 5.72a and 5.72b and not gauge invariant by themselves. For the pseudo-scalar coupling case, in the Guidal-Laget-Vanderhaeghen (GLV) [138] model, the t-channel term (Eq. 5.72b) is combined with the pseudo-scalar s-channel electric term in Eq. 5.72a to give a gauge-invariant Born amplitude

$$\mathcal{A}_{KY}^{\text{GLV}} = ieg_{KYp}\bar{u}_Y\gamma_5\left(\frac{\not{k}\not{\varepsilon}_\gamma}{2p\cdot k} + \left(\frac{p\cdot\varepsilon_\gamma}{p\cdot k} - \frac{q\cdot\varepsilon_\gamma}{q\cdot k}\right)\right)u_i. \tag{5.74}$$

For the pseudo-vector case, preserving gauge-invariance requires the addition of an extra "contact" term

$$\mathcal{A}_{KY}^{\text{contact}} = -ie(1-\zeta)\left(\frac{f_{KYp}}{M_K}\right)\bar{u}_Y\gamma_5\not{\varepsilon}_\gamma u_i, \tag{5.75}$$

and the gauge-invariant pseudo-vector K^+ exchange Born term reads

$$\mathcal{A}_{KY}^{\text{contact}} = ie(1-\zeta)\left(\frac{f_{KYp}}{M_K}\right)\bar{u}_Y\gamma_5\left(\frac{\not{p}+\not{k}+M_p}{2p\cdot k}(\not{\varepsilon}_\gamma + \frac{\kappa_p}{2M_p}\not{k}\not{\varepsilon}_\gamma) - \frac{q\cdot\varepsilon_\gamma}{q\cdot k}(\not{q}-\not{k}) - \not{\varepsilon}_\gamma\right)u_i. \tag{5.76}$$

5.6.3.2 t-channel $K^*(892)$ exchange

The $K^*(892)$ exchange amplitude is

$$\mathcal{A}_{KY}^{t-ch.\ K^*} = -eg_{K^*YN}\left(\frac{g_{\gamma KK^*}}{M_0}\right)\frac{\epsilon_{\mu\nu\alpha\beta}q^\mu k^\alpha(\varepsilon_\gamma)^\beta}{t-M_{K^*}^2}\bar{u}_Y\left(\gamma^\nu + \frac{\kappa_{K^*YN}}{M_p+M_Y}\gamma^\nu(\not{q}-\not{k})\right)u_i \tag{5.77}$$

5.6.3.3 t-channel $K1(1270)$ exchange

The axial vector $K1(1270)$ exchange amplitude is

$$\mathcal{A}_{KY}^{t-ch.\ K1} = -\frac{eg_{\gamma KK1}}{M_0}\frac{(k\cdot q(\varepsilon_\gamma)^\alpha - q\cdot\varepsilon_\gamma k^\alpha)}{t-M_{K1}^2}\bar{u}_Y\left(g_{K1Yp}^E\gamma_\alpha + \frac{(\not{k}-\not{q})}{M_Y+M_p}g_{K1Yp}^M\gamma_\alpha\right)\gamma_5 u_i \tag{5.78}$$

5.6.3.4 u-channel Y' exchanges

The u-channel processes correspond to hyperon (Y') exchanges. For $J^P = \frac{1}{2}^+$ spinors such as $\Lambda(1115)$, $\Sigma^0(1192)$ and $\Lambda^*(1800)$, the amplitude is

$$\mathcal{A}_{KY}^{u-ch.\ Y'} = ie\frac{\kappa_{YY'}}{2M_p}\bar{u}_Y\left[\not{k}\not{\varepsilon}_\gamma\frac{\not{p}-\not{q}+M_{Y'}}{u-M_{Y'}^2}\left(g_{KpY'}\zeta\gamma_5 + (1-\zeta)\frac{f_{KpY'}}{M_K}\gamma_5\not{q}\right)\right]u_i. \tag{5.79}$$

5.6.3.5 t-channel tensor exchanges

Following the work of Yu-Choi-Kim (YCK) [190], the 2^{++} tensor meson $K_2(1430)$ exchange amplitude reads

$$\mathcal{A}_{KY}^{t-ch.\ K2} = \epsilon_{\alpha\beta\mu\nu}\varepsilon^\mu k^\nu q^\alpha q_\rho X_I\ \frac{P^{(2)\beta\rho\lambda\sigma}(p_t)}{t-M_T^2}\bar{u}_Y\left(G_T^1(\gamma_\lambda\bar{p}_\sigma + \gamma_\sigma\bar{p}_\lambda) + G_T^2\bar{p}_\lambda\bar{p}_\sigma\right)u_i, \tag{5.80}$$

where $p_t = (q-k)$ is the t-channel exchange momentum, $\bar{p} = (p+p')/2$, and the tensor polarization projection operator $P^{(2)}$ is of the same form as Eq. 5.38. The two couplings are further broken down as:

$$G_{K2}^1 = \frac{2g_{\gamma KK2}}{M_0^2}\frac{2g_{pYK2}^1}{m_p^2},\ \ G_{K2}^2 = -\frac{2g_{\gamma KK2}}{M_0^2}\frac{4g_{pYK2}^2}{m_p^2}. \tag{5.81}$$

5.6.4 ηp and $\eta' p$ amplitudes

The forms of the amplitudes remain exactly the same between the η and η' cases, so only the ηp amplitudes are given below. The spinors for the incoming and the outgoing proton are u_i and u_f, respectively.

5.6.4.1 t-channel ρ and ω exchanges

For vector meson $V = \{\rho, \omega\}$ exchanges, the form of the amplitude is the same as Eq. 5.77 and reads

$$\mathcal{A}_{\eta p}^{t-ch.\ V} = -eg_{VNN}\left(\frac{g_{\gamma\eta V}}{M_0}\right)\frac{\epsilon_{\mu\nu\alpha\beta}q^\mu k^\alpha(\varepsilon_\gamma)^\beta}{t-M_V^2}\bar{u}_f\left(\gamma^\nu + \frac{\kappa_{VNN}}{2M_p}\gamma^\nu(\not{q}-\not{k})\right)u_i \tag{5.82}$$

5.6.4.2 s- and u-channel proton exchange

The proton exchange Born terms are given by

$$\mathcal{A}_{\eta p}^{s-ch.\ \text{proton}} = ieg_{\eta pp}\bar{u}_f\left(\zeta\gamma_5 + (1-\zeta)\frac{\gamma_5\not{q}}{2M_p}\right)\frac{\not{p}+\not{k}+M_p}{s-M_p^2}\left(\not{\varepsilon}_\gamma + \frac{\kappa_p}{2M_p}\not{k}\not{\varepsilon}_\gamma\right)u_i \tag{5.83}$$

$$\mathcal{A}_{\eta p}^{u-ch.\ \text{proton}} = ieg_{\eta pp}\bar{u}_f\left(\not{\varepsilon}_\gamma + \frac{\kappa_p}{2M_p}\not{k}\not{\varepsilon}_\gamma\right)\frac{\not{p}-\not{q}+M_p}{u-M_p^2}\left(\zeta\gamma_5 + (1-\zeta)\frac{\gamma_5\not{q}}{2M_p}\right)u_i, \tag{5.84}$$

where both terms must be taken together to maintain gauge-invariance. A contact term for the pseudo-vector case can be added here as well [188]:

$$\mathcal{A}_{\eta p}^{\text{contact}} = ie(1-\zeta)\left(\frac{f_{\eta pp}}{M_pM_\eta}\right)\bar{u}_f\not{\varepsilon}_\gamma\not{k}\gamma_5 u_i. \tag{5.85}$$

5.6.5 π^+n and π^0p amplitudes

In the following, we will include an extra isospin factor X_I that equals $\sqrt{2}$ and 1 for the π^+n and π^0p channels, respectively [138, 190].

5.6.5.1 s- and t-channel Born terms

Due to C-parity conservation in π^0p channel, the t-channel π exchange and therefore the crossed nucleon exchange Born terms can occur only in the π^+n channel. The forms are the same as in Eq. 5.72:

$$\mathcal{A}_{\pi^+n}^{s-ch.\ \text{proton}} = ieX_I\ \bar{u}_n\left(\zeta g_{\pi NN}\gamma_5 + (1-\zeta)\frac{f_{\pi NN}}{M_\pi}\gamma_5\not{q}\right)\frac{\not{p}+\not{k}+M_p}{s-M_p^2}\left(\not{\varepsilon}_\gamma + \frac{\kappa_p}{2M_p}\not{k}\not{\varepsilon}_\gamma\right)u_i \tag{5.86a}$$

$$\mathcal{A}_{\pi^+n}^{t-ch.\ \pi^+} = \frac{2X_I\ ieq\cdot\varepsilon_\gamma}{t-M_\pi^2}\bar{u}_n\left(\zeta g_{\pi NN}\gamma_5 + (1-\zeta)\frac{f_{\pi NN}}{M_\pi}\gamma_5\not{q}-\not{k})\right)u_i, \tag{5.86b}$$

Similar to the K^+Y channel case, we have a gauge-invariant GLV term

$$\mathcal{A}_{\pi^+n}^{\text{GLV}} = ieX_I\ g_{\pi NN}\bar{u}_N\gamma_5\left(\frac{\not{k}\not{\varepsilon}_\gamma}{2p\cdot k} + \left(\frac{p\cdot\varepsilon_\gamma}{p\cdot k} - \frac{q\cdot\varepsilon_\gamma}{q\cdot k}\right)\right)u_i. \tag{5.87}$$

5.6.5.2 t-channel vector meson exchanges

For the t-channel vector meson exchanges, ρ^+ can be exchanged for the π^+n case, while both ρ^0 and ω exchanges can occur for π^0p. Following Eq. 5.77, the $V = \{\rho, \omega\}$ exchange amplitude is

$$\mathcal{A}_{\pi N}^{t-ch.\ V} = -eg_{VNN}X_I\ \left(\frac{g_{\gamma\pi V}}{M_0}\right)\frac{\epsilon_{\mu\nu\alpha\beta}q^\mu k^\alpha(\varepsilon_\gamma)^\beta}{t-M_V^2}\bar{u}_N\left(\gamma^\nu + \frac{\kappa_V}{2M_p}\gamma^\nu(\not{q}-\not{k})\right)u_i. \tag{5.88}$$

5.6.5.3 t-channel axial vector exchanges

Following the work of GLV [138] and YCK [190], we include t-channel exchanges of the axial vector mesons $V_a = \{a_1(1260)(1^-(1^{++})), b_1(1235)(1^+(1^{+-})), h_1(1170)(0^-(1^{+-}))\}$ [1]. The general form of the amplitude is the same as Eq. 5.78:

$$\mathcal{A}_{\pi N}^{t-ch.\ V_a} = -\frac{e g_{\gamma\pi V_a}}{M_0} X_I \ \frac{(k\cdot q(\varepsilon_\gamma)^\alpha - q\cdot\varepsilon_\gamma k^\alpha)}{t - M_{V_a}^2} \bar{u}_N \left(g_{V_a NN}^E \gamma_\alpha + \frac{(\not{k} - \not{q})}{2M_p} g_{V_a NN}^M \gamma_\alpha \right) \gamma_5 u_i. \quad (5.89)$$

5.6.5.4 t-channel tensor exchanges

The spin-2 tensor meson $a_2(1320)(1^-(2^{++}))$ exchange amplitude for the $\pi^+ n$ case (C-parity forbids this exchange in $\pi^0 p$) is:

$$\mathcal{A}_{\pi^+ n}^{t-ch.\ a2} = \epsilon_{\alpha\beta\mu\nu}\varepsilon^\mu k^\nu q^\alpha q_\rho X_I \ \frac{P^{(2)\beta\rho\lambda\sigma}(p_t)}{t - M_T^2} \bar{u}_n \left(G_T^1(\gamma_\lambda \bar{p}_\sigma + \gamma_\sigma \bar{p}_\lambda) + G_T^2 \bar{p}_\lambda \bar{p}_\sigma \right) u_i, \quad (5.90)$$

where

$$G_{a2}^1 = \frac{2 g_{\gamma\pi a2}}{M_0^2} \frac{2 g_{NNa2}^1}{m_p^2}, \ \ G_{a2}^2 = -\frac{2 g_{\gamma\pi a2}}{M_0^2} \frac{2 g_{NNa2}^2}{m_p^2}. \quad (5.91)$$

5.6.6 ωp and ϕp amplitudes

5.6.6.1 t-channel pseudo-scalar (π and η) exchanges

Continuing our notation set up in Sec. 5.6.1 we denote $\varphi = \{\pi, \eta\}$ and $V = \{\omega, \phi\}$. The pseudo-scalar exchange amplitudes then take the form

$$\mathcal{A}_{Vp}^{t-ch.\ \varphi} = -i \frac{e g_{\varphi NN} g_{\gamma\varphi V}}{M_0} \bar{u}_f \gamma_5 u_i \epsilon^{\mu\nu\alpha\beta} q_\mu (\varepsilon_V^*)_\nu k_\alpha (\varepsilon_\gamma)_\beta \frac{1}{t - M_\varphi^2} \quad (5.92)$$

5.6.6.2 t-channel scalar meson (σ, $f_0(980)$ and $a_0(980)$) exchanges

The scalar meson (S) exchange amplitudes read

$$\mathcal{A}_{Vp}^{t-ch.\ S} = \frac{e g_{\gamma SV} g_{SNN}}{M_0} \bar{u}_f u_i \frac{(k\cdot q \varepsilon_V^* \cdot \varepsilon_\gamma - k\cdot\varepsilon_V^* q\cdot\varepsilon_\gamma)}{t - M_S^2} \quad (5.93)$$

5.6.6.3 s- and u-channel nucleon exchanges

Since both ω and ϕ are isoscalars, only nucleons (and not Δ's) can be exchanged in the u- or s-channel (the former and latter are sometimes referred to as the "crossed" and "direct" terms, respectively). From the perspective of gauge invariance, the two amplitudes must be taken together, since the individual amplitudes break gauge invariance. The proton exchange amplitude can thus be put into a compact form

$$\mathcal{A}_{Vp}^{\text{proton}} = e g_{Vpp} \bar{u}_f \left(\Gamma_V \frac{\not{p}_s + M_p}{s - M_p^2} \Gamma_\gamma + \Gamma_\gamma \frac{\not{p}_u + M_p}{u - M_p^2} \Gamma_V \right) u_i \quad (5.94)$$

where

$$\Gamma_\gamma = \not{\varepsilon}_\gamma + \frac{\kappa_p}{2M_p} \not{k} \not{\varepsilon}_\gamma \quad (5.95a)$$

$$\Gamma_V = \not{\varepsilon}_V^* - \frac{\kappa_V}{2M_p} \not{q} \not{\varepsilon}_V^*, \quad (5.95b)$$

and $p_s = (p+k)$ and $p_u = (p-q)$ are the exchanged 4-momenta in the s and u-channel, respectively.

[1] The isospin, G-parity and spin, parity and charge-conjugation quantum numbers are denoted by $I^G(J^{PC})$

5.6.7 The Pomeron ($I\!P$) and related exchanges

For later convenience, we first list some of the general numerical values of the Regge trajectories, couplings, *et al.* The most basic $I\!P$ trajectory is the classical soft or diffractive Donnachie-Landshoff (DL) Pomeron

$$\alpha_{I\!P_1}(t) = \alpha_{I\!P_1}(0) + \alpha'_{I\!P_1} t \tag{5.96}$$

where $\alpha_{I\!P_1}(0) \approx 1.08$ is the intercept and $\alpha'_{I\!P_1} = 0.25$ GeV^{-2} is the slope. There is also a "hard" DL Pomeron given by [8]

$$\alpha_{I\!P_0}(t) = \alpha_{I\!P_0}(0) + \alpha'_{I\!P_0} t, \;\; \alpha_{I\!P_0}(0) = 1.44, \;\; \alpha'_{I\!P_0} = 0.1 \text{ GeV}^{-2}. \tag{5.97}$$

With a larger intercept, the hard-DL Pomeron is supposed to dominate at higher energies, especially in the charmonium sector. At lower energies, near threshold, some authors [165, 166, 25] postulate the existence of a daughter glueball trajectory

$$\alpha_{I\!P_2}(t) = \alpha_{I\!P_2}(0) + \alpha'_{I\!P_2} t, \;\; \alpha_{I\!P_2}(0) = -0.75, \;\; \alpha'_{I\!P_2} = 0.25 \text{ GeV}^{-2}. \tag{5.98}$$

The negative intercept indicates that this will contribute only at the lowest energies. Actually, the $\alpha_{I\!P_2}(t)$ is inspired by 0^{++} glueball with mass $M^2_{gb} \approx 3$ GeV^2 that is predicted from lattic QCD calculations [169].

Following the work of Titov *et al* [164, 165, 166, 167], we will denote

$$F_p(t) = \frac{4M_p^2 - 2.8t}{(4M_p^2 - t)(1 - t/t_0)^2} \tag{5.99a}$$

$$F_V(t) = \frac{1}{1 - t/M_V^2} \frac{2\mu_0^2}{2\mu_0^2 + M_V^2 - t} \tag{5.99b}$$

$$F_\phi^{phen.}(t) = \exp(-B_\phi |t - t_0|) \tag{5.99c}$$

$$C_V = \frac{12 \beta_q \beta_{q'} e}{\gamma_V} \tag{5.99d}$$

$$M_{I\!P}(s,t) = C_V F_p(t) F_V(t) \left(\frac{s}{s_0}\right)^{\alpha_{I\!P}(t)-1} e^{-i\frac{\pi}{2}\alpha_{I\!P}(t)} \tag{5.99e}$$

where F_p is the proton isoscalar form-factor, F_V is the $I\!P$-γ-V vertex form-factor ($F_\phi^{phen.}$ is a phenomenological ansatz for the ϕ case [166], B_ϕ being the exponential slope from Sec. 9.4) and $s_0 = 1/\alpha'$. The phenomenological momentum cut-off scales in the form-factors are $t_0 = 0.7$ GeV^2 and $\mu_0^2 = 1.1$ GeV^2. The vector meson decay constant are $\gamma_\omega = 17.05$, $\gamma_\phi = -13.13$ that follow from the decay width as [8]:

$$\Gamma_{V \to e^+e^-} = \frac{\alpha^2}{3} \frac{4\pi}{\gamma_V^2} m_V. \tag{5.100}$$

Note that γ_ϕ has a relative minus sign compared to γ_ρ and γ_ω from SU(3) [8]. The couplings of the Pomeron to the individual quarks are given by β, where $\beta_u = 2.05$ GeV^{-1} for the light quark sector and $\beta_s = 1.61$ GeV^{-1} for the strange quark. Therefore, for the ω channel, the coupling will be β_u^2, while for the ϕ, this will be $\beta_u \beta_s$.

5.6.7.1 How does the Pomeron couple?

We first note that the that the Pomeron is not a single particle, it is a Regge trajectory. From Regge theory, we only know that its overall energy behavior is like a spin-1 exchange. However, this does not tell us that that the Pomeron *couples* like a spin-1 particle, and this point was specifically

noted by Gilman *et al.* [134]. In the DL-model [8], taking a cue from the fact that the $I\!P$ exchange process seems to be universal, independent of isospin, charge conjugation and parity reveral, it was postulated that $I\!P$ couples to individual quarks as an isoscalar $J^{PC} = 1^{++}$ photon. The DL-model also assumes that $I\!P$ couples to individual quarks inside the hadrons, which lead to the so called additive quark rule [8]. This leads to πp cross-sections being 2/3 that of pp scattering, since mesons have two constituent quarks and baryons have three. Another property of the Pomeron exchange amplitude is that in the diffractive limit, this has to be almost purely imaginary (in the parlance of Regge theory, the Pomeron has an even signature factor). The optical theorem that relates the total cross section to the forward angle cross section:

$$\sigma_{total}(s) \approx s^{-1}\mathcal{A}(s, t = 0), \text{ at large } s \tag{5.101}$$

so that in the $t \to 0$ diffractive limit, $\mathcal{A}$ scales as $\sim s^1$ as well. Combining these facts, the Regge factor in the soft diffractive Pomeron amplitude behaves like [8]

$$\mathcal{A}_{I\!P_1} \propto \exp(-i\alpha_{I\!P_1}/2)(\alpha'_{I\!P_1} s)^{\alpha_{I\!P_1}-1}. \tag{5.102}$$

The only remaining part is the γ_μ (photon-like) coupling at the $I\!P$-q-q' vertex, which Donnachie and Landshoff put "by hand" [8]. From this, it follows that a vector coupling will preserve helicity (for approximately massless quarks). Therefore, the DL-model immediately explains the observed s-channel helicity conservation for the vector mesons in the diffractive limit (see also Ref. [134])[2]. At this point following Titov *et al* [165], we will combine the Regge and the form-factors into the expression:

(5.103)

and write the $I\!P$ exchange amplitude as [165]

$$\mathcal{A}^{I\!P}_{Vp} = -M_{I\!P}(s, t)(\varepsilon_V)^*_\mu(\varepsilon_\gamma)_\nu \bar{u}_f h^{\mu\nu} u_i. \tag{5.104}$$

The problem therefore reduces to determining the form of the tensor $h^{\mu\nu}$.

In the vector-meson-dominance (VMD) picture [110, 112], the incoming photon first converts into a vector meson ($q\bar{q}$ pair) which then scatters off the target nucleon. This is shown schematically in Fig. **??**. The diagram includes two $I\!P$-q-q' vertices and an integration over the internal quark loop. If the $I\!Pqq$ coupling is like a scalar ($J^P = 0^+$) [176, 165], $h^{\mu\nu}$ is

$$h^{\mu\nu}_{0^+} = (g^{\mu\nu} k \cdot q - k^\mu q^\nu). \tag{5.105}$$

If the coupling is like γ_α, then $h^{\mu\nu}$ takes the following gauge invariant form as given by Titov and Lee [165]

$$h^{\mu\nu}_{g.\,invar.} = \not{k}\left(g^{\mu\nu} - \frac{q^\mu q^\nu}{q^2}\right) - \gamma^\nu\left(k^\mu - \frac{q^\mu k\cdot q}{q^2}\right) - \left(q^\nu - \bar{p}^\nu \frac{k\cdot q}{\bar{p}\cdot k}\right)\left(\gamma^\mu - \frac{\not{q} q^\mu}{q^2}\right), \tag{5.106}$$

where $\bar{p} = (p + p')/2$. It can be checked that this form satisfies the transversality (gauge invariance) requirements $h^{\mu\nu} q_\nu = 0$ and $h^{\mu\nu} k_\mu = 0$ Since $\varepsilon^*_V \cdot q = 0$ (gauge condition), we can drop all q^μ terms in the above expression and cast it in the form

$$h^{Titov,\,\mu\nu}_{I\!P_1} = (\not{k} g^{\mu\nu} - k^\mu \gamma^\nu) - \gamma^\mu\left(q^\nu - \bar{p}^\nu \frac{k\cdot q}{\bar{p}\cdot k}\right) \tag{5.107}$$

We note that only the terms within the first set of parenthesis in Eq. 5.107 were used in several previous works [167, 164, 166]. Also, the $\not{k} g^{\mu\nu}$ term in Eq. 5.107 will give a $(\varepsilon^*_V \cdot \varepsilon_\gamma)$ term in the

[2]There are issues with a $C = +1$ vector current which will not be conserved, but we will not discuss this further here.

final amplitude that is helicity preserving. At high energies this term will dominate and lead to s-channel helicity conservation between the incoming photon and the outgoing vector meson, but at lower energies, the other terms in Eq. 5.107 will contribute as well and give rise to helicity flips. In the high energy limit with $\bar{p} \approx p \approx p'$ and $\gamma_\mu \sim p_\mu$ (inside the traces), Eq. 5.107 takes the form

$$h^{\mu\nu}_{2-gluon} = k \cdot p g^{\mu\nu} - k^\mu p^\nu - p^\mu \left(q^\nu - p^\nu \frac{k \cdot q}{p \cdot k} \right), \tag{5.108}$$

where the subscript refers to the fact that this form closely resembles the perturbative QCD 2-gluon exchange calculation by Ryskin and others [174].

5.6.7.2 f_2 (2^{++}) and glueball (0^{++}) exchanges

In Laget's model [171], the soft Pomeron is combined with the f_2 exchange to give a combined amplitude

$$\mathcal{A}^{Laget}_{I\!P_1+f_2} = C_V F_p(t) F_V(t) \, (\varepsilon^*_V)_\mu (\varepsilon_\gamma)_\nu \, h^{\mu\nu}_{2-gluon} \tag{5.109}$$

$$\times \left(\left(\frac{s}{s_0} \right)^{\alpha_{I\!P_1}(t)-1} e^{-i\frac{1}{2}\pi\alpha_{I\!P_1}(t)} + \kappa_{f_2} \left(\frac{s}{s_{f_2}} \right)^{\alpha_{f_2}(t)-1} \frac{(1+e^{-i\pi\alpha_{f_2}(t)})\pi\alpha'_{f_2}}{2\sin(\pi\alpha_{f_2}(t))\Gamma(\pi\alpha_{f_2}(t))} \right), \tag{5.110}$$

where $h^{\mu\nu}_{2-gluon}$ is of the same Titov form given in Eq. 5.108. The f_2 Regge trajectory is

$$\alpha_{f_2}(t) = \alpha_{f_2}(0) + \alpha'_{f_2} t, \;\; \alpha_{f_2}(0) = 0.55, \;\; \alpha'_{f_2} = 0.7 \text{ GeV}^{-2} \tag{5.111}$$

and the corresponding energy scale is set at $s_{f_2} = 1$ GeV^2. The relative strength factor κ is given as $\kappa_{f_2(1270)} = 9$ for the light quark sector (ω and ρ), while for the strange sector (ϕ), this is given as $\kappa_{f'_2(1525)} = -4.5$ [171]. It should be stressed upon here that the f_2 and the $I\!P_1$ coupling in the same fashion is an assumption which goes back to the work by Donnachie and Landshoff [8]. While it is correct that the Reggeon f_2 has the quantum numbers of the vacuum, as does does the Pomeron, it could be argued that it should couple as a rank-2 tensor. Following this idea, Titov and Lee [165] have calculated the 0^{++} glueball and 2^{++} f_2 Reggeon exchange amplitues assuming 1 and $\gamma_\alpha\gamma_\beta$ Reggeon-q-q' vertex couplings, respectively. The $h^{\mu\nu}$ for the glueball remains the same as given in Eq. 5.105, while that of the f_2 is [165]

$$h^{Titov,\,\mu\nu}_{2^+} = h^{\mu\nu}_{0^+} - 2i\sigma_{\alpha\beta} \left(g^{\alpha\mu} g^{\beta\nu} k \cdot q + q^\alpha k^\beta g^{\mu\nu} + g^{\alpha\nu} q^\beta k^\mu + g^{\beta\mu} k^\alpha q^\nu \right). \tag{5.112}$$

The 0^+ and 2^+ Regge trajectories are given by Eqs. 5.98 and 5.111, respectively. The corresponding Reggeon prefactor is

$$M_R(s,t) = C_R F_p(t) F_V(t) \frac{1}{N_R} \left(\frac{s}{s_R} \right)^{\alpha_R(t)} \frac{\eta_R(1+e^{-i\pi\alpha_R(t)})}{2\sin(\pi\alpha_R(t))\Gamma(\alpha_R(t))}, \tag{5.113}$$

where $s_{gl} = 1/\alpha'_{gl}$ and the normalization factors are $N_{gl} = M_p M_V^2$ and $N_{f_2} = 2sM_V$. The phase factors η_R and the coupling strength β_R^2 (this goes into C_R, as in Eq. 5.99d) need to be fixed by fits to the data.

5.6.7.3 Quark correlations in the 2-gluon exchange model

In the 2-gluon exchange model of the Pomeron,

$$\mathcal{A}^{Laget1}_{2-gluon} = \frac{12\sqrt{6}}{\gamma_V} \frac{1}{8\pi} \, (\varepsilon^*_V)_\mu (\varepsilon_\gamma)_\nu \, h^{\mu\nu}_{2-gluon}$$

$$\times \int_0^\infty dx [4\pi\alpha_n D(t/4-x)]^2 [F_p(t) - F_p(t/4-3x)] \frac{t+4x}{(1-t/M_V^2)(m_V^2+4x)}, \tag{5.114}$$

where $\alpha_n = 0.3$ is the non-perturbative quark-gluon coupling [170] and $D(q^2)$ is the "dressed" gluon propagator. In Refs. [170, 171], $D(q^2)$ is taken to be of the Gaussian form

$$\alpha_n D(q^2) = \frac{3\beta_0}{\sqrt{2\pi}\lambda_0} e^{-q^2/\lambda_0^2}, \tag{5.115}$$

with the value of of the cut-off factor is set at $\lambda_0^2 \approx 2.7$ GeV^2 [170]. In a latter version [173], following the work of Leinweber *et al* [179], this is given as

$$D(q^2) = Z\left(\frac{AM^{2\alpha}}{(q^2)^{1+\alpha} + (M^2)^{1+\alpha}} + \frac{L(q^2, M)}{q^2 + M^2}\right), \tag{5.116}$$

where $Z = 2.09$, $A = 2.29$, $M = 0.38$ and $\alpha = 1.09$ and

$$L(q,^2 M) = \left(\frac{1}{2}\ln[(q^2 + M^2)(1/q^2 + 1/M^2)]\right)^{-d_D},\ d_D = 13/22. \tag{5.117}$$

5.7 Vector meson radiative decay constants

From Eq. 5.69f, the transition matrix element for the decay $V \to \gamma\varphi$ is given by[3]

$$\mathcal{A}_{V\to\gamma\varphi} = \frac{e g_{\gamma\varphi V}}{M_0}\epsilon^{\mu\nu\alpha\beta}(p_V)_\mu(\varepsilon_V)_\nu k_\alpha(\varepsilon_\gamma)_\beta. \tag{5.118}$$

This amplitude is related to the decay width of the vector meson as:

$$d\Gamma = \frac{1}{32\pi^2}\sum_{spins}|\mathcal{A}|\frac{|\vec{p}|}{M^2}d\Omega, \tag{5.119}$$

where $|\vec{p}|$ is the decay 3-momentum of the outgoing particles in the overall rest frame and M is the total invariant mass (the vector meson mass, in this case). The summation is over the spins of the final states and includes an averaging over the initial state spins. Keeping all the spins and indices intact, the norm amplitude norm squared becomes

$$\begin{aligned}
\sum_{spins}|\mathcal{A}_{V\to\gamma\varphi}|^2 &= \sum_{spins}\left(\frac{e g_{\gamma\varphi V}}{M_0}\right)^2 q_\mu(\varepsilon_V)_\nu k_\alpha(\varepsilon_\gamma)_\beta\epsilon^{\mu\nu\alpha\beta}q_\rho(\varepsilon_V^*)_\lambda k_\gamma(\varepsilon_\gamma^*)_\delta\epsilon^{\rho\lambda\gamma\delta} \\
&= \left(\frac{e g_{\gamma\varphi V}}{M_0}\right)^2(-g_{\beta\delta})(-g_{\nu\lambda})q_\mu k_\alpha q_\rho k_\gamma\epsilon^{\mu\nu\alpha\beta}\epsilon^{\rho\lambda\gamma\delta} \\
&= \left(\frac{e g_{\gamma\varphi V}}{M_0}\right)^2 q_\mu k_\alpha q_\rho k_\gamma\epsilon^{\mu\nu\alpha\beta}\epsilon^{\rho\nu\gamma\beta},
\end{aligned} \tag{5.120}$$

where q and k are the momenta of the outgoing pseudo-scalar meson and photon, respectively. Since $q_V = q + k$, where q_V is the momentum of the decaying vector meson, the above can also be written as:

$$\begin{aligned}
\sum_{spins}|\mathcal{A}_{V\to\gamma\varphi}|^2 &= \left(\frac{e g_{\gamma\varphi V}}{M_0}\right)^2(q_V)_\mu k_\alpha(q_V)_\rho k_\gamma\epsilon^{\mu\nu\alpha\beta}\epsilon^{\rho\nu\gamma\beta} \\
&= \left(\frac{e g_{\gamma\varphi V}}{M_0}\right)^2 M^2(k_m)_{\text{c.m.}}(k_n)_{\text{c.m.}}\epsilon^{0lmo}\epsilon^{0lno} \\
&= \left(\frac{e g_{\gamma\varphi V}}{M_0}\right)^2 2M^2|\vec{k}|^2_{\text{c.m.}},
\end{aligned} \tag{5.121}$$

[3]Note that some authors [138, 153, 152] choose to normalize by the pseudo-scalar meson mass M_φ instead of M_0.

where we have substitued $q_V = (M, 0, 0, 0)$ in the overall c.m. frame, which is also the rest frame of the decaying particle. Substituting Eq. 5.121 in Eq. 5.119 and completing the phase-space integral $\int d\Omega = 4\pi$, we get

$$\begin{aligned}\Gamma_{V\to\gamma\varphi} &= \frac{\alpha}{3}\left(\frac{g_{\gamma\varphi V}}{M_0}\right)^2 |\vec{k}|^3_{\text{c.m.}} \\ &= \frac{\alpha}{3}\left(\frac{g_{\gamma\varphi V}}{M_0}\right)^2 \left(\frac{M_V^2 - M_\varphi^2}{2M_V}\right)^3 \end{aligned} \tag{5.122}$$

The extra factor of 1/3 comes from averaging over the three polarization states of the initial vector meson.

For the case of the η' meson decaying to $\gamma\omega$ and $\gamma\rho$, the forms of Eq. 5.119 and Eq. 5.121 remain the same, except that we do not need to add the extra factor of 1/3 as in Eq. 5.122 since the vector meson is a final state particle now. Hence, we have:

$$\Gamma_{\eta'\to\gamma V} = \alpha\left(\frac{g_{\gamma\eta' V}}{M_0}\right)^2 \left(\frac{M_{\eta'}^2 - M_V^2}{2M_{\eta'}}\right)^3 \tag{5.123}$$

We note that a different formula for $\Gamma_{\eta'\to\gamma V}$ is quoted in the work by Chiang *et al* [152], though our result agrees with that of Refs. [154, 155]. The partial widths are obtained by multiplying the total decay width by the relevant branching fraction and vary slightly between different versions of the PDG. The latest PDG [181] values of the partial widths and the resulting coupling constants are given in Table 5.7. For the ϕ decaying to the scalar mesons, we have adopted Eq. 5.122, following Ref. [166].

For the axial-vector meson radiative decays, we follow Ref. [192] and first write the general form of the decay-width $\Gamma_{V_a\to\varphi V}$

$$\Gamma_{V_a\to\varphi V} = \left(\frac{f_V g_{V_a\varphi V}}{M_0}\right)^2 \frac{|\vec{p}_\varphi|}{24\pi m_{V_a}^2}\left(2(p_\varphi\cdot p_V)^2 + m_V^2 E_\varphi^2\right), \tag{5.124}$$

where we have generalized Eq. 5.69g by replacing e with f_V, and everything is understood to be computed in the rest-frame of the decaying V_a. The vector-dominance-model (VDM) then relates the couplings as $g_{V_a\varphi V} = g_{V_a\varphi\gamma}$, so that Eq. 5.124 can equivalently written as

$$\Gamma_{V_a\to\varphi V} = \left(\frac{f_V g_{V_a\varphi\gamma}}{M_0}\right)^2 \frac{|\vec{p}_\varphi|}{24\pi m_{V_a}^2}\left(2(p_\varphi\cdot p_V)^2 + m_V^2 E_\varphi^2\right). \tag{5.125}$$

For $\Gamma_{b_1\to\pi\omega} = 142$ MeV and $f_\omega \approx 15.6$ [190], we get $g_{b_1\pi\omega} \approx 0.626$, while, due to lack of direct measurements, the chiral unitarity model predictions [193] of $g_{h_1(1170)\pi^0\gamma} = 1.337$ and $g_{K1K\gamma} = 0.808$ are assumed.[4] For the $a_1(1260)$ meson, the full width is somewhat uncertain. Yu *et al* [190] take $\Gamma_{a_1\to\pi\gamma} = 0.64$ MeV which gives $g_{a_1\pi\gamma} = 1.043$. From Eq. 5.69i, the radiative decay width of the tensor mesons is given by [190]

$$\Gamma_{T\to\varphi\gamma} = \frac{2\alpha}{5}\left(\frac{g_{T\varphi\gamma}}{M_0^2}\right)^2 \left(\frac{m_T^2 - m_\varphi^2}{2m_T}\right)^5 \tag{5.126}$$

With $\Gamma_{a2\to\pi\gamma} = 0.287$ MeV, $g_{a2\pi\gamma} = 0.915$, and with $\Gamma_{K2\to K\gamma} = 0.235$ MeV, $g_{K2K\gamma} = 0.914$.

[4] Note that the work of Yu *et al* [190] absorbs a factor of e into the radiative coupling.

Decay process	Partial width (keV)	Coupling constant (g)
$\rho \to \eta\gamma$	44.73	1.58
$\omega \to \eta\gamma$	3.9	0.45
$\eta' \to \rho\gamma$	56.84	1.317
$\eta' \to \omega\gamma$	5.34	0.4261
$\rho^+ \to \pi^+\gamma$	67.1	0.72
$\rho^0 \to \pi^0\gamma$	89.4	0.831
$\omega \to \pi^0\gamma$	702.97	2.3
$\phi \to \pi^0\gamma$	5.41	-0.133
$\phi \to \eta\gamma$	55.76	-0.693
$\phi \to \sigma(500)\gamma$	0.48	$\sqrt{3} \times 0.0583$
$\phi \to f_0(980)\gamma$	1.37	3.12
$\phi \to a_0(980)\gamma$	0.32	1.52
$K^{*+} \to K^+\gamma$	50.1	0.834
$a_1^+ \to \pi^+\gamma$	-	1.043
$h_1^+ \to \pi^0\gamma$	-	1.337
$b_1^+ \to \pi\gamma$	-	0.626
$K_1^+ \to K^+\gamma$	-	0.808
$a2^+ \to \pi^+\gamma$	287	0.915
$K2^+ \to K^+\gamma$	235	0.914

Table 5.1: Summary of the coupling constants for the various vector meson radiative decays.

5.8 Reggeization

A detailed account of Regge theory can be found in Refs. [5, 8, 144, 145]. For our purposes here, a particle of mass m, spin J and Regge trajectory $\alpha(x) = \alpha_0 + \alpha' x$, exchanged in the x-channel ($x = \{t, u\}$) will have the usual Feynman propagator $1/(x - m^2)$ replaced by the following Regge propagator

$$\mathcal{P}_{\text{Regge}}(\zeta, s, x) = \left(\frac{s}{s_0}\right)^{(\alpha(x)-J)} \frac{(1 + \zeta e^{-i\pi(\alpha(x)-J)})}{2} \frac{\beta(x)}{\sin(\pi(\alpha(x) - J))\Gamma(\alpha(x) + 1 - J))}, \quad (5.127)$$

where $\beta(x) = \pi\alpha'$ is the residue and $\zeta = \pm 1$ is the signature of the Regge trajectory. The above form of the propagator is for the so-called non-degenerate type. Sometime, the $\zeta = \pm 1$ trajectories overlap, and the ± 1 signature amplitudes can either add or subtract to produce the so-called degenerate propagators. The degenerate propagators have the phase either rotating ($e^{-i\pi(\alpha(x)-J)}$) or constant (1). The choice of the phase is not governed by Regge theory, but has be fixed by fits to the data. The Regge trajectories for the different exchanges are listed in Table 5.2.

5.9 Coupling Constants

Table 5.3 gives a brief summary of the hadrodynamic couplings relevant to this work. The values listed are taken from the work of several authors in this field and aside from $f_{\pi NN}$, wide disagreements exist between them. It should also be noted that the issue of phenomenological form-factors will also play an important role since the form-factors can effectively "kill" any large contribution from a coupling. From the form-factor perspective, the GLV type Regge models are somewhat attractive, since these models do not use any form-factors. However, given that mesons and baryons are indeed not point particles, the form-factor arguments do have a strong physical basis. In any

Exchange	α_0	α'	Reference
π	0	0.7	[138]
ρ	0.55	0.8	[138]
ω	0.44	0.9	[138]
f_2	0.55	0.7	[171]
$I\!P_1$	1.08	0.25	[8]
$I\!P_0$	1.44	0.1	[8]
$I\!P_2$	-0.75	0.25	[165]
K^+	0.2	0.8	[5]
K^*	0.25	0.83	[138]
N	-0.3	0.9	[5]
Λ	-0.6	0.9	[5]
Σ	-0.8	0.9	[5]

Table 5.2: Summary of the Regge trajectories $\alpha(x) = \alpha_0 + \alpha' x$ for different exchanges. The book by Collins [5] lists most of these, and sometimes differs slightly from the values quoted from other sources.

case, simply note here that caution must be taken while comparing different results because these are all effective models and do not arise from a fundamental theory.

5.10 Resonant Amplitudes

5.10.1 $J^P \to K^+\Sigma^0$ Amplitudes

Consider then a general J^P state (either N^* or Δ, Δ^*) with 4-momentum P and spin projection M decaying to $K^+\Sigma^0$. As explained above we will ignore all prefactors and write down a single amplitude for both the N^*'s and the Δ's.

5.10.1.1 J^P States with $P = (-)^{J-\frac{1}{2}} = (-)^{\ell-1}$, $\ell = J + \frac{1}{2}$ $\left(\frac{1}{2}^+, \frac{3}{2}^-, \frac{5}{2}^+ \ldots\right)$

Consider the state $J^P = \frac{1}{2}^+$ which decays to $K^+\Sigma^0$ $\left(0^- \frac{1}{2}^+\right)$ through a P-wave decay only. The amplitude can thus be written as

$$\mathcal{A}_{\frac{1}{2}^+ \to K^+\Sigma^0} \sim \bar{u}(p_{\Sigma^0}, m_{\Sigma^0}) L^{(1)}_{\mu}(p_{K^+\Sigma^0}) \gamma^{\mu}\gamma^5 u(P, M), \tag{5.128}$$

where $p_{K^+\Sigma^0} = \frac{1}{2}(p_{K^+} - p_{\Sigma^0})$ is the relative momentum used to define $L^{(1)}$ and the inclusion of γ^5 ensures parity conservation (K^+ is a pseudo-scalar). The general case for J^P with $P = (-)^{J-\frac{1}{2}}$, going to $0^- \frac{1}{2}^+$ occurs in an ℓ-wave with the angular momentum selection rule $\ell = J \pm \frac{1}{2}$. Only $\ell = J + \frac{1}{2}$ survives from parity considerations and we can write the following amplitude

$$\mathcal{A}^{P=(-)^{J-\frac{1}{2}}}_{J^P \to K^+\Sigma^0} \sim \bar{u}(p_{\Sigma^0}, m_{\Sigma^0}) L^{(\ell)}_{\mu_1 \cdots \mu_\ell}(p_{K^+\Sigma^0}) \gamma^{\mu_1}\gamma^5 u^{\mu_2 \cdots \mu_\ell}(P, M), \tag{5.129}$$

where $\ell = J + \frac{1}{2}$.

Coupling	Source									
	A	B	C	D	E	F	G	H	I	
α_D							[0.59,0.66]	0.644		
$g_{\pi NN}$	13.4			13.1	13.3		13	13.45		
$g_{\eta NN}$	[0,4.8]				9.8		[0,9]			
$g_{\eta' NN}$					10.5					
$g_{\sigma NN}$					17.9					
$g_{\rho NN}$	2.4	2.4	1.9	3.18	2.75	10	2.63	3.4		
κ_ρ	6.1	3.7	3.0	6.1	6.6	1.5	6.27	6.1		
$g_{\omega NN}$	16.0	9	14.6	15.9	12.5	30.2	10.09	15		
κ_ω	0	0	-0.25	0	0.66	-1.5	0.14	0		
$g_{\phi NN}$					3.47					
κ_ϕ					-2.47					
$g_{K\Lambda N}$								[-16,-10.6] (-11.54)	-13.7	
$g_{K\Sigma N}$								[3.2,4.7] (4.5)	4.25	
$g_{K^*\Lambda N}$								-6.08 (-23)	-7.61	
$g_{K^*\Sigma N}$								-3.51 (-25)	-4.62	
$\kappa_{K^*\Lambda N}$								3.66 (2.5)	-1.31	
$\kappa_{K^*\Sigma N}$								-1.22 (-1)	1.94	

Table 5.3: A rough summary of where the different coupling constants lie from a survey of the existing literature. The sources are: A (η-MAID-isobar [153]), B (η-MAID-Regge [152]), C (η-He-Saghai-Regge [184]), D (Bonn-potential [185]), E (Nijmegen potential [186]), F (Downum-Barnes [187]), G (Benmerrouche-ELA [188]), H (GLV [138]), I (Kaon-MAID) [148]. Numerical values within square brackets denote specified ranges, while those within parentheses are the final fit results that appear in the paper.

$j^p_{\gamma p} \otimes L$ (allowed) $\rightarrow J^P$	$1^-_\gamma \otimes L$ (allowed) $\rightarrow$ Multipole
$\frac{3}{2}^- \otimes L = 2 \rightarrow \frac{1}{2}^-$	$1^-_\gamma \otimes L = 2 \rightarrow 1^-, \not{2}^-, \not{3}^-$
$\frac{1}{2}^- \otimes L = 0 \rightarrow \frac{1}{2}^-$	$1^-_\gamma \otimes L = 0 \rightarrow 1^-$
$\frac{3}{2}^- \otimes L = 1, 3 \rightarrow \frac{3}{2}^+$	$1^-_\gamma \otimes L = 3 \rightarrow 2^+, \not{3}^+, \not{4}^+$
$\frac{1}{2}^- \otimes L = 1 \rightarrow \frac{3}{2}^+$	$1^-_\gamma \otimes L = 1 \rightarrow 1^+, 2^+$
$\frac{3}{2}^- \otimes L = 2, 4 \rightarrow \frac{5}{2}^-$	$1^-_\gamma \otimes L = 4 \rightarrow 3^-, \not{4}^-, \not{5}^-$
$\frac{1}{2}^- \otimes L = 2 \rightarrow \frac{5}{2}^-$	$1^-_\gamma \otimes L = 4 \rightarrow \not{1}^-, 2^-, 3^-$

Table 5.4: Evolution of multipole basis for a particular J^P resonance. In the left column, the photon and proton are first coupled together to give a $\frac{3}{2}^-$ and a $\frac{1}{2}^-$. These are subsequently coupled to those L states which can yield the final J^P state. The multipoles in the right column are formed by coupling the photon directly with these allowed L states. The crossed out multipoles are those which cannot combine with a $\frac{1}{2}^+$ proton to yield the final J^P.

5.10.1.2 J^P States with $P = (-)^{J+\frac{1}{2}} = (-)^{\ell+1}$, $\ell = J - \frac{1}{2}$ $\left(\frac{1}{2}^-, \frac{3}{2}^+, \frac{5}{2}^- \ldots\right)$

Now consider $J^P = \frac{1}{2}^-$, which can decay to $K^+\Sigma^0$ only through an S-wave decay, the amplitude being simply

$$\mathcal{A}_{\frac{1}{2}^- \rightarrow K^+\Sigma^0} \sim \bar{u}(p_{\Sigma^0}, m_{\Sigma^0})\gamma^5 u(P, M). \tag{5.130}$$

For the general case, the decay occurs in an ℓ-wave, again with $\ell = J \pm \frac{1}{2}$, but this time parity dictates that only the $\ell = J - \frac{1}{2}$ survive and the general amplitude can be written down as

$$\mathcal{A}^{P=(-)^{J+\frac{1}{2}}}_{J^P \rightarrow K^+\Sigma^0} \sim \bar{u}(p_{\Sigma^0}, m_{\Sigma^0}) L^{(\ell)}_{\mu_1 \cdots \mu_\ell}(p_{K^+\Sigma^0})\gamma^5 u^{\mu_1 \cdots \mu_\ell}(P, M), \tag{5.131}$$

where $\ell = J - \frac{1}{2}$.

5.10.2 $\gamma p \rightarrow J^P$ Amplitudes

5.10.2.1 J^P States with $P = (-)^{J+\frac{1}{2}}$ $\left(\frac{1}{2}^-, \frac{3}{2}^+, \frac{5}{2}^- \ldots\right)$

The crux of the discussion to follow is summarized in Table 5.4. We study the case J^P with $P = (-)^{J+\frac{1}{2}}$ with a few examples, but the trend should be obvious. First we couple the $\gamma\, p$ system ($1^- \otimes \frac{1}{2}^+$) together to give a $\frac{3}{2}^-$ state and a $\frac{1}{2}^-$ state. Next, $\frac{3}{2}^-$ and $\frac{1}{2}^-$ are individually coupled to the appropriate angular momentum L states which can yield the final J^P state. In the second column we have first coupled the photon 1^- to the allowed L states to give spin-parity states called *multipoles*. These are next coupled with the proton $\frac{1}{2}^+$ to give the final J^P state where we have crossed out the multipoles which do not work (that is, cannot combine with the proton to give the final J^P state).

Until now we have not utilized the fact that even though the photon is a spin-1 particle, its L_z components are only ± 1, there being no $L_z = 0$ state for a real massless photon. As as result, the amplitudes for a D-wave coupled with $\frac{3}{2}^-$ γp and an S-wave coupled with $\frac{1}{2}^-$ γp to produce the final $J^P = \frac{1}{2}^-$ state have the same angular distributions. Similarly, an F-wave coupled with $\frac{3}{2}^-$ γp and a P-wave coupled with $\frac{1}{2}^-$ γp to produce $J^P = \frac{3}{2}^+$ have the same angular distributions. And

J^P	Multipole	J^P	Multipole
$\frac{1}{2}^-$	$E1$	$\frac{1}{2}^+$	$M1$
$\frac{3}{2}^-$	$E1$, $M2$	$\frac{3}{2}^+$	$M1$, $E2$
$\frac{5}{2}^-$	$M2$, $E3$	$\frac{5}{2}^+$	$E2$, $M3$
$\frac{7}{2}^-$	$E3$, $M4$	$\frac{7}{2}^+$	$M3$, $E4$
$\frac{9}{2}^-$	$M4$, $E5$	$\frac{9}{2}^+$	$E4$, $M5$
$\frac{11}{2}^-$	$E5$, $M6$	$\frac{11}{2}^+$	$M5$, $E6$

Table 5.5: Multipoles associated with J^P's used in this analysis.

so on. We prove this for the $J^P = \frac{1}{2}^-$ case as follows. The two amplitudes are

$$\mathcal{A}^{L=0}_{\gamma p\to \frac{1}{2}^-} = \bar{u}(P,M)\gamma^\mu\gamma^5 u(p_i,m_i)\epsilon_\mu(k,m_\gamma), \quad \text{and} \tag{5.132a}$$

$$\mathcal{A}^{L=2}_{\gamma p\to \frac{1}{2}^-} = \bar{u}(P,M)L^{(2)}_{\mu\nu}(p_{p\gamma})\gamma^\mu\gamma^5 u(i_p,m_i)\epsilon^\nu(k,m_\gamma). \tag{5.132b}$$

However, $\mathcal{A}^{L=2}_{\gamma p\to \frac{1}{2}^-}$ can be written as

$$\begin{aligned}\bar{u}L^{(2)}_{\mu\nu}(p_{p\gamma})\gamma^\mu\gamma^5 u\epsilon^\nu &= \bar{u}(p^{p\gamma\,\perp}_\mu p^{p\gamma\,\perp}_\nu - \frac{1}{3}p^2_{p\gamma\,\perp}g^\perp_{\mu\nu})\gamma^\mu\gamma^5 u\epsilon^\nu \\ &\sim \bar{u}p^2_{p\gamma\,\perp}\epsilon_\mu\gamma^\mu\gamma^5 u \\ &= |L^{(1)}|^2 A^{L=0}_{\gamma p\to\frac{1}{2}^-},\end{aligned} \tag{5.133}$$

where we have used $p^\mu_{p\gamma\,\perp}\epsilon_\mu = 0$ and $g^\perp_{\mu\nu}\epsilon^\nu = \epsilon_\mu$ for a real photon (these relations are most easily proved in the c.m. frame of the γp system). Thus aside from the $|L^{(1)}|^2 \sim O(s)$ factor (which is just a multiplicative constant for us since we bin finely in $\sqrt{s}$), the two amplitudes are the same. The convenience of working in the multipole basis is that it neatly separates independent angular amplitudes. Following standard nomenclature, we will then call the j^p multipole with $p = (-)^j$ as the *electric*, and with $p = (-)^{j+1}$, as the *magnetic* multipole. Thus, $1^-, 2^+, \ldots$ are called $E1, E2, \ldots$ while $1^+, 2^-, \ldots$ are $M1, M2, \ldots$.

Getting back to the original problem at hand, we find that for J^P with $P = (-)^{J+\frac{1}{2}}$, there is an electric and an magnetic contribution, both of which can be built from an $\ell = J - 1/2$ wave. The difference is that we need to project out the j part where $j = J - 1/2$ is the magnetic part and $j = J + 1/2$ is the electric part. Thus

$$\mathcal{A}^{P=(-)^{J+\frac{1}{2}}}_{\gamma p\to J^P} = \bar{u}^{\mu_1\mu_2\ldots\mu_\ell}(P,M)\gamma^\nu\gamma^5 P^{(j)}_{\mu_1\mu_2\ldots\mu_\ell\nu\alpha_1\alpha_2\ldots\alpha_\ell\beta}(P)L^{(\ell)\alpha_1\alpha_2\ldots\alpha_\ell}(p_{p\gamma})\epsilon^\beta(p_\gamma,m_\gamma)u(p_p,m_p). \tag{5.134}$$

Note that since there is no 0 multipole, $\frac{1}{2}^-$ has an $E1$ contribution only.

5.10.2.2 J^P States with $P = (-)^{J-\frac{1}{2}}$ $\left(\frac{1}{2}^+, \frac{3}{2}^-, \frac{5}{2}^+ \ldots\right)$

The only thing which changes now is that $\ell = J + 1/2$. The electric part is now given by $j = J - 1/2$ while the magnetic part is from $j = J + 1/2$. Also, $\frac{1}{2}^+$ has an $M1$ contribution only. The amplitude is

$$\mathcal{A}^{P=(-)^{J-\frac{1}{2}}}_{\gamma p\to J^P} = \bar{u}^{\mu_1\ldots\mu_{\ell-1}}(P,M)\gamma^{\mu_\ell}\gamma^{\mu_{\ell+1}}P^{(j)}_{\mu_1\ldots\mu_{\ell+1}\nu_1\ldots\nu_{\ell+1}}(P)L^{(\ell)\nu_1\ldots\nu_\ell}(p_{p\gamma})\epsilon^{\nu_{\ell+1}}(k,m_\gamma)u(p_i,m_i). \tag{5.135}$$

For ease of reference we have tabulated the relevant multipoles for the J^P waves used in this analysis in Table 5.5

5.10.3 $\gamma p \to J^P \to K^+\Sigma^0 \to K^+\gamma\Lambda \to K^+\gamma p\pi^-$ Amplitude

The amplitude for the entire reaction chain is now easily formed by multiplying the individual components together. The only other thing we need to keep in mind is that all three J^P, Σ^0 and Λ are intermediate particles and thus their spins have to be summed over. Thus,

$$\mathcal{A}_{\gamma p\to J^P\to K^+\Sigma^0\to K^+\gamma\Lambda\to K^+\gamma p\pi^-} = \sum_{m_{J^P}}\sum_{m_{\Sigma^0}}\sum_{m_\Lambda}\mathcal{A}_{\gamma p\to J^P}\times\mathcal{A}_{J^P\to K^+\Sigma^0}\times\mathcal{A}_{\Sigma^0\to\gamma\Lambda}\times\mathcal{A}_{\Lambda\to p\pi^-}. \quad (5.136)$$

Note that, in the actual physics, there will be $\sqrt{s}$ dependent Breit-Wigner and other factors in this amplitude, but for our purposes, since we will run fits on bunches of events finely binned in $\sqrt{s}$, this is just an additional factor floating around, to be absorbed in the overall scale during the fits.

5.11 Gauge Invariance and Form Factors

All the amplitudes constructed above have to satisfy one general condition − the Ward-Takahashi identity for gauge invariance in QED [1]. The total amplitude can be written as $\mathcal{A} = \epsilon_\mu\mathcal{A}^\mu$ where ϵ_μ is the polarization of the incident external photon and $\mathcal{A}^\mu$ represents the hadronic current which the photon couples to. The Ward identity states that this current is conserved. That is, $\partial_\mu\mathcal{A}^\mu = 0$, or $k_\mu\mathcal{A}^\mu = 0$ for the photon momentum k_μ. Note that individual diagrams may not obey the Ward identity, but when summed up over all possible diagrams, the total amplitude has to be gauge invariant in this manner.

As an example, consider $\gamma p \to K^+\Sigma^0$ occuring via the simplest s, t and u channels with the exchange of a proton, a K^+ and a Σ^0 respectively. The amplitude is given by

$$\begin{aligned}\epsilon_\mu\mathcal{A}^\mu &= ge\bar{u}_\Sigma\gamma^5\tfrac{(p_p+k)\cdot\gamma+m_p}{s-m_p^2}\left[\epsilon\cdot\gamma-\tfrac{\kappa_p}{2m_p}\epsilon\cdot\gamma k\cdot\gamma\right]u_p \\ &\quad +2ge\bar{u}_\Sigma\tfrac{p_K\cdot\epsilon}{t-m_K^2}\gamma^5u_p \\ &\quad -ge\bar{u}_\Sigma\tfrac{\kappa_{\Sigma^0}}{2m_p}\epsilon\cdot\gamma k\cdot\gamma\tfrac{(p_\Sigma-k)\cdot\gamma+m_{\Sigma^0}}{u-m_{\Sigma^0}^2}\gamma^5u_p,\end{aligned} \quad (5.137)$$

where k is the incoming photon momentum and p_Σ is the outgoing Σ^0 momentum. Now if we replace ϵ_μ with k_μ everywhere, we first see that the magnetic terms ($\sim \not{\epsilon}\not{k}$) go to zero (because $\not{k}\not{k} = k^2 = 0$ for a real photon). Thus the magnetic terms individually satisfy the Ward identity and it is only the electric terms that we need to be concerned about. The remnant electric terms are

$$\epsilon_\mu\mathcal{A}'^\mu = ge\bar{u}_\Sigma\left[\frac{2p_p\cdot\epsilon}{s-m_p^2}+\frac{2p_K\cdot\epsilon}{t-m_K^2}\right]\gamma^5u_p, \quad (5.138)$$

where we have used the identity $\not{a}\not{b} = -\not{b}\not{a}+2a\cdot b$ (from the γ^μ anti-commutation relations), the fact that γ^5 anticommutes with all the γ^μ's and finally, $\not{p}_p u_p = m_p u_p$ from the Dirac equation. $k_\mu\mathcal{A}'^\mu$ is then easily seen to be zero after substituting $(k+p_p)^2$ for s and $(k-p_K)^2$ for t. Thus if we include the K^+ exchange t-channel process, we also have to include the proton exchange s-channel process to ensure that the Ward identity is satisfied.

The $K^*(892)$ exchange t-channel amplitude is gauge invariant by itself because of the $\epsilon^{\nu\alpha\beta\lambda}k_\beta\epsilon_\lambda$ term. The $K1(1270)$ exchange t-channel and the Y exchange u-channel terms too are manifestly

gauge invariant, being built out of $F_{\mu\nu}$.

The PWA resonant amplitudes contain electric terms and are thus *not* gauge invariant in general. However, our setup ensures that we do not run into gauge invariance violations using these. To understand why, note that if any amplitude is not gauge invariant as such, by multiplying it with $g^{\perp\perp}$ from Eq. 5.33, we can project out the gauge invariant part. Indeed one should actually be doing this, but also note from Eq. 5.32 that the way we have constructed our polarization vectors, $\epsilon^{\nu}(m_\gamma)g^{\perp\perp}_{\nu\mu} = \epsilon^{\mu}(m_\gamma)$. In other words, computationally, multiplying by $g^{\perp\perp}$ does not change anything, because of the particular choice of our polarization basis.

5.11.1 Form Factors and Contact Terms

Until now, we have assumed that the vertices have point particle interactions. In reality, the hadrons and mesons are extended particles and it is customary to put in phenomenological form factors to account for their finite sizes. These form factors involve a cutoff mass Λ which sets the short-range scale of our (effective) theory. However, it is well known that the addition of phenomenological form factors break gauge invariance even at the tree level. For example, if the s and t channels have different form factors F_s and F_t, Eq. 5.138 becomes

$$\epsilon_\mu \mathcal{A}'^{\mu}_{FF} = ge\bar{u}_\Sigma \left[\frac{2p_p\cdot\epsilon}{s-m_p^2}F_s + \frac{2p_K\cdot\epsilon}{t-m_K^2}F_t\right]\gamma^5 u_p, \tag{5.139}$$

and thus the cancellation does not occur and gauge-invariance is violated.

There are various prescriptions in the literature for the addition of form factors and ways to tackle the ensuing violation of gauge invariance [78, 79, 77, 80] . It must be kept in mind here that *all* these prescriptions are phenomenological after all, so their correctness goes as far as the fits match the data. It is generally agreed upon however that some sort of form factor *is* required, because otherwise the bare tree level Born diagrams give too large a cross-section. A widely used form factor in the literature [81] is of the dipole form

$$F_x(\Lambda) = \frac{\Lambda^4}{\Lambda^4 + (x-M_x^2)^2} \qquad (x \equiv s,t,u). \tag{5.140}$$

Since the problem lies in the s and t-channels getting different form factors in Eq. 5.139, Haberzettl *et al* [78] applied a common form factor $\hat{F}$ instead. That is, an $\epsilon_\mu \mathcal{A}'^{\mu}\hat{F}$ term is added to and subtracted from the total amplitude. After this, the electric terms which remain is what is called $-\epsilon_\mu \mathcal{A}'^{\mu}_{contact}$. To cancel this, one thus *adds* the term

$$\epsilon_\mu \mathcal{A}'^{\mu}_{contact} = ge\bar{u}_\Sigma \left[\frac{2p_p\cdot\epsilon}{s-m_p^2}(\hat{F}-F_s) + \frac{2p_K\cdot\epsilon}{t-m_K^2}(\hat{F}-F_t)\right]\gamma^5 u_p. \tag{5.141}$$

The contact terms represent 4-point interactions and thus cannot contain any pole. The original suggestion by Haberzettl [78] was

$$\hat{F}_H = a_s F_s(\Lambda) + a_t F_t(\Lambda) + a_u F_u(\Lambda), \quad a_x + a_t + a_u = 1, \tag{5.142}$$

which was shown to not be free of poles by Davidson and Workman [79] who subsequently suggested a different form,

$$\hat{F}_{DW} = F_s(\Lambda) + F_t(\Lambda) - F_s(\Lambda)F_t(\Lambda). \tag{5.143}$$

We will follow the DW model in this work.

To sum it up, the upshot of the above discussion is that the electric terms in the s and t-channels for the proton and the K^+ exchanges must get a common form factor $\hat{F}_{DW}$, while the magnetic terms can independently get (dipole) form factors based on whichever channel s, u or t they might be a part of.

5.12 Summary

We described the construction of our amplitudes in a fully covariant manner, following the Rarita-Schwinger formalism. Production amplitudes for both resonance and background processes were described. The problem of gauge invariance violation and a prescription for fixing it was also addressed.

Chapter 6

PWA Fit Formulæ and $K^+\Sigma^0$ Differential Cross Sections

Having described in detail the construction of amplitudes in the previous chapter, we move on to describing the setup for using these amplitudes to run fits on the three-track dataset. We follow closely the works of Williams [51] and Chung [82]. Three points are to be noted at the outset. First, that we employ the powerful (but computationally intensive) technique of *unbinned event-based maximum likelihood fitting* for our purposes. A dedicated computer cluster for the Medium Energy group at Carnegie Mellon reduces concern for computation related limitations but the result is a highly stable fitting procedure where every event effectively becomes a separate degree of freedom. Compare this with binned χ^2 fits where information is lost due to binning.

Second, our resonance amplitudes are model independent, in the sense that for a given spin-parity J^P, we do not make *ab initio* assumptions about the masses and widths of the exchange resonances. We run individual fits on events which are finely binned in energy, so that $\sqrt{s}$ is approximately a constant for every fit. Therefore, $\sqrt{s}$ dependent propagators and Breit-Wigners (which depend on which particular resonances are being included in one's model) feature only as an overall pre-factor in our fits. It is to be noted that traditionally, one fits to the full expressions for the s-channel resonant amplitudes, including resonance-dependent propagators and Breit-Wigners. In our case, if a resonance of a particular spin-parity J^P and mass M contributes to our channel, its signature should lie in appreciable contributions from the same J^P amplitude *around* $\sqrt{s} \approx M$ (there are issues with overlapping resonaces here which we will talk about later).

Finally, in this chapter we employ these fits to extract differential cross sections using s-channel J^P waves from $\frac{1}{2}^{\pm}$ up to $\frac{11}{2}^{\pm}$, for the three-track dataset. It is important to realize that in this particular fit (which we call the *mother fit*), we are not trying to interpret the fit results as *physics*. It is completely equivalent to using a (nearly) complete basis of sines and cosines to fit to a distribution, save that instead of harmonic functions, we use a (semi-)complete basis of J^P waves. As long as there are enough "wiggles" in these waves and as long as we use enough number of waves, we should be able to fit to any distribution.

The advantage of using the PWA procedure for cross-section extractions is that the accepted Monte Carlo events, weighted by our mother fit results, incorporates any *physics* dependency into our acceptance calculation. For the two-track dataset however, since the π^- and outgoing γ momenta are unknown, the amplitudes cannot be constructed any more. We thus have to fall back to the more conventional method of unweighted acceptance calculation to extract differential cross sections. Fortunately, the break-up angles for both the Σ^0 and Λ decays are small, so that the latter is a very

good approximation to the more correct physics incorporated acceptance (see Sec. 7.3).

6.1 The Maximum Likelihood Method

Suppose we have a set of n events, a set of variables $\hat{x}$ whose values we want to estimate with the i^{th} event having the kinematics X_i. The probability of occurance of the i^{th} event is given by the probability distribution function $\mathcal{P}(\vec{x}, X_i)$. The likelihood function is then defined as

$$\mathcal{L}(\vec{x}) = \prod_i^n \mathcal{P}(\vec{x}, X_i). \tag{6.1}$$

$\mathcal{L}(\vec{x}_0)$ is the *statistical inference* that, given the set of n observed events with the given kinematics, how likely it is that $\vec{x}_0$ were the *actual* values of the estimators. In reality one measures the intensities $\mathcal{I}(\vec{x}, X_i)$ and not the actual probabilities. The probabilities are obtained from dividing out the intensities by the normalization integral $\mathcal{N}(\vec{x})$:

$$\mathcal{N}(\vec{x}) = \sum_i^n \mathcal{I}(\vec{x}, X_i) \tag{6.2}$$

$$\mathcal{P}(\vec{x}, X_i) = \frac{\mathcal{I}(\vec{x}, X_i)}{\mathcal{N}(\vec{x})}. \tag{6.3}$$

The maximum likelihood method then says: *the best estimators are given by those which maximize the likelihood function.*

6.1.1 The Extended Maximum Likelihood Method (EMLM)

An important aspect of the above scheme is that it fits only to the *shape* of a particular distribution. The normalization integral always cancels out the overall normalization of the distribution. However, there are instances when one wants to fit not only to the shape but also to the overall number of events. For example, if one knows that events occur at a given rate $\bar{n}$, the probability of observing n events within a unit time interval is given by the Poisson distribution:

$$\mathcal{P}_n = \frac{\bar{n}^n}{n!} e^{-\bar{n}}, \tag{6.4}$$

so that the probability of observing n events with a particular shape per unit time is:

$$\mathcal{P}_{ext}(n, \vec{x}, X_i) = \left(\frac{\bar{n}^n}{n!} e^{-\bar{n}} \right) \mathcal{P}(\vec{x}, X_i), \tag{6.5}$$

where the subscript denotes that this is the *extended* maximum likelihood method. This is the probability distribution appropriate for differential cross section fits, where events are known to be occurring at a particular rate.

Note that the event rate is *not* known either. We will later write expressions for $\bar{n}$ in terms of the amplitudes themselves.

6.1.2 Amplitudes, Probabilities and Cross Sections

In the previous chapter we wrote down the formulae for the PWA amplitudes $\mathcal{A}^a_{m_i, m_{mi}, m_{mf}, m_f}(X)$ for $\gamma p \to K^+ p \pi^- \gamma$ where m_i, m_{gi}, m_{gf} and m_f are the spin projections of the target proton, the incident photon, the outgoing final photon and the outgoing final proton respectively. The

superscript a denotes the particular type of amplitude concerned − it may be a background process or a J^P wave. The Lorentz invariant transition probability is given as:

$$|\mathcal{M}(\vec{x},X)|^2 = \sum_{m_i,m_{gi},m_{gf},m_f} |\sum_a \alpha_a(\vec{x},X)\mathcal{A}^a_{m_i,m_{gi},m_{gf},m_f}(X)|^2, \tag{6.6}$$

with α_a being (complex) coefficients built from the fit parameters (and possibly the kinematic variables X).

$\mathcal{P}$ now become a probability density function and can be written as

$$\mathcal{P}(\vec{x},X) = \frac{|\mathcal{M}(\vec{x},X)|^2\eta(X)\phi(X)}{\mathcal{N}(\vec{x})}, \tag{6.7}$$

where $\phi(X) = d\Phi(X)/dX$ is the differential phase space element and $\eta(X)$ is the detector acceptance.

The cross-section is now defined as the transition rate per unit incident flux per target particle, or in terms of measurable quantities,

$$\sigma = \frac{N}{\mathcal{F}\rho_{target}\ell_{target}N_A/A_{target}}, \tag{6.8}$$

where N is the number of scattering events, $\mathcal{F}$ is the incident photon flux, ρ_{target}, ℓ_{target} and A_{target} are the target density, length and atomic weight and, N_A is Avogadro's number. Likewise, it can also be written in terms of the transition element as

$$\sigma = \frac{1}{4}\frac{(2\pi)^4}{2(s-w_p^2)}\int |\mathcal{M}(\vec{x},X)|^2 d\Phi(X). \tag{6.9}$$

where the factor of 1/4 comes from averaging over the target proton and incident photon spins. Combining the two, one gets

$$N = (\mathcal{F}\rho_{target}\ell_{target}N_A/A_{target})\,\frac{(2\pi)^4}{8(s-w_p^2)}\int |\mathcal{M}(\vec{x},X)|^2 d\Phi(X), \tag{6.10}$$

and incorporating the detector acceptance $\eta(X)$ gives the following *expected* rate of events

$$\bar{n} = (\mathcal{F}\rho_{target}\ell_{target}N_A/A_{target})\,\frac{(2\pi)^4}{8(s-w_p^2)}\int |\mathcal{M}(\vec{x},X)|^2\eta(X) d\Phi(X). \tag{6.11}$$

Since there is no analytical expression for $\eta(X)$, one has to resort to numerical computation using Monte Carlo techniques to calculate the last integral. We have already covered this in Chapter 4 where we described in detail how phase space "raw" $\gamma p \to K^+\Sigma^0 \to K^+\gamma\Lambda$ events are generated and passed through GSIM which simulates the CLAS detector and decays the various unstable particles as they "swim" though various detector components. In the end, $\eta(X_i)$ for the i^{th} event is either 1 or 0 according to whether the event was successfully "detected" or not. In this way, provided we have generated enough "raw" events everywhere in phase space, the numerical integral can be written as

$$\int |\mathcal{M}(\vec{x},X)|^2\eta(X) d\Phi(X) \approx \Phi(s)\left(|\mathcal{M}(\vec{x},X)|^2\eta(X)\right)_{avg} \tag{6.12}$$

where $\Phi(s) = \int d\Phi(X)$ is the total phase space volume, while the average transition element is given by

$$\begin{aligned} \left(|\mathcal{M}(\vec{x}, X)|^2 \eta(X)\right)_{avg} &\equiv \frac{\sum_i^{N_{raw}} |\mathcal{M}(\vec{x}, X_i)|^2 \eta(X_i)}{N_{raw}} \\ &= \frac{\sum_i^{N_{acc}} |\mathcal{M}(\vec{x}, X_i)|^2}{N_{raw}} \end{aligned} \tag{6.13}$$

with N_{raw} as the total number of "raw" Monte Carlo events generated and N_{acc} as the total number of "accepted" events after passage through GSIM.

The phase space volume can be broken down into three parts, the $\gamma p \to K^+\Sigma^0$ part, and the two subsequent decays. The latter was already assimilated by the amplitudes as explained in Sec. 5.5.4, while the former is the usual 2-body decay phase space factor, which, in our case is given by

$$\Phi(s)_{\gamma p \to K^+\Sigma^0} = \frac{\left[(s - (w_{K^+} + w_{\Sigma^0})^2)(s - (w_{K^+} - w_{\Sigma^0})^2)\right]^{1/2}}{4(2\pi)^5 s}, \tag{6.14}$$

which is also the total phase space factor $\Phi(s)$.

Combining Eqs. 6.11-6.14 we can then write

$$\bar{n} = \beta(s) \sum_i^{N_{acc}} |\mathcal{M}(\vec{x}, X_i)|^2, \tag{6.15}$$

where

$$\beta(s) = \frac{(2\pi)^4}{8(s - w_p^2)} \frac{\Phi(s)}{N_{raw}} \left(\frac{\mathcal{F} \rho_{target} \ell_{target} N_A}{A_{target}} \right). \tag{6.16}$$

Removing the detector acceptance now by summing over all of N_{raw} yields the total cross section

$$\sigma = \beta(s) \sum_i^{N_{raw}} |\mathcal{M}(\vec{x}, X_i)|^2. \tag{6.17}$$

6.1.3 Log Likelihood Formula

Instead of maximizing the likelihood function directly, most of the times, it is computationally simpler to maximize the the logarithm of the likelihood function. A heuristic argument is that near the maximum, the first derivative vanishes, so the the likelihood function looks like a Gaussian

$$\begin{aligned} \mathcal{L} &\sim \mathcal{L}_{max} + \frac{1}{2!}\mathcal{L}''\delta x^2 + \cdots \\ &\sim \mathcal{L}_{max} - \frac{1}{2c}\delta x^2 + \cdots \sim \exp(-\frac{\delta x^2}{2c}), \end{aligned} \tag{6.18}$$

where $c = -1/\mathcal{L}''$ which has to be positive at a mamimum. Since the logarithm is a monotonically increasing function in the range of the likelihood function, maximizing $\ln \mathcal{L}$ always ensures maximing $\mathcal{L}$ too. Also, instead of maximing $\ln \mathcal{L}$, it is conventional to minimize the negative of the log

likelihood. From Eq. 6.5 this is given by

$$\begin{aligned} -\ln\mathcal{L} &= -n\ln\bar{n} + \ln n! + \bar{n} - \sum_i^n \ln\mathcal{P}(\vec{x}, X_i) \\ &= -n\ln\bar{n} + \ln n! + \bar{n} - \sum_i^n \ln\left(|\mathcal{M}(\vec{x}, X_i)|^2\eta(X_i)\phi(X_i)\right) + n\mathcal{N}(\vec{x}). \end{aligned} \tag{6.19}$$

Now, from Eqs. 6.7 and 6.11,

$$\mathcal{N}(\vec{x}) = \mathcal{C}(s)\bar{n}, \tag{6.20}$$

where

$$\mathcal{C}(s) = \frac{8(s-w_p^2)}{(2\pi)^4}\frac{A_{target}}{\mathcal{F}\rho_{target}\ell_{target}N_A}. \tag{6.21}$$

Thus we can rewrite Eq. 6.19 as

$$\begin{aligned} -\ln\mathcal{L} &= -\sum_i^n \ln|\mathcal{M}(\vec{x}, X_i)|^2 + \bar{n} + C \\ &= -\sum_i^n \ln|\mathcal{M}(\vec{x}, X_i)|^2 + \beta(s)\sum_i^{N_{acc}}|\mathcal{M}(\vec{x}, X_i)|^2 + C, \end{aligned} \tag{6.22}$$

where we have accumulated all terms that are independent of the fit parameters in the term C.

Note that the pre-factor $\beta(s)$ is really superfluous here and can be absorbed into the amplitudes. If we scale the amplitudes by $1/\beta(s)$, $-\ln\mathcal{L}$ will still be minimized by the re-scaled amplitudes with the same fit parameters. If we want to estimate the yield $\bar{n}$, as long as we consistently use the same re-scaled amplituedes all over, we would get the same yield as earlier.

6.1.4 Including Background

In Sec. 3.11 we explained how we account for background for our analysis – every event gets a quality factor or Q between 0 and 1. Consider the hypothetically extreme case of Q being 0. This means that the event has been rejected altogether and will not contribute to -ln $\mathcal{L}$ at all. Likewise, if Q is 1 then the event fully contributes -ln $|\mathcal{M}(\vec{x}, X_i)|^2$ for the i^{th} event. It is clear now that for the general case, we will have:

$$-\ln\mathcal{L} = -\sum_i^n Q_i\ln|\mathcal{M}(\vec{x}, X_i)|^2 + \beta(s)\sum_i^{N_{acc}}|\mathcal{M}(\vec{x}, X_i)|^2 + C. \tag{6.23}$$

6.2 Least Squares Fitting

We had earlier emphasized on the fact that the likelihood method is an *un*binned method, every event being fitted to, all at once. While this lends stability to the fits, in some occassions, it becomes very computationally intensive. This is the case if our fit variable is a cutoff scale Λ in a form factor and value of the form factor has to be calculated event by event at every iteration from a complicated monopole or dipole expression (as opposed to, say, a simple multiplicative pre-factor like dependence). In such circumstances it is prudent to use the alternative method of least square fitting which fits to ~ 20 data points instead of $\sim 10,000$ events.

This is a *binned* method. As in the likelihood case, we are still trying to determine the estimators $\vec{x}$ from a set of n data samples. However, the sample space is not the set of events themselves but

a set of *measured* observables $\mathcal{O}_i(X_i)$ from those events, with kinematics X_i at particular values of a subset of X_i' according to some binning in X_i'. For our purposes, these observables will be the measured differential cross sections or recoil polarizations or both. The fit function that we will try to minimize is

$$\chi^2 = \sum_i^n \frac{\mathcal{O}_i(X_i) - \hat{\mathcal{O}}_i(\vec{x}, X_i)}{\sigma_i^2}, \tag{6.24}$$

where $\mathcal{O}_i(X_i)$ are the *measured* values, $\hat{\mathcal{O}}_i(\vec{x}, X_i)$ are the *estimated* values from the functional form $\hat{\mathcal{O}}$ (to be built out of our amplitudes) and $\sigma_i$are the errors in the measurement. This definition of χ^2 is consistent with the fact that if the measurement errors are small, the estimated values will have to be even closer to the measured values for the same χ^2.

6.2.1 Calculation of $d\sigma/dt$

For the differential cross sections $d\sigma/dt$, the functional form $\hat{\mathcal{O}}$ is obtained from

$$d\sigma(\vec{x}, X) = \frac{1}{4}\frac{(2\pi)^4}{2(s-w_p^2)}|\mathcal{M}(\vec{x}, X)|^2 d\Phi(X). \tag{6.25}$$

The phase space element is given by

$$\begin{aligned} d\Phi(X) &= \frac{1}{4(2\pi)^6}\frac{|\vec{p}_{\Sigma^0}|d\Omega}{\sqrt{s}} \\ &= \frac{1}{4(2\pi)^6}\frac{|\vec{p}_{\Sigma^0}|2\pi d\cos\theta_{CM}^{K^+}}{\sqrt{s}}. \end{aligned} \tag{6.26}$$

To convert $d\cos\theta_{CM}^{K^+}$ to dt we need the following relations:

$$\begin{aligned} t &= w_p^2 + w_{\Sigma^0}^2 + 2E_iE_{\Sigma^0} + 2|\vec{p}_i||\vec{p}_{\Sigma^0}|\cos\theta_{CM}^{K^+} \\ &= w_p^2 + w_{\Sigma^0}^2 + 2E_iE_{\Sigma^0} + \frac{s-w_p^2}{\sqrt{s}}|\vec{p}_{\Sigma^0}|\cos\theta_{CM}^{K^+}, \end{aligned} \tag{6.27}$$

where E_i and $\vec{p}_i$ are the energy and momentum of the target proton. Thus,

$$d\cos\theta_{CM}^{K^+} = \frac{\sqrt{s}}{s-w_p^2}\frac{dt}{|\vec{p}_{\Sigma^0}|}. \tag{6.28}$$

Substitution of Eqs. 6.26 and 6.28 in Eq. 6.25 yields

$$\begin{aligned} \frac{d\sigma(\vec{x}, X)}{dt} &= \frac{1}{4}\frac{(2\pi)^4}{2(s-w_p^2)}|\mathcal{M}(\vec{x}, X)|^2\frac{1}{4(2\pi)^6}\frac{|\vec{p}_{\Sigma^0}|}{\sqrt{s}}\frac{\sqrt{s}}{s-w_p^2}\frac{2\pi}{|\vec{p}_{\Sigma^0}|} \\ &= \frac{1}{64\pi(s-w_p^2)^2}|\mathcal{M}(\vec{x}, X)|^2. \end{aligned} \tag{6.29}$$

6.3 Multiple Dataset Fits

To fit to several datasets at once, for example when a particular parameter is constraied to be the same over several datasets, is easily achieved here. The fit function, either χ^2 or $-\ln\mathcal{L}$, will simply be the sum of the fit functions of the two separate datasets.

6.4 MINUIT

To run all these fits, with many degrees of freedom, significant hardware computing power and efficient minimization routines are needed. The software package we use for this purpose is MINUIT, an efficient and well-honed minimization routine widely used in the particle physics community [83].

The minimization algorithm we employ while running MINUIT is MIGRAD, which is based upon the Davidon-Fletcher-Powell (DFP) variable metric method. The DFP is an iterative process that assumes that the gradient $\vec{g}(\vec{x}) = \vec{\nabla}F(\vec{x})$ of the minimization function $F(\vec{x})$ with respect to the fit parameters $\vec{x}$ can be calculated explicitly. In the majority of our fits, we supply MIGRAD with randomized initial values, $\vec{x}_0$, of the fit parameters. MIGRAD then uses the gradient of $\vec{g}(\vec{x})$ to find another value of the fit parameters, $\vec{x}_1$, for which $F(\vec{x}_1) < F(\vec{x}_0)$. The $\vec{x}_0$ are then replaced by the $\vec{x}_1$, and a new set of fit parameters, $\vec{x}_2$ is found in the same manner. MIGRAD repeats this process until the difference in the minimization function between consecutive iterations, $\delta F \equiv F(\vec{x}_n) - F(\vec{x}_{n-1})$, is less than some user-defined tolerance.

Since MIGRAD requires the derivatives explicitly, to ease calculations, we also supply it the partial derivatives of the fit functions with respect to the fit parameters. For likelihood fits this is,

$$\frac{\partial(-\ln\mathcal{L})}{\partial x_j} = -\sum_i^n Q_i \left(\frac{1}{|\mathcal{M}(\vec{x}, X_i)|^2} \frac{\partial|\mathcal{M}(\vec{x}, X_i)|^2}{\partial x_j} \right) + \beta(s) \sum_i^{N_{\rm acc}} \frac{\partial|\mathcal{M}(\vec{x}, X_i)|^2}{\partial x_j}, \tag{6.30}$$

while for least squares fits it is,

$$\frac{\partial\chi^2}{\partial x_j} = \left(\frac{1}{64\pi(s-w_p^2)^2} \frac{\partial|\mathcal{M}(\vec{x}, X_i)|^2}{\partial x_j} \right) \sum_i^n \frac{2}{\sigma_i^2} \left(\frac{d\sigma}{dt}(\vec{x}, X_i) - \frac{d\sigma}{dt} \right). \tag{6.31}$$

For both cases, we compute the partial derivatives of the $|\mathcal{M}(\vec{x}, X)|^2$ as

$$\frac{\partial|\mathcal{M}(\vec{x}, X_i)|^2}{\partial x_j} = \sum_{\text{all spins}} 2\Re\left(\sum_a \frac{\partial\alpha_a(\vec{x}, X_i)}{\partial x_j} \mathcal{A}_a \sum_{a'} \alpha_{a'}(\vec{x}, X_i) \mathcal{A}^*_{a'}(X_i) \right), \tag{6.32}$$

where the spin sum is over all the external particle spins.

6.5 The Mother Fit

As mentioned earlier, the first step towards extraction of differential cross sections constitutes running a likelihood fit to all events using a "sufficient" number of J^P waves. We call this fit the mother fit. What we mean by "sufficient" is a semi-complete basis of functions in $\cos\theta^{K^+}_{CM}$ which we will take as the PWA amplitudes $\gamma p \to J^P \to K^+\Sigma^0 \to K^+\gamma_{out}\ \Lambda \to K^+\gamma_{out}\ p\pi^-$ for J^P from $\frac{1}{2}^\pm$ till $\frac{11}{2}^\pm$. That is, we are not concerned with representing actual physics, but that the fit function has enough freedom to properly describe all the distributions in every independent kinematic variable, including correlations between them.

6.5.1 Setup

We parameterize the complex prefactor $\alpha_a(\vec{x}, X)$ in Eq. 6.6 (with "a" now consisting of J^P and electric/magnetic multipole specifications) in terms of three real fit parameters θ_{J^P}, r_{J^P} and ϕ_{J^P} as

$$\alpha_a(\vec{x}, X) = f_{MP}(\theta_{J^P}) r_{J^P} \exp(i\phi_{J^P}), \tag{6.33}$$

where

$$f_{MP}(\theta_{J^P}) = \left\{ \begin{array}{ll} \cos\theta_{J^P} & \text{for electric multipoles} \\ \sin\theta_{J^P} & \text{for magnetic multipoles} \end{array} \right\} \text{ for } J^P \neq \frac{1}{2}^{\pm} . \tag{6.34}$$

Thus each J^P wave has an independent phase angle ϕ_{J^P} and decay magnitude r_{J^P} whilst between the two allowed monopole variants in each case we keep an extra factor which we parameterize by $\tan\theta_{J^P}$. For $J^P \neq \frac{1}{2}^{\pm}$ there is only one allowed monopole, so that there is no f_{MP} for these two cases. In this way, $J^P \neq \frac{1}{2}^{\pm}$ has $2+2=4$ independent parameters while $\frac{3}{2}^{\pm}$ till $\frac{11}{2}^{\pm}$ has $3\times 10 = 30$, resulting in 34 overall fit parameters and every fit was run for at least 4 iterations. For the results to follow, we used 10 iterations and present the result for the iteration with the least $-\ln\mathcal{L}$. All thoughout, we bin events in 10 MeV wide $\sqrt{s}$ bins and run individual fits for every $\sqrt{s}$ bin.

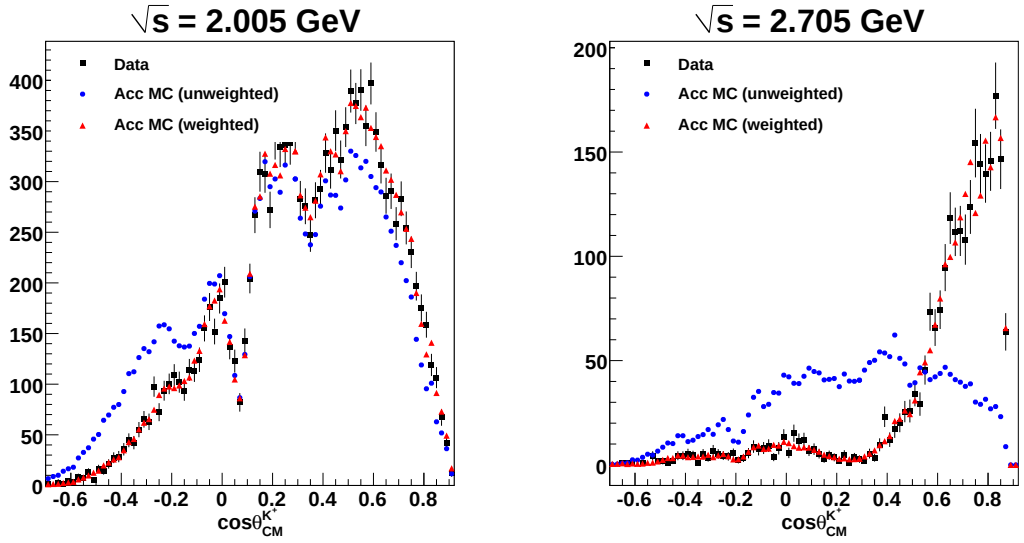

(a) (b)

Figure 6.1: Mother fit results: weighing by the mother fit results brings the accepted Monte Carlo into excellent agreement with the data.

6.5.2 Quality Checks on Fit Results

Fig. 6.5.2 shows the results of our mother fit at two center-of-mass energies, in a particular kinematic variable ($\cos\theta^{K^+}_{CM}$). The black squares represent the data and the blue circles are the unweighted accepted Monte Carlo. The red triangles show the accepted Monte Carlo weighted by the fit results. The weighted accepted Monte Carlo matches very well with the data.

It is however not enough that the fit reproduce the data distribution in just one particular kinematic variable. Recall that the mother fit was designed to match the data in *every single independent kinematic variable*. To ensure that our fits satisfy this criterion, we must look how the results look in multiple kinematic variables simultaneously. Fig. 6.5.2 shows $\phi^{\Lambda}_{\Sigma HF}$ plotted against $\cos\theta^{p}_{\Lambda HF}$ in eight different $\cos\theta^{K^+}_{CM}$ bins for $\sqrt{s} = 2.005$ GeV. The data and the weighted accepted Monte Carlo agree very well with each other.

6.6 Differential Cross Sections

We are in a position now to extract the differential cross section for $K^+\Sigma^0$ photoproduction. What is to follow is one of the central results from this thesis work. Though cross sections from previous experiments exist, our statistics and range in $\sqrt{s}$ represent a significant improvement over them. We follow the customary norm in the literature and report $d\sigma/d\cos\theta^{K^+}_{CM}$ instead of $d\sigma/dt$ or $d\sigma/du$, for every $\sqrt{s}$ bin, since this facilitates the study of the evolution of features in the cross sections with the CM energy (which is a monotonic function of $\sqrt{s}$).

6.6.1 Formula for Calculation

There are three parts to the formula for calculating differential cross sections. First comes the differential yield $\mathcal{Y}(\sqrt{s}, \cos\theta^{K^+}_{CM})$, next is the acceptance factor $\eta(\sqrt{s}, \cos\theta^{K^+}_{CM})$, and finally there is

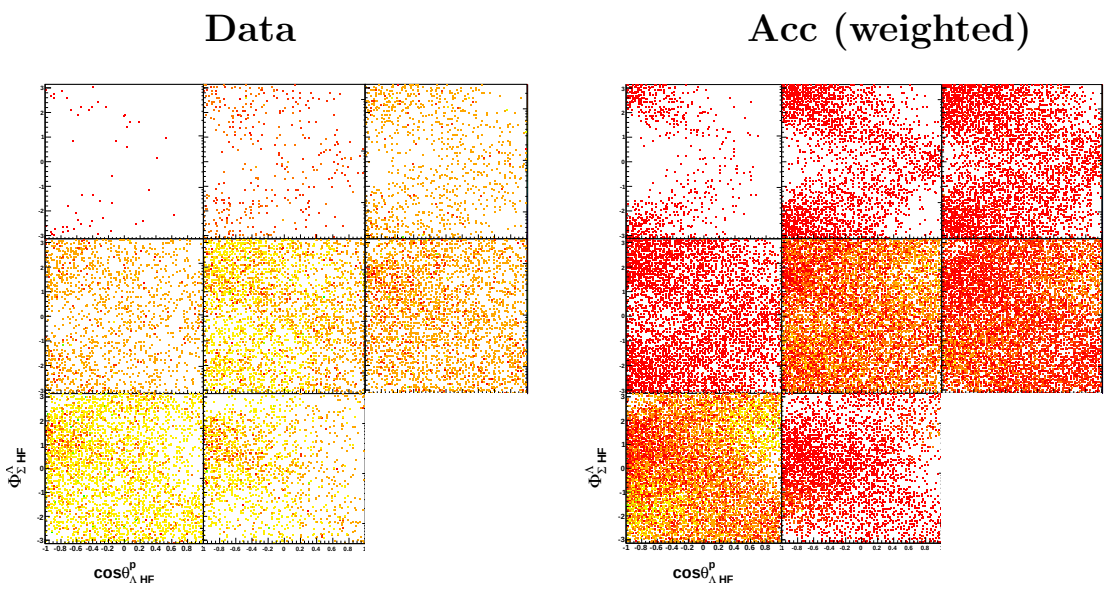

(a) (b)

Figure 6.2: Quality check for the mother fit: (a) data and (b) accepted Monte Carlo (weighted by the fit) at $\sqrt{s} = 2.005$ GeV. The plots show $\phi^{\Lambda}_{\Sigma HF}$ plotted against $\cos\theta^{p}_{\Lambda HF}$ in eight $\cos\theta^{K^+}_{CM}$ bins. Each bin is of width 0.2 and the bin centers increase from -0.6 to 0.8, top-left to bottom-right, thus traversing from backward angles to forward angles. All correlations presented in the data are faithfully represented in the accepted Monte Carlo after being weighted by the fit results

Factor	Value	Description
ρ_{target}	0.7177 g/cm^3	Target density (see Sec. 4.9)
ℓ_{target}	40 cm	Target length [39]
N_A	6.022 $\times 10^{23}$	Avogadro number
A_{target}	1.00794 $g/mole$	Target atomic weight

Table 6.1: Target factors used for $d\sigma/d\cos\theta^{K^+}_{CM}$ measurements.

a *target factor*. In all, it reads,

$$\frac{d\sigma}{d\cos\theta^{K^+}_{CM}} = \left(\frac{A_{target}}{\mathcal{F}(\sqrt{s})\rho_{target}\ell_{target}N_A}\right)\frac{\mathcal{Y}(\sqrt{s},\theta^{K}_{CM})}{(\Delta\cos\theta^{K^+}_{CM})\eta(\sqrt{s},\theta^{K^+}_{CM})}, \tag{6.35}$$

where A_{target}, ρ_{target}, and ℓ_{target} are the target atomic weight, density, and length respectively, N_A is the Avogadro number, $\mathcal{F}(\sqrt{s})$ is the corrected number of photons impingent on the target in each $\sqrt{s}$ bin, and $\Delta\cos\theta^{K^+}_{CM} = 0.1$ is the width of our binning in $\cos\theta^{K^+}_{CM}$, kept same for all kinematic regions. The values used for the target factors are listed in Table 6.1.

The detected data yield in each $(\sqrt{s},\theta^{K^+}_{CM})$ bin is obtained as

$$\mathcal{Y}(\sqrt{s},\theta^{K^+}_{CM}) = \sum_{i}^{N} Q_i, \tag{6.36}$$

where N is the number of detected events in the bin and Q_i are the Q-values obtained in Sec. 3.11. In this analysis, we employ two expressions for calculating acceptance in any particular $(\sqrt{s},\theta^{K^+}_{CM})$ bin:

$$\eta(\sqrt{s},\theta^{K^+}_{CM})_{\,\text{weighted}} = \frac{\sum_{i}^{N_{acc}}|\mathcal{M}_i|^2}{\sum_{j}^{N_{raw}}|\mathcal{M}_j|^2} \qquad \text{(three-track topology)} \tag{6.37a}$$

$$\eta(\sqrt{s},\theta^{K^+}_{CM})_{\,\text{unweighted}} = \frac{N_{acc}}{N_{raw}} \qquad \text{(two-track topology)}, \tag{6.37b}$$

where $N_{acc}(N_{raw})$ is the number of accepted(raw) Monte Carlo events in the bin and the $|\mathcal{M}|^2$'s are the *physics weighted* transition elements obtained from the mother fit (for the three-track topology).

Note that the expression in Eq. 6.37b ignores the *dynamics* of the reaction. This can be important in the present case since hyperons are known be produced with a high degree of polarization. In Eq. 6.37a, by weighing the Monte Carlo with results from the mother fit, we are properly accounting for the *physics*, in our acceptance calculation. However, for both Λ and Σ^0 decays, the breakup momenta/angles are small, so that in the laboratory/detector frame, the decays products keep travelling in almost the same direction as the decaying mother particle. Hence Eq. 6.37b should be a very good approximation to the more correct expression appearing in Eq. 6.37a. In Sec. 7.3 we will confirm this explicitly, when we compare the cross-sections for the three-track topology obtained by both expressions for acceptance and find them to agree very well.

Source	Value	Description
Confidence Level	3%	Kinematic Fitter Uncertainty (three-track) [16]
Particle Identification	0.62%	Signal loss to PID cut (three-track) (Sec. 3.6.6)
Particle Identification	1.8%	Signal loss to PID cuts (two-track) (Sec. 3.7.3)
Acceptance	3-6%	Sector-wise acceptance study (Sec. 4.8)
$\Lambda \to p\pi^-$ Branching Fraction	0.5%	PDG listed uncertainty [53]
Target Density	0.11%	Std. dev. of target measurement per run [51]
Target Length	0.125%	Target survey precision [39]
Photon Normalization	7.7%	Based upon run-to-run normalized yields [16]
Photon Transmission Efficiency	0.5%	Propagation of photons to target along beamline [16]
Live-time	3%	DAQ live time [51]

Table 6.2: Table of Systematic Uncertainties

6.6.2 Uncertainties

The statistical error in each $(\sqrt{s}, \theta^{K^+}_{CM})$ bin are given as

$$\sigma^2_{\mathcal{Y}} = \mathcal{Y} + (\sum_i^{N_{data}} \sigma_{Q_i})^2 \tag{6.38a}$$

$$\sigma^2_{acc} = N_{acc} \tag{6.38b}$$

$$\sigma^2_{raw} = N_{raw} \tag{6.38c}$$

where σ_{Q_i} is the error from our background fitting procedure in determining the quality factor Q_i for the i^{th} event (see Sec. 3.11.1). Note that by summing over the σ_{Q_i}'s, we are assuming that these errors are fully correlated with one another, which is an over-estimation. One could instead add the σ_{Q_i}'s in quadrature, but the difference is small. The total relative statistical error is:

$$\sigma^2_{rel} = \frac{\sigma^2_{\mathcal{Y}}}{\mathcal{Y}^2} + \frac{1}{N_{acc}} - \frac{1}{N_{raw}}, \tag{6.39}$$

where the negative sign before the σ^2_{raw} appears because N_{acc} is ultimately derived from N_{raw}. However, for all practical purposes, $\frac{1}{N_{raw}}$ is always negligibly small. The systematic uncertainties are summarized in Table 6.2. Due to the $\sqrt{s}$ dependence in the acceptance uncertainty, we will present a point-to-point systematic error, but overall, this ranges from about 10 to 12%.

6.7 Two- and Three-track Results

We now present the $\gamma p \to K^+\Sigma^0$ differential cross-section results for the $g11a$ dataset. Figs. 6.3 through 6.9 show the results from the the two-track and the three-track analyses in red and blue respectively. There are 112 $\sqrt{s}$ bins, each 10 MeV wide, from 1.695 to 2.835 GeV (bins $\sqrt{s} = 1.1955$, 2.735 and 2.745 GeV are skipped for reasons given in Sec. 4.10). Within each $\sqrt{s}$ bin, the $\cos\theta^{K^+}_{CM}$ bins in the x-axis are 0.1 wide.

A number of features are immediately apparent from these results. First, where the kinematics overlap, the two- and three-track results are in very good agreement with each other. As the two analyses employed entirely different event selection and PID schemes, the internal consistency of $g11a$ results thus bolsters our confidence in this analysis.

Secondly, the two-track analysis provides cross-sections in the backward-angle regions where the three-track dataset has little, or almost zero statistics. There there is a prominent rise in the cross-sections in this region, signaling the possible presence of u-channel contributions. Thus, the two-track dataset adds vital information to our overall understanding of $K^+\Sigma^0$ photoproduction.

Fig. 6.10 shows the the cumulative global difference between the two results. The quantity plotted here is:

$$\Delta(\sqrt{s}, \cos\theta^{K^+}_{CM}) = \frac{x_2 - x_3}{\sqrt{\sigma_2^2 + \sigma_3^2 + (\overline{x}\sigma_\eta(\sqrt{s}))^2}}, \tag{6.40}$$

where x_i and σ_i are the cross-section and its associated statistical error respectively, for the i-track topology, while $\overline{x}$ is the weighted mean of the two and $\sigma_\eta(\sqrt{s})$ is the $\sqrt{s}$ dependent systematic uncertainty provided by Eq. 4.3. A Gaussian fit to the the distribution yields a mean $\mu_\Delta = 0.558$ and standard deviation $\sigma_\Delta = 1.017$. That the Δ distribution is roughly normal with unit width shows that estimated errors correctly reflect the uncertainties. The mean shows that the two-track cross-sections are on the average ~ 0.5 standard deviations higher than the three-track. A possible explanation for this might be the different acceptance calculation techniques (*c.f.* Eqs. 6.37a and 6.37b).

6.8 Final Differential Cross-Sections

The consistency between the results for the two topologies allow us to quote our final cross-sections as a weighted mean of the two in regions where results from both datasets exist. In any such "overlap bin", let $\mu_{2,3}$ and $\sigma_{2,3}$ be the measured differential-cross section and its error from the 2- and 3-track datasets respectively. We then write the error matrix as

$$E = \begin{pmatrix} \sigma_2^2 & \rho_{23}\sigma_2\sigma_3 \\ \rho_{32}\sigma_3\sigma_2 & \sigma_3^2 \end{pmatrix}, \tag{6.41}$$

where the cross-terms denote the degree of correlation. Assuming $\rho = \rho_{23} = \rho_{32}$, we can invert this as

$$E^{-1} = \frac{1}{(1=\rho^2)\sigma_2^2\sigma_3^2} \begin{pmatrix} \sigma_3^2 & -\rho\sigma_2\sigma_3 \\ -\rho\sigma_2\sigma_3 & \sigma_2^2 \end{pmatrix}, \tag{6.42}$$

and thereby, obtain the χ^2 function

$$\chi^2 = \sum (\bar{\mu} - \mu_i) \left(E^{-1}\right)_{ij} (\bar{\mu} - \mu_j). \tag{6.43}$$

Minimising the χ^2 yields the requisite mean $\bar{\mu}$

$$\bar{\mu} = \frac{\mu_2\sigma_3^2 - \rho(\mu_2 + \mu_3)\sigma_2\sigma_3 + \mu_3\sigma_2^2}{\sigma_2^2 - 2\rho\sigma_2\sigma_3 + \sigma_3^2}, \tag{6.44}$$

and the error on the combined measurement

$$\bar{\sigma} = \left(\frac{1}{2}\frac{\partial^2\chi^2}{(\partial\bar{\mu})^2}\right)^{-1/2} = \left(\frac{1}{2}\sum_{i,j}\left(E^{-1}\right)_{ij}\right)^{-1/2} = \sqrt{\frac{\sigma_2\sigma_3(1-\rho^2)}{\sigma_2/\sigma_3 - 2\rho + \sigma_3/\sigma_2}}. \tag{6.45}$$

This method is very similar to the so-called `BLUE` method [84, 85] employed elsewhere [86] and also boils down to the familiar expressions for uncorrelated measurements at $\rho = 0$. The only pathology of this method is the near $\rho \approx 1$ region where the error matrix becomes non-invertible, but as long as one is away from the high-correlation regime, the formula is pathology free (the $\rho \approx 1$ limit

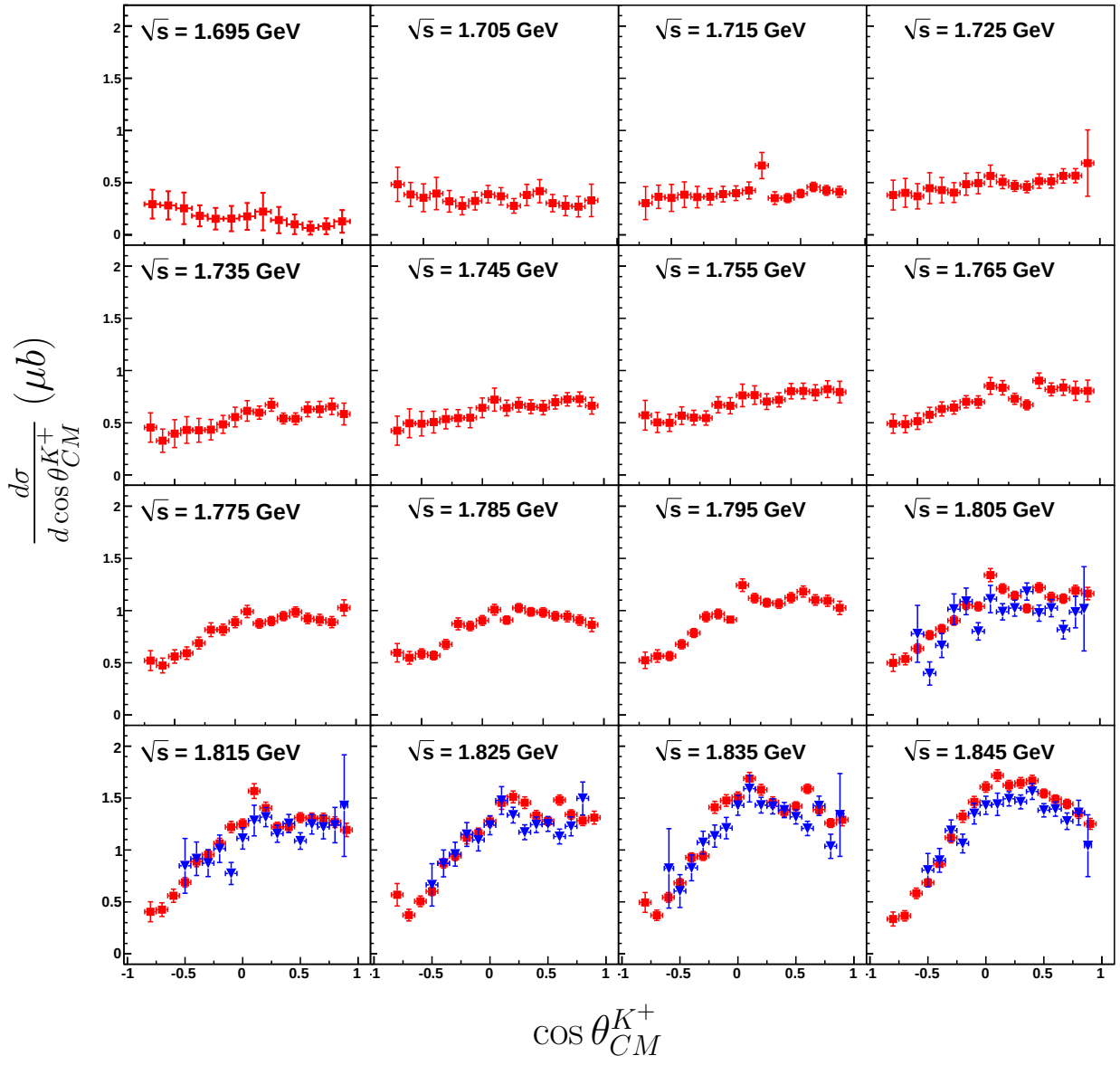

Figure 6.3: $\gamma p \to K^+\Sigma^0$ differential cross-sections for $g11a$: the **red** squares are the two-track results while the **blue** triangles are the three-track results. The vertical axis range is the same for all the plots in the canvas and is shown in the first column. All errors are statistical.

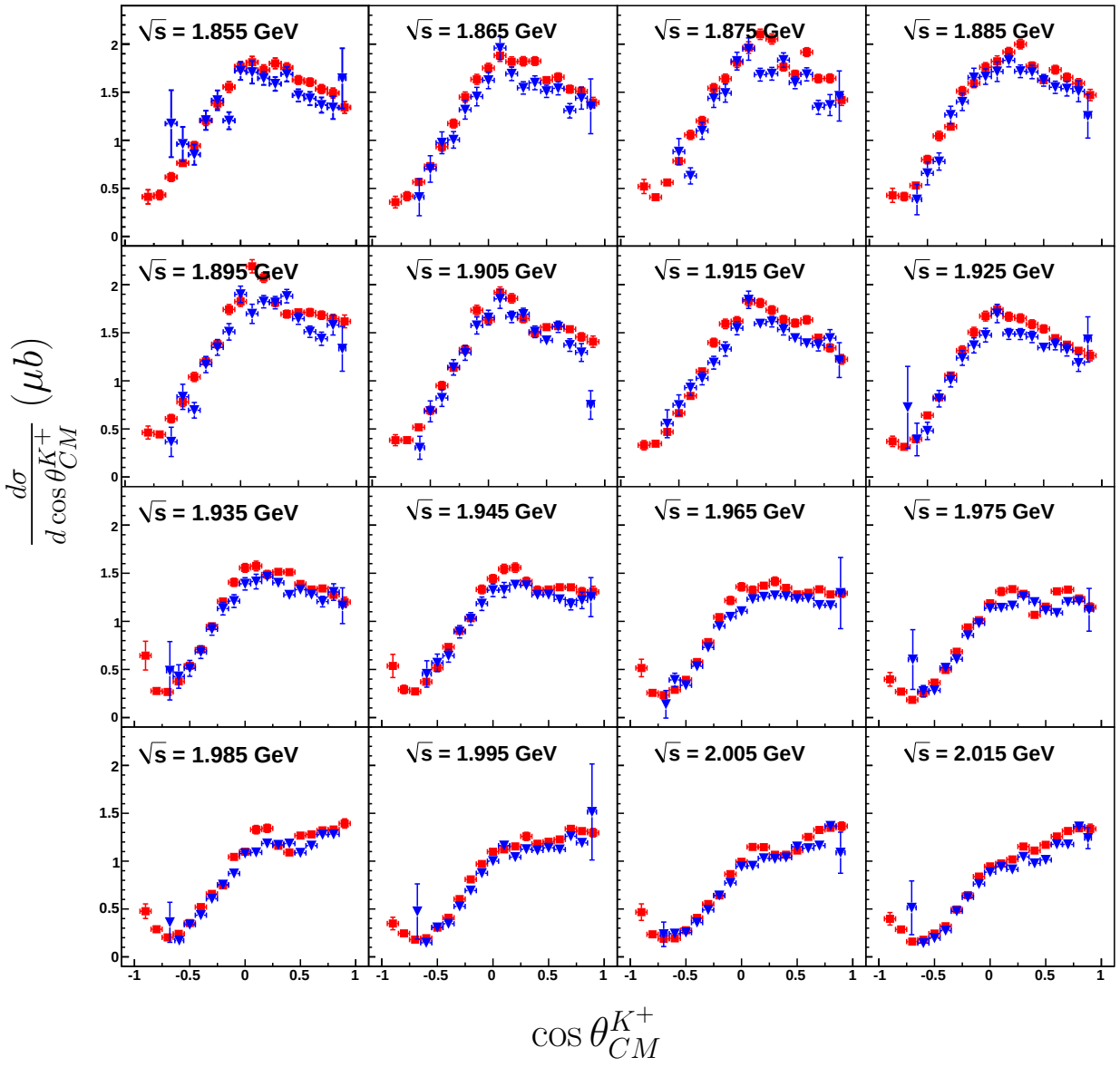

Figure 6.4: $\gamma p \to K^+\Sigma^0$ differential cross-sections for $g11a$: the **red** squares are the two-track results while the **blue** triangles are the three-track results. The vertical axis range is the same for all the plots in the canvas and is shown in the first column. All errors are statistical. No result is presented for the bin $\sqrt{s} = 1.955$ GeV due to reasons given in Sec. 4.10.

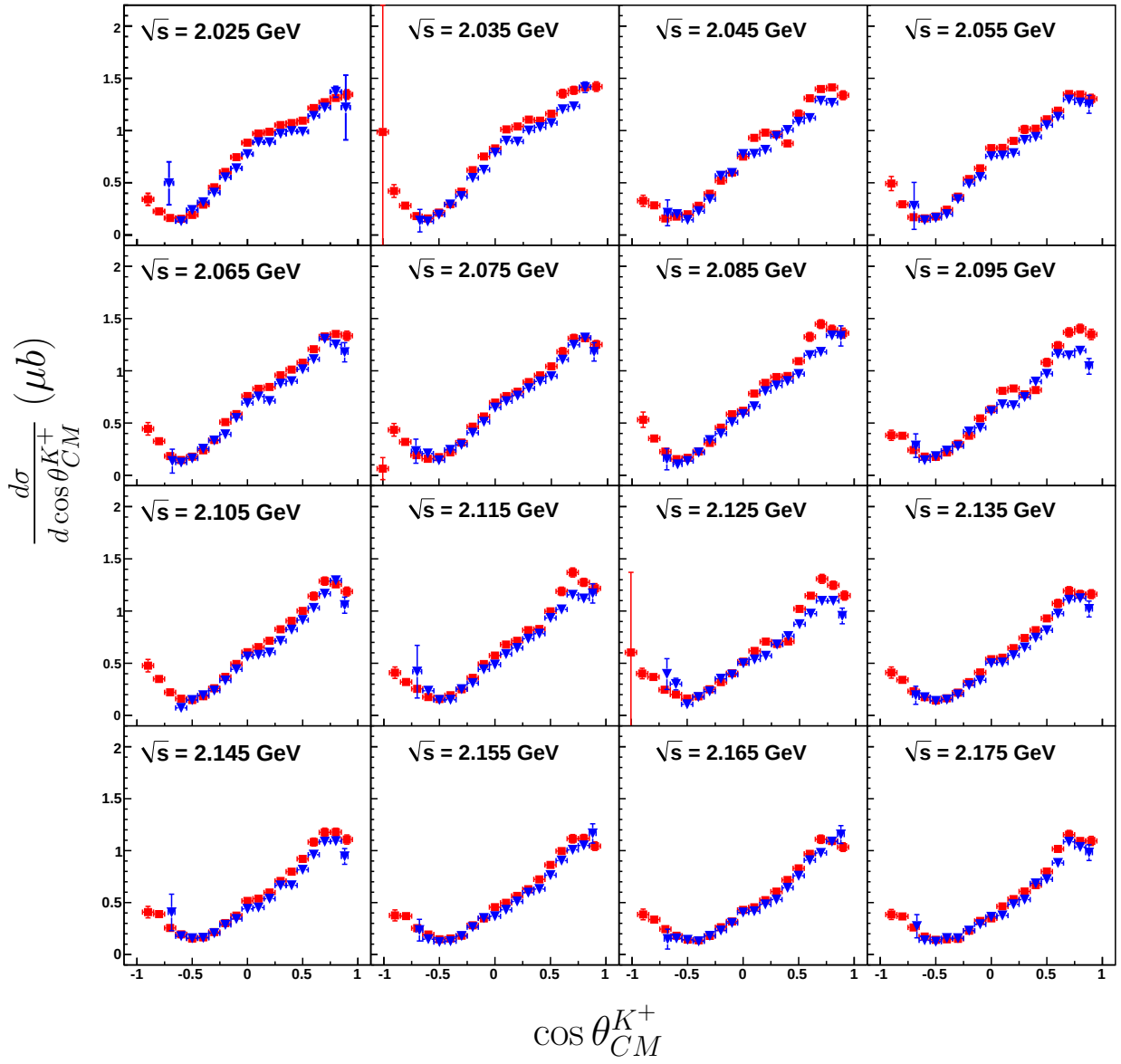

Figure 6.5: $\gamma p \to K^+\Sigma^0$ differential cross-sections for $g11a$: the **red** squares are the two-track results while the **blue** triangles are the three-track results. The vertical axis range is the same for all the plots in the canvas and is shown in the first column. All errors are statistical.

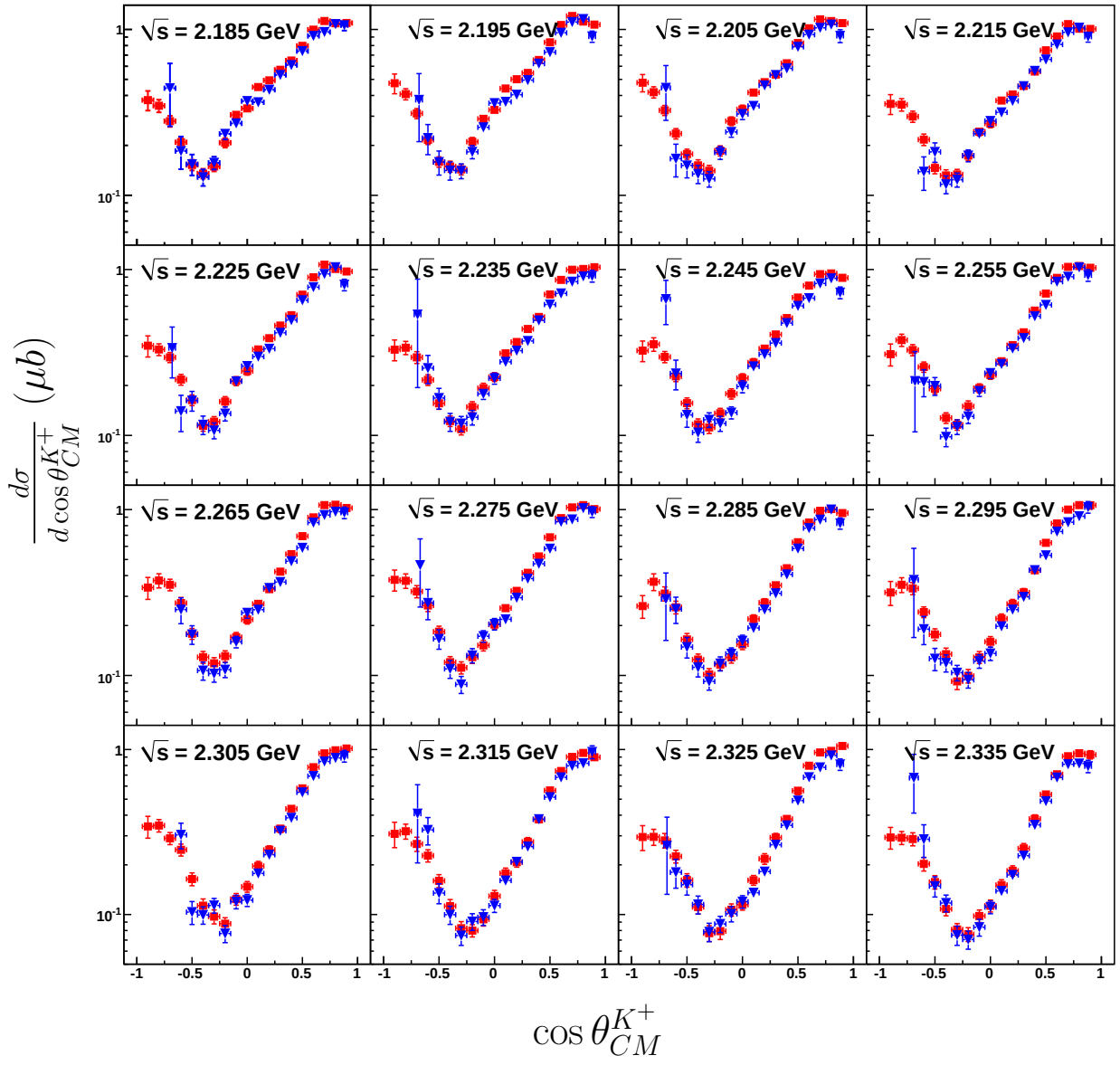

Figure 6.6: $\gamma p \to K^+\Sigma^0$ differential cross-sections for $g11a$: the **red** squares are the two-track results while the **blue** triangles are the three-track results. The vertical axis range (in logarithmic scale) is the same for all the plots in the canvas and is shown in the first column. All errors are statistical.

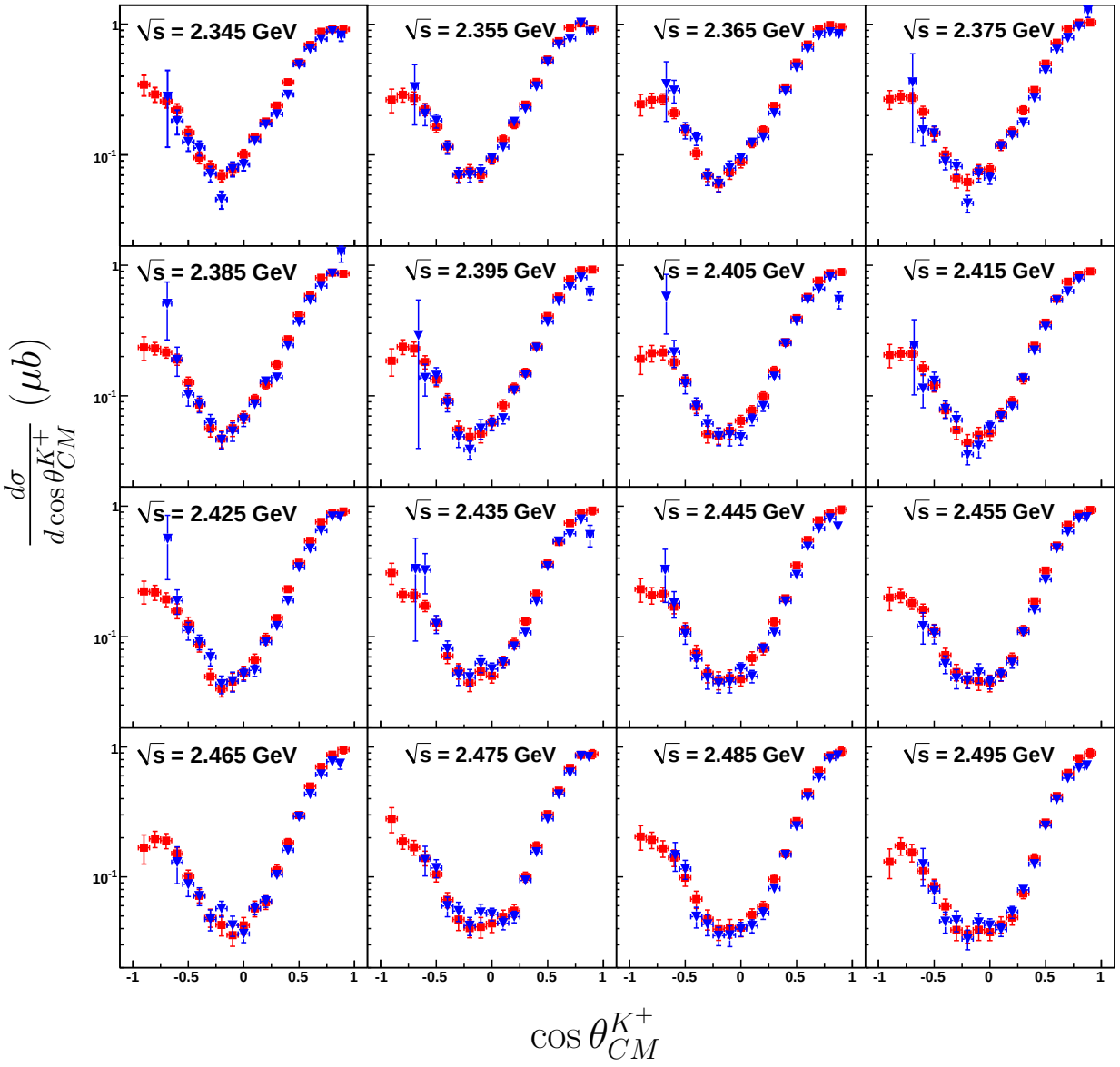

Figure 6.7: $\gamma p \to K^+\Sigma^0$ differential cross-sections for $g11a$: the **red** squares are the two-track results while the **blue** triangles are the three-track results. The vertical axis range (in logarithmic scale) is the same for all the plots in the canvas and is shown in the first column. All errors are statistical.

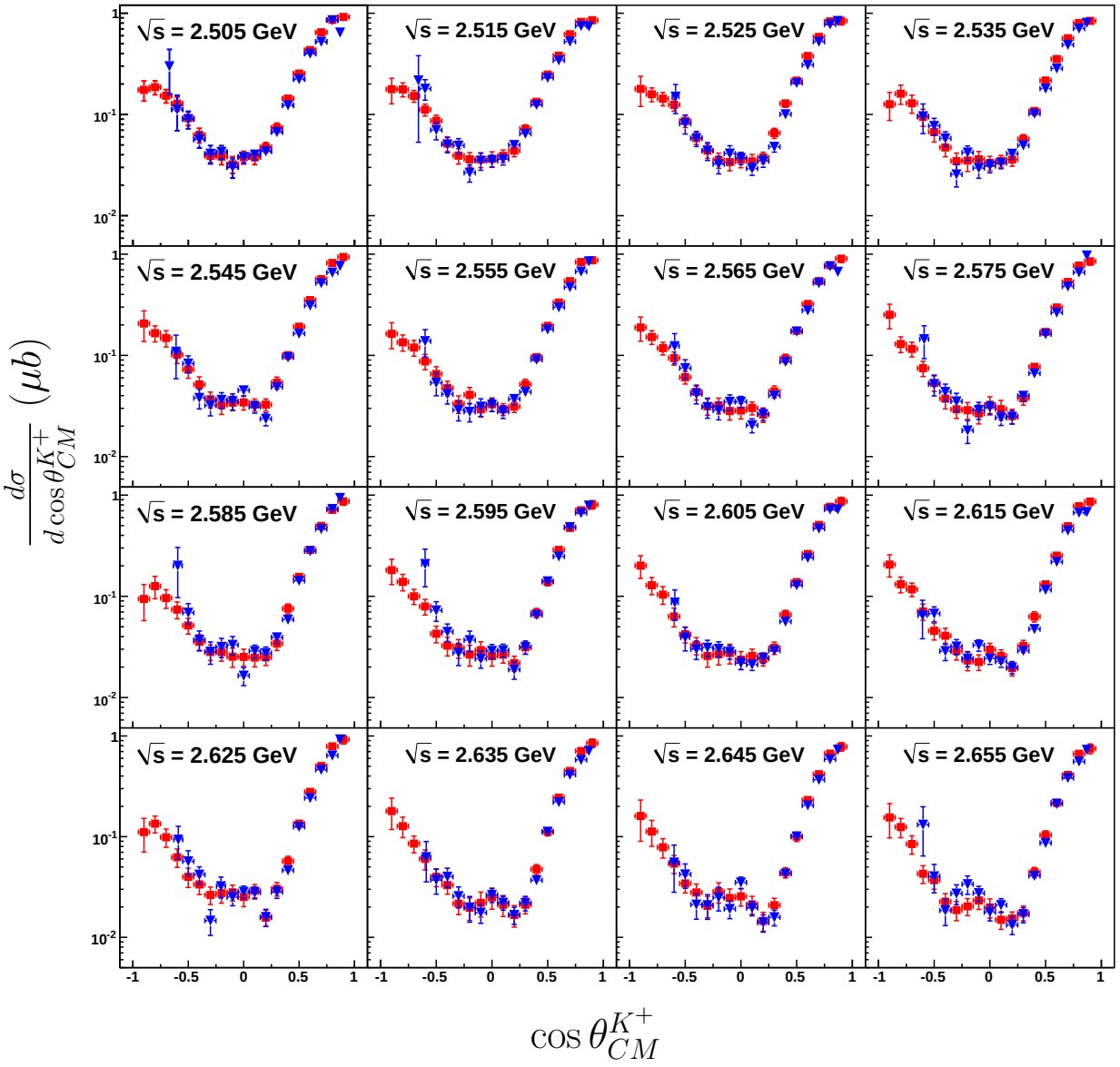

Figure 6.8: $\gamma p \to K^+\Sigma^0$ differential cross-sections for $g11a$: the **red** squares are the two-track results while the **blue** triangles are the three-track results. The vertical axis range (in logarithmic scale) is the same for all the plots in the canvas and is shown in the first column. All errors are statistical.

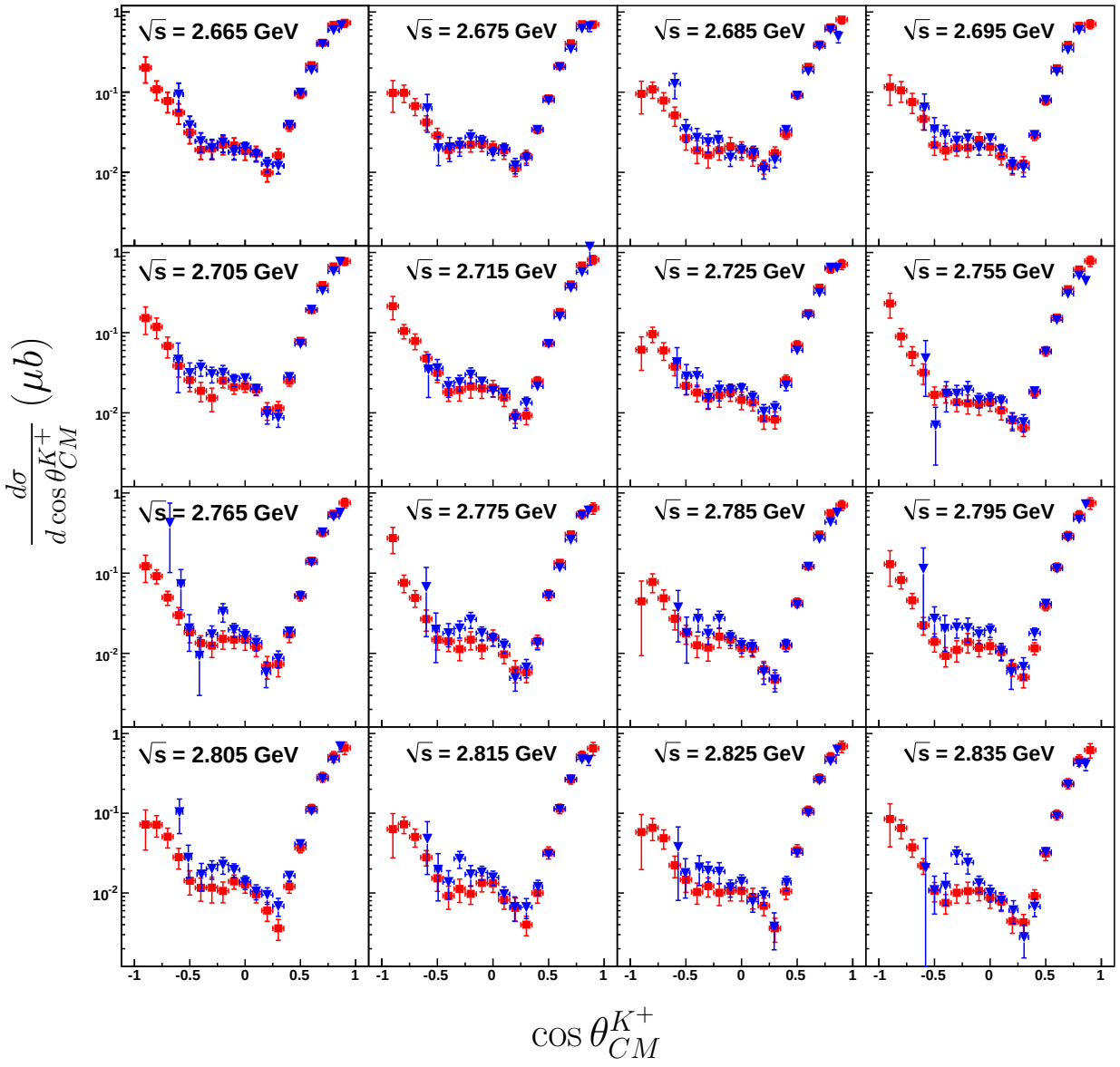

Figure 6.9: $\gamma p \to K^+\Sigma^0$ differential cross-sections for $g11a$: the **red** squares are the two-track results while the **blue** triangles are the three-track results. The vertical axis range (in logarithmic scale) is the same for all the plots in the canvas and is shown in the first column. All errors are statistical.No result is presented for the bins $\sqrt{s} = 2.735$ GeV and 2.745 GeV due to reasons given in Sec. 4.10.

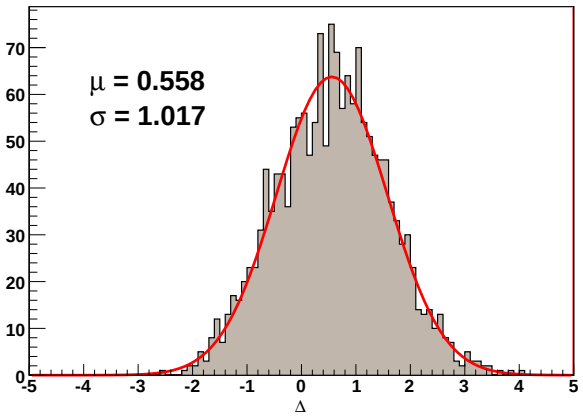

Figure 6.10: Δ (defined in Eq. 6.40) depicting the relative spread between the two- and three-track differential cross sections for $g11a$.

requires $\mu_2 \approx \mu_3$ and $\sigma_2 \approx \sigma_3$ and the formula becomes highly sensitive to small deviations from this behavior). Under the present circumstances, one can form *two* correlation factors. Since the entire 3-track dataset is (to a high approximation) present in the 2-track dataset, $\rho_{32} \approx 1.0$. However, from Sec. 3.11.1 the total occupancy after cuts and background separation is ~ 4.64 million for the 2-track and ~ 0.655 million for the 3-track dataset – hence $\rho_{23} \approx 0.14$. Taking the geometric mean of the two, one can get an *effective* correlation $\rho_{eff} \approx \sqrt{\rho_{23}\rho_{32}} \approx 0.37$.

Employing this method, our final differential cross-sections are shown in Figs. 6.11 and 6.12 as a function of the center-of-mass energy in different production angle regions. In all we have made measurements at 2133 individual kinematic points covering almost the entire angular range, barring the extreme forward and backward angles (the CLAS detector has holes in these regions) and threshold upwards till 2.84 GeV in energy.

6.8.1 A note on the errors

Before ending this section we want to point out that several other related expressions were tried out before finalizing on formulas 6.45 and 6.44. While it is true that some events are *physically* common between the two topologies, how we use the CLAS detector to *measure* these events are sufficiently different between the two topologies (event selection method, acceptance calculation, *et al*) that the degree of correlation might be less than 100% (that is, *all* 3-track events being included in the 2-track dataset). It is true however that certain segments of the measurements (the normalization, to be precise) which goes into the differential cross-section calculation is the same and thus highly correlated between the two measurements. The same might not apply for the apply to the acceptance calculation, however (see the discussion by Lyons [84]).

As a simple approximation, we tried a completely uncorrelated ($\rho = 0$) combination, both for μ and σ. Next, we tried keeping μ uncorrelated, but $\bar{\sigma} = \sqrt{\sigma_2\sigma_3}$. As an extreme, we also tried $\rho = 0.9$ – however, the errors seemed too small in this case, reflecting the near $\rho = 1$ pathology. The final correlation coefficient ρ_{eff} seemed the most plausible, both in terms of underlying justifiability and final results. However, we also found that to a large extent, as long as one stayed away from the $\rho = 1$ limit, the results (including taking the geometric mean of the errors) were very similiar. This

is probably due to the errors being small enough (as a reminder, we are *not* looking at the very backward angle regions here – which is where the largest statistical errors are) and also the fact that the agreement between the two datasets is generally very good.

6.9 Comparision With Previous Experiments

Figs. 6.13 and 6.14 show our final differential cross sections for CLAS $g11a$ in comparision with previously published high statistics measurements. The latter consists of results from the CLAS $g1c$ dataset by Bradford *et al* (2005) [87], a SAPHIR analysis by Glander *et al* (2004) [88] and a set of two more recent forward angle measurements using the LEPS detector by Kohri *et al* (2006) [89]. Overall, there is good consistency among the different datasets, with an enhancement at $\sqrt{s} \sim 1.9$ GeV prominent over the entire angular range. Some structures are also visible around $\sqrt{s} \sim 2.1$ GeV in the forward angles. Some interesting localized discrepancies also occur between the different results. Chiefly, this pertains to the "hump" in the backward angles at ~ 2.2 GeV seen in the CLAS $g1c$ results, but not prominent in the SAPHIR data. The present CLAS $g11a$ analysis however clearly confirms this structure.

In the kinematic region around $0.4 \leq \cos\theta^{K^+}_{CM} \leq 0.7$, 2.0 GeV $\leq \sqrt{s} <$ 2.2 GeV, $g11a$ seems to be slightly lower than $g1c$. The SAPHIR results seems to agree better with $g1c$ in this region. The difference is small and can be attributed to the systematics involved in the different analyses. In Chapter 7, we make a detailed study of $g11a$ to understand its systematics and find it to be self-consistent to a high degree. The particular kinematic region in question is neither statistics limited (see Figs. 3.25 and 8.4), nor falls in a region of questionable understanding of the detector acceptance (see Sec. 3.10.2). For $g11a$, the energy and momentum corrections for the proton and π^- should also be better because of the usage of the kinematic fitter in deriving them (the kinematic fitter was specially honed for the $g11a$ dataset [50]). This is especially true for the three-track topology where the secondary Λ decay vertex is reconstructed using tracking information on the proton and π^- trajectories and corrections for these two tracks subsequently derived using the Λ vertex as the source, instead of the event vertex, as used traditionally (see Sec. 3.4). Also note that only the three-track topology uses the more correct *physics-weighted* acceptance calculation, while we found in the previous section that the two-track results (which, like the previous $g1c$ and SAPHIR measurements, used *unweighted* acceptances) to be higher than the three-track results by around 0.5σ. While none of these effects are large enough to cause a $5-10\%$ difference, they do contribute to slight overall systematic shifts. Lastly, note that the more recent high statistics LEPS measurement roughly falls *between* the $g1c$ and $g11a$ results.

6.10 Summary

We extracted differential cross-sections for the $\gamma p \to K^+\Sigma^0$ for the CLAS $g11a$ dataset separately for the two- and three-track topologies. The agreement between herein, despite the fact that the two topologies are almost independent, employing significantly different analysis techniques, strengthens our faith in the overall consistency of this analysis. We have also compared our results with previous world data. Mild localized differences remain between the CLAS $g11a$ and $g1c$ results, but on the whole, world data, including our results, for $K^+\Sigma^0$ photoproduction seems largely consistent amongst different measurements.

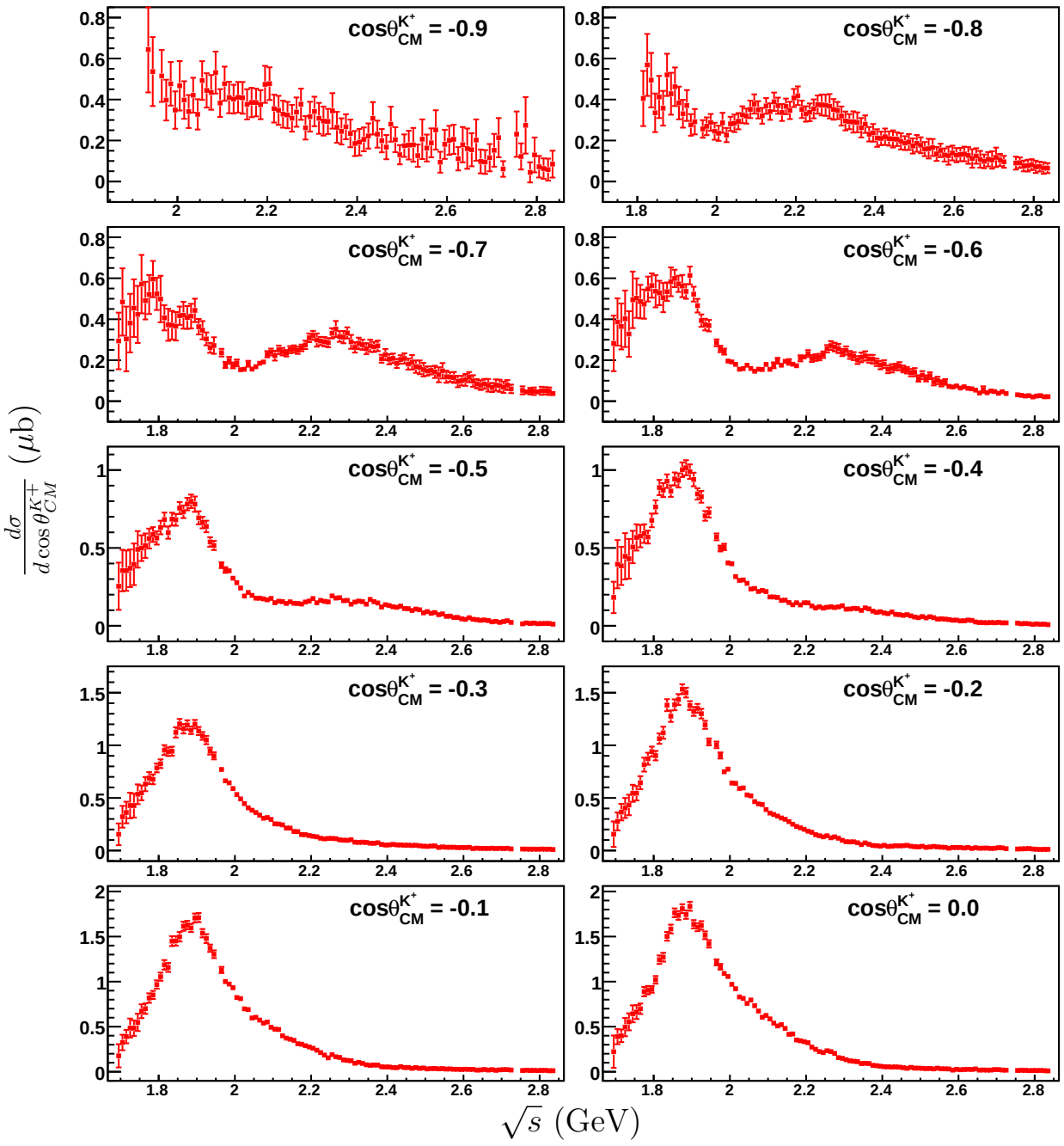

Figure 6.11: Final $\gamma p \to K^+\Sigma^0$ differential cross-sections for the $g11a$ dataset as a function of $\sqrt{s}$ in the backward angles. The results shown are a weighted average between the two- and three-track topology cross-sections. All errors shown are statistical.

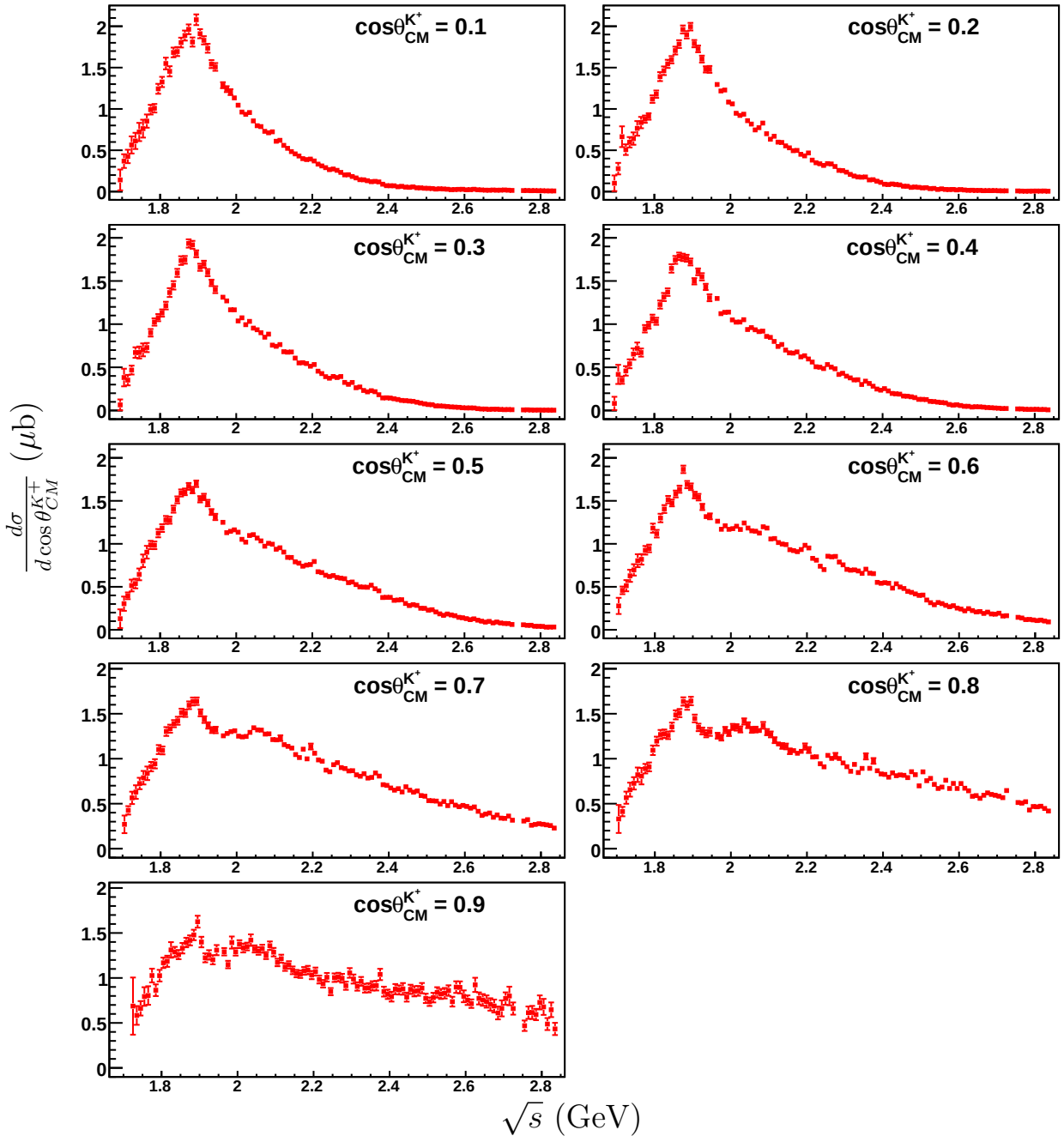

Figure 6.12: Final $\gamma p \to K^+\Sigma^0$ differential cross-sections for the $g11a$ dataset as a function of $\sqrt{s}$ in the forward angles. The results shown are a weighted average between the two- and three-track topology cross-sections. All errors shown are statistical.

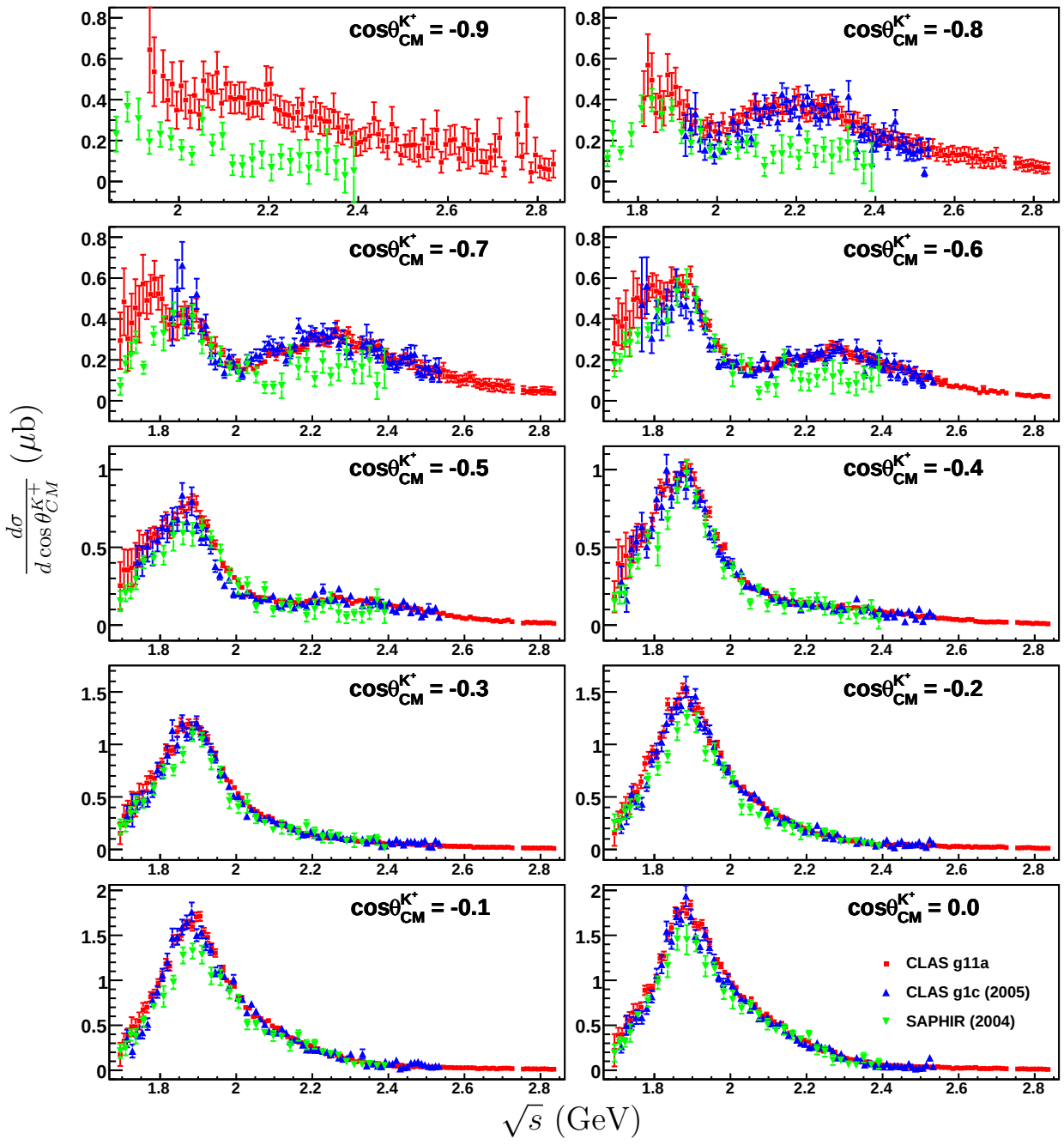

Figure 6.13: $\frac{d\sigma}{d\cos\theta^{K^+}_{CM}}$ (μb) *vs* $\sqrt{s}$ in the backward angles: final CLAS $g11a$ (this analysis) differential cross section results as the weighted average of the topologies are in **red** squares. Previous CLAS $g1c$ results are in **blue** up-triangles while **green** down-triangles are results from SAPHIR.

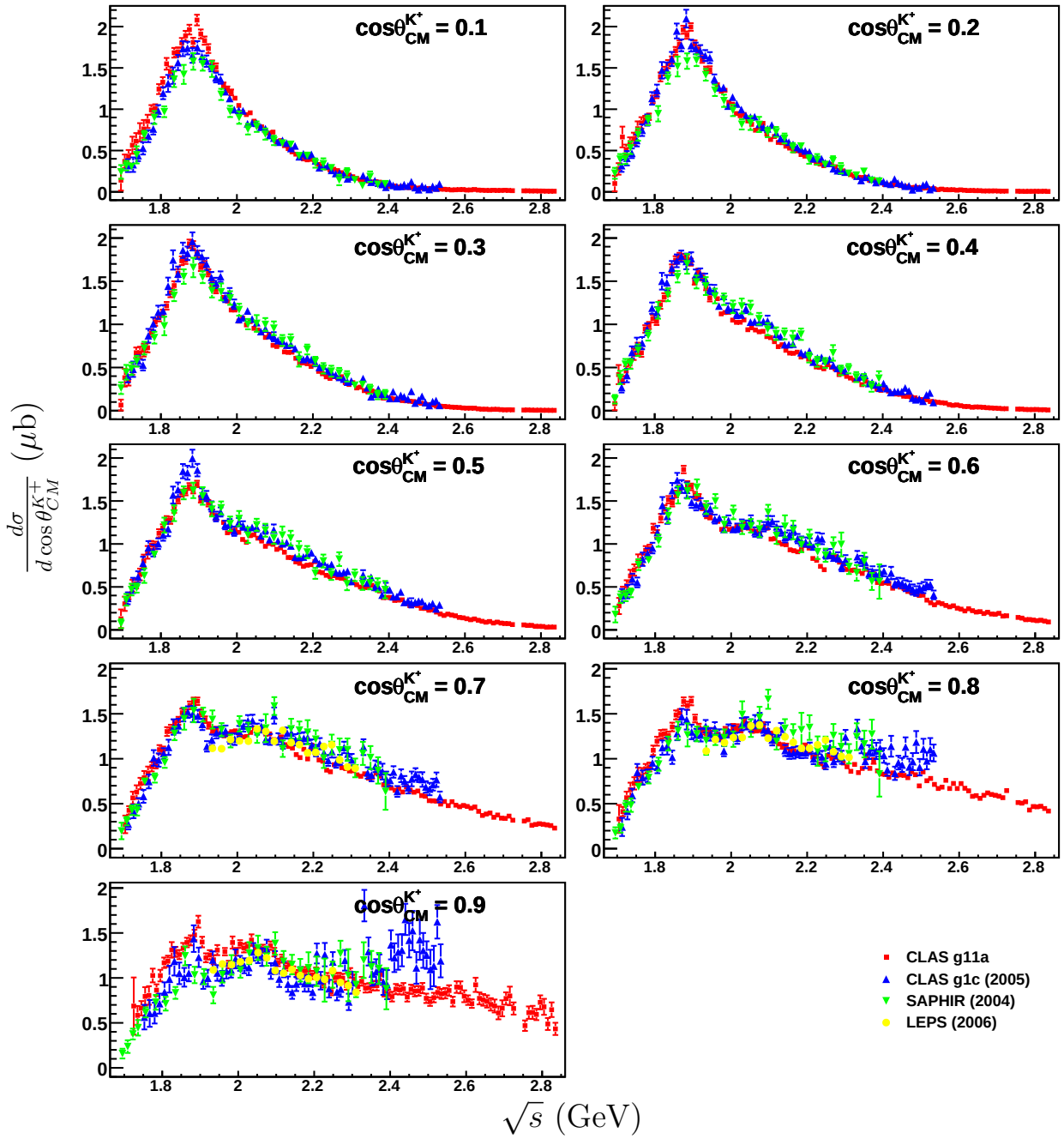

Figure 6.14: $\frac{d\sigma}{d\cos\theta^{K^+}_{CM}}$ (μb) *vs* $\sqrt{s}$ in the forward angles: final CLAS $g11a$ (this analysis) differential cross section results as the weighted average of the topologies are in red squares. Previous CLAS $g1c$ results are in **blue** up-triangles while **green** down-triangles are results from SAPHIR. The **yellow** circles represent LEPS measurements in the forward-most angular bins.

Chapter 7

Systematic Studies of $g11a$ for $K^+\Sigma^0$

In this chapter we address several issues that were previously either hinted at or touched upon. Though most of the checks described here pertains to the $K^+\Sigma^0$ analysis, they contribute towards our overall understanding of the systematics of CLAS and the $g11a$ dataset, and thereby, to the ϕp analysis as well. A chronological summary of our progress through the $K^+\Sigma^0$ analysis is useful here. We started off by analysing the three-track dataset. The kinematic fitter and the energy, momentum and tagger corrections, as well as the trigger efficiency maps for $g11a$ had already been scrupulously studied, well-established and applied to other channels [16, 18], which gave us confidence in using them. However, our preliminary differential cross sections showed significant discrepancies with Bob Bradford's CLAS $g1c$ results [87] over all energies and angles. Further investigation of $g11a$ [26] revealed that events where the Λ's decay outside the start counter are not triggered in the data, something which was not being accounted for in the Monte Carlo. Fine-tuning the Λ decay vertex position reconstruction (from tracking and momentum information) took us a while. The vertexing package [55] being used had its own idiosyncracies that had to be understood and at places, modified slightly. Note that the version of GSIM being employed at this time did not provide direct access to the decay vertices (see Sec. 4.1.2).

Including the correction for the Λ decay vertex pulled up our overall differential cross sections, but they were still lower than $g1c$ in a few places. We thus embarked upon a process of making various checks, as accounted in this chapter. This included a scrutiny of our background subtraction procedure, an extensive TOF-paddle survey, effects of possible K^+ decays in the far interiors of the drift chamber regions, differential cross-section extraction using unweighted acceptance calculations, amongst others. After all our corrections, in a *few* mid-energy, mid-angle bins, $g11a$ was lower than $g1c$ by $\sim 10\%$. In every other region, including the forward-most angles, the agreement between the two was excellent.

One of the remaining aspects left to check was to abandon the approach of *reconstructing* the Λ decay vertex, but to pull out the *actual* vertices directly from GSIM. GSIM was subsequently modified to churn out the Λ decay vertices directly and differential cross sections were extracted anew at five different center-of-mass energies − no systematic shift was noticed in the results. The silver lining however was that the updated version of GSIM enabled us to analyse the two-track dataset as well. The two-track analysis yielded measurements all the way into the backward angles, where the three-track had poor or no statistics at all.

The agreement between the two- and three-track analyses was found to be very good (Fig. 6.10). It has to be kept in mind here, how distinct the two analyses really are. Even though both employ the $g11a$ dataset, the three-track analysis makes heavy use of the kinematic fitter, besides employing

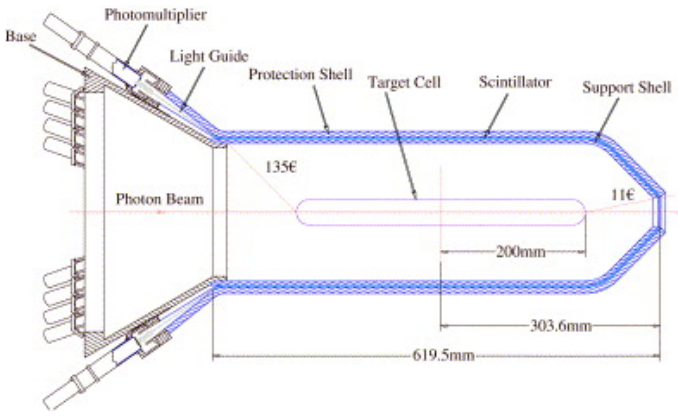

Figure 7.1: Cross-sectional view of the start counter for $g11a$ – it sits roughly 10 cms around the target, about the same as the Λ's characterestic path-length. (Source: [40])

a physics-weighted acceptance calculation, while the two-track does neither. Given these circumstances, the overall consistency within $g11a$ is noteworthy indeed.

7.1 Trigger Correction for Λ Decay

Fig. 7.1 shows a cross-sectional cutaway of the $g11a$ start counter. Recall that the $g11a$ trigger required a coincidence between a start counter hit and a TOF paddle hit in the same sector for at least two charged tracks in two different sectors. In the $\gamma p \to K^+\Sigma^0 \to K^+\gamma\Lambda \to K^+\gamma p\pi^-$ reaction chain, one of the hits has to come from the K^+ and the other from either the proton or the π^-, since the breakup momentum for the Λ decay is small and the proton and the π^- mostly go into the same sector, so that even if both the proton and the π^- triggers successfully, it still counts as a single sector-based hit.

The start counter is triggered by charged tracks only, while the Λ is a neutral particle. Coupled with the fact that the Λ decay pathlength is $c\tau \sim 7.89$ cm [53] while the start counter is positioned about 10 cms around the target cell [40], this means that there is a finite chance that the Λ decays *outside* the start counter, the proton/π^- (travelling radially outwards) miss it, and the event does not trigger. Such an effect is not compensated for in the Monte Carlo however, as trigger information from the start counter is not included in GSIM. Fig. 7.2 shows reconstructed Λ decay vertices for the data and the accepted Monte Carlo. The relative position of the start counter is marked by thick black lines. One can immediately spot the difference – for the data, there is a significant drop in occupancy whenever the Λs decay outside the start counter, while the accepted Monte Carlo occupancy is smooth across the start counter boundary.

As apparent from Fig. 7.2a, some "bleed through" occurs across the start counter boundary. This can be attibuted to the fact that the opening angle between the proton and the π^- for the Λ decay is small, leading to resolution issues in our reconstruction of the position of closest approach between the two tracks using *MVRT* [55]. Because of this "bleed through", instead of applying a hard-cut on both the data and the Monte Carlo based on the reconstructed secondary (Λ decay) vertex, we chose to apply a statistical based "trigger" cut only on the Monte Carlo, as explained below.

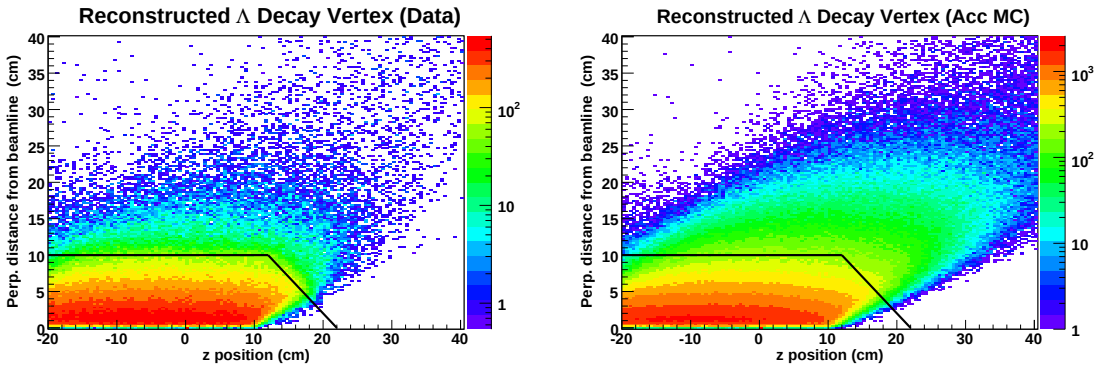

(a) (b)

Figure 7.2: Perpendicular distance from beamline versus z position along beamline for the reconstructed Λ decay vertex: (a) data and (b) Monte Carlo. The outline of the start counter is marked by the thick black lines. Aside from the "bleedthrough" (due to resolution issues in the reconstruction fit), there is a sharp drop in occupancy across the start counter boundary for the data.

7.1.1 Simulated Λ Decay Start Counter Trigger

Our starting point is the primary/event vertex $\vec{r}_0 = (x_0, y_0, z_0)$ which is the position of closest approach between the K^+ track and an idealized beam along the center of the target cell, calculated using *MVRT* [55]. We also calculate the Λ momentum $\vec{p}_\Lambda = (p_\Lambda, \theta, \phi)$ as the sum of proton and π^- momenta. The interaction vertex where $\vec{p}_\Lambda$ is projected to hit the start counter wall is denoted as $\vec{r}_{int} = (x_{int}, y_{int}, z_{int})$. If z_{int} lies prior to the "nose" of the start counter ($z_{nose} \sim 12$ cm), z_{int} and l (pathlength travelled by the Λ before it hits the start counter) are given by:

$$z_{int} = z_0 + \frac{d}{\tan\theta}, \quad \text{and} \tag{7.1a}$$

$$l = \frac{d}{\sin\theta\cos\phi'}, \tag{7.1b}$$

where $d \sim$10 cm is the shortest radial distance between the beamline and the start counter and ϕ' is the the azimuthal angle with respect to the azimuthal center of the CLAS sector in which $\vec{p}_\Lambda$ belongs (*i.e.*, $\phi' \in [-30°, 30°]$). However, if $z_0 + \frac{d}{\tan\theta} > z_{nose}$, this means that $\vec{p}_\Lambda$ enters the "nose" region, and the expression for l changes to:

$$l = \frac{z_{nose} + d - z_0}{\cos\theta + \sin\theta\cos\phi'}. \tag{7.2}$$

Using the Λ's characteristic lifetime $\tau = 2.63 \times 10^{-10}$ s, we can then calculate the characteristic lifetime of the Λ as observed in the laboratory frame to be

$$t = \gamma\tau = \frac{\tau}{\sqrt{1-\beta^2}}, \tag{7.3}$$

where β is calculated from $\vec{p}_\Lambda$. We also calculate the distance d_Λ that the Λ would have traveled in time t to be

$$d_\Lambda = \beta c t. \tag{7.4}$$

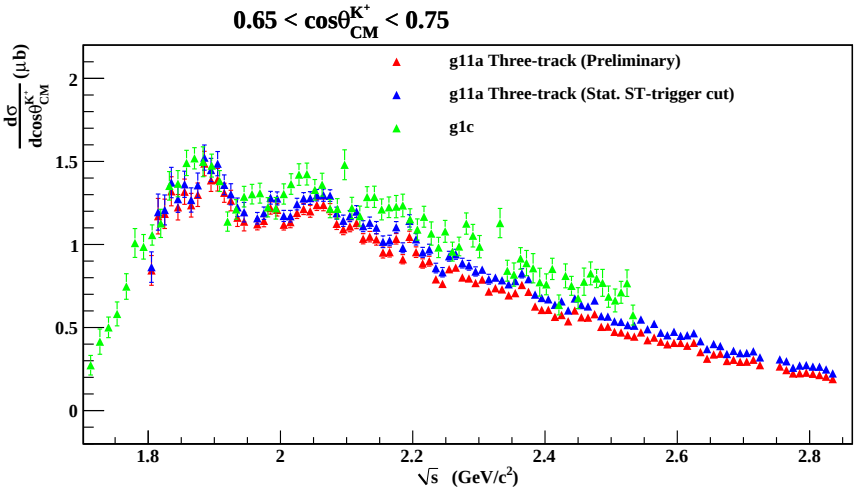

Figure 7.3: Effect of the simulated start counter trigger cut in one of the forward angle bins: in **red** are the preliminary cross-sections, in **blue** are the cross-section after including the cut, while in **green** are the $g1c$ results for comparison. Similar results were obtained for other angles as well.

Finally, we consider the exponential nature of the Λ decay and construct the probability $P(l,\beta)$ that the given Λ will intersect the start counter before it decays:

$$P(l,\beta) = \exp\{-l/d_\Lambda\} = \exp\{-l/(\beta ct)\}. \tag{7.5}$$

We then use $P(l,\beta)$ to generate a start counter trigger efficiency along the same lines as we had generated the trigger maps in Sec. 4.2: a random number x is generated between 0 and 1; if $P(l,\beta)$ is greater than x, we cut the event. In this fashion, we treat the Λ decay effect for the Monte Carlo in a purely statistical fashion, as nature does for the data. Some resolution issues remain, pertaining to how well r_0 and the proton/π^- momenta are known. To check for such effects we made slight variations in the parameters d and z_{nose}, but found minimal effect on the cross-sections.

The effect of the cut is ubiquitous and substantial. Fig. 7.3 shows the comparsion in one of the forward angle bins. Similar results are obtain in other angles as well – the cross-sections increase by 5-10% after the application of the cut.

7.1.2 Comparison With Hard Cut

To further check the credibility of the above cut, we generated Monte Carlo with a version of GSIM that provided direct access to the Λ vertices and placed a hard cut at the start counter limits. In cylindrical co-ordinates, let the secondary Λ decay vertex be $\vec{r}_{sec} = (\rho_{sec}, z_{sec}, \phi_{sec})$ and ϕ'_{sec} be the sector-based azimuthal angle. If $z_{sec} < z_{nose}$, we cut the event if

$$\rho_{sec}\cos\phi'_{sec} > d, \tag{7.6}$$

while if $z_{sec} > z_{nose}$, the event is cut if

$$\rho_{sec}\cos\phi'_{sec} > d - (z_{sec} - z_{nose}). \tag{7.7}$$

Instead of processing the entire dataset, we test-ran on five energy bins – $\sqrt{s}$ = 2.105, 2.135, 2.165, 2.205 and 2.235 GeV, that is, bins which have substantial difference between the $g11a$ and $g1c$

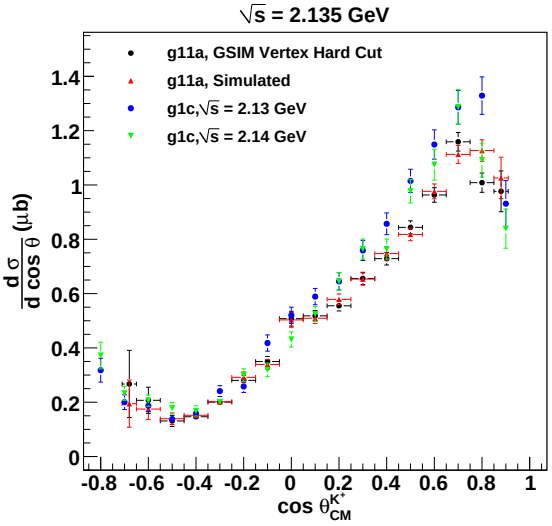

Figure 7.4: Comparison between the simulated trigger cut and a hard cut on GSIM secondary Λ decay vertices for $\sqrt{s} = 2.135$ GeV. No systematic difference is apparent between the two. Checks were also done at four other energies yielding similar results. Two overlapping bins from $g1c$ are also shown for comparison.

results. Fig. 7.4 compares the cross-sections between the simulated trigger and the hard cut, for the energy bin $\sqrt{s} = 2.135$ GeV. The difference between is well within statistical and systematic error limits. This lends further credence to our usage of the simulated start counter trigger – all final $g11a$ results quoted for the three-track topology are obtained using the simulated trigger cut while the two-track results are using the hard cut.

7.2 Background Subtraction Systematics Check

After the application of all our cuts, the three-track $K^+\Sigma^0$ dataset is a pretty clean channel. Some 5-15% background remains, which is subsequently removed by our background subtraction method. Furthermore, no systematic shifts are noticed by the usage of different background shapes, which points towards the fact that we are not truncating events from any specific kinematic region. As an extreme case, consider the following: suppose our background subtraction scheme is completely inaccurate. We can instead apply a hard cut on the Σ^0 invariant mass, demanding $MM(K^+)$ to be within 1.192 ± 0.02 GeV. This cut is applied on both the data and the Monte Carlo, but instead of weighing the data by Q-values from the background fits, we take all the Q's to be unity. By doing this we are intentionally over-estimating our data yields because we know that our background levels are not completely null.

Fig. 7.5 compares the cross-sections obtained by the above method to our original cross-sections as well as to $g1c$ results. From this plot we can conclude that everything else remaining the same, the discrepancy between $g1c$ and $g11a$ cannot be caused by our background subtraction method, since, even with the maximum over-estimated yield for the the data, $g11a$ is still lower than $g1c$.

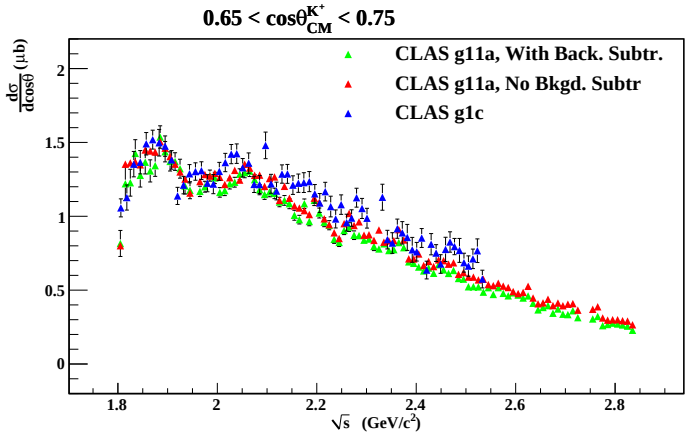

Figure 7.5: Cross-sections with $Q = 1$ for all events in **red** while original cross-sections are in **green**. Even after ignoring any background subtraction, the $g11a$ cross-sections are lower than $g1c$ (in **blue**)− the difference thus cannot be due to systematics in our background subtraction scheme.

7.3 Acceptance Calculation

One of the major differences between the (three-track) $g11a$ and (two-track) $g1c$ analyses is the way acceptance is calculated. Recall from Eq. 6.37 that the three-track $g11a$ calculation invokes a physics-weighted acceptance calculation, while $g1c$ employed a less sophisticated unweighted calculation. To check how this difference can potentially affect our results, we re-extracted our cross-sections using the unweighted acceptance method. The results are shown in Fig. 7.6. Though the cross-sections increase slightly with the unweighted acceptance, it cannot account for the larger difference between $g11a$ and $g1c$. Not that this was unexpected, but it serves as a confirmation on the fact that the physics model little impact on the cross-section calculation.

7.4 TOF Paddle Survey

A given value of $\sqrt{s}$ and $\cos\theta^{K^+}_{CM}$ roughly maps on to a small "band" of TOF scintillator paddles that the K^+s can hit in each sector. Since the difference between $g11a$ and $g1c$ cross-sections lies only in a few localized $\sqrt{s}$ and $\cos\theta^{K^+}_{CM}$ bins (mid-energy, mid-angles), we carried out a careful survey of the TOF paddle hit occupancies in these kinematic regions. Note that at the time of this analysis, a detailed study of the systematic uncertainties for $g11a$ had already been carried out using the much higher-statistics $\gamma p \to p\pi^+\pi^-$ channel [58]. Problematic TOF paddles identified therein were already removed at the start of this analysis. However, these studies did not make any direct observation of TOF paddle efficiencies for the K^+s.

Paddle 23 lies at the juncture of a discontinuity in the alignment of the scintillators giving rise to occassional physical overlaps between paddle 23 and 24. In this region, the tracking software cannot reliably decide on which of the two paddles a particular track passed through. On such occassions a default zero TOF paddle id is sometimes assigned to the track − to do away with these inconsistencies, we decided to remove paddle 23 altogether from this analysis.

Paddles 24 and 25 also seem questionable from the above point of view. However, removal of these paddles had almost no effect on the cross-sections, so we decided to keep them. Fig. 7.7 shows

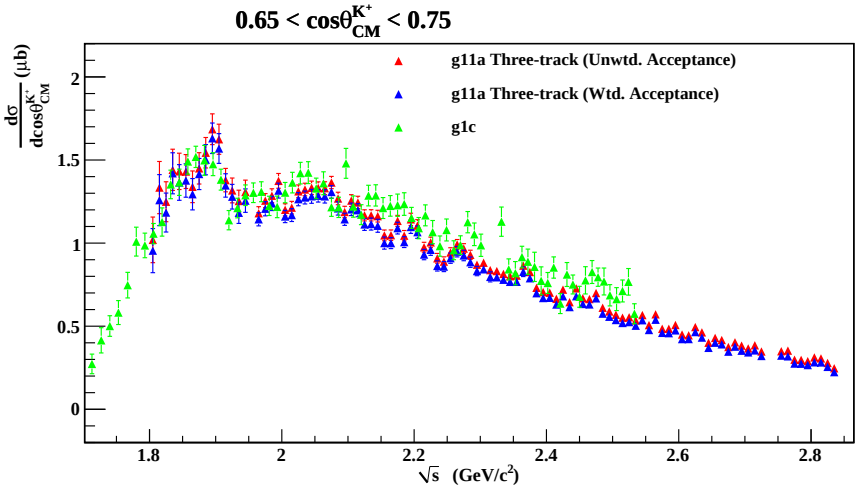

Figure 7.6: Effect of unweighted acceptance calculation as opposed to a physics-weighted acceptance, for the $g11a$ three-track dataset. The difference is small and cannot account for the $\sim 10\%$ difference between $g11a$ and $g1c$.

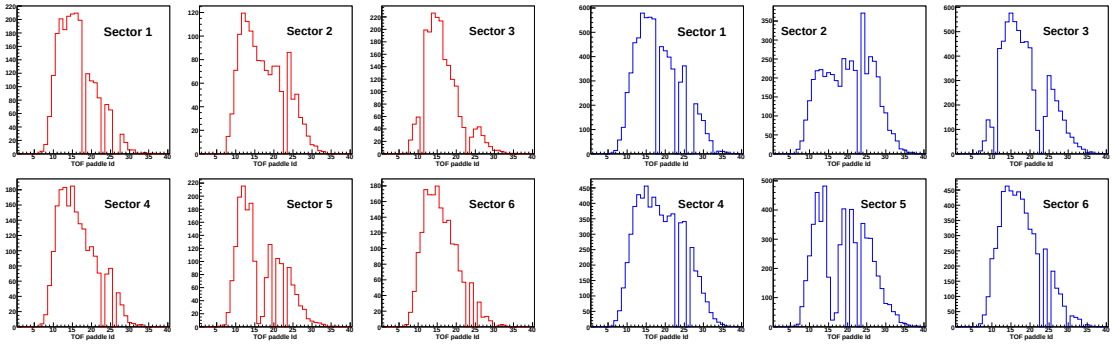

(a) (b)

Figure 7.7: TOF paddle survey for (a) data (b) accepted Monte Carlo in in the $\sqrt{s} = 2.135$ GeV bin. Paddle 23 is removed in all the sectors. Paddle 24 in sector 2 looks somewhat over-populated. This might be due to a spill-over from hits in Paddle 23. However, the effect occurs in both data and Monte Carlo. Cross-sections with this paddle removed over all sectors demonstrated no visible change either, so we chose to keep it.

a sector-wise comparison of TOF paddle occupancies between data and accepted Monte Carlo for the $\sqrt{s} = 2.135$ GeV bin. Overall, all the features present in the data are replicated in the Monte Carlo.

7.5 A Few Other Checks

7.5.1 Re-entry of proton/π^- Into Start Counter Region

The trigger correction in Sec. 7.1 assumes that the proton or the π^- from the Λ decay does not *re*-enter the start counter region again. To check for the frequency of such events, we generated a "trigger bit" using Monte Carlo $\gamma p \to K^+\Sigma^0 \to K^+\gamma\Lambda \to K^+\gamma p\pi^-$ events where the Λ was propagated in space and decayed by the event generator before submitting the event to GSIM. The propagation of the proton and the π^- from the Λ decay vertex onwards were then reconstructed using their individual momenta. In case any of the projected proton/π^- trajectories re-entered the start counter region, their corresponding start counter sector id's were noted. If the track satisfied the "Level 1" trigger condition (that is, the start counter sector id and the TOF paddle sector id matched) the trigger bit was set to 1 for the particular track. The event was cut unless at least two tracks "triggered" in this fashion (for the K^+, the propagation vertex was simply the event vertex). In other words, the Level 1 trigger for $g11a$ was reconstructed "by hand". Inclusion of the above cut was found to have almost zero influence on the differential cross sections. We therefore concluded that the frequency of events where the Λ decays outside the start counter but the proton/π^- re-enters it and triggers the event, is very small.

7.5.2 Trigger Map For K^+

Recall from Sec. 4.2 that our trigger efficiency correction for K^+ uses the π^+ trigger map. This is justified on the account that K^+'s and π^+'s, having same the same charge and comparable masses, should have similar ionization properties. Given that the mass of K^+ lies mid-way between the proton and π^+ masses, the other possibility is to apply the p trigger map for the K^+. The cross-sections obtained by applying the proton map (instead of the π^+ map) for the K^+ is shown in Fig. 7.8 for one particular $\sqrt{s}$ bin − no systematic shift is noticeable.

7.5.3 Additional $MM(K^+)$ Cuts (Three-track Topology)

Fig. 7.9a shows the invariant (p, π^-) mass plotted versus the missing mass off K^+ ($MM(K^+)$) for the accepted Monte Carlo (three-track topology). The small "band" of events above $MM(K^+) = 1.24$ GeV passes all our event seclection and PID cuts but seems to have an incorrect mass for the Σ^0. However, the invariant (p, π^-) mass for these events seems to be around the correct Λ mass. Note that the (p, π^-) invariant mass reconstruction does not involve any K^+ momentum resolution (while $MM(K^+)$ obviously does). Furthermore, since only $K^+\Sigma^0$ events were thrown in the Monte Carlo, we know that the only way a well-resolved Λ can arise is from a decaying Σ^0. We thus conclude that these represent well-identified $K^+\Sigma^0$ events after all, but where the K^+ decays somewhere deep inside the Drift Chamber regions. Since all the prominent K^+ decay modes produce a single positively charged track (along with other neutral tracks), the topology of the reaction is maintained; save that the reconstructed K^+ momentum gets affected in the process.

To avoid systematic errors due to such events, we place additional $\sqrt{s}$ dependent $MM(K^+)$ cuts on both the data and the Monte Carlo as follows. Fig. 7.9b shows the Q-value weighted (background subtracted) occupancy for the data for every $\sqrt{s}$ bin. The $MM(K^+)$ cut limits are shown by the heavy red lines in this plot − they mark the $MM(K^+)$ values where the occupancy drops below 1% of the maximum on either side *for that particular* $\sqrt{s}$ *bin*. The cut does not have a significant

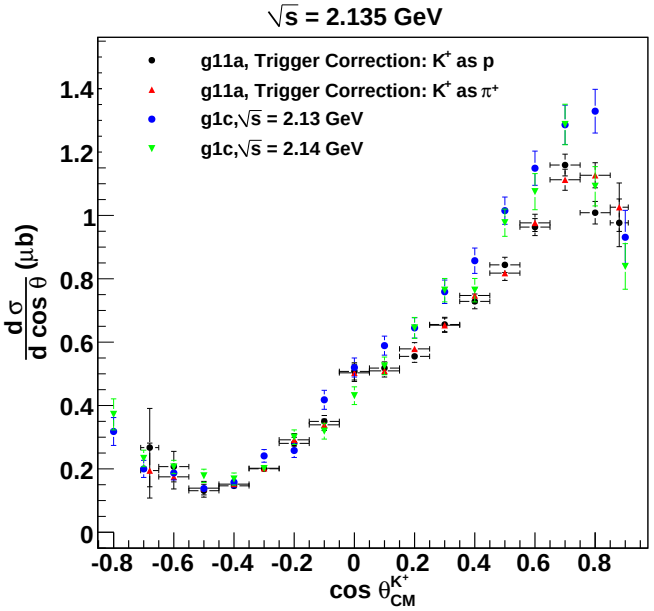

Figure 7.8: Effect of using the proton trigger efficiency map for K^+ instead of the π^+ map (used for rest of the analysis). No systematic shift is noticeable. Overlaid are the CLAS $g1c$ results for comparison.

effect on the cross-sections, but this study contributes towards a better understanding of some of the subtler aspects of this channel.

7.5.4 Additional $MM(K^+)$ Cuts (Two-track Topology)

Inkeeping with the discussion in the previous sub-section, we also make a similar cut for the 2-track datset. The $\sqrt{s}$ dependent $MM(K^+)$ limits in the cut are shown by the heavy red lines in Fig. 7.10.

7.5.5 Additional Sector 5 Fiducial Cut

Sector-based studies of $g11a$ using the $\gamma p \rightarrow K^+\Lambda$ channel by McCracken [26] indicated some additional inconsistencies in our understanding of certain regions of the CLAS detector pertaining to Sector 5. The effect seemed to be localized in $0.45 < \theta_{lab}^{K^+} < 0.55$ (Sector 5) but independent of the K^+ track momentum. McCracken *et al* thus chose to remove events that included *any* track (proton/K^+/π^-) belonging to Sector 5 and satisfying $0.45 < \theta_{lab} < 0.55$. The effect of the cut on the overall dataset was small but it resulted in greater consistency in the $\gamma p \rightarrow K^+\Lambda$ differential cross sections among the six sectors of CLAS. Our statistics for the $\gamma p \rightarrow K^+\Sigma^0$ channel did not suffice for a similar sector based study of the differential cross sections, but given the similarity in kinematics between the two hyperon reactions, we found it prudent to include this cut in our present analysis too.

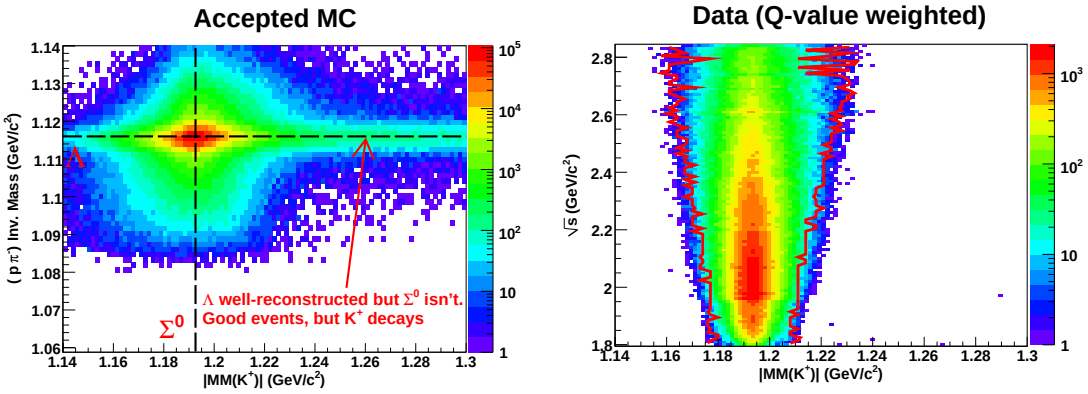

(a) (b)

Figure 7.9: Three-track topology: (a) Possible K^+ decay inside CLAS during $K^+\Sigma^0$ photoproduction. The effect is explained in the text. (b) $\sqrt{s}$ dependent $MM(K^+)$ cuts demarcated by the bold red lines – only events lying between these demarcations were accepted (both for data and Monte Carlo).

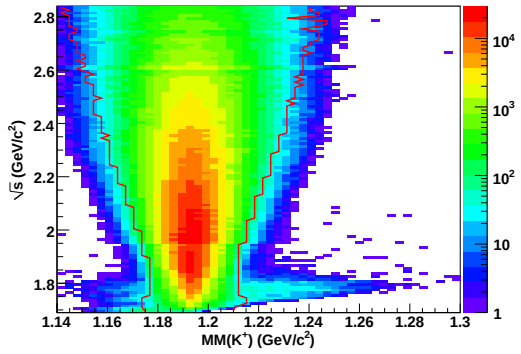

Figure 7.10: Two-track topology: Q-value weighted data events. The slightly long "tail" in $MM(K^+)$ near the threshold bins occured at the very backward angles, due to extremely limited statistics for these kinematics. The $\sqrt{s}$ dependent $MM(K^+)$ cuts limits are shown by the thick red lines, as for the 3-track case in Fig. 7.9b.

7.6 Summary

We studied possible avenues for systematics issues in our analysis techniques and the $g11a$ dataset *per se*. Nuances in the kinmatics of the $\gamma p \to K^+\Sigma^0$ channel in conjugation with the $g11a$ trigger results in subtle issues in event triggering. We described in detail the resolution of this and some other minor effects. After all corrections, our final differential cross sections for $g11a$ is in fair to very good agreement with previous CLAS $g1c$ results (see also Sec. 6.9).

Chapter 8

$K^+\Sigma^0$ Recoil Polarizations

A generic feature of hyperon physics is that over a large variety of production mechanisms, the hyperons come out often strongly polarized [91, 92]. For a pseudo-scalar meson photoproduction reaction like $\vec{\gamma}\vec{p} \to K^+\vec{\Sigma}^0$, where the beam, target and recoiling baryon can be all polarized, the most general production amplitude involves $2\times2\times2 = 8$ complex amplitudes, depending on the spin states of the photon, target and the outgoing baryon. The reaction can be simplified by considering the parity invariance of the strong and electromagnetic interactions, reducing the number of independent complex amplitudes to four. As shown originally by Barker, Donnachie and Storrow (BDS) [98], this leads to fifteen experimentally observable single- and double-polarization observables, in addition to the unpolarized differential cross-section. These sixteen observables occur as bilinears in the four independent amplitudes. However, several ambiguities originate with the BDS work. BDS treats reactions with the four amplitudes in the helicity basis (non-flip, N, double-flip, D, and two single-flip amplitudes, S_1 and S_2), but does not clearly specify to which helicity configurations the amplitudes S_1 and S_2 refer. Other authors [97, 94] follow different schemes for enumerating the four amplitudes and sign ambiguities are known to exist in the literature [182]. Chiang and Tabakin (CT) [93] later showed that to completely characterize the full production amplitude, measurements of the differential cross-section and a carefully chosen set of only seven polarization observables is required. These type of measurements are therefore known as "complete experiments" and represent a major part of the ongoing experimental effort within the Hall B Collaboration at JLab [102]. In this chapter, we will first give a detailed description of the general theory of polarization observables for such "complete measurements" in pseudo-scalar meson photoproduction.

For the $g11a$ dataset, with an unpolarized beam and an unpolarized target, parity conservation dictates that the outgoing baryon (Σ^0, in our case) can have a polarization only in the direction perpendicular to the production plane. This is known as the "recoil" polarization, P_Σ, and this can be measured due to the self-analysing nature of the hyperon decays. In this chapter we will present the recoil polarization results for $K^+\Sigma^0$ extracted from the $g11a$ dataset. We note here that an additional problem occurs for the $K^+\Sigma^0$ channel (compared to $K^+\Lambda$ case) – the measured polarization is inherently "diluted" because the spin of the undetected outgoing photon in the $\Sigma^0 \to \Lambda\gamma_f$ decay is unknown. This is because all experiments to date (including the present case) do not detect the γ_f directly, leave alone measure its polarization. For our $K^+\Sigma^0$ three-track topology, even though the γ_f momentum is re-constructed as the total missing momentum, the γ_f polarization remains unknown. For the two-track topology, neither the γ_f momentum. nor its polarization is accessible to us.

An additional step of dilution occurs in going from the three-track to the two-track topology. Since the three-track topology has access to the Λ momentum, this topology preserves the spin-transfer information between the Σ^0 and the intermediate Λ. In contrast, for the two-track case, the

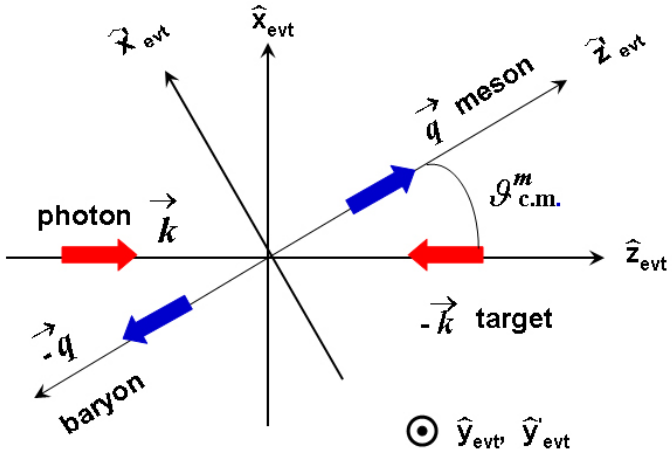

Figure 8.1: Axes for pseudo-scalar meson photoproduction in the c.m. frame for a particular event. See text for details.

Λ momentum is unknown and one needs to average over the intermediate Λ directions. The latter represents an extra factor of dilution in the extracted polarizations. Hence, the main bulk of the polarization results that we quote will be from the three-track dataset (1.8 GeV $\leq \sqrt{s} \leq$ 2.84 GeV, $-0.55 \leq \cos\theta^{K^+}_{\rm c.m.} \leq 0.95$). We will quote results from the two-track dataset only in the near-threshold energy and backward-angle kinematic regions, where the three-track dataset is severely limited by statistics.

8.1 The general theory of polarization observables in pseudo-scalar meson photoproduction

In this section, we first derive the general expression for the reaction intensity with all three polarizations (beam, target, and recoil). Our motivation is the density matrix approach of Fasano, Tabakin and Saghai (FTS) [94], the power of which is compactness of notation. The full expression consists of $4 \times 4 \times 4 = 64$ terms. Invariance under mirror symmetry transformations (a parity inversion followed by a rotation, see Sec. 8.1.4) removes half of these terms. In the remaining terms, each of the sixteen physically measurable observables occurs twice. All results herein follow simply from the properties of the Pauli matrices and the mirror symmetry operator acting on the spin density matrices of the photon and baryons. Second, we provide amplitude-level expressions for the polarization observables corresponding to measurable particle momentum distributions, carefully keeping track of the relative signs between experimental measurements and amplitude-level expressions. Our amplitudes are constructed in the longitudinal basis, that is, with spin projections for *all* particles quantized along a single direction, the beam direction. For reactions with multiple decays and non-zero spins for the the final-state particles, a single spin-quantization axis enables one to write the full production amplitude in a manifestly Lorentz-invariant fashion. Finally, we list and numerically validate the various "consistency relations" connecting the different spin observables. These consistency relations provide important checks for both theoretical analyses and constraints in the case of future experiments which will have access to polarizations of the beam and target and recoil baryons.

8.1.1 Axis conventions

In the case of single pseudo-scalar meson photoproduction, let $\vec{k}$, $-\vec{k}$, $\vec{q}$ and $-\vec{q}$ be the momenta of the incoming photon, target baryon, outgoing meson, and outgoing baryon, respectively, in the overall c.m. frame. This is shown in Fig. 8.1. The beam direction defines the z-axis, $\hat{z}_{\rm evt} = \vec{k}/|\vec{k}|$. The y-axis is taken to be normal to the reaction plane established by the photon and meson momenta, $\hat{y}_{\rm evt} = \vec{k} \times \vec{q}/|\vec{k} \times \vec{q}|$. The x-axis is then simply $\hat{x}_{\rm evt} = \hat{y}_{\rm evt} \times \hat{z}_{\rm evt}$. Here the subscript "evt" denotes that these axes, with $\hat{x}_{\rm evt}$ and $\hat{y}_{\rm evt}$ parallel and perpendicular to the reaction plane, are defined on an event-by-event basis.

The above-mentioned axes will is often referred to as the "unprimed" basis and will be the coordinate basis adopted in this work. In the literature [98, 100, 94], authors also make use of the so-called "primed" axes, where the z-axis points along the direction of the outgoing meson. The primed and the unprimed axes are related by a rotation about the normal to the production plane. Therefore, the observables in the two frames are related by

$$\mathcal{O}_x = \mathcal{O}_{x'} \cos(\vartheta^m_{\rm c.m.}) + \mathcal{O}_{z'} \sin(\vartheta^m_{\rm c.m.}) \tag{8.1a}$$

$$\mathcal{O}_z = -\mathcal{O}_{x'} \sin(\vartheta^m_{\rm c.m.}) + \mathcal{O}_{z'} \cos(\vartheta^m_{\rm c.m.}), \tag{8.1b}$$

where $\vartheta^m_{\rm c.m.}$ is the meson scattering angle in the c.m. frame. In the Adelseck-Saghai work [100], the z'-axis is chosen along the direction of the outgoing baryon and therefore has an an overall 180° flip with respect to the BDS "primed" frame. Furthermore, although the BDS article describes both the primed and the unprimed reference frames, it lists the observables in the unprimed frame, when it actually means to list them in the primed frame. To avoid such inconsistencies, we will not refer to the primed frames from here onwards. Unless otherwise mentioned, our z-axis will always be along the longitudinal beam direction.

8.1.2 The photon polarization state and density matrix

There is some disparity between the optics and particle-physics community in the nomenclature of the right- and left-handed polarization states. Particle physicists define the right-handed polarization state following the right-hand rule for the transverse electric polarization vector. The spin of the photon points along its momentum for the right-handed polarization state (or positive helicity state). The left-handed polarization state has the photon spin anti-parallel to its direction of motion. The optics community swaps the definitions for the right- and left-handed states, though the notions of positive- and negative-helicity states are the same in both treatments. Here, we adhere to the particle-physics convention and define the polarization basis states for the photon as

$$|\epsilon^+_{\rm evt}\rangle = -(|\hat{x}_{\rm evt}\rangle + i|\hat{y}_{\rm evt}\rangle)/\sqrt{2} \tag{8.2a}$$

$$|\epsilon^-_{\rm evt}\rangle = (|\hat{x}_{\rm evt}\rangle - i|\hat{y}_{\rm evt}\rangle)/\sqrt{2}, \tag{8.2b}$$

where $|\epsilon^+\rangle$ is the right-handed (positive-helicity) state, $|\epsilon^-\rangle$ is the left-handed (negative-helicity) state, and $|\hat{x}_{\rm evt}\rangle$ and $|\hat{y}_{\rm evt}\rangle$ are states of transverse polarization along $\hat{x}_{\rm evt}$ and $\hat{y}_{\rm evt}$, respectively. Looking *into* the incoming beam, the y-component phase leads (trails) the x-component phase for the positive (negative) helicity states and the polarization vector rotates counter-clockwise (clockwise) for the positive (negative) helicity states, in accordance with the right-hand rule.

For a general mixed state, it is useful to switch to the density matrix notation for describing the polarization state of the photon. We follow the work of Adelseck and Saghai (AS) [100] and

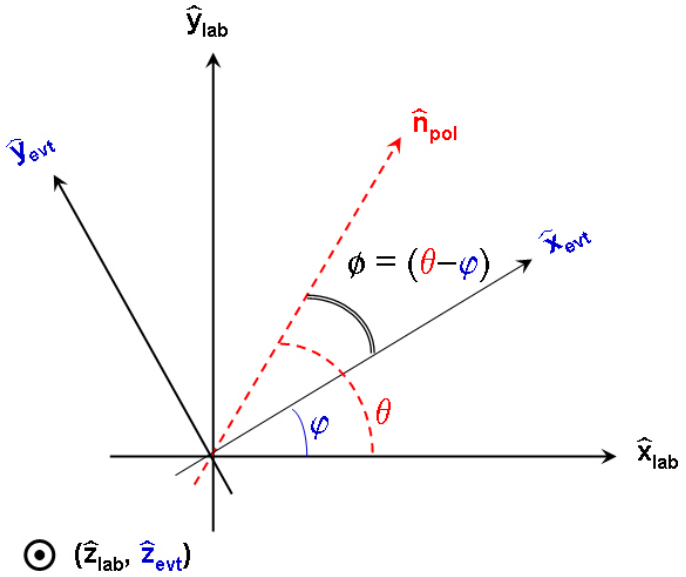

Figure 8.2: For a linearly polarized beam, $\{\hat{x}_{\rm lab}, \hat{y}_{\rm lab}, \hat{z}_{\rm lab}\}$ defines the fixed laboratory axis of the experiment. The polarization direction ($\hat{n}_{\rm pol}$) is at an angle θ to the laboratory x-axis. For a given event, the reaction plane is at angle φ to the laboratory x-axis. Therefore, the polarization vector is at an angle $\phi = (\theta - \varphi)$ relative to the reaction plane.

FTS [94] and write the photon spin density matrix as

$$\begin{aligned} \rho^\gamma &= \frac{1}{2}\begin{bmatrix} 1+P_C^\gamma & -P_L^\gamma \exp(-2i(\theta-\varphi)) \\ -P_L^\gamma \exp(2i(\theta-\varphi)) & 1-P_C^\gamma \end{bmatrix}_{\rm AS} \\ &= \frac{1}{2}\begin{bmatrix} 1+P_z^S & P_x^S - iP_y^S \\ P_x^S + iP_y^S & 1-P_z^S \end{bmatrix}_{\rm FTS}. \end{aligned} \tag{8.3}$$

In the AS prescription, the quantities P_L^γ and P_C^γ denote the degree of linear (L) and circular (C) polarization. In the FTS treatment, $\vec{P}^S$ is the Stokes' vector common in optics, with x-, y-, and z-components indicating the amount of polarization along each spatial direction. The kinematic variable φ is the azimuthal angle between the reaction plane and the laboratory $\hat{x}_{\rm lab}$ for a linearly polarized photon for a given event. The linear polarization vector relative to the laboratory frame is

$$\hat{n}_{\rm lab} = \cos\theta\, \hat{x}_{\rm lab} + \sin\theta\, \hat{y}_{\rm lab}. \tag{8.4}$$

For the circularly polarized photon (or unpolarized beam) case, the production amplitude is azimuthally symmetric about the beam direction. However, for the linearly polarized case, $\hat{x}_{\rm lab}$ and $\hat{y}_{\rm lab}$ define a preferred transverse coordinate system. The experimental conditions define $\hat{n}_{\rm lab}$ and $\theta = 0^\circ$ (90°) correspond to parallel (perpendicular) plane polarizations according to the experimentalist. For a given event, relative to the reaction plane, the polarization vector is

$$\hat{n}_{\rm evt} = \cos(\theta-\varphi)\hat{x}_{\rm evt} + \sin(\theta-\varphi)\hat{y}_{\rm evt}, \tag{8.5}$$

Polarization	P_x^S	P_y^S	P_z^S
(r) Circular helicity +1	0	0	+1
(l) Circular helicity -1	0	0	-1
$(\perp)$ Linear $(\phi = \pi/2)$	+1	0	0
$(\parallel)$ Linear $(\phi = 0)$	-1	0	0
$(-t)$ Linear $(\phi = -\pi/4)$	0	+1	0
$(+t)$ Linear $(\phi = \pi/4)$	0	-1	0

Table 8.1: Stokes' vector $\vec{P}^S$ for different photon polarization configurations (adapted from Ref. [94]). The right- (r) and left-handed (l) circular polarizations are our basis states. The different configurations for the linearly polarized states can be expressed in terms of these basis states. ϕ is the angle the linear polarization direction makes with $\hat{x}_{\rm evt}$. See text for details.

and the Stokes' vector $\vec{P}^S$ may be related to the circular polarization quantities by

$$P_z^S = P_C^\gamma \tag{8.6a}$$
$$P_x^S = -P_L^\gamma \cos(2\phi) \tag{8.6b}$$
$$P_y^S = -P_L^\gamma \sin(2\phi) \tag{8.6c}$$

in the basis formed by $\{\hat{x}_{\rm evt}, \hat{y}_{\rm evt}, \hat{z}_{\rm evt}\}$ and $\phi = (\theta - \varphi)$. The angles φ, θ, and ϕ are shown schematically in Fig. 8.2 and the connection between $\vec{P}^S$ and the different polarization states are given in Table 8.1. Apart from the right- (r) and left-handed (l) circular polarizations, which are our basis states, there are the perpendicular $(\perp)$ and parallel $(\parallel)$ states, corresponding to photons linearly polarized along the y- and x-axes, respectively, and two linearly polarized states at $\pm 45^\circ$ to the x-axis (in the $\hat{x}$-$\hat{y}$ plane), labelled as $\pm t$.

8.1.3 The intensity profile and T_{lmn} elements

We first note that as far as the *theoretical* definitions of the polarization observables are concerned, the only relevant kinematic variables for a given total energy (W) in the c.m. frame are the angle between the photon polarization vector and the reaction plane, $\phi = (\theta - \varphi)$ (for a linearly polarized beam), and the polar meson production angle $\vartheta^m_{\rm c.m.}$. This is because the observables are defined as asymmetries relative to the reaction-plane coordinate system $\{\hat{x}_{\rm evt}, \hat{y}_{\rm evt}, \hat{z}_{\rm evt}\}$. It is only when we will need to connect the observables to experimentally measurable intensity distributions, that the orientation between reaction plane, photon polarization vector, and the lab frame (quantified by angles θ and φ) will be required. We will return to this point later in Sec. 8.1.11. In what follows (as in the FTS conventions) we will refer to the Pauli matrices operating in the spin spaces of the beam, target baryon, and outgoing baryon as σ^γ, σ^i, and σ^b, respectively. The density matrices are then given by

$$\rho^\gamma = \frac{1}{2}(1 + \vec{P}^S \cdot \vec{\sigma}^\gamma) \tag{8.7a}$$
$$\rho^i = \frac{1}{2}(1 + \vec{P}^i \cdot \vec{\sigma}^i) \tag{8.7b}$$
$$\rho^b = \frac{1}{2}(1 + \vec{P}^b \cdot \vec{\sigma}^b). \tag{8.7c}$$

The vectors $\vec{P}^S$, $\vec{P}^i$, and $\vec{P}^b$ denote the polarization vectors of the beam, target and recoiling baryon, respectively. If any of the beam, target or recoil polarization is not measured, the corresponding $\vec{P}$

is the zero vector.

We define $\mathcal{A}_{m_\gamma m_i m_b}$ to be the reaction amplitude for a particular spin configuration of the photon (m_γ), target (m_i) and baryon (m_b), with the spin-quantization axes for all particles along $\hat{z}$, the beam direction. For a given photon spin, m_γ, the four $\mathcal{A}$ amplitudes correspond to the elements of a 2×2 matrix J_{m_γ} in the space of transition elements for a target spin state $|m_i\rangle$ going to the baryon spin state $|m_b\rangle$. Therefore the matrix elements of J_{m_γ} are $(J_{m_\gamma})_{m_b m_i} = \langle m_b|J_{m_\gamma}|m_i\rangle$ and J and $\mathcal{A}$ are connected via

$$\langle m_b|J_{m_\gamma}|m_i\rangle = \mathcal{A}_{m_\gamma m_i m_b}. \tag{8.8}$$

For experiments with "mixed" states $\rho_{\rm in}$ and $\rho_{\rm out}$ as the initial prepared (input) and final measured (output) configurations connected by the transition operator J, the intensity profile is proportional to the trace $\mathrm{Tr}[\rho_{\rm out} J \rho_{\rm in} J^\dagger]$. In the present case, $\rho_{\rm in} = \rho^i \otimes \rho^\gamma$ and $\rho_{\rm out} = \rho^b$. Therefore, the most general intensity expression for the profile dependent upon beam, target, and recoil polarizations is given by

$$\mathcal{I} = \mathcal{I}_0 \left(\frac{\mathrm{Tr}[\rho^b J \rho^i \rho^\gamma J^\dagger]}{\mathrm{Tr}[J J^\dagger]/8} \right), \tag{8.9}$$

where $\mathcal{I}_0$ is the unpolarized cross-section and the traces are over the beam, target and recoil spins. This derivation can be found in FTS [94] and in an equivalent form, in the paper by Goldstein, *et al* [95]. The main utility of this formulation is its symbolic compactness which enables easy derivation of other observables and their correlations. In Sec. 8.1.12 we will describe in detail how to expand these traces to give amplitude-level expressions for the polarization observables.

We now establish a notation for the Pauli matrices and the polarization vectors as four-component vectors, wherein

$$\{\sigma_0, \sigma_1, \sigma_2, \sigma_3\} \equiv \{I, \sigma_x, \sigma_y, \sigma_z\} \tag{8.10a}$$

$$\{P_0, P_1, P_2, P_3\} \equiv \{1, P_x, P_y, P_z\}. \tag{8.10b}$$

Since each density matrix in Eqs. 8.7 has four terms, the full profile in Eq. 8.9 has $4 \times 4 \times 4 = 64$ terms. We will also adopt the convention:

$$T_{lmn} \equiv \frac{\mathrm{Tr}[\sigma_n^b J \sigma_m^i \sigma_l^\gamma J^\dagger]}{\mathrm{Tr}[J J^\dagger]}, \tag{8.11}$$

so that Eq. 8.9 can be compactly represented as

$$\mathcal{I} = \mathcal{I}_0 \left(\sum_{lmn \,\in\, \{0,1,2,3\}} P_l^S P_m^i P_n^b \, T_{lmn} \right). \tag{8.12}$$

8.1.4 Mirror symmetry transformations

Following the work of Artru *et al* [101], we first define the mirror inversion operator

$$M = \Pi \exp(-i\pi J_y), \tag{8.13}$$

which describes a parity inversion (Π) followed by a 180° rotation about the $\hat{y}$ axis. We list the effects of M on the relevant particle types labeled by their spin and parity quantum numbers, J^P:

- $J^P = 0^-$ pseudo-scalar meson: Only the parity inversion contributes. Thus, $M = \Pi = -1$ is a simple sign flip.

- $J^P = \frac{1}{2}^+$ baryons: Here $\Pi = 1$ and $J_y = \sigma_2/2$. Therefore $M = \Pi \exp(-i\pi J_y) = -i\sigma_2$. In terms of the spin states, the transformation is given by $|+\rangle \to |-\rangle$ and $|-\rangle \to -|+\rangle$.
- $J^P = 1^-$ photon: A 180° rotation about the $\hat{y}$ axis leaves $|\hat{y}\rangle$ unchanged but changes $|\hat{x}\rangle$ to $|-\hat{x}\rangle$. Substituting this in Eq. 8.2a leads to an interchange between $|\epsilon^+_{\rm evt}\rangle$ and $|\epsilon^-_{\rm evt}\rangle$. Including $\Pi = -1$ for a vector particle leads to $M = -\sigma_1$ for the photon in the Pauli basis. In terms of the spin states, the transformation is $|\epsilon^+_{\rm evt}\rangle \leftrightarrow -|\epsilon^-_{\rm evt}\rangle$.

There are two main effects of the M transformation of which we make use. First, M acting on any T_{lmn} element results in a reshuffle in the Pauli operators for the incoming states:

$$\{0,1,2,3\} \;\Rightarrow\; \{-1,\,-0,-i3,\,i2\} \;\text{(photon)} \tag{8.14}$$
$$\{0,1,2,3\} \;\Rightarrow\; \{-i2,-3,-i0,\,1\} \;\text{(target)}. \tag{8.15}$$

where we have transformed the matrices as

$$\sigma_l \Rightarrow M\sigma_l, \quad l \in \{0,1,2,3\}, \tag{8.16}$$

M being the corresponding mirror tranformation matrix for the particular state. However, Eq. 8.15 does not quite work for the outgoing baryon density matrix, since the effect of the pseudo-scalar meson in the outgoing system needs to be incorporated as well. For the outgoing meson-baryon system, the reshuffle is given by

$$\{0,1,2,3\} \Rightarrow \{-i2,3,-i0,\,-1\} \;\text{(outgoing system)}, \tag{8.17}$$

where we have added an extra sign flip for σ_1 and σ_3 compared to Eq. 8.15, that comes from the parity of the pseudo-scalar meson. The σ_0 terms do not acquire this extra sign flip, since they physically correspond to the situation where the experiment is "blind" to the spins of the outgoing states. Also, since σ_2 is connected to the identity matrix by the M transform, it does not acquire a sign flip.

Second, the action of M on the production amplitudes and invariance under this transformation lead to relations between the amplitudes for positive and negative photon helicities:

$$L_1 \;\equiv\; \mathcal{A}_{+++} = +\mathcal{A}_{---} \tag{8.18a}$$
$$L_2 \;\equiv\; \mathcal{A}_{++-} = -\mathcal{A}_{--+} \tag{8.18b}$$
$$L_3 \;\equiv\; \mathcal{A}_{+--} = +\mathcal{A}_{-++} \tag{8.18c}$$
$$L_4 \;\equiv\; \mathcal{A}_{+-+} = -\mathcal{A}_{-+-}, \tag{8.18d}$$

where the four independent amplitudes L_i will be called the *longitudinal basis amplitudes.*

8.1.5 Connection with the CGLN amplitudes

The L_i amplitudes are very closely related to the standard CGLN amplitudes [96], since they are both in the Cartesian basis. We first write the general differential cross-section for polarized beam, target and recoil baryon as

$$\frac{d\mathcal{I}}{d\Omega}(m_\gamma, m_i, m_b) = \frac{1}{(4\pi)^2}\frac{1}{4W^2}\left(\frac{|\vec{q}|}{|\vec{k}|}\right)_{\rm c.m.} |\mathcal{A}_{m_\gamma m_i m_b}|^2, \tag{8.19}$$

where we have adopted the Peskin-Schroeder [1] normalization for the Dirac spinors, $\bar{u}u = 2m$, m being the mass of the particle, and W is the c.m. energy of the system. In the CGLN approach, the

cross-section is written as

$$\frac{d\mathcal{I}}{d\Omega}(m_\gamma, m_i, m_b) = \left(\frac{|\vec{q}|}{|\vec{k}|}\right)_{\text{c.m.}} |\langle m_b|\mathcal{F}_{m_\gamma}|m_i\rangle|^2, \tag{8.20}$$

which leads to the simple relation:

$$\mathcal{A}_{\lambda m_i m_b} = (8\pi W)\left[\ \chi^\dagger(m_b)\mathcal{F}(\lambda)\chi(m_i)\ \right]_{m_b m_i}, \tag{8.21}$$

where $\chi(m_i)$ and $\chi(m_b)$ are the two-component spinors of the initial target and the final baryon, respectively, and $\lambda = \pm 1$ is the photon helicity. Since the amplitude $\mathcal{A}$ is a Lorentz invariant quantity, one can calculate this in any reference frame. In the c.m. frame, the matrix $\mathcal{F}(\lambda)$ is expanded in terms of the four CGLN amplitudes F_i as

$$\mathcal{F}(\lambda) = i(\vec{\sigma}\cdot\hat{\epsilon})F_1 + (\hat{\sigma}\cdot\hat{q})(\hat{\sigma}\times\hat{k})\cdot\hat{\epsilon}F_2 + i(\hat{\epsilon}\cdot\hat{q})(\vec{\sigma}\cdot\hat{k})F_3 + i(\hat{\epsilon}\cdot\hat{q})(\vec{\sigma}\cdot\hat{q})F_4, \tag{8.22}$$

where the unit vectors $\hat{\epsilon}$, $\hat{q}$ and $\hat{k}$ are in the c.m. frame. Since the $\lambda = \pm 1$ amplitudes are related via Eq. 8.18, we only need to calculated the F_i's for any of $\lambda = \pm 1$. Doing this for $\lambda = +1$ leads to

$$\mathcal{F}(+1) = \frac{-i}{\sqrt{2}}\begin{bmatrix} sF_3 + csF_4 & 2F_1 - 2cF_2 + s^2F_4 \\ s^2F_4 & -2sF_2 - sF_3 - csF_4 \end{bmatrix}, \tag{8.23}$$

where we have abbreviated $s = \sin(\vartheta^m_{\text{c.m.}})$ and $c = \cos(\vartheta^m_{\text{c.m.}})$ in terms of the polar meson production angle in the c.m. frame, $\vartheta^m_{\text{c.m.}}$ (see Fig. 8.1). Neglecting any irrelevant overall phase, the connections between the L_i amplitudes and the CGLN amplitudes F_i are:

$$L_1 = 4\sqrt{2}\pi W(sF_3 + csF_4) \tag{8.24a}$$
$$L_2 = 4\sqrt{2}\pi W(s^2F_4) \tag{8.24b}$$
$$L_3 = 4\sqrt{2}\pi W(-2sF_2 - sF_3 - csF_4) \tag{8.24c}$$
$$L_4 = 4\sqrt{2}\pi W(2F_1 - 2cF_2 + s^2F_4), \tag{8.24d}$$

where the normalization factor $4\sqrt{2}\pi W$ is important only for the total intensity and can be neglected as far as the polarizations are concerned.

We emphasize again that our longitudinal amplitude formalism is essentially the same as the CGLN formalism. It may also be worth noting that the original CGLN work already pointed out that there are only four independent complex amplitudes. Aside from the extra factor of $4\pi W$ in Eq. 8.21, our amplitudes match exactly with the CGLN matrix elements. The only difference between the L_i's and the F_i's is that the F_i amplitudes are computed in a particular reference frame, the c.m. frame, whereas the L_i's are the invariant amplitudes, "as is". Therefore, the L_i's can be computed in any reference frame.

8.1.6 The Polarization observables

We first define the sixteen observables as the various T_{lmn} elements (see Table 8.2) noting that each observable occurs twice in the expansion given by Eq. 8.12. Our definitions for the observables follow those in FTS [94]. It is to be noted that there are minus signs in front of the defining T_{lmn} elements for the four double-polarization observables that use a linearly polarized beam (G, H, O_x, and O_z). These extra sign flips are needed to preserve the definitions of these variables as *physical asymmetries*, as given in FTS [94]. The signs for G, H, O_x, and O_z, in terms of the *density matrix trace calculations*, as given in Appendix A in the FTS article will therefore acquire sign flips (see

Type	Observable	Definition	M transform
Unpolarized	1	(000)	(122)
Single-pol.	P	(002)	(120)
”	Σ	(100)	(022)
”	T	(020)	(102)
Beam-target	E	(330)	(212)
”	F	(310)	-(232)
”	G	-(230)	(312)
”	H	-(210)	-(332)
Beam-recoil	C_x	(301)	(223)
”	C_z	(303)	-(221)
”	O_x	-(201)	(323)
”	O_z	-(203)	-(321)
Target-recoil	T_x	(011)	(133)
”	T_z	(013)	-(131)
”	L_x	(031)	-(113)
”	L_z	(033)	(111)

Table 8.2: The definition of the 16 observables as the T_{lmn} correlations in Eq. 8.12. The defining T_{lmn} elements are listed as (lmn) in the third column and the corresponding M transformed elements are listed in the last column. Invariance under the M transform results in each observable occurring twice. The full intensity expansion is given in Eq. 8.25.

Sec. 8.1.8 and Sec. 8.1.9 for further details). We now write the full intensity profile in terms of the polarization observables as:

$$\begin{aligned}\mathcal{I} \;=\; & \mathcal{I}_0\,\{(1+P_x^S P_y^i P_y^b)+P(P_y^b+P_x^S P_y^i)+\Sigma(P_x^S+P_y^i P_y^b)+T(P_y^i+P_x^S P_y^b)\\ & +E(P_z^S P_z^i+P_y^S P_x^i P_y^b)+F(P_z^S P_x^i-P_y^S P_z^i P_y^b)+G(-P_y^S P_z^i+P_z^S P_x^i P_y^b)\\ & +H(-P_y^S P_x^i-P_z^S P_z^i P_y^b)+C_x(P_z^S P_x^b+P_y^S P_y^i P_z^b)+C_z(P_z^S P_z^b-P_y^S P_y^i P_x^b)\\ & +O_x(-P_y^S P_x^b+P_z^S P_y^i P_z^b)+O_z(-P_y^S P_z^b-P_z^S P_y^i P_x^b)+T_x(P_x^i P_x^b+P_x^S P_z^i P_z^b)\\ & +T_z(P_x^i P_z^b-P_x^S P_z^i P_x^b)+L_x(P_z^i P_x^b-P_x^S P_x^i P_z^b)+L_z(P_z^i P_z^b+P_x^S P_x^i P_x^b)\}. \end{aligned} \tag{8.25}$$

We note that the three single polarizations (P, Σ and T) occur again as double correlations and the twelve double polarizations (E, F, G, H, C_x, C_z, O_x, O_z, T_x, T_z, L_x and L_z) occur again as triple correlations.

8.1.7 The 32 vanishing terms

The expansion in Eq. 8.12 has 64 terms, while Eq. 8.25 has only 32 terms. The rest of the 32 terms vanish under M invariance. T_{001} and T_{003} are examples of such terms (they do not occur in Table 8.2). Physically, these two elements correspond to recoil polarizations (with unpolarized beam and target) along the $\hat{x}$ and $\hat{z}$ directions, which are required by M invariance to be zero. The general structure of these vanishing terms can be understood from the following example. From Eq. 8.15 for the photon, under a M transform, σ_1 is connected to the the identity matrix (σ_0). Similarly, from Eqs. 8.15 and 8.17 for the baryons, it is σ_2 that is connected to the identity matrix. We group σ_0 and the Pauli matrix connected to σ_0 by the M operator as “E” (type +1), and the rest (σ_2 and σ_3 for the photon, and σ_1 and σ_3 for the baryons) as of the “O” (type -1). A general correlation T_{lmn}

vanishes if the product of the "types" of l, m, and n is -1, since these are not invariant under the mirror symmetry transformation.

8.1.8 Beam-target type experiments

We will show that our expressions for the intensity profiles as measured by the experimentalist conform to the definition of these observables as asymmetries. Following the notation set up in FTS [94] we will denote the cross-section for any configuration of the beam, target and recoil polarizations as $\mathcal{I}^{(\gamma,i,b)}$ [1]. For beam-target type experiments, $\vec{P}^b = \vec{0}$, and Eq. 8.25 becomes

$$\mathcal{I}^{(\gamma,i,0)} = \mathcal{I}_0\{1 + P_x^S\Sigma + P_x^i(-P_y^S H + P_z^S F) + P_y^i(T + P_x^S P) + P_z^i(-P_y^S G + P_z^S E)\}. \tag{8.26}$$

The beam asymmetry is defined as

$$\Sigma = \frac{\mathcal{I}^{(\perp,0,0)} - \mathcal{I}^{(\parallel,0,0)}}{\mathcal{I}^{(\perp,0,0)} + \mathcal{I}^{(\parallel,0,0)}}, \tag{8.27}$$

where $\parallel$ and $\perp$ correspond to a beams with polarizations along the $\hat{x}_{\rm evt}$ ($\phi = 0$) and $\hat{y}_{\rm evt}$ ($\phi = \pi/2$) directions, respectively, and 0 denotes an unpolarized configuration. The target asymmetry is defined as

$$T = \frac{\mathcal{I}^{(0,+y,0)} - \mathcal{I}^{(0,-y,0)}}{\mathcal{I}^{(0,+y,0)} + \mathcal{I}^{(0,-y,0)}}, \tag{8.28}$$

and the four double polarizations are defined as

$$E = \frac{\mathcal{I}^{(r,+z,0)} - \mathcal{I}^{(r,-z,0)}}{\mathcal{I}^{(r,+z,0)} + \mathcal{I}^{(r,-z,0)}} \tag{8.29a}$$

$$F = \frac{\mathcal{I}^{(r,+x,0)} - \mathcal{I}^{(r,-x,0)}}{\mathcal{I}^{(r,+x,0)} + \mathcal{I}^{(r,-x,0)}} \tag{8.29b}$$

$$G = \frac{\mathcal{I}^{(+t,+z,0)} - \mathcal{I}^{(+t,-z,0)}}{\mathcal{I}^{(+t,+z,0)} + \mathcal{I}^{(+t,-z,0)}} \tag{8.29c}$$

$$H = \frac{\mathcal{I}^{(+t,+x,0)} - \mathcal{I}^{(+t,-x,0)}}{\mathcal{I}^{(+t,+x,0)} + \mathcal{I}^{(+t,-x,0)}}, \tag{8.29d}$$

where "r" denotes a right-handed circularly polarized beam (all photons in the state $|\epsilon^+_{\rm evt}\rangle$), and "$+t$" denotes a linearly polarized beam with $\phi = +\pi/4$ with respect to $\hat{x}_{\rm evt}$. The full expression for the cross-section in beam-target experiments reads

$$\begin{aligned}\mathcal{I}^{(\gamma,i,0)}_{\rm theory} &= \mathcal{I}_0\{1 - P_L^\gamma\Sigma\cos(2\phi) + P_y^i\left(T - P_L^\gamma P\cos(2\phi)\right) \\ &\quad + P_x^i\left(P_C^\gamma F + P_L^\gamma H\sin(2\phi)\right) + P_z^i\left(P_C^\gamma E + P_L^\gamma G\sin(2\phi)\right)\}\end{aligned} \tag{8.30}$$

where we have added a subscript "theory" to remind the reader that this is for the theoretical formalism only. It can easily be checked that the definitions in Eqs. 8.27-8.29 are consistent with the intensity profile given by Eq. 8.30. Recall that $\phi = +\pi/4$ corresponds to $P_y^S = -1$ (see Table 8.1), explaining the extra minus signs for G and H in the definitions of the corresponding T_{lmn} elements in Table 8.2.

It is to be noted that one has access to an "extra" single-polarization observable, the recoil polarization P, even though the polarization of the recoiling baryon is not measured here. This is again due to the M transform relations. In fact, any double-polarization experiment has access to all the three single polarization observables. The definition of P as an asymmetry is given in the next sub-section.

[1] FTS defines the cross-section as $\sigma^{(\gamma,i,b)}$, whereas we define it as $\mathcal{I}^{(\gamma,i,b)}$, to avoid confusion with the Pauli σ matrices

8.1.9 Beam-recoil type experiments

For an experiment with beam and recoil baryon polarization information, we follow a similar logic. Here, $\vec{P}^i = \vec{0}$, and the beam-recoil expression is

$$\begin{aligned}\mathcal{I}^{(\gamma,0,b)}_{\text{theory}} &= \mathcal{I}_0\{1 - P^\gamma_L \Sigma\cos(2\phi) + P^b_y(P - P^\gamma_L T\cos(2\phi)) \\ &\quad + P^b_x\left(P^\gamma_C C_x + P^\gamma_L O_x \sin(2\phi)\right) + P^b_z\left(P^\gamma_C C_z + P^\gamma_L O_z \sin(2\phi)\right)\},\end{aligned}$$

where the recoil polarization P is defined as

$$P = \frac{\mathcal{I}^{(0,0,+y)} - \mathcal{I}^{(0,0,-y)}}{\mathcal{I}^{(0,0,+y)} + \mathcal{I}^{(0,0,-y)}}. \tag{8.31}$$

The four beam-recoil double polarizations are

$$C_z = \frac{\mathcal{I}^{(r,0,+z)} - \mathcal{I}^{(r,0,-z)}}{\mathcal{I}^{(r,0,+z)} + \mathcal{I}^{(r,0,-z)}} \tag{8.32a}$$

$$C_x = \frac{\mathcal{I}^{(r,0,+x)} - \mathcal{I}^{(r,0,-x)}}{\mathcal{I}^{(r,0,+x)} + \mathcal{I}^{(r,0,-x)}} \tag{8.32b}$$

$$O_z = \frac{\mathcal{I}^{(+t,0,+z)} - \mathcal{I}^{(+t,0,-z)}}{\mathcal{I}^{(+t,0,+z)} + \mathcal{I}^{(+t,0,-z)}} \tag{8.32c}$$

$$O_x = \frac{\mathcal{I}^{(+t,0,+x)} - \mathcal{I}^{(+t,0,-x)}}{\mathcal{I}^{(+t,0,+x)} + \mathcal{I}^{(+t,0,-x)}}. \tag{8.32d}$$

The "extra" single polarization observable accessible here is the target asymmetry T, defined in Eq. 8.28.

As in the case of G and H, the definitions of O_x and O_z as asymmetries use $\phi = +\pi/4$ that corresponds to $P^S_y = -1$. This explains the extra minus signs in the defining T_{lmn} elements in Table 8.2 for O_x and O_z.

8.1.10 Target-recoil type experiments

The target-recoil expression is

$$\mathcal{I}^{(0,i,b)} = \mathcal{I}^0\{1 + P^i_y T + P^b_y(P + \Sigma P^i_y) + P^i_z\left(P^b_z L_z + P^b_x L_x\right) + P^i_x\left(P^b_x T_x + P^b_z T_z\right)\},$$

where the four target-recoil double polarizations are

$$T_z = \frac{\mathcal{I}^{(0,+x,+z)} - \mathcal{I}^{(0,+x,-z)}}{\mathcal{I}^{(0,+x,+z)} + \mathcal{I}^{(0,+x,-z)}} \tag{8.33a}$$

$$T_x = \frac{\mathcal{I}^{(0,+x,+x)} - \mathcal{I}^{(0,+x,-x)}}{\mathcal{I}^{(0,+x,+x)} + \mathcal{I}^{(0,+x,-x)}} \tag{8.33b}$$

$$L_z = \frac{\mathcal{I}^{(0,+z,+z)} - \mathcal{I}^{(0,+z,-z)}}{\mathcal{I}^{(0,+z,+z)} + \mathcal{I}^{(0,+z,-z)}} \tag{8.33c}$$

$$L_x = \frac{\mathcal{I}^{(0,+z,+x)} - \mathcal{I}^{(0,+z,-x)}}{\mathcal{I}^{(0,+z,+x)} + \mathcal{I}^{(0,+z,-x)}}. \tag{8.33d}$$

8.1.11 Connection with experimental intensity profiles

Until now, we have been careful to distinguish the "theoretical" intensity profiles from what experimentalists will actually measure. The only difference lies in the case of a linearly polarized beam where the laboratory analyzing direction set by the choice of the angle θ (see Fig. 8.2) can vary.

Eq. 8.33 remains the same between the theory and experimental formalisms, since it is independent of θ. For Eqs. 8.30 and 8.31, however, we need to get back to the relation $\phi = (\theta - \varphi)$ in Fig. 8.2. The easiest choice is to measure everything with respect to $\hat{x}_{\rm lab}$, which usually represents the experimentalist's choice of photon polarization axis. Therefore, we take $\theta = 0$ (also called "para" setting), so that $\phi = -\varphi$ and Eqs. 8.30 and 8.31 become

$$\begin{aligned}\mathcal{I}^{(\gamma,i,0)}_{\rm para} &= \mathcal{I}_0\{1 - P^\gamma_L \Sigma\cos(2\varphi) + P^i_y\,(T - P^\gamma_L P\cos(2\varphi)) \\ &\quad + P^i_x\,(P^\gamma_C F - P^\gamma_L H\sin(2\varphi)) + P^i_z\,(P^\gamma_C E - P^\gamma_L G\sin(2\varphi))\},\end{aligned} \tag{8.34}$$

and

$$\begin{aligned}\mathcal{I}^{(\gamma,0,b)}_{\rm para} &= \mathcal{I}_0\{1 - P^\gamma_L \Sigma\cos(2\varphi) + P^b_y(P - P^\gamma_L T\cos(2\varphi)) \\ &\quad + P^b_x\,(P^\gamma_C C_x - P^\gamma_L O_x\sin(2\varphi)) + P^b_z\,(P^\gamma_C C_z - P^\gamma_L O_z\sin(2\varphi))\},\end{aligned} \tag{8.35}$$

respectively. Similarly, for $\theta = \pi/2$ (also called "perp" setting), we get

$$\begin{aligned}\mathcal{I}^{(\gamma,i,0)}_{\rm perp} &= \mathcal{I}_0\{1 + P^\gamma_L \Sigma\cos(2\varphi) + P^i_y\,(T + P^\gamma_L P\cos(2\varphi)) \\ &\quad + P^i_x\,(P^\gamma_C F + P^\gamma_L H\sin(2\varphi)) + P^i_z\,(P^\gamma_C E + P^\gamma_L G\sin(2\varphi))\},\end{aligned} \tag{8.36}$$

and

$$\begin{aligned}\mathcal{I}^{(\gamma,0,b)}_{\rm perp} &= \mathcal{I}_0\{1 + P^\gamma_L \Sigma\cos(2\varphi) + P^b_y(P + P^\gamma_L T\cos(2\varphi)) \\ &\quad + P^b_x\,(P^\gamma_C C_x + P^\gamma_L O_x\sin(2\varphi)) + P^b_z\,(P^\gamma_C C_z + P^\gamma_L O_z\sin(2\varphi))\}.\end{aligned} \tag{8.37}$$

It is important to note that the sine and cosine terms in Eqs. 8.30 and 8.31 alter signs differently in going from the "theory" expressions to the "para" and "perp" settings, and this directly affects the signs of the extracted polarization observables. Therefore, care must be taken by the experimentalist to conform to a definition of the "para" and "perp" settings that matches with the theoretical definitions. Finally, we also note that it is beneficial to measure the intensity profiles for both the "para" and "perp" settings and extract the polarizations from the asymmetries between the two settings. This removes the overall normalization factor (the unpolarized cross-section), and therefore, any dependence on the detector acceptance (see Ref. [103] for details).

8.1.12 Computation of polarization expressions in the longitudinal basis

We list some basic caveats that will be useful during the computations.

1. The matrix representation of an operator is $\mathcal{O}_{nm} = \langle n|\mathcal{O}|m\rangle$ (note order of subscripts). For the Pauli matrices for example, $(\sigma_y)_{+-} = -i$, $(\sigma_z)_{--} = -1$, etc.

2. FTS uses $m_{s'}$ and m_s for outgoing baryon and incoming (target) spins. We adopt m_b and m_i as the final baryon and initial proton spins, respectively, and denote the photon spin by $m_\gamma = \lambda$. Any other index will be a dummy index for summation purposes. Also, unless otherwise mentioned, it is understood that repeated indices are to be summed over.

3. A useful relation is that for the conjugate operator $J^\dagger_\lambda$, the matrix elements are $(J^\dagger_\lambda)_{m_i m_b} = (J_\lambda)^*_{m_b m_i} = \mathcal{A}^*_{\lambda m_b m_i}$.

4. There are two types of traces in the FTS paper. "Tr" implies a trace over all spins, while "tr" implies a trace over the baryon spins, assuming that the photon spins have been traced over. To go from "Tr" to "tr", that is, the procedure of doing the photon spin trace, is as follows. Let Ω_b and Ω_i be any operator in the final baryon and initial target proton spin space

respectively. For the three Pauli matrices σ_x^γ, σ_y^γ and σ_z^γ, the photon traces are computed as follows:

$$\begin{aligned}\mathrm{Tr}[\Omega_b J \Omega_i \sigma_x^\gamma J^\dagger] &= \sum_{\lambda\lambda'} \mathrm{tr}[\Omega_b J_\lambda \Omega_i (\sigma_x^\gamma)_{\lambda\lambda'} (J^\dagger)_{\lambda'}] \\ &= \mathrm{tr}[\Omega_b J_+ \Omega_i (J^\dagger)_- + \Omega_b J_- \Omega_i (J^\dagger)_+] \end{aligned} \tag{8.38a}$$

$$\begin{aligned}\mathrm{Tr}[\Omega_b J \Omega_i \sigma_y^\gamma J^\dagger] &= \sum_{\lambda\lambda'} \mathrm{tr}[\Omega_b J_\lambda \Omega_i (\sigma_y^\gamma)_{\lambda\lambda'} (J^\dagger)_{\lambda'}] \\ &= -i\ \mathrm{tr}[\Omega_b J_+ \Omega_i (J^\dagger)_- - \Omega_b J_- \Omega_i (J^\dagger)_+] \end{aligned} \tag{8.38b}$$

$$\begin{aligned}\mathrm{Tr}[\Omega_b J \Omega_i \sigma_z^\gamma J^\dagger] &= \sum_{\lambda\lambda'} \mathrm{tr}[\Omega_b J_\lambda \Omega_i (\sigma_z^\gamma)_{\lambda\lambda'} (J^\dagger)_{\lambda'}] \\ &= \mathrm{tr}[\Omega_b J_+ \Omega_i (J^\dagger)_+ - \Omega_b J_- \Omega_i (J^\dagger)_-]. \end{aligned} \tag{8.38c}$$

Note that these expressions for the summations over the photon states are equivalent to those from the more conventional forms that can be found in Ref. [95], for example. The trace notation is simply a more compact way of expressing the spin sums.

5. Overall normalization factor. All 15 polarization observables will be normalized by the intensity factor $\mathrm{Tr}[JJ^\dagger]$. This is given as

$$\mathrm{Tr}[JJ^\dagger] = \sum_{\lambda m_i m_b} |\mathcal{A}_{\lambda m_i m_b}|^2. \tag{8.39}$$

This will not appear in our expressions below, but it is understood that this normalization always goes into the computations.

8.1.13 The 15 polarization expressions

The detailed computation of the 15 polarizations are given below:

$$\begin{aligned} P &= \mathrm{Tr}[\sigma_y^b J J^\dagger] \\ &= \langle m_b|\sigma_y|m_b'\rangle \langle m_b'|J_\lambda|m_i\rangle \langle m_i|J_\lambda^\dagger|m_b\rangle \\ &= \langle m_b|\sigma_y|m_b'\rangle \langle m_b'|J_\lambda|m_i\rangle (\langle m_b|J_\lambda|m_i\rangle)^* \\ &= -i\ \langle -|J_\lambda|m_i\rangle (\langle +|J_\lambda|m_i\rangle)^* + i\langle +|J_\lambda|m_i\rangle (\langle -|J_\lambda|m_i\rangle)^* \\ &= \sum_{\lambda m_i} -2\,\mathrm{Im}\left(\mathcal{A}_{\lambda m_i +} \mathcal{A}^*_{\lambda m_i -}\right) \end{aligned} \tag{8.40a}$$

$$\begin{aligned} \Sigma &= \mathrm{Tr}[J \sigma_x^\gamma J^\dagger] \\ &= \langle m_b|J_+|m_i\rangle \langle m_i|J_-^\dagger|m_b\rangle + \langle m_b|J_-|m_i\rangle \langle m_i|J_+^\dagger|m_b\rangle \\ &= \langle m_b|J_+|m_i\rangle (\langle m_b|J_-|m_i\rangle)^* + \langle m_b|J_-|m_i\rangle (\langle m_b|J_+|m_i\rangle)^* \\ &= \sum_{m_i m_b} 2\,\mathrm{Re}\left(\mathcal{A}_{+ m_i m_b} \mathcal{A}^*_{- m_i m_b}\right) \end{aligned} \tag{8.40b}$$

$$
\begin{aligned}
T &= \mathrm{Tr}[J\sigma_y^i J^\dagger] \\
&= -i\langle m_b|J_\lambda|+\rangle\langle -|J_\lambda^\dagger|m_b\rangle + i\langle m_b|J_\lambda|-\rangle\langle +|J_\lambda^\dagger|m_b\rangle \\
&= -i\langle m_b|J_\lambda|+\rangle(\langle m_b|J_\lambda|-\rangle)^* + i\langle m_b|J_\lambda|-\rangle(\langle m_b|J_\lambda^\dagger|+\rangle)^* \\
&= \sum_{\lambda m_b} -2\,\mathrm{Im}\left(\mathcal{A}_{\lambda -m_b}\mathcal{A}^*_{\lambda +m_b}\right)
\end{aligned} \tag{8.40c}
$$

$$
\begin{aligned}
E &= \mathrm{Tr}[J\sigma_z^i\sigma_z^\gamma J^\dagger] \\
&= \langle m_b|J_+|m_b'\rangle\langle m_b'|\sigma_z|m_i'\rangle\langle m_i'|J_+^\dagger|m_b\rangle - \langle m_b|J_-|m_b'\rangle\langle m_b'|\sigma_z|m_i'\rangle\langle m_i'|J_-^\dagger|m_b\rangle \\
&= \langle m_b|J_+|m_b'\rangle\langle m_b'|\sigma_z|m_i'\rangle(\langle m_b|J_+|m_i'\rangle)^* - \langle m_b|J_-|m_b'\rangle\langle m_b'|\sigma_z|m_i'\rangle(\langle m_b|J_-|m_i'\rangle)^* \\
&= \langle m_b|J_+|+\rangle(\langle m_b|J_+|+\rangle)^* - \langle m_b|J_+|-\rangle(\langle m_b|J_+|-\rangle)^* \\
&\qquad\qquad - \langle m_b|J_-|+\rangle(\langle m_b|J_-|+\rangle)^* + \langle m_b|J_-|-\rangle(\langle m_b|J_-|-\rangle)^* \\
&= \sum_{m_b}\left(|\mathcal{A}_{++m_b}|^2 - |\mathcal{A}_{+-m_b}|^2 - |\mathcal{A}_{-+m_b}|^2 + |\mathcal{A}_{--m_b}|^2\right)
\end{aligned} \tag{8.40d}
$$

$$
\begin{aligned}
F &= \mathrm{Tr}[J\sigma_x^i\sigma_z^\gamma J^\dagger] \\
&= \langle m_b|J_+|m_b'\rangle\langle m_b'|\sigma_x|m_i'\rangle\langle m_i'|J_+^\dagger|m_b\rangle - \langle m_b|J_-|m_b'\rangle\langle m_b'|\sigma_x|m_i'\rangle\langle m_i'|J_-^\dagger|m_b\rangle \\
&= \langle m_b|J_+|m_b'\rangle\langle m_b'|\sigma_x|m_i'\rangle(\langle m_b|J_+|m_i'\rangle)^* - \langle m_b|J_-|m_b'\rangle\langle m_b'|\sigma_x|m_i'\rangle(\langle m_b|J_-|m_i'\rangle)^* \\
&= \langle m_b|J_+|+\rangle(\langle m_b|J_+|-\rangle)^* + \langle m_b|J_+|-\rangle(\langle m_b|J_+|+\rangle)^* \\
&\qquad\qquad - \langle m_b|J_-|+\rangle(\langle m_b|J_-|-\rangle)^* - \langle m_b|J_-|-\rangle(\langle m_b|J_-|+\rangle)^* \\
&= \sum_{m_b} 2\mathrm{Re}\left(A_{++m_b}A^*_{+-m_b} - A_{-+m_b}A^*_{--m_b}\right)
\end{aligned} \tag{8.40e}
$$

$$
\begin{aligned}
G &= -\mathrm{Tr}[J\sigma_z^i\sigma_y^\gamma J^\dagger] \\
&= i\langle m_b|J_+|m_b'\rangle\langle m_b'|\sigma_z|m_i'\rangle\langle m_i'|J_-^\dagger|m_b\rangle - i\langle m_b|J_-|m_b'\rangle\langle m_b'|\sigma_z|m_i'\rangle\langle m_i'|J_+^\dagger|m_b\rangle \\
&= i\langle m_b|J_+|m_b'\rangle\langle m_b'|\sigma_z|m_i'\rangle(\langle m_b|J_-|m_i'\rangle)^* - i\langle m_b|J_-|m_b'\rangle\langle m_b'|\sigma_z|m_i'\rangle(\langle m_b|J_+|m_i'\rangle)^* \\
&= i\langle m_b|J_+|+\rangle(\langle m_b|J_-|+\rangle)^* - i\langle m_b|J_+|-\rangle(\langle m_b|J_-|-\rangle)^* \\
&- i\langle m_b|J_-|+\rangle(\langle m_b|J_+|+\rangle)^* + i\langle m_b|J_-|-\rangle(\langle m_b|J_+|-\rangle)^* \\
&= \sum_{m_b} 2\mathrm{Im}\left(\mathcal{A}_{+-m_b}\mathcal{A}^*_{--m_b} + \mathcal{A}_{-+m_b}\mathcal{A}^*_{++m_b}\right)
\end{aligned} \tag{8.40f}
$$

$$
\begin{aligned}
H &= -\mathrm{Tr}[J\sigma_x^i\sigma_y^\gamma J^\dagger] \\
&= i\langle m_b|J_+|m_b'\rangle\langle m_b'|\sigma_x|m_i'\rangle\langle m_i'|J_-^\dagger|m_b\rangle - i\langle m_b|J_-|m_b'\rangle\langle m_b'|\sigma_x|m_i'\rangle\langle m_i'|J_+^\dagger|m_b\rangle \\
&= i\langle m_b|J_+|m_b'\rangle\langle m_b'|\sigma_x|m_i'\rangle(\langle m_b|J_-|m_i'\rangle)^* - i\langle m_b|J_-|m_b'\rangle\langle m_b'|\sigma_x|m_i'\rangle(\langle m_b|J_+|m_i'\rangle)^* \\
&= i\langle m_b|J_+|+\rangle(\langle m_b|J_-|-\rangle)^* + i\langle m_b|J_+|-\rangle(\langle m_b|J_-|+\rangle)^* \\
&\qquad\qquad - i\langle m_b|J_-|+\rangle(\langle m_b|J_+|-\rangle)^* - i\langle m_b|J_-|-\rangle(\langle m_b|J_+|+\rangle)^* \\
&= \sum_{m_b} 2\mathrm{Im}\left(\mathcal{A}_{--m_b}\mathcal{A}^*_{++m_b} + \mathcal{A}_{-+m_b}\mathcal{A}^*_{+-m_b}\right)
\end{aligned} \tag{8.40g}
$$

$$
\begin{aligned}
C_x &= \mathrm{Tr}[\sigma_x^b J \sigma_z^\gamma J^\dagger] \\
&= \langle m_b|\sigma_x|m_i'\rangle\langle m_i'|J_+|m_i\rangle\langle m_i|J_+^\dagger|m_b\rangle - \langle m_b|\sigma_x|m_i'\rangle\langle m_i'|J_-|m_i\rangle\langle m_i|J_-^\dagger|m_b\rangle \\
&= \langle m_b|\sigma_x|m_i'\rangle\langle m_i'|J_+|m_i\rangle(\langle m_b|J_+|m_i\rangle)^* - \langle m_b|\sigma_x|m_i'\rangle\langle m_i'|J_-|m_i\rangle(\langle m_b|J_-|m_i\rangle)^* \\
&= \langle -|J_+|m_i\rangle(\langle +|J_+|m_i\rangle)^* - \langle -|J_-|m_i\rangle(\langle +|J_-|m_i\rangle)^* \\
&\qquad\qquad + \langle +|J_+|m_i\rangle(\langle -|J_+|m_i\rangle)^* - \langle +|J_-|m_i\rangle(\langle -|J_-|m_i\rangle)^* \\
&= \sum_{m_i} 2\mathrm{Re}\left(\mathcal{A}_{+m_i-}\mathcal{A}_{+m_i+}^* - \mathcal{A}_{-m_i-}\mathcal{A}_{-m_i+}^*\right) \qquad (8.40\text{h})
\end{aligned}
$$

$$
\begin{aligned}
C_z &= \mathrm{Tr}[\sigma_z^b J \sigma_z^\gamma J^\dagger] \\
&= \langle m_b|\sigma_z|m_i'\rangle\langle m_i'|J_+|m_i\rangle\langle m_i|J_+^\dagger|m_b\rangle - \langle m_b|\sigma_z|m_i'\rangle\langle m_i'|J_-|m_i\rangle\langle m_i|J_-^\dagger|m_b\rangle \\
&= \langle m_b|\sigma_z|m_i'\rangle\langle m_i'|J_+|m_i\rangle(\langle m_b|J_+|m_i\rangle)^* - \langle m_b|\sigma_z|m_i'\rangle\langle m_i'|J_-|m_i\rangle(\langle m_b|J_-|m_i\rangle)^* \\
&= \langle +|J_+|m_i\rangle(\langle +|J_+|m_i\rangle)^* - \langle +|J_-|m_i\rangle(\langle +|J_-|m_i\rangle)^* \\
&\qquad\qquad - \langle -|J_+|m_i\rangle(\langle -|J_+|m_i\rangle)^* + \langle -|J_-|m_i\rangle(\langle -|J_-|m_i\rangle)^* \\
&= \sum_{m_i} \left(|\mathcal{A}_{+m_i+}|^2 - |\mathcal{A}_{-m_i+}|^2 - |\mathcal{A}_{+m_i-}|^2 + |\mathcal{A}_{-m_i-}|^2\right) \qquad (8.40\text{i})
\end{aligned}
$$

$$
\begin{aligned}
O_x &= -\mathrm{Tr}[\sigma_x^b J \sigma_y^\gamma J^\dagger] \\
&= i\langle m_b|\sigma_x|m_i'\rangle\langle m_i'|J_+|m_i\rangle\langle m_i|J_-^\dagger|m_b\rangle - i\langle m_b|\sigma_x|m_i'\rangle\langle m_i'|J_-|m_i\rangle\langle m_i|J_+^\dagger|m_b\rangle \\
&= i\langle m_b|\sigma_x|m_i'\rangle\langle m_i'|J_+|m_i\rangle(\langle m_b|J_-|m_i\rangle)^* - i\langle m_b|\sigma_x|m_i'\rangle\langle m_i'|J_-|m_i\rangle(\langle m_b|J_+|m_i\rangle)^* \\
&= i\langle -|J_+|m_i\rangle(\langle +|J_-|m_i\rangle)^* - i\langle -|J_-|m_i\rangle(\langle +|J_+|m_i\rangle)^* \qquad (8.40\text{j}) \\
&\qquad\qquad + i\langle +|J_+|m_i\rangle(\langle -|J_-|m_i\rangle)^* - i\langle +|J_-|m_i\rangle(\langle -|J_+|m_i\rangle)^* \\
&= \sum_{m_i} 2\mathrm{Im}\left(\mathcal{A}_{-m_i-}\mathcal{A}_{+m_i+}^* + \mathcal{A}_{-m_i+}\mathcal{A}_{+m_i-}^*\right) \qquad (8.40\text{k})
\end{aligned}
$$

$$
\begin{aligned}
O_z &= -\mathrm{Tr}[\sigma_z^b J \sigma_y^\gamma J^\dagger] \\
&= i\langle m_b|\sigma_z|m_i'\rangle\langle m_i'|J_+|m_i\rangle\langle m_i|J_-^\dagger|m_b\rangle - i\langle m_b|\sigma_z|m_i'\rangle\langle m_i'|J_-|m_i\rangle\langle m_i|J_+^\dagger|m_b\rangle \\
&= i\langle m_b|\sigma_z|m_i'\rangle\langle m_i'|J_+|m_i\rangle(\langle m_b|J_-|m_i\rangle)^* - i\langle m_b|\sigma_z|m_i'\rangle\langle m_i'|J_-|m_i\rangle(\langle m_b|J_+|m_i\rangle)^* \\
&= i\langle +|J_+|m_i\rangle(\langle +|J_-|m_i\rangle)^* - i\langle +|J_-|m_i\rangle(\langle +|J_+|m_i\rangle)^* \\
&\qquad\qquad - i\langle -|J_+|m_i\rangle(\langle -|J_-|m_i\rangle)^* + i\langle -|J_-|m_i\rangle(\langle -|J_+|m_i\rangle)^* \\
&= \sum_{m_i} 2\mathrm{Im}\left(\mathcal{A}_{-m_i+}\mathcal{A}_{+m_i+}^* + \mathcal{A}_{+m_i-}\mathcal{A}_{-m_i-}^*\right) \qquad (8.40\text{l})
\end{aligned}
$$

$$
\begin{aligned}
T_x &= \mathrm{Tr}[\sigma_x^b J \sigma_x^i J^\dagger] \\
&= \langle m_b|\sigma_x|m_i\rangle\langle m_i|J_\lambda|m_i'\rangle\langle m_i'|\sigma_x|m_b'\rangle\langle m_b'|J_\lambda^\dagger|m_b\rangle \\
&= \langle m_b|\sigma_x|m_i\rangle\langle m_i|J_\lambda|m_i'\rangle\langle m_i'|\sigma_x|m_b'\rangle(\langle m_b|J_\lambda|m_b'\rangle)^* \\
&= \langle -|J_\lambda|m_i'\rangle\langle m_i'|\sigma_x|m_b'\rangle(\langle +|J_\lambda|m_b'\rangle)^* + \langle +|J_\lambda|m_i'\rangle\langle m_i'|\sigma_x|m_b'\rangle(\langle -|J_\lambda|m_b'\rangle)^* \\
&= \langle -|J_\lambda|+\rangle(\langle +|J_\lambda|-\rangle)^* + \langle +|J_\lambda|+\rangle(\langle -|J_\lambda|-\rangle)^* + \langle -|J_\lambda|-\rangle(\langle +|J_\lambda|+\rangle)^* + \langle +|J_\lambda|-\rangle(\langle -|J_\lambda|+\rangle)^* \\
&= \sum_{\lambda} 2\mathrm{Re}\left(\mathcal{A}_{\lambda+-}\mathcal{A}_{\lambda-+}^* + \mathcal{A}_{\lambda++}\mathcal{A}_{\lambda--}^*\right) \qquad (8.40\text{m})
\end{aligned}
$$

$$
\begin{aligned}
T_z &= \mathrm{Tr}[\sigma_z^b J \sigma_x^i J^\dagger] \\
&= \langle m_b|\sigma_z|m_i\rangle\langle m_i|J_\lambda|m_i'\rangle\langle m_i'|\sigma_x|m_b'\rangle\langle m_b'|J_\lambda^\dagger|m_b\rangle \\
&= \langle m_b|\sigma_z|m_i\rangle\langle m_i|J_\lambda|m_i'\rangle\langle m_i'|\sigma_x|m_b'\rangle(\langle m_b|J_\lambda|m_b'\rangle)^* \\
&= \langle +|J_\lambda|m_i'\rangle\langle m_i'|\sigma_x|m_b'\rangle(\langle +|J_\lambda|m_b'\rangle)^* \\
&\quad - \langle -|J_\lambda|m_i'\rangle\langle m_i'|\sigma_x|m_b'\rangle(\langle -|J_\lambda|m_b'\rangle)^* \\
&= \langle +|J_\lambda|+\rangle(\langle +|J_\lambda|-\rangle)^* - \langle -|J_\lambda|+\rangle(\langle -|J_\lambda|-\rangle)^* + \langle +|J_\lambda|-\rangle(\langle +|J_\lambda|+\rangle)^* - \langle -|J_\lambda|-\rangle(\langle -|J_\lambda|+\rangle)^* \\
&= \sum_\lambda 2\mathrm{Re}\left(\mathcal{A}_{\lambda++}\mathcal{A}_{\lambda-+}^* - \mathcal{A}_{\lambda+-}\mathcal{A}_{\lambda--}^*\right) \qquad (8.40n)
\end{aligned}
$$

$$
\begin{aligned}
L_x &= \mathrm{Tr}[\sigma_x^b J \sigma_z^i J^\dagger] \\
&= \langle m_b|\sigma_x|m_i\rangle\langle m_i|J_\lambda|m_i'\rangle\langle m_i'|\sigma_z|m_b'\rangle\langle m_b'|J_\lambda^\dagger|m_b\rangle \\
&= \langle m_b|\sigma_x|m_i\rangle\langle m_i|J_\lambda|m_i'\rangle\langle m_i'|\sigma_z|m_b'\rangle(\langle m_b|J_\lambda|m_b'\rangle)^* \\
&= \langle -|J_\lambda|m_i'\rangle\langle m_i'|\sigma_z|m_b'\rangle(\langle +|J_\lambda|m_b'\rangle)^* + \langle \\
&\quad + |J_\lambda|m_i'\rangle\langle m_i'|\sigma_z|m_b'\rangle(\langle -|J_\lambda|m_b'\rangle)^* \\
&= \langle -|J_\lambda|+\rangle(\langle +|J_\lambda|+\rangle)^* + \langle +|J_\lambda|+\rangle(\langle -|J_\lambda|+\rangle)^* - \langle -|J_\lambda|-\rangle(\langle +|J_\lambda|-\rangle)^* - \langle +|J_\lambda|-\rangle(\langle -|J_\lambda|-\rangle)^* \\
&= \sum_\lambda 2\mathrm{Re}\left(\mathcal{A}_{\lambda+-}\mathcal{A}_{\lambda++}^* - \mathcal{A}_{\lambda--}\mathcal{A}_{\lambda-+}^*\right) \qquad (8.40o)
\end{aligned}
$$

$$
\begin{aligned}
L_z &= \mathrm{Tr}[\sigma_z^b J \sigma_z^i J^\dagger] \\
&= \langle m_b|\sigma_z|m_i\rangle\langle m_i|J_\lambda|m_i'\rangle\langle m_i'|\sigma_z|m_b'\rangle\langle m_b'|J_\lambda^\dagger|m_b\rangle \\
&= \langle m_b|\sigma_z|m_i\rangle\langle m_i|J_\lambda|m_i'\rangle\langle m_i'|\sigma_z|m_b'\rangle(\langle m_b|J_\lambda|m_b'\rangle)^* \\
&= \langle +|J_\lambda|m_i'\rangle\langle m_i'|\sigma_z|m_b'\rangle(\langle +|J_\lambda|m_b'\rangle)^* - \langle -|J_\lambda|m_i'\rangle\langle m_i'|\sigma_z|m_b'\rangle(\langle -|J_\lambda|m_b'\rangle)^* \\
&= \langle +|J_\lambda|+\rangle(\langle +|J_\lambda|+\rangle)^* - \langle -|J_\lambda|+\rangle(\langle -|J_\lambda|+\rangle)^* - \langle +|J_\lambda|-\rangle(\langle +|J_\lambda|-\rangle)^* + \langle -|J_\lambda|-\rangle(\langle -|J_\lambda|-\rangle)^* \\
&= \sum_\lambda \left(|\mathcal{A}_{\lambda++}|^2 - |\mathcal{A}_{\lambda+-}|^2 - |\mathcal{A}_{\lambda-+}|^2 + |\mathcal{A}_{\lambda--}|^2\right) \qquad (8.40p)
\end{aligned}
$$

8.1.14 Expressions in terms of L_i amplitudes

A summary of the expressions for the 16 observables in terms of the L_i amplitudes as given below:

$$
\begin{aligned}
\mathcal{I}_0/2 &= (|L_1|^2 + |L_2|^2 + |L_3|^2 + |L_4|^2) && (8.41a)\\
P &= -2\mathrm{Im}(L_1L_2^* + L_4L_3^*)/\mathcal{N} && (8.41b)\\
\Sigma &= 2\mathrm{Re}(L_1L_3^* - L_4L_2^*)/\mathcal{N} && (8.41c)\\
T &= 2\mathrm{Im}(L_1L_4^* + L_2L_3^*)/\mathcal{N} && (8.41d)\\
E &= (|L_1|^2 + |L_2|^2 - |L_3|^2 - |L_4|^2)/\mathcal{N} && (8.41e)\\
F &= 2\mathrm{Re}(L_1L_4^* + L_2L_3^*)/\mathcal{N} && (8.41f)\\
G &= -2\mathrm{Im}(L_1L_3^* - L_2L_4^*)/\mathcal{N} && (8.41g)\\
H &= 2\mathrm{Im}(L_1L_2^* + L_3L_4^*)/\mathcal{N} && (8.41h)\\
C_x &= 2\mathrm{Re}(L_1L_2^* + L_3L_4^*)/\mathcal{N} && (8.41i)\\
C_z &= (|L_1|^2 - |L_2|^2 - |L_3|^2 + |L_4|^2)/\mathcal{N} && (8.41j)\\
O_x &= 2\mathrm{Im}(L_1L_4^* - L_2L_3^*)/\mathcal{N} && (8.41k)\\
O_z &= -2\mathrm{Im}(L_1L_3^* + L_2L_4^*)/\mathcal{N} && (8.41l)\\
T_x &= 2\mathrm{Re}(L_1L_3^* + L_2L_4^*)/\mathcal{N} && (8.41m)\\
& && (8.41n)
\end{aligned}
$$

$$T_z = 2\mathrm{Re}(L_1 L_4^* - L_2 L_3^*)/\mathcal{N} \tag{8.41o}$$
$$L_x = 2\mathrm{Re}(L_1 L_2^* - L_3 L_4^*)/\mathcal{N} \tag{8.41p}$$
$$L_z = (|L_1|^2 - |L_2|^2 + |L_3|^2 - |L_4|^2)/\mathcal{N}, \tag{8.41q}$$

where $N = \mathcal{I}_0/2$ is the normalization factor for the polarizations.

8.1.15 The consistency relations

It is well known that the fifteen polarization observables occurring as bilinears in Eq. 8.41 can be connected by various identities. These are also called constraint equations, because they interconnect and place restrictions on the physical values these observables can take. Simply put, these equations are nothing but identities in the four independent amplitudes L_i. Chiang and Tabakin [93] have showed that these identities can be derived in a more sophisticated fashion by considering the complex space spanned by the four amplitudes. The observables can then be expanded in terms of the sixteen 4×4 Dirac gamma matrix bilinears $\{1, \gamma^\mu, \sigma^{\mu\nu}, \gamma^{\mu\nu\rho}, \gamma^{\mu\nu\rho\sigma}\}$ and the constraint relations emerge from the various Fierz identities connecting products of the Dirac bilinears. We list the set of relations (Eqs. L.0-S.r) that we find to be valid while maintaining the equation-numbering as in Chiang-Tabakin [93]:

$$\begin{aligned} 1 = \{&\Sigma^2 + T^2 + P^2 + E^2 + G^2 + F^2 + H^2 \\ &+ O_x^2 + O_z^2 + C_x^2 + C_z^2 + L_x^2 + L_z^2 + T_x^2 + T_z^2\}/3 \end{aligned} \tag{L.0}$$
$$\Sigma = TP + T_x L_z - T_z L_x \tag{L.tr}$$
$$T = \Sigma P - (C_x O_z - C_z O_x) \tag{L.br}$$
$$P = \Sigma T + GF - EH \tag{L.bt}$$
$$G = PF + O_x L_x + O_z L_z \tag{L.1}$$
$$H = -PE + O_x T_x + O_z T_z \tag{L.2}$$
$$E = -PH + C_x L_x + C_z L_z \tag{L.3}$$
$$F = PG + C_x T_x + C_z T_z \tag{L.4}$$
$$O_x = TC_z + GL_x + HT_x \tag{L.5}$$
$$O_z = -TC_x + GL_z + HT_z \tag{L.6}$$
$$C_x = -TO_z + EL_x + FT_x \tag{L.7}$$
$$C_z = TO_x + EL_z + FT_z \tag{L.8}$$
$$T_x = \Sigma L_z + HO_x + FC_x \tag{L.9}$$
$$T_z = -\Sigma L_x + HO_z + FC_z \tag{L.10}$$
$$L_x = -\Sigma T_z + GO_x + EC_x \tag{L.11}$$
$$L_z = \Sigma T_x + GO_z + EC_z \tag{L.12}$$
$$0 = C_x O_x + C_z O_z - EG - FH \tag{Q.b}$$
$$0 = GH + EF - L_x T_x - L_z T_z \tag{Q.t}$$
$$0 = C_x C_z + O_x O_z - L_x L_z - T_x T_z \tag{Q.r}$$
$$0 = -\Sigma G + TF + O_z T_x - O_x T_z \tag{Q.bt.1}$$
$$0 = -\Sigma H - TE - O_z L_x + O_x L_z \tag{Q.bt.2}$$
$$0 = \Sigma E + TH - C_z T_x + C_x T_z \tag{Q.bt.3}$$
$$0 = -\Sigma F + TG - C_z L_x + C_x L_z \tag{Q.bt.4}$$

$$0 = -\Sigma O_x + PC_z - GT_z + HL_z \quad \text{(Q.br.1)}$$
$$0 = -\Sigma O_z - PC_x + GT_x - HL_x \quad \text{(Q.br.2)}$$
$$0 = -\Sigma C_x - PO_z - ET_z + FL_z \quad \text{(Q.br.3)}$$
$$0 = -\Sigma C_z + PO_x + ET_x - FL_x \quad \text{(Q.br.4)}$$
$$0 = TT_x - PL_z - HC_z + FO_z \quad \text{(Q.tr.1)}$$
$$0 = TT_z + PL_x + HC_x - FO_x \quad \text{(Q.tr.2)}$$
$$0 = TL_x + PT_z - GC_z + EO_z \quad \text{(Q.tr.3)}$$
$$0 = TL_z - PT_x + GC_x - EO_x \quad \text{(Q.tr.4)}$$
$$1 = G^2 + H^2 + E^2 + F^2 + \Sigma^2 + T^2 - P^2 \quad \text{(S.bt)}$$
$$1 = O_x^2 + O_z^2 + C_x^2 + C_z^2 + \Sigma^2 - T^2 + P^2 \quad \text{(S.br)}$$
$$1 = T_x^2 + T_z^2 + L_x^2 + L_z^2 - \Sigma^2 + T^2 + P^2 \quad \text{(S.tr)}$$
$$0 = G^2 + H^2 - E^2 - F^2 - O_x^2 - O_z^2 + C_x^2 + C_z^2 \quad \text{(S.b)}$$
$$0 = G^2 - H^2 + E^2 - F^2 + T_x^2 + T_z^2 - L_x^2 - L_z^2 \quad \text{(S.t)}$$
$$0 = O_x^2 - O_z^2 + C_x^2 - C_z^2 - T_x^2 + T_z^2 - L_x^2 + L_z^2 \quad \text{(S.r)}$$

The above relations have been numerically verified by assigning random values to the four complex L_i amplitudes and calculating the polarizations employing Eqs. 8.41a-p. The relations consisting of only squares of the observables (Eqs. L.0 and S.bt-S.r) have no sign ambiguities. However, the signs in the remaining set of relations depend on the conventions adopted while defining the polarizations.

8.2 Sign Conventions for Polarization Observables

There appears to be some disagreement between different groups in the sign conventions for the polarizations, most likely arising from differences in the physics motivation. For example, in the CLAS C_x/C_z measurements for $K^+\Lambda$ photoproduction [108], it was found that $C_z \to +1$ at $\vartheta^{K^+}_{\text{c.m.}} \to 0$ and C_z was seen as the *spin*-transfer from a right-handed circularly polarized photon to the recoiling baryon. Other groups [104] prefer to have $C_z \to +1$ at $\vartheta^{\Lambda}_{\text{c.m.}} \to 0$, with the interpretation that C_z is the transfer of *helicity* from a right-handed circularly polarized photon to the Λ. Whatever be the choice of convention, the important issue is that the intensity profile the experimentalist uses must match with the asymmetry definitions that give the amplitude-level expressions. This point was detailed in Sec. 8.1.11. We also note that except for a sign flip for the variable E, our consistency relations match those found by Sandorfi *et al.* in Ref. [163].

8.2.1 The translation "dictionary"

In this work, we are following the FTS sign conventions as enlisted in Appendix A of the FTS paper [94]. It is important to note here that FTS first gives the definitions as *asymmetries*, which we agree with. Next, FTS also gives their definitions in the density matrix langauge. As pointed out earlier in Secs. 8.1.6B and 8.1.6C, for the double-polarization observables with a linearly polarized beam, *viz.*, G, H, O_x and O_z, these FTS *density matrix expressions should have extra negative signs.* Therefore, except for these extra four sign flips, the conventions in this current work (CMU) agree with FTS.

To find how our signs relate to those from the work of other authors, the simplest way is to do a term-by-term check of what signs the different polarization observables carry in the full intensity expression. In our case, this is given by Eq. 8.25. Making comparisons with the corresponding expressions for SAID/MAID [104] and EBAC [163], we arrive at the following translation "dictionary" for the signs:

1. CMU/FTS $\leftrightarrow$ SAID/MAID : flip signs of H, E, C_x, C_z, O_x, O_z and L_x.
2. CMU/FTS $\leftrightarrow$ EBAC : flip sign of E.

For the experimentalist, we urge that the particular sign convention chosen be clearly mentioned and care be taken that the "para" and "perp" definitions are correctly adhered to in going from ϕ to φ (as defined in Fig. 8.2). Also, while showing the full intensity profile, it should be clearly mentioned which of the angles ϕ and φ is being referred to.

8.3 "Traditional" methods of extracting P_Σ

Once the production amplitudes L_i's are extracted by a Partial Wave Analysis (PWA), the recoil polarization can be extracted by directly employing Eq. 8.41b. We will denote this as the "PWA" method of extracting P_Σ.

The more conventional methods of extracting polarizations involve a fit to an intensity distribution, such as given in Eq. 8.25. To derive the requisite intensity destribution, we need to first define what we mean by the "helicity frame" of a particle. The helicity frame (HF) of any particle is given by an initial rotation that aligns its direction of motion along the z-axis, followed by a subsequent boost to its rest frame. $\theta^p_{\Lambda HF}$ is then defined as the angle between the proton and the Λ momenta, as measured in the Λ helicity frame, while $\theta^\Lambda_{\Sigma HF}$ is the angle between the normal to the production plane (assumed to be the y-axis) and the Λ direction, as measured in the Σ^0 helicity frame. A pictorial description of these two angles is given in Fig. 8.3. Fig. 8.3a shows $\gamma p \to K^+\Sigma^0$ reaction in the c.m. frame, where the z-axis is along the beam direction and the y-axis is normal to the production plane. As mentioned earlier, if both the beam and target are unpolarized, as in the case of $g11a$, parity considerations imply that the induced Σ^0 polarization can only be along the normal to the production plane. This is shown by the bold arrow in red in Fig. 8.3a.

To go the Σ^0 helicity frame from the c.m. frame, we first rotate our system so that the Σ^0 momentum points along the z-axis and then perform a boost to the Σ^0 rest frame. Fig. 8.3b shows the $\Sigma^0 \to \Lambda\gamma$ decay in the Σ^0 helicity frame. Since the outgoing photon (shown by the dotted arrow) was not detected in our experiment, the polarization transfer from the Σ^0 to the Λ is given by (see Sec. 8.4 for a derivation)

$$P_\Lambda = -P_\Sigma \cos\theta^\Lambda_{\Sigma HF}. \tag{8.42}$$

Note that in terms of spin structure, the $\Sigma^0 \to \Lambda\gamma$ reaction is a $\frac{1}{2} \to \frac{1}{2} \oplus 1$ decay, while Eq. 8.42 is obtained after averaging over the spin projections of the unobserved outgoing photon. Thus, there is a step of "dilution" in the accessible Σ^0 spin information that occurs here. In the next step, we go to the Λ helicity frame from the Σ^0 helicity frame by making a rotation that aligns the z-axis with the Λ direction, followed by a boost to the Λ rest frame. The $\Lambda \to p\pi^-$ decay (see Fig. 8.3c) is a *self-analyzing* reaction. That is, the Λ polarization information is contained in the intensity distribution as

$$\mathcal{I} \sim (1 + \alpha P_\Lambda \cos\theta^p_{\Lambda HF}), \tag{8.43}$$

where $\alpha = 0.642 \pm 0.013$ is the Λ weak decay asymmetry [53]. Combining Eqs. 8.42 and 8.43, the final intensity distribution is given as

$$\mathcal{I} \sim (1 - \alpha P_\Sigma \cos\theta^\Lambda_{\Sigma HF} \cos\theta^p_{\Lambda HF}). \tag{8.44}$$

Traditionally, the extraction of P_Σ has been made using this intensity distribution.

In addition to the "dilution" mentioned earlier, a further step of "dilution" occurs if one does not have access to the Λ momentum. It can be shown (see Appendix A in Ref. [108]) that if the Σ^0-Λ spin-transfer information is averaged over, then Eq. 8.44 is replaced by

$$\mathcal{I} \sim (1 - \nu\alpha P_\Sigma \cos\theta^p_{\Sigma HF}), \tag{8.45}$$

where $\theta^p_{\Sigma HF}$ is the angle between the outgoing proton's momentum and the normal to the $K^+\Sigma^0$ production plane as measured in the Σ^0 helicity frame and $\nu \approx \frac{1}{3.90}$ is a "dilution factor". Since the π^- from the Λ decay was not detected in the two-track topology, the Λ momentum could not be reconstructed. Therefore, Eq. 8.45 applies instead of Eq. 8.44 for the two-track topology.

8.4 Polarization Transfer Between Σ^0-Λ

In this section we give the proof for Eq. 8.42; that is, in the electromagnetic decay $\Sigma^0 \to \Lambda\gamma$, *if we do not measure the final photon polarization*, then *in the* Σ^0 *rest frame*, the polarizations of the Λ and the Σ^0 are related as

$$\langle \vec{P}_\Lambda \rangle = -\left(\langle \vec{P}_\Sigma \rangle \cdot \hat{p}_\Lambda\right) \hat{p}_\Lambda, \tag{8.46}$$

where $\langle \vec{P}_\Lambda \rangle$ and $\hat{p}_\Lambda$ are the polarization and direction respectively of the produced Λ and $\langle \vec{P}_\Sigma \rangle$ is the initial polarization of the decaying Σ^0. The proof apprears in several places [105, 106] and we will sketch the one given by Feldman and Fulton here.

The starting point is Eq. 5.61. Since we are dealing with mixed states we need to take the density matrix approach to find expectation values. The initial density matrix for the Σ^0 with polarization $\vec{P}_\Sigma$ is given by

$$\rho = \frac{1}{2}\left(1 + \langle \vec{P}_\Sigma \rangle \cdot \vec{\sigma}\right) \tag{8.47}$$

where the σ's are the usual Pauli matrices and $\vec{\sigma} = \langle \sigma_x, \sigma_y, \sigma_z \rangle$. The expectation value of the Λ polarization is then given as

$$\langle \vec{P}_\Lambda \rangle = \frac{\mathrm{Tr}\left[T\rho T^\dagger \vec{\sigma}\right]}{\mathrm{Tr}\left[T\rho T^\dagger\right]} = \frac{\mathrm{Tr}\left[TT^\dagger\vec{\sigma} + T\langle \vec{P}_\Sigma \rangle T^\dagger \vec{\sigma}\right]}{\mathrm{Tr}\left[TT^\dagger + T\langle \vec{P}_\Sigma \rangle T^\dagger\right]}. \tag{8.48}$$

where T is the transition matrix for $\Sigma^0 \to \Lambda\gamma$ and $T\rho T^\dagger$ is the final density matrix for the Σ^0.

To evaluate this expression we will need the following properties of the Pauli matrices

$$\begin{aligned}
\sigma^\dagger &= \sigma \text{ (Hermitian)} && \text{(8.49a)}\\
\mathrm{Tr}[\sigma_i] &= 0 \text{ (traceless)} && \text{(8.49b)}\\
\mathrm{Tr}[\sigma_i\sigma_j] &= 2\delta_{ij}, \text{ from which it follows} && \text{(8.49c)}\\
\mathrm{Tr}[(\vec{u}\cdot\vec{\sigma})\,\vec{\sigma}] &= 2\vec{u} && \text{(8.49d)}\\
(\vec{u}\cdot\vec{\sigma})\,(\vec{v}\cdot\vec{\sigma}) &= (\vec{u}\cdot\vec{v})\,I + i\,(\vec{u}\times\vec{v})\cdot\vec{\sigma}, \text{ which leads to} && \text{(8.49e)}\\
\mathrm{Tr}[(\vec{u}\cdot\vec{\sigma})(\vec{v}\cdot\vec{\sigma})] &= 2(\vec{u}\cdot\vec{v}) \text{ and} && \text{(8.49f)}\\
\mathrm{Tr}[(\vec{u}\cdot\vec{\sigma})\,(\vec{v}\cdot\vec{\sigma})\,\vec{\sigma}] &= 2i\,(\vec{u}\times\vec{v}) && \text{(8.49g)}\\
\mathrm{Tr}[(\vec{u}\cdot\vec{\sigma})\,(\vec{v}\cdot\vec{\sigma})\,(\vec{w}\cdot\vec{\sigma})] &= 2i\vec{w}\cdot(\vec{u}\times\vec{v}) && \text{(8.49h)}\\
\mathrm{Tr}[(\vec{u}\cdot\vec{\sigma})\,(\vec{v}\cdot\vec{\sigma})\,(\vec{w}\cdot\vec{\sigma})\,\vec{\sigma}] &= 2\left[(\vec{u}\cdot\vec{v})\,\vec{w} + (\vec{w}\cdot\vec{v})\,\vec{u} - (\vec{w}\cdot\vec{u})\,\vec{v}\right] && \text{(8.49i)}
\end{aligned}$$

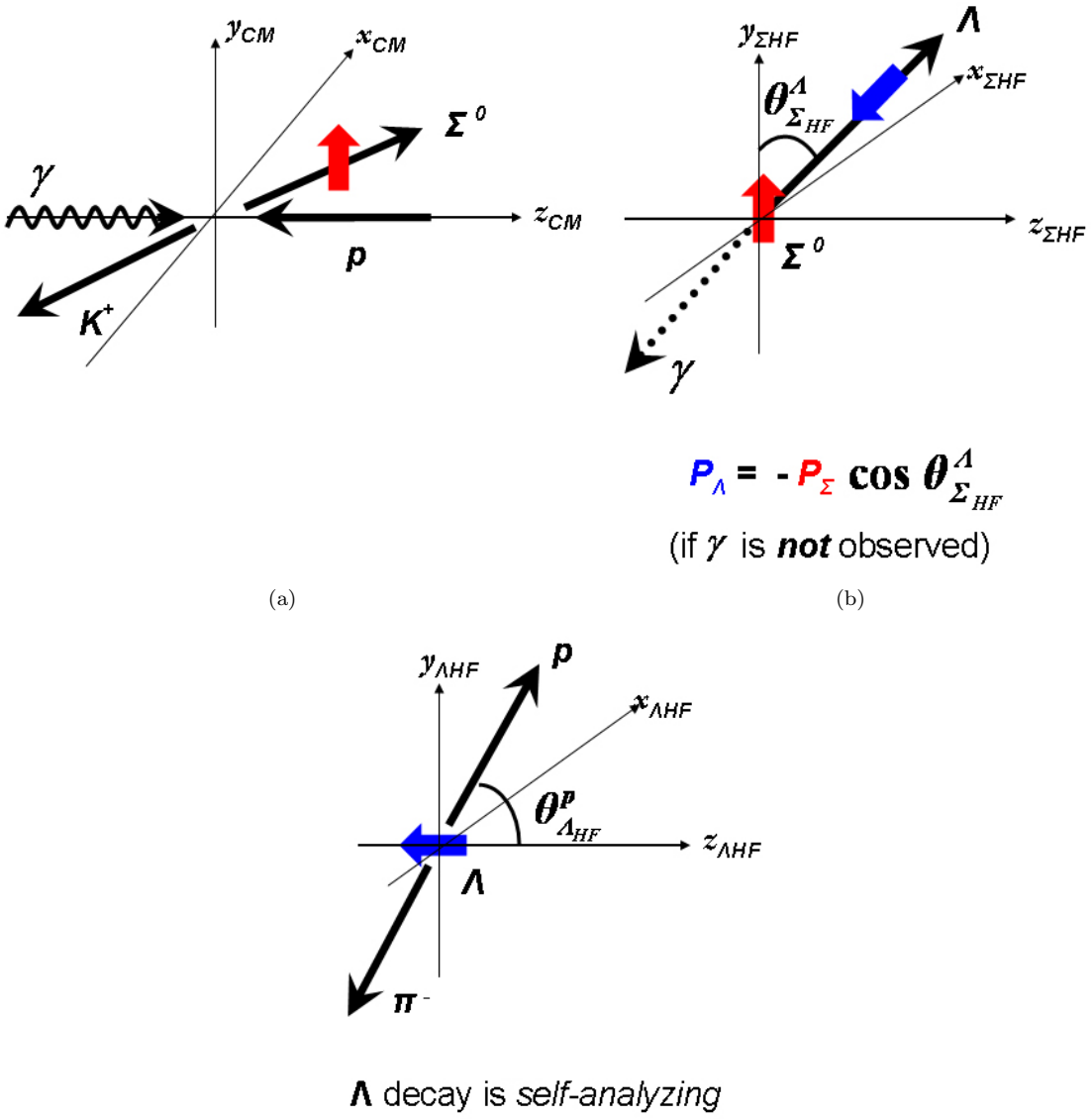

Figure 8.3: A pictorial representation of the helicity angles $\theta^{\Lambda}_{\Sigma_{HF}}$ and $\theta^{p}_{\Lambda_{HF}}$ and the polarization transfer between the Σ^0 and the Λ. (a) Shows the $\gamma p \to K^+\Sigma^0$ reaction in the c.m. frame with the y-axis as the normal to the production plane. The only component of the induced Σ^0 spin measurable in the current experiment is along the normal to the production plane, shown by the bold arrow in red. (b) Shows the $\Sigma^0 \to \Lambda\gamma$ decay in the Σ^0 helicity frame and (c) shows the $\Lambda \to p\pi^-$ decay in the Λ helicity frame. See text for details.

Going back to Eq. 5.61, we had chosen the polarization 3-vectors as the positive and negative helicity vectors $\vec{\epsilon}_\pm = (1/\sqrt{2})(\vec{\epsilon}_1 i \pm \vec{\epsilon}_2)$ where $\vec{\epsilon}_1$ and $\vec{\epsilon}_2$ are orthogonal unit vectors in the plane transverse to the photon momentum $\vec{p}_\gamma$ such that $\vec{\epsilon}_1 \times \vec{\epsilon}_2 = \hat{p}_\gamma$. We then showed that the photon "spin" is along its direction of motion and can be expresed in terms of the the $\vec{\epsilon}_\pm$ components of the photon field. The helicity vectors have the following properties

$$
\begin{aligned}
(\vec{\epsilon}_\pm)^* &= \vec{\epsilon}_\mp && (8.50a)\\
\vec{\epsilon}_\pm \times \hat{p}_\gamma &= \pm i\vec{\epsilon}_\pm && (8.50b)\\
\vec{\epsilon}_+ \cdot \vec{\epsilon}_+ = \vec{\epsilon}_- \cdot \vec{\epsilon}_- &= 0 && (8.50c)\\
\vec{\epsilon}_+ \cdot \vec{\epsilon}_- &= 1, \text{ so that} && (8.50d)\\
|\vec{\epsilon}_\pm| = (\vec{\epsilon}_\pm)^* \cdot \vec{\epsilon}_\mp &= 1 && (8.50e)\\
\vec{\epsilon}_+ \times \vec{\epsilon}_- &= -i\vec{p}_\gamma && (8.50f)
\end{aligned}
$$

Then in Eq. 5.61, we see that the transition matrix T goes like $(\vec{\epsilon} \times \vec{p}_\gamma) \cdot \vec{\sigma}$. So if $\vec{\epsilon}$ is one of $\vec{\epsilon}_{1,2}$ then $T_{1,2} \sim \vec{\epsilon}_{2,1} \cdot \vec{\sigma}$ and if it is one of $\vec{\epsilon}_\pm$ then $T_\pm \sim \vec{\epsilon}_\pm \cdot \vec{\sigma}$. Note that $\mathrm{Tr}[TT^\dagger] = 2\vec{\epsilon} \cdot \vec{\epsilon}^* \sim 1$ for either case so that unitarity of the scattering matrix is maintained. For ease of computation, since they are real, we will use the $\vec{\epsilon}_{1,2}$ basis for the rest of the computation.

Then, putting it all together, the numerator of Eq. 8.48 becomes

$$
\mathrm{Tr}[(\vec{\epsilon} \cdot \vec{\sigma})\,(\vec{\epsilon} \cdot \vec{\sigma})\vec{\sigma}] + \mathrm{Tr}[(\vec{\epsilon} \cdot \vec{\sigma})\,(\langle \vec{P}_\Sigma \rangle \cdot \vec{\sigma})\,(\vec{\epsilon} \cdot \vec{\sigma})\,\vec{\sigma}] = 4(\vec{\epsilon} \cdot \hat{P}_\Sigma)\hat{\epsilon} - 2\langle \hat{P}_\Sigma \rangle, \tag{8.51}
$$

while the denominator is

$$
\mathrm{Tr}[(\vec{\epsilon} \cdot \vec{\sigma})(\vec{\epsilon} \cdot \vec{\sigma})] + \mathrm{Tr}[(\vec{\epsilon} \cdot \vec{\sigma})(\vec{P}_\Sigma \cdot \vec{\sigma})(\vec{\epsilon} \cdot \vec{\sigma})] = 2. \tag{8.52}
$$

Thus for the two polarization states $\vec{\epsilon}_1$ and $\vec{\epsilon}_2$

$$
\langle \vec{P}_{\Lambda,\vec{\epsilon}_{1,2}} \rangle = -\langle \vec{P}_\Sigma \rangle + 2(\vec{\epsilon}_{2,1} \cdot \vec{P}_\Sigma)\vec{\epsilon}_{2,1} \tag{8.53}
$$

If we fix our cordinate axes as $\hat{x} = \vec{\epsilon_1}$, $\hat{y} = \vec{\epsilon_2}$ and $\hat{z} = \hat{p}_\Lambda$ the above two equations take the form

$$
\begin{aligned}
\langle \vec{P}_{\Lambda,\vec{\epsilon}_2} \rangle &= -\vec{P}_\Sigma + 2(\vec{P}_\Sigma)_x \hat{x} \text{ and} && (8.54a)\\
\langle \vec{P}_{\Lambda,\vec{\epsilon}_1} \rangle &= -\vec{P}_\Sigma + 2(\vec{P}_\Sigma)_y \hat{y}. && (8.54b)
\end{aligned}
$$

Averaging over the two photon polarizations immediately gives

$$
\langle \vec{P}_\Lambda \rangle = -\langle \vec{P}_\Sigma \rangle_z \hat{z} = -(\langle \vec{P}_\Sigma \rangle \cdot \hat{p}_\Lambda)\hat{p}_\Lambda. \tag{8.55}
$$

8.5 Preliminary Measurement Results and Discussion

For the three-track topology, we have then at our disposal two equivalent ways of extracting the polarizations – the "traditional" way using Eq. 8.44, or the PWA method (Eq. 8.41b) using the Mother Fit results from Ch. 6. However, before embarking on that, we need to reconsider our binning first to ensure that we have enough statistics for every polarization extraction point. Recall that earlier we binned the data very finely in 10 MeV $\sqrt{s}$ bins. The final distribution of "good" (Q-value weighted)

data events after this binning is shown in Fig. 3.25a for the three-track dataset.

This is however not the complete story, because we are dealing with an essentially two dimensional problem here (in $\sqrt{s}$ and $\cos\theta^{K^+}_{\rm c.m.}$). In the higher $\sqrt{s}$ bins, most of the events are very forward peaked, and thus, assymetrically distributed in $\cos\theta^{K^+}_{\rm c.m.}$ as apparent from Fig. 8.4a.

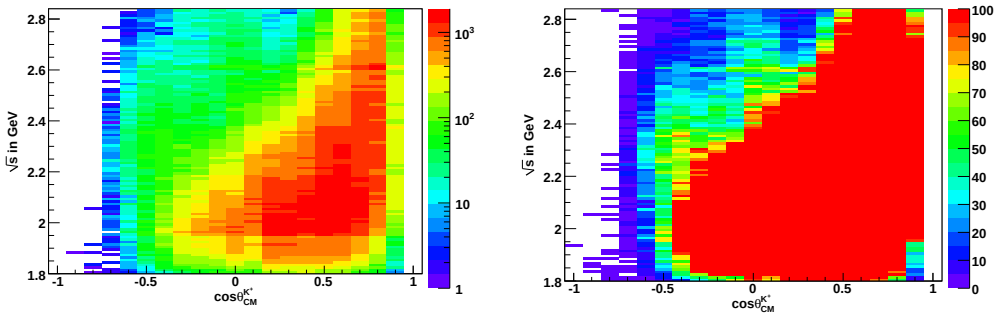

Figure 8.4: Q-value (from background subtraction fits) weighted data occupancies in both $\sqrt{s}$ and $\cos\theta^{K^+}_{\rm c.m.}$ for the three-track dataset: (a) log scale (b) normal scale with a cap at 100 events. Binning in both axes was set according to how we binned our data in $\sqrt{s}$ and where we extracted differential cross sections in $\cos\theta^{K^+}_{\rm c.m.}$. See text for details.

The y-axis bins in this plot are 10 MeV wide in $\sqrt{s}$ with bin centers at 1.805 GeV, 1.815 GeV, ..., 2.835 GeV and the x-axis bins are 0.1 wide in $\cos\theta^{K^+}_{\rm c.m.}$ with bin centers at -1.0, -0.9, ..., 1.0. That is, the binning is set according to where we measured our differential cross sections. If we now look at the same histogram but place an upper cap on the occupancy at 100 events (Fig. 8.4b), we see that a lot of these bins have much fewer than 50 "good" events. If we tried to extract the polarizations in these regions with our present binning, we would be severely limited by statistics. We thus need to find a plausible way to merge our bins. To do this, we preserve the same 0.1 binning in $\cos\theta^{K^+}_{\rm c.m.}$ but use wider bins in $\sqrt{s}$. Also, guided by Fig. 8.4a, we will limit our $\cos\theta^{K^+}_{\rm c.m.}$ bin center range from -0.5 to 0.9 for our polarization extractions.

Fig. 8.5 shows the extracted polarizations with our initial 10 MeV wide $\sqrt{s}$ binning. The errors (estimated from the scatter between adjacent $\sqrt{s}$ bins) seem large, but the gross structures are clearly evident. It is to be noted here that we are limited not only by statistics but also by the fact in the Σ^0 decay, with spin-1/2 going to spin-1/2 plus spin-1, we are not observing the spin-1 particle (the "missing" outgoing photon). Thus, the polarization information in Eq. 8.44 is "diluted". For example, for $\cos\theta^{K^+}_{\rm c.m.} = 0.8$ in Fig. 8.5, where we have excellent statistics for most $\sqrt{s}$, the polarizations are not as smooth as might have been expected.

8.6 Re-binned Polarizations

To choose an optimal binning such that we have reasonable statistics while retaining as fine a $\sqrt{s}$ binning as possible, we tried setting a minimum $\sqrt{s}$ bin-width of 20 and then 30 MeV, and required a minimum number of "good" events to be present per bin. The latter was gradually varied from 50, 75, ..., to 500 events per bin. We found that a 30 MeV minimum $\sqrt{s}$ bin-width and a minimum

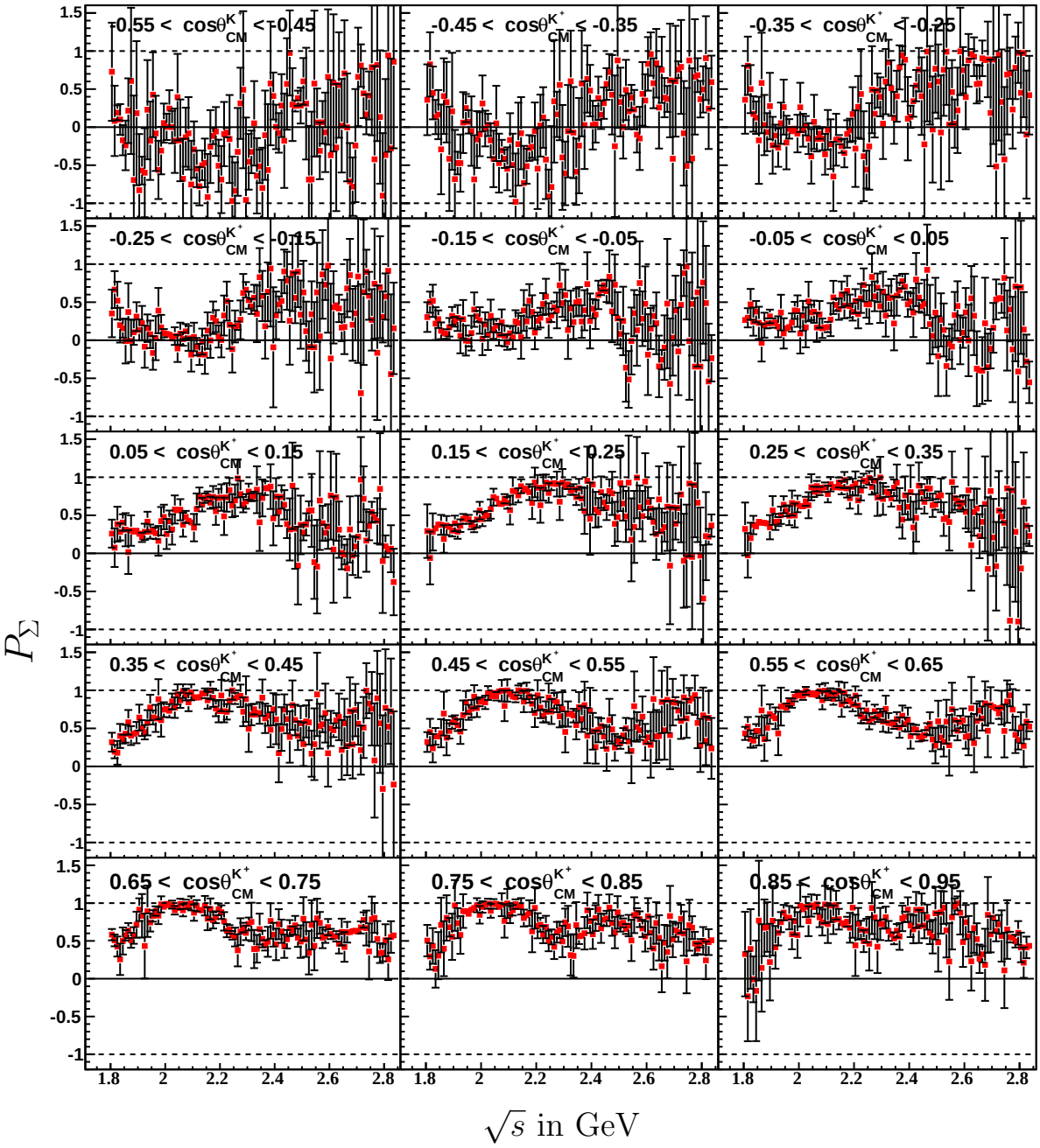

Figure 8.5: P_Σ from the PWA extraction method with 10 MeV wide $\sqrt{s}$ binning. The error bars are derived from the scatter between adjacent $\sqrt{s}$ bins. The large errors arise from the small statistics and mean that we need coarser binning in $\sqrt{s}$.

requirement of 200 events per bin was optimal. Fig. 8.6 shows the polarizations after merging bins according to this criterion. The scatter in the points are much less now and the overall structures evolve quite smoothly.

8.6.1 Statistical Error Estimation for the PWA method

Unfortunately, there is no *a priori* way of estimating the statistical errors in the PWA method of polarization extraction. Ideally, in an asymmetry measurement, one needs to know $N_\pm$ *separately* to estimate the statistical errors. In our case, we are extracting the polarization information by *fitting to a distribution*, without directly measuring $N_\pm$. The error bars in Figs. 8.5 and 8.6 have been estimated by looking at the scatter between adjacent $\sqrt{s}$ points inside a given $\cos\theta^{K^+}_{\rm c.m.}$ bin. This method was also used in previous $g11a$ PWA analyses like $p\omega$, $K^+\Lambda$, *et al* [51, 26] and gave reasonable results. The statistics in those channels were high enough to maintain a 10 MeV $\sqrt{s}$ binning. The scatter estimate, although *ad hoc*, appeared reasonable because the physics should remain essentially the same between two $\sqrt{s}$ points just 10 MeV apart. Thus the scatter in the recoil polarization measurements should mainly arise out of statistical fluctuations.

In our case, even though the $\sqrt{s}$ binning is not as fine after our re-binning, as we show below, this *ad hoc* method gives a good error estimate. The final statistical errors we will quote are from a more direct estimation, as explained in Sec. 8.8.

8.7 "Traditional" Method Polarizations

Fig. 8.7 shows the polarizations extracted using the "traditional" way of fitting the data to the intensity profile appearing in Eq. 8.44 (plotted in blue) and compared to the PWA results (in red). The fits were run using the unbinned maximum likelihood method and the errors are the errors that Minuit provides. The agreement between the two methods is remarkable (especially in regions of good statistics). This underscores the fact that the underlying physics is the same.

Note that, *by definition*, the polarizations from the PWA method are bound between ±1, while the "traditional" method involves a fit to a slope and can jump beyond the physical limits, as evident from some of the bins in Fig. 8.7. If we constrain the fit to remain within ±1, we found the reults to always cap off at ±1 if the unconstrained result was already beyond ±1. Thus, no new information is gained by constraining the fits in this fashion.

The "traditional" method seems to be somewhat overestimating the polarizations in the forward-most angular bin. The reason is two-fold. Firstly, the statistics is not as good here as the next lower couple of angular bins. Secondly, note that the polarizations are typically very high in this region. In the PWA method, for a particular $\sqrt{s}$ bin, we fit over the entire $\cos\theta^{K^+}_{\rm c.m.}$ range as a whole. Thus, the polarization results at a particular $\sqrt{s}$ and $\cos\theta^{K^+}_{\rm c.m.}$ is somewhat constrained by the PWA fit results in the neighbouring angular bins for the same $\sqrt{s}$. Since our angular binning is quite fine (0.1 in $\cos\theta^{K^+}_{\rm c.m.}$), we expect the physics to be continuous between adjacent angular bins, which is exactly what the PWA method results show. For the traditional method, fits to the intensity profile are run independently in a particular $\sqrt{s}$ and $\cos\theta^{K^+}_{\rm c.m.}$ bin. Thus, these results are less constrained than the PWA results and for a high degree of polarization, tends to overestimate at the forward-most angles.

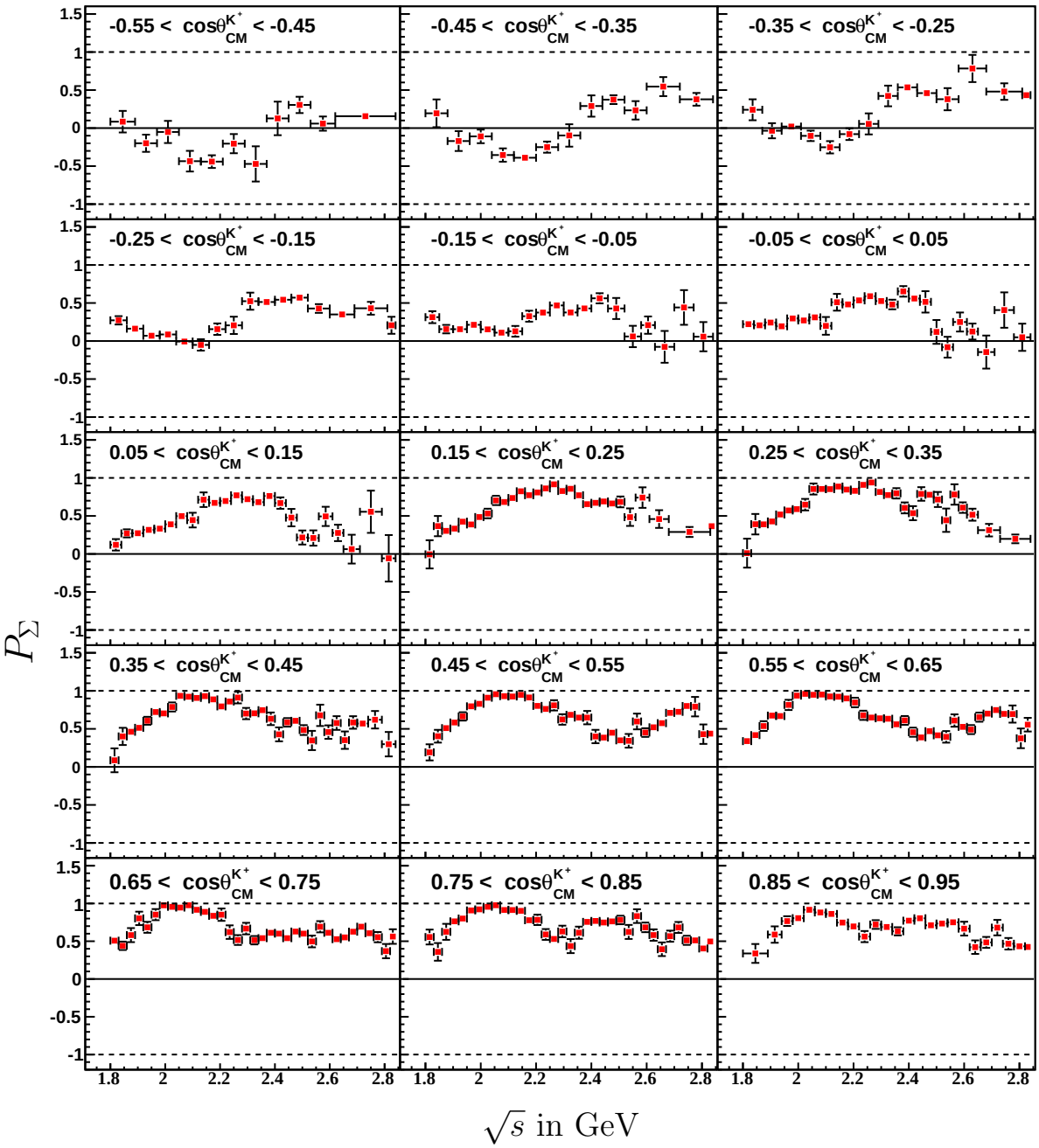

Figure 8.6: Re-binned P_Σ from the PWA extraction method. Every point is at least 30 MeV wide in $\sqrt{s}$ and has a minimum of 200 events. Error estimates are from the scatter between adjacent $\sqrt{s}$ bins.

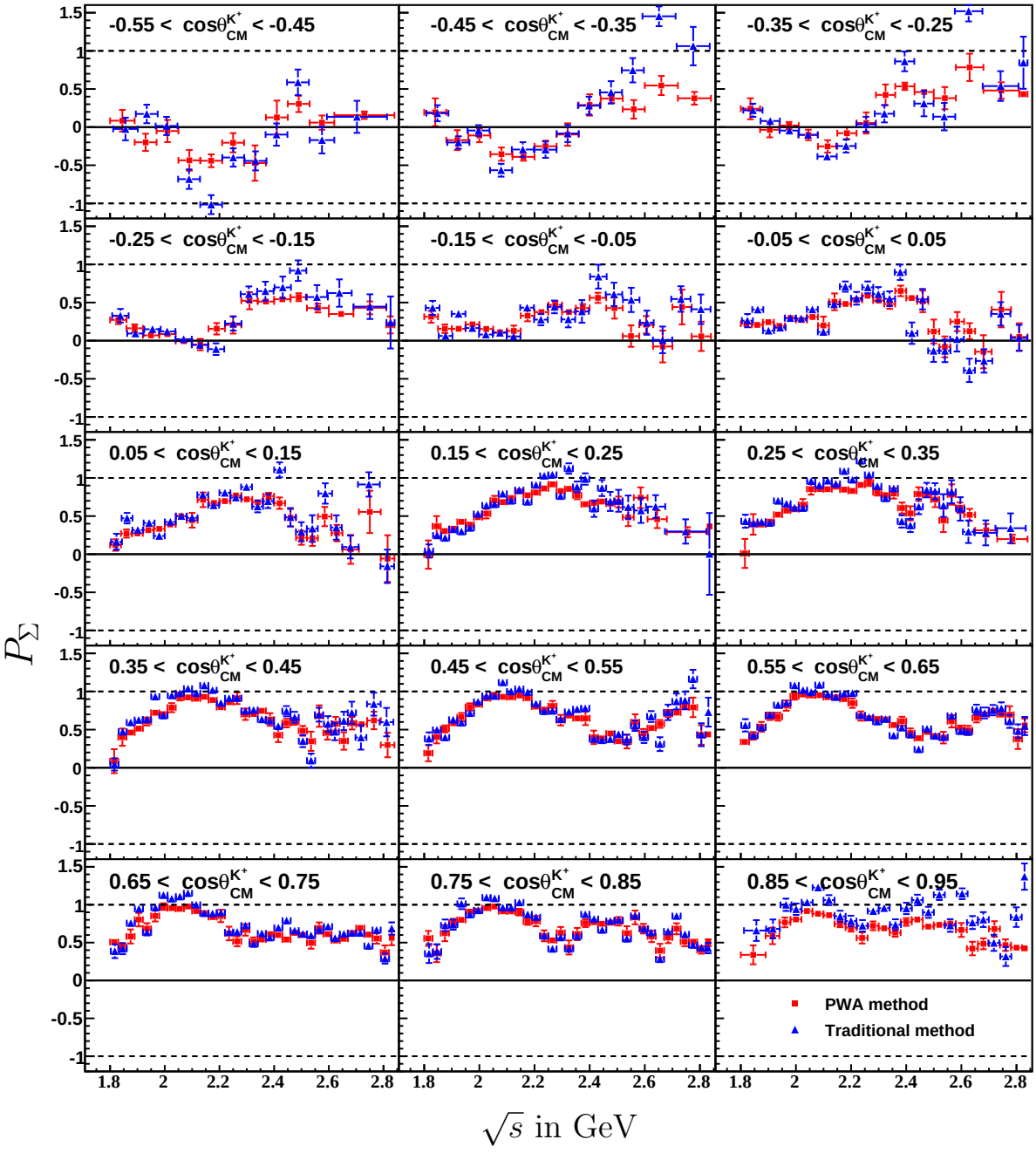

Figure 8.7: Compare P_Σ obtained from the PWA method (**red** squares) versus the "traditional" method (**blue** up-triangles). Within the statistical uncertainties, the agreement is excellent. The forward-most angle bin is both statistics limited and is highly polarized. The "traditional" method seems to be systematically overestimating the polarizations here. Errors for the PWA method are from the scatter between adjacent $\sqrt{s}$ bins while for the "traditional" method, they are the Minuit errors.

8.8 Final Polarization Results and Statistical Errors

8.8.1 Three-track results

It is clear from the previous sections that the two methods for polarization extraction agree very well with each other in regions of high statistics. The advantage of the PWA method lies in the polarizations being within the physical limits of ± 1 and also because of the reasons outlined in latter part of the last section. The disadvantage, however, is that there is no direct handle on the error estimates.

The polarizations from the "traditional" method, on the other hand, are less constrained, but here we have a direct access to the errors. Also, from Fig. 8.7, these errors are quite comparable to the PWA errors obtained from the scatter in the measured polarizations. This shows that the errors from Minuit in the "traditional" method are a true reflection of the statistical uncertainties.

With these considerations in mind, we will present our final recoil polarization measurements for the three-track dataset in the following fashion − the *values* of the polarizations will be the ones from the PWA method, while the statistical *errors* will be the errors obtained from the "traditional" method. Our final P_Σ measurements and the final estimated errors are shown in Figs. 8.13 and 8.14. A systematic account for differences between the two methods is given in Sec. 8.9.

8.8.2 Including Two-track results

We noted earlier that our P_Σ measurements from the intensity profile in Eq. 8.44 are already diluted because the polarization of the outgoing photon is not being measured. Going from Eq. 8.44 to Eq. 8.45 represents a further step of dilution. To check this effect, for the three-track dataset, we measured P_Σ using the "approximate" expression (using Eq. 8.45) and compared it to our previous measurements. The results are shown in Fig. 8.8 − the effect of the dilution is clear. Quantitatively, we plot distribution of the ratio

$$r = \frac{\sigma_{approx}}{\sigma_{original}} \tag{8.56}$$

in Fig. 8.9, where $\sigma_{original}$ (σ_{approx}) are the P_Σ errors from using Eq. 8.44 (Eq. 8.45). The peak at $r \approx 2.5$ indicates the degree of dilution introduced by averaging over the intermediate Λ directions.

Keeping in mind the above considerations, and the fact that the two-track dataset can use only the "approximate" expression for P_Σ extraction, we will quote results from the two-track analysis *only at those kinematic points where we do not have results from the three-track dataset* (recall that due to higher acceptance, the two-track dataset has a wider kinematic coverage than the three-track dataset). Though the two-track results have, in general, larger error bars than the three-track results, by including them, we are able to extend our $\sqrt{s}$ coverage till the the production threshold (~ 1.69 GeV) and our backward angle coverage all the way till $\cos\theta^{K^+}_{\rm c.m.} = -0.85$.

Our re-binning for the two-track dataset follows the method outlined in Sec. 8.6 for the three-track case. The only change is that instead of a minimum of 200 events, we now require at least 300 "good" events per kinematic point. While re-binning, we also ensure that the bin-edge around $\sqrt{s} \sim 1.8$ GeV is always *at* $\sqrt{s} = 1.8$ GeV for all values of $\cos\theta^{K^+}_{\rm c.m.}$, so that there is no overlap with the three-track dataset (which extends from $\sqrt{s} \geq 1.8$ GeV onwards). The 2-track P_Σ results appeared to be be unstable at the very backward angle bin, so we will not be presenting results for $\cos\theta^{K^+}_{\rm c.m.} = -0.9$. Our final kinematic coverage for P_Σ extraction is as follows:

$$\begin{aligned}
\text{Three-track} \quad &: \quad -0.55 \leq \cos\theta^{K^+}_{\rm c.m.} \leq 0.95, \ \text{AND}, \ 1.8 \text{ GeV} \leq \sqrt{s} \leq 2.84 \text{ GeV} \\
\text{Two-track} \quad &: \quad -0.85 \leq \cos\theta^{K^+}_{\rm c.m.} < -0.55, \ \text{OR}, \ 1.69 \text{ GeV} \leq \sqrt{s} < 1.8 \text{ GeV}
\end{aligned}$$

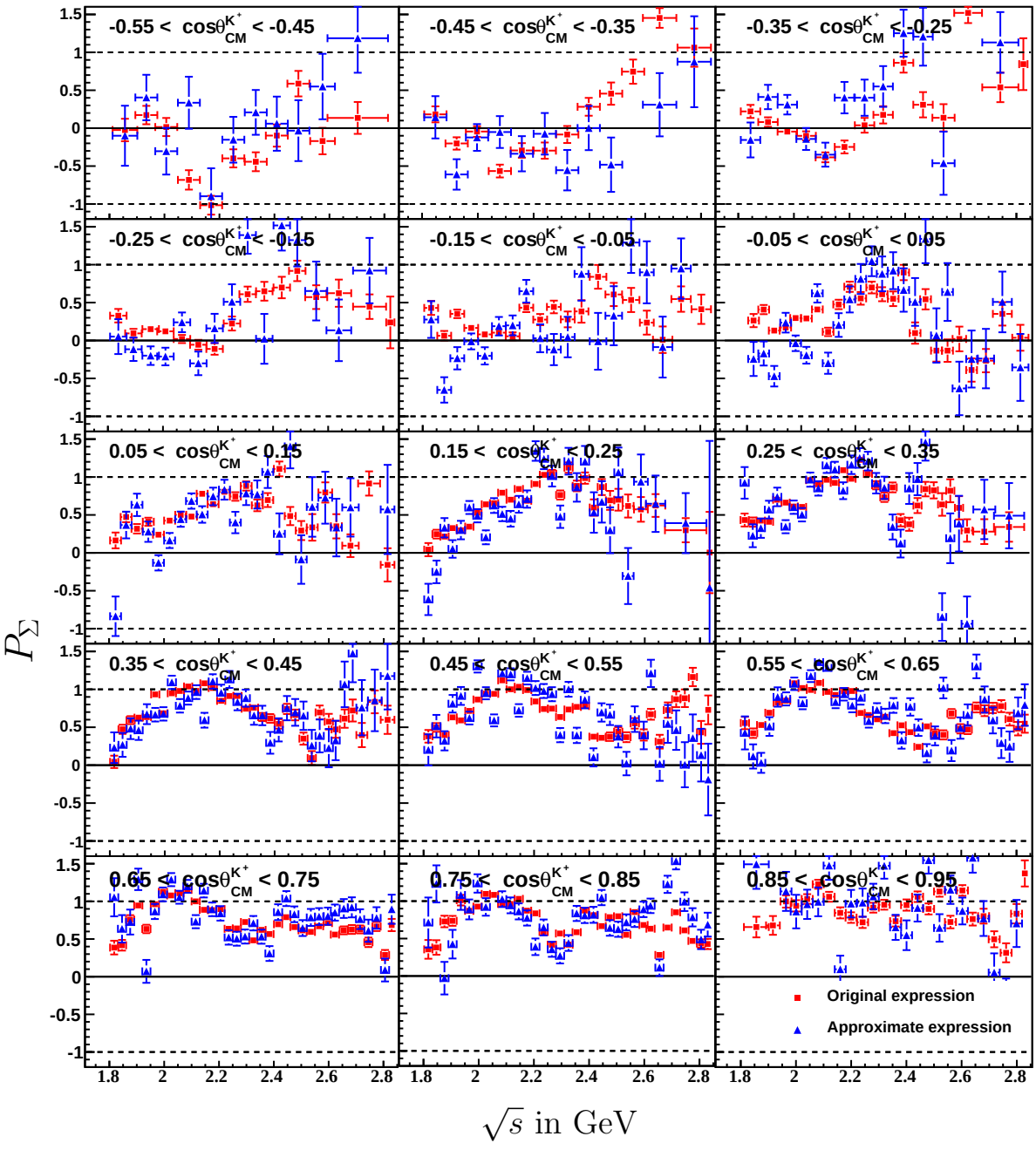

Figure 8.8: Compare P_Σ results for the three-track dataset: original expression using Eq. 8.44 (**red** squares) versus the approximate expression using Eq. 8.45 (**blue** up-triangles) for the three-track dataset. Both have the same binning in $\sqrt{s}$ and $\cos\theta^{K^+}_{\text{c.m.}}$ and utilized unbinned maximum likelihood fits, but the latter is more scattered, reflecting the effect of the "dilution".

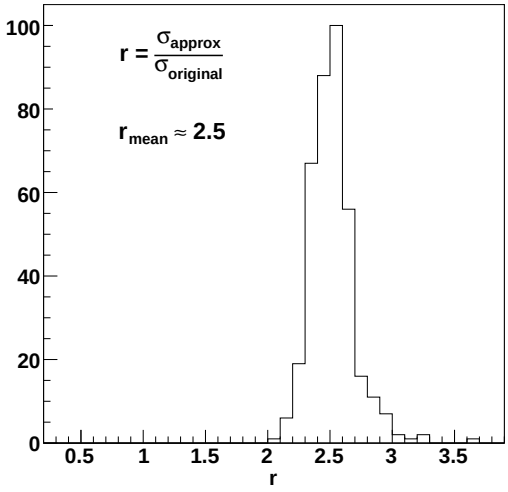

Figure 8.9: Distribution of the ratio between the errors in P_Σ measurements from the intensity profiles in Eqs. 8.44 and 8.45 for the three-track dataset.

In all, we present results at 472 independent kinematic points.

8.9 Systematic Error Estimation

The systematic errors for polarization measurements are of a different nature than those for the differential cross-sections. Since normalizations cancel out, the photon flux normalization does not conribute to the errors. We thus need only the systematic errors in our acceptance calculation. However, our acceptance calculation involved measuring the total yield N_{total} and not $N_\pm$ (yields for opposite spin orientations of the Σ^0). Thus, there is no straight-forward (or rigorous) way to calculate the polarization systematic errors.

As a reasonable estimate, we chose to look at the difference between the polarization results obtained from the two methods of polarization extraction for the three-track results − the PWA method and the "traditional" method. Since the underlying physics is the same, within statistical fluctuations, both methods should yield the same results. Fig. 8.12 shows the difference between the two measurements accumulated over the regions with reasonable statistics ($-0.05 \leq \cos\theta^{K^+}_{\rm c.m.} \leq 0.85$). A Gaussian fit to the distribution gives a mean $\mu \sim -0.028$ and a width $\sigma \sim 0.1$. The width is due to statistical fluctuations, while the mean represents an overall *systematic* shift, and its absolute value will be quoted as our systematic error. As a check, we note that systematic errors in polarizations from previous CLAS analyses using the same dataset ($p\omega$ [51], $K^+\Lambda$ [26], *et al*) were in the same range. Since the systematic errors are ultimately dependent on the detector acceptance, 2.8% is reasonable estimate for the $K^+\Sigma^0$ channel as well. For the two-track results, to incorporate the dilution in averaging over the Λ directions, we include a $(1 + r)$ multiplicative factor, where $r = 2.5$ from Fig. 8.9.

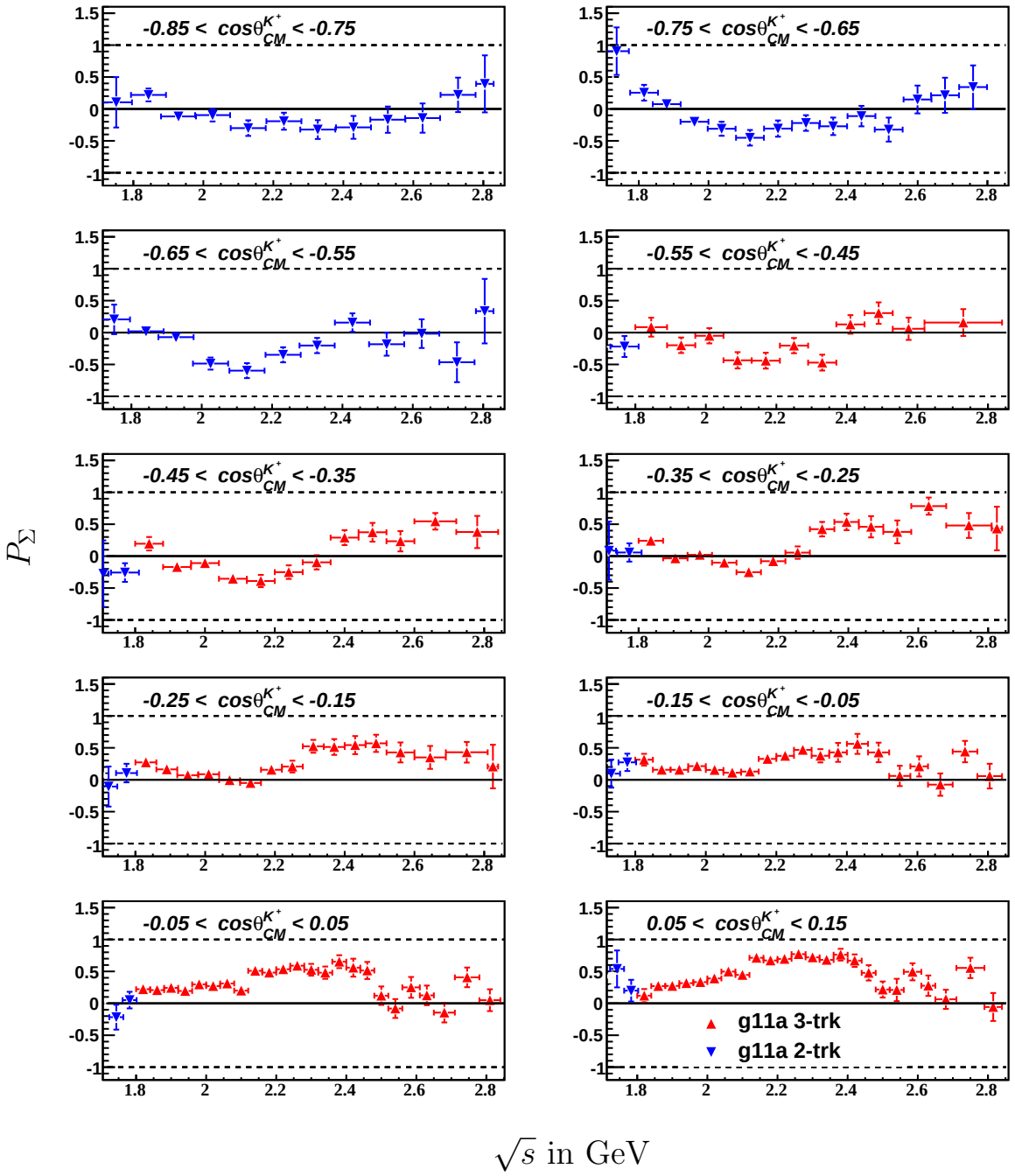

Figure 8.10: Final recoil polarization results from the CLAS $g11a$ dataset. Apart from the very backward angles and near-threshold regions, results are available from the 3-track dataset (in red). In the remaining kinematic regions, we present results from the 2-track topology (in blue), which involves an averaging over the Σ^0-Λ spin transfer information.

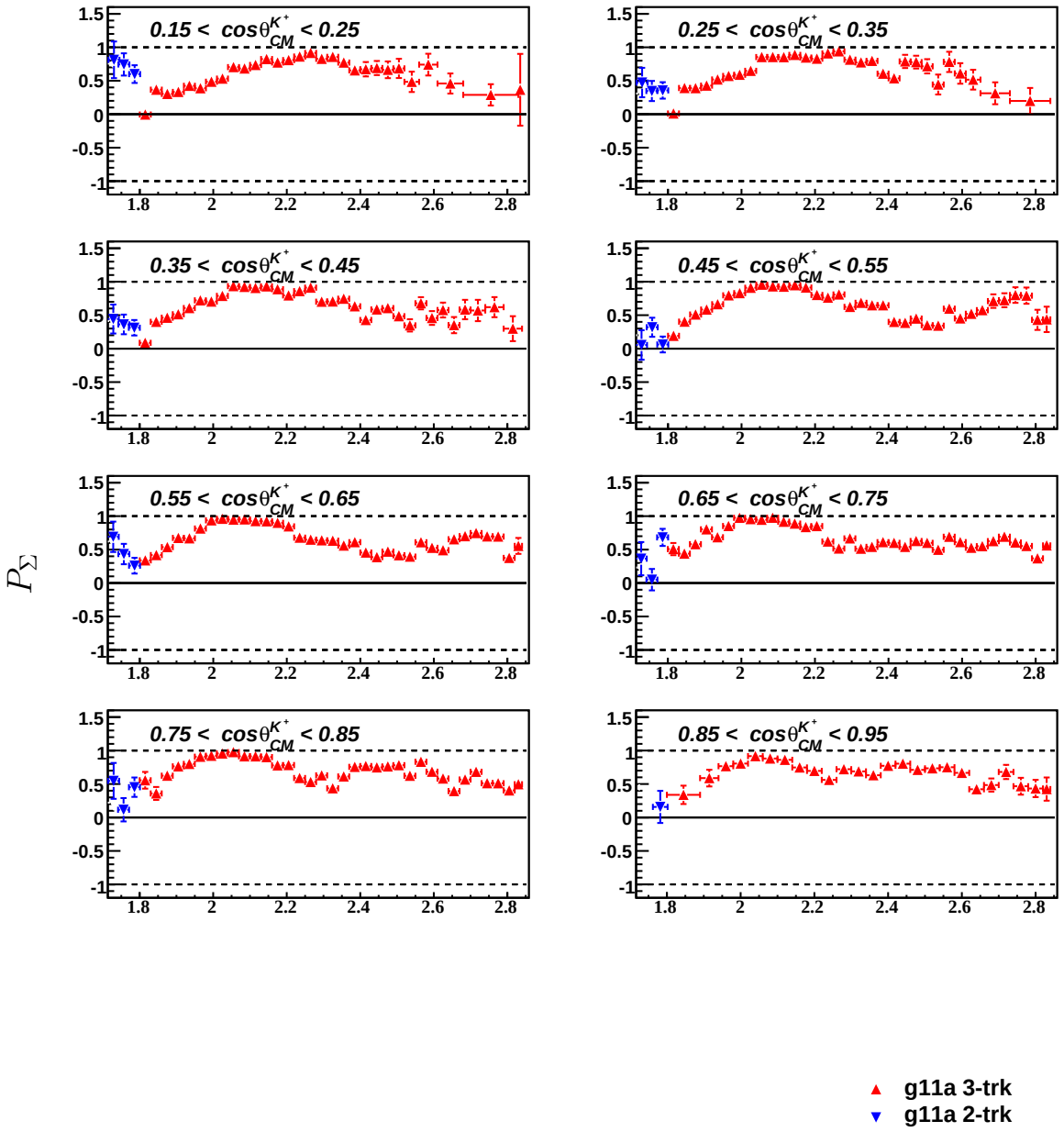

Figure 8.11: Final recoil polarization results from the CLAS $g11a$ dataset. Apart from the very backward angles and near-threshold regions, results are available from the 3-track dataset (in red). In the remaining kinematic regions, we present results from the 2-track topology (in blue), which involves an averaging over the Σ^0-Λ spin transfer information.

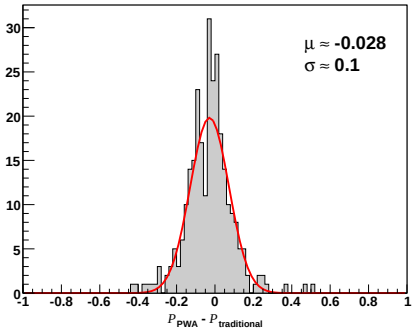

Figure 8.12: Systematic Error Calculation for P_Σ: difference in the extracted polarizations from two different but equivalent methods give an estimate of the systematic uncertainty in our P_Σ calculation.

8.10 Comparison With Previous Measurements

Previous world data on P_Σ is generally sparse. There are three other measurements – a Bonn measurement using the SAPHIR detector, published in 2004 (Glander *et al* [88]), an earlier CLAS analysis on the $g1$ dataset in 2004 (McNabb *et al* [107]) and a more recent GRAAL analysis in 2007 (Lleres *et al* [109]).

SAPHIR published results at four $\cos\theta^{K^+}_{\rm c.m.}$ (-0.75, -0.25, 0.25 and 0.75) points for each of three $\sqrt{s}$ points – 1.847, 2.029 and 2.279 GeV. The CLAS $g1$ results consisted of measurements at $\cos\theta^{K^+}_{\rm c.m.}$ = -0.7, -0.5, ..., 0.9 with $\sqrt{s}$ ranging from 1.79 to 2.29 GeV – a total of seventy data points. Finally, the GRAAL results were at two $\sqrt{s}$ points – 1.762 and 1.85 GeV with two forward angle and two backward angle measurments at each $\sqrt{s}$; a total of eight measurements. The present results cover 472 individual kinematic points, vastly increasing our overall knowledge of P_Σ, both in statistics and kinematic coverage.

As shown in Figs. 8.13 and 8.14, agreement between our results and previous world data is generally good. Even in the bins where the previous results seem to differ from ours, they either have large error bars or show a localized deviation from a smooth variation between angular bins. There are prominent structures present which the present results map out in much greater detail that before. In the $\cos\theta^{K^+}_{\rm c.m.} = 0.7$ bin, the $g1$ polarizations seem to get flatter than $g11a$. Note however, that $g11a$ maintains its shape between the two neighbouring angular bins, while $g1$ goes down and comes back up again. Our agreement with the latest GRAAL results is especially good. In the bin $\cos\theta^{K^+}_{\rm c.m.} = -0.7$, there seemed to be considerable disparity between previous CLAS $g1$ and SAPHIR results with both datasets having wide error bars. The new results smoothly varies between consecutive angular bins and seems to support the general trend of P_Σ tending towards negative values in the backward angle regions.

8.11 Discussion

The overall trend of the polarization seems to be that P_Σ is large and positive in the forward angles and tends toward zero or negative values in the backward angles. Many local structures are visible, especially in the backward-angle bins, possibly from resonance contributions, though the variations are smoother than seen in $K^+\Lambda$ [19]. In the static quark model, assuming an approximate

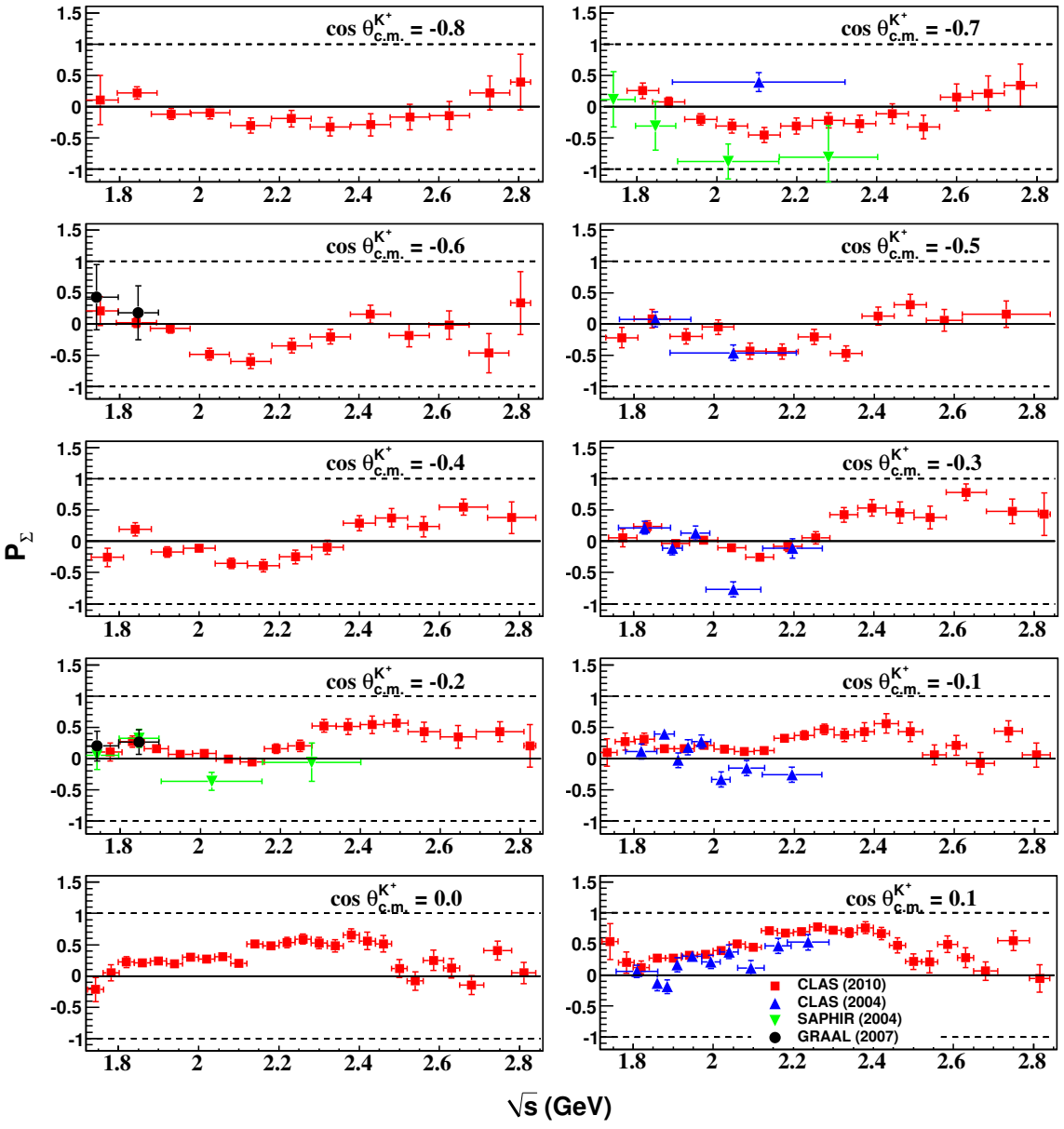

Figure 8.13: P_Σ *vs.* $\sqrt{s}$: Recoil polarization world data in the backward angles. CLAS [20] (present analysis) results are in red squares, earlier CLAS [107] results in blue up-triangles, SAPHIR [88] in green down-triangles, GRAAL [109] are in black circles. The error bars represent the statistical uncertainties.

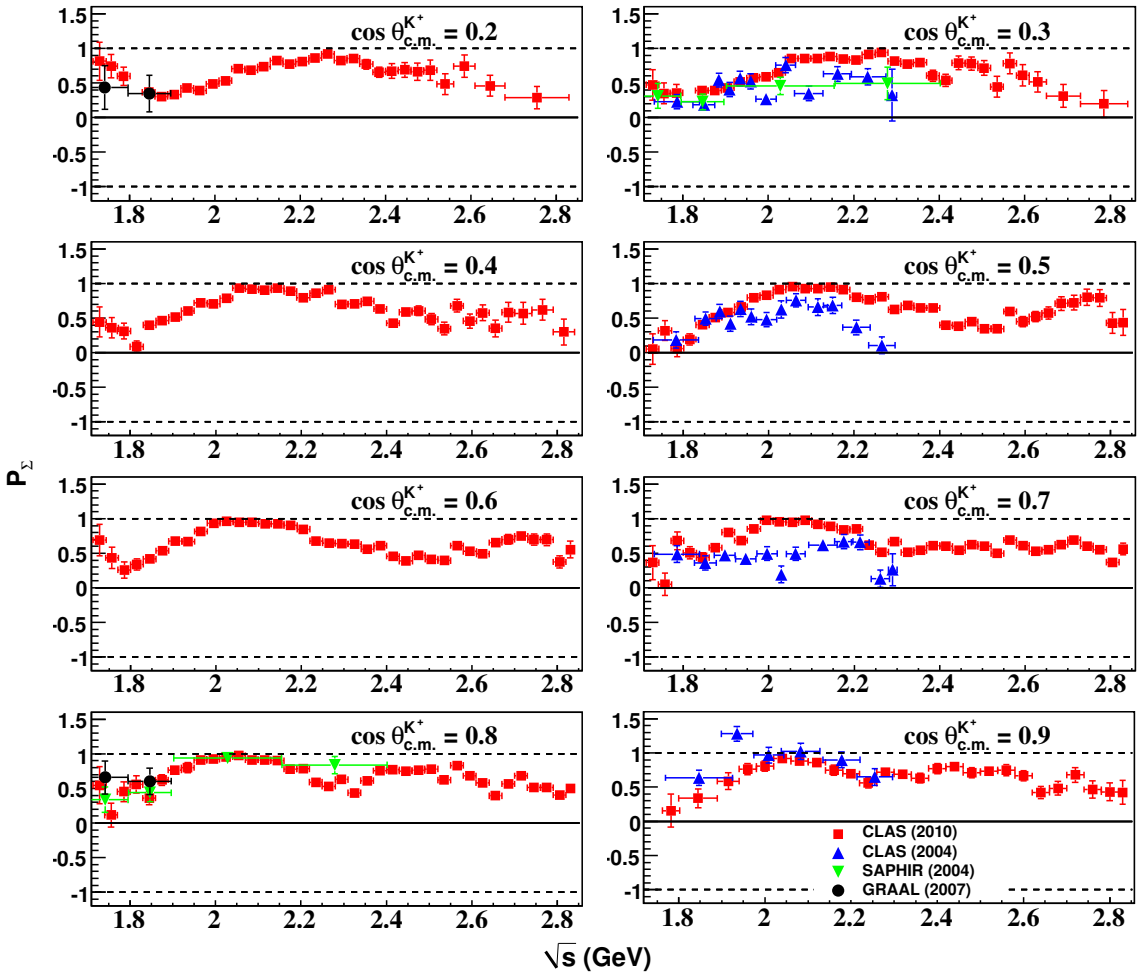

Figure 8.14: P_Σ *vs.* $\sqrt{s}$: Recoil polarization world data in the forward angles. CLAS [20] (present analysis) results are in red squares, earlier CLAS [107] results in blue up-triangles, SAPHIR [88] in green down-triangles, GRAAL [109] are in black circles. The error bars represent the statistical uncertainties.

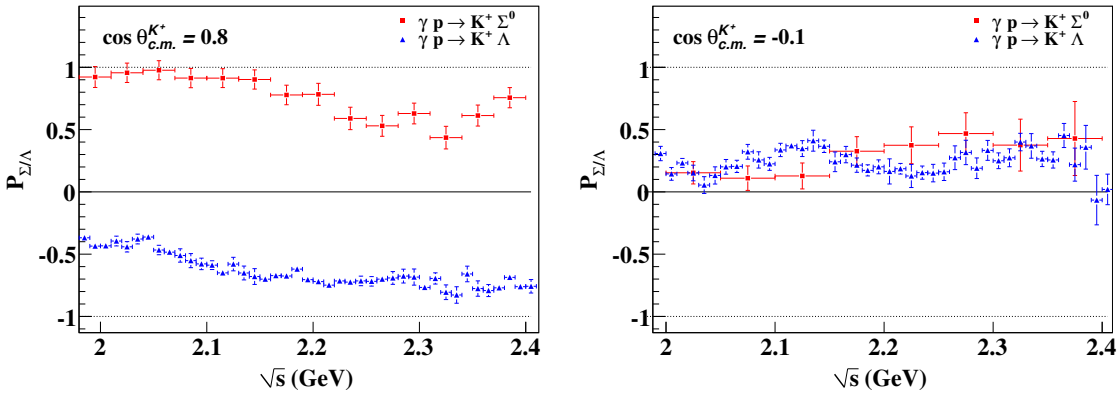

(a) (b)

Figure 8.15: The $SU(6)$ prediction of $P_\Sigma \approx -P_\Lambda$ is seen to hold at (a) forward angles, but is broken for certain (b) mid- and backward-angle kinematics. The P_Λ values are taken from Ref. [19].

$SU(6)$ symmetry [183], the spin-flavor configurations of the two hyperons are $|\Lambda^\uparrow\rangle = |u^\uparrow d^\downarrow s^\uparrow\rangle$ and $|\Sigma^{0\,\uparrow}\rangle = |u^\uparrow d^\uparrow s^\downarrow\rangle$. Therefore, it follows that $P_\Sigma \approx -P_\Lambda$. A new feature that we see from the present results is that this prediction is explicitly broken in certain kinematic regions. Fig. 8.15 shows this for one region, where P_Λ [19] and P_Σ are both non-zero and have the same sign. Similar features are visible in several other mid- and backward-angle bins, but not in any of the forward-angle bins. In other words, the $SU(6)$ prediction is not observed globally. Of course, $SU(6)$ is known to be a broken symmetry, and it is an interesting question by itself, as to why the $P_\Sigma \approx -P_\Lambda$ prediction seems to hold at high $\sqrt{s}$ and forward angles. A possible answer may lie in the fact that the static quark model assumes that the production mechanisms for both hyperons are the same. This hypothesis no longer holds if Δ^* resonances contribute to the $K^+\Sigma^0$ production, and $SU(6)$ can be broken explicitly.

8.12 Summary

Recoil polarizations for $K^+\Sigma^0$ photoproduction in the CLAS $g11a$ dataset were presented in this chapter. For the three-track dataset, two equivalent methods of polarization extraction along with their pros and cons were discussed. Our final results incorporate the best features of both methods. Systematic errors were extracted by looking at the difference between the two methods. For the two-track dataset, the polarization information is diluted because the Λ momentum is not acessible. We thus chose to present results from the two-track analysis only at kinematic points where the three-track dataset is limited by statistics. We also compared our results with previous world data and found good agreement. The present results however represent a many fold improvement in both statistics and kinematic coverage over previous world data and maps out in great detail, the structures only *hinted at* previously.

Chapter 9

ϕ Differential Cross Sections

In this chapter we apply the "mother fit" PWA formalism of Ch. 6 to the $\gamma p \to \phi p$ channel. The only additional element required here is the $\phi \to KK$ branching fraction, which was unity for the $\Sigma^0 \to \Lambda\gamma$ decay. The differential cross-section formula appearing in Eq. 6.35 is scaled up by $1/b.f.$, where $b.f.$ is the appropriate branching fraction – 34.0% for the neutral-mode and 49.1% for the charged-mode decay of the ϕ [53].

9.1 The Mother Fits

The basic set-up for the mother-fits in the ϕp channel is the same as described in Sec. 6.5 for the $K^+\Sigma^0$ case. We use J^P waves from $\frac{1}{2}^{\pm}, \ldots, \frac{11}{2}^{\pm}$ and following Eq. 6.33, for each J^P wave, there is a phase angle ϕ_{J^P}, a production angle θ_{J^P} and three decay parameters $r_{J^P,L\cdot S}$ corresponding to the triplet of spin-projections for a vector particle (this is different from the pseudoscalar meson case). The $J^P = \frac{1}{2}^{\pm}$ waves are special cases again, since only a single $L \cdot S$ projection is possible. Therefore, the $J^P = \frac{1}{2}^{\pm}$ waves contribute three fit parameters each, while $J^P \neq \frac{1}{2}^{\pm}$ waves have five fit parameters each. For J^P from $\frac{1}{2}^{\pm}$ till $\frac{11}{2}^{\pm}$, there are 56 independent fit parameters in all.

Figs. 9.1 and 9.2 show the mother fit results for the charged-mode topology at the energy bin-centers $\sqrt{s} = 2.155$, 2.455 and 2.755 GeV (10-MeV bins) and for the charged-mode topology at the energy bin-centers $\sqrt{s} = 2.135$ and 2.455 GeV (30-MeV-wide bins), respectively. For each energy bin, comparisons are shown in the angular variables $\cos\theta^K_{Adair}$, ϕ^K_{Adair} and $\cos\theta^{\phi}_{\rm c.m.}$. The real data is shown in black, the unweighted accepted monte carlo in blue, and the monte carlo weighted by the fit results, in red. The weighted monte carlo matches the real data very well in all three kinematically independent variables.

Fig. 9.3 shows an example of a multi-dimensional quality-check for the PWA fit shown in a particular energy-bin ($\sqrt{s} = 2.155$ GeV) for the charge-mode topology. The events have been divided into three regions in the $\theta^{\phi}_{c.m.}$, backward-, mid- and forward-angles. In each angular region, we look at the ϕ decay distributions in the Adair frame. The top, middle and bottom rows represent the data, accepted monte carlo prior to being weighted by the fit results and accepted monte carlo after being weighted by the fit results, respectively. The fit pulls the monte carlo distributions closer to the data in each localized region of phase-space.

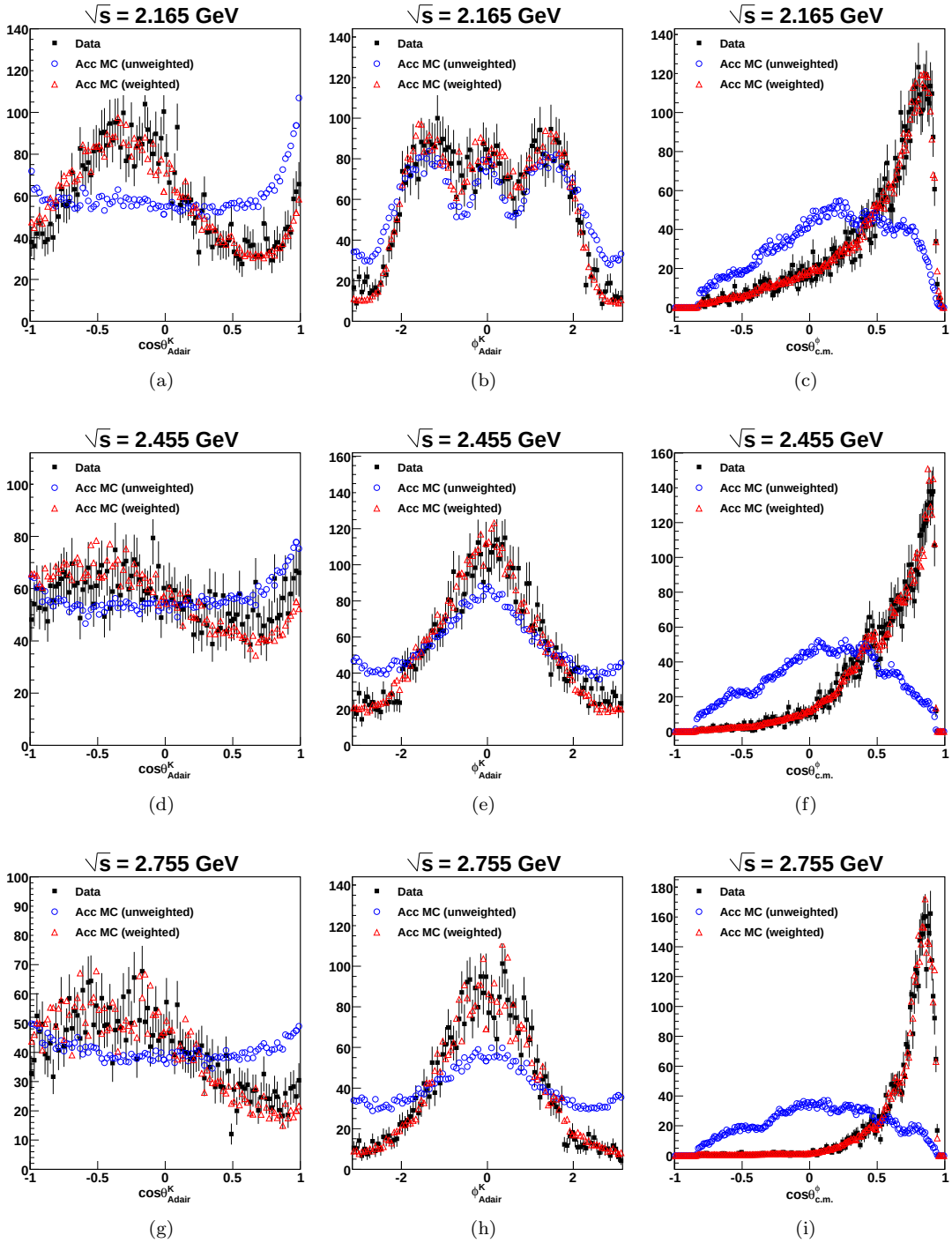

Figure 9.1: Mother fit results for the ϕp charged-mode topology using J^P waves from $\frac{1}{2}^{\pm}$ till $\frac{11}{2}^{\pm}$. The rows correspond to three different energy bins. The first, secodn and third columns show the $\cos\theta^{K^+}_{Adair}$, $\phi^{K^+}_{Adair}$ and $\cos\theta^{\phi}_{\rm c.m.}$ distributions respectively. For each plot, the black points are the actual data, the blue points are the initial unweighted accepted monte carlo data while the red points are the accepted monte carlo weighted by the mother fit results. As evident from the plots, the weighted monte carlo follows the real data quite well.

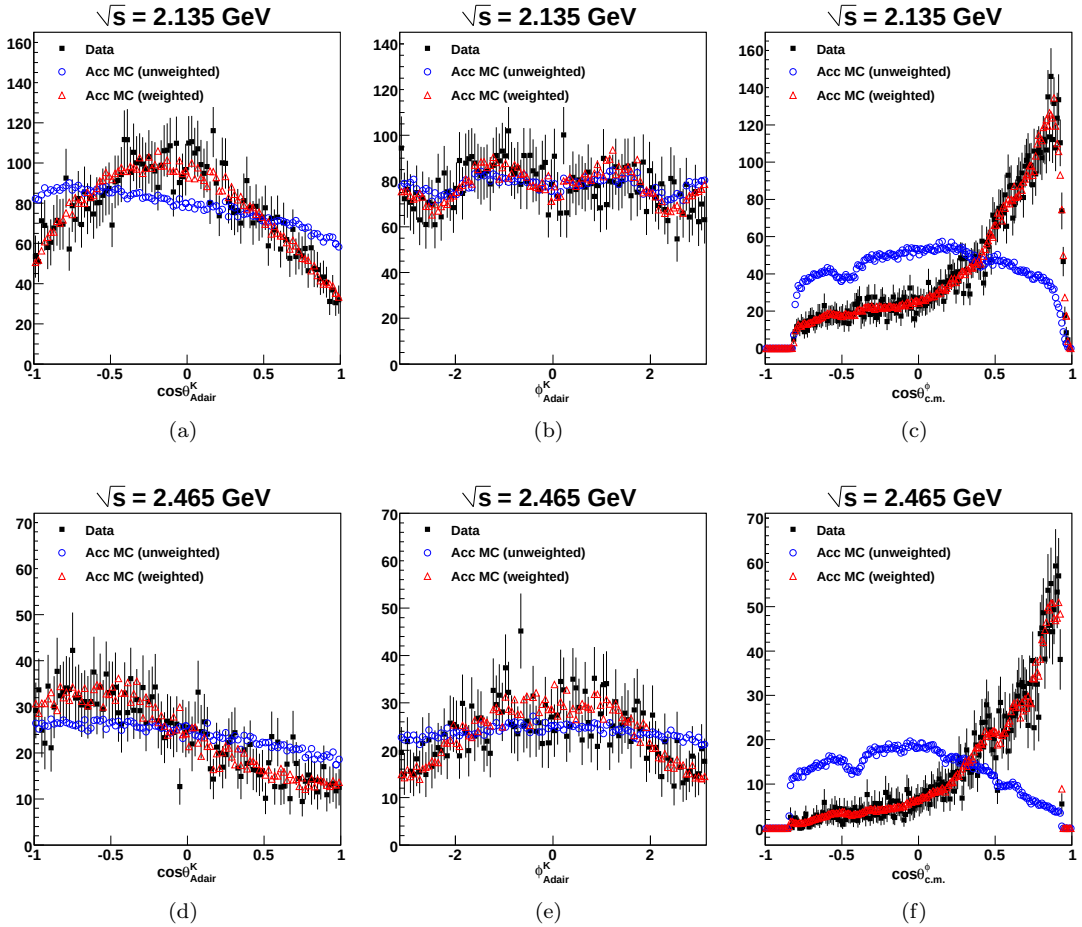

Figure 9.2: Mother fit results for the ϕp neutral-mode topology using J^P waves from $\frac{1}{2}^{\pm}$ till $\frac{11}{2}^{\pm}$. The rows correspond to two different energy bins. The first, second and third columns show the $\cos\theta^{K^0_S}_{Adair}$, $\phi^{K^0_S}_{Adair}$ and $\cos\theta^{\phi}_{\rm c.m.}$ distributions respectively. For each plot, the black points are the actual data, the blue points are the initial unweighted accepted monte carlo data while the red points are the accepted monte carlo weighted by the mother fit results. As evident from the plots, the weighted monte carlo follows the real data quite well.

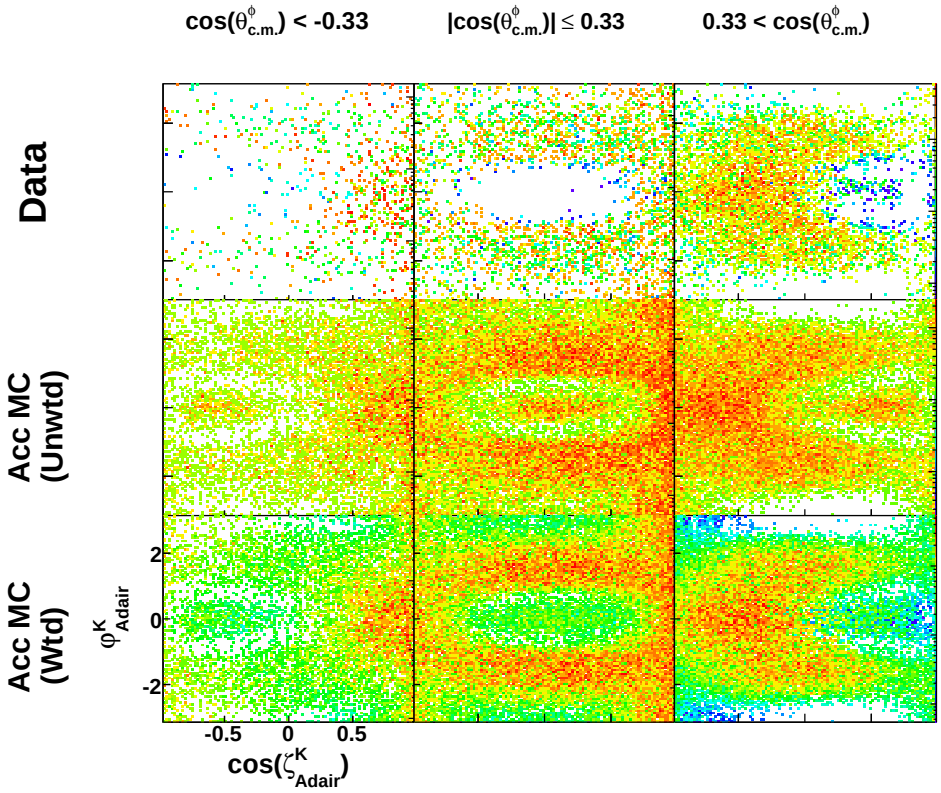

Figure 9.3: Multi-dimensional fit-quality check for the ϕp charged-mode in a single enery bin, $\sqrt{s} = 2.165$ GeV. Column-wise, the events are divided into backward-, mid- and forward-angles. Row-wise, the top row is the data, the middle row is the accepted monte carlo, and the bottom row is the accepted monte carlo weighted by the PWA fit results. Each panel shows the $\phi \to KK$ decay angular distributions in the Adair frame – the PWA fit pulls the monte carlo distributions to resemble the data in all regions of phase-space.

Source	Value	Description
Confidence Level	3%	Kinematic Fitter Uncertainty [16]
Particle Identification	4.2%	Signal loss to PID cut (charged-mode) (Sec. 3.8.2)
K^0_S Selection	5%	Signal loss to K^0_S selection cut (neutral-mode) (Sec. 3.9.3)
Acceptance	3-6%	Sector-wise acceptance study (Sec. 4.8)
$\phi \to K^+K^-$ Branching Fraction	0.6%	PDG listed uncertainty [53]
$\phi \to K^0_S K^0_L$ Branching Fraction	0.5%	PDG listed uncertainty [53]
Target Density	0.11%	Std. dev. of target measurement per run [51]
Target Length	0.125%	Target survey precision [39]
Photon Normalization	7.7%	Based upon run-to-run normalized yields [16]
Photon Transmission Efficiency	0.5%	Propagation of photons to target along beamline [16]
Current-dependent live-time	3%	Current-dependent DAQ live time correction [51]

Table 9.1: Table of systematic uncertainties for the ϕp channel.

9.2 Uncertainties

The statistical uncertainties were calculated as described earlier in Sec. 6.6.2. The systematic uncertainties are listed in Table 9.1.

9.3 Cross section results

Figs. 9.4, 9.5 and 9.6 show the differential cross section results for the charged-mode topology (with a $|M(p,K^-) - 1.52| \leq 15$ MeV cut). Our energy coverage is from near production threhold, $\sqrt{s} = 1.97$ GeV, to 2.84 GeV in 10-MeV-wide $\sqrt{s}$ bins. The angular binning is 0.1 in $\cos\theta^{\phi}_{\text{c.m.}}$ and our angular coverage is $-0.85 \leq \cos\theta^{\phi}_{\text{c.m.}} \leq 0.95$ at most energy bins. Also, no cross section result is presented at the bins $\sqrt{s} = 2.735$ and 2.745 GeV due to the normalization issues described in Sec. 4.10.3.

Fig. 9.7 shows the differential cross sections for the neutral-mode topology. The energy bins are at least 30-MeV-wide $\sqrt{s}$, with some 40-MeV bins at the higher energies. The angular binning remains 0.1 in $\cos\theta^{\phi}_{\text{c.m.}}$, as for the charged-mode, but the angular coverage at backward-angles is more restricted, especially at higher energies, due to very low available statistics for these kinematics.

Figs. 9.8 and 9.9 show the comparison between the charged- and neutral-mode differential cross section results. In keeping with the diffractive nature of vector meson photoproduction, we have chosen to present our results as $d\sigma/dt$ here, with the conversion being

$$\frac{d\sigma}{dt} = \frac{1}{2}\left(\frac{1}{E_\gamma|\vec{p}_\phi|}\right)_{c.m.}\left(\frac{d\sigma}{d\cos\theta^{\phi}_{\text{c.m.}}}\right). \tag{9.1}$$

The diffractive Pomeron exchange mechanism is clearly borne out in the very forward-most angular bin ($t \to 0$), where $d\sigma/dt$ remains almost constant above $\sqrt{s} > 2.3$ GeV. It is interesting to note that the structure around $\sqrt{s} \approx 2.1$ GeV is clearly present in both topologies. Above $\sqrt{s} > 2.3$ GeV, the two topologies are in very good agreement, except in the $\cos\theta^{\phi}_{\text{c.m.}} = 0.8$ and 0.9 bins, where the neutral-mode cross sections tend to be slightly lower.

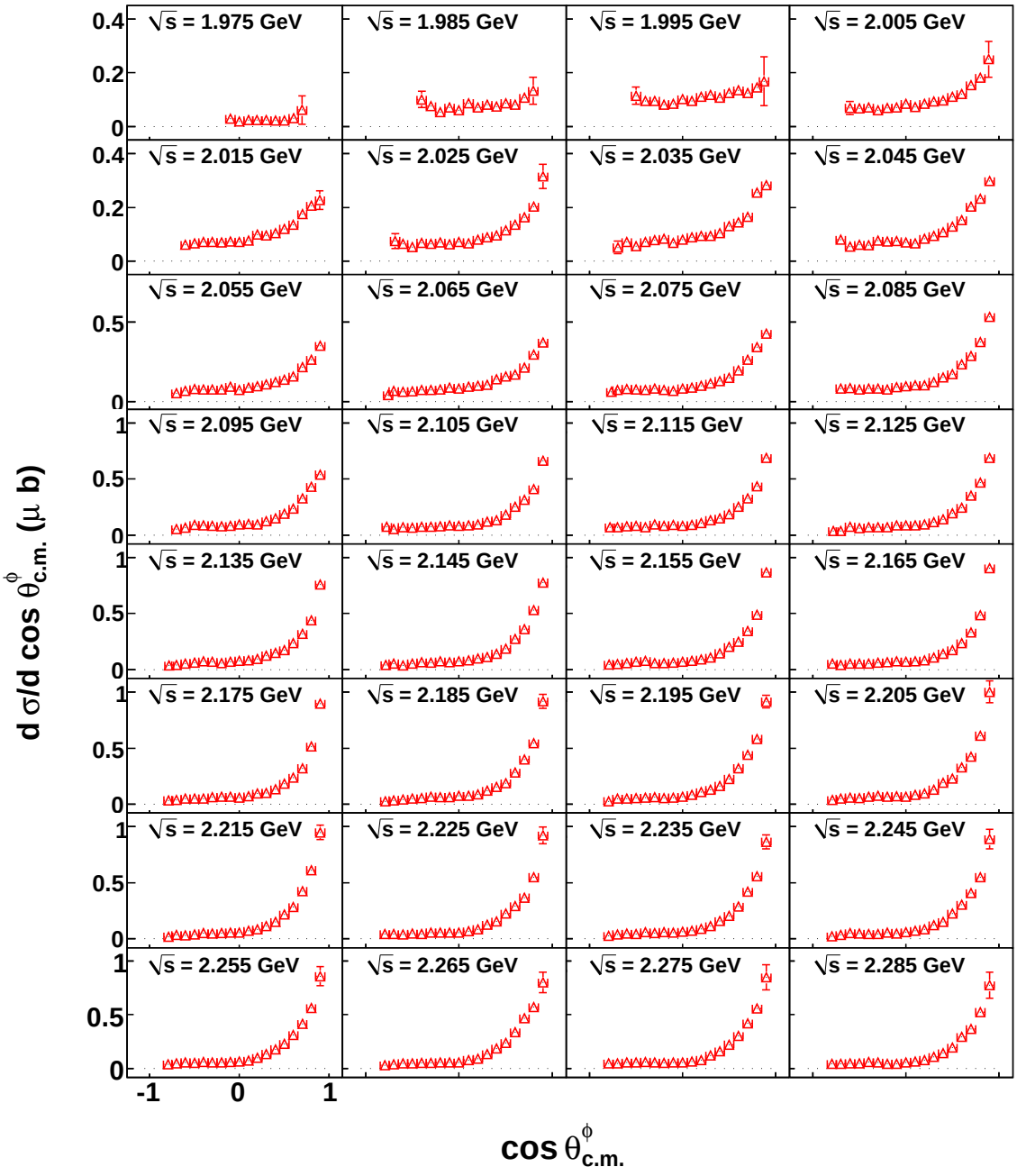

Figure 9.4: $\frac{d\sigma}{d\cos\theta^{\phi}_{\rm c.m.}}$ (μb) *vs.* $\sqrt{s}$: Differential cross section results for the charged-mode topology in the energy range 1.97 GeV $\leq \sqrt{s} <$ 2.29 GeV. The centroid of each 10-MeV-wide bin is printed on the plots. The y-axis range is constant over each horizontal row and is shown in the left-most column for every row. All error bars represent statistical uncertainties only.

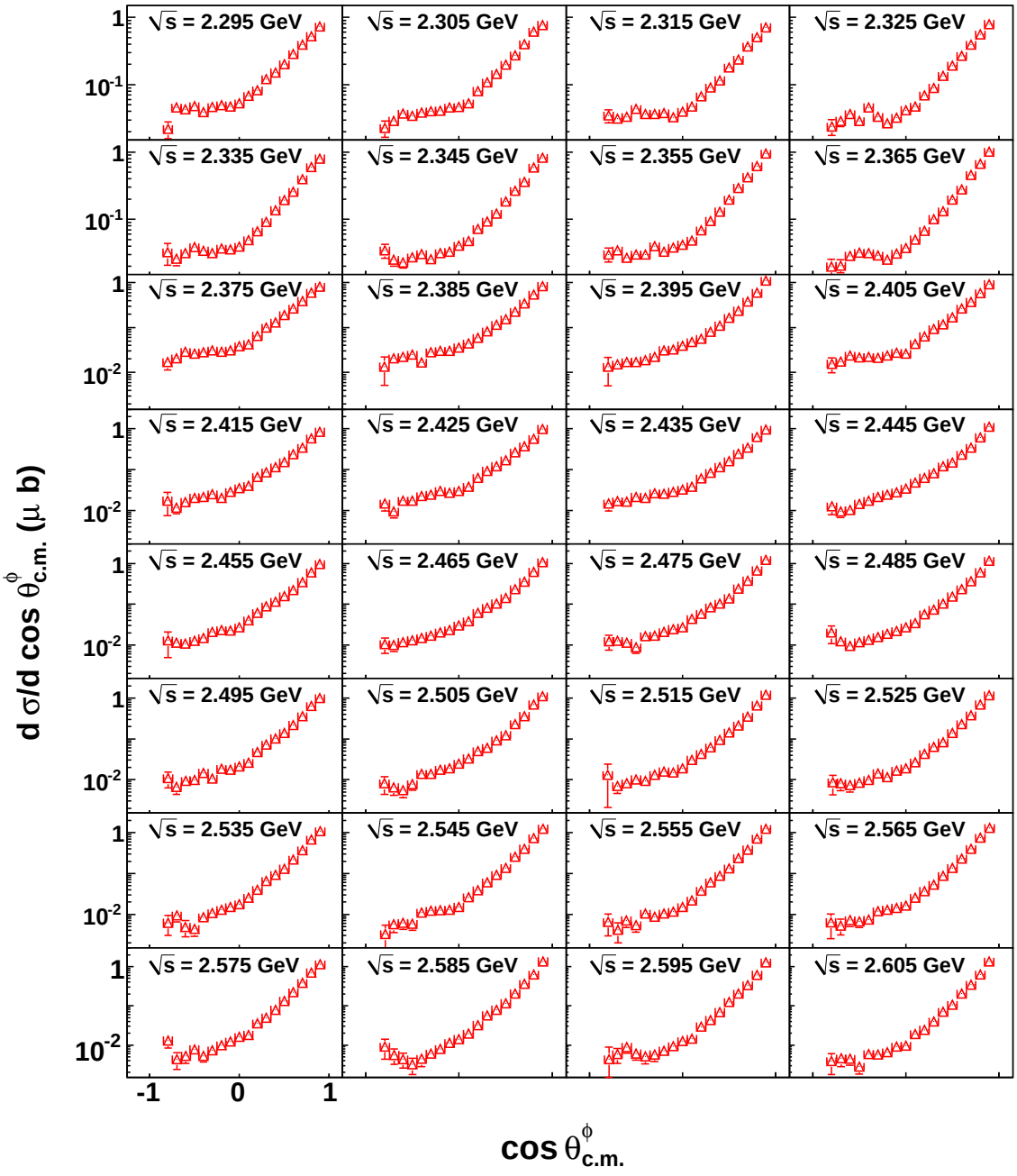

Figure 9.5: $\frac{d\sigma}{d\cos\theta^{\phi}_{\rm c.m.}}$ (μb) *vs.* $\sqrt{s}$: Differential cross section results for the charged-mode topology in the energy range 2.29 GeV $\leq \sqrt{s} <$ 2.61 GeV. The centroid of each 10-MeV-wide bin is printed on the plots. The y-axis range is constant over each horizontal row and is shown in the left-most column for every row. All error bars represent statistical uncertainties only.

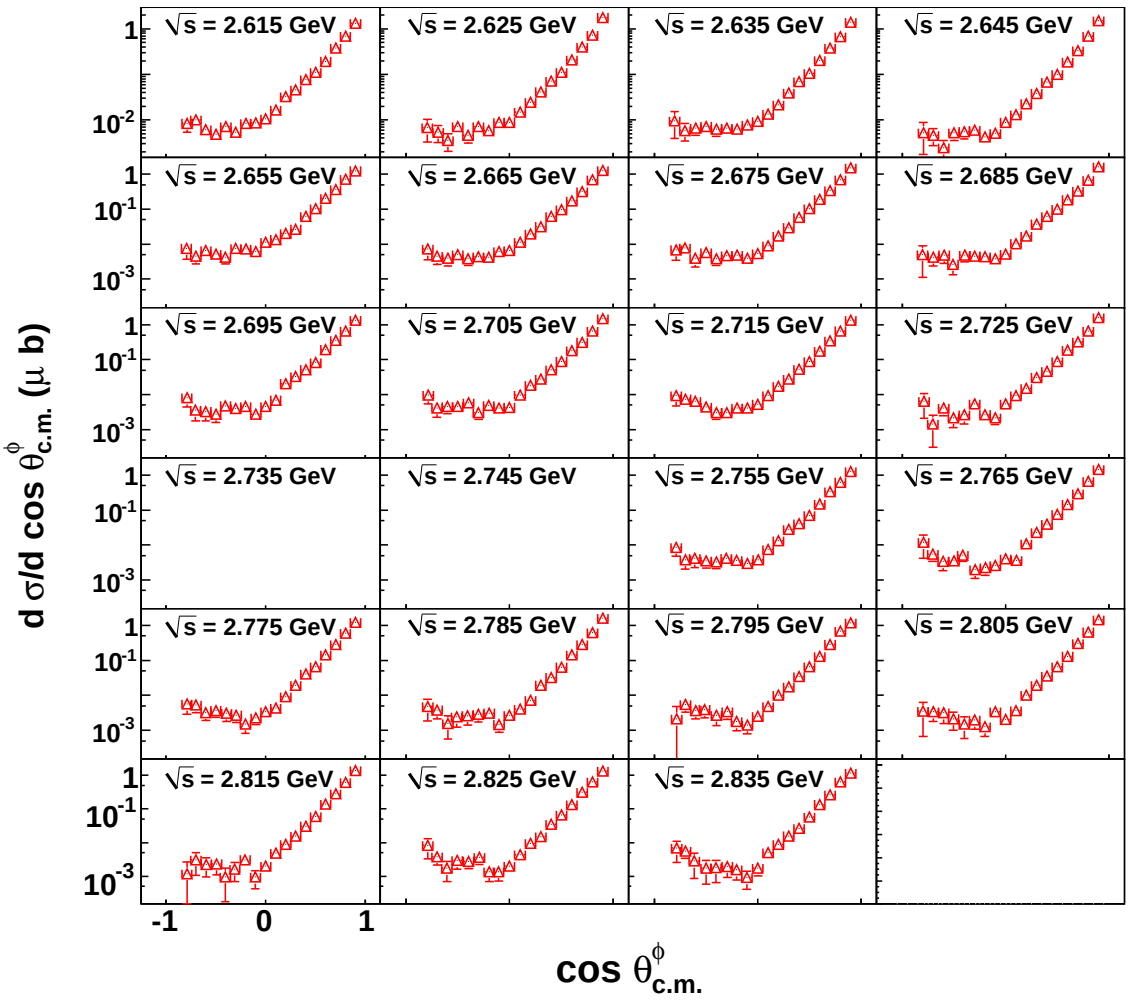

Figure 9.6: $\frac{d\sigma}{d\cos\theta^{\phi}_{\rm c.m.}}$ (μb) *vs.* $\sqrt{s}$: Differential cross section results for the charged-mode topology in the energy range 2.61 GeV $\leq \sqrt{s} <$ 2.84 GeV. The centroid of each 10-MeV-wide bin is printed on the plots. The y-axis range is constant over each horizontal row and is shown in the left-most column for every row. No results are presented for the bins $\sqrt{s} = 2.735$ and 2.745 GeV due to the normalization issues, as described in Sec. 4.10.3. All error bars represent statistical uncertainties only.

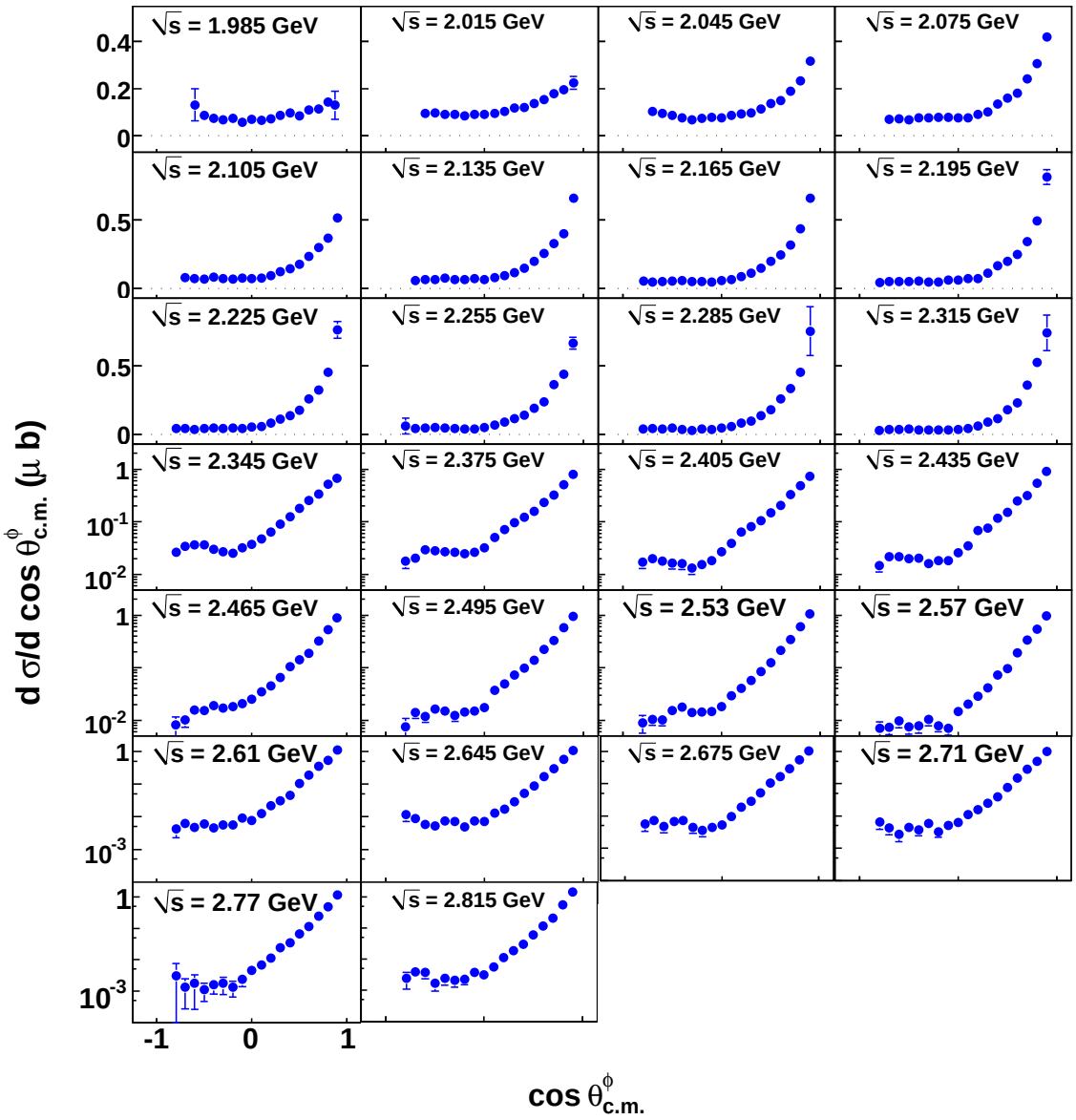

Figure 9.7: $\frac{d\sigma}{d\cos\theta^{\phi}_{\rm c.m.}}$ (μb) *vs.* $\sqrt{s}$: Differential cross section results for the neutral-mode topology. The minimum bin-width is 30-MeV and the bin-centroid is printed on the plots. The y-axis range is constant over each horizontal row and is shown in the left-most column for every row. All error bars represent statistical uncertainties only.

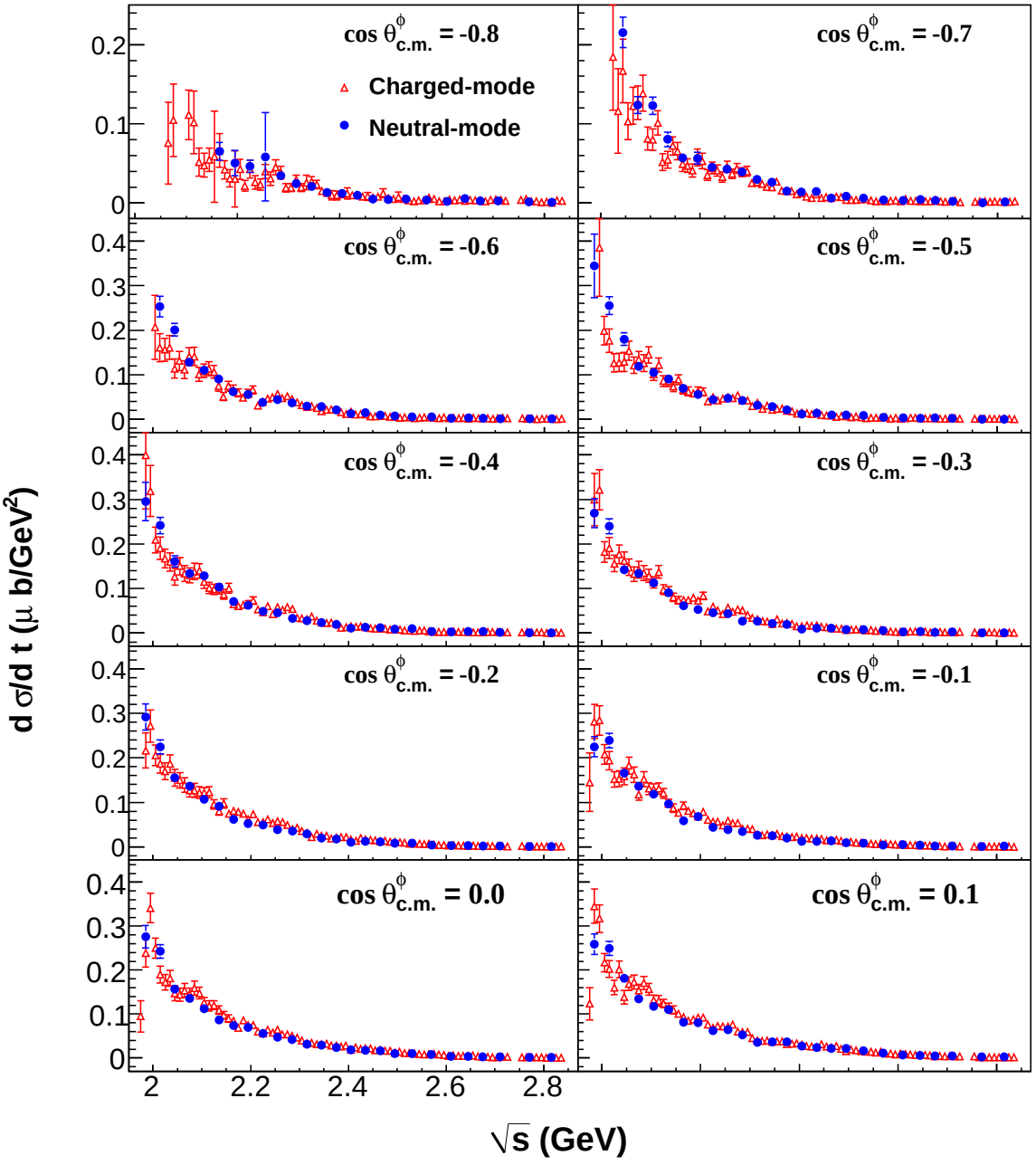

Figure 9.8: Comparison of the charged- and neutral-mode $d\sigma/dt$ results in the mid- and backward-angle bins. All error bars represent statistical uncertainties only.

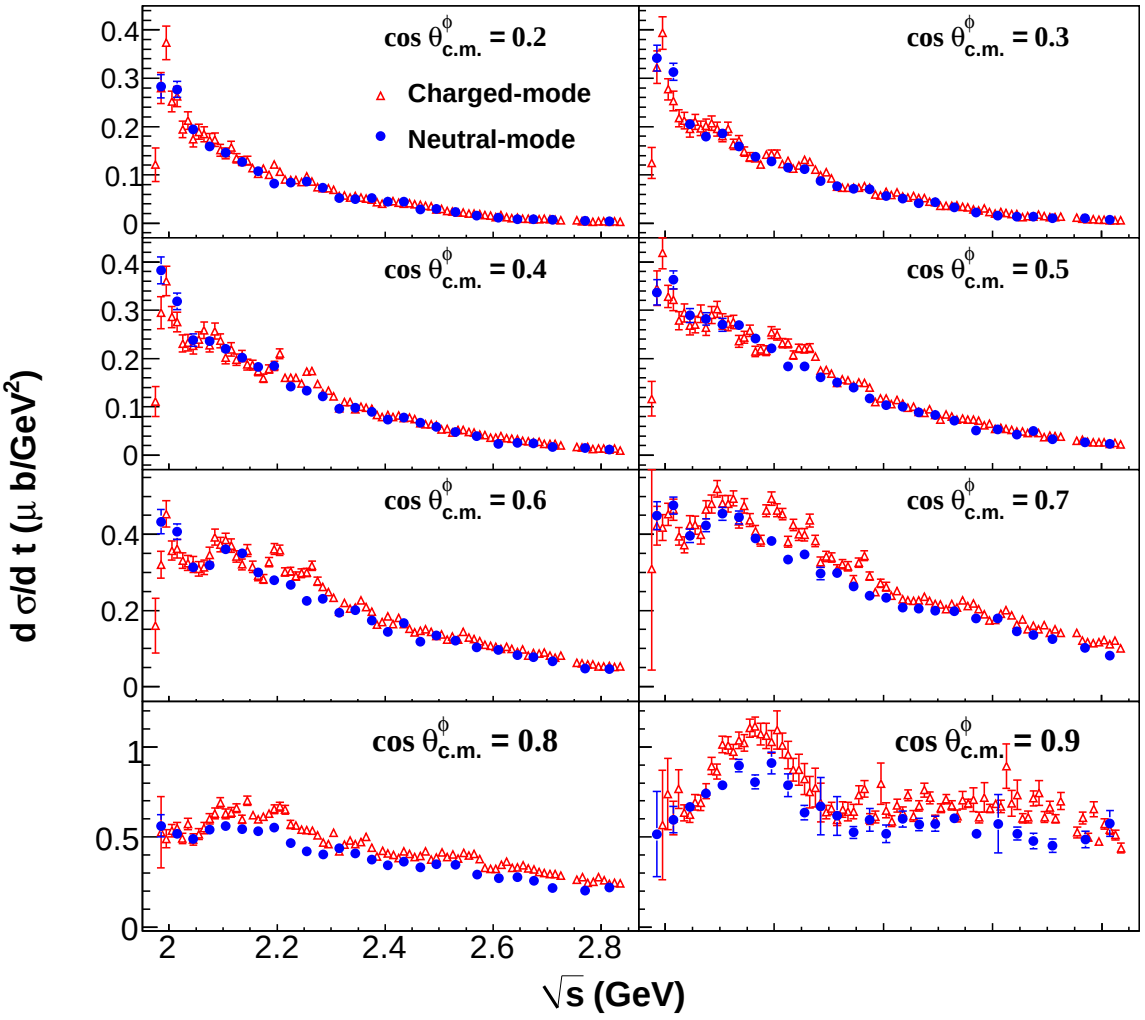

Figure 9.9: Comparison of the charged- and neutral-mode $d\sigma/dt$ results in the mid- and forward-angle bins. Both topologies show the $\sqrt{s} \approx 2.1$ GeV structure in the forward-most angular bins. $d\sigma/dt$ appears almost constant above $\sqrt{s} \approx 2.3$ GeV for $\cos\theta^{\phi}_{\rm c.m.} = 0.9$ ($t \to 0$), as expected for diffractive photoproduction. All error bars represent statistical uncertainties only.

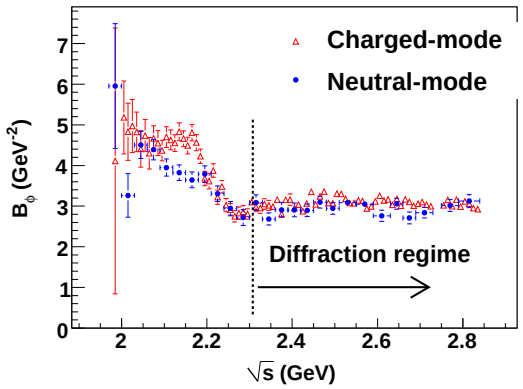

Figure 9.10: Extracted Pomeron slope parameter B_ϕ by fitting $d\sigma/dt$ to the functional form $C_\phi \exp(-B_\phi|t-t_0|)$.

9.4 Extraction of the Pomeron parameters

Fig. 9.10 shows the extracted constant slope (B_ϕ) parameter, for both the charged- and neutral-mode topologies. The exponential fitting function was of the form $C_\phi \exp(-B_\phi|t-t_0|)$, where t_0 refers to the minimum value of $|t|$ for a given $\sqrt{s}$ bin, that is, the value of t at $\cos\theta^\phi_{\rm c.m.} = 0$. Since we are interested in the forward-angle diffractive regime only points with $\cos\theta^\phi_{\rm c.m.} \geq 0.5$ were included in the fits.

9.5 Comparison with previous world data

9.5.1 Differential cross-sections

Previous world data for ϕ photoproduction cross sections are generally scarce and no detailed results exist for the neutral-mode topology at all. We therefore restrict our discussion to the charged-mode topology only. For low energy and forward-angle kinematics, there are three previous results from DESY (1968, ABBHHM Group [121]), Bonn (1973, Besch *et al* [120]), SAPHIR (2003, Barth *et al.* [65]) and LEPS (2004, Mibe *et al* [66]). In general, these older results have wide energy bins. The ABBHHM results are quoted with E_γ from 1.58 to 2.5 GeV with extremely limited statistics. The Bonn measurements [120] are quoted at $E_\gamma = 2.0$ GeV, but incorporate limited control over the ϕ decay distributions. The more recent SAPHIR and LEPS have energy bin-widths of $E_\gamma \approx 200$ and 100 MeV, respectively, which are still quite broad compared to our 10-MeV-wide $\sqrt{s}$ binning. However, the common feature in the SAPHIR/LEPS results is the mention of a prominent "enhancement" around $E_\gamma \approx 2$ GeV ($\sqrt{s} \approx 2.2$ GeV) in the forward-angle $d\sigma/dt$, in agreement with our current results.

Fig. 9.11 shows the comparison between the present CLAS and the 1973 results from Bonn at $E_\gamma = 2$ GeV. SAPHIR [65] and LEPS [66] reported results as $d\sigma/dt$ *vs.* $|t-t_0|$. The conversion from $\cos\theta^\phi_{\rm c.m.}$ to t or $|t-t_0|$ depends on $\sqrt{s}$. With wide energy bins, it is not immediately clear which $\sqrt{s}$ should be chosen for this conversion. Therefore, we convert our results in to the units chosen by SAPHIR and LEPS and make independent comparisons with both of them. Since our energy binning is much finer (10-MeV-wide in $\sqrt{s}$), we overlay our results at the energy bin-center of the SAPHIR or LEPS results. Figs. 9.12 and 9.13 show the comparison between our results with SAPHIR and LEPS, respectively.

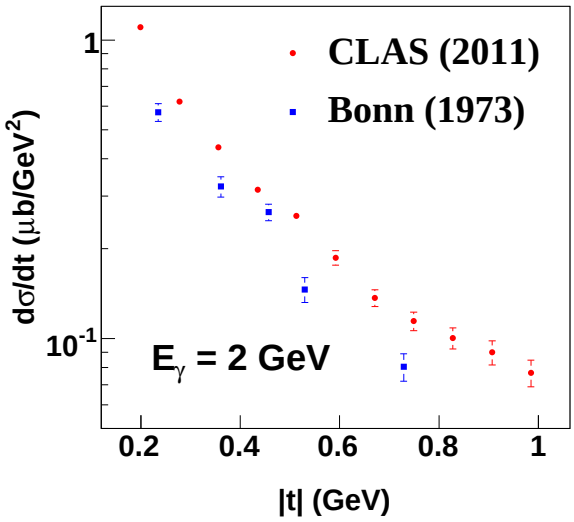

Figure 9.11: Comparison between the present CLAS 2011 (red circles) and Bonn 1973 $E_\gamma = 2$ GeV (Besch *et al.*, Ref. [120] results (blue squares) for the charged-mode topology. All error bars represent statistical uncertainties only.

The only existing world data for large $|t|$ are the CLAS (2000, Anciant *et al* [60]) results for a bin-center at $E_\gamma = 3.6$ GeV (tagged photon energy range 3.3 to 3.9 GeV). The chief motivation of the previous CLAS experiment was to investigate whether u-channel processes (at small u or large t) contribute to the ϕ channel. Assuming that the ϕ is almost pure $s\bar{s}$ and the strangeness content in ordinary nucleuons is small, the coupling constant $g_{\phi NN}$ is expected to be small and therefore nucleon exchanges in the u-channel are supposed to the suppressed. However, as shown in Fig. 9.14, both the CLAS 2000 and the current CLAS 2011 results show a small but distinct rise in the backward-angles, suggestive of a non-negligible value for $g_{\phi NN}$.

Lastly, we compare our results with the $E_\gamma = 3.3$ GeV bin-center results from Daresbury (1982, Barber *et al.* [118]). The Daresbury binning was 1-GeV in E_γ and away from the $t \to 0$ region, the error bars are large. Overall, within the limitations of statistical uncertainties, agreement between the two results is fair.

9.5.2 Pomeron parameters

It seems more or less "conventional" to compare the Pomeron parameters C_ϕ and B_ϕ while reporting new results for the ϕ. However, we point out that there are several issues that need to be kept in mind while making thse comparisons. Behrend [115] points out that the slope seems to show some t dependence as well. That is, the extracted C_ϕ and B_ϕ parameters depend on the t range in the exponential fit. In the highly forward angle region, Behrend [115] reports a relatively high t-slope of around $B_\phi \sim 6$ GeV^{-2} in the energy range $E_\gamma = 3.0$ to 6.7 GeV. Additionally, there is also some $\sqrt{s}$ dependence in these parameters.

Above around $\sqrt{s} \approx 2.2$ GeV, where the $\Lambda(1520)$ overlap ceases to be a factor, our slope is stable at $B_\phi \approx 3$ GeV^{-2} for both the charged- and neutral topologies (Fig. 9.10b). Fig. 9.16b shows the comparison with previous world results. We reiterate again that these parameters depend on the range of t in the fit. In our case, this corresponded to the angular range $0.5 \leq \cos\theta^\phi_{\rm c.m.} \leq 0.9$ in

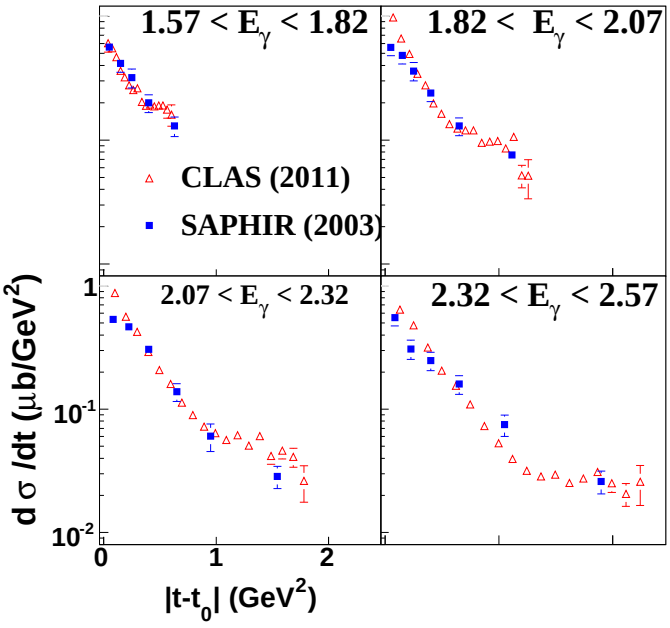

Figure 9.12: Comparison between the present CLAS 2011 (red circles) and SAPHIR 2003 (Barth *et al.*, Ref. [65] (blue squares) results. The SAPHIR binning in E_γ (GeV) is printed on each pad and the CLAS results are at the bin-centers for each SAPHIR energy bin. All error bars represent statistical uncertainties only.

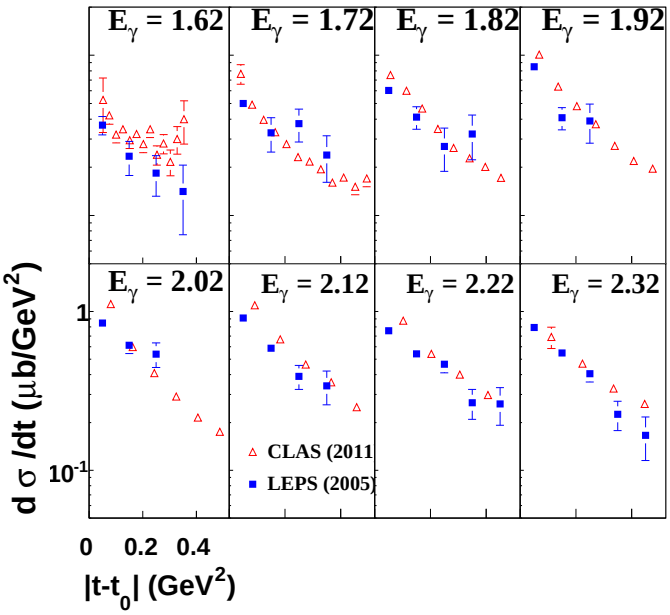

Figure 9.13: Comparison between the present CLAS 2011 (red circles) and LEPS 2004 (Mibe *et al*, Ref. [66]) (blue squares) results. The LEPS data had $E_\gamma = 200$ MeV wide bins (the bin-center is printed on each pad). All error bars represent statistical uncertainties only.

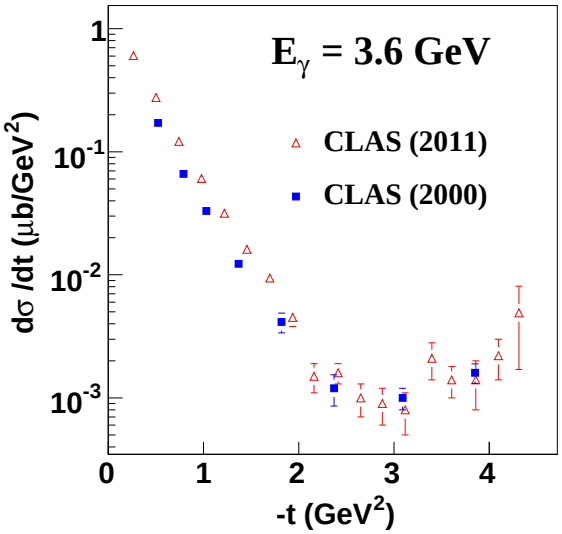

Figure 9.14: Comparison between the current CLAS (red circles) and 2000 CLAS [60] (blue squares) results at the energy bin-center $E_\gamma = 3.6$ GeV. The CLAS 2000 energy binning was 600-MeV in E_γ while the current CLAS binning is 10-MeV-wide in $\sqrt{s}$.

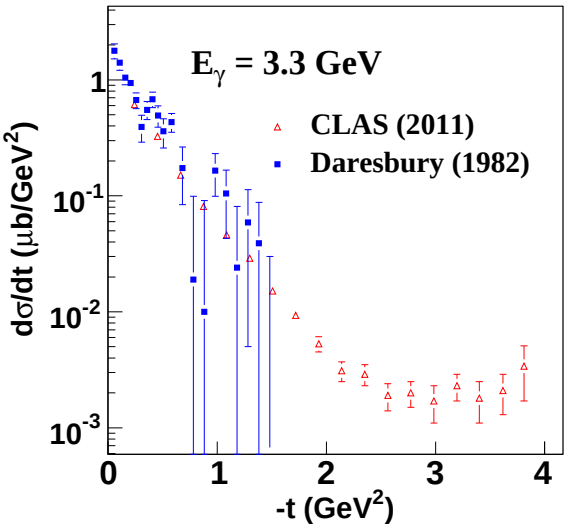

Figure 9.15: Comparison between the current CLAS (red circles) and Daresbury 1982 (Barber *et al* Ref. [118]) (blue squares) results at the bin-center $E_\gamma = 3.3$ GeV. The Daresbury energy bins were 1-GeV-wide in E_γ while the CLAS binning is 10-MeV-wide in $\sqrt{s}$.

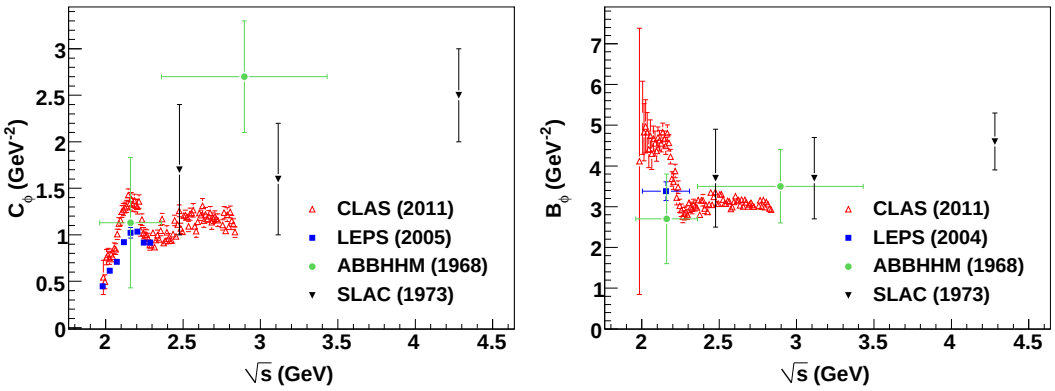

(a) (b)

Figure 9.16: Extracted Pomeron parameters by fitting $d\sigma/dt$ to the functional form $C_\phi \exp(-B_\phi|t-t_0|)$. (a) shows the extracted constant C_ϕ and (b) shows the slope B_ϕ.

every energy bin. Therefore, our results do not include the forward-most angular region. The C_ϕ results show some difference between the charged- and neutral-mode results (Fig. 9.10a). We also note that different authors treat the t_0 portion of $|t-t_0|$ differently. That is, some authors fold the t_0 dependence into the pre-factor of the exponential function. If the energy binning is wide, this can affect the extraction of C_ϕ. From Fig. 9.10a, above $\sqrt{s} \approx 2.2$ GeV, we see a slowly increasing C_ϕ, with an average value of about $1\mu b/\text{GeV}^2$. This slow rise of the forward $d\sigma/dt$ is the hallmark of diffractive phenomenology at work.

Below $\sqrt{s} \sim 2.2$ GeV, it is not even clear whether fitting $d\sigma/dt$ to an exponential is the correct approach, since there are clear deviations from a monotonically-rising forward cross-section, as expected from diffractive exchanges. The extracted C_ϕ and B_ϕ values as arising from a diffractive-type phenomenology, in this kinematic range should therefore be interpreted with caution while performing model fits.

9.6 The Forward-angle "Bump"

9.6.1 The Kiswandhi model

Fig. 9.17 shows a comparison between the present CLAS $g11a$ results and predictions from the model by Kiswandhi *et al.* model [161]. The Kiswandhi model came from a fit to the LEPS-2005-Mibe [66] data and older higher energy results. The claim of the Kiswandhi analysis was that the $\sqrt{s} \sim 2.1$ GeV "bump" structure could be explained by a $J^P = \frac{3}{2}^-$ resonant contribution. However, the LEPS data [66] covers only the forward-angle region and this is the only information that was available for the Kiswandhi model. As shown in Fig. 9.17a, the model does a reasonable job in showing a bump structure. However, as seen in Fig. 9.17b, away from the forward-angle region, the Kiswandhi model continues to feature the bump, while the CLAS results show a smooth monotonic structure. It is not difficult to understand the Kiswandhi model behavior, since a single J^P wave will never show a peak only a give central angle. Since the CLAS results indicate that the structure exists only at forward angle, the resonance interpretation seems somewhat difficult to believe.

It is also noteworthy that a similar analysis has been done on the $\Lambda(1520)$ side by Xie *et al.* [162]. As for the ϕp channel, the fits were made to forward-angle LEPS data, so it remains to be seen how

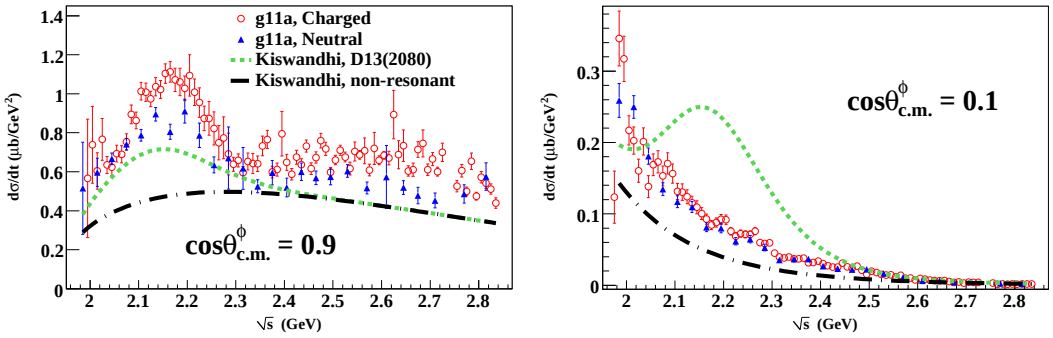

(a) (b)

Figure 9.17: Comparison between the CLAS ϕp results and the predictions from the Kiswandhi *et al.* model [161].

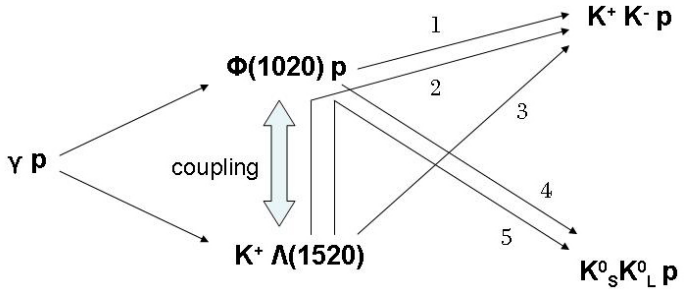

Figure 9.18: Pictorial representation of the channel-coupling between ϕp and $K^+\Lambda(1520)$.

the predictions work for the full angular range. Several groups within CLAS are currently working on the $\Lambda(1520)$ channel and we expect the wide-angle results to be available soon.

9.6.2 The Ozaki model

The Ozaki *et al.* model [160] attempts to explain the structure using a coupled-channel analysis of ϕp and $K^+\Lambda(1520)$ employing a K-matrix formalism. While the generic forward-angle structure is borne out, the model predicts the structure as a "dip", just after $\sqrt{s} \approx 2.2$ GeV, instead of a "bump" at $\sqrt{s} \sim 2.1$ GeV. The present CLAS data does not support this prediction. However, it is concievable that the *idea* of the "bump" structure being caused due to a re-scattering/coupled-channel effect is plausible. We give a pictorial description in Fig. 9.18. It is important to note that the bump structure exists for the neutral-mode as well. Therefore, if the coupling ansatz has to work, the two channels have to scatter prior to the decay of the ϕ. In addition, the charged-mode overlaps the K^+p mode of the $\Lambda(1520)$ in phase-space, so it is conceivable that the effect is enhanced for the charged-mode than for the neutral-mode. We hope that theoreticians will refit their models using our present results and be able to shed light on this problem.

9.7 Summary

In this chapter, we have presented differential cross section results for the ϕp channel. We examined both the charged and neutral decay modes of the ϕ. Around $\sqrt{s} \approx 2.1$ GeV, forward angles,

we see an interesting structure in both modes. In the forward-most angular bin, $d\sigma/dt$ shows an approxmimately constant behavior with $\sqrt{s}$, the signature behavior of diffractive Pomeron exchange. Comparisons with the few existing previous world data is generally fair, thought most of these earlier results have wide energy binning, limited statistics and kinematic coverage.

Chapter 10

Spin Density Matrix Elements for ϕ

In this chapter we describe the extraction of the spin density matrix elements (SDME's) for the ϕ vector meson. We first describe the general formulation of the density matrix for a spin-1 particle and the connection between the different SDME's and physically meaningful observables. Similar to our approach for the $K^+\Sigma^0$ channel, we extract the polarization information using both an intensity distribution fit and by using the spin-projections of our PWA aplitudes. The two methods are found to be in excellent agreement. We also discuss the interpretation of our results at the amplitude level in terms of both s- and t-channel helicity conservation (SCHC and TCHC, respectively).

10.1 The Density Matrix of a Massive Vector Particle

In Sec. 8.1.2, we showed that the spin density matrix of a massless vector particle (the photon) is given by the so-called Stokes parameters and the density matrix "lives" in the space spanned by the three Pauli matrices and $I_{2\times 2}$. The reduced space results from the fact that the same gauge symmetry that makes the photon massless also renders the polarization component along its momentum unphysical. Thus, a real photon is always transverse. For the massive case, this is no longer necessary and a massive spin-1 particle is allowed to have a longitudinal spin component. The three spin-1 operators are

$$S_x = \frac{1}{\sqrt{2}}\begin{pmatrix} 0 & 1 & 0 \\ 1 & 0 & 1 \\ 0 & 1 & 0 \end{pmatrix} \quad S_y = \frac{1}{\sqrt{2}}\begin{pmatrix} 0 & -i & 0 \\ i & 0 & -i \\ 0 & i & 0 \end{pmatrix} \quad S_z = \begin{pmatrix} 1 & 0 & 0 \\ 0 & 0 & 0 \\ 0 & 0 & -1 \end{pmatrix}, \tag{10.1}$$

and a pure spin state $|\alpha\rangle$ is an eigenstate of the full $\vec{S}$ operator. For a classical ensemble of states, the spin of the vector particle is described by the density matrix $\rho = \sum w_\alpha |\alpha\rangle\langle\alpha|$, where the sum is over a complete basis of states and w_α is the classical probability of finding the particle in the state $|\alpha\rangle$.

For the general case, however, ρ will not be diagonal and the different polarization states will be correlated. A general 3×3 complex matrix ρ has 2×3^2 real elements. Hermiticity constrains the diagonal elements of ρ to be real (3 real elements) and the off-diagonal elements to be conjugate transpose of each other (3 complex elements or 6 real elements). The unit trace constraint further reduces the number of independent elements by 1. Therefore, in all, the most general 3×3 density matrix will have 8 real and independent elements. A convenient basis to expand the density matrix

is given by three rank-1 tensors, S_i ($i = x$, y, z) and five rank-2 tensors τ_{ij} given by

$$\tau_{ij} = \frac{3}{2}(S_i S_j + S_j S_i) - 2\delta_{ij}. \tag{10.2}$$

Therefore, by construction, in the tensorial space indexed by the two rank-1 tensors S_i and S_j, τ_{ij} is symmetric and traceless.

The above tensors were written in the Cartesian basis. Following Ref. [131], we switch to the helicity basis where the spin-1 operators are written as $S_{1\pm1} = \mp(S_x \pm iS_y)/\sqrt{2}$ and $S_{10} = S_z$ [132]. Explicitly, they are

$$S_{10} = \begin{pmatrix} 1 & 0 & 0 \\ 0 & 0 & 0 \\ 0 & 0 & -1 \end{pmatrix} \quad S_{11} = -\begin{pmatrix} 0 & 1 & 0 \\ 0 & 0 & 1 \\ 0 & 0 & 0 \end{pmatrix} \quad S_{1-1} = \begin{pmatrix} 0 & 0 & 0 \\ 1 & 0 & 0 \\ 0 & 1 & 0 \end{pmatrix}. \tag{10.3}$$

In the helicity basis, the rank-2 operators $\tau_{2\mu}$ are given by the tensor products $[S_1 \otimes S_1]_\mu$, $\mu = \{0, \pm1, \pm2\}$. Substituting the appropriate Clebsch-Gordan coefficients, the tensor polarization operators are

$$\tau_{22} = S_{11}S_{11} \tag{10.4a}$$
$$\tau_{2-2} = S_{1-1}S_{1-1} \tag{10.4b}$$
$$\tau_{21} = \frac{1}{\sqrt{2}}(S_{11}S_{10} + S_{10}S_{11}) \tag{10.4c}$$
$$\tau_{2-1} = \frac{1}{\sqrt{2}}(S_{1-1}S_{10} + S_{10}S_{1-1}), \text{ and} \tag{10.4d}$$
$$\tau_{20} = \frac{1}{\sqrt{6}}(S_{11}S_{1-1} + 4S_{10}S_{10} + S_{1-1}S_{11}). \tag{10.4e}$$

For the sake of completeness, we give the explicit form of these five matrices:

$$\tau_{22} = \begin{pmatrix} 0 & 0 & 1 \\ 0 & 0 & 0 \\ 0 & 0 & 0 \end{pmatrix} \quad \tau_{2-2} = \begin{pmatrix} 0 & 0 & 0 \\ 0 & 0 & 0 \\ 1 & 0 & 0 \end{pmatrix} \quad \tau_{21} = -\frac{1}{\sqrt{2}}\begin{pmatrix} 0 & 1 & 0 \\ 0 & 0 & -1 \\ 0 & 0 & 0 \end{pmatrix}$$
$$\tau_{2-1} = -\frac{1}{\sqrt{2}}\begin{pmatrix} 0 & 0 & 0 \\ -1 & 0 & 0 \\ 0 & 1 & 0 \end{pmatrix} \quad \tau_{20} = \frac{1}{\sqrt{6}}\begin{pmatrix} 1 & 0 & 0 \\ 0 & -2 & 0 \\ 0 & 0 & 1 \end{pmatrix}. \tag{10.5}$$

The full expression of the density matrix is then given as

$$\rho = \frac{1}{3}\left[I + \frac{3}{2}\vec{S}\cdot\vec{P} + \sqrt{3}\tau\cdot T\right], \tag{10.6}$$

with the vector polarizations defined as

$$P_{1\pm1} = \mp\frac{P_x \pm iP_y}{\sqrt{2}}, \quad P_{10} = P_z, \tag{10.7}$$

and the sum over the tensor polarizations defined as

$$\tau\cdot T = \sum_{\mu=0,\pm1,\pm2} (-1)^\mu \tau_{2-\mu} T_{2\mu}. \tag{10.8}$$

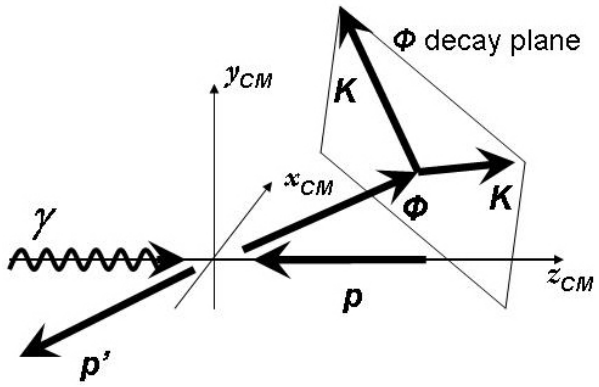

Figure 10.1: A schematic diagram of the reaction chain $\gamma p \to \phi p' \to KKp'$ in the overall center-of-mass frame. The beam direction is taken as the positive z-axis, and the y-axis is normal to the ϕ production plane.

Therefore, the density matrix can be written as

$$\rho_{\lambda\lambda'} = \begin{pmatrix} \rho_{-1-1} & \rho_{-10} & \rho_{-11} \\ \rho_{0-1} & \rho_{00} & \rho_{01} \\ \rho_{1-1} & \rho_{10} & \rho_{11} \end{pmatrix} \tag{10.9a}$$

$$= \frac{1}{3}\begin{pmatrix} 1+\frac{3}{2}P_{10}+\sqrt{\frac{1}{2}}T_{20} & -\frac{3}{2}P_{11}+\sqrt{\frac{3}{2}}T_{2-1} & \sqrt{3}T_{2-2} \\ \frac{3}{2}P_{1-1}-\sqrt{\frac{3}{2}}T_{21} & 1-\sqrt{2}T_{20} & -\frac{3}{2}P_{11}-\sqrt{\frac{3}{2}}T_{2-1} \\ \sqrt{3}T_{22} & +\frac{3}{2}P_{1-1}+\sqrt{\frac{3}{2}}T_{21} & 1-\frac{3}{2}P_{10}+\sqrt{\frac{1}{2}}T_{20} \end{pmatrix}. \tag{10.9b}$$

For photoproduction with an unpolarized beam and unpolarized target, the parity constraint $\rho^V_{\lambda\lambda'} = (-1)^{\lambda-\lambda'}\rho^V_{-\lambda-\lambda'}$ requires $P_{11} = P_{1-1}$ ($P_x = 0$), $P_{10} = 0$ ($P_z = 0$), $T_{2-1} = -T_{21}$ and $T_{2-2} = T_{22}$, so that the density matrix becomes

$$\rho_{\lambda\lambda'} = \frac{1}{3}\begin{pmatrix} 1+\sqrt{\frac{1}{2}}T_{20} & \frac{3}{2}\sqrt{\frac{1}{2}}(-iP_y)-\sqrt{\frac{3}{2}}T_{21} & \sqrt{3}T_{22} \\ \frac{3}{2}\sqrt{\frac{1}{2}}(iP_y)-\sqrt{\frac{3}{2}}T_{21} & 1-\sqrt{2}T_{20} & \sqrt{\frac{1}{2}}(-iP_y)+\sqrt{\frac{3}{2}}T_{21} \\ \sqrt{3}T_{22} & \sqrt{\frac{1}{2}}(iP_y)+\sqrt{\frac{3}{2}}T_{21} & 1+\sqrt{\frac{1}{2}}T_{20} \end{pmatrix}. \tag{10.10}$$

Therefore, for the unpolarized case, instead of eight, the density matrix has only four non-zero independent variables given by $\rho^0_{00} = \frac{1}{3}(1-\sqrt{2}T_{20})$, $\rho^0_{1-1} = T_{22}/\sqrt{3}$, $Re\rho^0_{10} = -1/\sqrt{6}T_{21}$ and $Im\rho^0_{10} = -1/(2\sqrt{2})P_y$. However, it turns out that for the decay of the vector meson through pseudoscalars ($\rho \to \pi\pi$, $\omega \to \pi\pi\pi$ or $\phi \to KK$), the element $Im\rho^0_{10}$ is also not physically measurable as well. Kloet *et al.* [131] has shown that the only way to measure the vector-polarization P_y is through leptonic decay modes of the vector mesons, with the additional requirement that the daughter leptons be detected as well. Therefore, we come to the following conclusion: *for unpolarized photoproduction of vector mesons, and subsequent detection through pseudoscalar decay modes, only the three tensor polarization components T_{20}, T_{22} and T_{21} are non-zero and physically measureable. In particular, the vector polarization $\vec{P}$ can not be measured at all.*

Fig. 10.1 shows our reaction of interest, $\gamma p \to \phi p$, with the subsequent decay of the ϕ into two kaons. This is a P-wave decay and the angular distribution of the daughter kaons is given by Schilling's equation [133]

$$W^0(\zeta,\varphi) \sim \left(\frac{1}{2}(1-\rho^0_{00}) + \frac{1}{2}(3\rho^0_{00}-1)\,\cos^2\zeta - \sqrt{2}\,Re\rho^0_{10}\sin 2\zeta\,\cos\varphi - \rho^0_{1-1}\,\sin^2\zeta\cos 2\varphi\right), \tag{10.11}$$

where ζ and φ are the polar and azimuthal angles of the K^+ unit vector (for $\phi \to K^+K^-$). Note that the element $Im\rho^0_{10}$ does not feature in Eq.10.11, so that, as explained above, P_y remains unmeasurable.

10.2 Amplitude Level Construction of $\rho^V_{\lambda\lambda'}$

The discussion of the previous section was pertitent only to an unpolarized beam-target configuration. For the general reaction $\gamma p \to Vp'$, the density matrices of the beam and the target proton also have to be considered. The non-spin-correlated observable is the overall spin-averaged differential cross-section, with several single, double, triple and even quadrauple spin-observables possible. We start with the basic amplitude for vector meson photoproduction

$$\mathcal{A} = \langle \vec{q}\lambda_V\lambda_2|T|\vec{k}\lambda_\gamma\lambda_1\rangle, \tag{10.12}$$

where λ_γ, λ_1, λ_V and λ_2 are the spin-components of the incoming photon, target proton, outgoing vector meson and outgoing proton respectively. The photon momentum is $\vec{k}$ and the vector meson momentum is $\vec{q}$. In the helicity basis, the spin-quantization axes are along the direction of each particle momentum. Counting the number of helicity states possible for each incoming and outgoing particle, there are $2\times2\times3\times2 = 24$ such complex $\mathcal{A}$ amplitudes. However, for parity conserving processes, we have the additional relation under parity-reversal

$$\langle \vec{q}\lambda_V\lambda_2|T|\vec{k}\lambda_\gamma\lambda_1\rangle = (-1)^{\lambda_{in}-\lambda_{out}}\langle \vec{q}-\lambda_V-\lambda_2|T|\vec{k}-\lambda_\gamma-\lambda_1\rangle, \tag{10.13}$$

where $\lambda_{in} = \lambda_\gamma - \lambda_1$ and $\lambda_{out} = \lambda_V - \lambda_2$ are the overall incoming- and outgoing-state helicities. Therefore there are only 12 independent complex amplitudes. Since the overall phase is irrelevant, there are 23 independent real observables to be measured. In the Pichowski-Savkli-Tabakin (PST) [132] formalism, these physical observables occur within the $12\times12 = 144$ bilinear products of the complex amplitudes. For a given beam helicity (the reverse helicity case is related by parity), the PST formalism breaks down the overall spin-space into a $\mathbf{4} = \mathbf{2}\otimes\mathbf{2}$ (enumerated by $a = \{1,2,3,4\}$) space for the initial- and final-state spin-$\frac{1}{2}$ protons and a $\mathbf{3}$ space for the vector meson ($\lambda_V = \{\pm1, 0\}$). The helicity amplitudes $H_{a\lambda_V}$ are written as

$$\begin{aligned}
H_{1\lambda_V} &= \langle\lambda_V,\lambda_2=+1/2|T|\lambda_\gamma=1,\lambda_1=-1/2\rangle\\
H_{2\lambda_V} &= \langle\lambda_V,\lambda_2=+1/2|T|\lambda_\gamma=1,\lambda_1=+1/2\rangle\\
H_{3\lambda_V} &= \langle\lambda_V,\lambda_2=-1/2|T|\lambda_\gamma=1,\lambda_1=-1/2\rangle\\
H_{4\lambda_V} &= \langle\lambda_V,\lambda_2=-1/2|T|\lambda_\gamma=1,\lambda_1=+1/2\rangle
\end{aligned} \tag{10.14}$$

In this "split" space, any general observable Ω can be written in the form

$$\Omega = \pm\frac{1}{2}\sum_{a,b,\lambda_V,\lambda'_V} H^*_{a\lambda_V}\Gamma^\alpha_{ab}\omega^\beta_{\lambda_V\lambda'_V}H_{b\lambda'_V}, \tag{10.15}$$

where the 16 Γ^α's are the usual Dirac bilinears [1] and the 9 ω^β's "live" in the vector meson spin-space spanned by the identity matrix the 3 vector polarizations and the 5 tensor polarizations. It turns

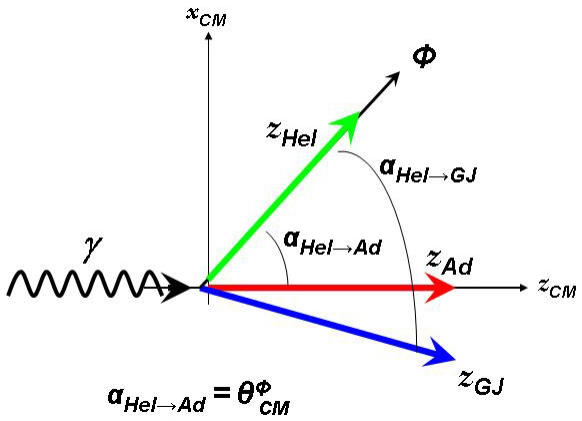

Figure 10.2: The spin-quantization axes for the Helicity (Hel, in green), Adair (Ad, in red) and Gottfried-Jackson (GJ, in blue) frames, in relation to the overall center-of-mass (c.m.) frame. The z-axis for the overall c.m. frame points along the beam direction and coincides with z_{Ad}. Since z_{Hel} points along the direction of the ϕ meson, the angle between the Helicity and Adair frames is just $\theta^{\phi}_{c.m.,}$. The Gottfried-Jackson frame is defined as the direction of the incoming photon, as seen in the rest frame of the ϕ meson. The angle between the Helicity and Gottfried-Jackson frame is given by Eq, 10.22b.

out that there are 290 possible (single, double, triple and quadruple) polarization observables [132]. Many of these observables include a similar set of bilinear $\Gamma^{\alpha}\omega^{\beta}$ observables leading to redundancies, and the question of what constitutes a "complete" set of measurements to determine the full 12 complex amplitude still remains to be answered.

10.3 Reference Frames and Helicity Conservation

The choice of the reference frame for the two decay angles in the intensity distribution of Eq. 10.11 depends on the production mechanism under examination. Three prevelant choices exist in the literature, the Adair frame, the Helicity frame, and the Gottfried-Jackson frame (see Fig. 10.2). We go over each of these below.

In the Adair (Ad) frame, the polarization axes from both the incoming and outgoing states are chosen as the z-axis (along the beam direction). With an unpolarized beam ($\rho^{\gamma} = \frac{1}{2}I$) and target, the vector meson density matrix elements are [133]

$$\begin{aligned}\rho^{0}_{m_\phi m'_\phi} &= \frac{\sum_{m_f m_\gamma m_i m'_\gamma} \mathcal{A}_{m_\phi m_f m_i m_\gamma} (\rho^{\gamma})_{m_\gamma m'_\gamma} \mathcal{A}^{*}_{m'_\phi m_f m_i m'_\gamma}}{1/2 \sum_{m_\phi m_f m_\gamma m_i} |\mathcal{A}_{m_\phi m_f m_i m_\gamma}|^2} \\ &= \frac{\sum_{m_f m_\gamma m_i} \mathcal{A}_{m_\phi m_f m_i m_\gamma} \mathcal{A}^{*}_{m'_\phi m_f m_i m_\gamma}}{\sum_{m_\phi m_f m_\gamma m_i} |\mathcal{A}_{m_\phi m_f m_i m_\gamma}|^2},\end{aligned} \tag{10.16}$$

where $\mathcal{A}_{m_\phi m_f m_i m_\gamma}$ are the same amplitudes as in the Mother Fit in Sec. 9.1. In the "PWA" method

of SDME extraction, we get the ρ^0 elements in the Adair frame by directly employing Eq. 10.16. The Adair frame is convenient when the production mechanism conserves spin in the s-channel c.m. frame. The Helicity (Hel) frame has already been defined in the earlier sections of this chapter. Here the vector meson direction in the c.m. frame defines the quantization axis. This is the preferred system for s-channel helicity conservation (SCHC). Under the assumptions of SCHC, $\rho^0_{00} = \rho^0_{10} = \rho^0_{1-1} = 0$ in the Helicity frame [134]. For the Gottfried-Jackson (GJ) frame, one makes a further boost from the overall c.m. frame to the vector meson rest-frame, and the quantization axis is along the direction of the incoming photon, *as seen in the vector meson rest-frame*. For a t-channel exchange of X, the momentum of the incoming photon and X is collinear in the GJ frame. Therefore, in the GJ frame, the ρ^0 elements measure the degree of helicity flip due to the t-channel exchange of X. For example, if the t-channel exchange particle is a 0^+, then no helicity flip will occur (TCHC) and the vector meson will have the same helicity as the incoming photon. For this case $\rho^{GJ}_{00} = \rho^{GJ}_{10} = \rho^{GJ}_{1-1} = 0$ [134].

Note that for $m_\phi = m'_\phi = 0$, ignoring the initial and final proton spins (which are not measured)

$$\rho^0_{00} \sim |\mathcal{A}_{m_\phi=0,m_\gamma=1}|^2 + |\mathcal{A}_{m_\phi=0,m_\gamma=-1}|^2. \tag{10.17}$$

Therefore a non-zero value of ρ^0_{00} is a direct measurement of the helicity flip between the incoming photon and the outgoing vector meson.

10.3.1 Conversion between the Adair, Helicity and GJ frames

It is clear that knowing the ρ elements in one frame, one can immediately calculate them in any other frame by a Wigner rotation. The y-axis is always the normal to the vector meson production plane; $\vec{y} = \vec{k} \times \vec{q}$, where $\vec{k}$ is the incoming photon direction and $\vec{q}$ is the outgoing vector meson (ϕ) direction. The choice of the z-axis is frame dependent, as described above. For the Adair frame $\vec{z} = \vec{k}$, for the Helicity frame, $\vec{z} = \vec{q}$, and for the GJ frame, $\vec{z} = \vec{k'}$, where $\vec{k'}$ points along the incoming photon direction in the vector meson rest frame. Once the y- and the z-axis has been fixed, $\vec{x} = \vec{y} \times \vec{z}$. Let $\hat{\pi}$ be the direction of the daughter K^+ (for $\phi \to K^+K^-$) in the chosen reference frame. Then the angles ζ and φ in Eq. 10.11 are given as [133]:

$$\cos\zeta = \hat{\pi} \cdot \hat{z}, \quad \cos\varphi = \frac{\hat{y} \cdot (\hat{z} \times \hat{\pi})}{|\hat{z} \times \hat{\pi}|}, \quad \sin\varphi = -\frac{\hat{x} \cdot (\hat{z} \times \hat{\pi})}{|\hat{z} \times \hat{\pi}|}, \tag{10.18}$$

In the Rose convention of the signs for the Wigner matrices (this is the followed by the Schilling paper [133]), the general form of the density matrix (after parity, Hermiticity and trace conditions have been placed) is

$$\rho = \begin{pmatrix} \frac{1}{2}(1-\rho_{00}) & \rho_{10} & \rho_{1-1} \\ \rho_{10} & \rho_{00} & -\rho_{10} \\ \rho_{1-1} & -\rho_{10} & \frac{1}{2}(1-\rho_{00}) \end{pmatrix}, \tag{10.19}$$

where we remind the reader that this is for unpolarized beam and unpolarized target. The Wigner rotation matrix for spin-1 is[1]

$$d^1(\alpha) = \begin{pmatrix} \frac{1+\cos\alpha}{2} & -\frac{\sin\alpha}{\sqrt{2}} & \frac{1-\cos\alpha}{2} \\ \frac{\sin\alpha}{\sqrt{2}} & \cos\alpha & -\frac{\sin\alpha}{\sqrt{2}} \\ \frac{1-\cos\alpha}{2} & \frac{\sin\alpha}{\sqrt{2}} & \frac{1+\cos\alpha}{2} \end{pmatrix}. \tag{10.20}$$

To rotate the density matrix from refernce frame A to B, the transformation is

$$\rho^B = d^1(-\alpha_{A\to B})\rho^A d^1(\alpha_{A\to B}). \tag{10.21}$$

[1]In the Wigner convention, followed by the PDG [53] for example, the signs of α and ρ_{10} are reversed.

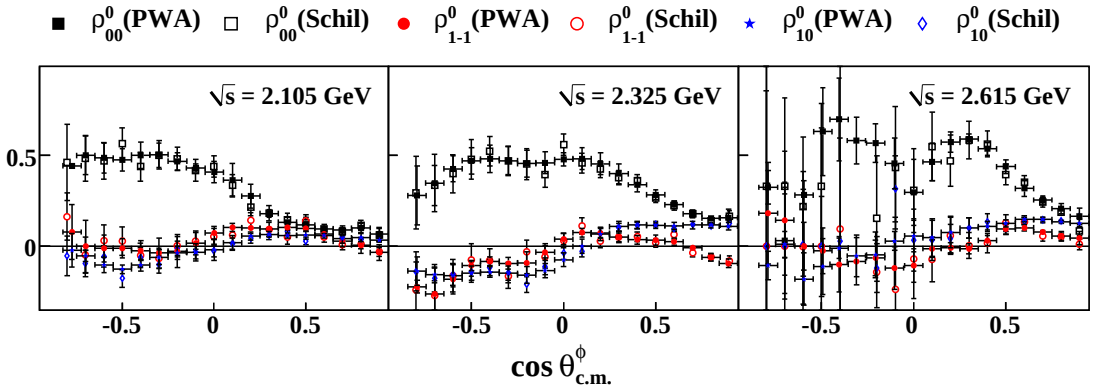

Figure 10.3: Comparison between SDME extraction using the PWA method and Schilling's method in the Adair frame. Within the limitations of statistical uncertainties, the agreement is excellent.

These rotation angles (counter-clockwise is positive) are given by

$$\alpha_{Ad\to Hel} = \theta^{\phi}_{c.m.} \tag{10.22a}$$

$$\alpha_{Hel\to GJ} = -\cos^{-1}\left(\frac{\beta-\cos\theta^{\phi}_{c.m.}}{\beta\cos\theta^{\phi}_{c.m.}-1}\right) \tag{10.22b}$$

$$\alpha_{Ad\to GJ} = \alpha_{Ad\to Hel}+\alpha_{Hel\to GJ}, \tag{10.22c}$$

where $\beta=\frac{|\vec{p}_K|}{E_K}$ is the velocity of the daughter kaon in the ϕ rest frame (for the $\phi\to KK$ decay).

10.4 Statistical Uncertainties for the PWA method

Following previous work on the ω channel [51], we compute the statistical uncertainties for the SDME's extracted using the PWA method from the statistical spread relative to the adjacent W-bins. That is, our estimated statistical error on $\rho^0_{MM'}(W_i,\cos\theta^{\phi}_{c.m.})$ at the i^{th} W-bin is obtained by comparing it to $\rho^0_{MM'}(W_{i\pm1},\cos\theta^{\phi}_{c.m.})$ as

$$\sigma^2(W_i,\cos\theta^{\phi}_{c.m.})=\frac{1}{2}\sum_{j=-1}^{1}\left(\rho^0_{MM'}(W_{i+j},\cos\theta^{\phi}_{c.m.})-\bar{\rho}^0_{MM'}(W_i,\cos\theta^{\phi}_{c.m.})\right)^2, \tag{10.23}$$

where $\bar{\rho}^0_{MM'}(W_i,\cos\theta^{\phi}_{c.m.})$ is the mean value of the three measurements. Subsequently, a smoothing algorithm is applied that sets the statistical error on $\rho^0_{MM'}(W_i,\cos\theta^{\phi}_{c.m.})$ as the mean value of the estimated errors at $(W_{i\pm1},\cos\theta^{\phi}_{c.m.})$.

10.5 Comparison of PWA and Schilling Methods

As mentioned earlier the density matrix in the Adair frame can be directly projected out using Eq. 10.16 and the PWA Mother Fit amplitudes. Eqivalently, one can also employ the Schilling's equation (Eq. 10.11). Fig. 10.3 shows a comparison between the two methods of extraction using the charged-mode topology. Within the limitations of experimental uncertainties, the agreement is excellent.

10.6 Systematic Uncertainties

As for the $K^+\Sigma^0$ polarization results, there is no standardized method for calculating the systematic uncertainties for the SDME's. We adopt the results obtained in a previous CLAS analysis for the ωp channel. This study [51] examined the maximal (or rather, the extimated maximal) effect of an incorrect acceptance calculation on the SDME's. This would distort the acceptance corrected normalized intensity distribution given by Eq. 10.11 and would lead to incorrect values of the ρ elements. The deviation between the two results gave an estimation of the systematic uncertainties as

$$\sigma_{00} = 0.0175, \quad \sigma_{1-1} = 0.0125, \text{ and } \sigma_{10} = 0.01. \tag{10.24}$$

Since the underlying assumption for this study was that the intensity distribution for the vector meson decay was given by the Schilling's equation (Eq. 10.11) it is reasonable to adopt these results for the present analysis as well.

10.7 Final SDME results

Figs. 10.4-10.18 show the spin density matrix elements (SDME) for the charged-mode topology in all three (Adair, Helicity and GJ) frames. The most promiment feature is the large value of ρ^0_{00} (especially in the Adair and GJ frames), while ρ^0_{10} and ρ^0_{1-1} are small, but non-zero. In the Helicity frame, ρ^0_{00} remains relatively smaller, but still, non-zero. Therefore *SCHC and TCHC are both seen to be broken.* In the Adair frame in Figs. 10.4-10.4, there is a similarity with the corresponding results for the ωp channel [16] in the "hump-like" angular structure for ρ^0_{00}. At high $\sqrt{s}$, the ωp results have a distinct "dip" for ρ^0_{00} in the mid-forward angles. For the ϕp case, there are indications of a "dip" for ρ^0_{00} in the mid- to mid-backward angles, though the structure is much less well-defined due to statistical limitations at high $\sqrt{s}$ and $\cos\theta^{\phi}_{c.m.} < 0$. Figs. 10.19-10.27 shows the SDME's for the neutral-mode topology in the Adair frame. The energy bins are at least 30-MeV-wide in $\sqrt{s}$.

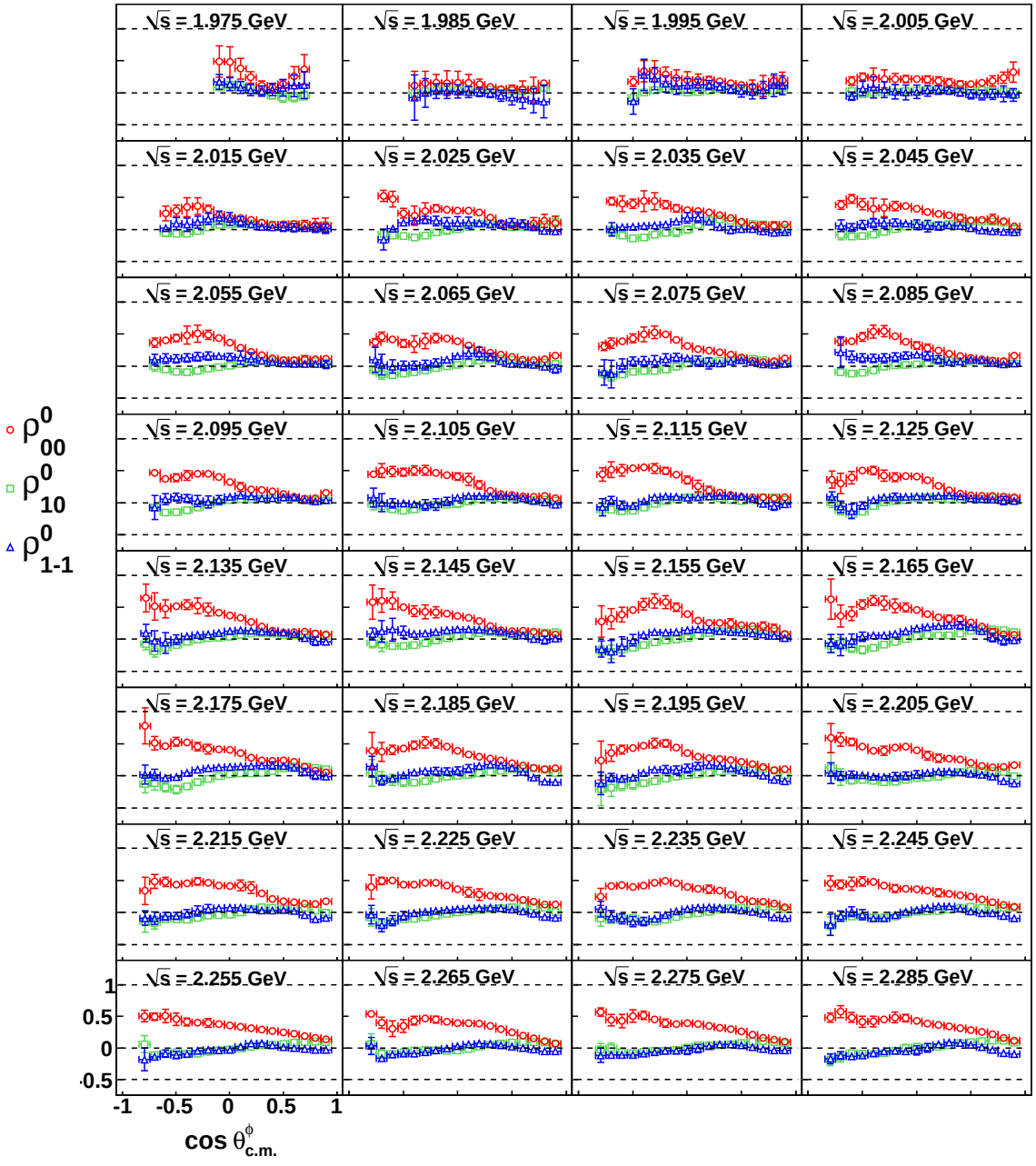

Figure 10.4: SDME *vs.* $\cos\theta^{\phi}_{\mathrm{c.m.}}$: spin density matrix elements in the Adair frame for the charged-mode topology in the energy range 1.97 GeV $\leq \sqrt{s} <$ 2.29 GeV. The centroid of each 10-MeV-wide bin is printed on the plots. All error bars represent statistical uncertainties only.

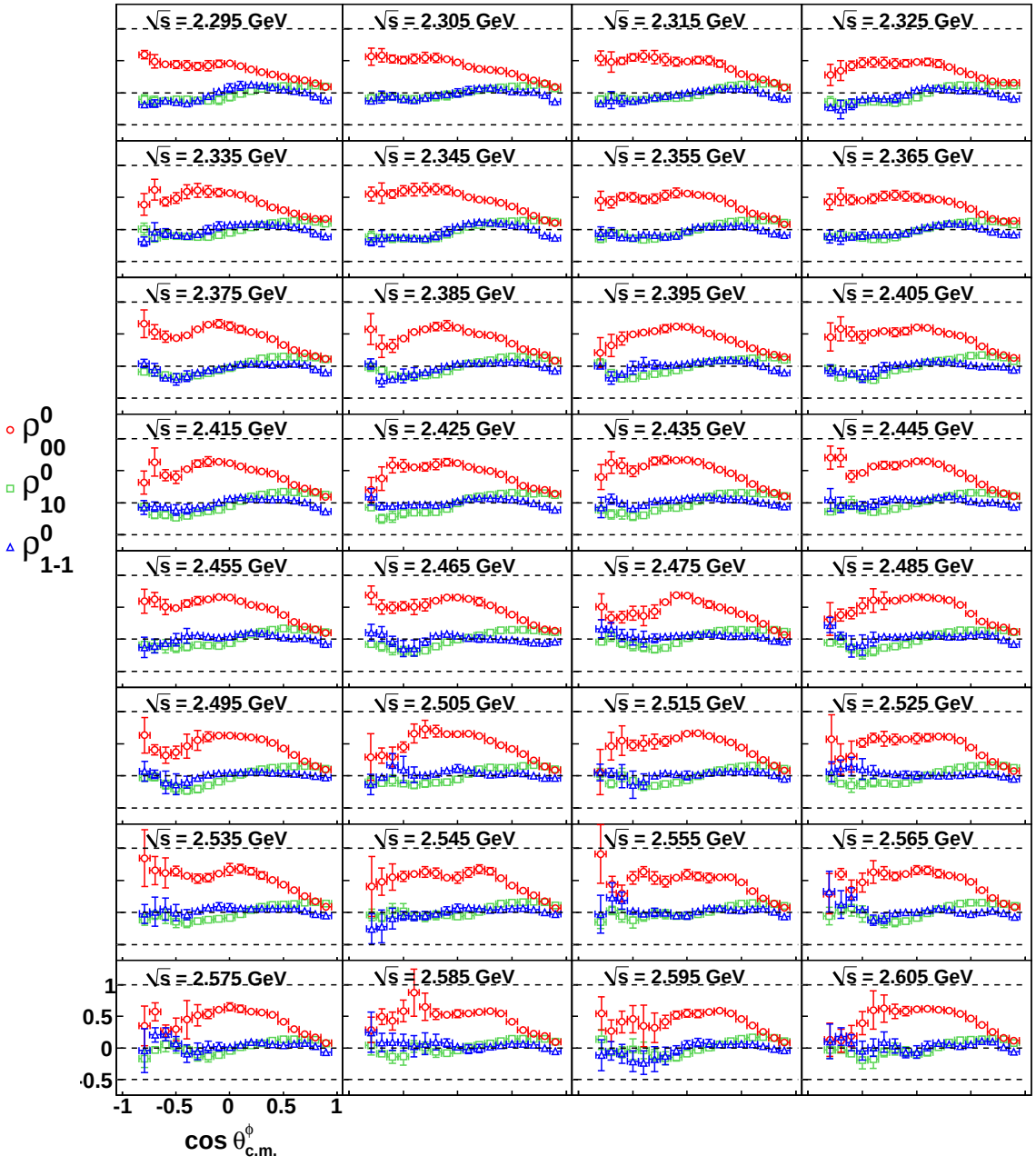

Figure 10.5: SDME *vs.* $\cos\theta^{\phi}_{\mathrm{c.m.}}$: spin density matrix elements in the Adair frame for the charged-mode topology in the energy range 2.29 GeV $\leq \sqrt{s} <$ 2.61 GeV. The centroid of each 10-MeV-wide bin is printed on the plots. All error bars represent statistical uncertainties only.

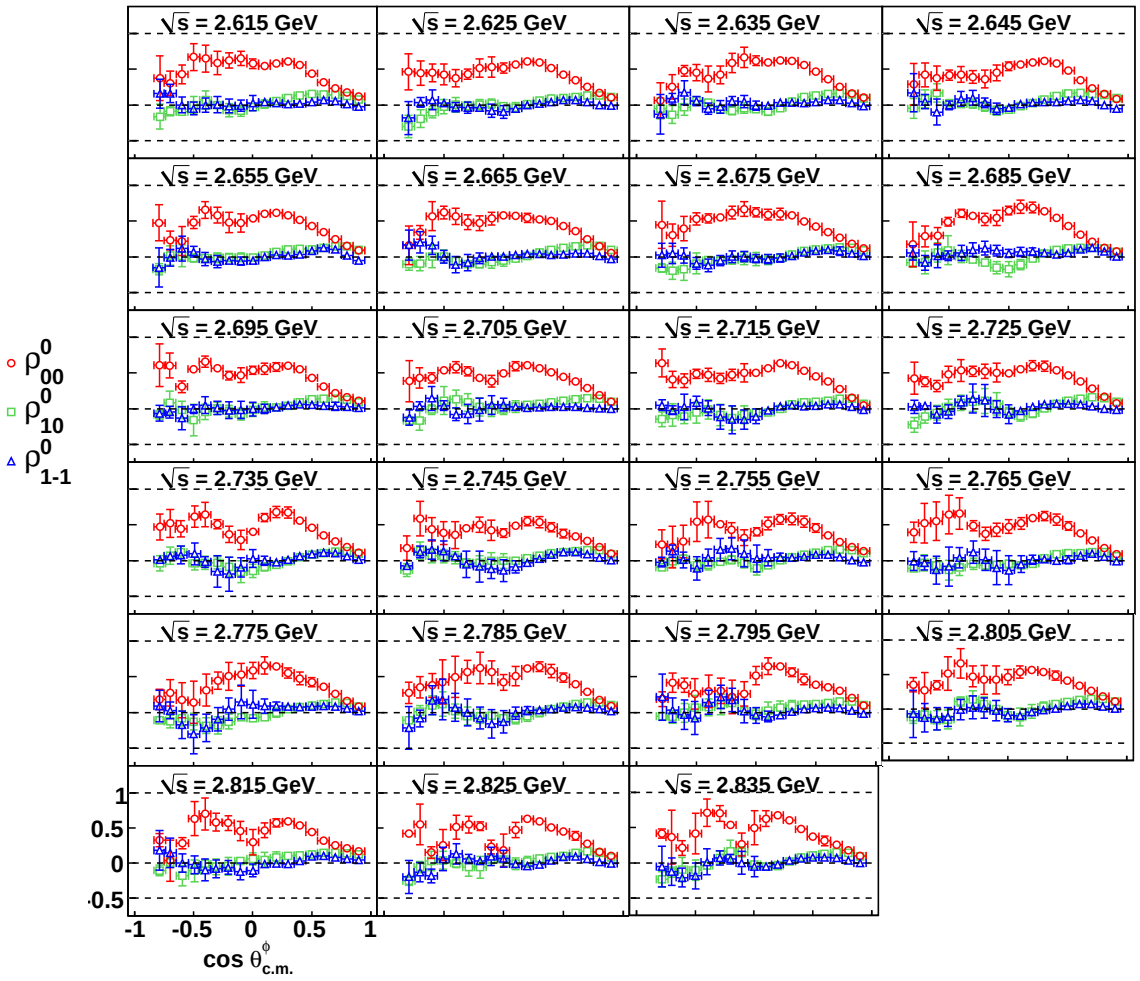

Figure 10.6: SDME *vs.* $\cos\theta^{\phi}_{\mathrm{c.m.}}$: spin density matrix elements in the Adair frame for the charged-mode topology in the energy range 2.61 GeV $\leq \sqrt{s} <$ 2.84 GeV. The centroid of each 10-MeV-wide bin is printed on the plots. All error bars represent statistical uncertainties only.

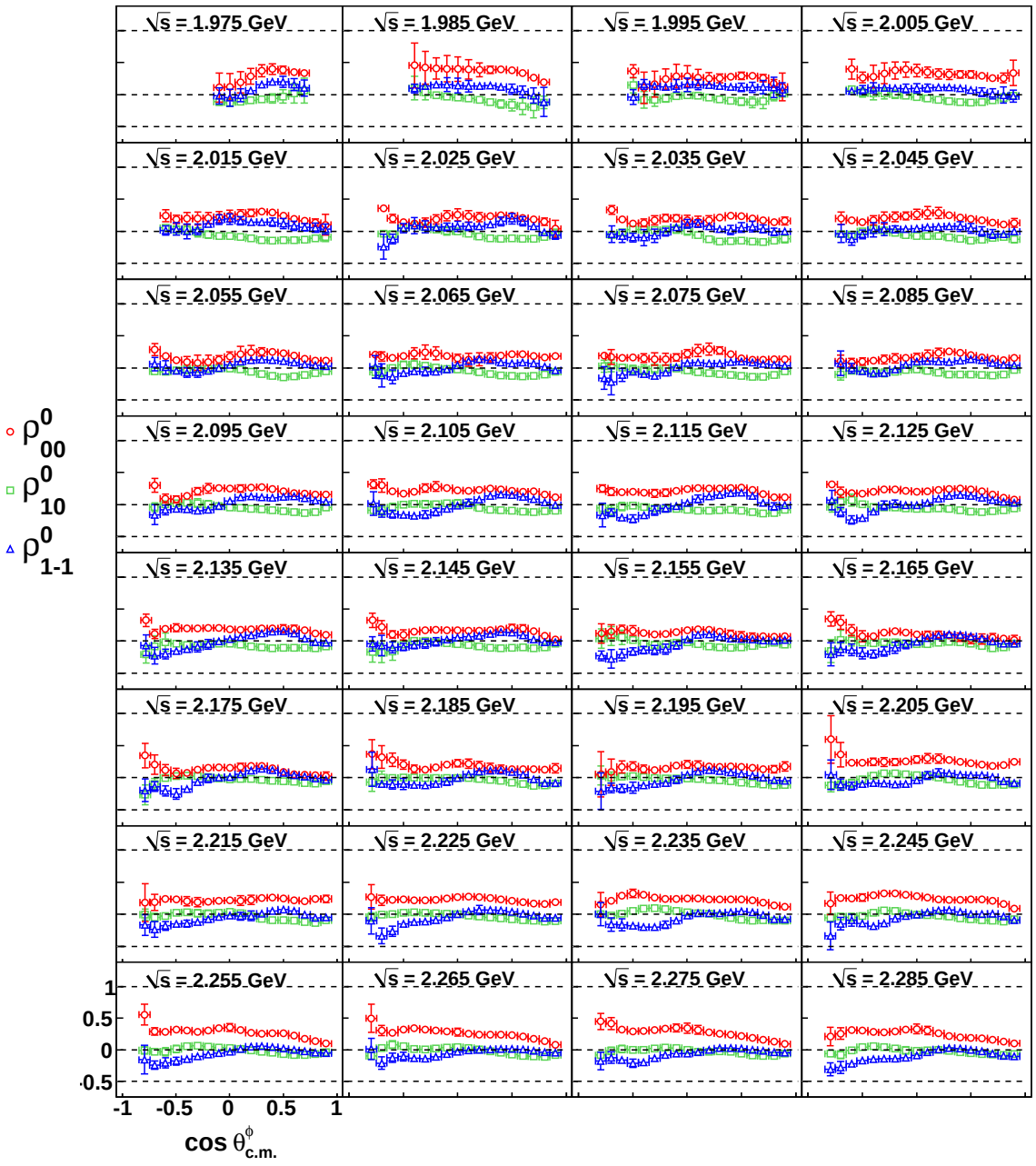

Figure 10.7: SDME *vs.* $\cos\theta^{\phi}_{\mathrm{c.m.}}$: spin density matrix elements in the Helicity frame for the charged-mode topology in the energy range 1.97 GeV $\leq \sqrt{s} <$ 2.29 GeV. The centroid of each 10-MeV-wide bin is printed on the plots. All error bars represent statistical uncertainties only.

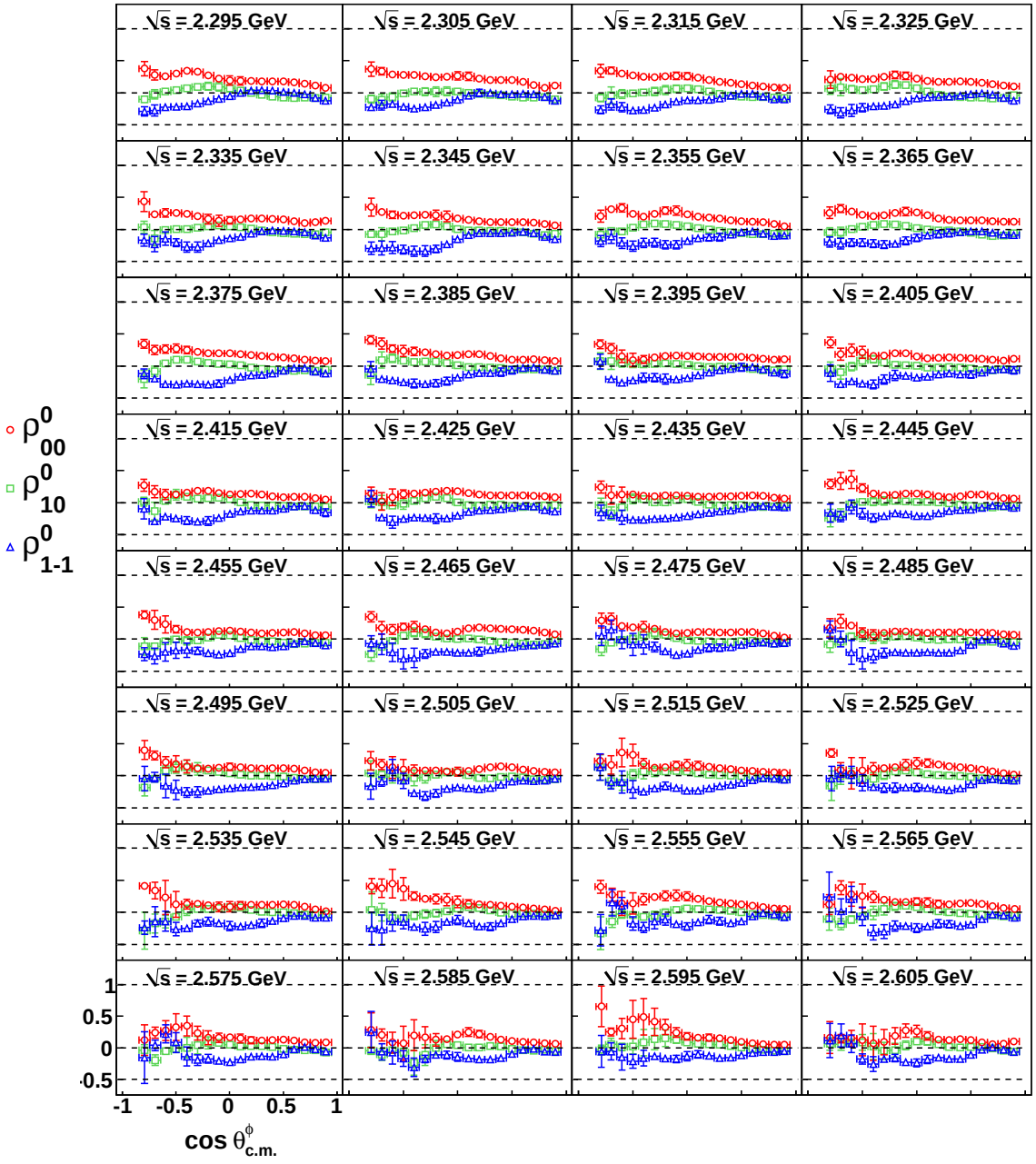

Figure 10.8: SDME *vs.* $\cos\theta^{\phi}_{\mathrm{c.m.}}$: spin density matrix elements in the Helicity frame for the charged-mode topology in the energy range 2.29 GeV $\leq \sqrt{s} <$ 2.61 GeV. The centroid of each 10-MeV-wide bin is printed on the plots. All error bars represent statistical uncertainties only.

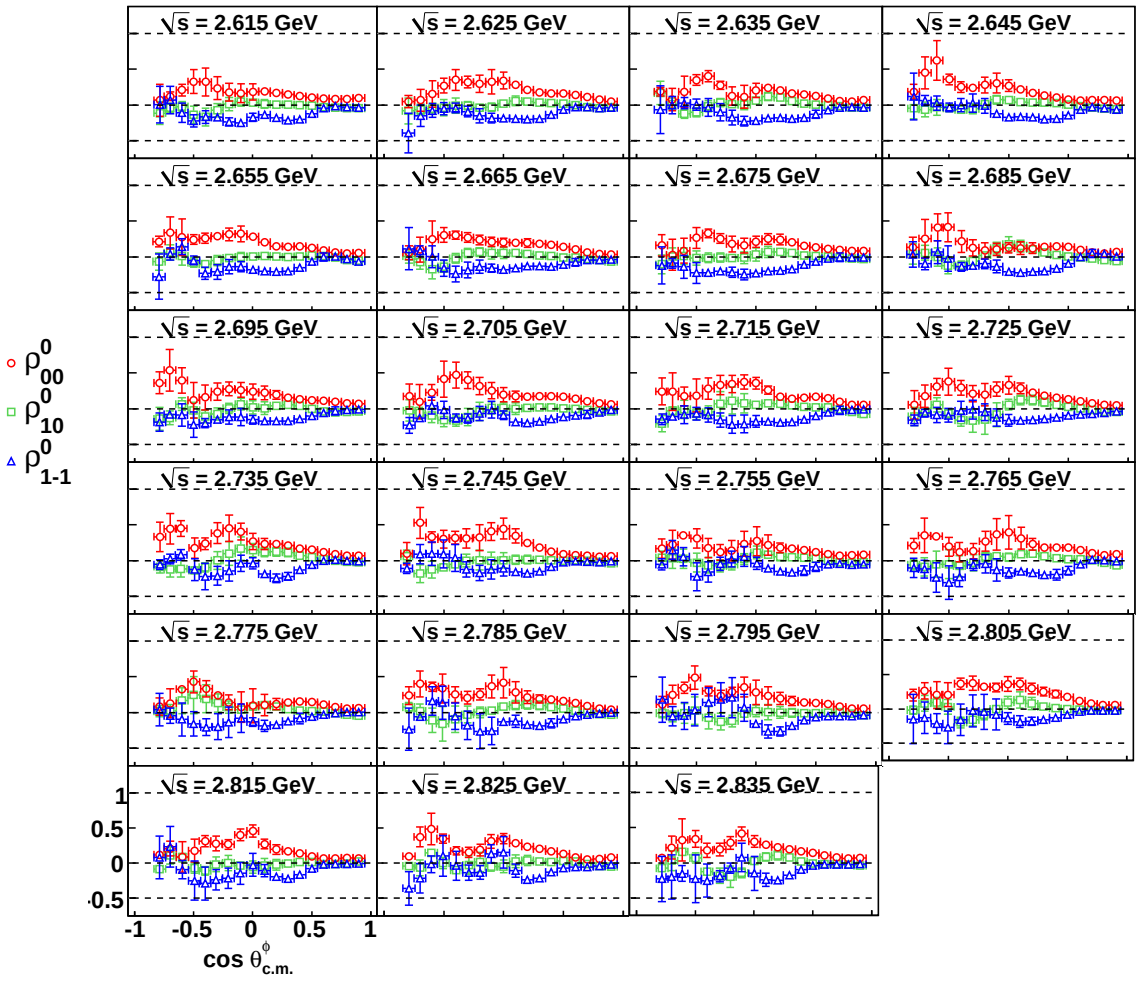

Figure 10.9: SDME *vs.* $\cos\theta^{\phi}_{\mathrm{c.m.}}$: spin density matrix elements in the Helicity frame for the charged-mode topology in the energy range 2.61 GeV $\leq \sqrt{s} <$ 2.84 GeV. The centroid of each 10-MeV-wide bin is printed on the plots. All error bars represent statistical uncertainties only.

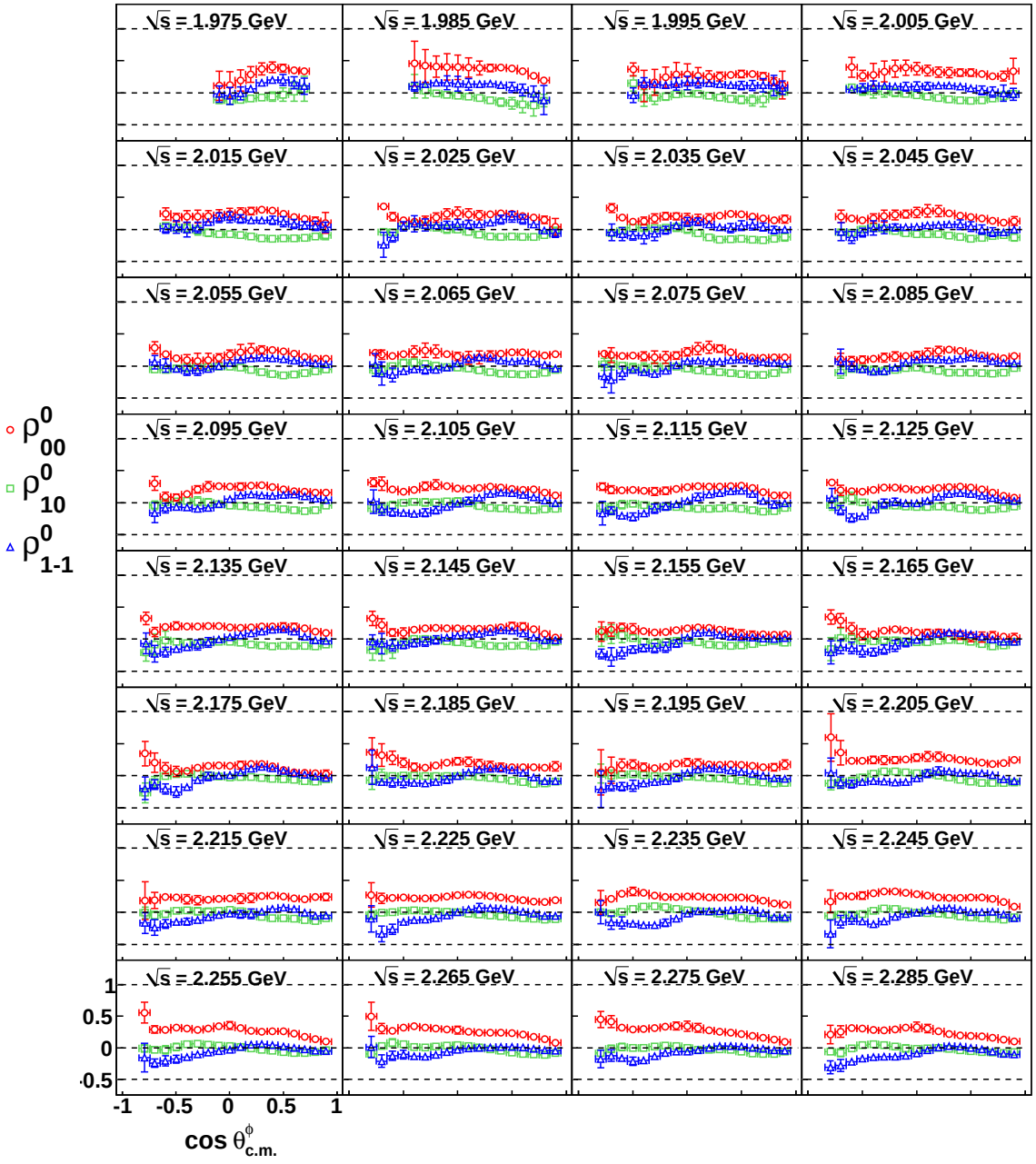

Figure 10.10: SDME *vs.* $\cos\theta^{\phi}_{\mathrm{c.m.}}$: spin density matrix elements in the GJ frame for the charged-mode topology in the energy range 1.97 GeV $\leq \sqrt{s} <$ 2.29 GeV. The centroid of each 10-MeV-wide bin is printed on the plots. All error bars represent statistical uncertainties only.

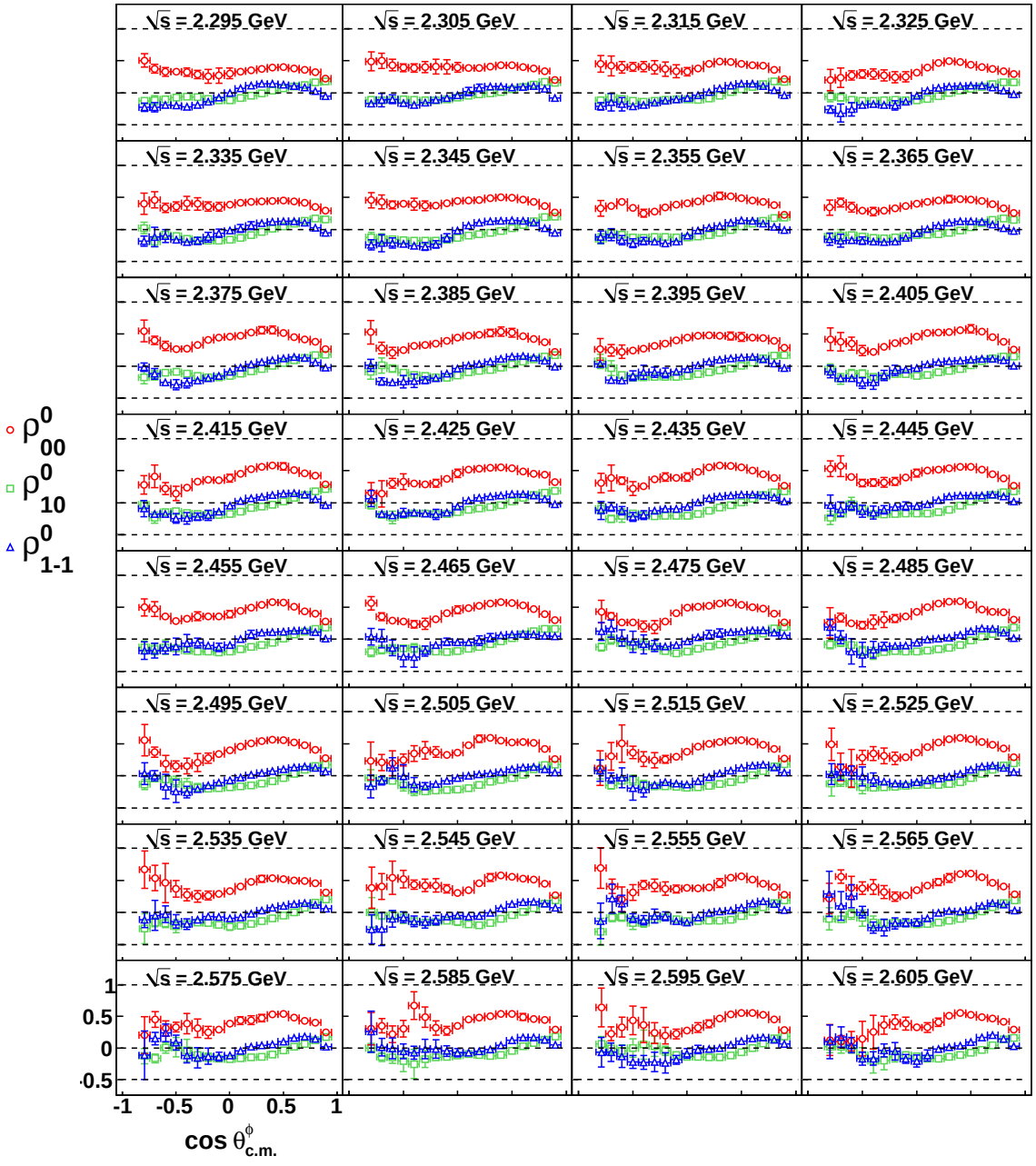

Figure 10.11: SDME *vs.* $\cos\theta^{\phi}_{\mathrm{c.m.}}$: spin density matrix elements in the GJ frame for the charged-mode topology in the energy range 2.29 GeV $\leq \sqrt{s} <$ 2.61 GeV. The centroid of each 10-MeV-wide bin is printed on the plots. All error bars represent statistical uncertainties only.

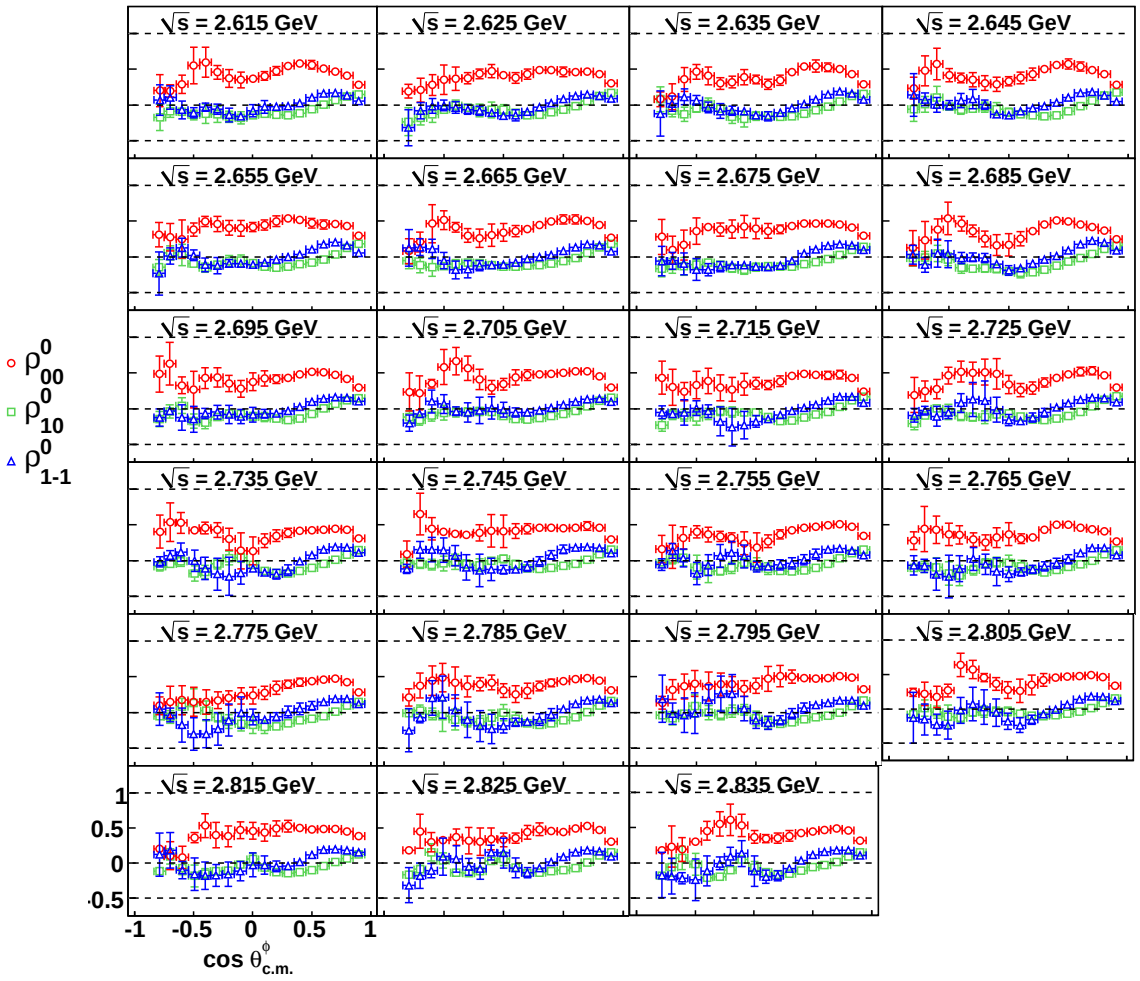

Figure 10.12: SDME *vs.* $\cos\theta^{\phi}_{\mathrm{c.m.}}$: spin density matrix elements in the GJ frame for the charged-mode topology in the energy range 2.61 GeV $\leq \sqrt{s} <$ 2.84 GeV. The centroid of each 10-MeV-wide bin is printed on the plots. All error bars represent statistical uncertainties only.

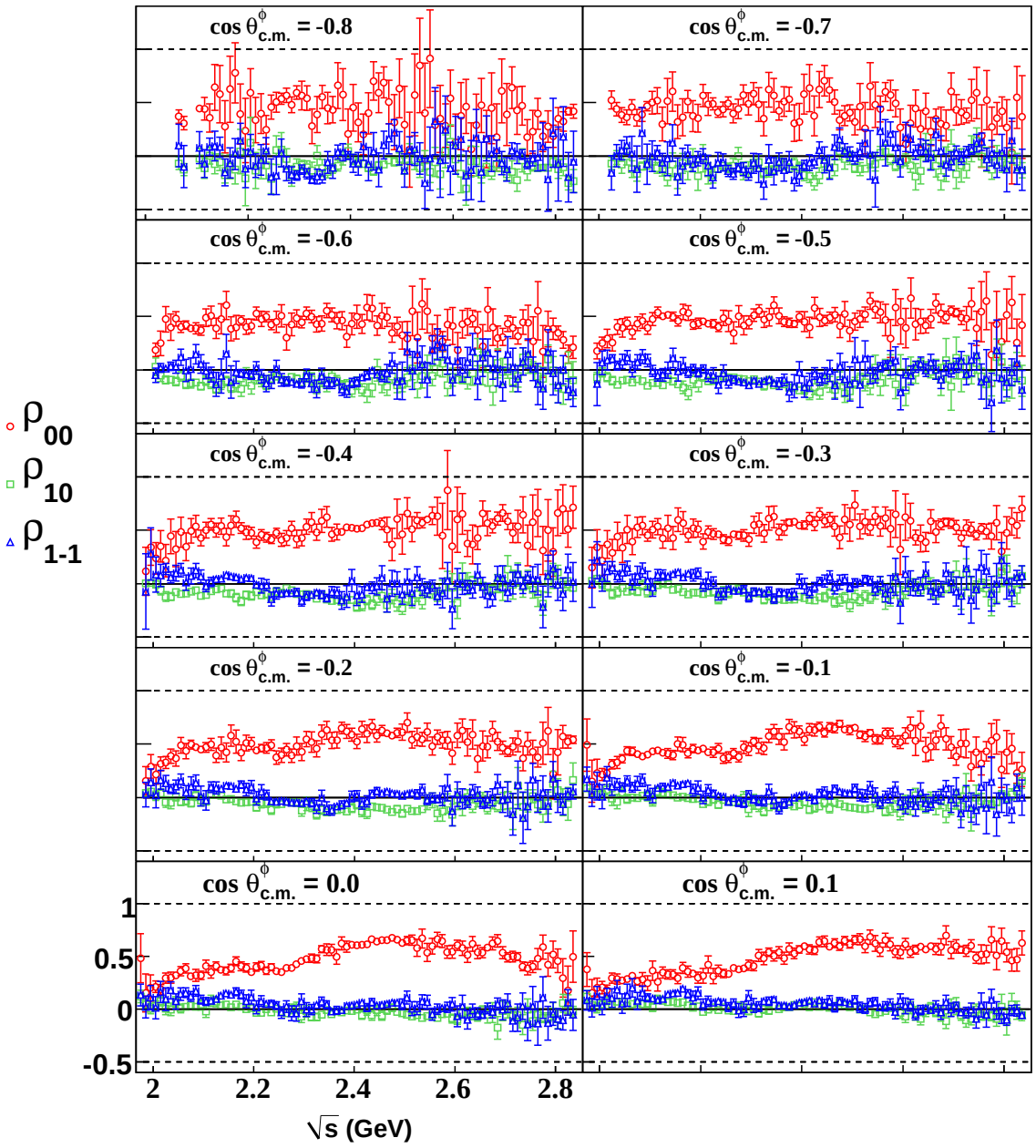

Figure 10.13: The energy dependence of SDME's (Adair frame) in the backward- and mid-angle bins for the charged-mode topology. All error bars represent statistical uncertainties only.

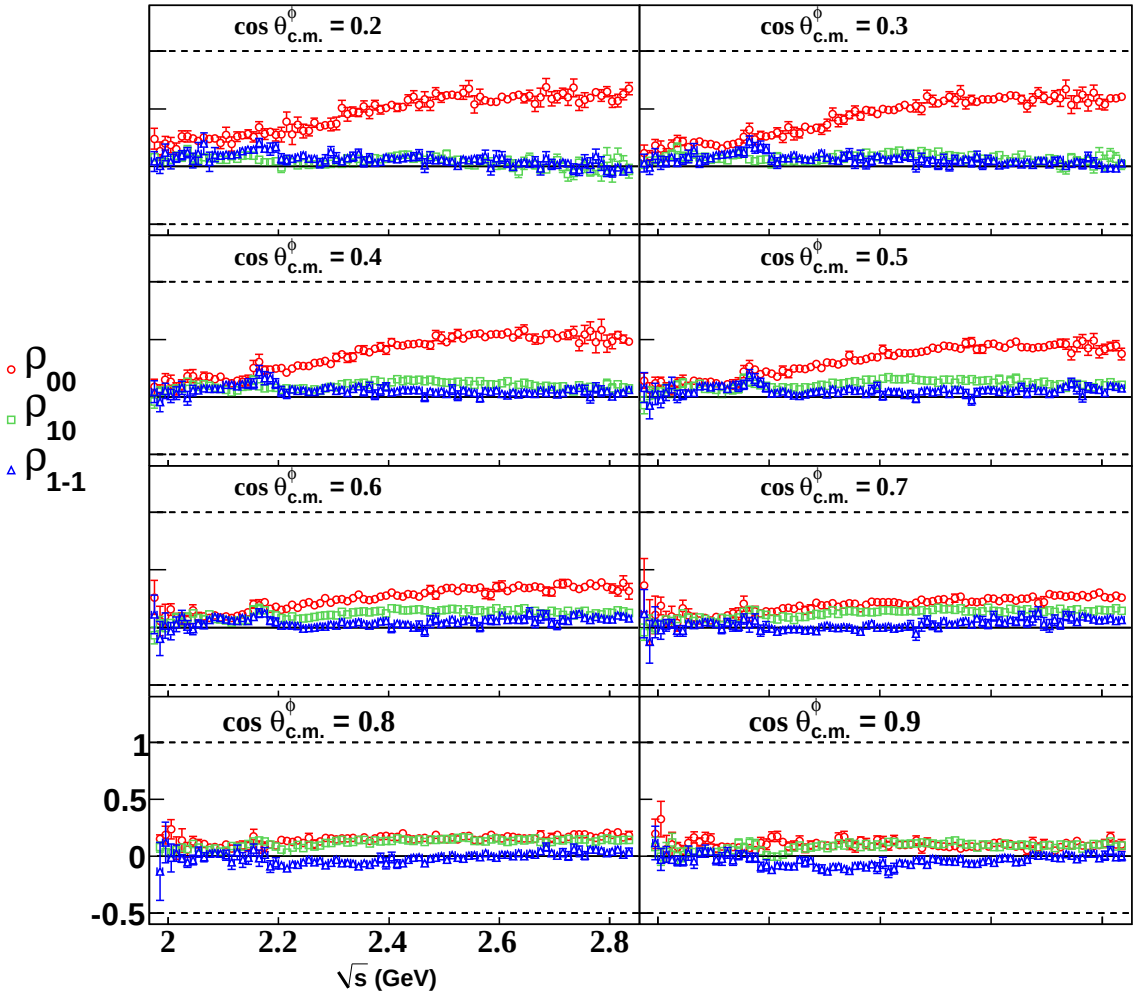

Figure 10.14: The energy dependence of SDME's (Adair frame) in the backward- and mid-angle bins for the charged-mode topology. All error bars represent statistical uncertainties only.

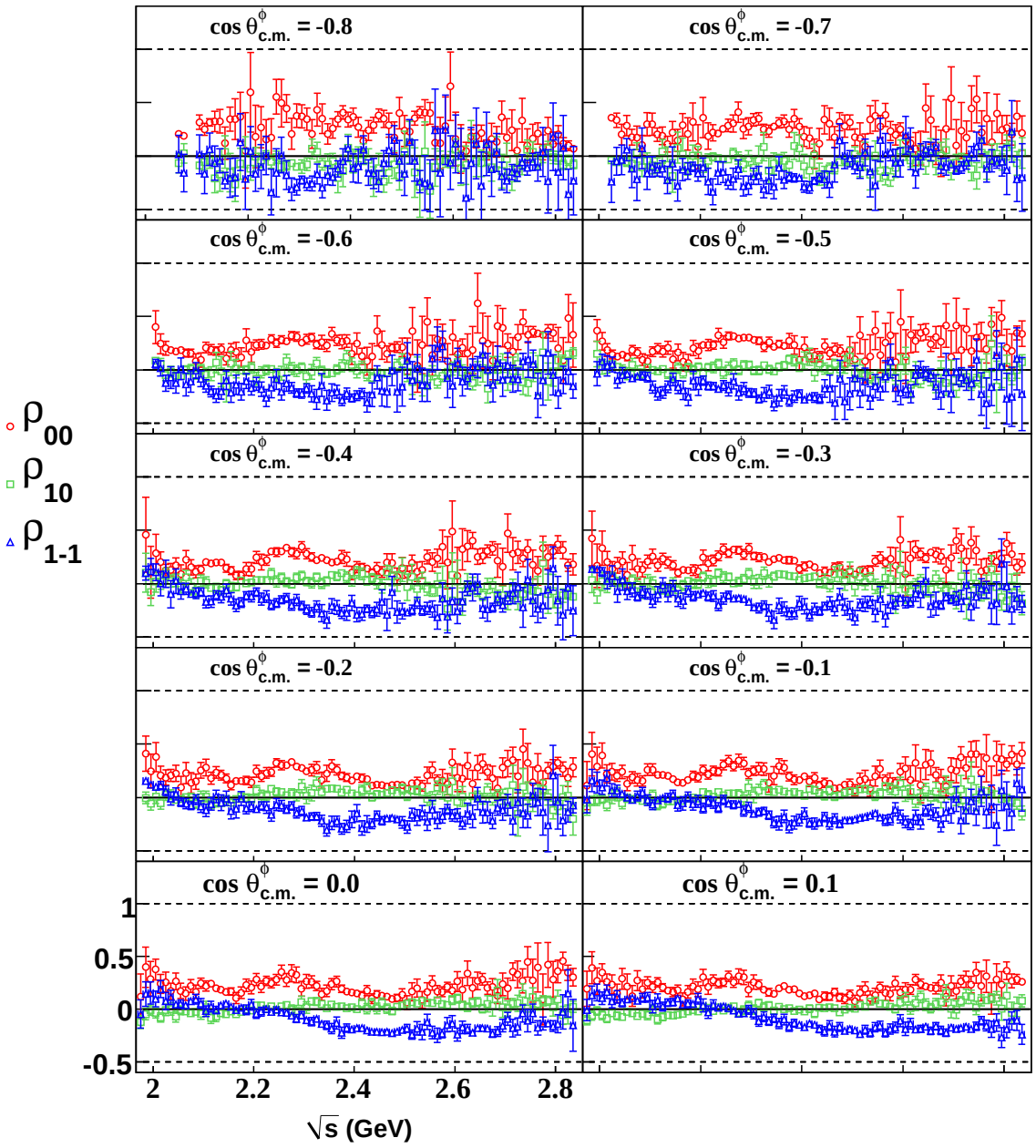

Figure 10.15: The energy dependence of SDME's (Helicity frame) in the backward- and mid-angle bins for the charged-mode topology. All error bars represent statistical uncertainties only.

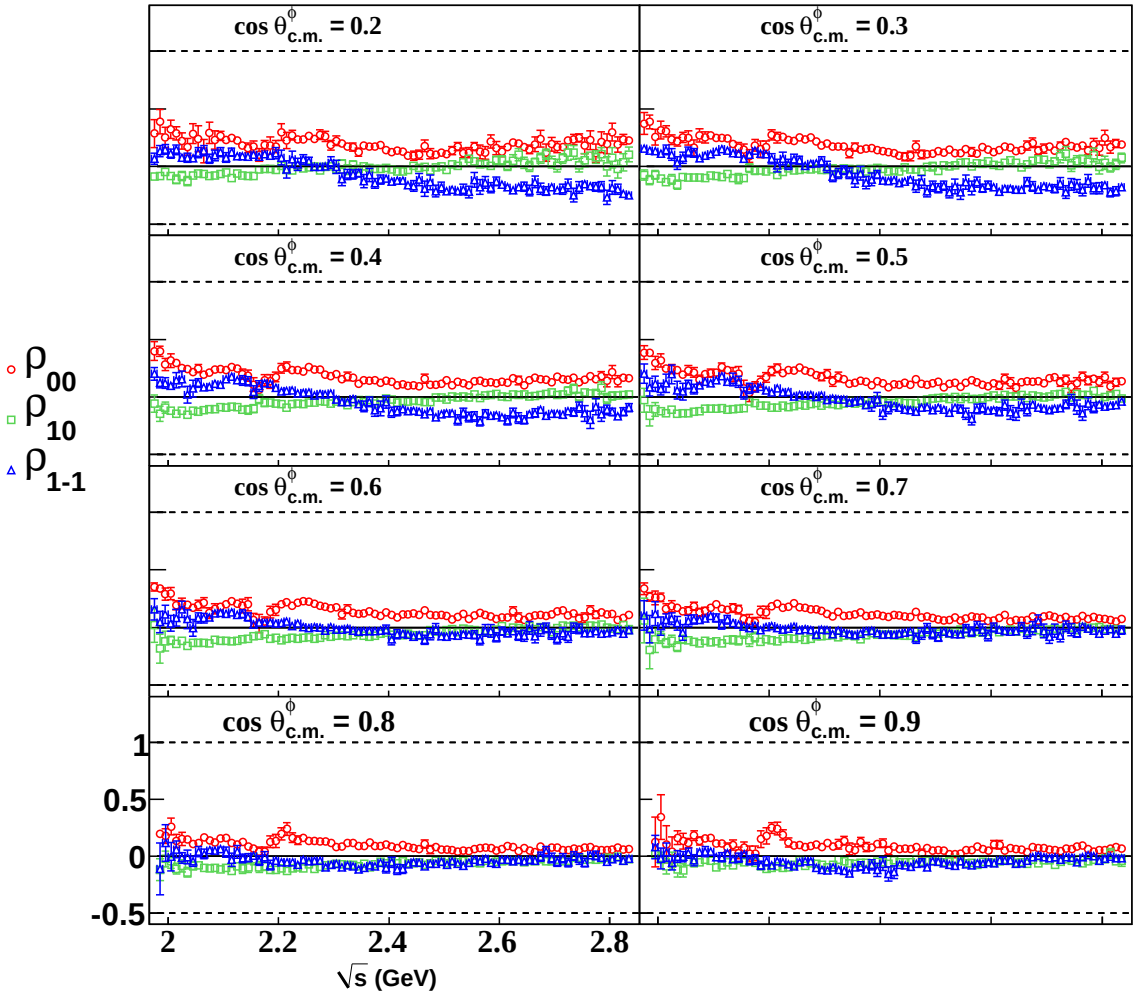

Figure 10.16: The energy dependence of SDME's (Helicity frame) in the backward- and mid-angle bins for the charged-mode topology. All error bars represent statistical uncertainties only.

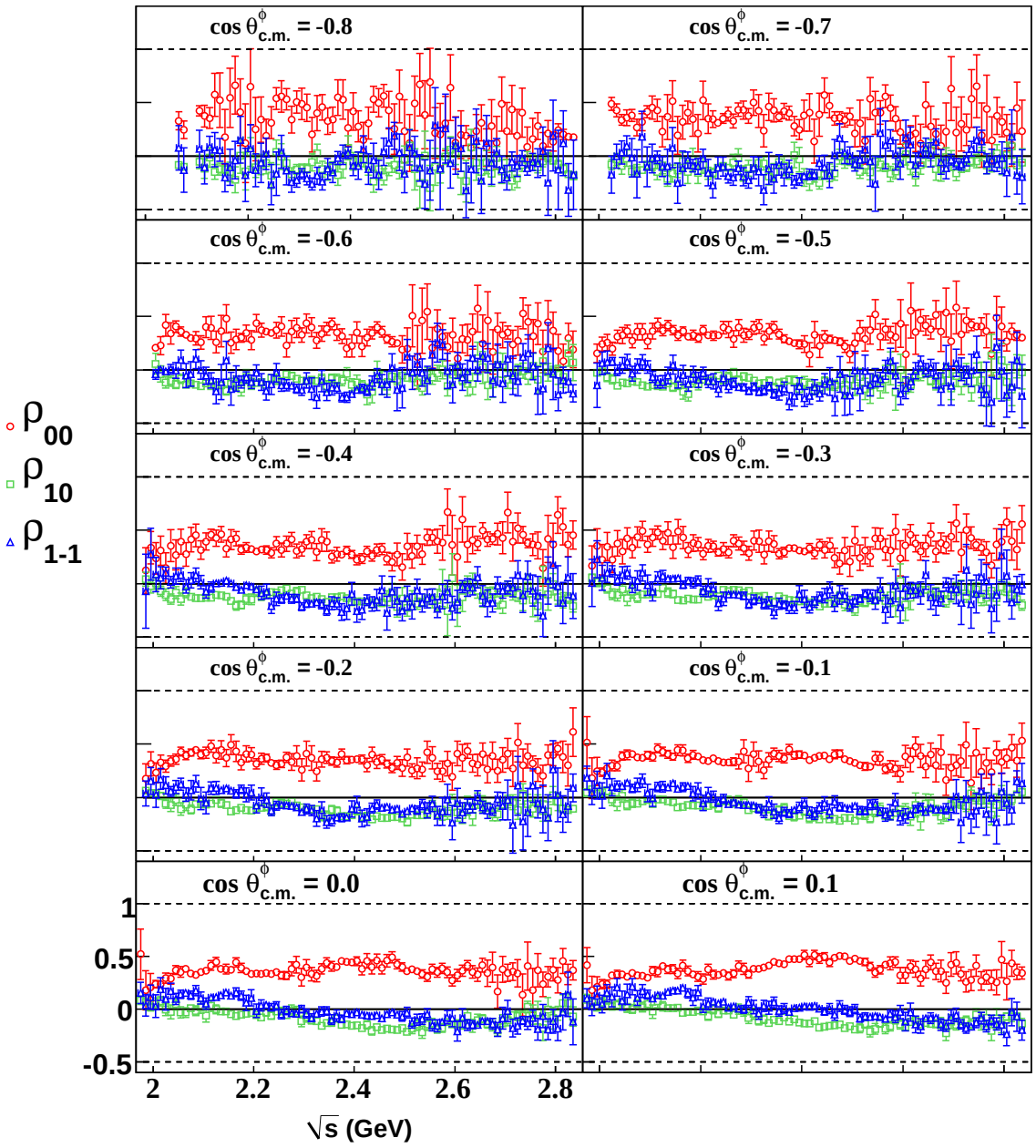

Figure 10.17: The energy dependence of SDME's (GJ frame) in the backward- and mid-angle bins for the charged-mode topology. All error bars represent statistical uncertainties only.

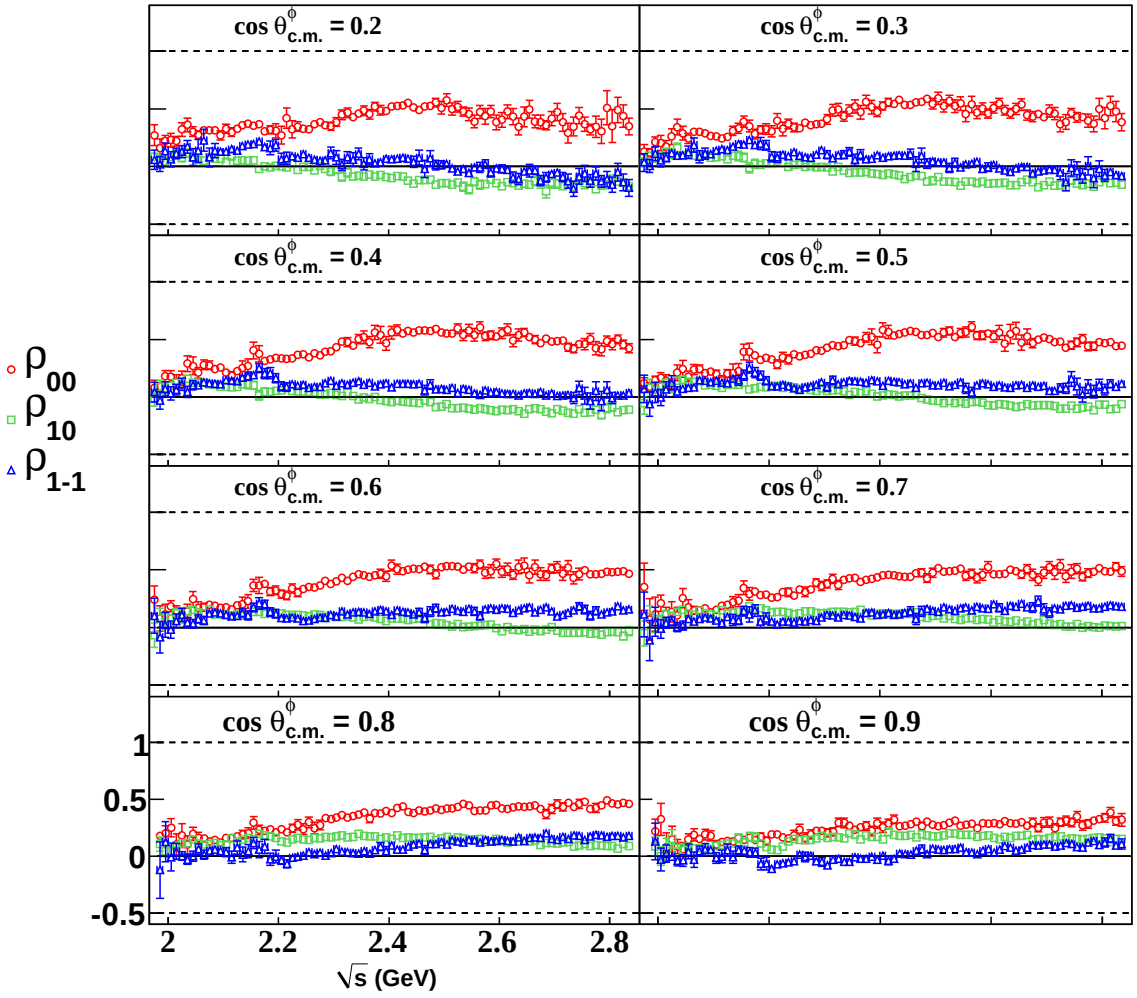

Figure 10.18: The energy dependence of SDME's (GJ frame) in the backward- and mid-angle bins for the charged-mode topology. All error bars represent statistical uncertainties only.

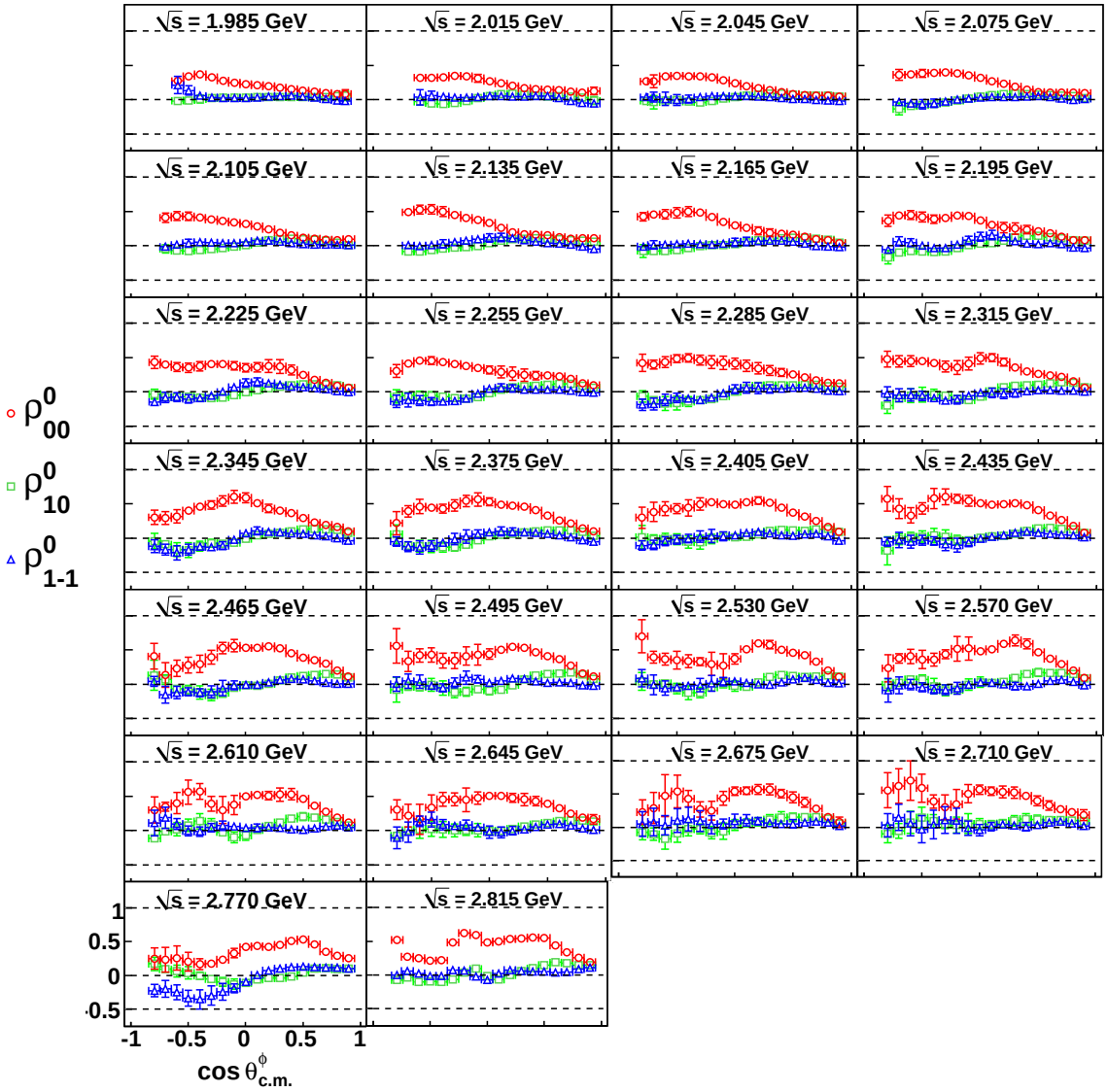

Figure 10.19: SDME *vs.* $\cos\theta^{\phi}_{c.m.}$: spin density matrix elements in the Adair frame for the neutral-mode topology. The minimum bin-width is 30-MeV in $\sqrt{s}$ and the centroid of each bin is printed on the plots. All error bars represent statistical uncertainties only.

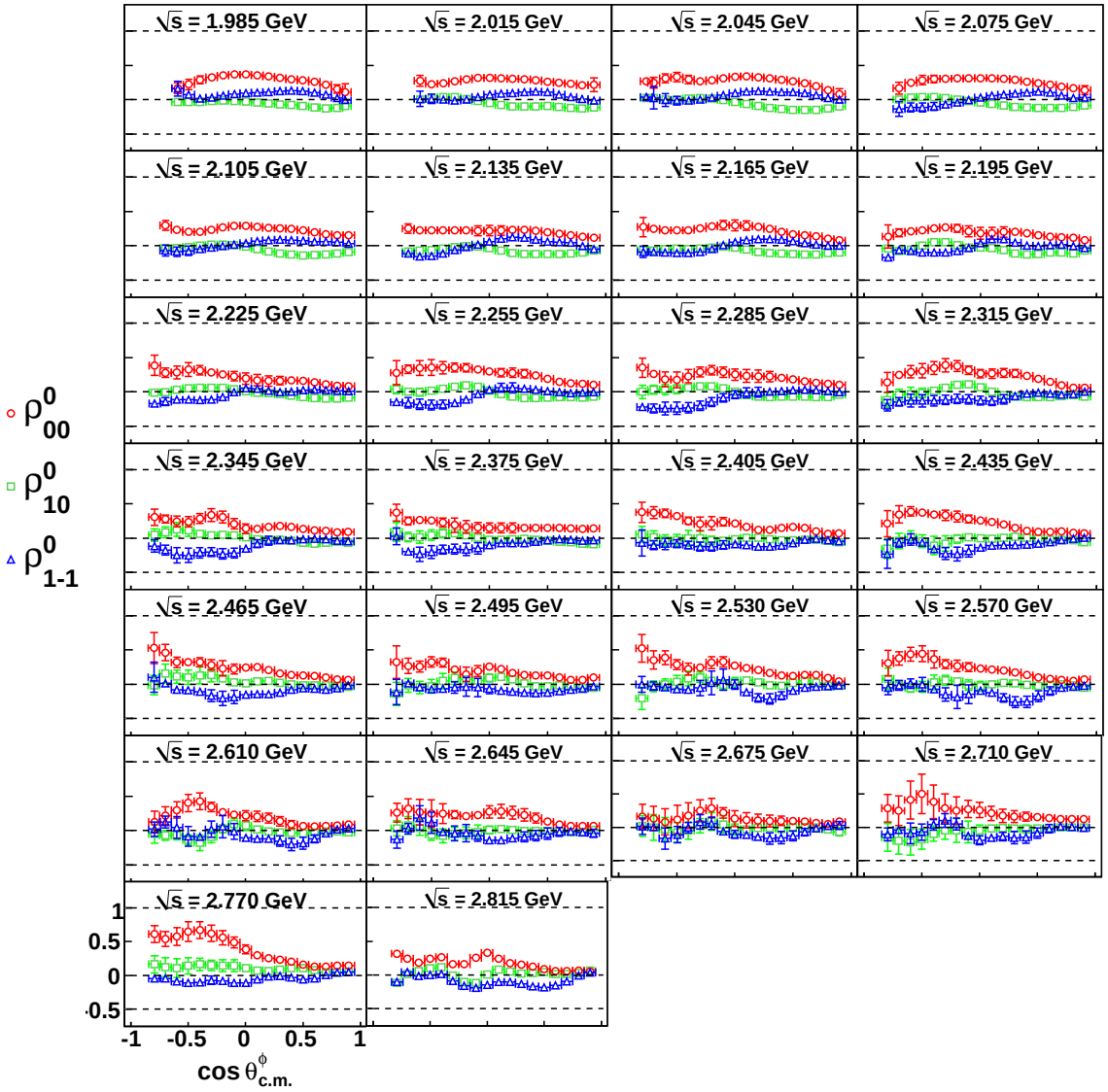

Figure 10.20: SDME *vs.* $\cos\theta^{\phi}_{c.m.}$: spin density matrix elements in the Helicity frame for the neutral-mode topology. The minimum bin-width is 30-MeV in $\sqrt{s}$ and the centroid of each bin is printed on the plots. All error bars represent statistical uncertainties only.

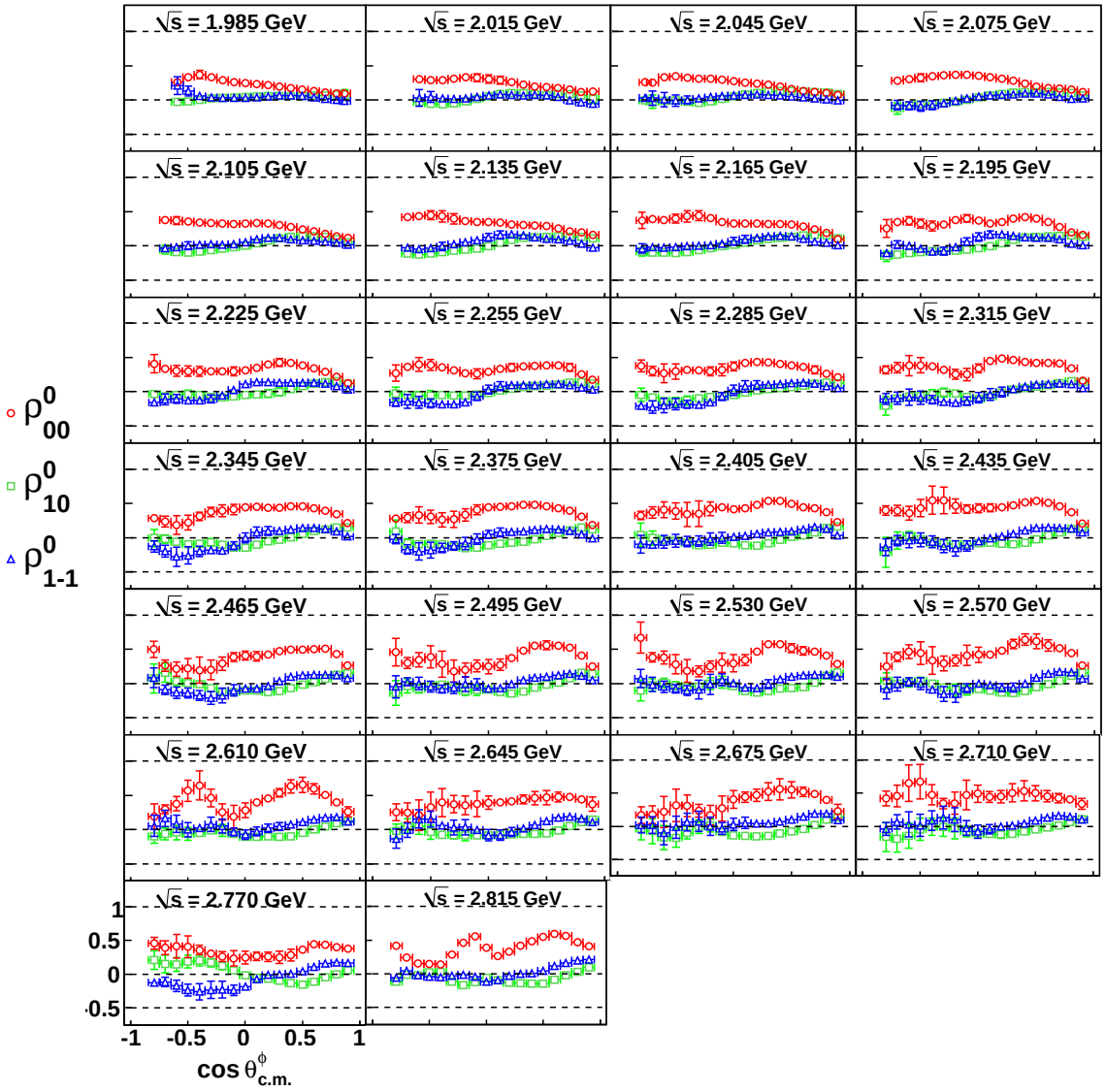

Figure 10.21: SDME *vs.* $\cos\theta^{\phi}_{c.m.}$: spin density matrix elements in the GJ frame for the neutral-mode topology. The minimum bin-width is 30-MeV in $\sqrt{s}$ and the centroid of each bin is printed on the plots. All error bars represent statistical uncertainties only.

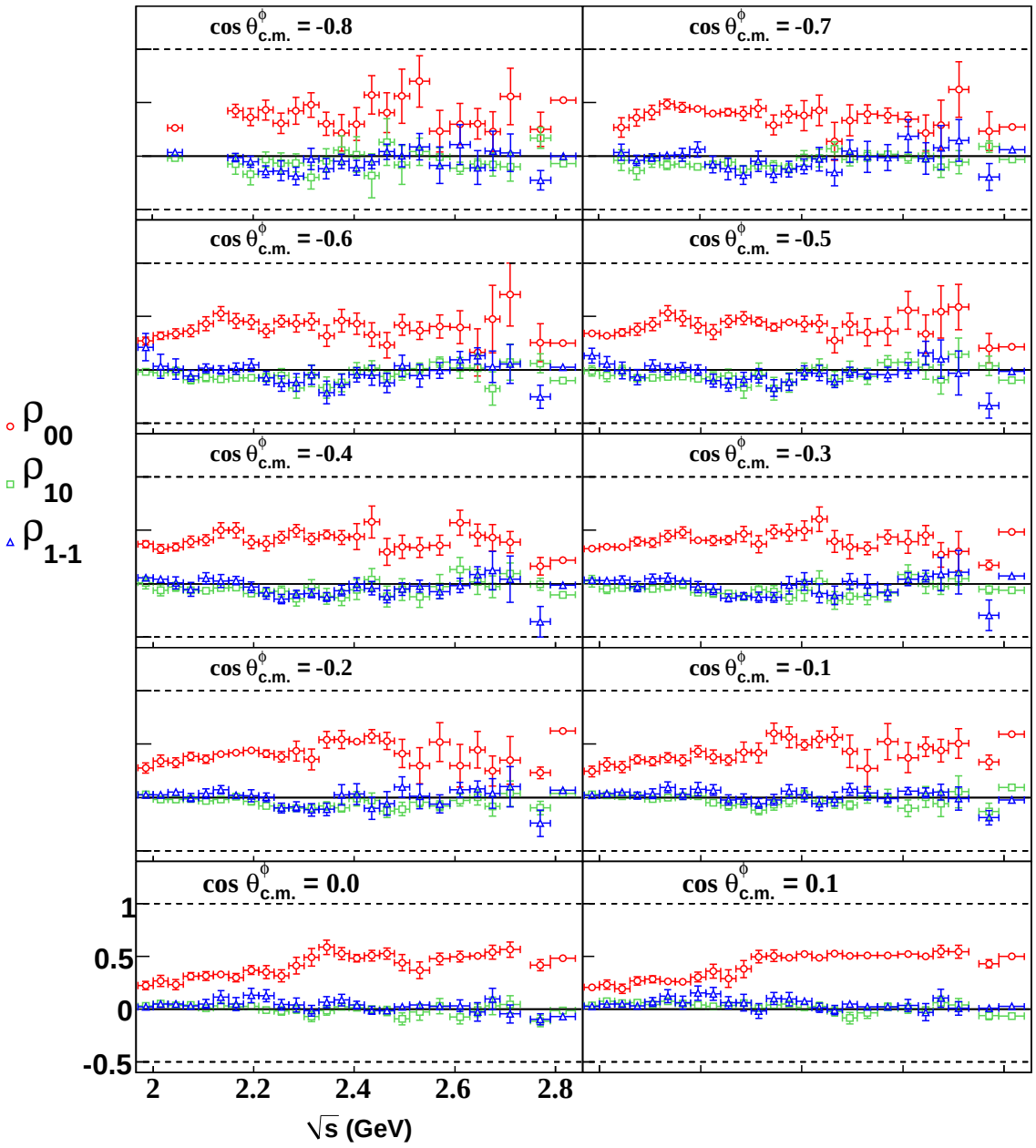

Figure 10.22: The energy dependence of SDME's (Adair frame) in the backward- and mid-angle bins for the neutral-mode topology. All error bars represent statistical uncertainties only.

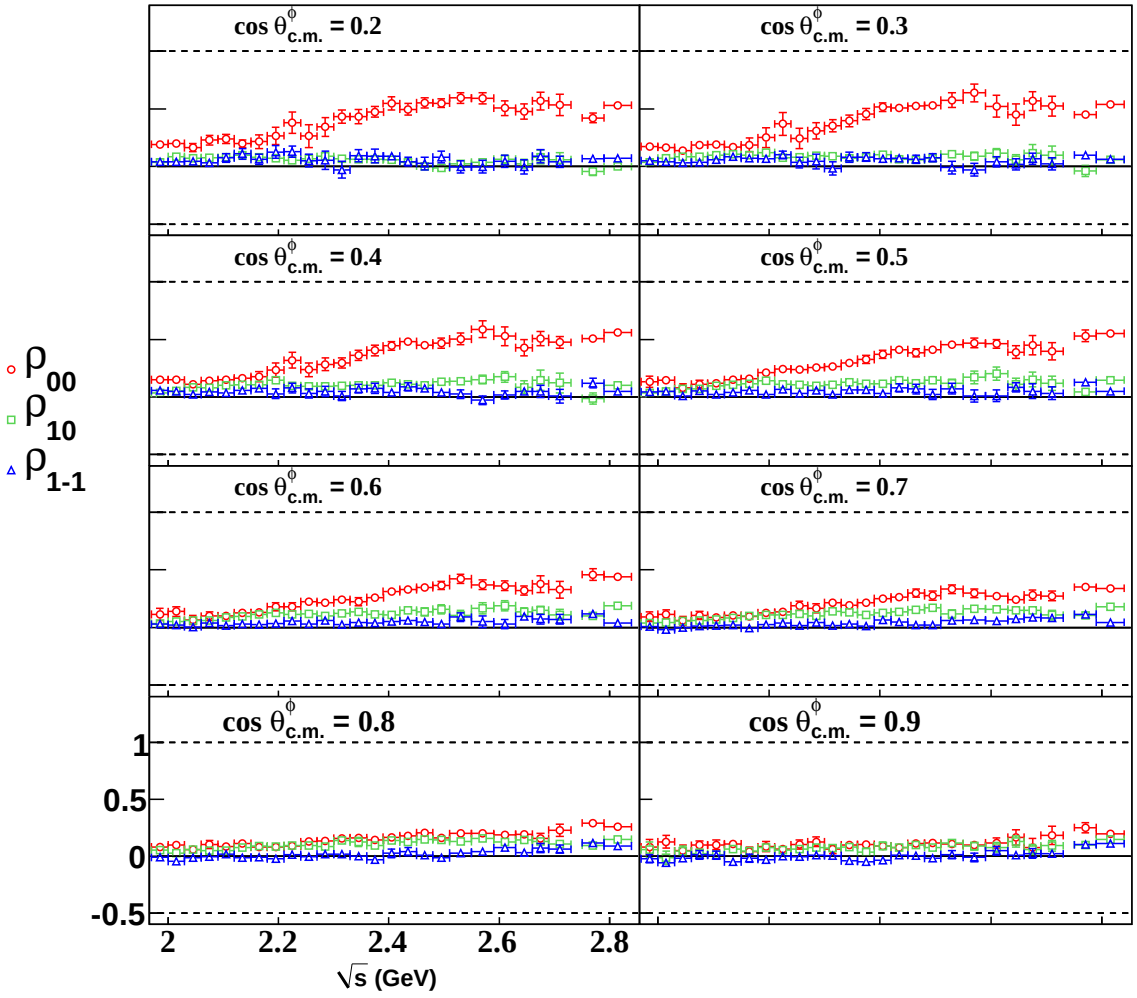

Figure 10.23: The energy dependence of SDME's (Adair frame) in the mid- and forward-angle bins for the neutral-mode topology. All error bars represent statistical uncertainties only.

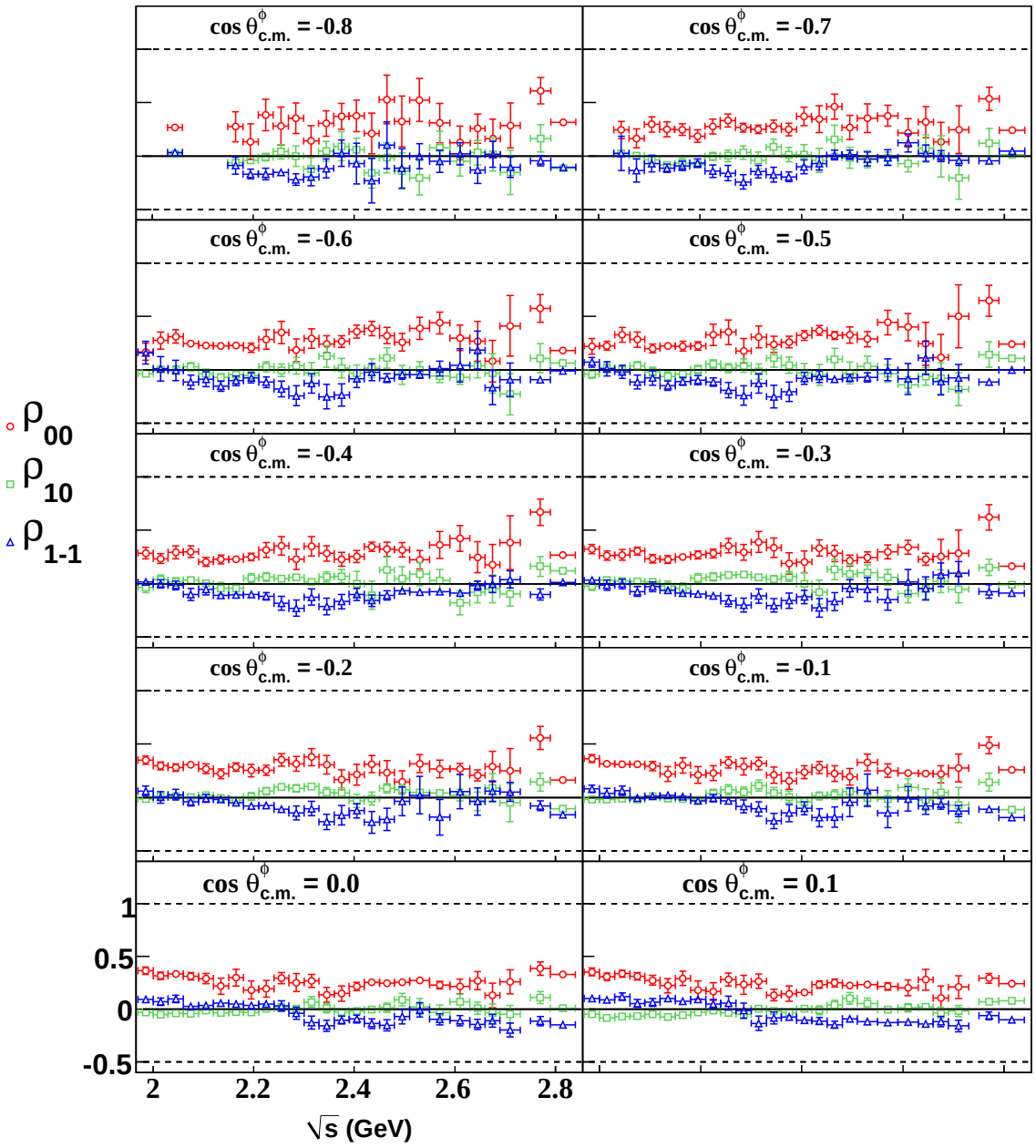

Figure 10.24: The energy dependence of SDME's (Helicity frame) in the backward- and mid-angle bins for the neutral-mode topology. All error bars represent statistical uncertainties only.

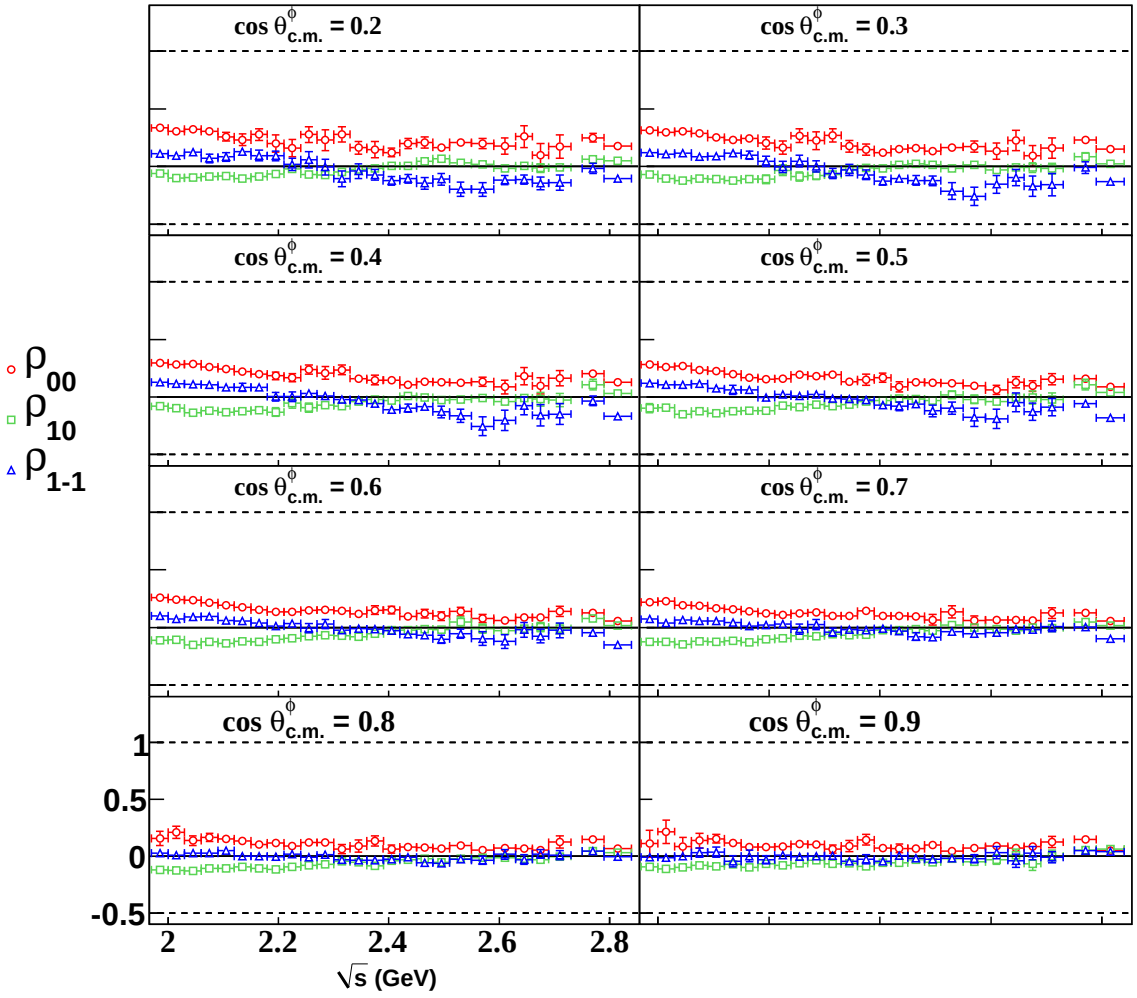

Figure 10.25: The energy dependence of SDME's (Helicity frame) in the mid- and forward-angle bins for the neutral-mode topology. All error bars represent statistical uncertainties only.

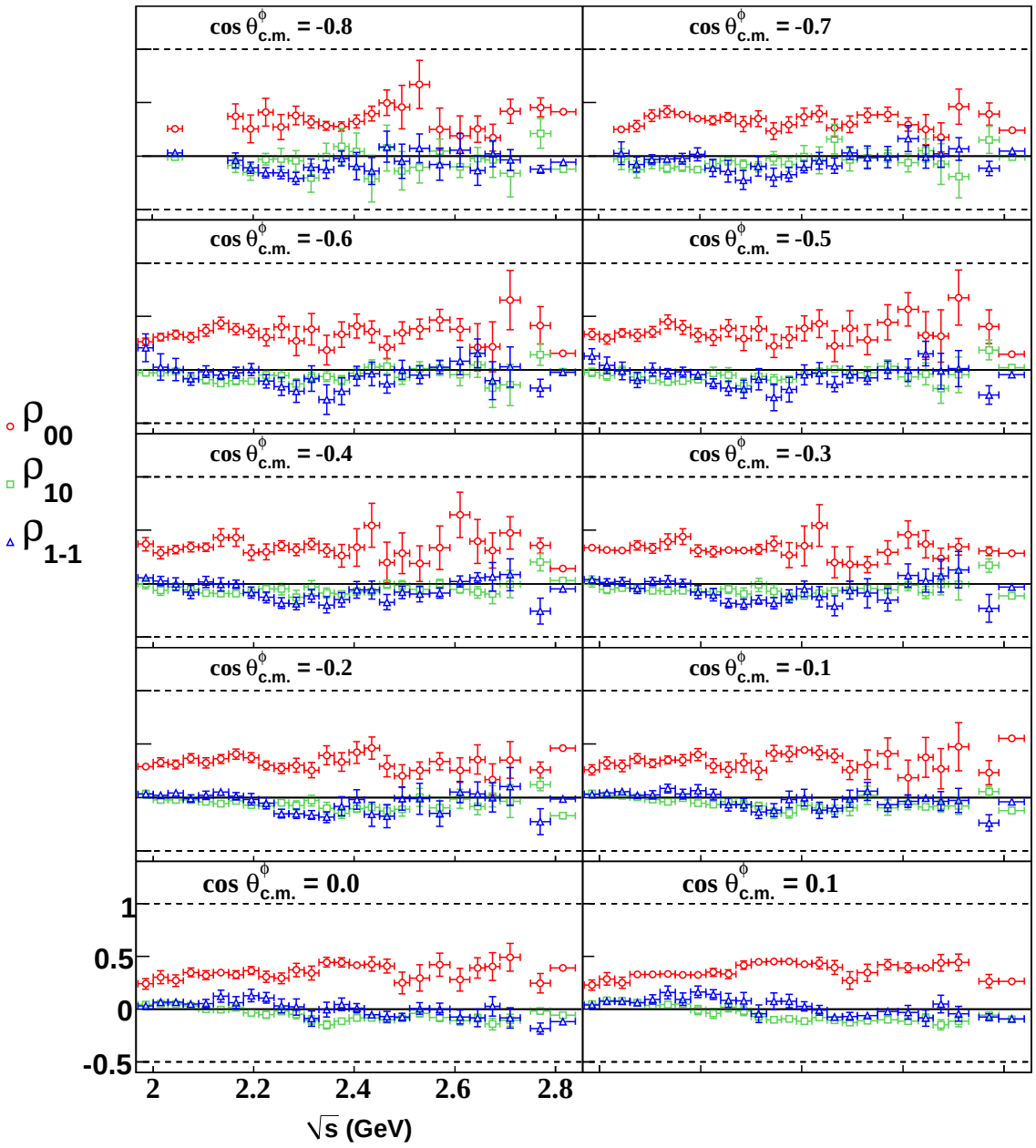

Figure 10.26: The energy dependence of SDME's (GJ frame) in the backward- and mid-angle bins for the neutral-mode topology. All error bars represent statistical uncertainties only.

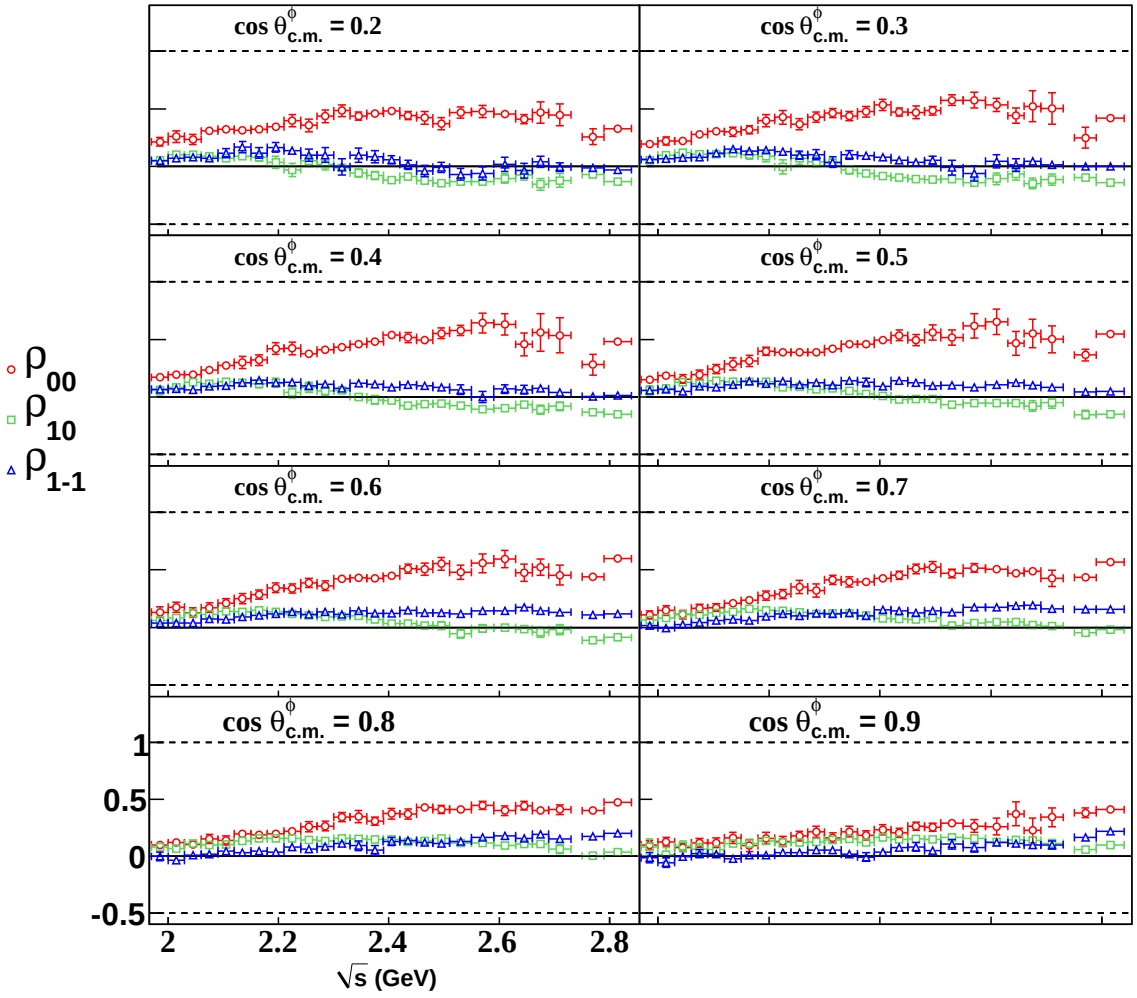

Figure 10.27: The energy dependence of SDME's (GJ frame) in the mid- and forward-angle bins for the neutral-mode topology. All error bars represent statistical uncertainties only.

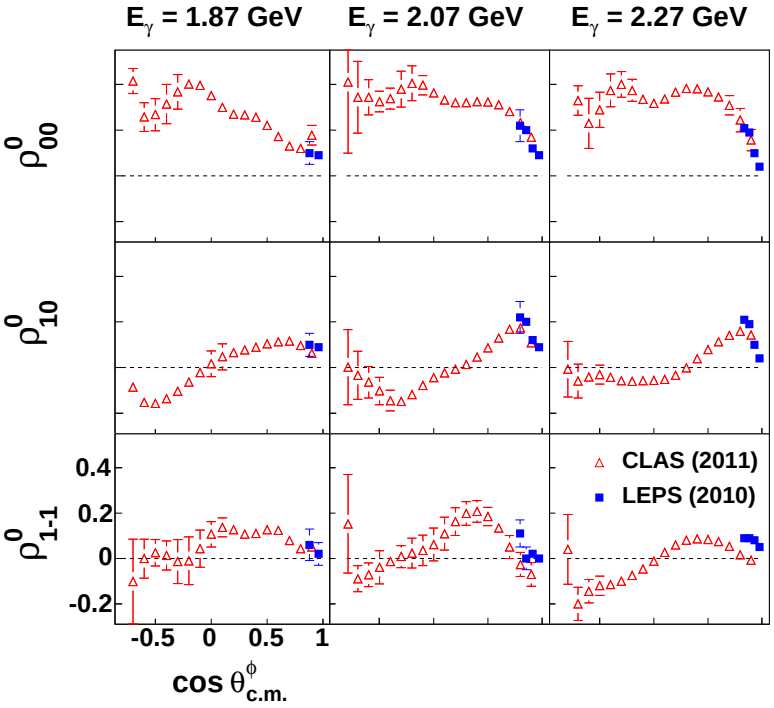

Figure 10.28: Comparison between the present CLAS (2011) and LEPS (Chang *et al.* 2010) charged-mode SDME's in the GJ frame. The LEPS bin-width was 200 MeV in E_γ. The CLAS results shown are at the $\sqrt{s}$ bins closest to the LEPS E_γ bin-centers (printed on the plot). All error bars represent statistical uncertainties only.

10.8 Comparison with previous world data

All previous measurements of the SDMEs for ϕ suffered from *extremely* limited statistics. As a result the SDMEs were extracted from data samples that incorporated wide energy bins and mostly, without any binning in the ϕ production angle. The other important feature of these earlier measurements were they were often not acceptance corrected. To explain this further, we look at the original Schilling's expression given in Eq. 10.11 and rewrite it in the form

$$W^0_{\rm meas}(\zeta,\varphi,\sqrt{s},\cos\theta^\phi_{\rm c.m.}) = \eta(\zeta,\varphi,\cos\theta^\phi_{\rm c.m.})W^0_{\rm Sch.}(\zeta,\varphi,\sqrt{s},\cos\theta^\phi_{\rm c.m.}), \qquad (10.25)$$

where the original Schilling distribution given by $W^0_{\rm Sch.}$ is modulated by the acceptance of the detector, η, to produce the experimentally measureable distribution $W^0_{\rm meas}$, and we have specifically highlighted the kinematical dependence of all three quantities. To bolster statistics, previous analyses often integrated the $W^0_{\rm meas}$ distribution over one or more of the variables $\{\zeta,\varphi,\sqrt{s},\cos\theta^\phi_{\rm c.m.}\}$, *without prior correction for the acceptance* η. The overall consensus of these previous measurements has been that ρ^0_{00} is predominantly small in the helicity frame. It has also been claimed from measurements following the procedure outlined above, that the fits require an additional S-wave contribution [135]. While there is certainly an S-P interference between the ϕ and the underlying $f_0(980)$, conclusions on the *degree* of that interference and its effect on the ϕ SDME extraction, based on fits with multiple levels of dilution and no reliable correction for the detector acceptance, seem somewhat unjustified (see also discussion in Sec. 3.12).

Recently, the LEPS Collaboration [136] (Chang *et al.*, 2010) has published results for ρ^0, ρ^1 and

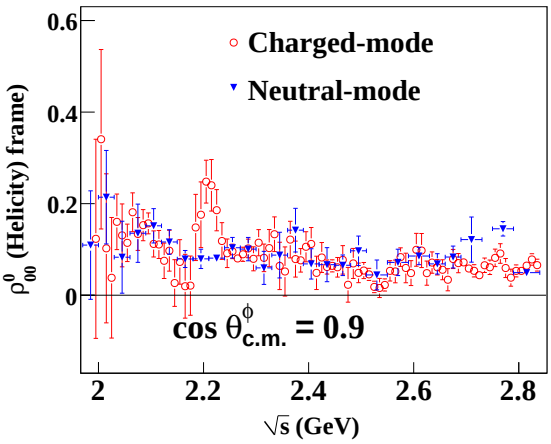

Figure 10.29: Comparison between the charged- and neutral-mode ρ^0_{00} results in the Helicity frame for a forward-angle bin. The agreement is good, expect around $\sqrt{s} \approx 2.1$ GeV, where the charged-mode shows localized structures, while the neutral-mode results are smooth.

ρ^2, using a linearly polarized beam. Their results cover the energy range $E_\gamma = 1.77$ to 2.37 GeV in 200 MeV wide ΔE_γ bins and only in the forward ϕ production angles. The important feature of these results is that the incorporated an acceptance corrected SDME extraction and a fit to the full Schilling's equation. The comparison with these and the present CLAS results in the Gottfried-Jackson frame are shown in Fig. 10.28. Within binning and statistical errors, the agreement is excellent.

10.9 Features in the Data

10.9.1 Charged and Neutral-mode comparison at forward angles

Fig. 10.29 shows the comparison between the charged- and neutral-mode ρ^0_{00} results in the Helicity frame for a particular forward-angle bin. The agreement is fair to good at most places, except around $\sqrt{s} \approx 2.1$ GeV, where the charged-mode results show localized "structures". The neutral-mode is relatively monotonic in comparison. It is possible that the ϕ-$\Lambda(1520)$ overlap is responsible for this difference, but this will need further investigation.

10.9.2 Comparison between ωp and ϕp results

Fig. 10.30a shows the comparison between the ϕp charged-mode (this work) and ωp [16] results for ρ^0_{00}. Traversing from forward to mid-angles, both vector-mesons seem to indicate an initial "rise", followed by a "dip" structure. The angular position of the "dip" is different for the two channels. For the ϕ, it occurs at a relatively backward angle, compared to ωp. Fig. 10.30b shows an extract from CLAS-2009 PWA paper for the ωp channel [17]. The theoretical prediction based on a non-resonant model by Oh, Titov and Lee [164] clearly fails to reproduce the local dip feature.

10.9.3 Helicity non-conservation

As mentioned in Sec. 10.3, a long held *assumption* in diffractive vector-meson production phenomenology is that helicity in conserved in the s-channel (Helicity frame) and not in the t-channel (Gottfried-Jackson frame). Fig. 10.31 shows the ρ^0_{00} for the ϕp charged-mode in all three reference-frames for a forward-angle bin. Since ρ^0_{00} is clearly not zero in the GJ frame, TCHC is broken.

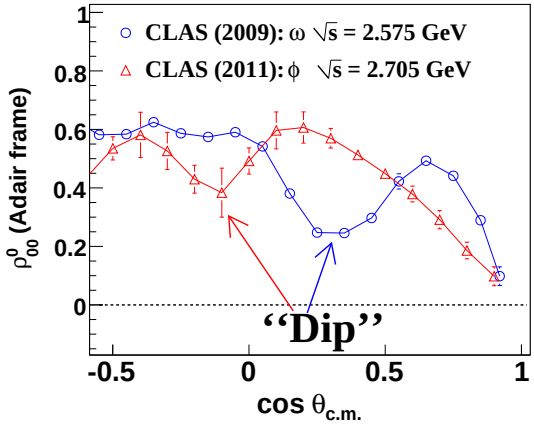

(a)

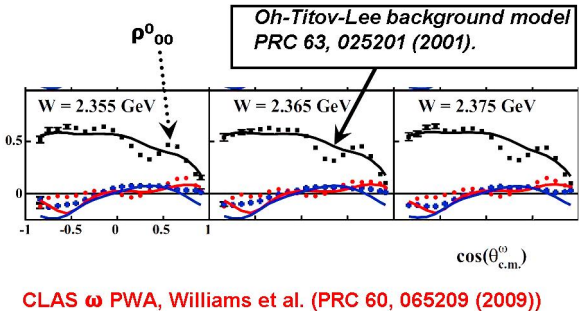

CLAS ω PWA, Williams et al. (PRC 60, 065209 (2009))

(b)

Figure 10.30: Comparison between the $g11a$ ωp [16] and ϕp charged-mode results (this work): (a) shows the similarity in the "dip" structure present in ρ^0_{00} for both channels. (b) shows that present theory models can not accomodate this feature (image source [17])

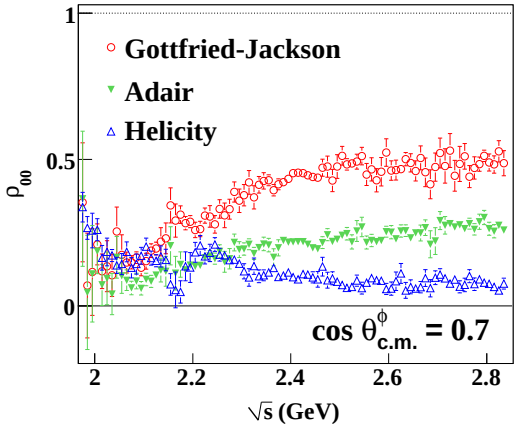

Figure 10.31: The ρ^0_{00} element for the ϕp charged-mode in a forward-angle bin, for all three reference frames. Note that $\rho^0_{00} \neq 0$ in the Helicity frame, indicating SCHC violation.

However, it is also non-zero in the Helicity frame, indicating SCHC violation as well. More generically, ρ^0_{00} is non-zero in *all* three reference frames. One can only state that SCHC violation is the least of all, but our data shows that SCHC can not be taken as a fundamental constraint. In fact, a similar behavior is also visible in the ωp sector [16], but since the ω is not supposed to be as strongly dominated by Pomeron production, helicity non-conservation is probably less of a surprise in that case.

10.10 Summary

The extraction of the spin density matrix elements for the ϕ vector meson was described in detail in this chapter. Results for both the charged- and neutral-modes were presented in all three reference frames, Adair, Helicity and Gottfried-Jackson frames. The current results represent a *huge* improvement over previously available world data and have several interesting features.

Chapter 11

Normalization discrepancies in photoproduction

In Chs. 6, 8, 9 and 10, we presented our extracted cross-section and polarization results for the $K^+\Sigma^0$ and ϕp channels. The $K^+\Sigma^0$ data are now published in Ref. [20], along with results for several other non-πN ground meson photoproduction channels, $K^+\Lambda$ [19], $\eta p/\eta' p$ [18] and ωp [16], using the same CLAS $g11a$ dataset. These new $g11a$ data extend upon results from a previous lower-energy $g1c$ dataset [27], and in regions of kinematic overlap, the two datasets are found to be in excellent agreement with each other. It seems, however, that a persistent normalization discrepancy exists between CLAS and some other world datasets. To wit, the CLAS differential cross sections for the pseudoscalar meson channels ($K^+\Lambda$ [19, 87], $K^+\Sigma^0$ [20, 87], ηp [18], $\pi^0 p$ [197], $\pi^+ n$ [196]) are systematically lower that those from older high-energy and forward meson production-angle SLAC/DESY/CEA data [200, 201, 202, 211]. On the other hand, the CLAS $K^+\Lambda/K^+\Sigma^0$ results agree well with the latest LEPS forward-angle data [90], although CLAS is lower than CB-ELSA [158, 157] for the ηp channel. Also, the CLAS vector-meson results for ωp [16] and ϕp (this work) are in generally good agreement with SLAC [114] and Daresbury [116, 118].

Given that the quoted systematic uncertainties in most places are of the order of $\sim 10\%$, a discrepancy as large as a factor of two is a matter of concern and any PWA based on these data

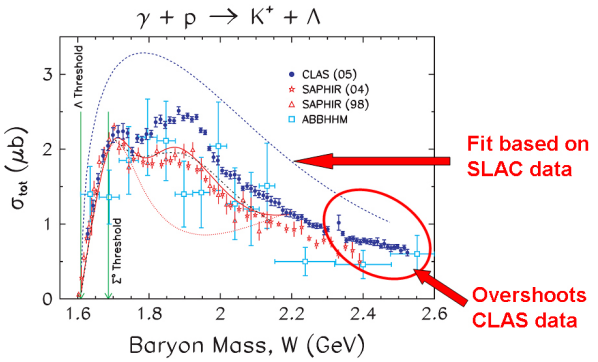

Figure 11.1: The dashed-blue lines show a prediction from a Regge-based model [138] from fits to older SLAC data. At higher energies, the model overpredicts the CLAS-2006 data almost by a factor of two. Figure taken from the CLAS-2006 paper by Bradford *et al* [87].

Characterestics	CLAS experiment	
	$g11a$	$g1c$
Run year	2004	1999
Cryotarget length	40 cm	17.85 cm
Start counter	new	older
Trigger setting	2-prong	1-prong
πN-channels accessible?	no	yes
Kinematic fitter used?	yes	no
Physics-weighted acceptance?	yes	no
Maximum $\sqrt{s}$ (GeV)	2.84	2.55
Tagged photon beam?	yes	yes

Table 11.1: Some characterestics of the two CLAS experiments of concern in this chapter. The two datasets had several distinguishing features and were analyzed by completely different groups. However, in the regions of kinematic overlap, the results from $g11a$ and $g1c$ were in excellent agreement with each other.

is bound to be affected by this. For example, Fig. 11.1 shows a plot taken from the CLAS-2006 $K^+\Lambda/K^+\Sigma^0$ paper [87]. The dashed blue curve shows a model prediction [138] based on fits to the SLAC data and at the higher end of the energy spectrum, overshoot the CLAS results by almost a factor of two. The effect of these discrepancies on PWA's has already been discussed by Sibirtsev *et al.* [150] for the ηp sector. Inkeeping with the fact that our final goal is to perform PWA's on these data and look for resonances, it is essential to attend to this issue. In this chapter we present a systematic global overview of these discrepancies taking into account several different channels from the CLAS results and provide detailed descriptions of the various internal checks that have been performed. Next, using a Regge-based formalism, we show how much the different hadrodynamic coupling constants are affected depending on which dataset is being fit to. For the pseudoscalar channels, in contrast to the recent work by Yu *et al.* [190, 191] who have conjectured the relevance of tensor exchanges to "resolve" this discrepancy, we show that once the CLAS $g11a$ data is taken into consideration, it becomes clear that *it is impossible to reconcile the old SLAC data and the CLAS data within a single fit.*

11.1 The CLAS $g11a$ and $g1c$ experiments

A detailed description of the $g11a$ experiment was provided in Chs. 2 and 3. We also note here that since $g11a$ was a high-precision experiment designed to search for an exotic particle, the data underwent an extensive calibration by several groups within CLAS working independently during this process. Sophisticated analysis tools such as a dedicated $g11a$ kinematic fitter [50] was developed to add to the robustness of the results. Care was also taken to keep the data analysis cuts to be as loose as possible. An event-based signal-background separation method and a physics-weighted detector acceptance calculation from a unbinned maximum likelihood partial wave analysis fit ensured that all correlations present in the data were faihfully represented during the yield extraction and acceptance calculation procedures. It is also worth noting at this point that all the six $g11a$ results of concern here ($K^+\Lambda$ [19], $K^+\Sigma^0$ [20], $\eta p/\eta' p$ [18], ωp [16] and ϕp) utilized the same set of data analysis tools and photon flux nomalizations, which should keep the systematic uncertainties under better control, as well.

The CLAS $g1c$ experiment [27] was an earlier (1999) photoproduction experiment that also utilized a tagged beam facility but ran at a lower photon energy. The maximum $\sqrt{s}$ accessible here

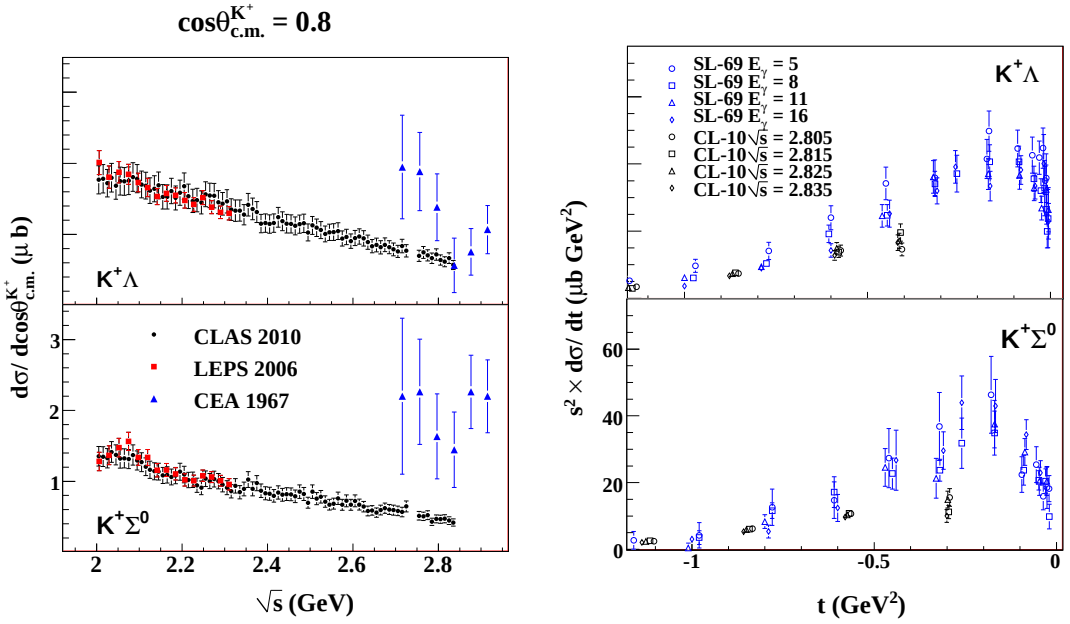

(a) (b)

Figure 11.2: (a) Comparison between the CLAS $g11a$ [19, 20], CEA-Elings-1967 [201] and LEPS-Sumihama-2006 [90] results for a forward-angle bin in the hyperon channels. While CLAS and LEPS are in excellent agreement with each other, the older CEA data is systematically higher. (b) Comparison between the CLAS $g11a$ [19, 20] (CL-10) and SLAC-Boyarski-1969 [200] (SL-69) scaled cross section results for the two hyperons. The energies are listed in E_γ for SLAC and $\sqrt{s}$ for CLAS, in units of GeV. Both sets of results (SLAC and CLAS) agree to a $d\sigma/dt \propto 1/s^2$ behavior as depicted by the tightly bunched set of points, but differ by a normalization factor. All error bars represent the statistical and systematic uncertainties added in quadrature.

was ~ 2.55 GeV. The other distinction from $g11a$ was that $g1c$ utilized a less-restrictive single-prong trigger setting that allowed it to analyze the single pion channels ($\pi^0 p$ [197] and $\pi^+ n$ [196]) as well. Compared to $g11a$, $g1c$ had completely different target characterestics, trigger settings and analysis personnel. Several of the sophisticated analysis tools that $g11a$ used (the kinematic fitter, for example) were also not available at the time of $g1c$. A flat phase-space Monte Carlo generator was used in the case of $g1c$, in contrast to a physics-weighted acceptance calculation that is used in $g11a$. Therefore, although the same CLAS detector was employed in both cases, by and large, the two sets of results can be termed as "independent". However, *in the regions where kinematics overlapped, the two CLAS experiments are in excellent agreement with each other, lending support to the internal consistency of the CLAS results.*

11.2 The discrepancies

11.2.1 $K^+\Lambda$ and $K^+\Sigma^0$

In what follows, we will broadly refer to the following as the "SLAC results" for the two hyperon channels: SLAC-Boyarski-1969 [200], CEA-Elings-1967 [201], CEA-Joseph-1967 [202] and SLAC-Quinn-1979 [203]. All of these results covered the high-energy ($E_\gamma > 3$ GeV) forward production

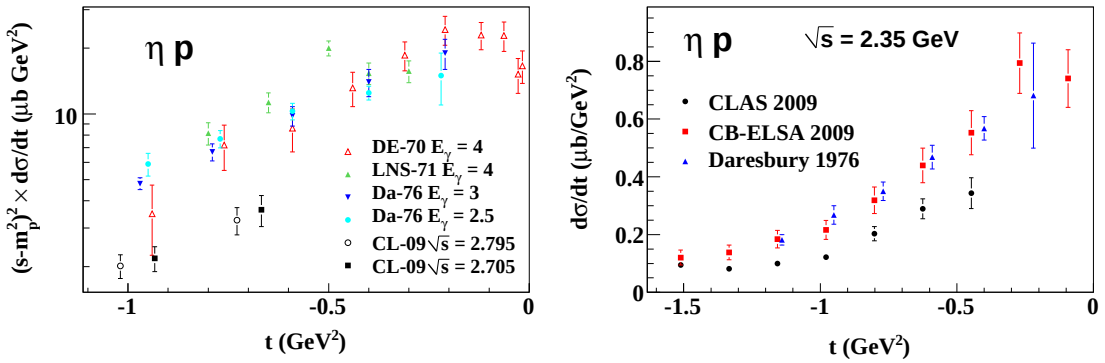

(a) (b)

Figure 11.3: ηp comparisons: CLAS $g11a$ [18] (CL-09), DESY-Braunschweig-1970 [156] (DE-70), LNS-Dewire-1971 [205] (LNS-71) and Daresbury-Bussey-1976 [207] (Da-76) scaled cross sections. The energies are listed in E_γ for DESY/LNS/Daresbury and $\sqrt{s}$ for CLAS, in units of GeV. Both sets of results (DESY/LNS/Daresbury and CLAS) agree to a $d\sigma/dt \propto 1/(s-m_p^2)^2$ behavior as depicted by the tightly bunched set of points, but differ by a normalization factor. (b) CLAS $g11a$ [18], CB-ELSA-2009 [158] and Daresbury-Bussey-1976 [207] in the energy bin $\sqrt{s} \approx 2.35$ GeV. CLAS appears to be systematically lower than both Daresbury and ELSA at forward-angles. The error bars represent the statistical and systematic uncertainties added in quadrature.

angle (small $|t|$) regime and between themselves, agree quite well with each other. These results also exhibit a t-channel Regge-type $d\sigma/dt \propto 1/s^2$ scaling behavior. On the other hand, none of these results had a tagged photon beam, but quoted the photon-energy E_γ as the end-point energy of the bremsstrahlung spectrum. As was already pointed out in the CLAS $g11a$ $K^+\Sigma^0$ paper [20], the CLAS results also agree well to a $d\sigma/dt \propto 1/s^2$ Regge-type behavior. Therefore, the CLAS and SLAC data agree well in *shape*. However, the CLAS cross sections are systematically lower than SLAC in *scale* by roughly a factor of two. Unfortunately, the kinematics of two sets of results (*i.e.* CLAS and SLAC) do not overlap much, which makes a direct comparison somewhat difficult. The SLAC results typically cover the extreme forward angle region, where CLAS has a hole for the beam-dump. The only kinematics where a direct comparison is possible is between the CLAS $g11a$ data and the CEA-Elings results at $\cos\theta^{K^+}_{\rm c.m.} \sim 0.81$, as shown in Fig. 11.2a. We have also overlaid in this plot, the latest LEPS forward-angle data that are in excellent agreement with CLAS. Fig. 11.2b shows the comparison of $s^2 \times d\sigma/dt$ scaled cross sections between CLAS and SLAC-Boyarski – while the shapes agree very well, the disagreement in scale is clearly visible.

11.2.2 ηp

The older high-energy forward-angle cross section data for this channel comprise of the following: CEA-Bellenger-1969 [204], DESY-Braunschweig-1970 [156], LNS-Dewire-1971 [205], SLAC-Anderson-1971 [206] and Daresbury-Bussey-1976 [207]. As in the case of the KY channels, a smooth $d\sigma/dt \propto 1/(s-m_p^2)^2$ behavior is reported in all these datasets that are also in fair to good agreement with each other. As shown in Fig. 11.3a, the CLAS data also shows a scaling behavior. However, while the scaled DESY/LNS/Daresbury cross-sections agree with each other, CLAS appears to be systematically lower. We also note here that none of the older experiments used a tagged beam.

In the previous sub-section, for the hyperons, we pointed out that CLAS is is good agreement with another recent experiment (LEPS) that had comparable statistical precision and employed a tagger photon beam. A perplexing issue for the ηp channel is that the CLAS results do not seem to

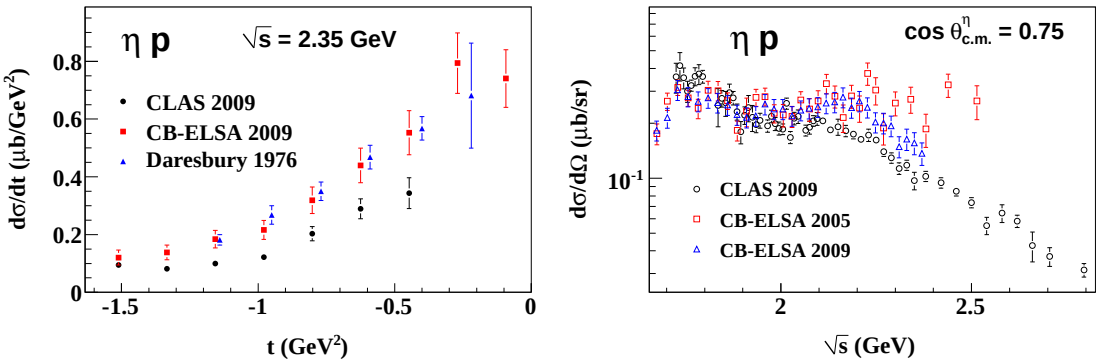

(a) (b)

Figure 11.4: ηp comparisons: (a) CLAS $g11a$ [18], CB-ELSA-2009 [158] and Daresbury-Bussey-1976 [207] in the energy bin $\sqrt{s} \approx 2.35$ GeV. CLAS appears to be systematically lower than both Daresbury and ELSA at forward-angles. (b) The error bars represent the statistical and systematic uncertainties added in quadrature.

agree with recent CB-ELSA measurements. Fig. 11.3b shows the comparison between CLAS [18], CB-ELSA-2009 [158] and Daresbury-Bussey-1976 [207] in the energy bin $\sqrt{s} \approx 2.35$ GeV. At forward-angles, CB-ELSA and Daresbury seem to agree well with each other, while CLAS is systematically lower. This issue was also mentioned in the work by Sibirtsev *et al.* [150]. While we do not have a resolution for the CB-ELSA/CLAS discrepancy at the moment, we make two comments on the issue. First, the CLAS $g11a$ results were found to be in fair agreement with an earlier (unpublished) $g1c$ analysis, pointing towards internal constistency within CLAS. Second, on the other hand, the recent ELSA-2009 [158] results show a marked difference from ELSA-2005 [157] in the foward-angle region above $\sqrt{s} \approx 2.1$ GeV. In the ELSA-2005 version, $d\sigma/d\Omega$ vs. $\sqrt{s}$ appears almost flat, while in the ELSA-2009 version, $d\sigma/d\Omega$ starts falling off with $\sqrt{s}$, as seen by CLAS. In the ELSA-2009 paper [158], this shift is attributed to an underestimated background at forward-angle and high $\sqrt{s}$ in ELSA-2005. While ELSA-2009 is still higher than CLAS, it is encouraging to see that at least the cross-section shape is in better agreement between the two datasets.

11.2.3 πN

Since pions are most copiously produced in hadronic reactions, the single pion channels are where most of the world data reside. The πN channels have also been commonly used as the "normalization channels" between different world datasets. On many occassions, the K^+Y ($Y = \Lambda, \Sigma^0$) and ηp results came from parasite analyses from an original $\pi^+ n$ and $\pi^0 p$ dataset. As an example, the high energy forward-angle SLAC-Boyarski $\pi^+ n$ [211] results were first published in 1968, followed by the K^+Y results in 1969 [200]. The other relevant πN world data in this kinematic regime include CEA-Joseph-1967 [202], CEA-Elings-1967 [201], DESY-Buschhorn-1966 [208], DESY-Buschhorn-1967 [209], DESY-Heide-1968 [210], DESY-Braunschweig-1967 [213], *et al.* Within themselves, agreement between these older results is fair to good.

Since the trigger setting for the CLAS $g11a$ experiment require detection of at least two charged particles, the single-pion channels are not accessible here. The CLAS $g1c$ $\pi^+ n$ [196] and $\pi^0 p$ [197] results go till about $\sqrt{s} \approx 2.55$ GeV, and have restricted coverage in the forward angles. Fig. 11.5a shows the DESY-Buschhorn-1966 [208] and CLAS-Dugger-2009 [196] at $E_\gamma \approx 2.88$ GeV together. Unfortunately, the two datasets do not have a direct overlap. To guide the eye, we have overlaid a Regge-model prediction based on the work by Guidal-Laget-Vanderhaeghen (GLV) [138]. The

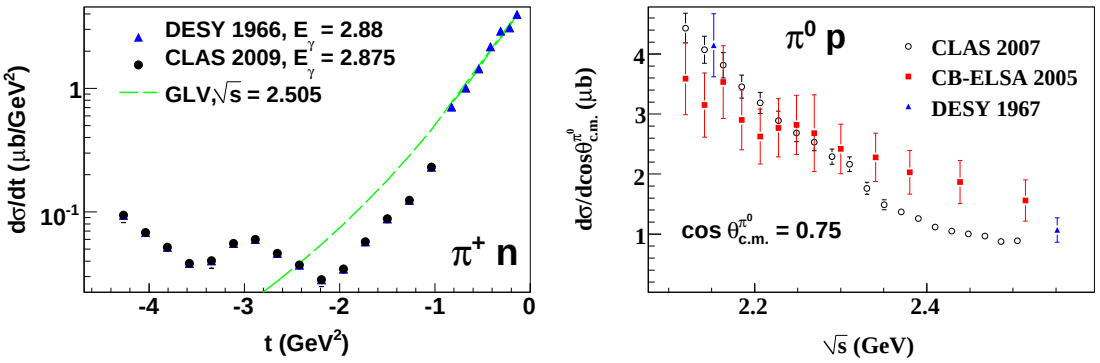

(a) (b)

Figure 11.5: πN comparisons: (a) CLAS-Dugger-2009 [196] and DESY-Buschhorn-1966 [208] results for the $\pi^+ n$ channel. The dashed green lines show a Regge-model prediction that fits well to the DESY data, but the projected model over-predicts the cross-sections at the CLAS kinemtics. (b) CLAS-Dugger-2009 [197], CB-ELSA-Bartholomy-2005 [214] and DESY-Braunschweig-1967 [213] results for the $\pi^0 p$ channel. At higher energies and forward-angles, there is a scale discrepancy, most prominently visible between the CLAS and CB-ELSA results.

projected model prediction at the CLAS energies seems to hint that a scale discrepancy exists for the $\pi^+ n$ channel as well, though we underscore the fact that this is not a direct evidence. A direct comparison between CLAS and the older high-energy forward-angle SLAC/CEA/DESY data is also not possible in the $\pi^0 p$ sector due to non-overlapping kinematics. However, there are previous CB-ELSA [214] data that overlap with the CLAS kinematics. Fig. 11.5b shows a comparison between CLAS-Dugger-2009 [197], CB-ELSA-Bartholomy-2005 [214] and DESY-Braunschweig-1967 [213] for the $\pi^0 p$ channel. As for the ηp channel, CB-ELSA results show a scale discrepancy with CLAS (and possibly a shape discrepancy as well).

11.2.4 ωp and ϕp

For the vector meson channels, ωp and ϕp, most of the previous world data reside only in the diffractive region (large s and $|t| \to 0$) and data at CLAS kinematics is scarce. The two previous vector meson world datasets that we compare the CLAS results to are SLAC-Ballam-1973 [114] and Daresbury-Barber [116, 118]. Figs. 11.6a and 11.6b show the CLAS-SLAC cnd CLAS-Daresbury comparisons, respectively, for the ωp channel. In Ch. 9, Fig. 9.15, we showed the comparison between CLAS and Daresbury for ϕp. For either vector-mesons, the older data have lower statistical precision and much wider energy bins compared to CLAS. However, within error bars, the agreement is fair to good.

11.3 Internal consistency checks within CLAS $g11a$

As already mentioned, in the regions of overlapping kinematics, the results from $g11a$ and $g1c$ are in excellent agreement with each other. Given the very different analysis tools, trigger settings and acceptance calculation methods employed for the two experiments, this agreement is very encouraging. In the next step, several internal checks were run within $g11a$ to ensure that the systematics were being understood well enough. The calculation of the differential cross section comprises of three elements – yield extraction, detector acceptance and normalization (photon flux and target characterestics). If we assume that CLAS ωp results are correct, since they match very well with

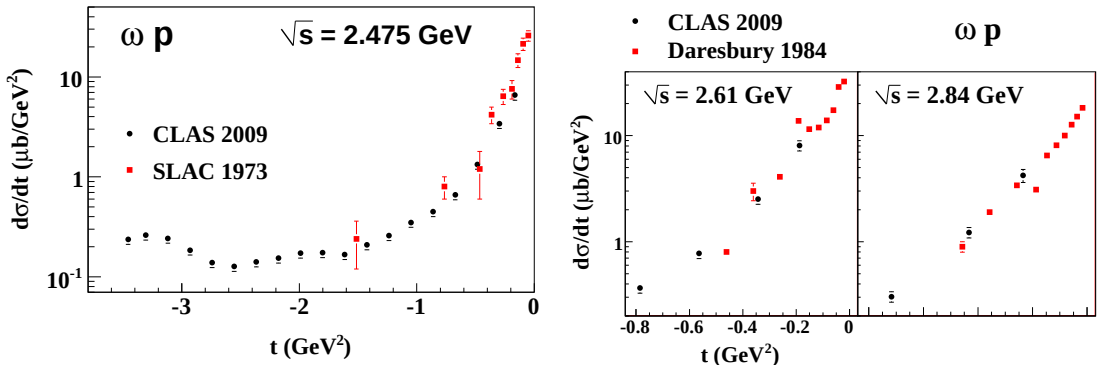

(a) (b)

Figure 11.6: ωp comparisons: CLAS $g11a$ [16] and SLAC-Ballam-1973 [114] results at $\sqrt{s}$ = 2.475 GeV. (b) CLAS $g11a$ [16] and Daresbury-Barber [116] results. The agreements are fair to good.

SLAC and Daresbury, we can rule out any discrepancy arising from the normalization part in the cross section calculation, since this is completely channel independent.

To check the reliability of our acceptance calculation, several steps were taken. The CLAS detector has a forward angle hole for the beam-dump. It is convievable that our understanding of the detector acceptance worsens as we approach the forward angle region. However, as shown in Fig. 11.2a our agreement with LEPS, which is a dedicated forward-angle detector facility, shows that this is probably not the case. The magnetic setting for the CLAS spectrometer results in negatively charged tracks (corresponding to K^- or π^-) being bent inwards toward the beam-dump hole. Therefore, the CLAS acceptance is generally lower for negatively tracks as compared to the positive ones. To check for possible shortcomings in our understanding of the K^-/π^- acceptances, different reaction topologies were analyzed that included/excluded the detection of negative tracks. A summary of these topologies for each channel within CLAS $g11a$ is listed in Table 11.2. There are several noteworthy points here. First, any topology having more than one undetected final-state particle could not make use of the kinematic fitter. This pertains to the two-track topologies for the $K^+\Sigma^0$ and ηp channels. The fact that the two- and three-track topologies agree with each other for these channels therefore indirectly strengthens our faith in the kinematic fitting procedure. Second, our partial wave analysis based physics-weighted acceptance calculation method required knowledge of all the final-state 4-momenta and was therefore limited to fully exclusive or a single final-state missing particle topologies. Since this was not available for the two-track $K^+\Sigma^0$ and ηp topologies, a flat phase-space Monte Carlo event generator was used here. In fact, recall from Table 11.1, a phase-space Monte Carlo generator was also used in the case of the $g1c$ analyses. If the energy bin-width is small enough such that the physics does not vary too much across the bin and the break-up energies of the decays are small enough, a flat phase-space Monte Carlo should suffice. The fact that the different topologies agree well with each other shows that our understand of the CLAS accepatnce (in the fiducial regions) os reliable. Third, given that the ωp and ηp three-track topologies involve the same set of detected final-state particles, it would be somewhat surprising if our acceptances for the p, π^+ and π^- tracks are well understood for the ωp case, but not for ηp. A similar argument could be made between the ϕp charged-mode and $K^+\Lambda$ two-track topologies where the only difference is that the undetected particle is K^- and π^-, respectively.

CLAS $g11a$ Reaction Topologies		
Channel	Topology	Name
$K^+\Lambda \rightarrow$	$pK^+\pi^-$	three-track
	$pK^+(\pi^-)$	two-track
$K^+\Sigma^0 \rightarrow$	$K^+\Lambda\gamma_f \rightarrow pK^+\pi^-(\gamma_f)$	three-track
	$K^+\Lambda\gamma_f \rightarrow pK^+(\pi^-\gamma_f)$	two-track
$\eta p \rightarrow$	$p\pi^+\pi^-(\pi^0)$	three-track
	$p\pi^+(\pi^-\pi^0)$	two-track
$\eta' p \rightarrow$	$p\pi^+\pi^-(\eta)$	three-track
$\omega p \rightarrow$	$p\pi^+\pi^-(\pi^0)$	three-track
$\phi p \rightarrow$	$pK^+(K^-)$	charged-mode
	$pK^0_S(K^0_L) \rightarrow p\pi^+\pi^-(K^0_L)$	neutral-mode

Table 11.2: The reaction topologies for the six channels from the CLAS g11a experiment. Since a 2-prong trigger was used here, at least two charged particles were required to be detected. The undetected final-state particle(s) is(are) shown within parentheses for each case.

11.4 Tagged and untagged photon experiments

One of the recurring aspects of the older SLAC/DESY/CEA experiments (for the pseudoscalar channels) is that they did not have a tagged photon beam. The energy bin-widths in these results were large ($\Delta E_\gamma \sim \mathcal{O}(1\text{ GeV})$) and with large uncertainties in the quoted E_γ. Aside from the fact that with a wide binning, the cross-section can vary considerably across the bin-wdith, another concern is that the conversion between the variables t and $\cos\theta^{\text{meson}}_{\text{c.m.}}$, which depends on E_γ. Some of the older experiments even quote the electron beam energy as the estimated photon beam energy. It is also possible that the older experiments had been normalized to each other, which could explain their mutual agreement. In fact, the CLAS $g11a$ data is the first photoproduction dataset that "bridges" the higher energy forward-angle regime (where discrepancies exist) with the lower energy regime (where there is no apparent discrepancy). The only problem with this explanation is that the CB-ELSA $\pi^0 p$ [214] and ηp [158, 157] data, which is more recent, and did use a tagged photon beam, also differs from CLAS at the forward-angles. Therefore, the CLAS-ELSA discrepancy remains an outstanding issue that needs to be resolved by future experiments.

For the two vector meson (channels ωp and ϕp) where we do not find a discrepancy, the SLAC-Ballam [114] data did not use a bremsstrahlung beam. In this case, a nearly mono-chromatic linearly polarized photon beam was produced by a collimated laser-backscattering procedure. The Daresbury-Barber [116, 118] used a tagged bremsstrahlung beam.

11.5 Effect on the hadrodynamic coupling constants

Before proceeding further, we first clarify that our aim in this section is not to investigate photoproduction mechanisms *per se*, but to demonstrate that irrespective of the physics model chosen, a normalization discrepancy at the higher energies will have a significant bearing on future resonances searches at lower energies.

We follow the Regge-based work outlined in GLV [138] and adopted by the Ghent-RPR group [140, 141] and others [152], and limit our discussion to the three channels $\pi^+ n$, $K^+\Lambda$ and $K^+\Sigma^0$. The first indication of a normalization problem between CLAS and SLAC can be found in the CLAS $g1c$ $K^+\Lambda/K^+\Sigma^0$ paper [87] where the GLV model from a fit to the SLAC high-energy results and projected down to CLAS energies consistently overpredicts the $K^+\Lambda$ cross-sections (see Fig. 20 in

Ref. [87] for example). In the basic GLV model, there are just two Reggeized t-channel exchange processes, a pseudo-scalar ($J^P = 0^-$) exchange and a vector meson ($J^P = 1^-$) exchange. GLV also assumes these exchange processes to be strongly degenerate with the higher spin exchanges (lying on the same Regge trajectory). As a result, incorporating just the lowest spin exchanges can suffice, and the model does a reasonable job in predicting the high energy data. The issue of degeneracy has been re-visited by Yu *et al.* in their recent work [190, 191], where, instead of a strong degeneracy (both the couplings and the phases are degenerate), they assume a weak degeneracy (only the phases are degerate). In the Yu work, higher spin tensor exchanges are taken into account as a simple extension of the basic GLV model.

As such, we do not have any complaints about the physics motivation in this extended-GLV model of Yu. The problem is that Yu claims that within the Regge framework, addition of the tensor exchanges can lead to a reduction of the projected $K^+\Lambda$ cross-sections at the CLAS energies, and therefore, these tensor exchanges are *necessary*. We also note that the Yu article does not incorporate the CLAS $g11a$ data, which has a much closer kinematic proximity to the SLAC data. Once the CLAS $g11a$ results are taken into account, it becomes amply clear that the problem lies not in the model, but in the data itself, as we showed in Sec. 11.2.1. Therefore, attempts to reconcile both the CLAS and SLAC data within a single fit are essentially misleading.

11.5.1 Coupling constants

To our knowledge, the only coupling that is relatively well known is $g_{\pi NN}$. Most authors place its value around 13 and GLV takes $g_{\pi NN} \approx 13.45$. Assuming a 20% broken SU(3), GLV places the following limits on $g_{Kp\Lambda}$ and $g_{Kp\Sigma}$:

$$-16 \leq \quad g_{Kp\Lambda} \quad \leq -10.6 \tag{11.1a}$$

$$3.2 \leq \quad g_{Kp\Sigma} \quad \leq 4.7. \tag{11.1b}$$

These couplings enter via the Born terms, t-channel pion/kaon exchange and s-channel nucleon/hyperon exchange. The latter is required for restoration of gauge symmetry, since the sole t-channel Born term breaks gauge invariance. Aside from these Born terms, t-channel vector meson exchanges can also occur. The couplings for this case are much less well known. For example, $g_{\rho NN}$ varies from 1.9 [151] to 3.4, as taken by GLV. Similarly, $\kappa_{\rho NN}$ is found to vary between 1.5 and 6.6 in the literature; GLV takes $\kappa_{\rho NN} = 6.1$. Given $g_{\rho NN}$ and $\kappa_{\rho NN}$, it is possible to estimate g_{K^*pY} and κ_{K^*pY} for the hyperons (Y) using SU(3) [138]:

$$g_{K^*p\Lambda} = -6.08 \qquad \kappa_{K^*p\Lambda} = +3.66 \tag{11.2a}$$

$$g_{K^*p\Sigma} = -3.51 \qquad \kappa_{K^*p\Lambda} = -1.22. \tag{11.2b}$$

However, given how much uncertainty there is in the values of the ρ couplings themselves, even assuming unbroken SU(3), it is clear that the K^* couplings remain poorly known. Finally, we also point out that the values of these couplings are model-dependent. The isobar-models (instead of the Regge-based models) include phenomenological form-factors that bring in further model-dependence.

11.5.2 The SLAC forward-angle shapes

Fig. 11.7 shows the forward-angle SLAC-Boyarski [211, 200] results at $E_\gamma = 5$ GeV for the π^+n, $K^+\Lambda$ and $K^+\Sigma^0$ channels overlaid with the GLV [138] model fit results. The notable feature of interest we want to point out here is the $|t| \to 0$ behavior. For π^+n, the cross-section shows a steep peak; for $K^+\Lambda$, this is more a flat plateau, while, for $K^+\Sigma^0$, it shows a fall off. In the GLV picture, this forward-angle behavior is dictated by the ratio between the Born term and the vector meson exchang term. The Born term consists of two pieces, the conventional t-channel π^+/K^+ exchange,

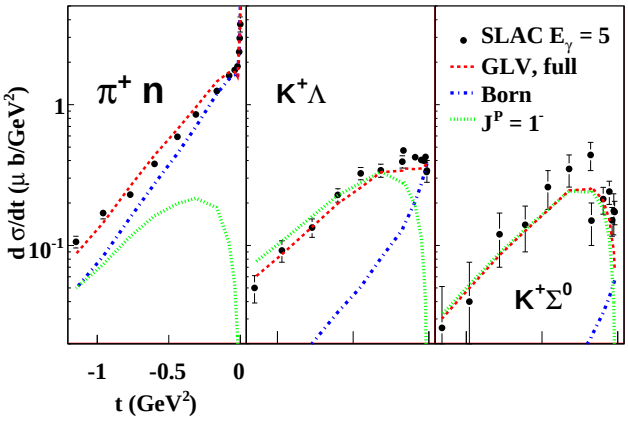

Figure 11.7: Comparison between the forward-angle $d\sigma/dt$ for the $\pi^+ n$ [211], $K^+\Lambda$ [200] and $K^+\Sigma^0$ [200] channels from SLAC-Boyarski at $E_\gamma = 5$ GeV. At $|t| \to 0$, $\pi^+ n$ shows a rise, $K^+\Lambda$ shows more of a plateau, while $K^+\Sigma^0$ shows a fall-off. The curves show the GLV [138] Regge-model results. See text for details.

plus, the electric part of the s-channel nucleon/hyperon exchange that is added to restore gauge invariance. The sharp rise for the $\pi^+ n$ case is due to a large $g_{\pi NN}$ in the s-channel Born term. Relative to $g_{\pi NN}$, $g_{\rho NN}$ (for the vector-meson $J^P = 1^-$ exchange) is small, and therefore, the Born term dominates. In the case of the hyperon (KY) channels, since there is no sharp rise at $|t| \to 0$, this means, g_{KpY} has to be relatively smaller than g_{K^*pY} and the ratio of these two couplings determines whether the $|t| \to 0$ should be a plateau ($K^+\Lambda$) or a drop-off ($K^+\Sigma^0$). *At $|t| \approx 0$, the cross-section is completely fixed by g_{KpY} in the Born term, since the K^* exchange contribution vanishes here.*

Furthermore, it can be see from Fig. 11.7 that in the case of the hyperons, away from $|t| = 0$, the natural-parity K^* exchange term dominates, which would signify that the beam-asymmetry observable (Σ) be close to $+1$. This is indeed what is seen in the 16-GeV SLAC results [203].

Since the forward-angle coverage in the CLAS $g11a$ results [19, 20] extends till $\cos\theta^{K^+}_{\rm c.m.} \leq 0.95$ only, these results do not contain information on the shape of the cross-section at $|t| \to 0$. Therefore, if we neglect the older SLAC results, ab initio, we do know whether the forward-angle cross-section is a rise, or plateau or a fall-off. On the other hand, the LEPS detector is a dedicated forward-angle detector, and as shown in Fig. 11.2, in regions where the kinematics overlap, the CLAS results are in excellent agreement with LEPS. The LEPS hyperon data [90] in the forward-most angular bin show a slight fall-off in the cross-sections at $|t| \to 0$, in agreement with the SLAC-Boyarski results. Therefore, even if we do not include the SLAC data directly, it is plausible to incorporate the shapes of the forward-angle SLAC results. More specifically, we impose the restriction that the extrapolation of any PWA fit results into the $|t| \to 0$ region should not show a rise for the $K^+\Lambda$ and $K^+\Sigma^0$ channels.

11.5.3 New fits incorporating the CLAS data

The results of our fit using the GLV model and all CLAS data points $\sqrt{s} \geq 2.6$ GeV (high energy), $|\cos\theta^{K^+}_{\rm c.m.}| > 0.5$ (forward- and backward-angle) as well as the SLAC $E_\gamma = 16$ GeV beam-asymmetry results [203] are shown in Fig. 11.8. We assume a rotating phase for all the Regge amplitudes and the the $K^+\Lambda$ and $K^+\Sigma^0$ channels were coupled together. The latter implies that the u-channel terms (involving $g_{Kp\Lambda}$ and $g_{Kp\Sigma}$) did not involve any new coupling. This adds to the internal

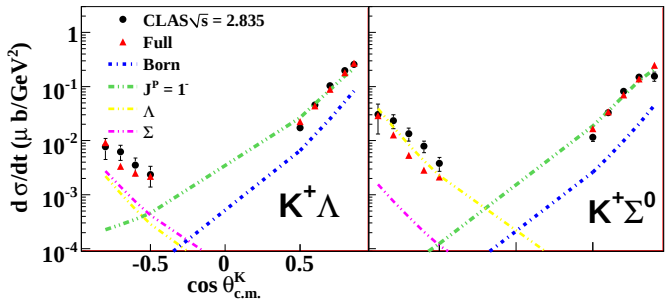

(a)

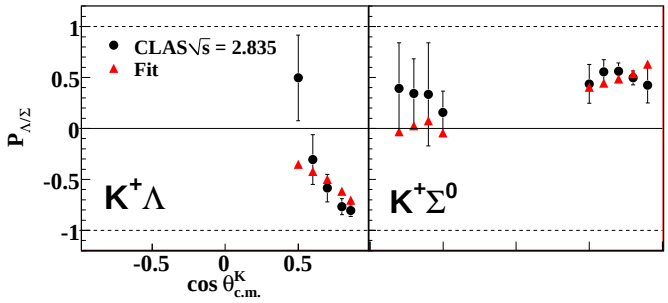

(b)

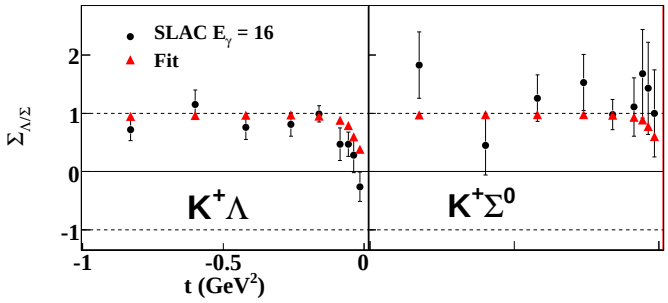

(c)

Figure 11.8: Results from a fit using the GLV model and incorporating all CLAS data points with $\sqrt{s} \geq 2.6$ GeV and $|\cos\theta^{K^+}_{\text{c.m.}}| > 0.5$, as well as the $E_\gamma = 16$ GeV SLAC beam-asymmetry results [203].

consistency of our fit results. The values of the couplings we obtained are: $g_{Kp\Lambda} = -9.5$, $g_{Kp\Sigma} = 5.6$, $g_{K^*p\Lambda} = -14.5$, $\kappa_{K^*p\Lambda} = 1.7$, $g_{K^*p\Sigma} = -14.5$ and $\kappa_{K^*p\Sigma} = -1.3$. We note here that the exact values of the couplings could depend on the choice of the phase choices and a more exhaustive study of the phases is currently underway . However, the values of the three couplings $g_{Kp\Lambda}$, $g_{K^*p\Lambda}$ and $g_{K^*p\Sigma}$ will certainly be lower than what was found in the original GLV work. The value of the $g_{Kp\Lambda}$ turns out to be especially important, since this contributes to the Born term in $K^+\Lambda$, that dominates at near-threshold. Therefore, from the perspective of searches for s-channel resonances, it is very important that $g_{Kp\Lambda}$ be well-known. For $K^+\Sigma^0$, the Born-term plays a less dominant role, so that the contribution from $g_{Kp\Sigma}$ is small. However, the K^* couplings $g_{K^*p\Lambda}$ and $g_{K^*p\Sigma}$ again play important roles.

11.6 Future work involving the ηp channnel

The main hurdle to our argument in Sec. 11.4 that the old results suffer from issues related to an untagged photon beam, is the CLAS/ELSA discrepancy for the η and π^0 channels, since the ELSA experiments did use a tagged beam. At the time of this writing, the ELSA Collaboration is analyzing a newer high-statistics dataset [215] and preliminary results from this work were presented at the NSTAR 2011 conference at JLab [216]. The goal of this new ELSA analysis is to extract cross-sections for the ω and compare them to CLAS, since the ω channel does not seem to have the CLAS/SLAC discrepancy. For the η channel, their preliminary results seem to indicate that the CLAS/ELSA discrepancy exists, not just at forward-angles (as noted in the CLAS-2009 work by Williams *et al* [18]), but over the entire angular range. Therefore, their conclusion is that the discrepancy is a purely *energy-dependent* normalization issue.

Inkeeping with this development, we are currently re-visiting the CLAS η analysis employing the full $g11a$ two-track dataset for the following reaction topologies

$$\gamma p \to \eta p \to (\pi^-, \pi^0)\pi^+ p \tag{11.3a}$$

$$\gamma p \to \eta p \to (\pi^+, \pi^0)\pi^- p \tag{11.3b}$$

where the undetected final-state particles are shown within parentheses. The first case was studied by Williams *et al* for a few energy bins. As noted earlier in Sec. 11.2.2 the conclusion was that the $g11a$ two- and three-track results were consistent with each other. The present study will extend upon this earlier work and will also investigate the missing (π^+, π^0) case.

11.7 Summary

In this chapter we have given a detailed account of the normalization discrepancies between CLAS and other photo-production experiments. The discrepancy pertains to the pseudo-scalar sector, at higher energies, where the CLAS cross-sections are lower by a factor of about two, than older SLAC/DESY/CEA results. The discrepancy persists with more rescent ELSA data, although CLAS agrees with LEPS for the $K^+\Lambda$ and $K^+\Sigma^0$ channels. We have pointed out a "probable" reason being the older data using an untagged beam, but this issue needs to be investigated further.

Chapter 12

Outlook and future work

The CLAS $g11a$ dataset has proved to be an enormously rich source of high quality data. The Carnegie Mellon PWA group has accumulated high-statistics and wide kinematic coverage results for six ground-state meson protoproduction channels using this dataset. Combined with our powerful analysis tools, we look forward to completing the PWA work. For the $K^+\Lambda$ and $K^+\Sigma^0$ channels, preliminary results from the CLAS $g8$ experiment (linearly polarized beam) are also available and fits incorporating these new data are currently in progress. In this last chapter, we briefly discuss our goals for the near future:

1. Coupled-channel fits:
   In Secs. 5.9 and 11.5, we discussed the wide uncertainties prevelant many of the coupling constants. An interesting example is the value of $\kappa_{\omega NN}$, which most analyses take to be zero. This coupling occurs in the backward-angle nucleon exchange process for ωp. Williams *et al.* [51] found that the large ρ^0_{00} for ωp at high-energies, backward-angles could not be explained if $\kappa_{\omega NN}$ was taken to be zero. Since $\kappa_{\omega NN}$ also occurs in the t-channel ω exchange process for the ηp channel, it is conceivable that we can better constrain the value of $\kappa_{\omega NN}$ by fitting the ωp and ηp channels simultaneously. In fact, many of the other couplings recur in different channels (see Fig. 12.1), either directly, or via SU(3) relations and coupled-channel fits will be very useful for this purpose.

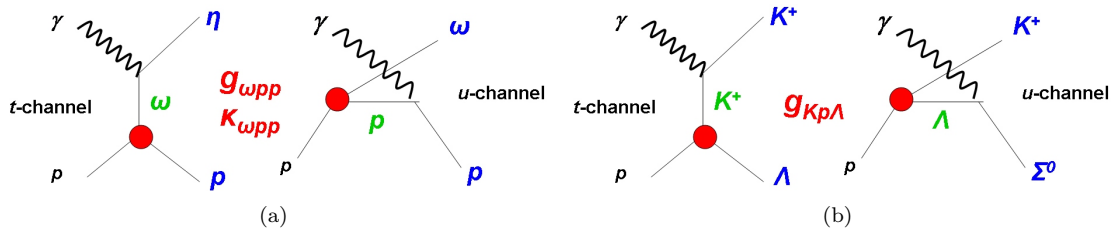

Figure 12.1: Examples of channel-coupling: (a) ηp and ωp (b) $K^+\Lambda$ and $K^+\Sigma^0$. The common coupling constants are shown in red.

2. $K^+\Lambda/K^+\Sigma^0$ PWA:

   Much work have already been done for the hyperons and some preliminary results were presented at NSTAR 2011 [217]. An interesting feature seen in the latest extended $K^+\Lambda$ results (see App. A) is the presence of a *narrow* peak at around $\sqrt{s} \approx 1650$ MeV, as shown in Fig. 12.2. A recent paper by T. Mart [218] has studied this near-theshold region using the

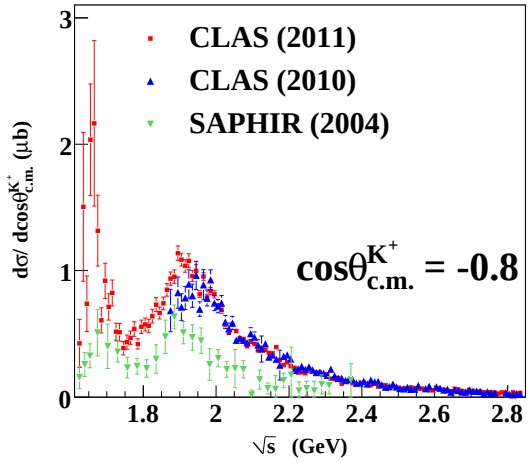

Figure 12.2: The $K^+\Lambda$ differential cross-sections for a backward-angle bin. The red points are the latest CLAS-2011 results (this work); in blue are results from CLAS-2010-McCracken [19] while the green points show results from SAPHIR-2004-Glander [88]. Note the the sharp peak around 1650 MeV.

available SAPHIR data [88]. From Fig. 12.2, SAPHIR evidently shows signs of this structure, but the newer CLAS data shows a much more sharp structure. While there is a **** $S_{11}(1650)$ resonance listed in the PDG, that has a significant branching ratio to $K\Lambda$, the S_{11} is a *broad* resonance which can not explain the narrowness of the structure under discussion. Mart conjectures the possibility of a narrow S_{11} *or* a P_{11} as a viable explanation. We hope that the inclusion of our CLAS-2011 results will help shed further light on this.

3. The Pomeron coupling:

   In Sec. 10.9.2 we pointed out that the older non-resonant models can not explain many of the finer detains present in the latest CLAS ωp results. Given the statistical precision of the new CLAS ωp and ϕp results, we expect the older models to be put to stringent tests. One of our goals is to better understand the structure of the Pomeron coupling and we hope to extend upon the earlier work done by Laget *et al.* [170] on the CLAS-200 ϕp data [60].

4. The ϕp forward-angle structure:

   Our results on the ϕp forward-angle "bump" structure (Sec. 9.6) have also evoked interest among theoreticians. We are in correspondance with Alvin Kiswandhi at the National Taiwan University, Taipei, who has expressed interest in re-fitting his model [161] incorporating our data.

Bibliography

[1] M. E. Peskin and D. V. Schroeder, *An Introduction to Quantum Field Theory*, Westview Press (1995).

[2] J. D. Gross and F. Wilczek, *Ultraviolet Behavior of Non-Abelian Gauge Theories*, Phys. Rev. Lett. **30**, 1343 (1973).

[3] H. D. Politzer, *Reliable Perturbative Results for Strong Interactions?*, Phys. Rev. Lett. **30**, 1346 (1973).

[4] G. F. Chew, *S-Matrix Theory of Strong Interactions without Elementary Particles*, Rev. Mod. Phys. **34**, 394 (1962).

[5] P. D. B. Collins, *An Introduction to Regge Theory and High-Energy Physics* (Cambridge University Press, Cambridge, 1977).

[6] E. D. Bloom and F. J. Gilman, *Scaling and the Behavior of Nucleon Resonances in Inelastic Electron-Nucleon Scattering*, Phys. Rev. D **4**, 2901 (1971).

[7] J. R. Forshaw and D. A. Ross, *Quantum Chromodynamics and the Pomeron* (Cambridge University Press, Cambridge, UK, 1997)

[8] S. Donnachie, G. Dosch, P. Landshoff, and O. Nachtmann, *Pomeron Physics and QCD* (Cambridge University Press, Cambridge, 2002).

[9] R. H. Dalitz, *Les Houches Lectures*, 1965 (Gordon and Breach Science Publishers, Inc. New York, 1965).

[10] D. Faiman and A. W. Hendry, *Harmonic-Oscillator Model for Baryons*, Phys. Rev. **173**, 1720 (1968).

[11] R. Koniuk and N. Isgur, *Baryon decays in a quark model with chromodynamics*, Phys. Rev. D **21**, 1868 (1980).

[12] S. Capstick, Photo- and electroproduction of nonstrange baryon resonances in the relativistic quark model, Phys. Rev. D, **46**, 2864 (1992).

[13] S. Capstick and W. Roberts, *$N\pi$ decays of baryons in a relativised model*, Phys. Rev. D, **47**, 1994 (1993).

[14] S. Capstick and W. Roberts, *Quasi-two-body decays of nonstrange baryons*, Phys. Rev. D, **49**, 4570 (1994).

[15] S. Capstick and W. Roberts, *Strange decays of nonstrange baryons*, Phys. Rev. D, **58**, 074011 (1998).

[16] M. Williams *et al.* (CLAS Collaboration), *Differential Cross Sections and Spin Density Matrix Elements for $\gamma p \to p\omega$*, Phys. Rev. C **80**, 065208 (2009).

[17] M. Williams *et al.* (CLAS Collaboration), *Partial wave analysis of the reaction $\gamma p \to p\omega$ and the search for nucleon resonances*, Phys. Rev. C **80**, 065209 (2009).

[18] M. Williams, *et al.*, *Differential cross sections for the reactions $\gamma p \to p\eta$ and $\gamma p \to p\eta'$*, Phys. Rev. C **80**, 045213 (2009).

[19] M. E. McCracken *et al.* (CLAS Collaboration), *Differential cross section and recoil polarization measurements for the $\gamma p \to K^+\Lambda$ reaction using CLAS at Jefferson Lab*, Phys. Rev. C **81**, 025201 (2010).

[20] B. Dey *et al.* (CLAS Collaboration), *Differential cross sections and recoil polarizations for the reaction $\gamma p \to K^+\Sigma^0$*, Phys. Rev. C **82**, 025202 (2010).

[21] D. B. Lichtenberg, L. J. Tassie and P. J. Keleman, *Quark-Diquark Model of Baryons and SU(6)*, Phys. Rev. **167**, 1535 (1968).

[22] D. B. Lichtenberg, W. Namgung, E. Predazzi, and J. G. Wills, *Baryon Masses in a Relativistic Quark-Diquark Model*, Phys. Rev. Lett. **48**, 1653 (1982).

[23] R. G. Edwards, J. J. Dudek, D. G. Richards, S. J. Wallace, *Excited state baryon spectroscopy from lattice QCD*, arXiv:1104.5152v1 [hep-ph].

[24] B. Povh, K. Rith, C. Scholz and F. Zetsche, *Particles and Nuclei – An INtroduction to the Physical Concepts*, Springer (2006).

[25] T. Nakano and H. Toki, *Proceedings of the International Workshop on Exciting Physics with New Accelerator Facilities*, SPring-8, Hyogo, 1997 (World Scientific, Singapore, 1998), p. 48.

[26] M. E. McCracken, *A Study of $K^+\Lambda$ Photoproduction in the CLAS* g11a *Dataset: Differential Cross Section, Recoil Polarization, and a Partial-Wave Analysis*. Ph.D. Thesis, Carnegie Mellon University (2008).

[27] Information on the "g11a" (E-04-021), "g1c" (E-89-004) and other CLAS run-periods can be found at:
`http://www.jlab.org/Hall-B/physics/experiments/run_period.html`.

CLAS running-periods,
`http://www.jlab.org/Hall-B/physics/experiments/run_period.html`.

[28] M. Battaglieri *et al.*, *Spectroscopy of Exotic Baryons with CLAS: Search for ground and first excited states*, CLAS Analysis Proposal PR04-021.

[29] The GlueX experiment, `http://portal.gluex.org/`.

[30] The JLab Picture Exchange, `http://www1.jlab.org/ul/jpix`.

[31] Jefferson Lab, `http://www.jlab.org/`.

[32] The 12 GeV JLab Upgrade, `http://www.jlab.org/12GeV/`.

[33] B. M. Dumham, *Jefferson Lab, a status report*, Thomas Jefferson National Accelerator Facility, 1997.

[34] Electronic logs recorded during *g11a* CLAS shifts, `http://clasweb.jlab.org/shift/g11/`.

[35] S. Gagnon. *Jefferson Lab Site Tour*, `http://education.jlab.org/sitetour/guidedtour05.1.alt.html`.

[36] D. I. Sober, *et al. The bremsstrahlung tagged photon beam in Hall B at JLab*. Nucl Inst Meth A **440**, 263 (2000).

[37] Jefferson Lab. *Experimental Hall B*, `http://www.jlab.org/Hall-B/`

[38] B. A. Mecking *et al*, *The CEBAF large acceptance spectrometer (CLAS)*, Nucl. Inst. Meth. A **440**, 263-284 (2000).

[39] S. Christo, *The g11a Target Cell*, `http://www.jlab.org/~christo/g11a_target.html`.

[40] Y. G. Sharabian *et al.*, *A new highly segmented start counter for the CLAS detector*. Nucl. Inst. Meth. A **556**, 246 (2006).

[41] A. J. Street *et al.*, *Final site assembly and testing of the superconducting toroidal magnet for the CEBAF Larege Acceptance Spectrometer (CLAS)*, IEEE Trans. Mag. **32**, No. 4, 2074 (1996).

[42] M. D. Mestayer *et al.*, *The CLAS drift chamber system*, Nucl. Inst. Meth. A **449**, 81 (2000).

[43] D. S. Carman *et al.*, *The Region One drift chamber for the CLAS spectrometer*, Nucl. Inst. Meth. A **419**, 315 (1998).

[44] Y. M. Qin *et al.*, *Prototype studies and design considerations for the CLAS Region Two drift chambers*. Nucl. Inst. Meth A **367**, 316 (1995).

[45] F. J. Barbosa *et al.*, *A drift chamber system for a toroidal detector*, Nucl. Inst. Meth. A **323**, 19 (1992).

[46] E. S. Smith *et al.*, *The time-of-flight system for CLAS*, Nucl. Inst. Meth A **432**, 265 (1999).

[47] J. Ball and E. Pasyuk, *Photon Flux Determination Through Sampling of "out-of-time" Hits with the Hall B Photon Tagger*. CLAS Note 2005-002.

[48] M. Battaglieri and R. DeVita, *The g11 Triggers efficiency*, unpublished CLAS-note (2005).

[49] M. Ungaro, R. DeVita, and L. Elouadrhiri, *g11a data processing*, CLAS-note 2005-014 (2005).

[50] M. Williams and C. A. Meyer. *Kinematic Fitting in CLAS*. CLAS-note 2003-017.

[51] M. Williams, *Measurement of Differential Cross Sections and Spin Density Matrix Elements along with a Partial Wave Analysis for $\gamma p \to p\omega$ using CLAS at Jefferson Lab*. Ph.D. Thesis, Carnegie Mellon University (2007).

[52] R. K. Bradford, *Measurement of differential cross sections and C_X and C_Z for $\gamma p \to K^+\Lambda$ and $\gamma p \to K^+\Sigma^0$ using CLAS at Jefferson Lab*, Ph.D. Thesis, Carnegie Mellon University (2005).

[53] W.-M. Yao *et al. Review of Particle Physics*. J. Phys. G **33**, 1 (2006).

[54] E. Pasyuk, *The CLAS ELOSS Package*. Software available via the CLAS CVS repository under `clas/utilities/packages/eloss`.

[55] J. McNabb, *Photoproduction of Λ and Σ^0 Hyperons off Protons in the Nucleon Resonance Region using CLAS at Jefferson Lab*, Ph.D. Thesis, Carnegie Mellon University (2004).

[56] M. Williams, D. Applegate, and C. A. Meyer, *Determining Momentum and Energy Corrections for g1c Using Kinematic Fitting*.

[57] D. Sober, H. Crannell, and F. Klein, *The Tagger Energy Scale: Interpreting the CMU Kinematic Fit Results*, CLAS-note 2004-019 (2004).

[58] D. Applegate, M. Bellis, Z. Krahn, C. Meyer, and M. Williams, *A Detailed Study of the Sources of Systematic Errors in the CLAS g11 Data*, CLAS-note 2006-017 (2006).

[59] K. Lukashin *et al.* (The CLAS Collaboration),*Exclusive electroproduction of ϕ mesons at 4.2 GeV*, Phys. Rev. C **63**, 065205 (2001).

[60] E. Anciant *et al.* (CLAS Collaboration), *Photoproduction of $\phi(1020)$ mesons on the proton at large momentum transfer*, Phys. Rev. Lett. **85** 4682 (2000).

[61] E. Anciant, *g6a* analysis note,
`http://www.jlab.org/Hall-B/secure/analysis/clas_analysis00/2000-106.ps`

[62] E. Anciant, *Photoproduction de Mesons Phi a Grand Moment Transfere* (in French). Ph.D. Thesis, CEA-Saclay (2000),
`http://www.jlab.org/Hall-B/general/thesis/Anciant_thesis.pdf`.

[63] L. Bibrzycki, L. Lesniak1 and A. P. Szczepaniak, *$K\overline{K}$ photoproduction and S-P-wave interference*, Eur. Phys. J. C **34**, 335-344 (2004).

[64] D. C. Fries *et al.*, *S-P wave interference in K^-K^- photoproduction near K^-K^- threshold*, Nucl. Phys. **B143**, 408-416 (1978).

[65] J. Barth *et al.* (SAPHIR Collaboration), *Low-energy photoproduction of ϕ-mesons*, Eur. Phys. J. A **17**, 269 (2003).

[66] T. Mibe *et al.* (LEPS Collaboration), *Near-Threshold Diffractive ϕ-Meson Photoproduction from the Proton*, Phys. Rev. Lett. 95, **182001** (2005).

[67] M. Holtrop, *GSIM: CLAS GEANT Simulation*,
http://www.physics.unh.edu/maurik/Gsim/gsim_current_code_dev.shtml

[68] R. Schumacher. *Photon Attenuation in the CLAS Beam Line*. CLAS-note 2001-010 (2001).

[69] W. Rarita and J. Schwinger, *On a Theory of Particles with Half-Integral Spin*, Phys. Rev. **60**, 61 (1941).

[70] C. Zemach, *Three-Pion Decays of Unstable Particles*, Phys. Rev. B **133**, 1201-1220 (1964).

[71] S. U. Chung, *Spin Formalisms*, BNL Preprint BNL-QGS-02-0900 (2004).

[72] S. Weinberg, *The Quantum Theory of Fields, Vol. 1: Foundations*, Cambridge University Press (1995).

[73] C. Itzykson and J-B. Zuber. *Quantum Field Theory*, Dover Publications (2006).

[74] A. V. Anisovich, E. Klempt, A. V. Sarantsev and U. Thoma, *Partial-wave decomposition of pion and photoproduction amplitudes*, Eur. Phys. J. A **24**, 111-128 (2005).

[75] J. D. Jackson. *Classical Electrodynamics*, Wiley 3 ed. (1998).

[76] E. D. Commins and P. H. Bucksbaum, *Weak interactions of leptons and quarks*, Cambridge University Press (1983).

[77] S. Janssen, J. Ryckebusch, D. Debruyne, and T. Van Cauteren, *Kaon photoproduction: Background contributions, form factors, and missing resonances*, Phys. Rev. C **65**, 015201 (2001).

[78] H. Haberzettl, C. Bennhold, T. Mart, and T. Feuster, *Gauge-invariant tree-level photoproduction amplitudes with form factors*, Phys. Rev. C **58**, R40–R44 (1998).

[79] R. M. Davidson and R. Workman, *Form factors and photoproduction amplitudes*, Phys. Rev. C **63**, 025210 (2001).

[80] A. Usov and O. Scholten, *KLambda and KSigma photoproduction in a coupled-channels framework*, Phys. Rev. C **72**, 025205 (2005).

[81] B. C. Pearce and B. K. Jennings, *A relativistic, meson exchange model of pion-nucleon scattering*, Nucl. Phys. **A528**, 655 (1991).

[82] S. U. Chung, *Formulas for Partial Wave Analysis, Version II*, Brookhaven National Laboratory Preprint BNL-QGS-93-05 (1993).

[83] F. James, *MINUIT: Function Minimization and Error Analysis, v. 94.1.* CERN Program Library D506.

[84] L. Lyons *et al.*, *How to combine correlated estimates of a single physical quantity*, Nucl. Inst. Meth. A **270**, 110 (1988).

[85] A. Valassi, *Combining correlated measurements of several different physical quantities*, Nucl. Inst. Met. A *500*, 391 (2003).

[86] T. Aaltonen, *et al.* (CDF collaboration), *Measurement of W-boson helicity fractions in top-quark decays using* $\cos\theta^*$, Phys. Lett. **B674**, Issue 3, 160-167 (2009).

[87] R. Bradford, *et al.* (CLAS Collaboration), *Differential cross sections for* $\gamma p \to K^+ Y$ *for* Λ *and* Σ^0 *hyperons*, Phys. Rev. C **73**, 035202 (2006).

[88] K. H. Glander, *et al.* (SAPHIR Collaboration), *Measurement of* $\gamma p \to K^+\Lambda$ *and* $\gamma p \to K^+\Sigma^0$ *at photon energies up to 2.6 GeV*, Eur. Phys. J. **A19**, 2 (2004).

[89] H. Kohri *et al.* (LEPS Collaboration), *Differential Cross Section and Photon-Beam Asymmetry for the* $\vec{\gamma}n \to K^+\Sigma^-$ *Reaction at* E_γ*=1.5-2.4 GeV*, Phys. Rev. Lett. **97**, 082003 (2006).

[90] M. Sumihama *et al.* (LEPS Collaboration), *The* $\gamma p \to K^+\Lambda$ *and* $\gamma p \to K^+\Sigma^0$ *reactions at forward angles with photon energies from 1.5 to 2.4 GeV*, Phys. Rev. C **73**, 035214 (2006).

[91] G. Bunce *et al.*, *Hyperon Polarization in Inclusive Production by 300-GeV Protons on Beryllium*, Phys. Rev. Lett. **36**, 1113-1116 (1976).

[92] H-W. Siebert, *The challenge of polarizations in hadronic hyperon production*, Eur. Phys. J. Special Topics **162**, 147 (2008)

[93] W-T. Chiang and F. Tabakin, *Completeness rules for spin observables in pseudoscalar meson photoproduction*, Phys. Rev. C **55** 2054 (1997).

[94] C. G. Fasano, F. Tabakin, and B. Saghai, *Spin observables at threshold for meson photoproduction*, Phys. Rev. C **46** 2430 (1992).

[95] G. R. Goldstein, J. F. Owens III, J. P Rutherfoord, and M. J. Moravcsik, Nucl. Phys. **B80**, 164 (1974).

[96] G. F. Chew, M. L. Goldberger, F. E. Low and Y. Nambu,, *Relativistic dispersion relation approach to photomeson production*, Phys. Rev. **106** 1345 (1957).

[97] R. L. Walker, *Phenomenological analysis of single-pion photoproduction*, Phys. Rev. **182** 1729 (1969).

[98] I. S. Barker, A. Donnachie and J. K. Storrow, *Complete experiments in pseudoscalar photoproduction*, Nucl. Phys. B **95** 347 (1975).

[99] N. Levy *et al.*, *Kaon photoproduction*, Nucl. Phys. B **55** 493-512 (1973).

[100] R. A. Adelseck and B. Saghai, *Kaon photoproduction: data consistency, coupling constants, and polarization observables*. Phys. Rev. C **42** 108-127 (1990).

[101] X. Artru, M. Elchikh, J.-M. Richard, J. Soffer, and O. V. Teryaev, Phys. Rept., 470, 1 (2009).

[102] P. Eugenio *et al.*, (CLAS Collaboration), *Search for Missing Nucleon Resonances in the Photoproduction of Hyperons Using A Polarized Photon Beam and A Polarized Target*, Jefferson Lab Experiment E-02-112.

[103] Craig Paterson, *Polarization Observables in Strangeness Photoproduction with CLAS at Jefferson Lab*, Ph.D. Thesis, Glasgow University (2008).

[104] SAID database `http://gwdac.phys.gwu.edu/`; MAID database `http://wwwkph.kph.uni-mainz.de/MAID//`; for the SAID/MAID signs, we refer to Eqs. 13-15 in G. Knöchlein, D. Drechsel and L. Tiator, Z. Phys. A **352**, 327 (1995).

[105] R. Gatto, *Relations between the Hyperon Polarizations in Associated Production*, Phys. Rev. **109**, 610 - 611 (1958).

[106] G. Feldman and T. Fulton, *Determination of the relative* Σ-Λ *parity*, Nucl. Phys.**8**, 106 (1958).

[107] J. W. C. McNabb, *et al.* (CLAS Collaboration), *Hyperon photoproduction in the nucleon resonance region*. Phys. Rev. C **69**, 042201 (2004).

[108] R. Bradford, *et al.*, *First measurement of beam-recoil observables* C_x *and* C_z *in hyperon photoproduction*, Phys. Rev. C **75**, 035205 (2007).

[109] A. Lleres, *et al.* (GRAAL Collaboration), *Polarization observable measurements for* $\gamma p \to K^+\Lambda$ *and* $\gamma p \to K^+\Sigma^0$ *for energies up to 1.5 GeV*, Eur. Phys. J. **A31**, 79 (2007).

[110] J. J. Sakurai, *Currents and Mesons*, The University of Chicago Press (1969).

[111] R. P. Feynman, *Photon-hadron Interactions*, W. A. Benjamin, Inc. (1972).

[112] T. H. Bauer, R. D. Spital, D. R. Yennie and F. M. Pipkin, *The hadronic properties of the photon in high-energy interactions*, Rev. Mod. Phys. **50**, 261436 (1978).

[113] R. M. Egloff *et al.*, *Measurements of Elastic* ρ- *and* ϕ-*Meson Photoproduction Cross Sections on Protons from 30 to 180 GeV*, Phys. Rev. Lett. **43**, 657660 (1979)

[114] J. Ballam *et al.*, Vector-Meson Production by Polarized Photons at 2.8, 4.7, and 9.3 GeV, Phys. Rev. D **7**, 31503177 (1973).

[115] H.-J. Behrend *et al.*, *Elastic and inelastic photoproduction*, Nucl. Phys. **B144**, 22-60 (1978).

[116] D. P. Barber *et al.* (LAMP2 Group Collaboration), Z. Phys. C, **26**, 343 (1984).

[117] D. P. Barber et al., Phys. Lett. **79B**, 150 (1978).

[118] D. P. Barber *et al.*, *A study of elastic photoproduction of low massK+K pairs from hydrogen in the energy range 2.84.8 GeV* Z. Phys. C **12**, 1 (1982).

[119] M. Derrick *et al.* (ZEUS Collaboration), *Measurement of elastic phi photoproduction at HERA*, Phys. Lett. **B377** 259-272 (1996).

[120] H. J. Besch *et al.*, *Photoproduction of mesons on protons at 2.0 GeV*, Nucl. Phys. B **70**, 257 (1974).

[121] R. Erbe *et al.* (ABBHHM Collaboration), *Photoproduction of Meson and Baryon Resonances at Energies up to 5.8 GeV*, Phys. Rev. **175** 1669-1696 (1968).

[122] H. Alvensleben *et al.*, Phys. Rev. Lett. **28**, 6669 (1972).

[123] G. McClellan *et al*, Phys. Rev. Lett. **26**, 15931596 (1971)

[124] C. Berger *et al.*, Phys. Lett. **39B**, 659 (1972)

[125] R. L. Anderson *et al.*, Phys. Rev. Lett. **30**, 149152 (1973).

[126] R. Anderson *et al.*, Phys. Rev. D **1**, 2747 (1970).

[127] J. Busenitz *et al.* Phys. Rev. D **40**, 121 (1989).

[128] J. Breitweg *et al.* (ZEUS Collaboration), *Measurement of diffractive photoproduction of vector mesons at large momentum transfer at HERA* Eur. Phys. J. C **14**, 213-238 (2000).

[129] A. Sibirtsev, Ulf-G. Meißner, and A. W. Thomas, *Okubo-Zweig-Iizuka rule violation in photoproduction*, Phys. Rev. D **71**, 094011 (2005).

[130] A. Donnachie and P. V. Landshoff, Phys. Lett. B **185**, 403 (1987); Nucl. Phys. **B244**, 322 (1984); **B267**, 690 (1986).

[131] W. M. Kloet, W-T. Chiang and F. Tabakin, *Spin information from vector-meson decay in photoproduction* Phys. Rev. C *58*, 1086 (1998).

[132] M. Pichowsky, C. Savkli and F. Tabakin, *Polarization observables in vector meson photoproduction* Phys. Rev. C *53*, 593 (1995).

[133] K. Schilling, P. Seyboth and G. Wolf, *On the analysis of vector-meson production by polarized photons*. Nucl. Phys. **B15**, 397 (1970).

[134] F. J. Gilman, J. Pumplin, A. Schwimmer, and L. Stodolsky, *Helicity conservation in diffractive scattering*, Phys. Lett. **B31**, 387 (1970).

[135] K. McCormick *et al.* (CLAS Collaboration),*Tensor polarization of the phi meson photoproduced at high t*, Phys. Rev. C **69**, 032203(R) (2004).

[136] W. C. Chang *et al.* (LEPS Collaboration), *Measurement of spin-density matrix elements for ϕ-meson photoproduction from protons and deuterons near threshold*, Phys. Rev. C **82**, 015205 (2010).

[137] M. Guidal, J.-M. Laget, and M. Vanderhaeghen, *Pseudoscalar meson photoproduction at high energies: from the Regge regime to the hard scattering regime*, Phys. Lett. B **400**, 6 (1997).

[138] M. Guidal, J.-M. Laget, and M. Vanderhaeghen, *Pion and kaon photoproduction at high energies: forward and intermediate angles* Nucl. Phys. **A627**, 645 (1997).

[139] M. Guidal, J.-M. Laget, and M. Vanderhaeghen, *Exclusive electromagnetic production of strangeness on the nucleon: Regge analysis of recent data*, Phys. Rev. C **68**, 058201 (2003).

[140] T. Corthals, J. Ryckebusch, and T. Van Cauteren, *Forward-angle $K^+\Lambda$ photoproduction in a Regge-plus-resonance approach*, Phys. Rev. C **73**, 045207 (2006).

[141] T. Corthals, T. Van Cauteren, J. Ryckebusch, and D. G. Ireland, *Regge-plus-resonance treatment of the $p(\gamma, K^+)\Sigma^0$ and $p(\gamma, K^0)\Sigma^+$ reactions at forward kaon angles*, Phys. Rev. C **75**, 045204 (2007).

[142] S. Janssen, J. Ryckebusch, D. Debruyne, and T. Van Cauteren, Phys. Rev. C **66**, 035202 (2002).

[143] S. Janssen, D. G. Ireland, and J. Ryckebusch, *Kaon photoproduction: Background contributions, form factors, and missing resonances*, Phys. Rev. C **65**, 015201 (2001).

[144] S. Janssen, *Strangeness production on the nucleon*, Ph. D thesis, Ghent University (2002), `http://inwpent5.ugent.be/papers/thesis_stijn.pdf`.

[145] S. Janssen, *Constructing observables for strangeness production* (technical note, 2004), `http://inwpent5.ugent.be/papers/formalism.pdf`.

[146] T. Corthals, *Regge-plus-resonance approach to kaon production from the proton*, Ph. D. thesis, Ghent University (2007), `http://inwpent5.ugent.be/papers/phdtamara.pdf`.

[147] T. Mart, *Electromagnetic production of kaons near threshold*, Phys. Rev. C **82**, 025209 (2010).

[148] F. X. Lee, T. Mart, C. Bennhold, H. Haberzettl, L. E. Wright, *Quasifree Kaon Photoproduction on Nuclei*, Nucl. Phys. A **695**, 237 (2001).

[149] W.-T. Chiang, B. Saghai, F. Tabakin, and T.-S. H. Lee, *Dynamical coupled-channel model of kaon-hyperon interactions*, Phys. Rev. C **69**, 065208 (2004).

[150] A. Sibirtsev, J. Haidenbauer, S. Krewald, U.-G. Meiner, *Analysis of recent η photoproduction data*, Eur. Phys. J. A *46*, 359371 (2010).

[151] J. He and B. Saghai, *η production off the proton in a Regge-plus-chiral quark approach*, Phys. Rev. C *82*, 035206 (2010).

[152] W.-T. Chiang, S. N. Yang, L. Tiator, M. Vanderhaeghen, and D. Drechsel, *Reggeized model for η and η photoproduction*, Phys. Rev. C **68**, 045202 (2003).

[153] W.-T. Chiang, S. N. Yang, L. Tiator, and D. Drechsel, *An isobar model for η photo- and electroproduction on the nucleon*, Nucl. Phys. A700, 429 (2002).

[154] A. Sibirtsev, C. Elster, S. Krewald and J. Speth, *Photoproduction of eta-prime-mesons from the proton* AIP Conf. Proc. 717, 837 (2004) [arXiv:nucl-th/0303044].

[155] J. M. Laget, *The Primakoff effect on a proton target*, Phys. Rev. C **72**, 022202 (2005).

[156] W. Braunschweig *et al.*, *Single photoproduction of η-mesons on hydrogen in the forward direction at 4 and 6 GeV*, Phys. Lett. 33B, 236 (1970).

[157] V. Crede *et al.* (CB-ELSA Collaboration), Phys. Rev. Lett. **94**, 012004 (2005).

[158] V. Crede *et al.* (CB-ELSA Collaboration), *Photoproduction of η and η' mesons off protons*, Phys. Rev. C **80**, 055202 (2009).

[159] D. Elsner *et al.* (CBELSA/TAPS Collaboration), *Measurement of the beam asymmetry in η photoproduction off the proton*, Eur. Phys. J. A **33**, 147 (2007).

[160] S. Ozaki, A. Hosaka, H. Nagahiro, and O. Scholten, *Coupled-channel analysis for ϕ photoproduction with $\Lambda(1520)$*, Phys. Rev. C 80, 035201 (2009).

[161] A. Kiswandhi, J-J. Xie, S. N. Yang, *Is the nonmonotonic behavior in the cross section of ϕ photoproduction near threshold a signature of a resonance?*, Phy. Lett. **B691**, 214 (2010).

[162] J-J.Xie and J. Nieves, *Role of the $N^*(2080)$ resonance in the $\vec{\gamma}p \to K^+\Lambda(1520)$ reaction*, Phys. Rev. C **82**, 045205 (2010).

[163] A. M. Sandorfi, S. Hoblit, H. Kamano, T.-S. H. Lee, *Calculations of Polarization Observables in Pseudoscalar Meson Photo-production and Experimental Constraints on the $\gamma p \to K^+\Lambda$ Multipoles*, J. Phys. G: Nucl. Part. Phys. **38** 053001.

[164] Y. Oh, A. I. Titov, and T.-S. H. Lee, *Nucleon resonances in ω photoproduction*, Phys. Rev. C **63**, 025201 (2001).

[165] A. I. Titov and T.-S. H. Lee, *Spin effects and baryon resonance dynamics in -meson photoproduction at few GeV* Phys. Rev. C **67**, 065205 (2003).

[166] A. I. Titov, T.-S. H. Lee, H. Toki, and O. Streltsova, *Structure of the ϕ photoproduction amplitude at a few GeV*, Phys. Rev. C **60**, 035205 (1999).

[167] Y. Oh, and H. C. Bhang, *Asymmetries in ϕ photoproduction and the Okubo-Zweig-Iizuka violation*, Phys. Rev. C 64, 055207 (2001).

[168] A. I. Titov and B. Kämpfer, *Photoproduction of the ϕ meson off the deuteron near threshold*, Phys. Rev. C **76**, 035202 (2007).

[169] H. Suganuma, S. Sasaki, and H. Toki, *Color confinement, quark pair creation and dynamical chiral-symmetry breaking in the dual Ginzburg-Landau theory* Nucl. Phys. **B435**, 207 (1995).

[170] J.-M. Laget and R. MendezGalain, *Exclusive photoproduction and electroproduction of vector mesons at large momentum transfer*, Nucl. Phys. **A581**, 397 (1995).

[171] J.-M. Laget, *Photoproduction of vector mesons at large momentum transfer*, Phys. Lett. B **489**, 313 (2000)

[172] J.-M. Laget, *The Photoproduction of vector mesons* Nucl. Phys. **A699**, 184 (2002).

[173] F. Cano and J.-M. Laget, *Compton scattering, vector-meson photoproduction, and the partonic structure of the nucleon*, Phys. Rev. D **65**, 074022 (2002).

[174] M. G. Ryskin, *Diffractive J/Ψ electroproduction in LLA QCD*, Z. Phys. C **57**, 89 (1993).

[175] J. R. Cudell and I. Royen, *Elastic vector-meson production at HERA*, Phys. Lett. B **397**, 317 (1997).

[176] R. A. Williams, *ϕ photoproduction near threshold with Okubo-Zweig-Iizuka evading ϕNN interactions*, Phys. Rev. C **57**, 223232 (1998).

[177] A. Donnachie, P. V. Landshoff, *Gluon condensate and pomeron structure*, Nucl. Phys. B **311**, 509 (1989).

[178] P. V. Landshoff and O. Nachtmann, *Vacuum structure and diffraction scattering*, Z. Phys. C **35**, 405 (1987).

[179] D. B. Leinweber, J. I. Skullerud, A. G. Williams and C. Parrinello, *Asymptotic scaling and infrared behavior of the gluon propagator*, Phys. Rev. D **60**, 094507 (1999).

[180] R. L. Jaffe, *Stranger than fiction: The strangeness radius and magnetic moment of the nucleon*, Phys. Lett. B **229**, 275 (1984).

[181] K. Nakamura *et al.* (Particle Data Group), *Review of Particle Physics*, J. Phys. G **37**, 075021 (2010).

[182] B. Dey, M. E. McCracken, D. G. Ireland and C. A. Meyer, *Polarization observables in the longitudinal basis for pseudo-scalar meson photoproduction using a density matrix approach*, arXiv:1010.4978v2 [hep-ph].

[183] David J. Griffiths *Introduction to Elementary Particles*, Wiley-VCH (2008).

[184] J. He and B. Saghai, *η production off the proton in a Regge-plus-chiral quark approach*, Phys. Rev. C **82**, 035206 (2010).

[185] R. Machleidt, *High-precision, charge-dependent Bonn nucleon-nucleon potential*, Phys. Rev. C **63**, 024001 (2001).

[186] M. M. Nagels, T. A. Rijken, and J. J. de Swart, *Baryon-baryon scattering in a one-boson-exchange-potential approach. III. A nucleon-nucleon and hyperon-nucleon analysis including contributions of a nonet of scalar mesons*, Phys. Rev. D **20**, 16331645 (1979).

[187] C. Downum, T. Barnes, J. R. Stone and E. S. Swanson, *Nucleon-meson coupling constants and form-factors in the quark model*, Phys. Lett. B **638**, 455-460 (2006).

[188] M. Benmerrouche, N. C. Mukhopadhyay and J. F. Zhang *Effective Lagrangian approach to the theory of η photoproduction in the $N^*(1535)$ region*, Phys. Rev. D **51**, 32373266 (1995).

[189] S. Godfrey and N. Isgur, *Mesons in a relativized quark model with chromodynamics*, Phys. Rev. D **32**, 189 (1985).

[190] Byung Geel Yu, Tae Keun Choi, and W. Kim,*Regge phenomenology of pion photoproduction off the nucleon at forward angles*, Phys. Rev. C **83**, 025208 (2011).

[191] B. G. Yu, T. K. Choi and W. Kim, arXiv:1104.3672v1 [nucl-th].

[192] L. Xiong, E. Shuryak, and G. E. Brown, *Photon production through A_1 resonance in high-energy heavy-ion collisions*, Phys. Rev. D **46**, 37983801 (1992).

[193] H. Nagahiro, L. Roca, and E. Oset *Radiative decay into γP of the low lying axial-vector mesons*, Phys. Rev. D **77**, 034017 (2008).

[194] E. Klempt and J-M. Richard, Rev. Mod. Phys. **82**, 1095-1153 (2010).

[195] S. Capstick and W. Roberts, Phys. Rev. D **47**, 1994 (1993); Phys. Rev. D **49**, 4570 (1994); Phys. Rev. D **58**, 074011 (1998).

[196] M. Dugger *et al.* (CLAS Collaboration), Phys. Rev. C, **79** 065206 (2009).

[197] M. Dugger *et al.* (CLAS Collaboration), Phys. Rev. C **76**, 025211 (2007).

[198] M. Dugger *et al.* (CLAS Collaboration), Phys. Rev. Lett. **89**, 222002 (2002).

[199] M. Williams *et al.*, JINST **4**, P10003 (2009).

[200] A. M. Boyarski *et al.* (SLAC), Phys. Rev. Lett. **22** 1131 (1969).

[201] V. B. Elings *et al.* (CEA), Phys. Rev. **156**, 1433 (1967).

[202] P. M. Joseph *et al.*, Phys. Lett. **26B**, 41 (1967).

[203] D. J. Quinn *et al.* (SLAC), Phys. Rev. D **20**, 1553 (1979).

[204] D. Bellenger *et al.*, Phys. Rev. Lett. **23**, 540 (1969).

[205] J. Dewire *et al.*, Phys. Lett. **37B**, 326 (1971).

[206] R. L. Anderson *et al.*, Phys. Rev. Lett. **26**, 30 (1971).

[207] P. L. Bussey *et al.*, Phys. Lett. **61B**, 479 (1976).

[208] G. Buschhorn *et al.* (DESY), Phys. Rev. Lett, **17**, 1027 (1966).

[209] G. Buschhorn *et al.* (DESY), Phys. Rev. Lett, **18**, 571 (1966).

[210] P. Heide *et al.* (DESY), Phys. Rev. Lett. **21**, 248 (1968).

[211] A. M. Boyarski *et al.* (SLAC), Phys. Rev. Lett. **20**, 300 (1968).

[212] G. Vogel *et al.* (DESY), Phys. Lett. **40B**, 513 (1972).

[213] M. Braunschweig *et al.* (DESY), Phys. Lett. **26B**, 405 (1967).

[214] O. Bartholomy *et al.* (CB-ELSA Collaboration), Phys. Rev. Lett. **94**, 012003 (2005).

[215] Volker Crede, private communication.

[216] Talk given at NSTAR'11, Andrew Wilson, *ω Photoproduction at the CBELSA/TAPS Experiment*
`http://conferences.jlab.org/nstar2011/NStar%20-%20Parallel%20III-C%20-%20Thursday/NStar2011_AWilson.pdf`

[217] Talk given at NSTAR'11, B. Dey, *Partial wave analysis for $K^+\Lambda$ and $K^+\Sigma^0$ photoproduction*
`http://conferences.jlab.org/nstar2011/Tuesday%20Nstar%20Parallels%20I-B/Dey_NSTAR.pdf`

[218] T. Mart, *Evidence for the $J^P = 1/2^+$ narrow state at 1650 MeV in the photoproduction of $K\Lambda$*, Phys. Rev. D **83**, 094015 (2011).

Appendix A

Extension of the CLAS-2010 $K^+\Lambda$ results

In this Appendix we present an extension of the published CLAS-2010-McCracken $K^+\Lambda$ [19] results by employing the full two-track $g11a$ dataset. The McCracken results used 28% of the full two-track statistics. By employing the full dataset, we now have much better coverage in the near-threshold and backward-angle kinematic regimes. Our definition of the "full" two-track $g11a$ dataset here is the same as was used for the ϕp charged-mode analysis. In particular, from Sec. 3.2 we note that around a hundred files were lost during transfer from the magnetic tape. Still, the resulting two-track dataset has considerably greater statistics than the CLAS-2010 [19] results. The two-track $K^+\Lambda$ topology is defined as:

$$\gamma p \rightarrow K^+\Lambda \rightarrow K^+ p(\pi^-), \tag{A.1}$$

where the missing π^- momentum is re-constructed using a kinematic fit to a missing m_π mass. The CLAS torus magnet bends negatively charged particles towards the CLAS forward-angle beam-dump hole; therefore *not* detecting the π^- increases the acceptance and this is the prime motivation of analysing this topology.

Since this is a repetition of the McCracken analysis [26, 19] only employing a larger dataset, we give a brief synopsis of the analysis chain. We start by selecting "+:+" events, that is, events with at least two positively charged particles detected. Next, we make an event hypothesis of these particles being as "p:K^+", or "K^+:p" (both combinations checked) and make a 1-C kinematic fit to a missing π^- mass. Only events with a confidence level greater than 2% are retained. To reduce background, we next place the "iron-cross" timing cut described in Fig. 3.5a. Our fiducial cuts, efficiency corrections, Monte Carlo processing and acceptance calculation using the PWA Mother Fits remain the same as the McCracken analysis. The only two minor changes are, first, for the event-based signal-background separation (Sec. 3.11), McCracken used a linear background function, while we use a more general quadratic background. Second, for the Λ vertex cut that plays a significant role in the $g11a$ trigger (Sec. 7.1), McCracken used the simulated version of the trigger cut (Sec. 7.1.1), while we use the hard-cut version (Sec. 7.1.2). Our results are shown in Figs. A.1 to A.4. Within statistical fluctuations, the agreement is excellent. We also note that the photon flux normalization file had to be re-generated completely anew. Since this flux file is the same as the ϕp charged-mode analysis, the agreement with the McCracken results lend confidence in the normalization of our ϕp results, as well.

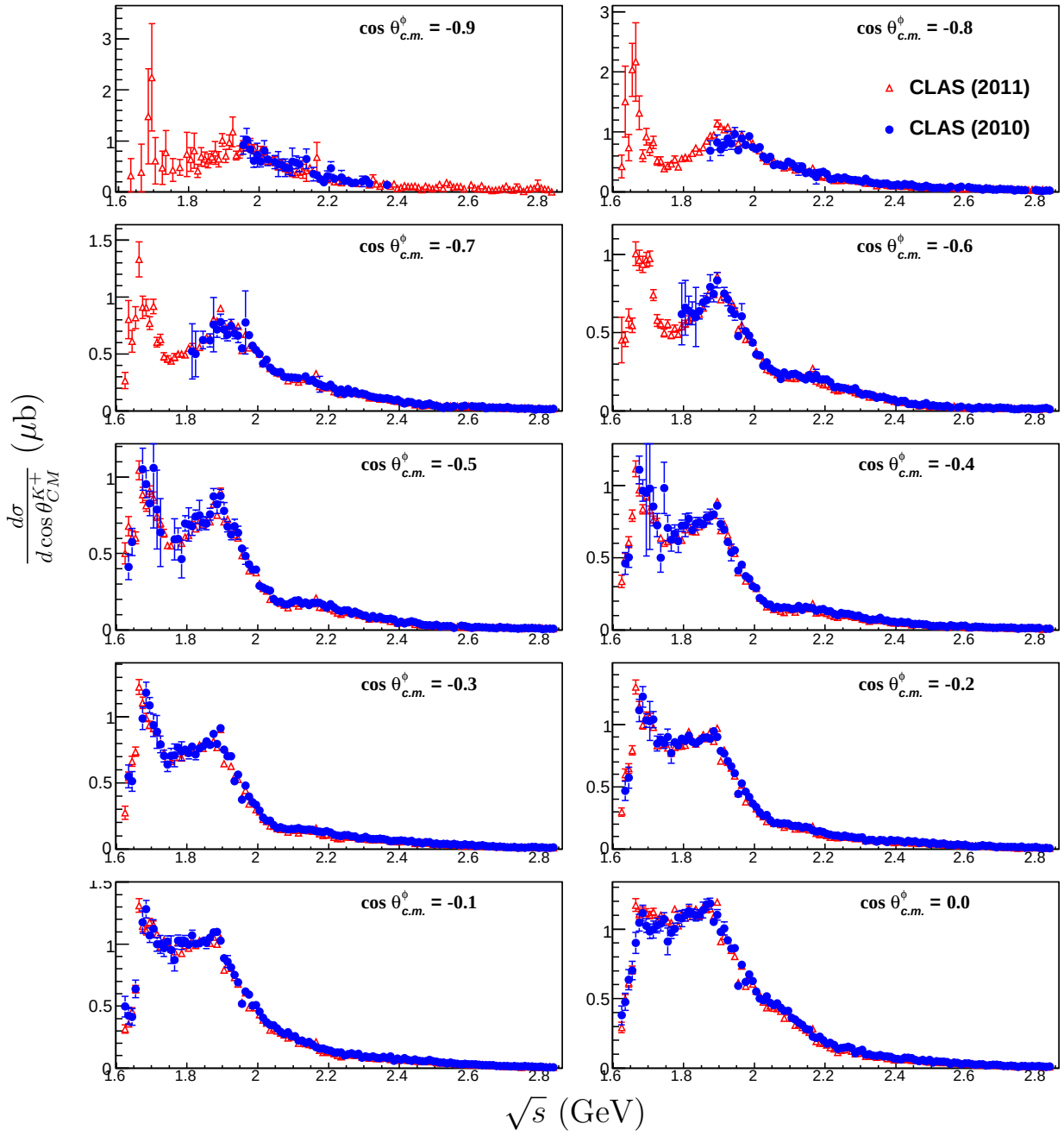

Figure A.1: Extended $\gamma p \rightarrow K^+\Lambda$ differential cross-sections for the two-track $g11a$ dataset as a function of $\sqrt{s}$ in the backward angles. The CLAS (2011) results in red are this work, and the CLAS (2010) are results from the McCracken analysis [19]. All errors shown are statistical.

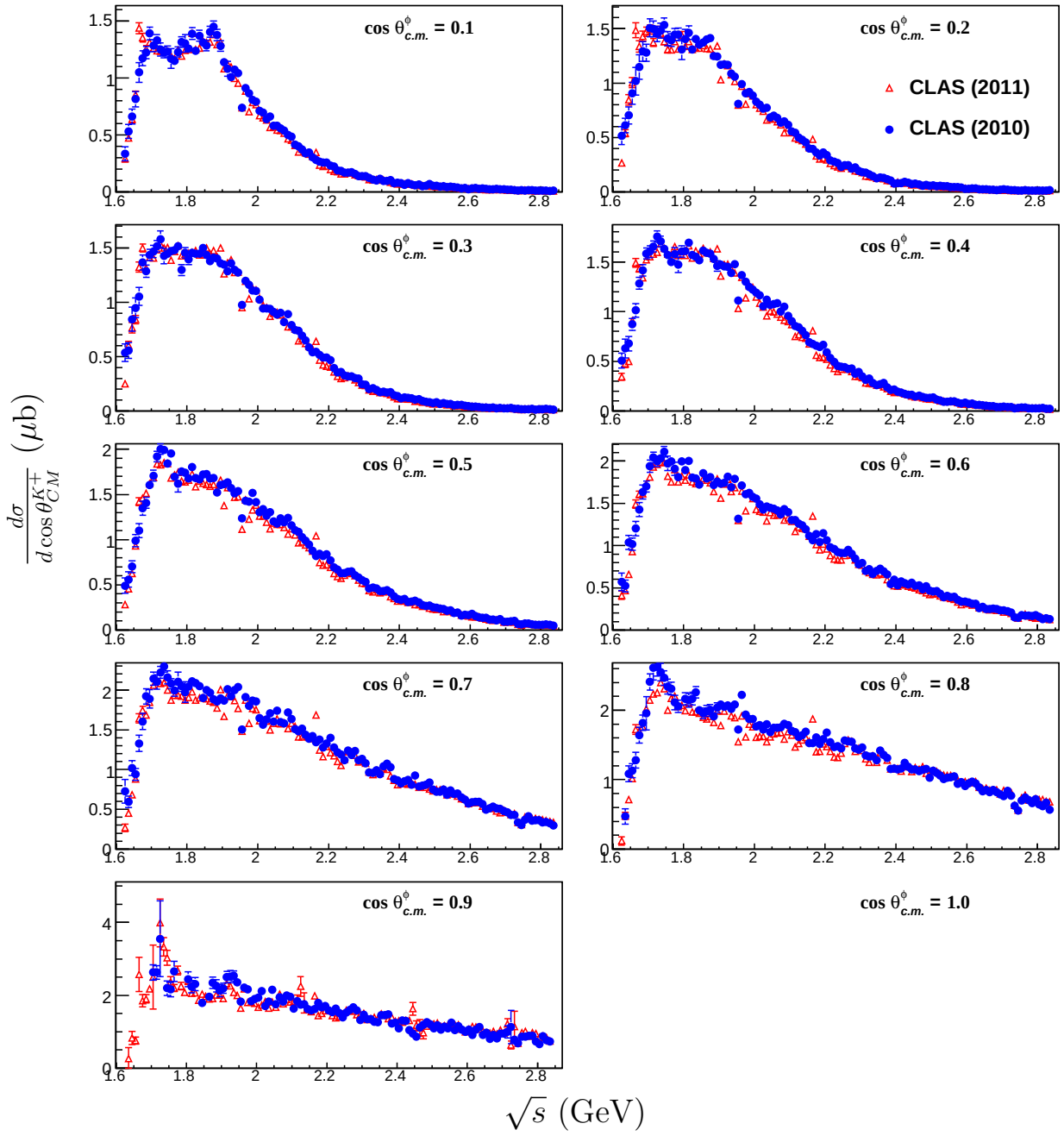

Figure A.2: Extended $\gamma p \rightarrow K^+\Lambda$ differential cross-sections for the two-track $g11a$ dataset as a function of $\sqrt{s}$ in the forward angles. The CLAS (2011) results in red are this work, and the CLAS (2010) are results from the McCracken analysis [19]. All errors shown are statistical.

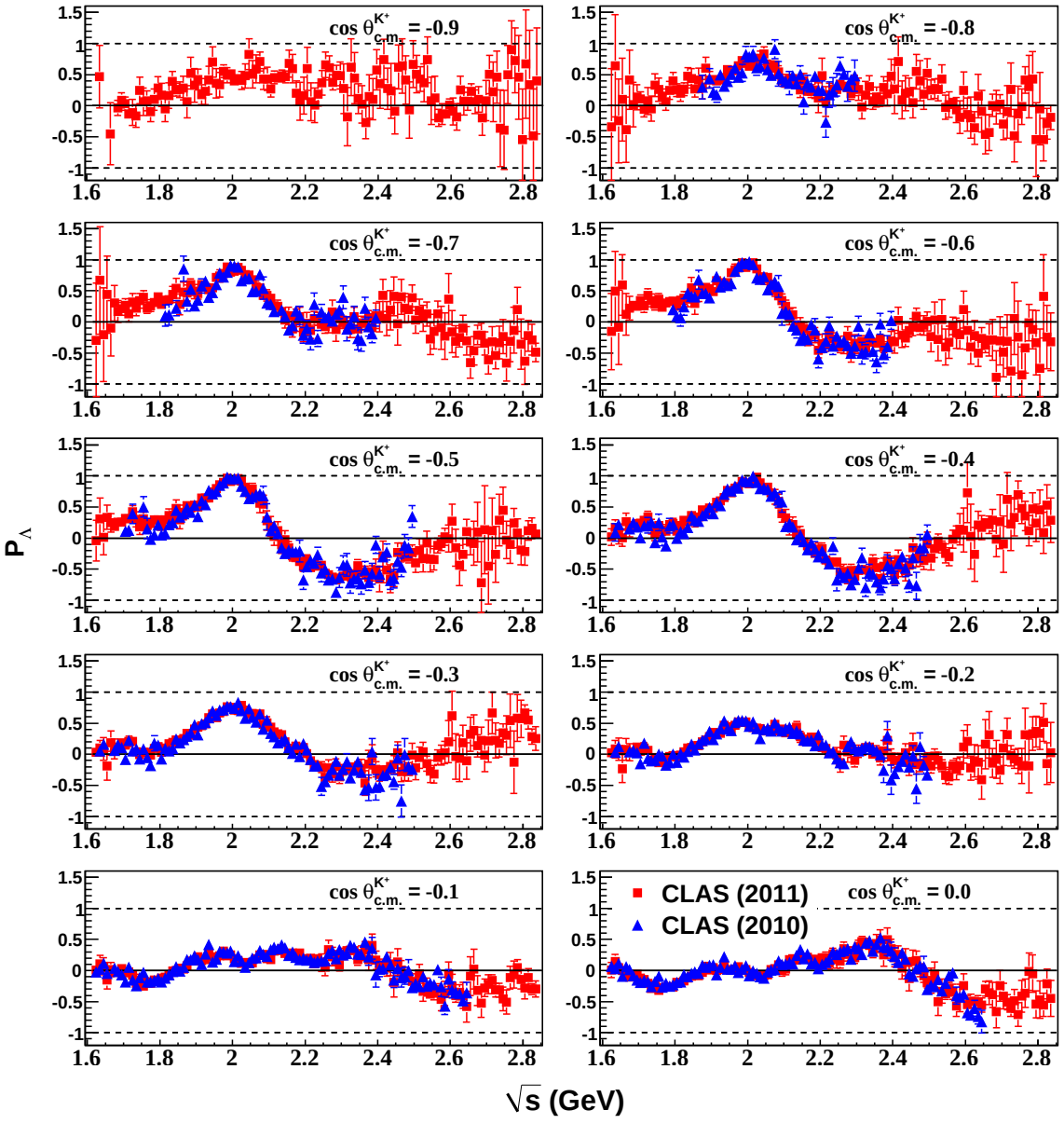

Figure A.3: Extended $\gamma p \to K^+\Lambda$ recoil polarizations for the two-track $g11a$ dataset as a function of $\sqrt{s}$ in the backward angles. The CLAS (2011) results in red are this work, and the CLAS (2010) are results from the McCracken analysis [19]. All errors shown are statistical.

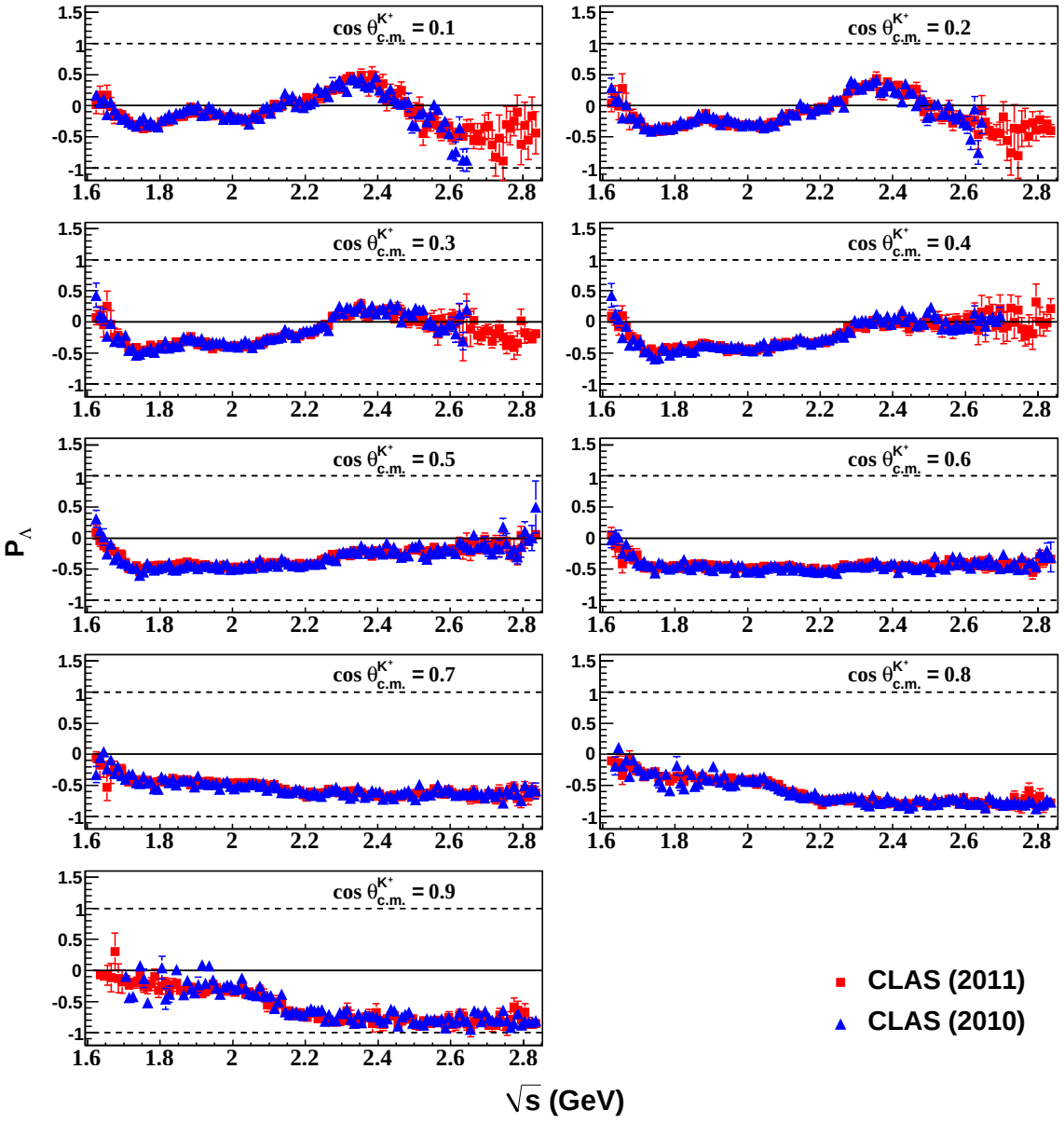

Figure A.4: Extended $\gamma p \to K^+\Lambda$ recoil polarizations for the two-track $g11a$ dataset as a function of $\sqrt{s}$ in the forward angles. The CLAS (2011) results in red are this work, and the CLAS (2010) are results from the McCracken analysis [19]. All errors shown are statistical.